

cy2



# TRANSMISSION OF INFRARED MATERIALS AND CONDENSED GASES AT CRYOGENIC TEMPERATURES

VON KÁRMÁN GAS DYNAMICS FACILITY  
ARNOLD ENGINEERING DEVELOPMENT CENTER  
AIR FORCE SYSTEMS COMMAND  
ARNOLD AIR FORCE STATION, TENNESSEE 37389

September 1977

Final Report for Period July 26, 1973 — June 30, 1975

Approved for public release; distribution unlimited.

PROPERTY OF U.S. AIR FORCE  
AEDC TECHNICAL LIBRARY  
ARNOLD AFB, TN 37389

Prepared for

DIRECTORATE OF TEST ENGINEERING  
DEPUTY FOR OPERATIONS  
ARNOLD ENGINEERING DEVELOPMENT CENTER  
AIR FORCE SYSTEMS COMMAND  
ARNOLD AIR FORCE STATION, TENNESSEE 37389

## NOTICES

When U. S. Government drawings specifications, or other data are used for any purpose other than a definitely related Government procurement operation, the Government thereby incurs no responsibility nor any obligation whatsoever, and the fact that the Government may have formulated, furnished, or in any way supplied the said drawings, specifications, or other data, is not to be regarded by implication or otherwise, or in any manner licensing the holder or any other person or corporation, or conveying any rights or permission to manufacture, use, or sell any patented invention that may in any way be related thereto.

Qualified users, may obtain copies of this report from the Defense Documentation Center.


References to named commercial products in this report are not to be considered in any sense as an endorsement of the product by the United States Air Force or the Government.


This report has been reviewed by the Information Office (OI) and is releasable to the National Technical Information Service (NTIS). At NTIS, it will be available to the general public, including foreign nations.

## APPROVAL STATEMENT

This technical report has been reviewed and is approved for publication.

FOR THE COMMANDER

  
MARION L. LASTER  
Director of Test Engineering  
Deputy for Operations

  
ALAN L. DEVEREAUX  
Colonel, USAF  
Deputy for Operations

# UNCLASSIFIED

REPORT DOCUMENTATION PAGE		READ INSTRUCTIONS BEFORE COMPLETING FORM
1. REPORT NUMBER AEDC-TR-77-71	2. GOVT ACCESSION NO.	3. RECIPIENT'S CATALOG NUMBER
4. TITLE (and Subtitle) TRANSMISSION OF INFRARED MATERIALS AND CONDENSED GASES AT CRYOGENIC TEMPERATURES		5. TYPE OF REPORT & PERIOD COVERED Final Report - July 26, 1973 - June 30, 1975
		6. PERFORMING ORG. REPORT NUMBER
7. AUTHOR(s) J. G. Pipes, J. A. Roux, and A. M. Smith, ARO, Inc. and H. E. Scott, Arnold Engineering Development Center		8. CONTRACT OR GRANT NUMBER(s)
9. PERFORMING ORGANIZATION NAME AND ADDRESS Arnold Engineering Development Center (DO) Air Force Systems Command Arnold Air Force Station, Tennessee 37389		10. PROGRAM ELEMENT, PROJECT, TASK AREA & WORK UNIT NUMBERS Program Element 65807F
11. CONTROLLING OFFICE NAME AND ADDRESS Arnold Engineering Development Center (XRFIS) Air Force Systems Command Arnold Air Force Station, Tennessee 37389		12. REPORT DATE September 1977
		13. NUMBER OF PAGES 289
14. MONITORING AGENCY NAME & ADDRESS (if different from Controlling Office)		15. SECURITY CLASS. (of this report)  UNCLASSIFIED
		15a. DECLASSIFICATION/DOWNGRADING SCHEDULE  N/A
16. DISTRIBUTION STATEMENT (of this Report)  Approved for public release; distribution unlimited.		
17. DISTRIBUTION STATEMENT (of the abstract entered in Block 20, if different from Report)		
18. SUPPLEMENTARY NOTES  Available in DDC		
19. KEY WORDS (Continue on reverse side if necessary and identify by block number)		
infrared radiation infrared transmitting materials wavelengths optical materials	windows cryogenics germanium gases	deposition polystyrene
20. ABSTRACT (Continue on reverse side if necessary and identify by block number)		
<p>An infrared optical transmission chamber was developed to measure the spectral transmission of cryogenically cooled (20°K and 80°K) optical windows, filters, etc., both with and without cryodeposit contamination. An FTS-14 Interferometer Spectrometer recorded transmission measurements for 20 and 80°K germanium windows both clean and with the following contaminants condensed on them: NH<sub>3</sub>, CO<sub>2</sub>, CO, CH<sub>4</sub>, HCl, and air. These measurements were made for many different contaminant<sup>4</sup> thicknesses. From 20 and 80°K data the optical constants (complex</p>		

# UNCLASSIFIED

UNCLASSIFIED

20. ABSTRACT (Continued)

refractive index) for  $\text{NH}_3$  were determined. Further, the transmission measurement of 20 and 80°K polystyrene was recorded and showed that the standard absorption bands observed at 300°K do not shift in wavenumber more than 1  $\text{cm}^{-1}$  when the polystyrene is cooled to 20°K. Hence, polystyrene is a reliable wavelength calibrator when used at 20°K.

UNCLASSIFIED



## PREFACE

The research reported herein was performed by the Arnold Engineering Development Center (AEDC), Air Force Systems Command (AFSC) under Program Element 65807F. Work and analysis for this research was done by personnel of ARO, Inc. (a Sverdrup Corporation Company), operating contractor of AEDC, AFSC, Arnold Air Force Station, Tennessee. The work covered the period from July 26, 1973 to June 30, 1975, and was done under ARO Project Numbers VF469, V35S-61A, and V32S-A5A. The authors of this report were J. G. Pipes, J. A. Roux, and A. M. Smith, of ARO, Inc. and H. E. Scott of Arnold Engineering Development Center. Dr. H. E. Scott was also the Air Force project manager. The manuscript (ARO Control No. ARO-VKF-TR-75-108) was submitted for publication on June 30, 1975.

## CONTENTS

	<u>Page</u>
1.0 INTRODUCTION . . . . .	13
2.0 SCIENTIFIC OBJECTIVES	
2.1 Transmission of Cryocooled Windows . . . . .	14
2.2 Optical Constants of Contaminants . . . . .	16
3.0 EXPERIMENTAL LAYOUT OF IROTC	
3.1 Chamber Layout . . . . .	17
3.2 Prism System: PE-99 . . . . .	21
3.3 Interferometer: Digilab FTS-14 . . . . .	23
4.0 RESULTS AND DISCUSSION	
4.1 Transmission of Germanium at 300, 200, 80 and 20°K . . . . .	24
4.2 Transmission of Polystyrene at 20°K . . . . .	27
4.3 IR Spectra of Solid NH <sub>3</sub> , CO <sub>2</sub> , CO, CH <sub>4</sub> , and HCl Thin Films on 20 and 80°K Germanium Windows . . . . .	30
5.0 OPTICAL CONSTANTS OF CONDENSED GASES . . . . .	37
6.0 CONCLUSIONS AND SUMMARY . . . . .	45
REFERENCES . . . . .	46

## ILLUSTRATIONS

Figure

1. Analytical Model for Transmission Through a Plane- Parallel Slab . . . . .	49
2. Analytical Model for Transmission Through an Interface . . . . .	50
3. Plan View of IROTC Chamber with Perkin-Elmer 99 . . . . .	51
4. Plan and Elevation Views of Cryogenically Cooled Window Holder . . . . .	52
5. Photographs of Cryogenic Holder and Holder Assembly	
a. Cryogenic Holder . . . . .	53
b. Holder Assembly . . . . .	53

<u>Figure</u>	<u>Page</u>
6. Residual Gas Analyzer Scan . . . . .	54
7. Results of Surface Figure Test for a Germanium Window	
a. One Side . . . . .	55
b. Opposite Side . . . . .	55
8. Gas Induction System . . . . .	56
9. Contamination Subcell	
a. Sketch . . . . .	57
b. Photograph . . . . .	58
10. Electron Gun	
a. Assembly . . . . .	59
b. Electronics . . . . .	60
11. Calibration Curves for KBr Prism	
a. Drum Number versus Wavelength . . . . .	61
b. Spectral Resolution versus Slit Width . . . . .	62
12. Plan View Schematic of the Infrared Optical Transmission Chamber with FTS-14 Interferometer . . . . .	63
13. Photograph of FTS-14 Interferometer . . . . .	64
14. Radiation Background Scan for Interferometer . . . . .	65
15. Infrared Transmission of Germanium as a Function of Temperature . . . . .	66
16. Transmission of Germanium Window as a Function of Absorption Coefficient with Thickness as a Parameter . . . . .	67
17. Transmission of an 80°K Germanium Window as a Function of NH <sub>3</sub> Deposit Thickness	
a. $\lambda = 4 \mu\text{m}$ . . . . .	68
b. $\lambda = 5 \mu\text{m}$ . . . . .	68
c. $\lambda = 6 \mu\text{m}$ . . . . .	68
d. $\lambda = 7 \mu\text{m}$ . . . . .	69
e. $\lambda = 8 \mu\text{m}$ . . . . .	69
f. $\lambda = 9.8 \mu\text{m}$ . . . . .	69
18. Transmission of 300°K Germanium Window Measured with PE-99 and FTS-14 . . . . .	70

<u>Figure</u>	<u>Page</u>
19. Transmission of an 80°K, 4-mm-Thick Germanium Window . . . . .	71
20. Correction Percentage ( $C(\sigma)$ ) for FTS-14 80°K Germanium Transmission Data Attributable to Emission Problem . . . . .	72
21. Summary of Transmission Data for 300°K and 80°K Germanium Windows . . . . .	73
22. Transmission of 300°K Polystyrene Sandwiched Between Two 4-mm-Thick NaCl Windows . . . . .	74
23. Transmission of 20°K Polystyrene . . . . .	75
24. 25-cm <sup>-1</sup> /in. Plots of 300°K Polystyrene	
a. 2,800 to 3,200 cm <sup>-1</sup> Region . . . . .	76
b. 1,900 to 2,000 cm <sup>-1</sup> Region . . . . .	77
c. 1,550 to 1,650 cm <sup>-1</sup> Region . . . . .	78
d. 900 to 1,200 cm <sup>-1</sup> Region . . . . .	79
25. 25-cm <sup>-1</sup> /in. Plots of 20°K Polystyrene	
a. 2,800 to 3,200 cm <sup>-1</sup> Region . . . . .	80
b. 1,900 to 2,000 cm <sup>-1</sup> Region . . . . .	81
c. 1,550 to 1,650 cm <sup>-1</sup> Region . . . . .	82
c. 900 to 1,200 cm <sup>-1</sup> Region . . . . .	83
26. Conversion Plot for a 1-cm <sup>-1</sup> Increment in Wavenumber to the Corresponding Increment in Wavelength . . . . .	84
27. Equilibrium Vapor Pressure as a Function of Temperature for Gases Investigated in This Study . . . . .	85
28. Photograph of 5.0-μm-Thick CO <sub>2</sub> Deposit on an 80°K Germanium Window . . . . .	86
29. Transmission of 80°K Germanium Window with Various NH <sub>3</sub> Deposit Thicknesses	
a. 0.111-μm-Thick Deposit . . . . .	87
b. 0.334-μm-Thick Deposit . . . . .	88
c. 0.557-μm-Thick Deposit . . . . .	89
d. 0.780-μm-Thick Deposit . . . . .	90
e. 1.003-μm-Thick Deposit . . . . .	91
f. 1.225-μm-Thick Deposit . . . . .	92
g. 1.449-μm-Thick Deposit . . . . .	93
h. 1.671-μm-Thick Deposit . . . . .	94
i. 1.894-μm-Thick Deposit . . . . .	95

<u>Figure</u>		<u>Page</u>
j.	2.117- $\mu\text{m}$ -Thick Deposit . . . . .	96
k.	2.340- $\mu\text{m}$ -Thick Deposit . . . . .	97
l.	2.562- $\mu\text{m}$ -Thick Deposit . . . . .	98
m.	2.785- $\mu\text{m}$ -Thick Deposit . . . . .	99
n.	3.010- $\mu\text{m}$ -Thick Deposit . . . . .	100
o.	3.231- $\mu\text{m}$ -Thick Deposit . . . . .	101
p.	3.454- $\mu\text{m}$ -Thick Deposit . . . . .	102
q.	3.676- $\mu\text{m}$ -Thick Deposit . . . . .	103
r.	3.990- $\mu\text{m}$ -Thick Deposit . . . . .	104
s.	4.120- $\mu\text{m}$ -Thick Deposit . . . . .	105
t.	4.340- $\mu\text{m}$ -Thick Deposit . . . . .	106
u.	4.570- $\mu\text{m}$ -Thick Deposit . . . . .	107
v.	4.790- $\mu\text{m}$ -Thick Deposit . . . . .	108
w.	5.010- $\mu\text{m}$ -Thick Deposit . . . . .	109
30.	Transmission of 20°K Germanium Window with Various NH <sub>3</sub> Deposit Thicknesses	
a.	0.111- $\mu\text{m}$ -Thick Deposit . . . . .	110
b.	0.334- $\mu\text{m}$ -Thick Deposit . . . . .	111
c.	0.557- $\mu\text{m}$ -Thick Deposit . . . . .	112
d.	0.780- $\mu\text{m}$ -Thick Deposit . . . . .	113
e.	1.003- $\mu\text{m}$ -Thick Deposit . . . . .	114
f.	1.225- $\mu\text{m}$ -Thick Deposit . . . . .	115
g.	1.448- $\mu\text{m}$ -Thick Deposit . . . . .	116
h.	1.671- $\mu\text{m}$ -Thick Deposit . . . . .	117
i.	1.894- $\mu\text{m}$ -Thick Deposit . . . . .	118
j.	2.117- $\mu\text{m}$ -Thick Deposit . . . . .	119
k.	1.80-2.10- $\mu\text{m}$ -Thick Deposit . . . . .	120
31.	Transmission of 80°K Germanium Window with Various CO <sub>2</sub> Deposit Thicknesses	
a.	0.111- $\mu\text{m}$ -Thick Deposit . . . . .	121
b.	0.334- $\mu\text{m}$ -Thick Deposit . . . . .	122
c.	0.446- $\mu\text{m}$ -Thick Deposit . . . . .	123
d.	0.557- $\mu\text{m}$ -Thick Deposit . . . . .	124
e.	0.668- $\mu\text{m}$ -Thick Deposit . . . . .	125
f.	0.780- $\mu\text{m}$ -Thick Deposit . . . . .	126
g.	0.891- $\mu\text{m}$ -Thick Deposit . . . . .	127
h.	1.003- $\mu\text{m}$ -Thick Deposit . . . . .	128
i.	1.114- $\mu\text{m}$ -Thick Deposit . . . . .	129
j.	1.225- $\mu\text{m}$ -Thick Deposit . . . . .	130
k.	1.337- $\mu\text{m}$ -Thick Deposit . . . . .	131
l.	1.448- $\mu\text{m}$ -Thick Deposit . . . . .	132

<u>Figure</u>	<u>Page</u>
m. 1.560- $\mu\text{m}$ -Thick Deposit . . . . .	133
n. 1.670- $\mu\text{m}$ -Thick Deposit . . . . .	134
o. 1.780- $\mu\text{m}$ -Thick Deposit . . . . .	135
p. 1.890- $\mu\text{m}$ -Thick Deposit . . . . .	136
q. 2.000- $\mu\text{m}$ -Thick Deposit . . . . .	137
32. Transmission of 80°K Germanium Window with a 2,000- $\mu\text{m}$ -Thick CO <sub>2</sub> Deposit, Expanded Abscissa Scale	
a. 650-cm <sup>-1</sup> Region . . . . .	138
b. 2,300-cm <sup>-1</sup> Region . . . . .	139
33. Transmission of Germanium Window with a 2.000- $\mu\text{m}$ -Thick CO <sub>2</sub> Deposit after Warming to 100°K and Cooling Back Down to 80°K . . . . .	140
34. Transmission of 20°K Germanium Window with Various CO <sub>2</sub> Deposit Thicknesses	
a. 0.668- $\mu\text{m}$ -Thick Deposit . . . . .	141
b. 1.114- $\mu\text{m}$ -Thick Deposit . . . . .	142
c. 1.890- $\mu\text{m}$ -Thick Deposit . . . . .	143
d. 2.560- $\mu\text{m}$ -Thick Deposit . . . . .	144
35. Transmission of Germanium Window with a CO <sub>2</sub> Deposit after Warming	
a. From 20°K to 50°K . . . . .	145
b. From 20°K to 100°K . . . . .	146
36. Transmission of 20°K Germanium Window with Various CO Deposit Thicknesses	
a. 0.130- $\mu\text{m}$ -Thick Deposit . . . . .	147
b. 0.390- $\mu\text{m}$ -Thick Deposit . . . . .	148
c. 0.648- $\mu\text{m}$ -Thick Deposit . . . . .	149
d. 0.908- $\mu\text{m}$ -Thick Deposit . . . . .	150
e. 1.167- $\mu\text{m}$ -Thick Deposit . . . . .	151
37. Transmission of 20°K Germanium Window with Various CO Deposit Thicknesses	
a. 1.167- $\mu\text{m}$ -Thick Deposit (Expanded Abscissa Scale in 2,200-cm <sup>-1</sup> Region) . . . . .	152
b. 1.426- $\mu\text{m}$ -Thick Deposit . . . . .	153
c. 1.686- $\mu\text{m}$ -Thick Deposit . . . . .	154
d. 1.945- $\mu\text{m}$ -Thick Deposit . . . . .	155
e. 1.945- $\mu\text{m}$ -Thick Deposit (Expanded Abscissa Scale in 2,200-cm <sup>-1</sup> Region) . . . . .	156

<u>Figure</u>	<u>Page</u>
f. 2.204- $\mu\text{m}$ -Thick Deposit . . . . .	157
g. 2.464- $\mu\text{m}$ -Thick Deposit . . . . .	158
h. 2.723- $\mu\text{m}$ -Thick Deposit . . . . .	159
i. 2.982- $\mu\text{m}$ -Thick Deposit . . . . .	160
j. 2.982- $\mu\text{m}$ -Thick Deposit (Expanded Abscissa Scale in 2,200- $\text{cm}^{-1}$ Region) . . . . .	161
k. 3.242- $\mu\text{m}$ -Thick Deposit . . . . .	162
l. 3.501- $\mu\text{m}$ -Thick Deposit . . . . .	163
m. 3.760- $\mu\text{m}$ -Thick Deposit . . . . .	164
n. 4.020- $\mu\text{m}$ -Thick Deposit . . . . .	165
o. 4.280- $\mu\text{m}$ -Thick Deposit . . . . .	166
p. 4.538- $\mu\text{m}$ -Thick Deposit . . . . .	167
q. 4.798- $\mu\text{m}$ -Thick Deposit . . . . .	168
r. 5.057- $\mu\text{m}$ -Thick Deposit . . . . .	169
s. 5.316- $\mu\text{m}$ -Thick Deposit . . . . .	170
t. 5.576- $\mu\text{m}$ -Thick Deposit . . . . .	171
u. 5.835- $\mu\text{m}$ -Thick Deposit . . . . .	172
v. 6.095- $\mu\text{m}$ -Thick Deposit . . . . .	173
w. 6.354- $\mu\text{m}$ -Thick Deposit . . . . .	174
38. Transmission of Germanium Window with a 15- $\mu\text{m}$ -Thick CO Deposit after Warming from 20°K to 40°K . . . . .	175
39. Transmission of 20°K Germanium Window with Various CH <sub>4</sub> Deposit Thicknesses	
a. 0.114- $\mu\text{m}$ -Thick Deposit . . . . .	176
b. 0.229- $\mu\text{m}$ -Thick Deposit . . . . .	177
c. 0.344- $\mu\text{m}$ -Thick Deposit . . . . .	178
d. 0.458- $\mu\text{m}$ -Thick Deposit . . . . .	179
e. 0.573- $\mu\text{m}$ -Thick Deposit . . . . .	180
f. 0.688- $\mu\text{m}$ -Thick Deposit . . . . .	181
g. 0.802- $\mu\text{m}$ -Thick Deposit . . . . .	182
h. 0.917- $\mu\text{m}$ -Thick Deposit . . . . .	183
i. 1.030- $\mu\text{m}$ -Thick Deposit . . . . .	184
j. 1.150- $\mu\text{m}$ -Thick Deposit . . . . .	185
k. 1.260- $\mu\text{m}$ -Thick Deposit . . . . .	186
l. 2.290- $\mu\text{m}$ -Thick Deposit . . . . .	187
m. 3.44- $\mu\text{m}$ -Thick Deposit . . . . .	188
n. 4.127- $\mu\text{m}$ -Thick Deposit . . . . .	189
o. 4.580- $\mu\text{m}$ -Thick Deposit . . . . .	190
p. 5.040- $\mu\text{m}$ -Thick Deposit . . . . .	191
q. 5.500- $\mu\text{m}$ -Thick Deposit . . . . .	192

<u>Figure</u>	<u>Page</u>
r. 5.960- $\mu\text{m}$ -Thick Deposit . . . . .	193
s. 6.420- $\mu\text{m}$ -Thick Deposit . . . . .	194
t. 6.880- $\mu\text{m}$ -Thick Deposit . . . . .	195
u. 8.710- $\mu\text{m}$ -Thick Deposit . . . . .	196
v. After Warming from 20°K to 50°K . . . . .	197
w. Just Before CH <sub>4</sub> Evaporated . . . . .	198
x. After CH <sub>4</sub> Deposit Had Completely Evaporated . . . . .	199
40. Transmission of 20°K Germanium Window with an HCl Deposit (See Table 5)	
a. First Interference Minimum . . . . .	200
b. Second Interference Minimum . . . . .	201
c. Third Interference Minimum . . . . .	202
41. Transmission of 300°K HCl, 95-cm Path Length . . . . .	203
42. Transmission of 20°K Germanium Window with an Air Cryodeposit	
a. 1-min Deposition Time . . . . .	204
b. 3-min Deposition Time . . . . .	205
43. Geometry Depicting Analytical Model for a Thin Film Formed Upon a Thick Film . . . . .	206
44. Comparison of Theory and Transmission Data for NH <sub>3</sub> Deposits on 80°K Germanium	
a. $\lambda = 15.873 \mu\text{m}$ . . . . .	207
b. $\lambda = 15.625 \mu\text{m}$ . . . . .	207
c. $\lambda = 14.286 \mu\text{m}$ . . . . .	208
d. $\lambda = 13.889 \mu\text{m}$ . . . . .	208
e. $\lambda = 13.514 \mu\text{m}$ . . . . .	209
f. $\lambda = 12.821 \mu\text{m}$ . . . . .	209
g. $\lambda = 12.500 \mu\text{m}$ . . . . .	210
h. $\lambda = 11.364 \mu\text{m}$ . . . . .	210
i. $\lambda = 10.989 \mu\text{m}$ . . . . .	211
j. $\lambda = 10.417 \mu\text{m}$ . . . . .	211
k. $\lambda = 10.101 \mu\text{m}$ . . . . .	212
l. $\lambda = 9.615 \mu\text{m}$ . . . . .	212
m. $\lambda = 9.524 \mu\text{m}$ . . . . .	213
n. $\lambda = 9.434 \mu\text{m}$ . . . . .	213
o. $\lambda = 9.346 \mu\text{m}$ . . . . .	214
p. $\lambda = 9.259 \mu\text{m}$ . . . . .	214
q. $\lambda = 8.772 \mu\text{m}$ . . . . .	215
r. $\lambda = 8.696 \mu\text{m}$ . . . . .	215



<u>Figure</u>	<u>Page</u>
s. $\lambda = 8.621 \mu\text{m}$ . . . . .	216
t. $\lambda = 7.812 \mu\text{m}$ . . . . .	216
u. $\lambda = 7.519 \mu\text{m}$ . . . . .	217
v. $\lambda = 6.250 \mu\text{m}$ . . . . .	217
w. $\lambda = 6.024 \mu\text{m}$ . . . . .	218
x. $\lambda = 5.780 \mu\text{m}$ . . . . .	218
y. $\lambda = 3.584 \mu\text{m}$ . . . . .	219
z. $\lambda = 3.135 \mu\text{m}$ . . . . .	219
aa. $\lambda = 3.003 \mu\text{m}$ . . . . .	220
bb. $\lambda = 2.994 \mu\text{m}$ . . . . .	220
cc. $\lambda = 2.967 \mu\text{m}$ . . . . .	221
dd. $\lambda = 2.924 \mu\text{m}$ . . . . .	221
ee. $\lambda = 2.710 \mu\text{m}$ . . . . .	222
45. Complex Refractive Index for $\text{NH}_3$ on $80^\circ\text{K}$ Germanium	
a. Real Component . . . . .	223
b. Imaginary Component . . . . .	224
46. Comparison of Theory and Transmission Data for $\text{NH}_3$ on $20^\circ\text{K}$ Germanium	
a. $\lambda = 14.085 \mu\text{m}$ . . . . .	225
b. $\lambda = 13.514 \mu\text{m}$ . . . . .	225
c. $\lambda = 11.628 \mu\text{m}$ . . . . .	226
d. $\lambda = 11.364 \mu\text{m}$ . . . . .	226
e. $\lambda = 10.870 \mu\text{m}$ . . . . .	227
f. $\lambda = 10.753 \mu\text{m}$ . . . . .	227
g. $\lambda = 10.000 \mu\text{m}$ . . . . .	228
h. $\lambda = 9.709 \mu\text{m}$ . . . . .	228
i. $\lambda = 9.615 \mu\text{m}$ . . . . .	229
j. $\lambda = 9.524 \mu\text{m}$ . . . . .	229
k. $\lambda = 9.434 \mu\text{m}$ . . . . .	230
l. $\lambda = 9.346 \mu\text{m}$ . . . . .	230
m. $\lambda = 9.259 \mu\text{m}$ . . . . .	231
n. $\lambda = 9.174 \mu\text{m}$ . . . . .	231
o. $\lambda = 9.091 \mu\text{m}$ . . . . .	232
p. $\lambda = 9.009 \mu\text{m}$ . . . . .	232
q. $\lambda = 8.929 \mu\text{m}$ . . . . .	233
r. $\lambda = 8.850 \mu\text{m}$ . . . . .	233
s. $\lambda = 8.772 \mu\text{m}$ . . . . .	234
t. $\lambda = 8.696 \mu\text{m}$ . . . . .	234
u. $\lambda = 8.621 \mu\text{m}$ . . . . .	235
v. $\lambda = 8.547 \mu\text{m}$ . . . . .	235
w. $\lambda = 8.475 \mu\text{m}$ . . . . .	236

<u>Figure</u>	<u>Page</u>
x. $\lambda = 7.194 \mu\text{m}$ . . . . .	236
y. $\lambda = 6.211 \mu\text{m}$ . . . . .	237
z. $\lambda = 6.135 \mu\text{m}$ . . . . .	237
aa. $\lambda = 6.061 \mu\text{m}$ . . . . .	238
bb. $\lambda = 5.952 \mu\text{m}$ . . . . .	238
cc. $\lambda = 5.650 \mu\text{m}$ . . . . .	239
dd. $\lambda = 5.494 \mu\text{m}$ . . . . .	239
ee. $\lambda = 5.102 \mu\text{m}$ . . . . .	240
ff. $\lambda = 4.739 \mu\text{m}$ . . . . .	240
gg. $\lambda = 4.464 \mu\text{m}$ . . . . .	241
hh. $\lambda = 4.273 \mu\text{m}$ . . . . .	241
ii. $\lambda = 4.098 \mu\text{m}$ . . . . .	242
jj. $\lambda = 3.584 \mu\text{m}$ . . . . .	242
kk. $\lambda = 3.106 \mu\text{m}$ . . . . .	243
ll. $\lambda = 2.985 \mu\text{m}$ . . . . .	243
mm. $\lambda = 2.967 \mu\text{m}$ . . . . .	244
nn. $\lambda = 2.941 \mu\text{m}$ . . . . .	244
oo. $\lambda = 2.865 \mu\text{m}$ . . . . .	245
pp. $\lambda = 2.786 \mu\text{m}$ . . . . .	245
47. Complex Refractive Index for $\text{NH}_3$ on $20^\circ\text{K}$ Germanium	
a. Real Component . . . . .	246
b. Imaginary Component . . . . .	247

## TABLES

1. Growth Conditions for Solid Gases Studied . . . . .	248
2. Transmission of Germanium as a Function of Temperature . . . . .	249
3. Transmission Measurements of $80^\circ\text{K}$ Germanium Using PE-99 and Correction Factor C for FTS-14 . . . . .	250
4. Summary of Band Center Frequencies for $300^\circ\text{K}$ and $20^\circ\text{K}$ Polystyrene . . . . .	251
5. Summary of Film Thicknesses, Gas Species, and Substrate Temperature for Plots Given in Figs. 29 through 42 . . . . .	253

	<u>Page</u>
6. Molecular Band of 20°K and 80°K Solid NH <sub>3</sub> . . . . .	255
7. Complex Refractive Index ( $\bar{n} = n - ik$ ) for NH <sub>3</sub> on 80°K Germanium . . . . .	256
8. Complex Refractive Index ( $\bar{n} = n - ik$ ) for NH <sub>3</sub> on 20°K Germanium . . . . .	267

**APPENDIXES**

A. $\Delta n_g / \Delta t$ OF GERMANIUM AT 10.6 $\mu m$ . . . . .	277
B. REFLECTANCE OF 77°K NH <sub>3</sub> FROSTS BETWEEN 0.5 AND 3.0 $\mu m$ . . . . .	283
C. NOTES ON NONCUBIC NH <sub>3</sub> . . . . .	286

## 1.0 INTRODUCTION

To provide an environment in which the effects of infrared (IR) radiation can be studied experimentally, as in several of the AEDC space simulation chambers, the walls that enclose this environment as well as all components within it must be cryogenically cooled. Of course this requirement is a direct result of the Stefan-Boltzmann law -- blackbodies emit thermal radiation in proportion to the fourth power of absolute temperature (Ref. 1). The only other means of controlling the radiant emittance of a surface is to reduce the emissivity, a technique that is quite limited. Elements within a space chamber usually include a target which consists of various optical components. Until recently the effects of cryogenically cooling optical components were not well documented and available data are generally for the effects of cryocooling reflection optics (Ref. 2).

The objective of this research was to characterize the effects of cryogenic temperatures and associated cryodeposit contamination on the infrared spectral transmission by optical materials. Specific goals were to obtain the IR transmittance of cryogenically cooled optical components such as windows and interference filters and to study the spectral transmission of these same components after being contaminated with condensed gases. Such information is required not only in the development of space simulation chambers but also in the prediction and control of spacecraft contamination. Other useful results include the optical properties of materials at very low temperatures and the degradation of special coatings (e.g., thermal control, solar cell, etc.) attributable to cryodeposit contamination.

The investigation was performed in a cryogenic cell that had been employed previously for ultrahigh-vacuum studies and therefore required only modest modifications. This research cell has been designated the infrared optical transmission chamber (IROTC).

This report documents the development of the IROTC hardware and the infrared transmission data for a cryogenically cooled germanium (Ge) window both clean and with condensed gas contamination in the form of thin solid films of ammonia ( $\text{NH}_3$ ), carbon dioxide ( $\text{CO}_2$ ), carbon monoxide ( $\text{CO}$ ), methane ( $\text{CH}_4$ ), and hydrogen chloride ( $\text{HCl}$ ). Spectra of 300 and 20°K polystyrene are also presented. The data were recorded with two different spectrometers: a Perkin-Elmer Model 99 double-pass prism monochromator and a Digilab FTS-14<sup>®</sup>

Michelson interferometer. These two experimental arrangements are discussed in Section 3.0. Most of the transmittance data were obtained with the interferometer system which includes a dedicated minicomputer for processing and displaying the spectra; the interferometer was configured to cover the spectral range from 400 to  $3960\text{ cm}^{-1}$  (25 to  $2.5\text{ }\mu\text{m}$ ). In contrast, the data acquired with the PE-99 system required manual reduction to obtain only low resolution spectra. Nevertheless, important transmission data were obtained with each system. Other experiments performed in areas closely related to the primary subject matter are described in Appendices A, B, and C.

## 2.0 SCIENTIFIC OBJECTIVES

### 2.1 TRANSMISSION OF CRYOCOOLED WINDOWS

A review of the formalism for the transmission of electromagnetic energy through a homogeneous plane parallel slab of dielectric or conductive material is presented for completeness, for guidelines in design of hardware, and because published literature is often inconsistent in the choice of nomenclature. The measurement made in the IROTC was the ratio of energy emerging normal to the face of a slab of material to the energy incident normally on the opposite face. Figure 1 depicts schematically a conductive slab of material normally illuminated and also the light rays involved in measuring the transmission of the slab. The ratio of total emerging energy to total incident energy is termed the "total external transmittance" or simply the "transmission" of the window. This quantity is distinguished from the internal transmittance, which is defined as the ratio of the energy reaching the back interface of the slab to the energy leaving the front interface. The internal transmittance does not include the Fresnel reflection losses and multiple internal reflections. In contrast, transmission accounts for all such losses and reflections. For the general case of a conductive material, or one having both real and imaginary index of refraction components, the transmission can be analytically derived by tracing an incident light ray through the slab while summing the Fresnel reflection and absorption losses which occur during each multiple reflection. For a slab of thickness  $D$  the resulting transmission is given by the expression (see Fig. 1.)

$$T = \tau^2 e^{-\alpha_2 D} [1 + \rho^2 e^{-2\alpha_2 D} + \rho^4 e^{-4\alpha_2 D} + \rho^6 e^{-6\alpha_2 D} + \dots] \quad (1)$$

or

$$T = \frac{\tau^2 e^{-\alpha_2 D}}{1 - \rho^2 e^{-2\alpha_2 D}} = \frac{(1 - \rho)^2 e^{-\alpha_2 D}}{1 - \rho^2 e^{-2\alpha_2 D}} \quad (2)$$

where  $\rho$  is the Fresnel "intensity" reflection at a refractive boundary (see Fig. 2 for illustrations of pure Fresnel reflections for normal incidence);  $\tau = 1 - \rho$ ;  $\alpha_2 = \frac{4\pi k_2}{\lambda}$  where  $k_2$  is the absorption or the imaginary part of the refractive index and thus does not include extinction in the form of scattering; and  $D$  is the absolute thickness of the slab. In the case of germanium, for example, at a wavelength of  $\lambda = 10.0 \mu\text{m}$ , where

$$n_2(\text{real}) = n_g = 4.00 \text{ (Ref. 3) and } \alpha_2 = \alpha_g = 0 \quad (3)$$

$$\rho = \left( \frac{n_2 - 1}{n_2 + 1} \right)^2 = \left( \frac{3}{5} \right)^2 = 0.360 \quad (4)$$

and

$$T = \frac{(0.64)^2}{1 - (0.36)^2} = 0.47058 \quad (5)$$

Equation (2) can be further simplified if the window is a dielectric or  $k_2 = 0$  ( $\alpha_2 = 0$ ) and  $\rho = [(n_2 - 1)/(n_2 + 1)]^2$ . Substitution for  $\rho$  yields the expression

$$T = \frac{2n_2}{n_2^2 + 1} \quad (6)$$

and for  $n_2 = 4.00$ ,  $T = 0.47058$ .

Thus a germanium window has a transmission of 0.47 at  $10 \mu\text{m}$ , or more than half the incident energy is reflected. For Eqs. (2) and (6) to be realized experimentally it is evident that the slab must be illuminated normally or not more than five degrees off normal, that

scattering at interfaces and grain boundaries must be negligible, and that no coherent phase relation can exist between multiple reflected rays. If a coherent phase relation were maintained, the slab would be treated analytically as a thin film where  $n_2 D < 2.5 \lambda$ ; thick and thin films are discussed in Ref. 4. Later in this report an analytical model for the transmission of a cryocooled window (thick film) having a thin cryodeposit film on one side is presented. This model enables one to obtain the complex refractive index,  $\bar{n} = n - ik$ , of the cryodeposit from the transmission measurements of a contaminated window.

The accuracy of a normal incidence transmission measurement depends upon an accumulative error associated with such problem areas as source stability, uniformity in radiant sensitivity of detector, stray radiation, optical tolerance of sample, degree of monochromaticity of transmitted beam, electronics and detector linearity. The IROTC was designed for samples whose transmission is between 100 and 1 percent. (For transmission below 1 percent the apparatus becomes rather complex. See Refs. 5 and 6 for discussions of high accuracy room temperature spectrophotometers.) This limited dynamic range was acceptable because the added complexity of cryogenically cooled samples was the primary goal. Since, in some cases, the problems associated with operation were different for the prism and interferometer systems, they are discussed separately in Section 3.0 where the experimental apparatus is described. However, the evaluation of transmission accuracy was not done by determining the error of each subsystem but rather from comparing transmission values taken in the IROTC of a sample of known transmission. An uncoated germanium window was selected as a known sample for the following reasons: (1) the transmission of germanium is well known at 300°K and data were available for 80°K germanium from D. L. Stierwalt, Naval Electronics Laboratory, San Diego, CA; (2) the transmission of germanium is a constant 47 percent over most of the wavelength range of the IROTC; and (3) germanium is a semiconductor of high refractive index and reasonable thermal conductivity, making it an ideal cryodeposit substrate. The resulting transmission accuracy is given for the prism and interferometer systems in Section 3.0.

## 2.2 OPTICAL CONSTANTS OF CONTAMINANTS

A second goal in the development of the IROTC was to devise a means by which the IR optical constants of contaminants could be

obtained experimentally. The optical constants referred to here are the real refractive index,  $n$ , and the imaginary refractive index,  $k$ , which are functions of wavelength and combined give the complex refractive index,  $\bar{n} = n - ik$ . The Lambertian absorption coefficient,  $\alpha$ , is related to  $k$  by the relation

$$\alpha(\lambda) = \frac{4\pi k(\lambda)}{\lambda} \quad (7)$$

The requirement for optical properties of condensed gases, especially rocket exhaust plume species, is directly related to the need to predict and control the contamination of cryogenically cooled optics and thermal control surfaces on spacecraft. It should also be noted that optical constants of condensed gases are needed for preparation of upper atmospheric models of the Jovian planets. If the optical constants of the contaminant are known, the effects of contamination can be predicted. Since the IROTC was designed to measure the transmission of cryocooled windows, it was a simple matter to extend the capability to the transmission of cryocooled windows with thin films of condensed gases of known thickness. The optical properties of the substrate (germanium) were known, and the optical constants of the contaminant were determined through comparison with an analytical model. This second objective was implemented by depositing  $\text{NH}_3$ ,  $\text{CO}_2$ ,  $\text{CO}$ ,  $\text{CH}_4$ , and  $\text{HCl}$  at  $20^\circ\text{K}$ , and in some cases  $80^\circ\text{K}$ , onto the germanium window to various thicknesses and measuring the infrared transmission of the window plus thin film. For  $80$  and  $20^\circ\text{K}$  solid  $\text{NH}_3$  the optical constants were extracted from the transmission data. Complete details of the technique are provided in Section 5.0.

### 3.0 EXPERIMENTAL LAYOUT OF IROTC

#### 3.1 CHAMBER LAYOUT

The IROTC was constructed by modifying a chamber previously employed for ultrahigh-vacuum research. The chamber is an all-stainless-steel cell 28 in. (71 cm) in diameter by 33-1/2 in. (85 cm) in height. The centerline of the cell is 47 in. (119 cm) above the floor. In order to make transmission measurements six 6-in. (15.2-cm)-high vacuum CONFLAT® ports were added midway on the cell as shown in Fig. 3. The two ports flanking the IR beam entrance port in Fig. 3 are located at an angle of 23 deg from the



centerline of the IR beam. A liquid nitrogen (LN<sub>2</sub>) liner within the cell provides an efficient means of cryopumping residual water (H<sub>2</sub>O) and CO<sub>2</sub>, thus preventing uncontrolled contamination of the 80°K IR window. The liner also provides a cold radiative background. With the liner in the IROTC the work space is a cylindrical volume that is 23 in. (58.4 cm) in diameter by 22 in. (56 cm) in height. An oil diffusion pump is used to pump the chamber to 10<sup>-7</sup> torr, and when the LN<sub>2</sub> liner is activated the chamber pressure falls to a minimum of 10<sup>-8</sup> torr. If 20°K gaseous helium (GHe) is used to cool the sample, the sample holder (see Figs. 4 and 5) cryopumps to some extent and reduces the chamber pressure even further to near 1 x 10<sup>-9</sup> torr.

To verify that condensed gases were not migrating from the LN<sub>2</sub> liner to the 20°K germanium substrate, a helium-neon laser beam was reflected off the 20°K substrate, and the reflector energy was monitored for several hours. No interference pattern was observed in the reflected beam, as would be if the substrate cryopumped significant deposits.

For contamination studies performed in the IROTC, it is important that the cell be as clean as possible. The IROTC was therefore baked out at 300°F for several days with the LN<sub>2</sub> liner warm in order to clean the chamber walls. Further, the cryogenically cooled optical component holder (see Fig. 4) was assembled in the AEDC-VKF class 10,000 clean room. The residual gas analyzer scan shown in Fig. 6 was taken just before IR transmission measurements were started. It is clear that no oils in the heavy AMU range were present and only the typical residual gases, H<sub>2</sub>O, CO, NH<sub>3</sub>, hydroxyl gas molecule (OH), etc., were present. The bulk of the residual was H<sub>2</sub>O which is pumped on the LN<sub>2</sub> liner when it is cooled. Using DC 705 diffusion pump oil and a Mexican cold cap in the diffusion pump were key factors minimizing backstreaming. In fact, the IROTC is a very clean vacuum chamber and quite adequate for cryodeposit contamination research.

As noted in Section 2.1, two germanium windows, purchased from a commercial manufacturer, served as test IR windows. Specifications for the germanium windows are listed below:

Dimensions: 70 mm x 70 mm x 4 mm

Material: intrinsic germanium, specific resistivity  $\geq$  40 ohm-cm

Surface Figure: 1/4 wave of Hg; 5,461 Å

Surface Quality: 40-20 (scratch-dig)

Wedge:  $\pm 5$  arc minutes

Coating: None

Aperture: 80% of full dimension

Upon delivery the germanium windows were checked for surface figure and thickness tolerance. They could not be accurately checked for wedge tolerance or resistivity. The result of the surface figure test is shown in Fig. 7 for the best window delivered. The second window was almost too poor in quality to be useful. The fringes seen in Fig. 7 are fringes of equal thickness or Fizeau fringes formed by placing the germanium window on a standard master flat ( $\lambda/100$ ) and illuminating it with monochromatic light. If the germanium window were perfectly flat, a dark (or light) fringe would run straight across the window and all fringes would be parallel. One side of the germanium window, Fig. 7a, was clearly of good quality, so it was employed as the cryodeposit substrate. On the reverse side the central portion of the window was reasonably flat. The thickness was measured, and the results are noted in Fig. 7b. If the thickest value and thinnest value are used to compute a worst-case wedge value, the result is approximately 20 arc sec, a value well within the specification. The value of specific resistivity, an indicator of purity, could not be checked. However, if some impurities, usually carbon, were present in the germanium, they would have been detected in the form of long wavelength absorption bands when the window was cooled to 20°K (Ref. 7). No such absorptions were found in the IR spectrum of the 20°K germanium window.

The system employed to deposit various gases onto the cryocooled germanium window is shown schematically in Fig. 8. The baffle on the back side of the window holder that extends from the rear CONFLAT prevents gas from cryodepositing on the backside of the germanium window. The flow rate is controlled by an MKS Baratron® pressure readout. In most cases the inlet pressure was kept below 500 millitorr (mtorr) which resulted in a chamber background pressure of not more than  $1 \times 10^{-6}$  torr, as measured by an ionization gage located on the lid of the IROTC. An ideal cryodeposit formation exhibits uniform thickness and clarity; that is, it does not have a cloudy or polycrystalline appearance when observed in visible light. There are several deposition factors that affect the structure of the thin film of condensed gas. Some are more fully understood than others, and each new experiment with thin film cryodeposits leaves some unexplained observations. With the arrangement shown in Fig. 8 a thin

film deposit could be formed successfully with all the gases and conditions employed except 80°K CO<sub>2</sub> which always exhibited a cloudy appearance. Results for each gas are discussed in Section 4.0; however, it is noted that the gas deposition arrangement of the IROTC is somewhere between a completely diffuse deposition (Ref. 8) and a molecular-beam-type deposition (Ref. 2), and that it is best described as multiple free-jet expansions into a vacuum.

One of the important parameters required to obtain the optical constants of a thin film cryodeposit is the absolute thickness of the cryodeposit. The technique used here to measure cryodeposit thickness is one that is becoming quite popular because of its simplicity. At least two monochromatic collimated light beams (usually a He-Ne laser is used) are reflected off the cryodeposit substrate and the reflected energy is monitored with a photodetector. As the gas is deposited onto the substrate, a thin film interference pattern is observed for each beam with the periodicity depending on the angle of incidence. Provided the two angles of incidence are known to an accuracy of 0.25 deg or better, and the mass deposition rate is a constant, a real refractive index value for the cryodeposit can be computed from the expression

$$n = \frac{[\sin^2 v_2 - \beta^2 \sin^2 v_1]^{\frac{1}{2}}}{1 - \beta^2} \quad (8)$$

where  $\beta = \Delta t_1 / \Delta t_2$  and the  $\Delta t_i$ 's are the periods of the two interference patterns, and  $v_1$  and  $v_2$  are the angles of incidence. Equation (8) is also valid for a conductive substrate; therefore this technique can be used for metal as well as dielectric substrates. In the IROTC it was not feasible to measure  $v_1$  and  $v_2$  to an accuracy of 0.25 deg; therefore, a calibration was performed using H<sub>2</sub>O and CO<sub>2</sub> deposits at 80°K. The known values of  $n$  for H<sub>2</sub>O and CO<sub>2</sub> at the 0.6328- $\mu$ m He-Ne laser line were those of Ref. 8 and those provided by W.

Viehman, NASA Goddard Space Flight Center, Greenbelt, MD. This same laser interference scheme was also used in Ref. 2 for determining the refractive indices of H<sub>2</sub>O, CO<sub>2</sub>, NH<sub>3</sub>, N<sub>2</sub>, and O<sub>2</sub>. Table 1 is a summary of indices for solid gases at 0.6328  $\mu$ m, taken from Refs. 2 and 8, Mr. Viehman, and this work. Since one angle  $v_1$  in the IROTC arrangement is near zero,  $v_1 \cong 2$  deg, errors in  $v_1$  do not affect Eq. (3) significantly. The value of  $v_2$  can then be determined from Eq. (8) by measuring  $\beta$ ,  $v_1$ , and using the indices from Ref. 8 and Mr. Viehman for CO<sub>2</sub> and H<sub>2</sub>O. The value of  $v_2$  was determined by this means to be 18°51'. For 80°K solid NH<sub>3</sub>, the result was  $n = 1.42 \pm 0.02$  for data taken in the IROTC. This value compares favorably with the value of  $n = 1.415 \pm 0.005$  for 195°K solid NH<sub>3</sub>.

at the sodium-D line ( $0.5892 \mu\text{m}$ ), Ref. 9, since the dispersion of solid  $\text{NH}_3$  is probably very small over a range of visible wavelengths of  $400 \text{ \AA}$ .

In addition to the deposition system just described, an additional contaminant introduction system was designed that allows samples, paint for example, to be placed inside the IROTC and all outgassed constituents to be directed toward the cryocooled IR substrate. The samples can be heated if necessary. This second contamination subcell, shown in Figs. 9a and b, requires the cryocooled window to be rotated  $90^\circ$  so that essentially all contaminants emanating from the contamination subcell are captured by the cryocooled window. After a certain outgassing period the cryocooled window is rotated back into the IR beam, and an IR spectral scan is recorded.

Finally, there is one additional feature on the IROTC that warrants documentation even though it has not been employed to date. A 75-keV electron gun was fabricated (Fig. 10) with the intention of recording electron diffraction patterns of cryodeposits. In general, gases deposited on a substrate of temperature  $20^\circ\text{K}$  or below will form an amorphous solid; that is, no polycrystalline structure can be identified within the deposit. If the  $20^\circ\text{K}$  deposit is allowed to warm slightly or is annealed at an elevated temperature, it will often undergo a phase transition. The new phase is usually polycrystalline, cubic or hexagonal structured in most cases, and can therefore exhibit highly different radiometric characteristics than that of an amorphous solid. Further, the transition temperature for various condensed gases is different for each gas, and for some, such as  $\text{CO}_2$ , the phases are not categorized to a satisfying degree.

Electron diffraction patterns from condensed gases, deposited under various kinetic and geometric conditions, is but one technique that can be utilized to pinpoint phase transition temperatures. It is for this purpose that the electron gun on the IROTC was fabricated; however, it could also conceivably be used to ionize and/or dissociate the gases immediately before their deposition or to bombard cryodeposits with energetic electrons and thereby study the phenomenon of metamorphosis. These are just a few of the areas that can be investigated now that the IROTC hardware is completed.

### 3.2 PRISM SYSTEM: PE-99

The basic components of the PE-99 system are shown in Fig. 3. In this system a collimated quasi-monochromatic beam is directed

through the cryocooled infrared window and subsequently collected and imaged onto a TGS pyroelectric detector. The quasi-monochromatic beam is generated as follows. Radiation emitted by a 1,300°F stainless steel blackbody ( $L/R = 10$ ; effective emissivity  $\simeq 0.984$ ) is imaged by a potassium bromide (KBr) lens onto the entrance slit of the Perkin-Elmer Model 99 prism monochromator. The Model 99 employs a double-pass optical scheme in order to reduce scattered light for wavelengths beyond  $10\text{ }\mu\text{m}$ , and a KBr prism as a dispersive element. Figures 11a and b show the wavelength versus drum number calibration curve and the spectral resolution versus slit width curve, respectively, for a KBr prism.

The radiation leaving the monochromator is chopped at 13 Hz and collimated by an off-axis  $f/3.3$  parabolic mirror. The exit slit height of the Model 99 is stopped down such that the resulting size of the collimated beam at the germanium window is a 0.75- by 1.5-in. rectangle which underfills the clear 2-in. -diam aperture of the window. The collection optics are an  $f/3.3$  parabolic mirror, exactly the same as the collimating mirror, and a six-to-one off-axis ellipsoidal mirror. The image of the Model 99 exit slit is focused onto the 1- by 2-mm TGS element of the pyroelectric infrared detector,  $D^* = 4.05 \times 10^8\text{ cm (Hz)}^{1/2}\text{ w}^{-1}$ . The analog signal from the pyroelectric detector is amplified by a PAR<sup>®</sup> Model 113 pre-amplifier and processed by a PAR Model 120 lock-in amplifier. The 0- to 10-v output of the PAR 120 is recorded on a Honeywell Electronic 19 strip-chart recorder. A typical procedure for recording transmission spectra is as follows: the Model 99 slits and PAR 120 amplifier gain are adjusted until an increment of the wavelength range could be covered by scanning the Model 99 without saturating the amplifier. The background spectrum,  $I_0$ , is recorded; then the germanium window is rotated into the IR beam, and the transmitted spectrum,  $I_t$ , recorded. The slits and amplifier gain are re-adjusted and the basic sequence repeated until the 1.5- to 20- $\mu\text{m}$  wavelength range is covered. The signal-to-noise (S/N) ratio is 200:1 for wavelengths near the blackbody radiation peak but decreases monotonically to values as low as 20:1 for the long wavelengths. After a complete scan in wavelength is recorded, the  $I_t/I_0$  ratio is hand computed for every ten drum numbers and the drum numbers converted to wavelength. The  $I_t/I_0(\lambda)$  values are plotted to obtain a transmission versus wavelength plot.

Alignment of the germanium window normal to the IR beam is very important since the high refractive index of germanium would cause a lateral displacement of the final slit image on the pyroelectric detector if the window were tilted relative to the IR beam. Normal alignment is accomplished by sending visible light out of the PE-99

and autocollimating off the germanium window. When the reflected image of the exit slit is observed to pass directly back into the exit slit, the germanium window is exactly normal to the beam.

### 3.3 INTERFEROMETER SYSTEM: DIGILAB FTS-14

The Digilab FTS-14 Fourier Transform Spectrometer, shown in Figs. 12 and 13, is a modern spectrophotometer based on a Michelson interferometer and an online NOVA minicomputer for controlling the Michelson scanning mirror and performing the digital Fourier transform necessary to obtain spectra from interferograms. The nominal spectral resolution of the instrument can be chosen from discrete values between 0.5 and 16  $\text{cm}^{-1}$ . By choice of beamsplitter and detector, the interferometer can be set up to cover different spectral regions. In this application the beamsplitter was germanium on a KBr substrate, and the detector was a TGS pyroelectric providing good response over the broad spectral range of  $\sigma = 400$  to 3,950  $\text{cm}^{-1}$  (2.5 to 25  $\mu\text{m}$ ). The interferometer control, data collection, and display are determined by values assigned to a parameter list via a teletype interfaced with the minicomputer. These parameters specify the type of plot routine desired, resolution requested, number of scans to be co-added, etc.; for example, a typical set of parameters and commands for data presented in Section 4.0 is as follows:

#### Parameters

NSS = 64	number of interferograms co-added = 64
RES = 2	spectral resolution = 2 $\text{cm}^{-1}$
PLM = T	plot mode = transmission
STP = 450	start plot at 450 $\text{cm}^{-1}$
ENP = 3700	end plot at 3,700 $\text{cm}^{-1}$

#### Commands

COL	collect interferograms
CMP	compute spectrum
STO	store spectrum
SCN	collect, compute and plot spectrum

There are some 36 parameters that can be varied, but the ones listed above are most frequently changed. The interferometer was fitted with a dry nitrogen purge cover, as was the infrared source, but a 25-cm path in air remained for the IR beam. Because of this unpurged path the  $\text{H}_2\text{O}$  and  $\text{CO}_2$  absorption bands were very prominent as in Fig. 14, and on some occasions the bands did not divide out

completely in the transmission spectrum. This effect is easily identified in the spectra and the regions can be avoided in the data reduction.

There is one major shortcoming of the optical arrangement shown in Fig. 12, namely the interferometer received unmodulated radiation from the IROTC. The photometric accuracy of the interferometer was  $\pm 1$  percent for conditions of a warm (300°K) sample and LN<sub>2</sub> liner; however, when the liner and sample were cryogenically cooled the long wavelength transmission of the germanium window appeared lower than it should because of a long wavelength infrared emission component in the background spectrum that was not present in the sample spectrum. The reason for this is that the field of view of the interferometer, approximately 3 deg, was such that the sample holder was being viewed; therefore, in the sample spectrum the interferometer saw radiation from the source and the 20°K sample holder, but in the background spectrum it saw the source and a portion of the 300°K chamber wall. This situation was corrected by placing a 1.5-in. -diam stop in front of the 20°K sample such that the interferometer viewed the same background whether the sample was in or out of the measurement position. Such an arrangement worked well for the 20°K polystyrene data (Section 4.2); however, the aperture ahead of the sample holder disturbed the uniform flow field of the gas addition system. For the cryodeposit data discussed in Section 4.3 the background emission problem was not corrected, and therefore a correction was applied to the transmission of 20 and 80°K germanium as measured by the interferometer. The obvious solution to the background emission problem, when time permits, is to interchange the source and detector locations so the background radiation is not modulated. A further advantage of this rearrangement is a considerable reduction in total power passing through the cryocooled sample at any instant and thus a lower heat load on the sample and/or cryodeposit.

## 4.0 RESULTS AND DISCUSSION

### 4.1 TRANSMISSION OF GERMANIUM AT 300, 200, 80, AND 20°K

Initial checkout of the IROTC was accomplished by measuring the transmission of a germanium window at temperatures of 300, 200, 80, and 20°K. These temperatures were obtained by gaseous helium (GHe) for 20°K cooling, by LN<sub>2</sub> for 80°K cooling, and by cooling the IROTC liner only and allowing thermal equilibrium to be established overnight between sample and liner for 200°K cooling. Transmission measurements by the Model 99 system of germanium at these temperatures are presented in Fig. 15.

The difference between the 20 and 80°K transmission data was within the error bars; therefore, the two cases are not distinguishable. Table 2 is a list of the Model 99 germanium transmission values as a function of temperature and wavelength (or wavenumber,  $\sigma$ ).

It is evident from Fig. 15 that the germanium absorption coefficient is definitely temperature sensitive. The cuton wavelength shifted from 2.0  $\mu\text{m}$  for the 300°K germanium to 1.7  $\mu\text{m}$  for the 80°K germanium. Germanium is often employed as a cuton filter material, and this shift in cuton wavelength with temperature is relevant in this respect. For wavelengths beyond 10  $\mu\text{m}$ , germanium lattice vibrations cause IR absorption structure which is again temperature sensitive. In fact, germanium transmits nearly fifteen percent more energy, for some long wavelengths, when cooled to 80°K because of the lower vibrational intensity of the crystal lattice structure at the lower temperatures. In addition to a change in absorption strength with cooling, there is also a wavenumber shift in the absorption band centers. For example, the band center frequency for the 660- $\text{cm}^{-1}$  band shifted as much as 10  $\text{cm}^{-1}$ , or 0.20  $\mu\text{m}$ , toward the shorter wavelengths. Finally, it should be noted that the germanium transmission is about one percent higher for the 2- to 10- $\mu\text{m}$  range after cooling to 80°K. This effect is attributable to the decrease in real refractive index of the germanium,  $n_g$ , with cryocooling and hence a decrease in the Fresnel reflection loss. The changes of  $n_g$  are very small and difficult to quantitize from the transmission data; therefore, a more sensitive technique is warranted.

One technique for measuring  $\Delta n_g / \Delta t$  using a  $\text{CO}_2$  laser was employed during the course of the project and is fully described in Appendix A. Results were

$$\left. \frac{\Delta n_g}{\Delta t} \right|_{\substack{\text{Average} \\ 100 \rightarrow 300^\circ\text{K}}} = 3.0 \times 10^{-4} \text{ } ^\circ\text{K}^{-1} \quad (9)$$

for  $\lambda = 10.6 \mu\text{m}$ . Therefore, for  $\Delta t = -220^\circ\text{K}$ ,  $\Delta n_g = -0.066$  or  $n_g = 3.934$ .

The resulting transmission is given by

$$T = \frac{2n_g}{n_g^2 + 1} \cong 47.8 \text{ percent} \quad (10)$$

a value well in line with the prism 99 and also the interferometer transmission data.



In Section 5.0 a model is discussed that allows computation of the complex refractive index ( $n, k$ ) of a thin solid gas film on the 80°K germanium window. The model requires knowledge of the refractive index of the germanium substrate, film thickness, and transmission of the film plus substrate. For 80°K (and 20°K) germanium the optical constant " $k_g(\lambda)$ " can be extracted from the data in Fig. 15 combined with a graphical solution of Eq. (2), Section 2.1. The real refractive index, " $n_g(\lambda)$ " is also required and the dispersion relation of Ref. 3 has been employed. The dispersion of germanium past 13  $\mu\text{m}$  has been taken to be zero; therefore,  $n_g = \text{constant}$  (based on the results of Ref. 10). Furthermore, the value of  $\rho$  employed in Eq. (2) is based on a real refractive index since  $\alpha_g < 3.0 \text{ cm}^{-1}$  for germanium and therefore  $k_g \approx 0.0005$ , which is much less than  $n \approx 4.00$ . A plot of transmission versus  $\alpha_g$ , where  $\alpha_g = 4\pi k_g(\lambda)/\lambda$  is shown in Fig. 16, for window thicknesses employed in this work and that by Stierwalt, Naval Electronics Lab Center, and Randall and Rawcliffe (Ref. 10), so that for any given transmission, a value of  $\alpha_g$  can be read from the plot. Using this procedure the  $k_g(\lambda)$  values for 80°K germanium were determined and are listed for every 10  $\text{cm}^{-1}$  in Table 3 for the  $\sigma = 1,000\text{- to }500\text{-cm}^{-1}$  range where  $\sigma(\text{cm}^{-1}) = 10^4/\lambda(\mu\text{m})$ . Since the  $k_g(\lambda)$  is a characteristic of the bulk material, the values listed in Table 3 can be used for any window thickness and a transmission value computed from Eq. (2). This was done to check the  $k_g(\lambda)$  values of this study against the transmission measurement of Stierwalt. For all wavelengths selected, the  $T(\lambda)$  computed, using  $k_g(\lambda)$  from Table 3, were within 2.0 percent of the  $T(\lambda)$  values of Stierwalt. Thus the errors in the  $k_g(\lambda)$  values are not more than  $\pm 5$  percent.

After the transmission measurements of germanium were made as a function of temperature and the radiometric accuracy of the IROTC measurements was established, the next investigation conducted with the Model 99 system was to record spectra of a thin solid gas film deposited on the cryogenically cooled germanium window. The required data are the transmission spectra for various film thicknesses, and many different thicknesses are desirable. Attempts to record large numbers of spectra for a number of different gases of interest proved to be a formidable task and at this point inquiries were made to Wright-Patterson AFB, Ohio, concerning the Digilab FTS-14. During the interim, the Model 99 system was best employed by holding the wavelength fixed and recording transmission during the deposition of a particular gas. Conceptually this could be done for any number of wavelengths in

the 2- to 20- $\mu\text{m}$  range. The results of such a measurement for  $\text{NH}_3$  on 80°K germanium at selected wavelengths is shown in Figs. 17a through f. These  $\text{NH}_3$  data are useful because they can be compared with similar type data taken with interferometer.

After the interferometer was arranged as discussed in Section 3.3, spectral transmission scans of the bare germanium were made at 300 and 80°K. The 300°K transmission data are in excellent agreement with the Model 99 data (see Fig. 18); however, there was an emission problem when the 80°K data were taken (see Fig. 19), as outlined in Section 3.3. A percentage correction factor,  $C(\sigma)$ , to the interferometer data was deduced by comparison to the Model 99 data (see Figs. 19 and 20). The  $C(\sigma)$  values are listed in Table 3 and were used to adjust the interferometer absolute values of transmission in the 1,000- to 500- $\text{cm}^{-1}$  range, i. e. ,

$$C(\sigma) = T_{\text{Model 99}}(\sigma) - T_{\text{interferometer}}(\sigma) \quad (11)$$

A summary of 300 and 80°K germanium transmission data recorded during the project for wavenumbers 500 to 1,000  $\text{cm}^{-1}$  is given in Fig. 21 as are the data of Stierwalt.

## 4.2 TRANSMISSION OF POLYSTYRENE AT 20°K

Before recording IR spectra of condensed gases with the interferometer, measurements of the IR spectrum of 20°K polystyrene were made. Polystyrene  $(\text{C}_8\text{H}_8)_n$  has been extensively employed as an accepted IR wavelength calibrator since the publication by E. K. Plyler, et al. of Refs. 11 and 12 on the subject of wavelength calibration of infrared prism spectrometers. This material is easily manufactured in thin uniform films and also exhibits excellent temporal stability. A more recent review of polystyrene as an infrared wavelength calibration standard is contained in Ref. 13; however, no information on the temperature sensitivity of the location of the standard absorption bands can be found. Recently the need to employ polystyrene at 20°K has arisen in the AEDC 7V Aerospace Chamber. In connection with this need a study was conducted to determine if the standard bands of polystyrene shift when it is cooled to 20°K.

In order to measure the transmission of the 0.050-mm-thick polystyrene at 20°K the thin film was sandwiched between two salt (NaCl) windows 4 mm thick and then subsequently mounted into the

cryogenically cooled window holder. This ensured that the thin polystyrene film would be conductively cooled to near 20°K. The temperature of the polystyrene itself could not be measured directly, only the temperature of the aluminum holder was measured; however, calculations showed that for a cooling arrangement like the one employed (for a vacuum environment) the window temperature at its center is not more than 10°K above the temperature of the actively cooled aluminum holder. There is some disadvantage of such a NaCl-polystyrene-NaCl sandwich. The NaCl cuts off in the 600- (16.7- $\mu$ m) to 500- $\text{cm}^{-1}$  (20- $\mu$ m) range and no doubt increases in transmission when cooled to 20°K (see Ref. 14 for examples of transmission of cryocooled materials). The long wavelength cutoff is of little importance since the last standard absorption band occurs at 906.9 $^{-1}$  (11.027  $\mu$ m). The increased transmission of NaCl at 20°K does not allow the absolute change in transmission of the polystyrene with cryocooling to be observed; however, it was concluded that the assurance of a cold specimen was of top priority; hence the NaCl sandwich was employed. The polystyrene sample employed was ordered from Beckman, as was the sample employed in Chamber 7V. Unfortunately, no purity specifications are available. The sample was measured to be 0.050 mm thick.

The transmission of polystyrene was measured for temperatures of 300, 200, 100, and 20°K. The 300 and 20°K results are sufficient to draw conclusions from and are therefore the only spectra presented. Following the 300°K measurements the polystyrene was slowly cooled, one degree Kelvin per minute for 300 to 200°K, then three degrees Kelvin per minute for 200 to 20°K. The cooling rate was slow since the salt windows are sensitive to thermal shock. The polystyrene was left at 20°K for at least thirty minutes before transmission scans were made. The complete transmission spectrum of 300 and 20°K polystyrene from 3,700  $\text{cm}^{-1}$  (2.7  $\mu$ m) to 500  $\text{cm}^{-1}$  (20  $\mu$ m) is shown in Figs. 22 and 23, respectively. The spectral resolution of all transmission data was 1.0  $\text{cm}^{-1}$ . For the polystyrene calibration bands located at 3027.9  $\text{cm}^{-1}$  (3.303  $\mu$ m), 2851.5  $\text{cm}^{-1}$  (3.507  $\mu$ m), 1944.5  $\text{cm}^{-1}$  (5.143  $\mu$ m), 1601.8  $\text{cm}^{-1}$  (6.243  $\mu$ m), 1154.6  $\text{cm}^{-1}$  (8.661  $\mu$ m), 1028.3  $\text{cm}^{-1}$  (9.725  $\mu$ m), and 906.9  $\text{cm}^{-1}$  (11.027  $\mu$ m), the transmission measurements were plotted in an expanded abscissa scale of 25  $\text{cm}^{-1}$  per inch. Figures 24a through d are results of 300°K polystyrene transmission for 2,800 to 3,200  $\text{cm}^{-1}$ , 1,900 to 2,000  $\text{cm}^{-1}$ , 1,550 to 1,650  $\text{cm}^{-1}$ , and 900 to 1,200  $\text{cm}^{-1}$  wavenumber regions, respectively. Each figure has the band center wavenumber indicated. For 20°K polystyrene similar plots are shown in Figs. 25a through d. Table 4 is a summary of the calibration wavenumbers

for (1) a 300°K polystyrene sample taken from a Beckman wavelength calibrator card, (2) the 300°K results of Ref. 12, (3) the 300°K results of this study, and (4) the 20°K results of this study.

In this study band centers were obtained simply by inspection of the spectral plots. Through close examination of Figs. 24 and 25 it is evident that these plots can be read with an uncertainty of about  $0.5 \text{ cm}^{-1}$ . For some bands further uncertainty is introduced by noisy minima or by total absorption in the band center. Although the interferometer is capable of a wavenumber accuracy of at least  $0.025 \text{ cm}^{-1}$ , more elaborate techniques to locate the band centers were not warranted in this case.

Again, the primary objective of the study was to search for shifts caused by cryocooling to 20°K; thus even if a systematic error in absolute wavenumber exists, any shifts upon cooling the polystyrene can readily be detected. From the results listed in Table 4 it is evident that the wavenumbers for the standard calibration bands of 20°K polystyrene did not shift in wavenumber more than  $1 \text{ cm}^{-1}$  as compared to those of 300°K polystyrene. This upper limit can easily be converted to an incremental wavelength at any desired wavelength by reference to Fig. 26.

One readily observed characteristic in the 20°K polystyrene spectrum that is different from the 300°K polystyrene spectrum is the increased transmission in the  $500\text{--}(20\text{-}\mu\text{m})$  to  $900\text{-cm}^{-1}$  ( $11.1\text{-}\mu\text{m}$ ) range. This is without doubt caused by the increased transmission of the NaCl used in the sandwich arrangement and should not be totally associated with the polystyrene. However, even if the increase in the NaCl transmission is taken into account an increase in the depth and sharpness of the polystyrene absorption bands is noted in some instances. This effect is quite characteristic of cryocooling solid materials.

Finally, there are two absorption features located at  $590$  ( $16.95 \mu\text{m}$ ) and  $630 \text{ cm}^{-1}$  ( $15.97 \mu\text{m}$ ) that are unexplained. They could be a result of cryocontamination; however, no accompanying near-infrared absorption has been noted; thus it is equally plausible they are associated with the polystyrene.

### 4.3 IR SPECTRA OF SOLID $\text{NH}_3$ , $\text{CO}_2$ , $\text{CO}$ , $\text{CH}_4$ , AND $\text{HCl}$ THIN FILMS ON 20 AND 80°K GERMANIUM WINDOWS

The spectra will be presented by first describing general conditions that apply to all the gases studied and then each gas will be discussed individually. Table 1 gives values of substrate temperature, refractive index values of solid gases at  $0.6328 \mu\text{m}$ , growth rates employed in  $\mu\text{m}/\text{min}$ , upstream inlet pressure of gas, background pressure in IROTC, equilibrium vapor pressure, and purity grade of the gases studied. Table 5 serves as a table of contents giving the figure number and corresponding film thickness for each spectrum.

All of the gases were deposited from a 300°K reservoir as described in Section 3.1 and shown in Fig. 8. Since deposition of a gas onto a cryocooled surface is a condensation phenomenon, the governing parameter is the equilibrium vapor pressure for each gas at the temperature of the substrate. The equilibrium vapor pressure is of such importance that standard curves (Ref. 16) for those gases studied herein have been reproduced in Fig. 27. The curves are often divided into an " $\text{LN}_2$  range" and an " $\text{LH}_2$  range" since equilibrium vapor pressure for some gases is rather high,  $10^{-1}$  or 1 torr, at 77°K ( $\text{LN}_2$ ) and cannot be deposited "in vacuum" for this reason. In this study  $\text{NH}_3$  and  $\text{CO}_2$  can be readily deposited at 77°K, or actually 80°K for the IROTC, but 20°K cooling is required for  $\text{CO}$ ,  $\text{CH}_4$ , and  $\text{HCl}$ . The equilibrium vapor pressure must not be confused with the deposition background pressure which can assume almost any value since deposition is a nonequilibrium condition. The values of background pressure in the immediate vicinity of the germanium window could not be measured and are not easily computed since the effect of the  $\text{LN}_2$  liner geometry on the flow field inside the IROTC during deposition is unknown. The values of background pressure recorded by the ionization gage and given in Table 1 are only indicative of conditions within the IROTC since this pressure readout can be highly affected by noncondensable impurities in the primary gas. The ionization gage readout was most useful in observing the IROTC background pressure after the flow was shut off. In summary, all that is well known is the inlet pressure on the upstream side of the free-jet expansions and the final background pressure, typically  $1 \times 10^{-8}$  torr, after the flow was shut off. Even with these shortcomings, the gas addition system as shown in Fig. 8 worked well in that thin uniform films of solid gas could be deposited on the germanium window at a well-controlled rate. The growth rate upper limit was set only by the increased background pressure associated with a rapid growth rate and the high heat load on the germanium

window caused by the latent heat of condensation. There is no lower limit restriction other than time. In this study the linear growth rate ranged from 1.3 to 4.1  $\mu\text{m}/\text{min}$ .

A typical sequence of thin-film growth and recording of IR spectra is as follows:

1. Pumpdown IROTC with diffusion pump to  $10^{-7}$ -torr. This usually required three to four hours.
2. Cooldown  $\text{LN}_2$  liner and allow to soak over night. Pressure would fall to  $10^{-8}$ -torr range.
3. Cooldown of sample for at least one-half hour.
4. Record background IR spectrum with the interferometer and store in NOVA memory. Make all necessary adjustments to interferometer system, such as a baseline scan.
5. Slowly open variable leak valve until inlet pressure was near 500 mtorr and He-Ne interference patterns started. The diffusion pump is still pumping on IROTC. Continue growth until first He-Ne minimum is observed; then close variable leak valve.
6. Record IR spectrum transmitted through thin film plus germanium window.
7. Repeat Steps 5 and 6 until a sufficient number of thicknesses have been grown and IR spectra recorded.

Of the five gases studied, 20°K  $\text{NH}_3$  and 20 and 80°K  $\text{CO}_2$  did not produce clear thin films but rather a milky-cloudy-type film as seen in visible light. However, the films in all cases are believed to be uniform in thickness across the IR beam portion of the germanium window as is manifested by the IR interference pattern or "channel spectrum" in the transmission spectra. For thin films that were clear, the visible hue attributable to the visible channel spectrum was easily observed with the chamber lighting during early stages of deposition, but photographs did not show the color display. A cloudy  $\text{CO}_2$  deposit (80°K) roughly 5.0  $\mu\text{m}$  thick was photographed and is shown in Fig. 28. The  $\text{CO}_2$  appears to completely mask the germanium window; however, IR transmission data indicate that attenuation in the form of scattering is essentially zero since the

amplitude of the IR interference pattern is the same as that of a clear thin deposit. It is for this reason that the absorption coefficient employed in the theoretical model of Section 5.0 is a true absorption and not an extinction coefficient.

The transmission spectra for all the solid gases studied have two characteristics in common, that is, they all have absorption band structure caused by the fundamental absorption modes of the molecules and they all have the interference pattern attributable to the thin-film structure. The absolute level of transmission varies between that of the base substrate (48 percent) and a maximum of near 60 percent, depending on the optical constants of the solid gas film. In most cases the real refractive index of the film is near 1.40 so that the film tends to act as an antireflection coating. Thus except for the absorption band features the transmission always increases, above the substrate transmission, because of the cryodeposit.

There were a few observables in regard to deposition worth noting. The first, and most important, is a circumstance noted during CO<sub>2</sub> deposition on 80°K germanium. Since the CO<sub>2</sub> film was usually milky it was thought that if the leak valve was opened very slowly, the equilibrium vapor pressure would be reached gradually and the early stages of condensation at a very slow growth rate might lead to CO<sub>2</sub> deposits that were clear. When this was tried it was discovered that the LN<sub>2</sub> liner, as well as the germanium holder, was cryopumping the CO<sub>2</sub> at an equilibrium vapor pressure well below that necessary to realize condensation on the germanium. As stated previously in Section 4.2 the window temperature cannot be measured and it is a fact that some degree of temperature gradient exists between the center of the germanium window, a semiconductor, and the aluminum holder. Thus if the window center were 5°K higher in temperature than the 80°K holder, the equilibrium vapor pressure for CO<sub>2</sub> for the window would be  $7 \times 10^{-7}$  torr and the holder equilibrium vapor pressure for CO<sub>2</sub> would be  $8 \times 10^{-8}$  torr (see Fig. 27). Therefore, if the mass flow rate of CO<sub>2</sub> into the cell were very small, the partial pressure of the CO<sub>2</sub> would be nearly that corresponding to the 80°K equilibrium vapor pressure and no condensation could take place on the 85°K germanium window. This circumstance occurred solely because transmission measurements are being made in the IROTC and the window must be mounted and cooled around its periphery. In most previous investigations reflectance was the quantity measured. Thus, the sample was heat sunk along its back side as well as its periphery and if a temperature gradient existed across the substrate it was a very small one. In such a case the sample has

just as low a temperature as any other cooled material and condensation takes place on the sample as well as any other place. In short, for low mass addition rates, condensation will take place only at the coldest locations, and a 5°K differential can easily cause deposition only at the coldest location. For the IROTC the mass flow rate into the cell had to be large enough so that the local partial pressure at the germanium window was equal to or greater than the equilibrium vapor pressure of CO<sub>2</sub> at the window temperature. This usually occurred when the MKS Baratron indicated an inlet pressure between 300 and 500  $\mu$ m Hg. This same phenomenon of cryopumping (or condensation) only at the lowest temperature locations was also often observed on the LN<sub>2</sub> liner. The liner was formed from fins welded in spots to tubing containing the cryogen, and thus cryopumping was only seen (the thin-film channel spectrum could be seen with the chamber lights) where the fins were welded to the tubing. This phenomenon is a result of the equilibrium vapor pressure being a logarithmic function of the temperature. As was noted above for a 5°K change in temperature, the equilibrium vapor pressure differential is nearly an order of magnitude. What this immediately suggests is that if one desires to avoid deposition on a sensor mirror for example, the mirror could be kept slightly warmer than the surrounding structure. A 5°K differential would seem to be adequate and would not be detrimental from a radiometric emission standpoint. Since CO<sub>2</sub> was the only gas studied in this respect, it is clear that much more research effort is warranted in this area. The same applies to migration of cryodeposits from "warm" spots to colder locations.

The second phenomenon observed during deposition was the effect on disposition rate of background pressure. Normally the IROTC background pressure was in the 10<sup>-7</sup>-torr range during deposition since the diffusion pump was open to the IROTC and pumped out non-condensables. On several occasions the diffusion was valved off and the IROTC background pressure slowly rose to the 10<sup>-5</sup>-torr range. The He-Ne laser pattern indicated that deposition rate was slowing down even though the inlet pressure was constant. An explanation was the decrease in the mean free path for the condensable gas as the background pressure rose, which permitted fewer molecules to leave the free-jet expansion and reach the germanium before they were deflected to the LN<sub>2</sub> liner and captured. When the diffusion pump was opened to the IROTC the background pressure fell to 10<sup>-7</sup> torr and the period of the He-Ne pattern decreased, indicating faster deposition. Based on these results it seems that a helium (noncondensable) flush immediately in front of the mirror could be used to prevent condensable species from cryopumping on mirrors.



### 4.3.1 80 and 20°K NH<sub>3</sub>

The IR transmission spectra of 80 to 20°K solid NH<sub>3</sub> for various thicknesses is shown in Figs. 29a through w and Figs. 30a through k, respectively. In each figure parameters are given concerning thickness, pressure, growth rate, spectral resolution, and temperature. The wavenumbers range from 3,700 cm<sup>-1</sup> (2.703 μm) to 450 cm<sup>-1</sup> (22.2 μm). Below 450 cm<sup>-1</sup> the signal was too low to be useful because of the absorption by the germanium substrate, and above 3,700 cm<sup>-1</sup> the noise level was high because of a shortage in energy from the source. This wavenumber range applies to all of the IR spectra in this section. Where a "(+)" appears on a thickness value this implies that the deposition was not exactly valved off when the He-Ne interference pattern reached a minimum; thus the thickness value given is low by an amount between 1 and 5 percent.

Infrared spectra of solid NH<sub>3</sub> has been reported by Staats and Morgan (Ref. 17) and Reding and Hornig (Ref. 18). The crystalline structure of solid NH<sub>3</sub> has been investigated by F. A. Mauer, et al., at the National Bureau of Standards. The notes on their research on noncubic NH<sub>3</sub> are given in Appendix C. Solid NH<sub>3</sub> apparently can exist in four distinct phases: (1) the common cubic phase obtained by deposition above 140°K, (2) a metastable I (MI) phase, (3) a metastable II (MII) phase, and (4) an amorphous phase obtained by deposition below 40°K. The formation of the MI phase, for this study, was always obtained by deposition at 80°K, and the MII phase was obtained by warming the amorphous phase to near 100°K. The IR spectra of MI, amorphous, and MII are shown, respectively, in Figs. 29i and 30j and k. A cubic NH<sub>3</sub> film could not be obtained in the IROTC since a film temperature of 140°K or above is required. For such a high temperature the NH<sub>3</sub> would have evaporated from the substrate and cryopumped on the LN<sub>2</sub> liner. The conditions of deposition for each phase are not completely consistent with those of Refs. 17 and 18; thus the MI and MII phases are assigned based on the doublet feature near 1,075 cm<sup>-1</sup> which is assigned to the MII phase in Ref. 17. Arnold et al. (Ref. 2) have also observed the 1,075-cm<sup>-1</sup> doublet for deposition temperatures of 55, 57, and 58°K; however, they do not discuss the associated phase of these solid NH<sub>3</sub> deposits. Table 6 summarizes the molecular band center wavenumbers for each phase. It should also be noted that the absolute transmission level for the MII phase NH<sub>3</sub> dropped some three percent since the phase transition caused crystallization and some level of scattering is no doubt present.

### 4.3.2 80 and 20°K CO<sub>2</sub>

Transmission spectra of 80 and 20°K CO<sub>2</sub> are shown in Figs. 31 through 35. Only four thicknesses of 20°K CO<sub>2</sub> were recorded since there seemed to be little difference between the 80 and 20°K CO<sub>2</sub>. Figures 35a and b show data taken during warmup of the 20°K thin film. The vibrational modes of <sup>12</sup>CO<sub>2</sub> and <sup>13</sup>CO<sub>2</sub> have been identified in Fig. 31b. As was noted previously, the CO<sub>2</sub> films were all of a cloudy nature and no deposition combination could be found for producing clear films.

The refractive index value for 20°K CO<sub>2</sub> at 0.6328 μm was taken to be 1.42, the same as for 80°K CO<sub>2</sub> since an attempt to measure it in situ failed. This may lead to an error in the thickness values of up to 20 percent.

There is one noticeable difference between the 80 and 20°K spectra for the  $\nu_2$  band at 655 cm<sup>-1</sup>. The 660 cm<sup>-1</sup> band in the 20°K CO<sub>2</sub> is much broader than for the 80°K CO<sub>2</sub>: 2 cm<sup>-1</sup> as compared to 0.75 cm<sup>-1</sup>. Further, if the thickness values for the 20°K CO<sub>2</sub> are correct the line center absorption strength of the 20°K CO<sub>2</sub> vibrational bands are considerably less than the 80°K CO<sub>2</sub> (the same is true for the <sup>13</sup>CO<sub>2</sub> bands).

In comparing the CO<sub>2</sub> spectra with those given in Ref. 2 a number of differences are obvious. For the 655 cm<sup>-1</sup>  $\nu_2$  band the IROTC data show no features at 656 and 680 cm<sup>-1</sup>. Further, the <sup>13</sup>CO<sub>2</sub> line at 638 is not nearly as strong for the IROTC data, indicating a lesser concentration of isotope CO<sub>2</sub> (see Fig. 32a). For the  $\nu_3$  band structure (Fig. 32b) the feature near 2,370 cm<sup>-1</sup> was not observed and the lattice absorption at 2,382 cm<sup>-1</sup> was not seen in either the 80 or 20°K CO<sub>2</sub> IROTC data, even though the minimum at 2,460 cm<sup>-1</sup> caused by a lattice combination band is present. This paradox has not been explained.

Finally it is evident that thicknesses of solid CO<sub>2</sub> less than 1,000 Å could easily be detected by identifying the strong  $\nu_2$  and  $\nu_3$  bands. Also, there seems to be only one phase, cubic, of CO<sub>2</sub> since no large differences in 20, 50, 80, 100°K CO<sub>2</sub> spectra were observed.

### 4.3.3 20°K CO

Transmission spectra of 20°K CO is shown in Figs. 36 through 38. The main absorption feature is the fundamental stretching mode of CO at  $2,138\text{ cm}^{-1}$ . Other features are attributed to  $\text{CO}_2$  ( $2,347\text{ cm}^{-1}$ ) and isotopes of CO ( $2,090\text{ cm}^{-1}$ ) (Ref. 19). The absorption at  $2,095\text{ cm}^{-1}$  is not identified, whereas the broad absorption feature at  $2,210\text{ cm}^{-1}$  is thought to be a lattice combination band similar to the  $2,460\text{ cm}^{-1}$  band in solid  $\text{CO}_2$ . The thickness values shown are based on an  $n = 1.22$  at  $0.6328\text{ }\mu\text{m}$ . Only one other comparison is available for solid CO, Ref. 20, where  $n = 1.237$  at  $0.6328\text{ }\mu\text{m}$  and  $T = 31^\circ\text{K}$  (also  $n = 1.277$  at  $0.6328\text{ }\mu\text{m}$  and  $T = 20^\circ\text{K}$ ). The errors for these refractive index values are unknown; thus the thickness could not be determined. For this reason "max" and "min" values are given in Table 5 for the He-Ne interference pattern.

In Fig. 38 the 20°K CO was allowed to warm up to 40°K and then was recooled to 20°K before the transmission was recorded. No apparent changes occurred in the spectrum, and therefore no phase change seemed to have taken place. The  $2,138\text{-cm}^{-1}$  CO band has been investigated recently by Jiang, et al. (Ref. 21) in the 30 to 70°K range. They found that the absorption band occurred at  $2,138\text{ cm}^{-1}$  also. The thickness of the film in Fig. 38 was estimated by using  $n = 1.35 \pm 0.05$  at  $\nu = 1,000\text{ cm}^{-1}$  from Ref. 21 and the separation of the channel spectrum maxima in the  $1,000\text{-cm}^{-1}$  region. Also, as noted in Fig. 38 the amplitude of the channel spectrum is decreasing toward the higher wavenumbers. This could be attributable to a large value of the CO refractive index, but more likely it was caused by scattering since the film was rather thick.

### 4.3.4 20°K $\text{CH}_4$

The transmission of 20°K  $\text{CH}_4$  is shown in Figs. 39a through x for a number of different film thicknesses. The measured refractive index at  $0.6328\text{ }\mu\text{m}$  is  $1.38 \pm 0.02$ , which compares favorably with the value of  $1.30 \pm 0.01$  ( $T = 91^\circ\text{K}$ ) from Ref. 9 ( $\lambda = 0.5893\text{ }\mu\text{m}$ ). The two fundamental absorption modes are indicated in Fig. 39c, i. e.,  $\nu_3(\text{CH}_4) = 3,009\text{ cm}^{-1}$  and  $\nu_4(\text{CH}_4) = 1,300\text{ cm}^{-1}$  as compared to the gas,  $\nu_3(\text{CH}_4\text{ gas}) = 3020.3\text{ }\mu\text{m}$  and  $\nu_4(\text{CH}_4\text{ gas}) = 1306.2\text{ }\mu\text{m}$  (Ref. 22). Further, the  $2\nu_4$  ( $2,591\text{ cm}^{-1}$ ) and the  $\nu_2 + \nu_4$  ( $2,813\text{ cm}^{-1}$ ) are seen in the thicker film deposits (Fig. 39o for example) and again a lattice combination band is evident near  $3,050\text{ cm}^{-1}$ . The most interesting results for solid  $\text{CH}_4$  occurred during the warming of the film as shown in Figs. 39v and w.

As seen in visible light, the  $\text{CH}_4$  definitely passed into a different phase during warmup. All of the absorption features became much broader as compared to the 20°K  $\text{CH}_4$  spectra. This is just the opposite effect to that for  $\text{NH}_3$ . That is, the 20°K  $\text{NH}_3$  (amorphous) spectra had broad absorptions, and a phase transition caused the bands to narrow and also strengthen. This opposite phenomenon for solid  $\text{CH}_4$  has not been explained as yet and clearly exemplifies the need to complete the electron diffraction system on the IROTC so that phases can be identified. As shown in Fig. 39w, the widths of the  $\text{CH}_4$  bands continued to increase as the temperature rose, indicating an annealing effect or temperature dependence.

#### 4.3.5 20°K HCl and Air

These two solid gases were examined only in a qualitative manner. The scans are shown in Figs. 40, 41, and 42. The absorption by gaseous HCl is compared to solid HCl in Fig. 41 to exemplify the great difference between the two phases.

### 5.0 OPTICAL CONSTANTS OF CONDENSED GASES

With the data obtained from the interferometer the complex refractive index ( $\bar{n} = n - ik$ ) was computed for  $\text{NH}_3$  on 80°K and 20°K germanium. The measurement of the transmission of contaminated cooled optics is important to determine the behavior of the throughput of optical components. However, it is also important to have the capability to compute the anticipated behavior when designing an optical system. To compute the effect of thin contamination films as a function of film thickness and wavelength, it is necessary to have available the contaminant optical constants ( $n, k$ ). From the transmission data recorded at various thicknesses and the least squares technique used in conjunction with an analytical transmission model, the optical constants were obtained. The analytical model is based on the work in Ref. 23. The contamination film was modeled as a thin partially transmitting film deposited on a thick partially transmitting substrate. In the thin film the light waves were considered to be phase coherent, but in the thick substrate the light waves were assumed to be phase incoherent. In using the analytical model it is necessary to know the optical properties ( $n_g, k_g$ ) of the germanium substrate.

In the range from 2 to 13.5  $\mu\text{m}$  the germanium was assumed to have  $k_g = 0$  with the real refractive index given, from Ref. 3, by

$$n_g = A^1 + B^1 L + C^1 L^2 + D^1 \lambda^2 + E^1 \lambda^4 \quad (12)$$

where

$$L = (\lambda^2 - 0.028)^{-1}$$

$$A^1 = 3.99931$$

$$B^1 = 0.391707$$

$$C^1 = 0.163492$$

$$D^1 = -0.000006$$

$$E^1 = 0.000000053$$

To determine the optical properties it was necessary to derive an analytical model of the transmittance of a thin film deposited upon a thick, partially transmitting substrate. The geometry describing the transmittance is shown in Fig. 43. The derivation of the analytical expression for the transmittance is based upon the expressions in Ref. 23. For convenience the different layers have been numbered with subscripts 0, 1, 2, and 3, where subscripts 0 and 3 are vacuum conditions and subscripts 1 and 2 are the thin contamination film and the thick germanium substrate, respectively. Also the relative thickness of media 1 to media 2 is exaggerated for illustration purposes. Since all of the data obtained were for normal incidence, the analytical model will be derived for "normal incidence only"; however, the analysis can easily be extended to light incident at any angle. In Fig. 43  $E_O^+$  represents the incident radiation and the series of waves shown in media 1 are phase coherent for each packet and represent an infinite number of reflections back and forth. The resultant amplitude that transmits through the top interface is designated by B1 for the first packet, B2 for the second packet, etc.; the resultant amplitude that transmits into the substrate (media 2) is designated by  $E_2^+$  for the first packet, A2 for the second packet, A4 for the third packet, etc. Because the substrate behaves as a thick film the waves  $E_2^+$ , A2, A4, A6, etc. are not phase coherent; similarly, A1, A3, A5, etc. are not phase coherent; likewise C1, C2, C3, etc. are not phase coherent; and finally, B1, B2, B3, etc. are not phase coherent.

The relationships between the amplitudes of the various waves shown in Fig. 43 are the following:

$$\left. \begin{aligned} E_2^+ &= t_{012} E_o^+ \\ A2 &= A1 r_{210} \\ A4 &= A3 r_{210} \\ A6 &= A5 r_{210} \\ &\vdots \end{aligned} \right\} \quad (13)$$

with

$$\left. \begin{aligned} A1 &= E_2^+ r_2 \\ A3 &= A2 r_2 \\ A5 &= A4 r_2 \\ &\vdots \end{aligned} \right\} \quad (14)$$

with

$$\left. \begin{aligned} C1 &= t_2 E_2^+ \\ C2 &= t_2 A2 \\ C3 &= t_2 A4 \\ &\vdots \end{aligned} \right\} \quad (15)$$

and with

$$\left. \begin{aligned} B1 &= r_{012} E_o^+ \\ B2 &= A1 t_{210} \\ B3 &= A3 t_{210} \\ B4 &= A5 t_{210} \\ &\vdots \end{aligned} \right\} \quad (16)$$

where  $t_2$  designates the amplitude transmission of light traveling from medium 2 to medium 3; where  $r_2$  designates the amplitude reflection of light incident upon medium 3 from medium 2; where  $r_{012}$  designates the amplitude reflection of light which is incident from medium 0 and is reflected back into medium 0 after undergoing thin-film interference in medium 1; where  $r_{210}$  designates the amplitude reflection of light which is incident from medium 2 and is reflected back into medium 2 after undergoing thin-film interference in medium 1; where  $t_{012}$  designates the amplitude transmission of light incident from medium 0 and transmitted into medium 2 after undergoing thin-film interference in medium 1; and where  $t_{210}$  designates the amplitude transmission of light incident from medium 2 and transmitted into medium 0 after undergoing thin-film interference in medium 1.

The power transmitted through the thin-film, thick-film combination is given by

$$\xi = n_3 |C1|^2 + n_3 |C2|^2 + n_3 |C3|^2 + \dots \quad (17)$$

where  $n_3 = n_0$  since medium 3 and medium 0 are both considered as vacuum and with the constant  $c/4\pi$  ( $c$  being the speed of light in vacuum) being omitted for convenience since this constant will be lost when dividing to determine the overall transmittance.

Substituting Eq. (15) into Eq. (17) yields the transmitted power as

$$\xi = n_0 |t_2|^2 \left[ |E_2^+|^2 + |A2|^2 + |A4|^2 + |A6|^2 + \dots \right] \quad (18)$$

Next, combining Eqs. (13) and (14) yields

$$\left. \begin{aligned} |A2|^2 &= R_2 R_{210} |E_2^+|^2 \\ |A4|^2 &= R_2^2 R_{210}^2 |E_2^+|^2 \\ |A6|^2 &= R_2^3 R_{210}^3 |E_2^+|^2 \end{aligned} \right\} \quad (19)$$

where

$$R_2 = |r_2|^2 \quad (20)$$

$$R_{210} = |r_{210}|^2 \quad (21)$$

$$T_2 = |t_2|^2 \quad (22)$$

Inserting Eqs. (19-22) into Eq. (18) results in the transmitted power being given by

$$\xi = n_o T_2 |E_2^+|^2 [1 + R_2 R_{210} + R_2^2 R_{210}^2 + R_2^3 R_{210}^3 + \dots] \quad (23)$$

where the infinite sum converges to a closed form expression, hence giving

$$\xi = \frac{n_o T_2 |E_2^+|^2}{1 - R_2 R_{210}} \quad (24)$$

The transmittance is defined as the transmitted power divided by the incident power. The incident power is given by

$$\xi_o = n_o |E_o^+|^2 \quad (25)$$

and the expression for the overall transmittance is obtained by ratioing Eq. (24) to Eq. (25), i.e.,

$$T = \frac{\xi}{\xi_o} = \frac{T_2 |E_2^+|^2}{[1 - R_2 R_{210}] |E_o^+|^2} \quad (26)$$

but from Eq. (13)

$$\frac{|E_2^+|^2}{|E_o^+|^2} = |t_{012}|^2 = T_{012} \quad (27)$$

with the final result for the overall normal transmittance given by

$$T = \frac{T_2 T_{012}}{[1 - R_2 R_{210}]} \quad (28)$$

The result in Eq. (28) is valid only when the substrate is a nonabsorbing medium. If the substrate is also absorbing, i.e., the imaginary part of the complex refractive index of the substrate is nonzero, then Eq. (28) becomes

$$T = \frac{T_2 T_{012} e^{-\alpha_g D}}{1 - R_2 R_{210} e^{-2\alpha_g D}} \quad (29)$$



where

$D$  = the thickness of the substrate (germanium)

$\alpha_g = \frac{4\pi k_g}{\lambda}$  is the absorption coefficient of the substrate (germanium)

$k_g$  = imaginary component of complex refractive index of the substrate (germanium)

$\lambda$  = wavelength in vacuum

Having derived Eq. (29), which is the normal transmittance of a thin film deposited upon a thick partially transmitting film, it is now necessary to define the expressions  $T_2$ ,  $T_{012}$ ,  $R_2$ , and  $R_{210}$  in terms of the optical constants of the thin film, the substrate, and wavelength. The derivation of these quantities is straightforward, although tedious, and is outlined in detail in Ref. 23. For convenience, the expressions required to evaluate Eq. (29) are listed below (with the detailed derivation given in Ref. 23):

$$R_2 = |r_2|^2 = \left| \frac{\bar{n}_2 - n_o}{\bar{n}_2 + n_o} \right|^2 \quad (30)$$

$$T_2 = |t_2|^2 = \left| \frac{2\bar{n}_2}{(n_o + \bar{n}_2)} \right|^2 \quad (31)$$

The expressions for  $T_{012}$  and  $R_{210}$  are somewhat more complicated to evaluate and will be considered separate from  $R_2$  and  $T_2$ . The expressions for  $T_{012}$  and  $R_{210}$  based on the work of Ref. 23 are given by

$$T_{012} = \frac{|t_a|^2 |t_b|^2 e^{-2b}}{[1 + |r_a|^2 |r_b|^2 e^{-4b} + 2e^{-2b} \{ \text{Re}(r_a r_b) \cos 2a + \text{Im}(r_a r_b) \sin 2a \}]} \quad (32)$$

and

$$R_{210} = \frac{[|r_a|^2 + |r_b|^2 e^{-4b} + 2e^{-2b} \{ \text{Re}(r_b r_a^*) \cos 2a + \text{Im}(r_b r_a^*) \sin 2a \}]}{[1 + |r_a|^2 |r_b|^2 e^{-4b} + 2e^{-2b} \{ \text{Re}(r_a r_b) \cos 2a + \text{Im}(r_a r_b) \sin 2a \}]} \quad (33)$$

where

$$r_a = \frac{\bar{n}_2 - \bar{n}_1}{\bar{n}_2 + \bar{n}_1} \quad (34)$$

$$r_b = \frac{\bar{n}_1 - n_o}{\bar{n}_1 + n_o} \quad (35)$$

$$t_a = \frac{2\bar{n}_1}{\bar{n}_1 + \bar{n}_2} \quad (36)$$

$$t_b = \frac{2n_o}{n_o + \bar{n}_1} \quad (37)$$

$$\bar{n}_1 = n_1 - ik_1 = n - ik = \bar{n} \quad (38)$$

$$\bar{n}_2 = n_g - ik_g \quad (39)$$

$$a = \frac{2\pi d_1 n_1}{\lambda} \quad (40)$$

$$b = \frac{2\pi d_1 k_1}{\lambda} \quad (41)$$

$$d_1 = \text{cryodeposit thickness} \quad (42)$$

and \* denotes the complex conjugate.

For determining  $n_1 = n$  and  $k_1 = k$  for  $\text{NH}_3$  on 80°K germanium, 16 of the 23 film thicknesses were used in a least squares determination of the optical constants of  $\text{NH}_3$ . The quality of the agreement of the data with the analytical model, Eqs. (29-42), is shown in Figs. 44a through ee. These figures show excellent agreement between theory and data for all the various regions between 2.7 and 15.873  $\mu\text{m}$ . Even in the absorption bands there was no ambiguity in determining a unique value of  $n$  and  $k$ ; in the strong absorption band at  $\lambda = 9.346 \mu\text{m}$  (Fig. 44p) the theory and data are still in excellent agreement. Figures 44a through ee are included to demonstrate the agreement for a sampling of other wavelengths. The values of  $n$  and  $k$  for  $\text{NH}_3$  on 80°K germanium are plotted in Figs. 45a and b and are also shown tabulated in Table 7. The strong peak values of  $k$  are seen to appear in the

absorption bands and the anomalous dispersion of  $n$  is also seen to occur in the absorption bands. The results shown in Figs. 45a and b are shown to be in good agreement with the results from Ref. 24 which considered  $\text{NH}_3$  at 188°K. However, the maximum and minimum values of  $n$  in the absorption bands are seen to be higher and lower, respectively, than the results in Ref. 24. Also in Table 7, if the value of  $k$  was less than  $10^{-6}$  then the value of  $k$  was assumed to be equal to  $10^{-6}$ ; values of  $k \leq 10^{-6}$  appear to no longer affect the transmission in the analytical model.

In the determination of  $n$  and  $k$  for  $\text{NH}_3$  on 20°K germanium, only 10 film thicknesses of data were recorded and these were used in the least squares determination of the optical constants of 20°K  $\text{NH}_3$ . Again to show the agreement between theory and data for a range of wavelengths, Figs. 46a through pp are supplied. These figures again show the good agreement between theory and data. The only regions where the results did not appear to be unique were for a few points inside the long wavelength absorption band and for wavelengths greater than 14.286  $\mu\text{m}$ . However, the non-uniqueness only occurred for  $n$  and not for  $k$ . The least squares program converged on the same  $k$  values, but a range of  $n$  values appeared to yield equally good results. Inside the absorption band the curve in Fig. 47a was smoothed to match the unique values of  $n$ . It is believed that this non-uniqueness resulted because only 10 thicknesses were available for use in the least squares technique. The problem also only occurred at the long wavelengths; in the short wavelength absorption band there were no ambiguities encountered. It is believed that if 16 thicknesses of data had been available as in the 80°K case no ambiguities would have resulted in the long wavelength absorption band. The long wavelengths require more data to determine  $n$  and  $k$  since the period of thin-film interference is longer and requires more data to describe the interference. Hence more data at larger thicknesses are needed to converge upon a unique value of  $n$  and  $k$ . It should be noted that only a few of the data points ( $n$ ) in the long wavelength absorption band are not unique and that Fig. 47a is believed to be an accurate representation. The results in Figs. 46j through s show the good agreement between theory and data within the long wavelength absorption band. The values of  $n$  and  $k$  for  $\text{NH}_3$  on 20°K germanium are shown in Figs. 47a and b and in Table 8. It is recommended that for determining  $n$  and  $k$  from this technique that at least 16 values of thickness should be employed and that larger thickness values should be employed to adequately describe the long wavelength thin-film interference. Also, it should be noticed that all of the  $k$  values were of the same order of magnitude ( $\approx 10^{-2}$ ) as opposed to some of the 80°K data having very small

k values ( $\leq 10^{-6}$ ). Because of the uncertainty in thickness and the few number of films available a total error of 10 percent should be associated with the 20°K NH<sub>3</sub> n's and 30 percent with the 20°K NH<sub>3</sub> k's.

Because of the popularity and simplicity of employing the Kramers-Kronig relations between n and k, this relationship was used in comparison with the least squares determination of n and k. The Kramers-Kronig relation is given by

$$n = n_{\infty} + \frac{2}{\pi} P \int_0^{\infty} \frac{\sigma' k(\sigma') d\nu'}{\sigma'^2 - \sigma^2} \quad (43)$$

where  $n_{\infty}$  is the index of refraction at frequencies well above the infrared (in this case at  $\lambda = 0.6328 \mu$ ;  $n_{\infty} = 1.42$ ) and p means the Cauchy principal value of the integral. The integral was evaluated by the simple trapezoidal rule. The  $k(\sigma)$  values used in Eq. (43) are those listed in Tables 7 and 8. Shown in Figs. 45 and 47 is a comparison between the least squares and Kramers-Kronig determination of n. The 80°K data are in excellent agreement between the two techniques, whereas the 20°K agreement is not as good. The Kramers-Kronig results are only shown for comparison purposes; the least squares determination of n and k is believed to be accurate as is borne out by the agreement between theory and data.

## 6.0 CONCLUSIONS AND SUMMARY

The conclusions reached from this investigation are summarized as follows:

1. An IR optical transmission chamber was developed to provide the capability of measuring the spectral transmission by cryogenically cooled (20 and 80°K) optical materials, both with and without cryodeposit contamination.
2. The following condensed gases were studied: NH<sub>3</sub>, CO<sub>2</sub>, CO, CH<sub>4</sub>, HCl, and air. Measurements were made over a range of deposition conditions and cryodeposit thicknesses. Real and imaginary components of the index of refraction of NH<sub>3</sub> at 20 and 80°K were determined using a least squares technique in conjunction with an analytical model.

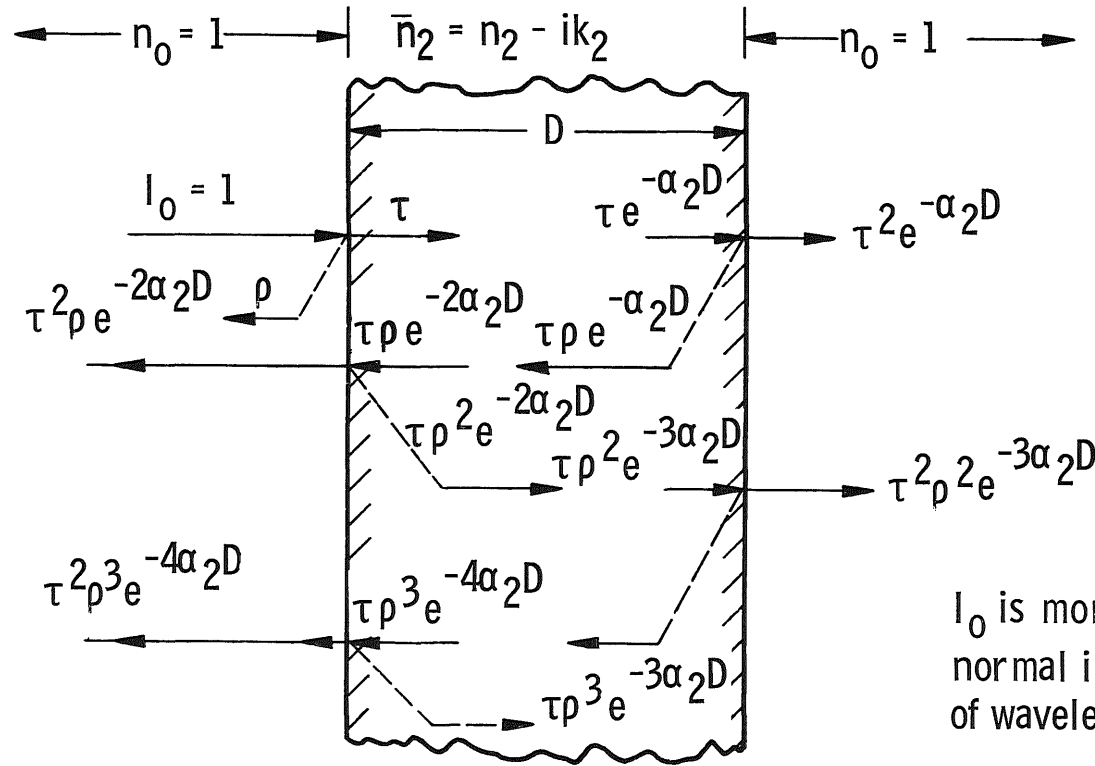
3. An analytic model for the transmission of a thin film cryo-deposit on a thick IR transmitting substrate was derived and demonstrated to be in excellent agreement with the experimental data.
4. A rapid-scan Michelson interferometer was successfully interfaced with a cryogenic cell to provide an excellent and flexible facility for IR spectral measurements on condensed gases and optical materials at cryogenic temperatures. The speed and throughput advantages of the interferometer proved to be valuable assets in the study of cryodeposits where measurement time is always limited.
5. The transmittance of polystyrene at 20 and 80°K was measured. Results indicate no shift (minimum detectable shift about  $0.5 \text{ cm}^{-1}$  in this study) in the location of the polystyrene absorption bands over the temperature range from 20 to 300°C. Hence, polystyrene is suitable for reliable wavelength calibration of instruments in space simulation chambers at cryogenic temperatures.

## REFERENCES

1. Hudson, R. D. Infrared System Engineering. John Wiley & Sons, New York, 1969.
2. Arnold, F., Sanderson, R. B., Mantz, A. W., and Thompson, S. B. "Infrared Spectral Reflectance of Plume Species on Cooled Low Scatter Mirrors." AFRPL-TR-73-52, Wright-Patterson Air Force Base, Dayton, Ohio.
3. Herzberger, M. and Salzberg, C. D. "Refractive Indices of Infrared Optical Materials and Color Correction of Infrared Lenses." Journal of the Optical Society of America, Vol. 52, No. 4, April 1962, pp. 420-426.
4. Vasicek, A. Optics of Thin Films. North-Holland Publishing Company, Amsterdam, 1960.
5. Mielenz, K. D., Eckerle, K. L., Madden, R. P., and Reader, J. "New Reference Spectrophotometer." Applied Optics, Vol. 12, No. 7, July 1973, pp. 1630-1641.

6. Speranskaya, N. I., Berdnikov, N. B., and Furtova, A. Z. "High-Accuracy Measurements of Spectral Transmittance." Optical Technology, Vol. 40, No. 3, March 1973, pp. 145-147.
7. Kizer, K. L. and Scott, M. W. "Semiconductor Impurity Measurements." Research/Development Magazine, December 1974, pp. 20-24.
8. Seiber, B. A., Smith, A. M., Wood, B. E., and Müller, P. R. "Refractive Indices and Densities of H<sub>2</sub>O and CO<sub>2</sub> Films Condensed on Cryogenic Surfaces." Applied Optics, Vol. 10, No. 9, September 1971, pp. 2086-2089.
9. Marcoux, J. E. "Indices of Refraction of Some Gases in the Liquid and Solid State." Journal of the Optical Society of America, Vol. 59, No. 8, August 1969, pp. 998.
10. Randall, C. M. and Rawcliffe, R. D. "Refractive Indices of Germanium, Silicon, and Fused Quartz in the Far Infrared." Applied Optics, Vol. 6, No. 11, November 1967, pp. 1889-1895.
11. Plyler, E. K. and Peters, C. W. "Wavelengths for Calibration of Prism Spectrometers." Journal of the National Bureau of Standards, Vol. 45, No. 6, December 1950.
12. Plyler, E. K., Blaine, L. R., Nowark, M. "Reference Wavelengths for Calibrating Prism Spectrometers." Journal of Research of the National Bureau of Standards, Vol. 58, No. 4, April 1957, pp. 195-200.
13. Hannah, R. W. and Farnum, R. J. "Polystyrene as an Infrared Standard." Perkin-Elmer Infrared Applications Study 12, Order No. IRAS-12, May 1973.
14. Linsteadt, G. F. and Leet, H. P. "The Infrared Transmission of Cooled Optical Materials." Proceedings of the IRIS, 6, No. 3, 1961.
15. Anon. "Tables of Wavenumbers for the Calibration of Infrared Spectrometers." Pure and Applied Chemistry, Vol. 1, No. 4, 1960, pp. 537.
16. Honig, R. E. and Hook, H. O. "Vapor Pressure Data for Some Common Gases." RCA Review, Vol. 21, No. 3, September 1960.

17. Staats, P. A. and Morgan, H. W. "Infrared Spectra of Solid Ammonia." Journal of Chemical Physics, Vol. 31, No. 2 August 1959, pp. 553-554.
18. Reding, F. P. and Hornig, D. F. "The Vibrational Spectra of Molecules and Complex Ions in Crystals. V. Ammonia and Deutero-Ammonia." Journal of Chemical Physics, Vol. 19, No. 5, May 1951, pp. 594-601.
19. Houghton, J. T. and Smith, S. D. Infrared Physics. Clarendon Press, Oxford, 1966, p. 77.
20. Arnold, F. "Degradation of Low Scatter Metal Mirrors." AEDC-TR-75-128 (AD-B007022L), October 1975.
21. Jaing, G. J., Person, W. B., and Brown, K. G. "Absolute Infrared Intensities and Band Shapes in Pure Solid CO and CO in Some Solid Matrices." Journal of Chemical Physics, Vol. 62, No. 4, February 1975, pp. 1201-1211.
22. Herzberg, G. Infrared and Raman Spectra of Polyatomic Molecules. D. Van Nostrand Company, Inc., Princeton, New Jersey, 1954.
23. Heavens, O. S. Optical Properties of Thin Solid Films. Academic Press, New York, 1955.
24. Robertson, C. W., Downing, H. D., Curnutte, B., and Williams, W. "Optical Constants of Solid Ammonia in the Infrared." Journal of the Optical Society of America, Vol. 65, No. 4, April 1975, pp. 432-435.



where:

$$\tau = 1 - \rho$$

$$\alpha_2 = \frac{4\pi k_2}{\lambda}$$

$I_0$  is monochromatic normal incidence beam of wavelength  $\lambda$ .

Energy Transmitted =  $T$

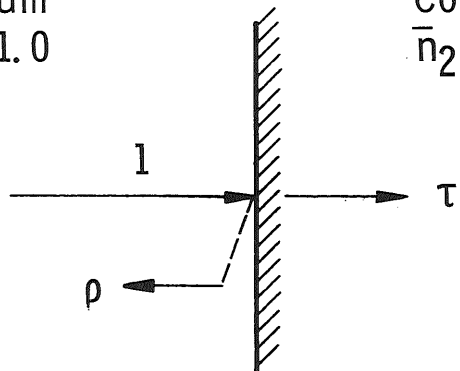
$$T = \tau^2 e^{-\alpha_2 D} \left[ 1 + \rho^2 e^{-2\alpha_2 D} + \rho^4 e^{-4\alpha_2 D} + \dots \right]$$

$$T = \frac{\tau^2 e^{-\alpha_2 D}}{1 - \rho^2 e^{-2\alpha_2 D}} = \frac{(1 - \rho)^2 e^{-\alpha_2 D}}{1 - \rho^2 e^{-2\alpha_2 D}}$$

Figure 1. Analytical model for transmission through a plane-parallel slab.



Vacuum  
 $n_0 = 1.0$



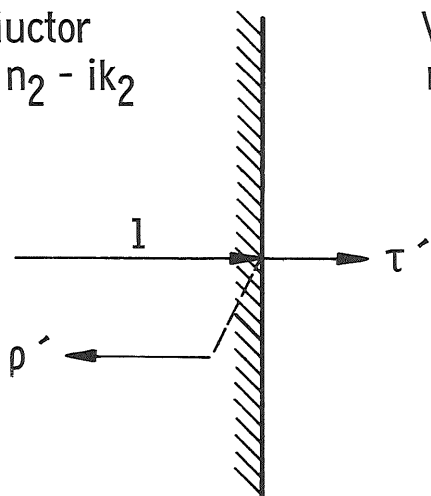
Conductor  
 $\bar{n}_2 = n_2 - ik_2$

$$\rho = \left| \left( \frac{\bar{n}_2 - 1}{\bar{n}_2 + 1} \right) \right|^2 \quad \text{Intensity}$$

$$r = \frac{\bar{n}_2 - 1}{\bar{n}_2 + 1} \quad \text{Amplitude}$$

$$\tau = 1 - \rho$$

Conductor  
 $\bar{n}_2 = n_2 - ik_2$



Vacuum  
 $n_0 = 1.0$

$$\rho' = \left| \left( \frac{1 - \bar{n}_2}{1 + \bar{n}_2} \right) \right|^2 \quad \text{Intensity}$$

$$r' = \frac{1 - \bar{n}_2}{1 + \bar{n}_2} \quad \text{Amplitude}$$

Figure 2. Analytical model for transmission through an interface.

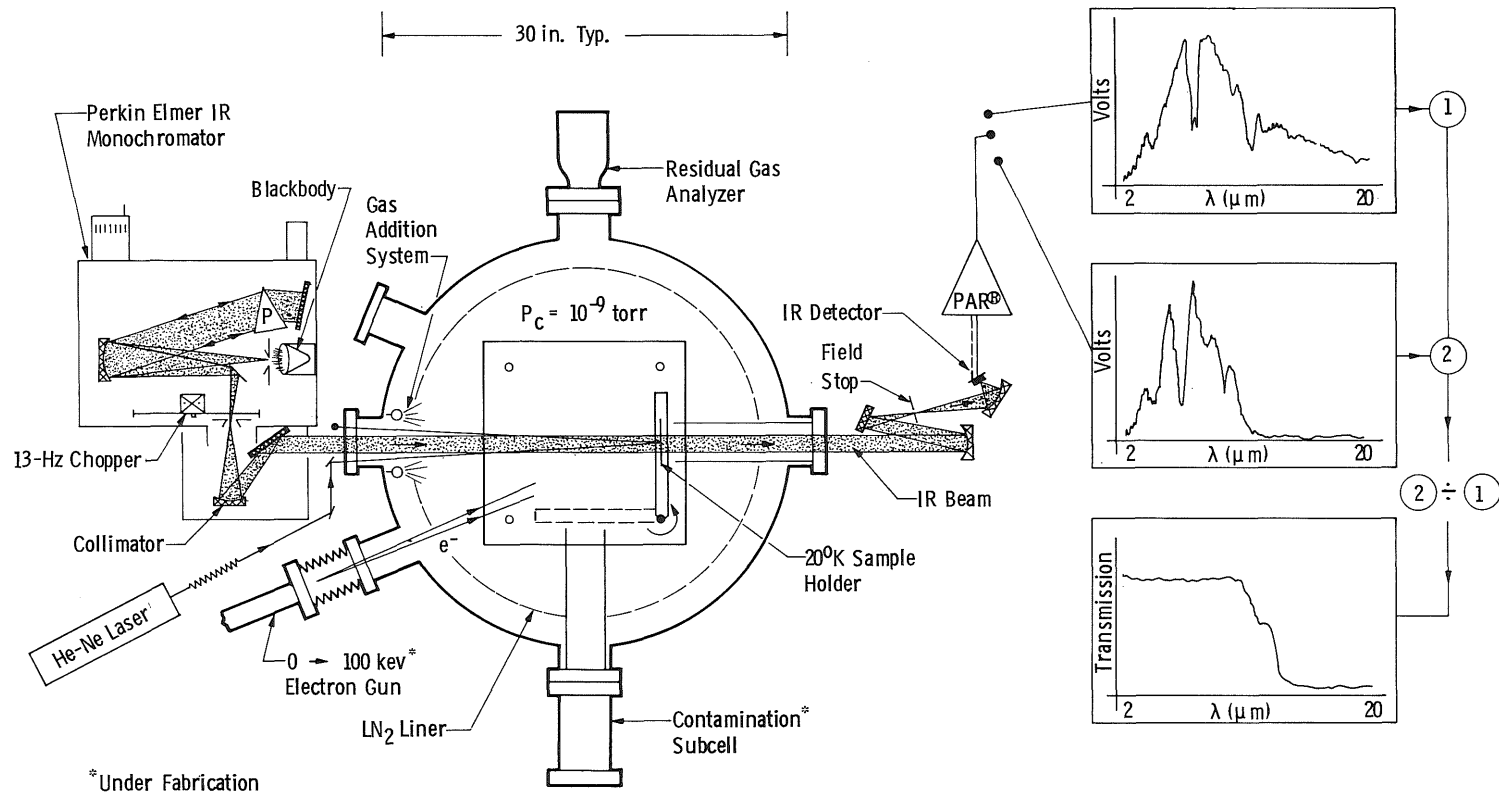


Figure 3. Plan view of IROTC chamber with Perkin-Elmer 99.

1. Infrared beam, 38-mm-diameter (1.5 in.).
2. Optical stop required to underfill cryo-cooled window with infrared beam. Also this stop is supported by a 3-in.-ID pipe that prevents gas added to chamber from cryopumping on rear of window.
3. Aluminum holder with cryogenic passageways.
4. Infrared window heat sunk with an indium gasket to the aluminum holder.
5. Cover plate.
6. Gaseous helium or liquid nitrogen inlet.
7. Gaseous helium or liquid nitrogen outlet.
8. Crosshatched area illustrates area of window heat sunk to holder. Clear diameter is 50.7 mm (2 in.) while infrared beam diameter is 38 mm (1.5 in.).

Note: Polystyrene is sandwiched between two 4-mm-thick by 70-mm-square salt windows. The salt is heat sunk to the aluminum holder by 0.254-mm-thick indium gaskets.

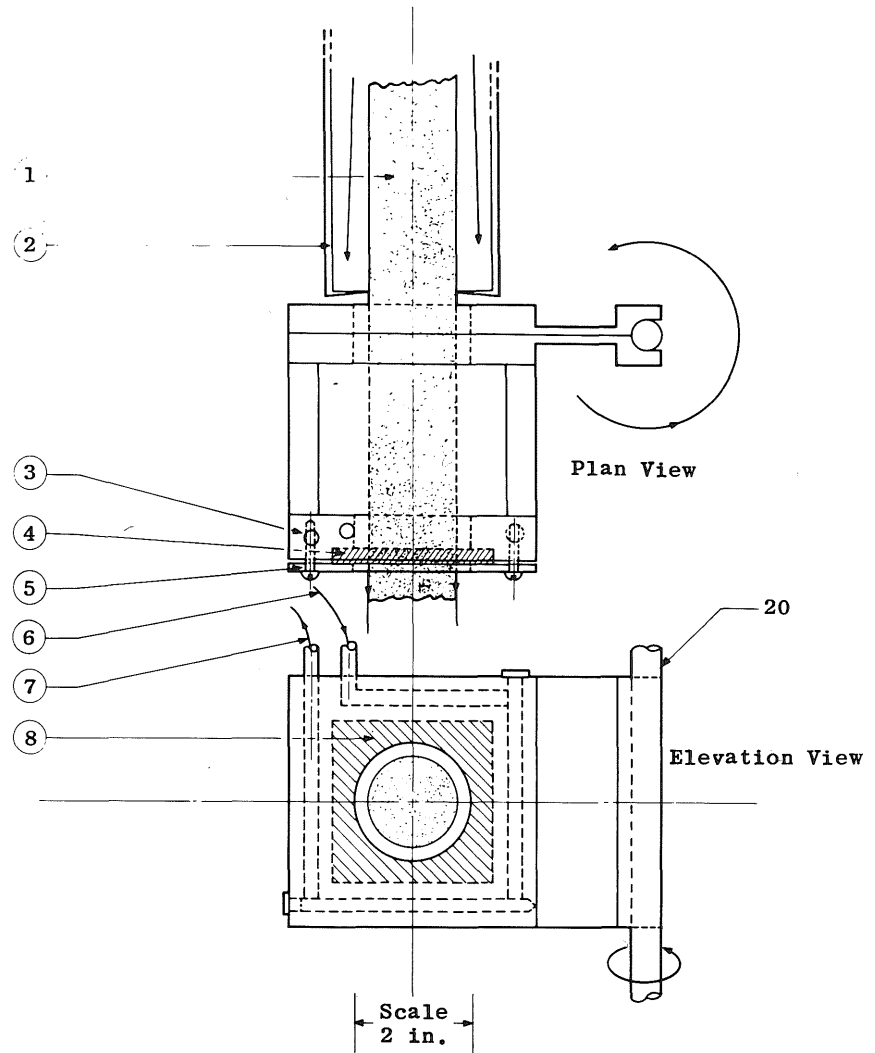
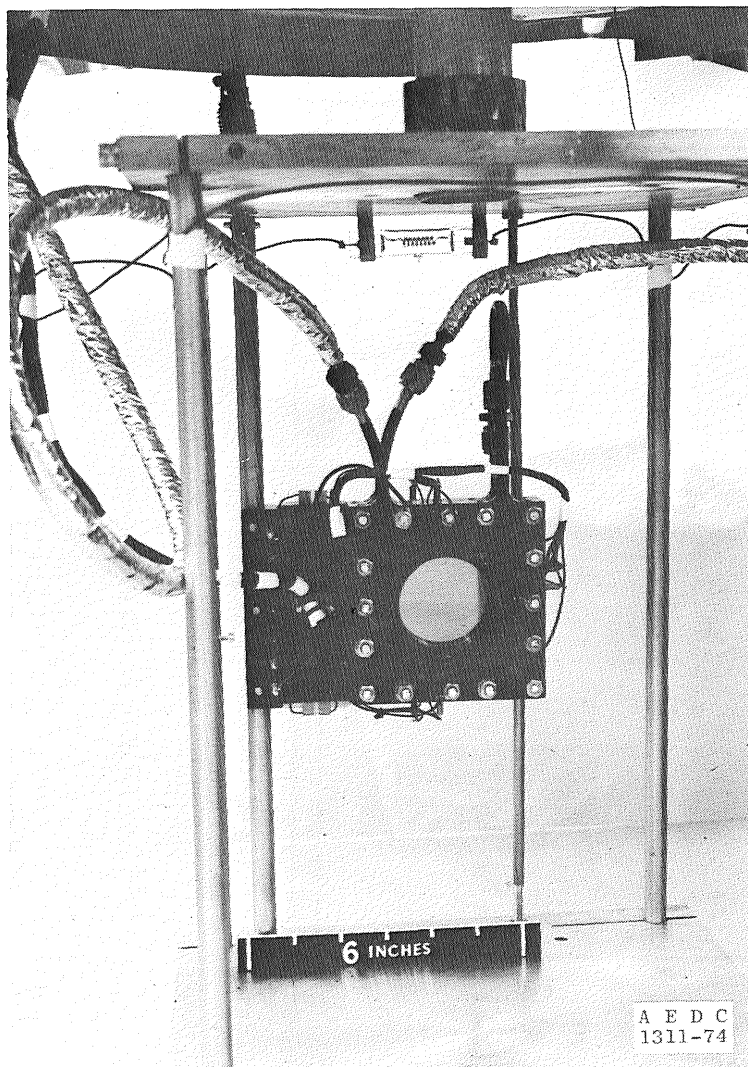
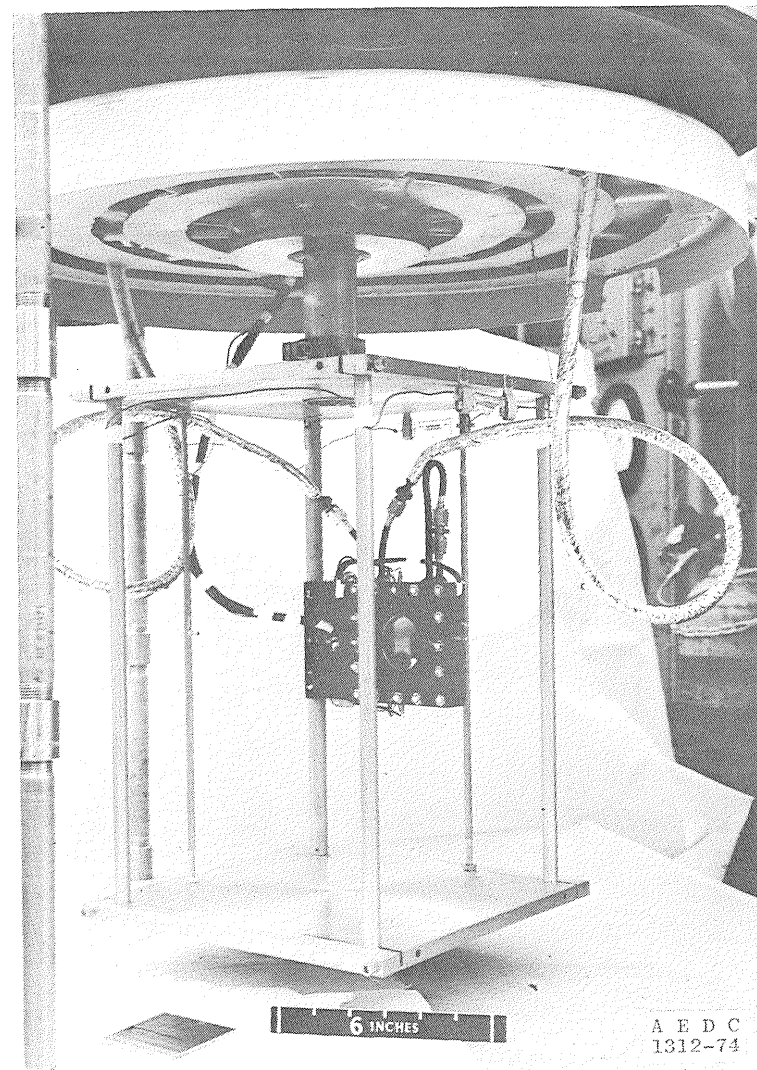


Figure 4. Plan and elevation views of cryogenically cooled window holder.



a. Cryogenic holder



b. Holder assembly

Figure 5. Photographs of cryogenic holder and holder assembly.

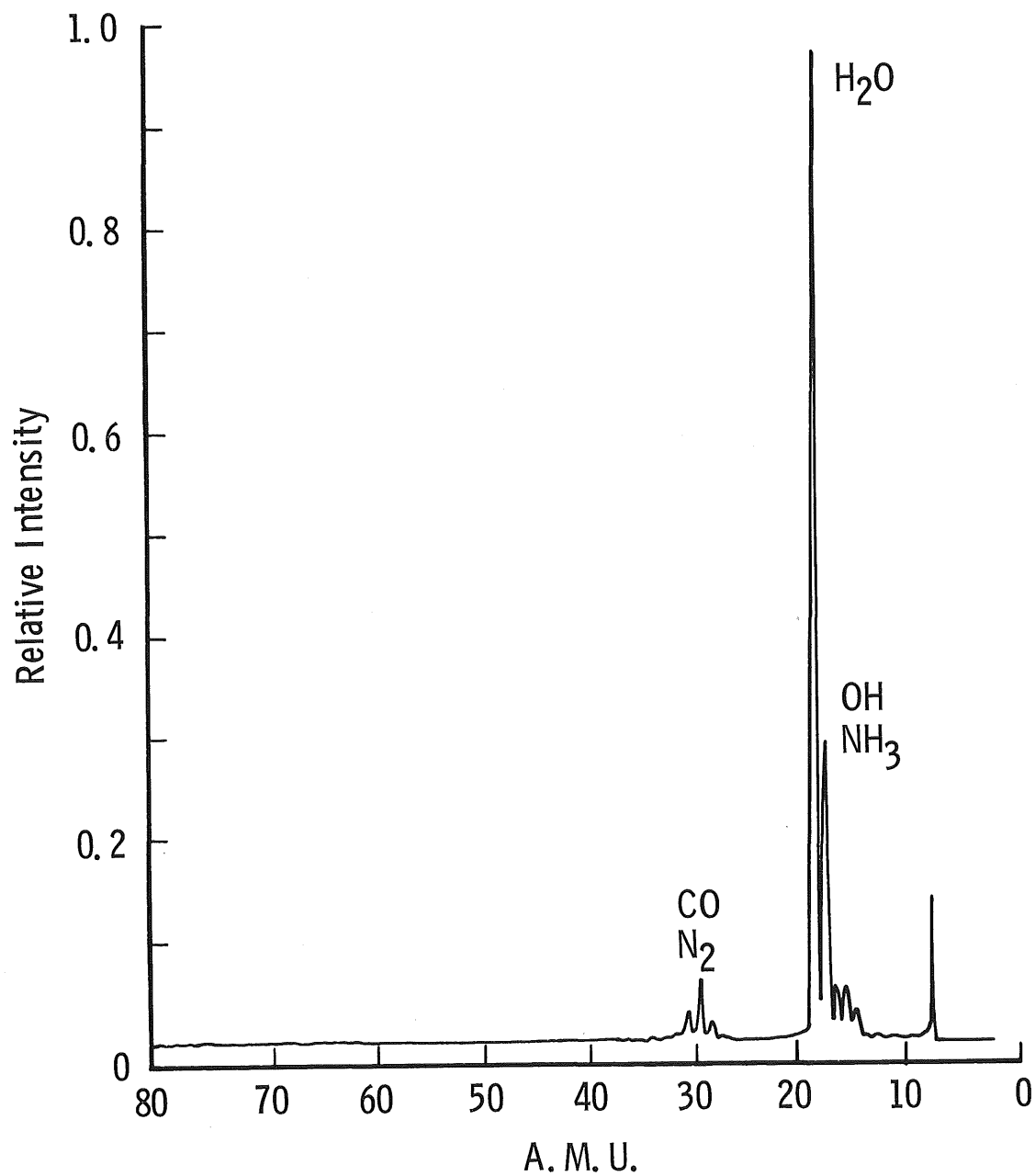
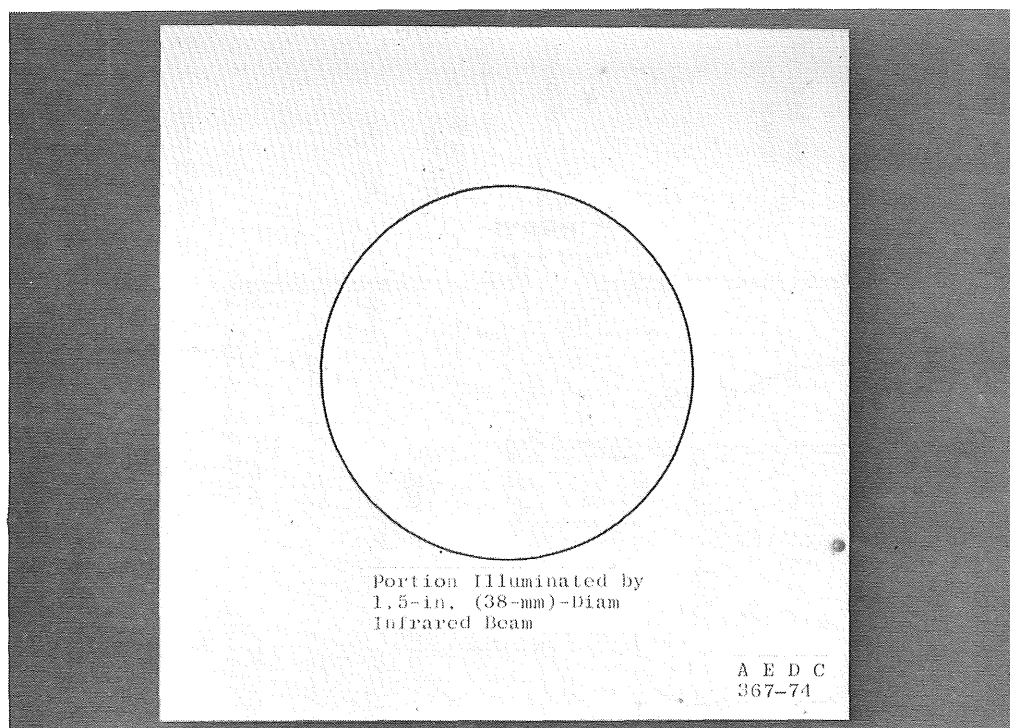
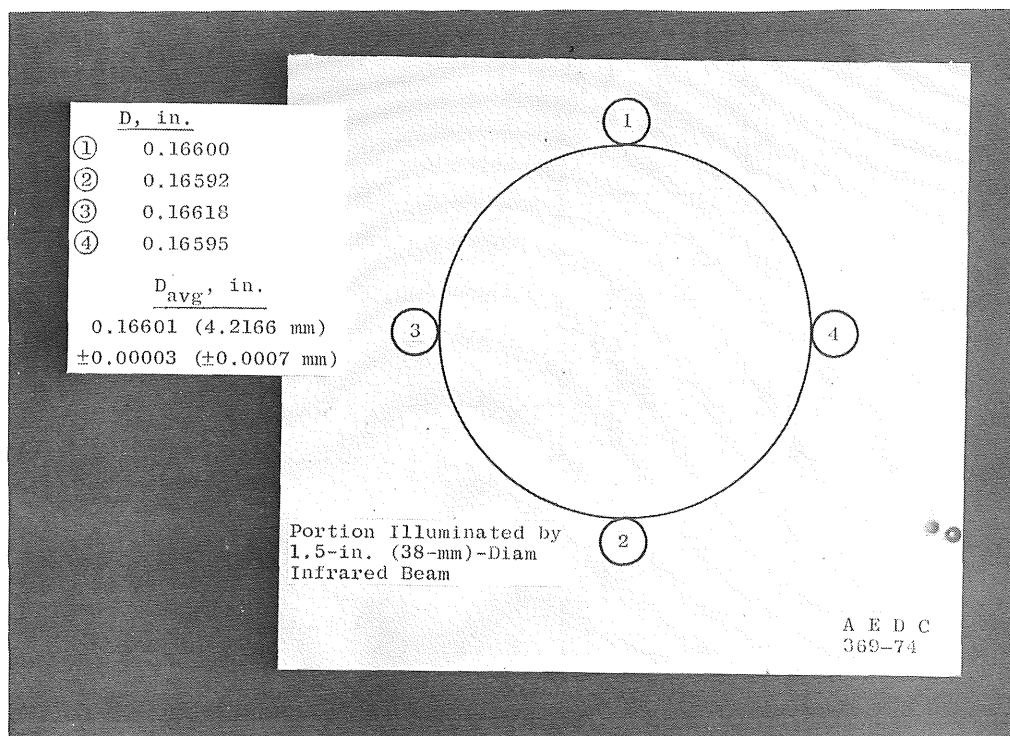


Figure 6. Residual gas analyzer scan.



a. One side



b. Opposite side

Figure 7. Results of surface figure test for a germanium window.

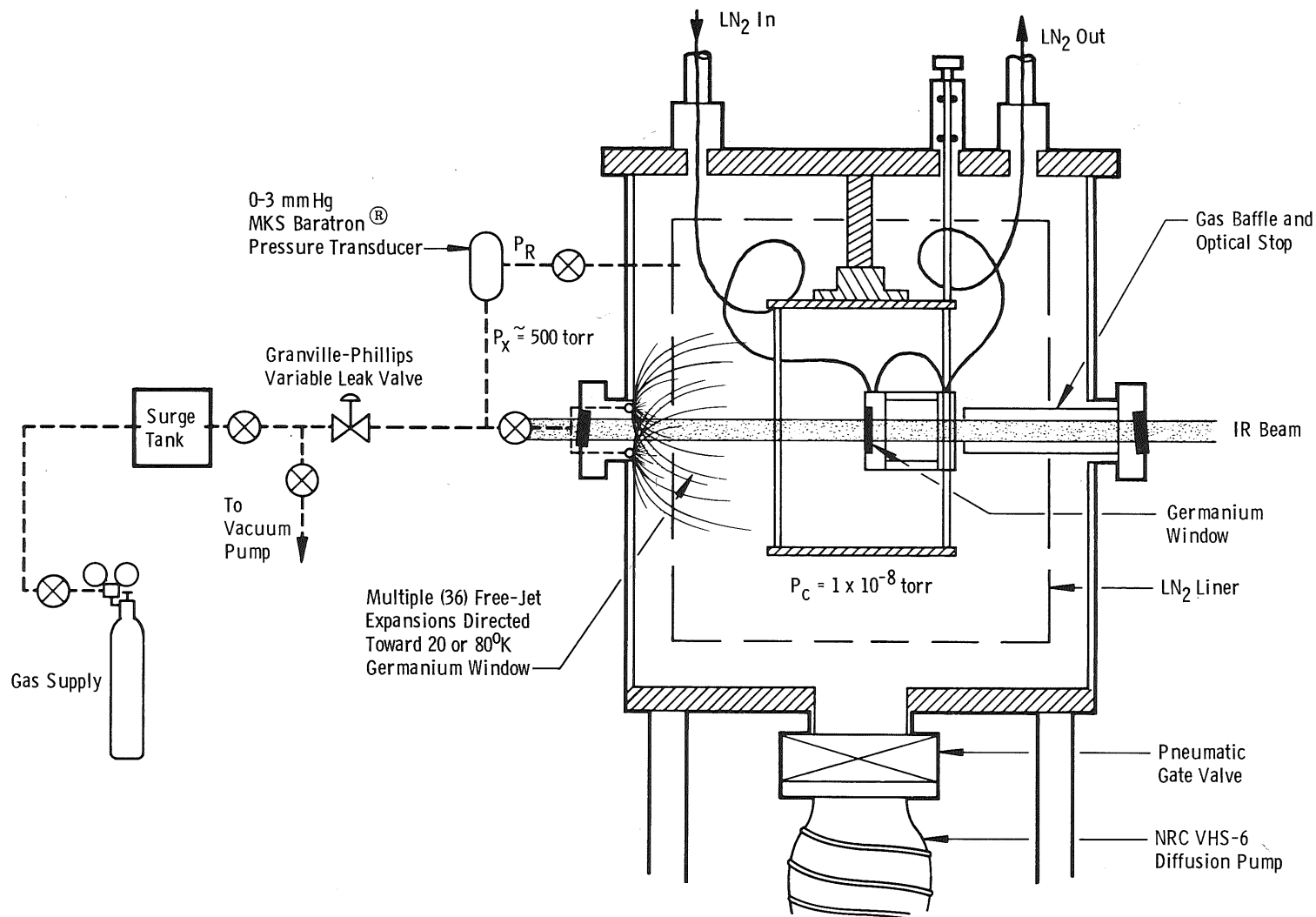
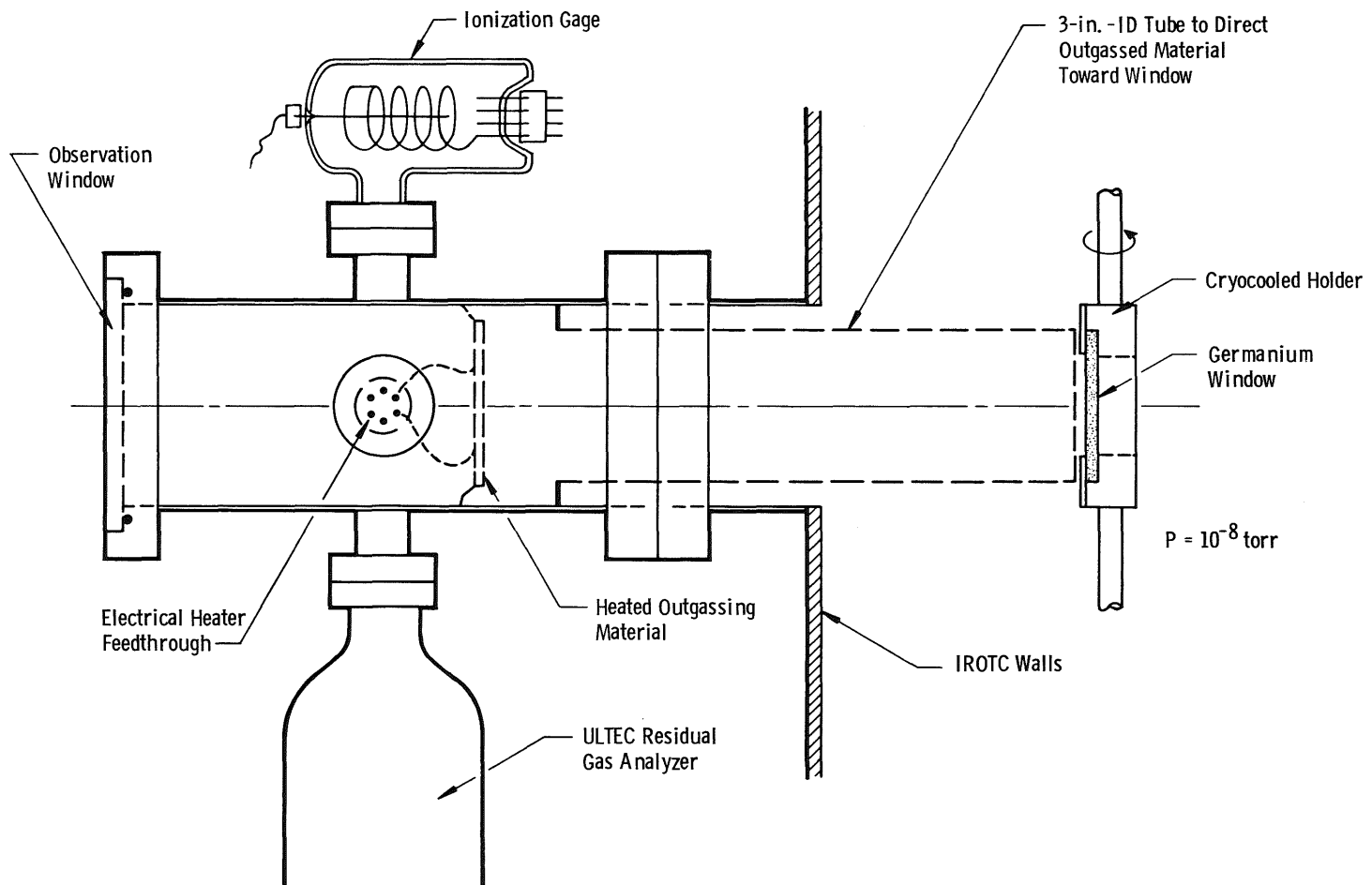
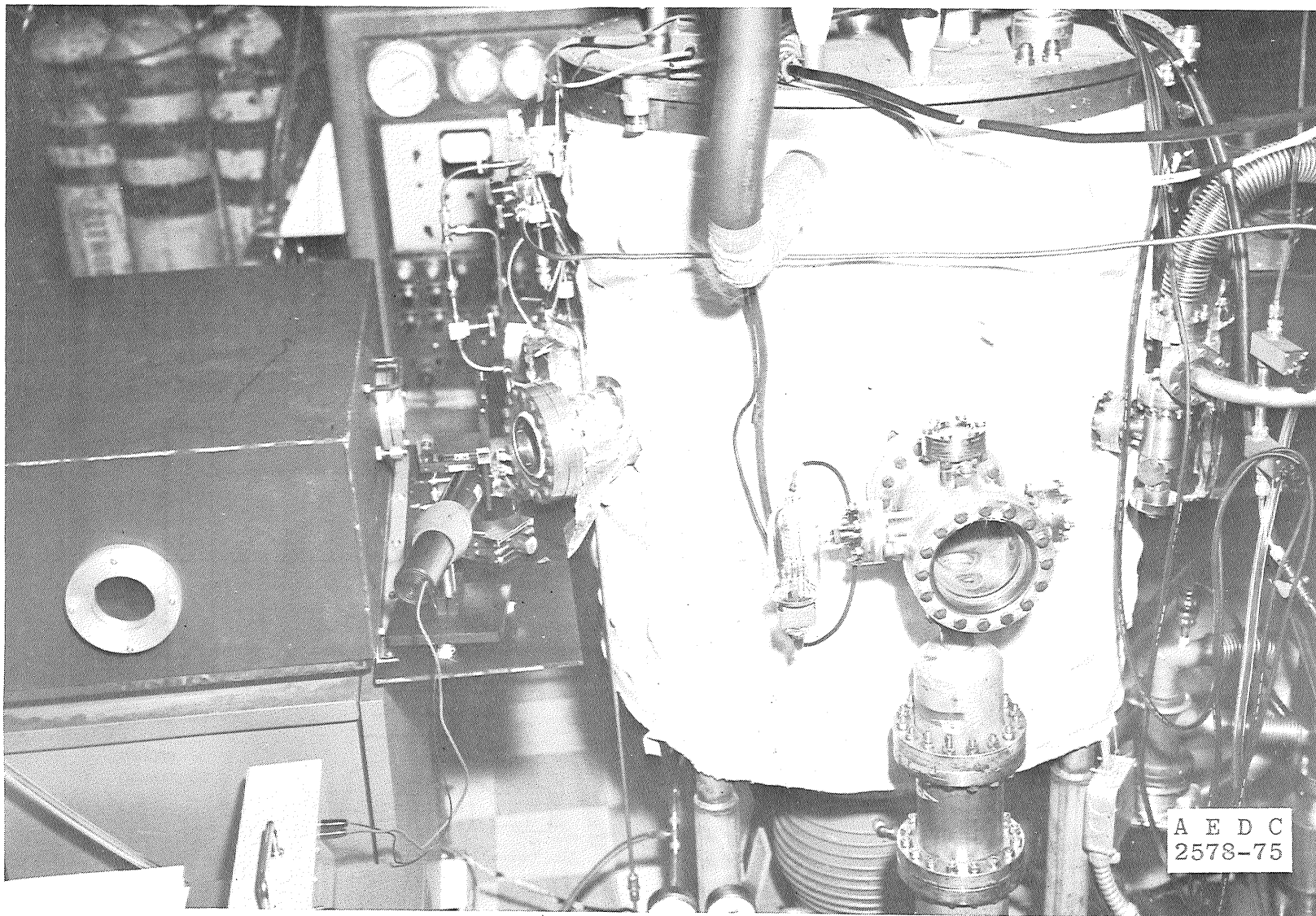


Figure 8. Gas induction system.

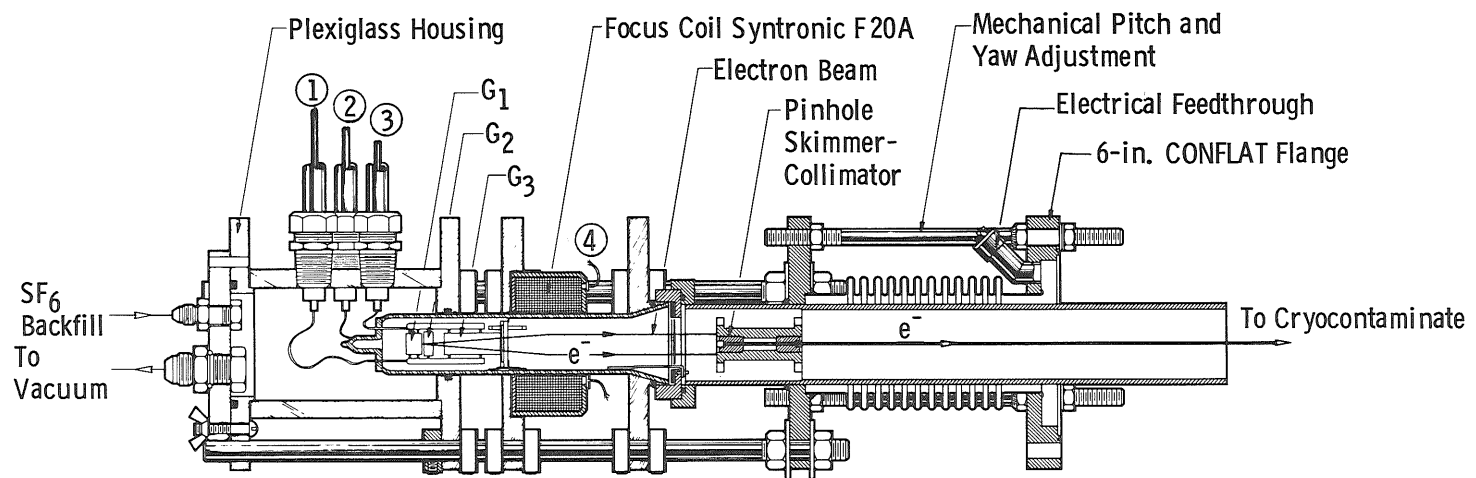


a. Sketch  
Figure 9. Contamination subcell

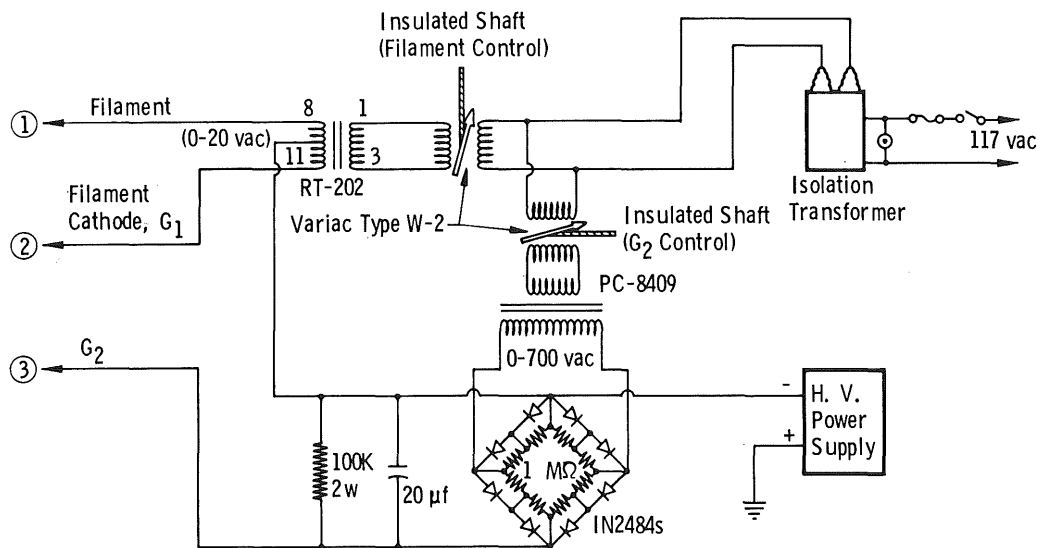




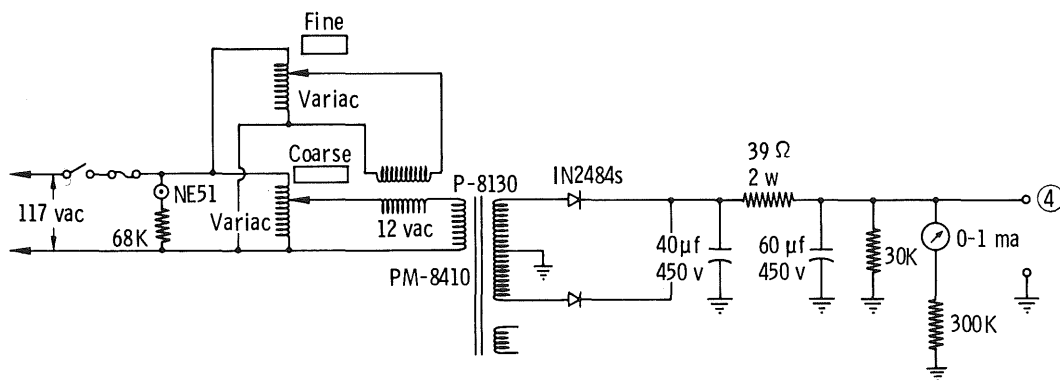
b. Photograph  
Figure 9. Concluded.



a. Assembly  
Figure 10. Electron gun



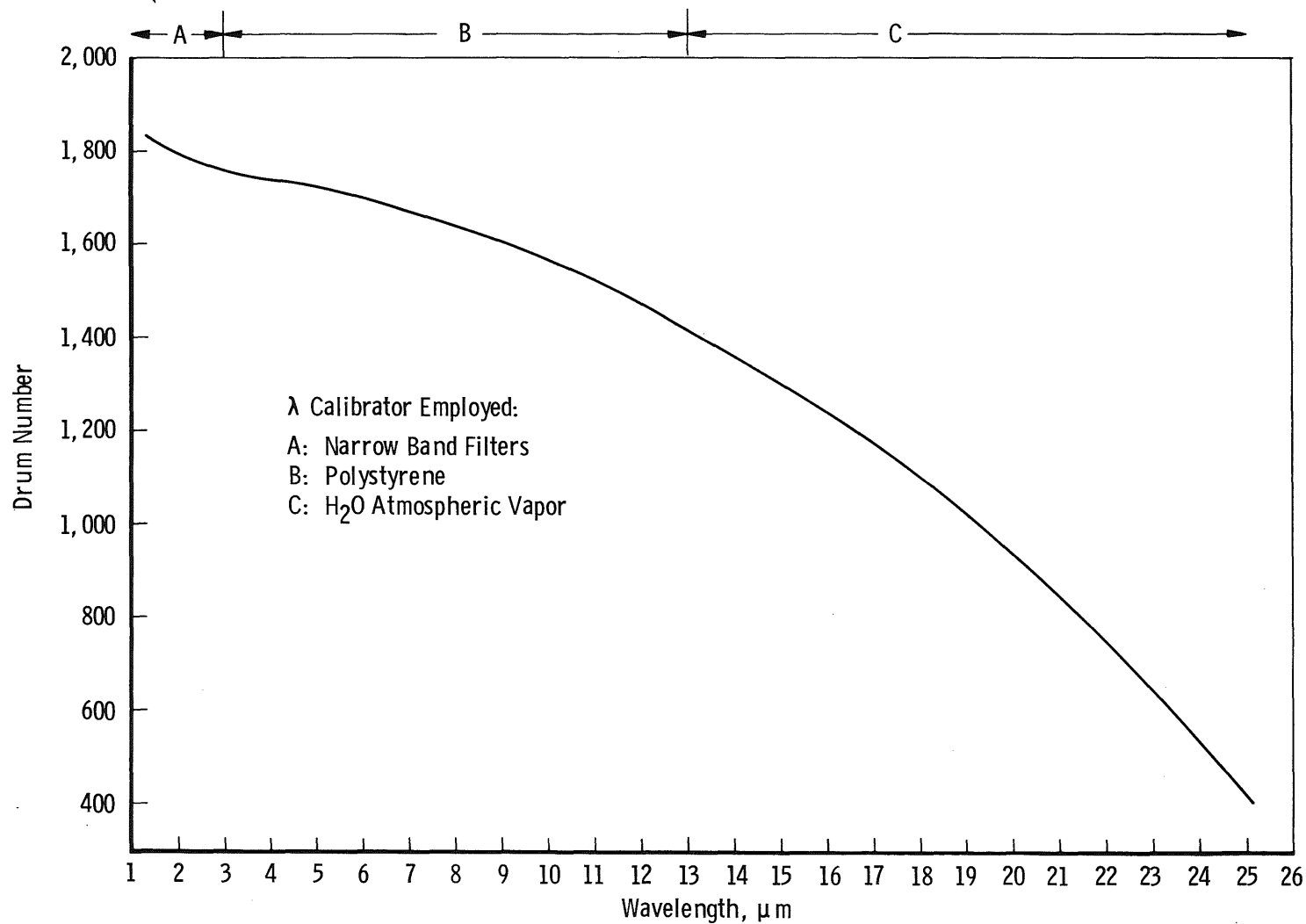
### Electron Gun High Voltage Supply



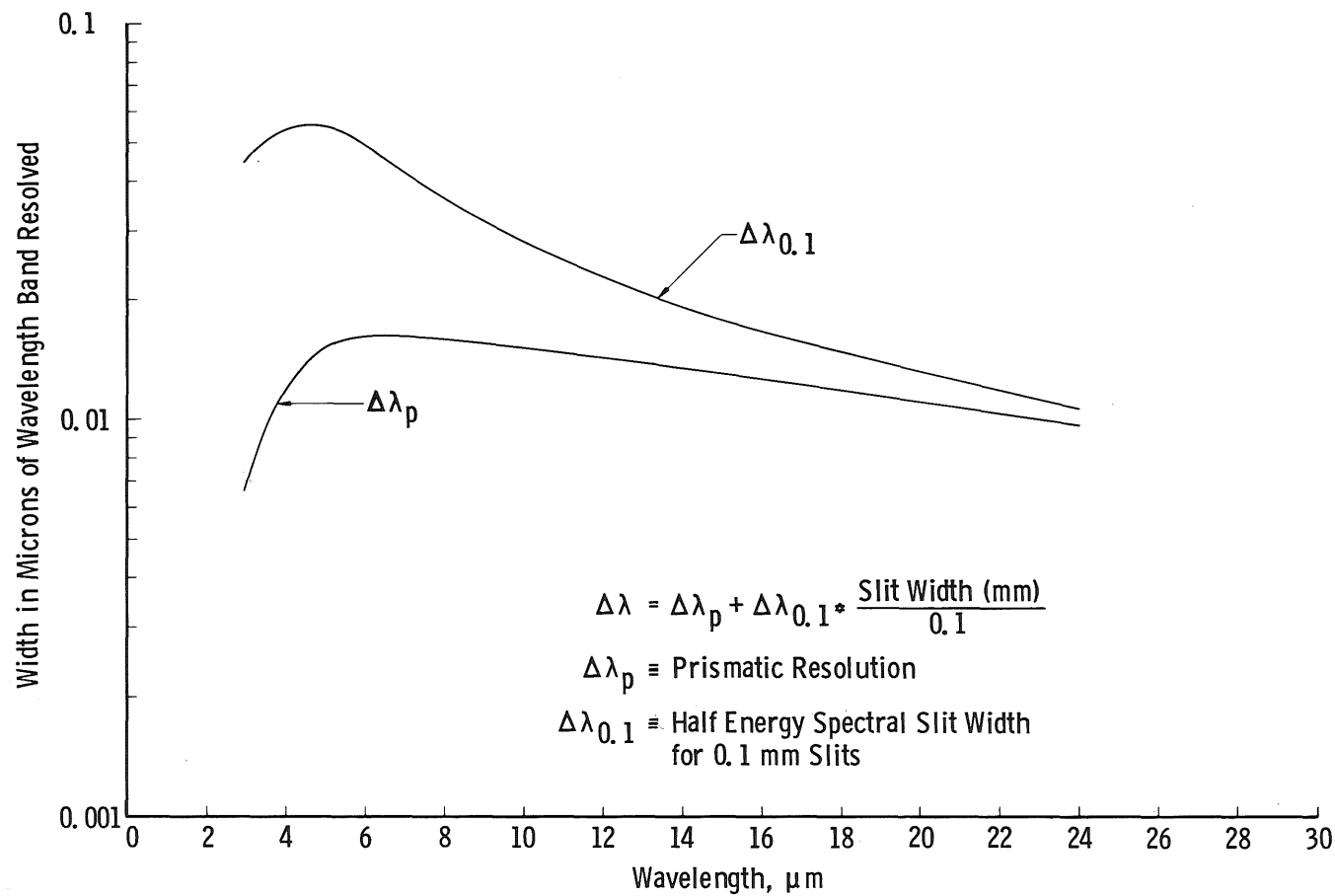
300-v Focus Power Supply 60 ma

### b. Electronics

**Figure 10. Continued.**



a. Drum number versus wavelength  
Figure 11. Calibration curves for KBr prism



b. Spectral resolution versus slit width  
Figure 11. Concluded.

1. Dry nitrogen purge box for infrared source.
2. Infrared source and collimator mirror.
3. KBr infrared window, 10 mm thick by 72 mm diameter (0.4-in. by 2.75-in. diameter).
4. Optical stop and also gas baffle.
5. LN<sub>2</sub>-cooled chamber liner.
6. Stainless-steel high-vacuum chamber, 85 cm tall by 70 cm diameter (33.5-in. by 27.5-in. diameter).
7. Cryogenically cooled optical component holder; either GHe (20°K) or LN<sub>2</sub> (80°K).
8. Observation port; 15-cm CONFLAT (6 in.).
9. Cryogenically cooled infrared window; usually germanium, 4 mm thick by 70 mm square (0.158 in. by 2.76 in.).
10. Helium-neon laser (0.6328- $\mu$ m) beam (one of two shown) employed to measure cryodeposit thickness.
11. Infrared beam, 38-mm diameter (1.5 in.).
12. Observation port; 15-cm CONFLAT (6 in.).
13. Gas addition header.
14. KBr infrared window, 10 mm thick by 72 mm diameter (0.4-in. by 2.75-in. diameter).
15. Observation port; He-Ne beam entry to chamber.
16. Hughes 1-mw He-Ne laser.
17. Michelson interferometer cube of Digilab FTS-14; KBr-germanium beamsplitter.
18. Collection optics of FTS-14.
19. Reduction optics and pyroelectric detector of FTS-14.
20. Contamination introduction subsystem.

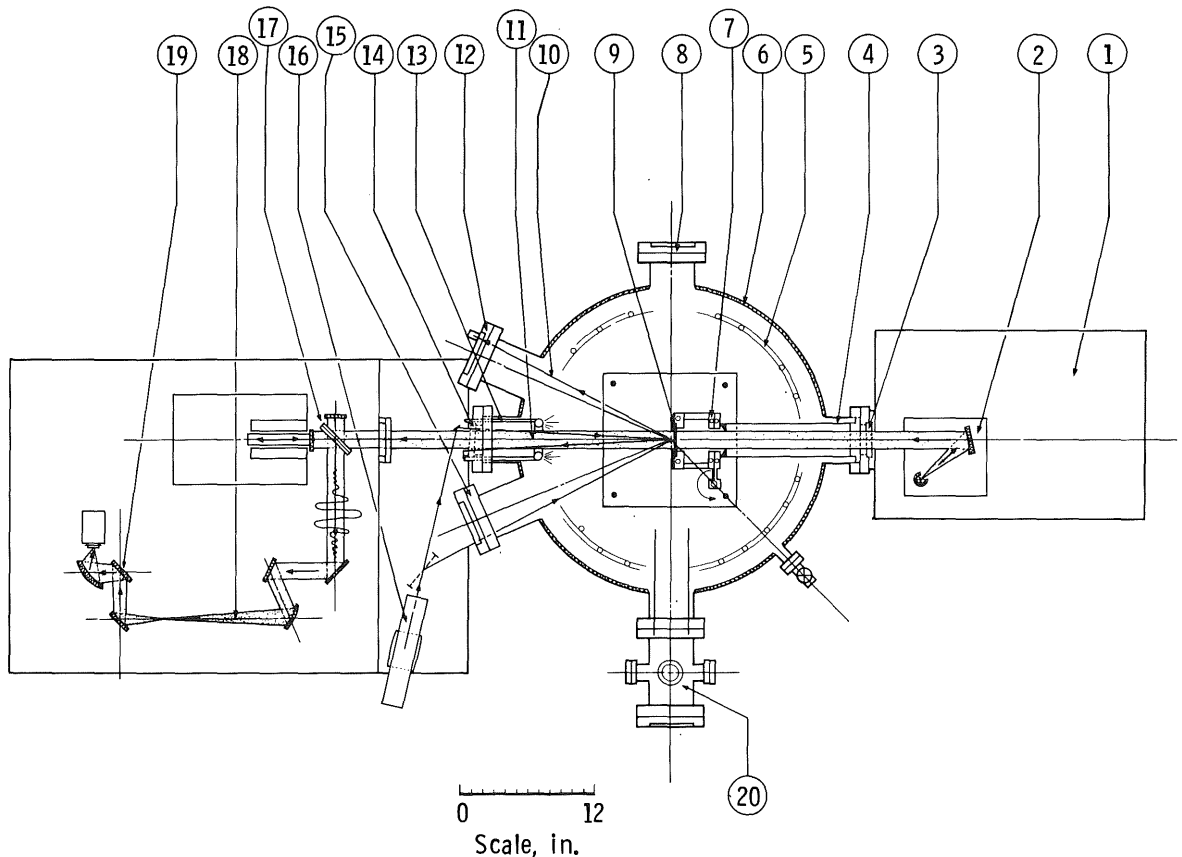


Figure 12. Plan view schematic of the infrared optical transmission chamber (IROT) with FTS interferometer.

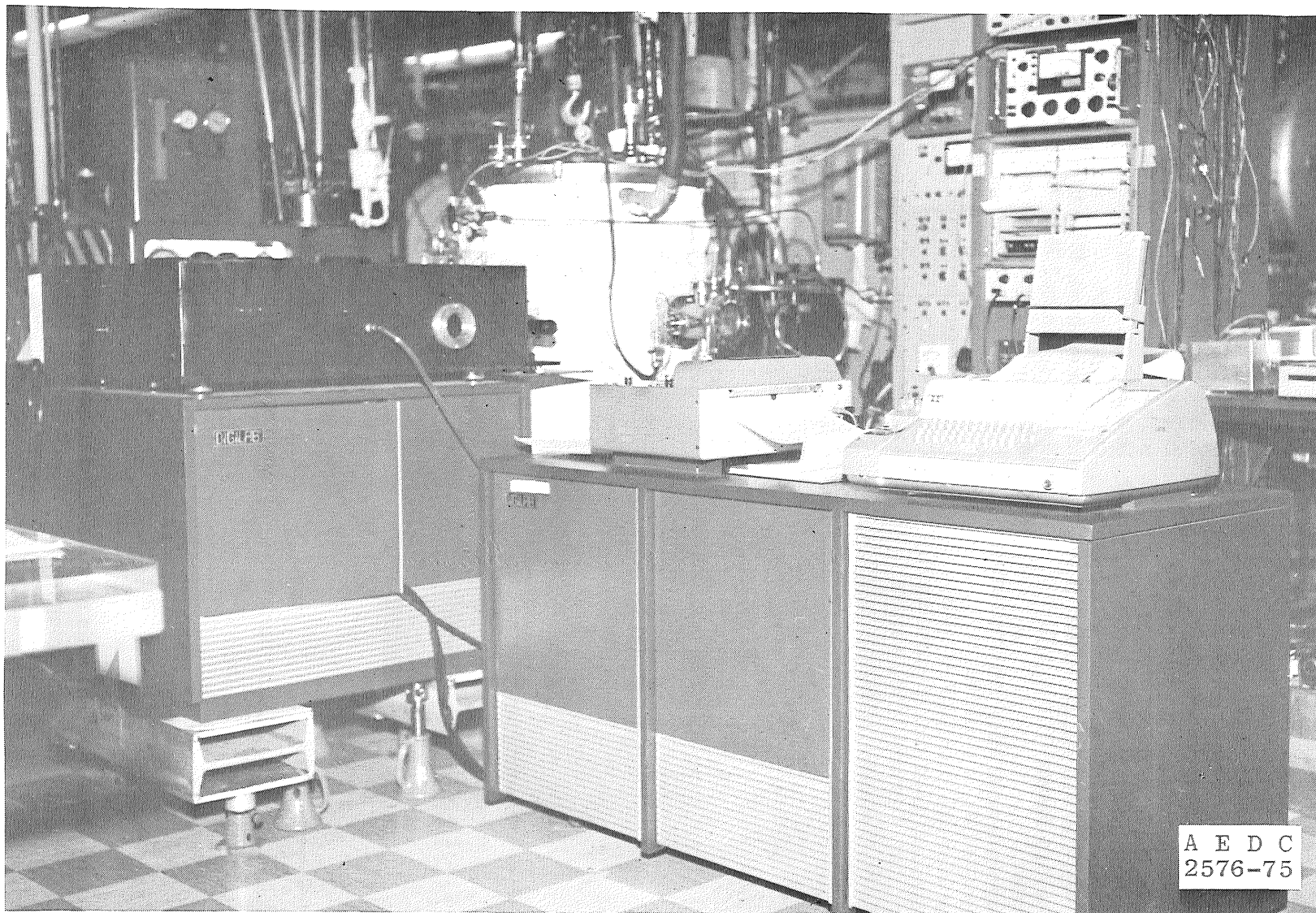


Figure 13. Photograph of FTS-14 interferometer-spectrometer.

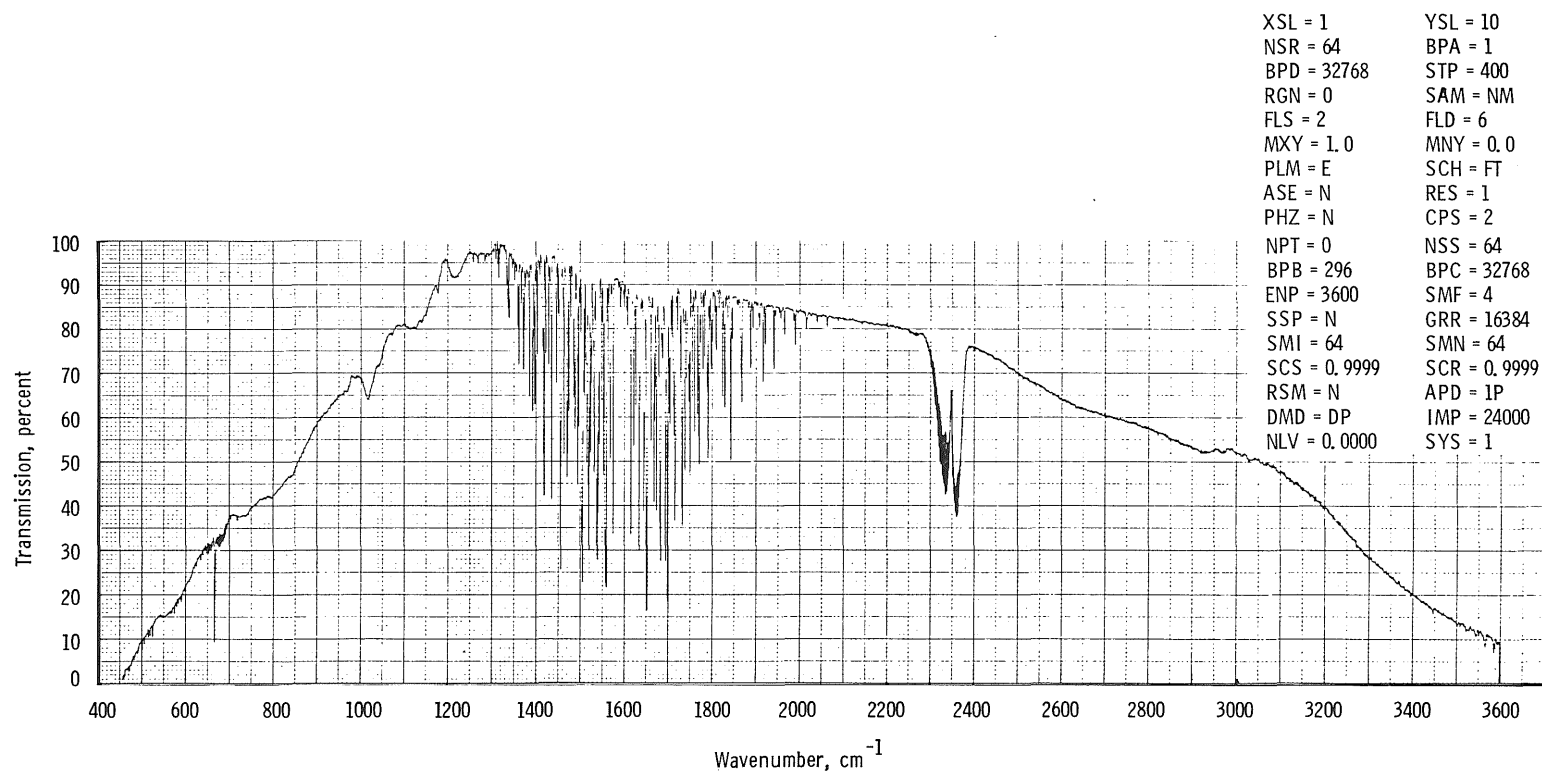


Figure 14. Radiation background scan for interferometer.



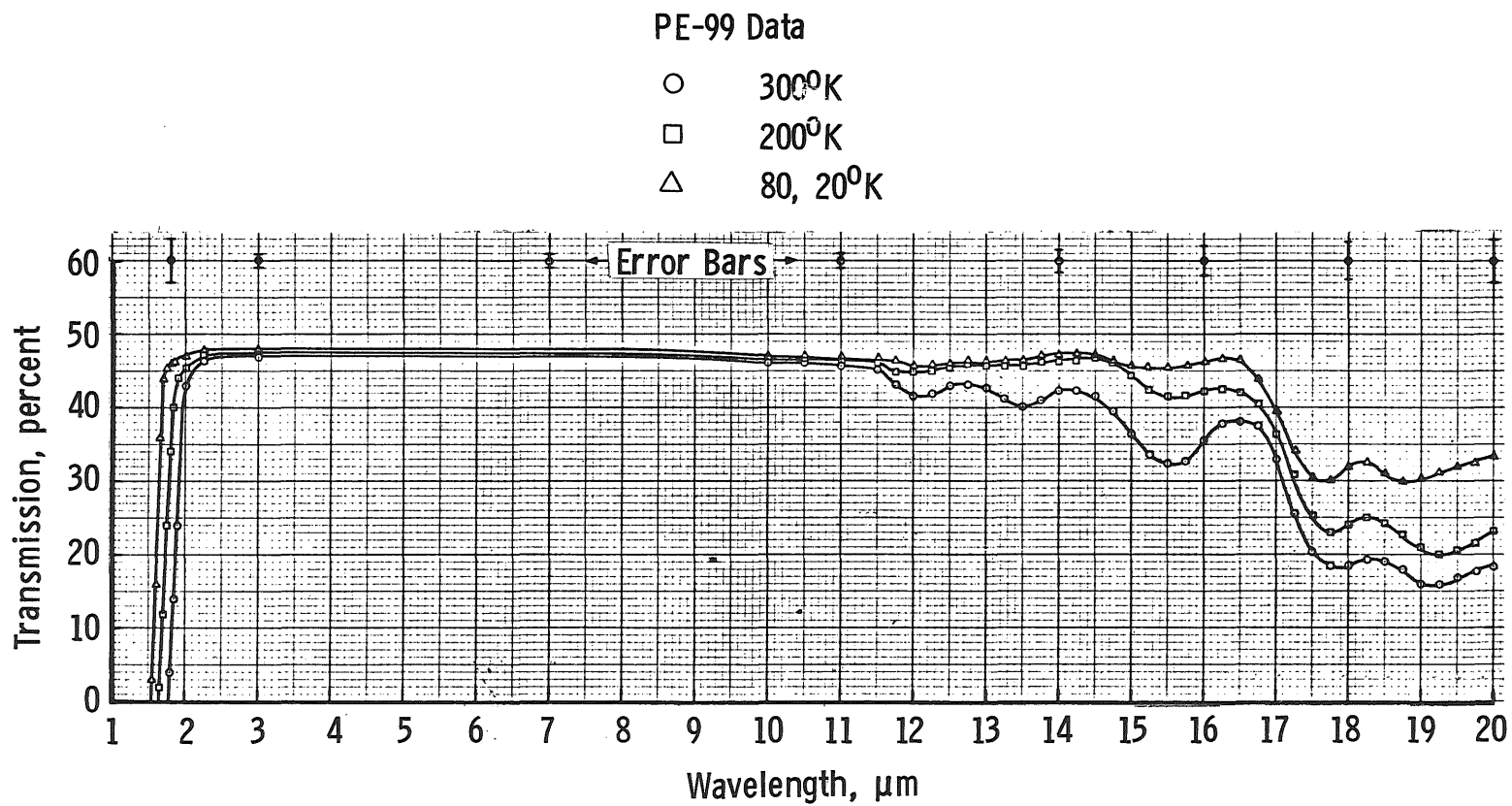


Figure 15. Infrared transmission of germanium as a function of temperature.

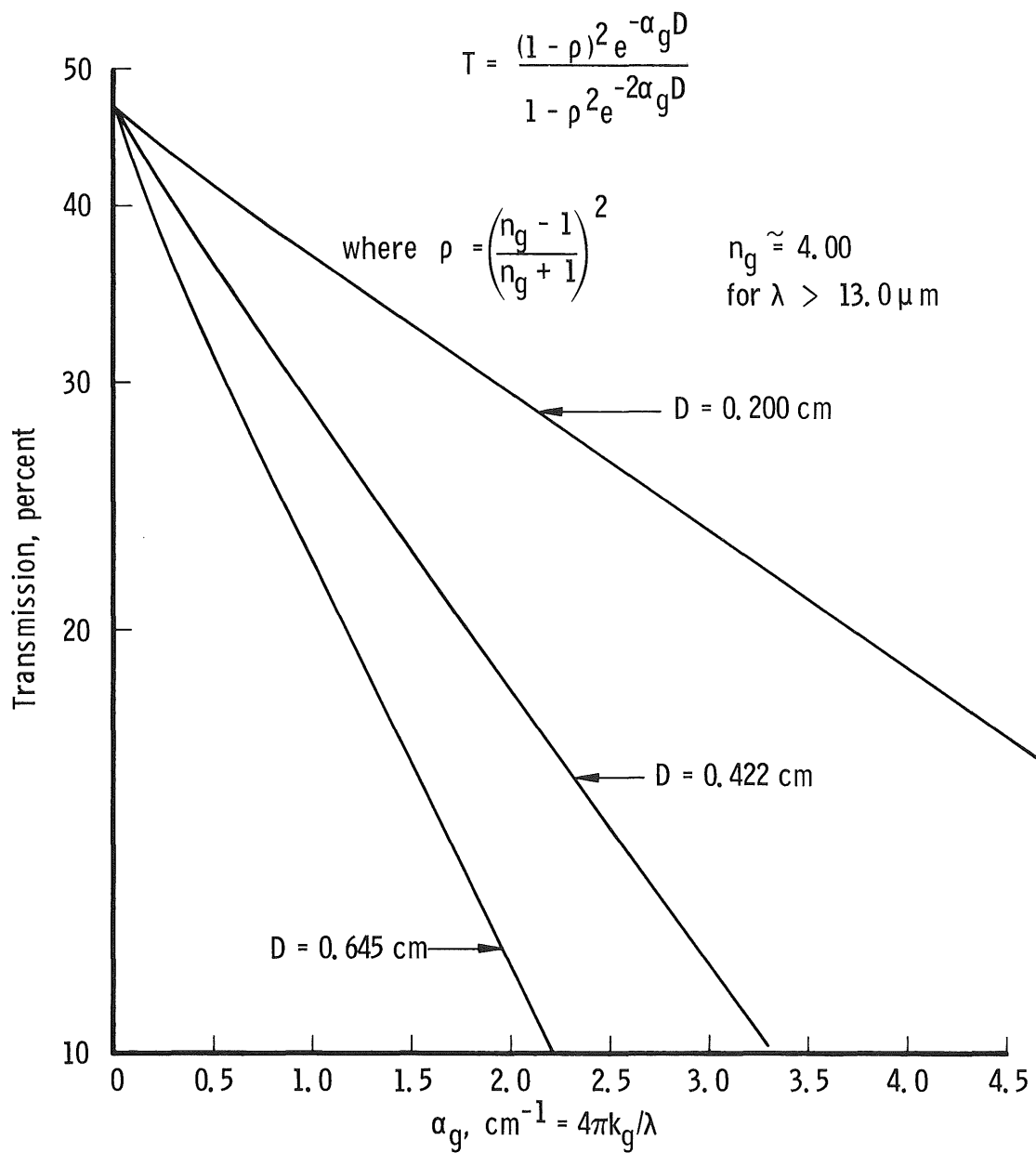


Figure 16. Transmission of germanium windows as a function of absorption coefficient with thickness as a parameter.

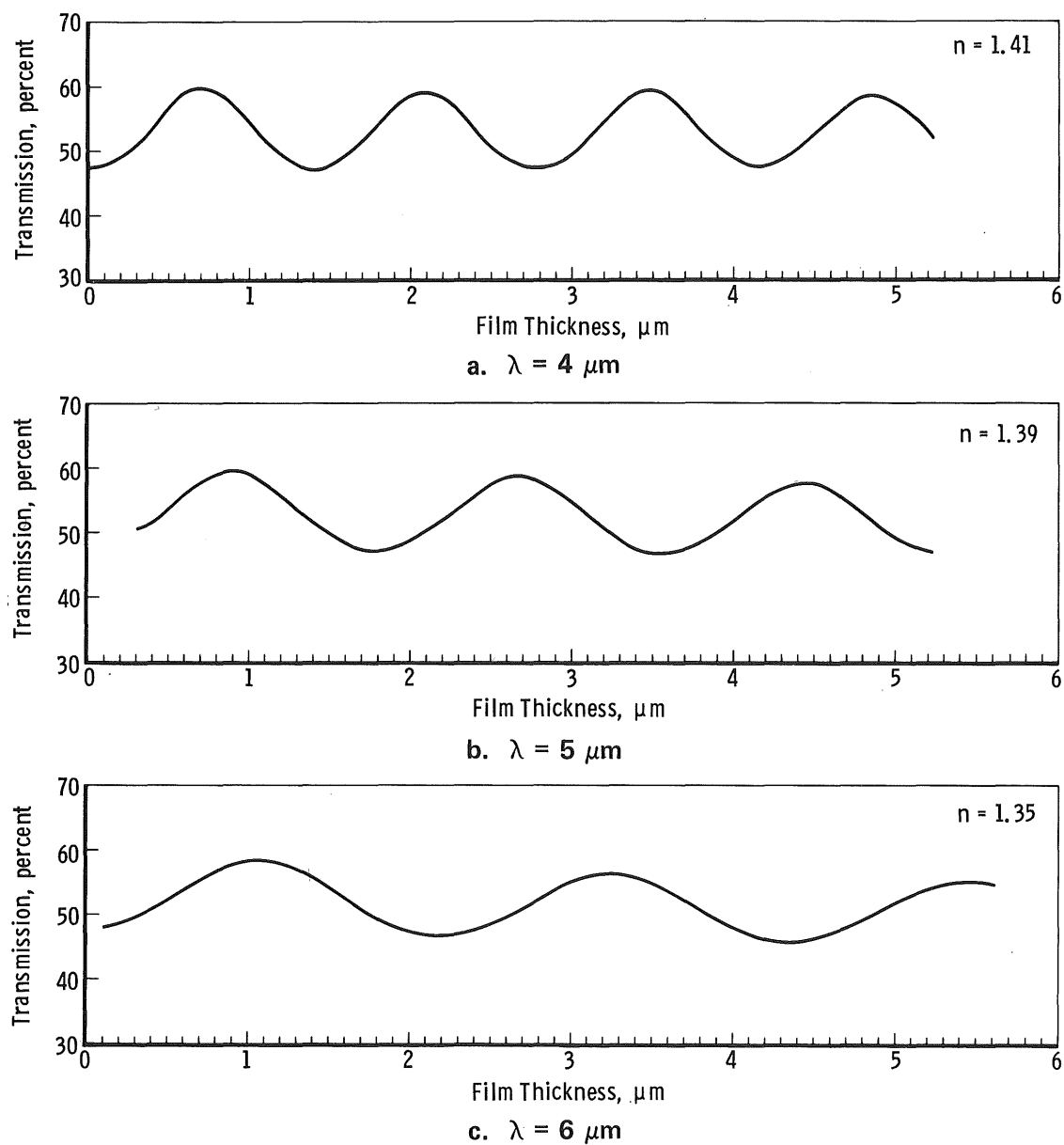
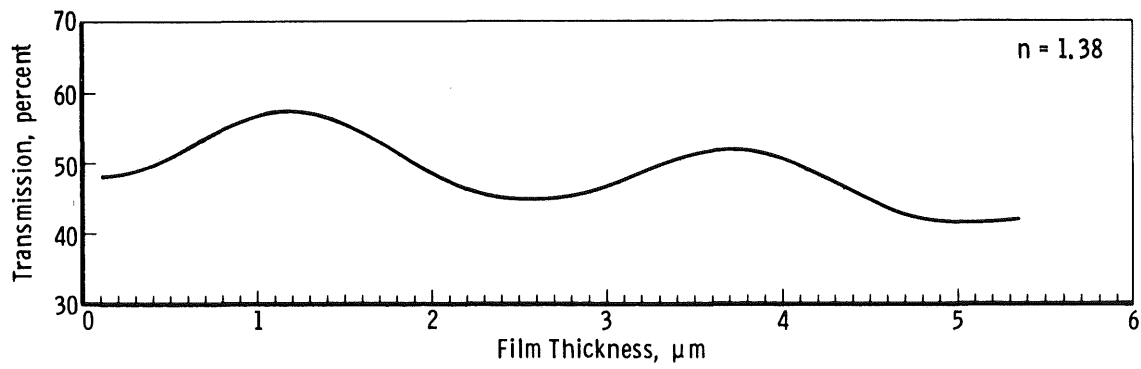
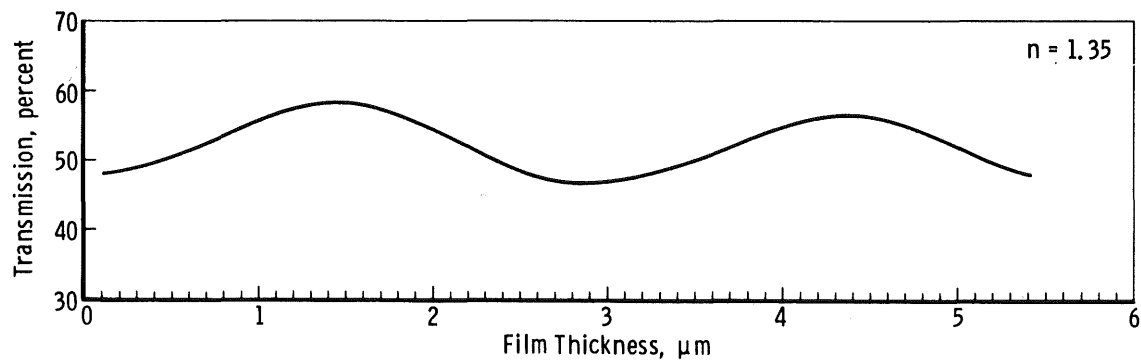


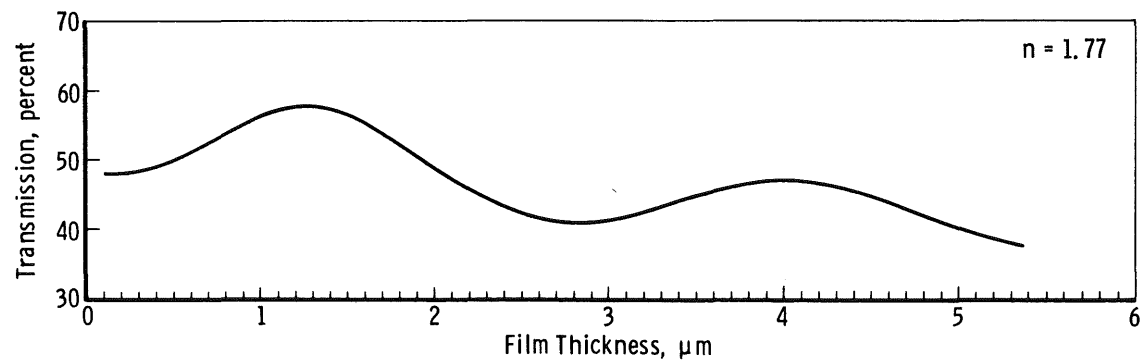
Figure 17. Transmission of an  $80^{\circ}\text{K}$  germanium window as a function of  $\text{NH}_3$  deposit thickness.



d.  $\lambda = 7 \mu\text{m}$



e.  $\lambda = 8 \mu\text{m}$



f.  $\lambda = 9.8 \mu\text{m}$

Figure 17. Concluded.

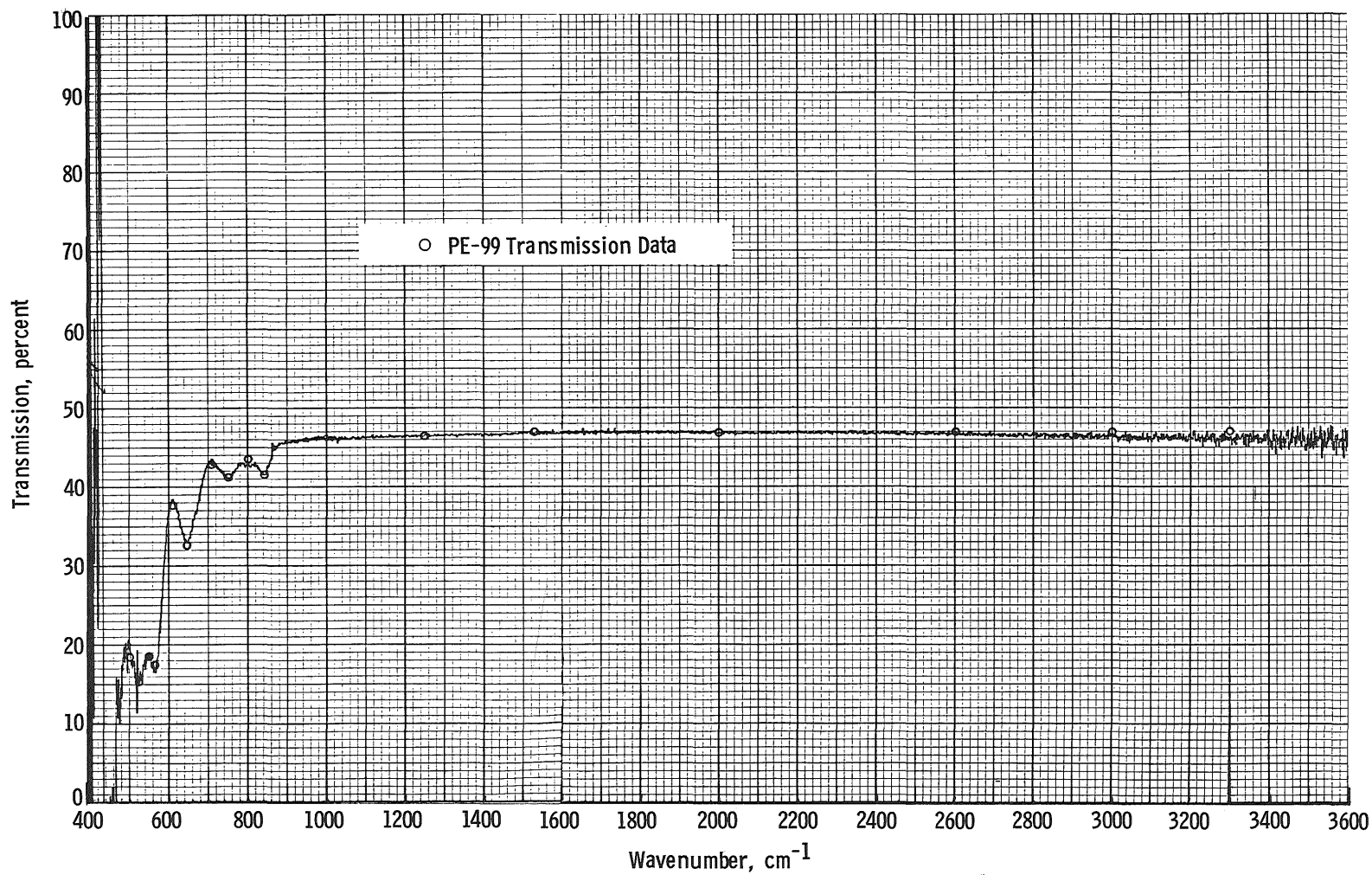


Figure 18. Transmission of 300°K germanium window measured with PE-99 and FTS-14.

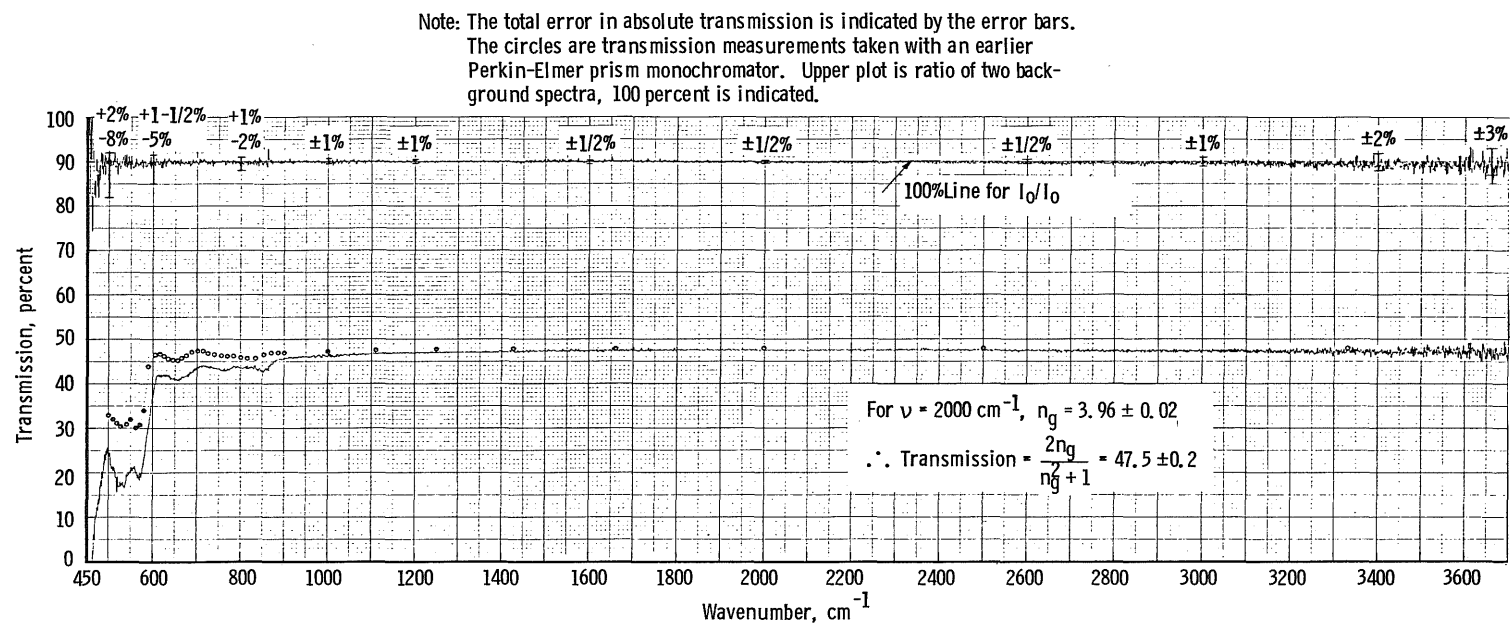


Figure 19. Transmission of an 80°K, 4-mm-thick germanium window.

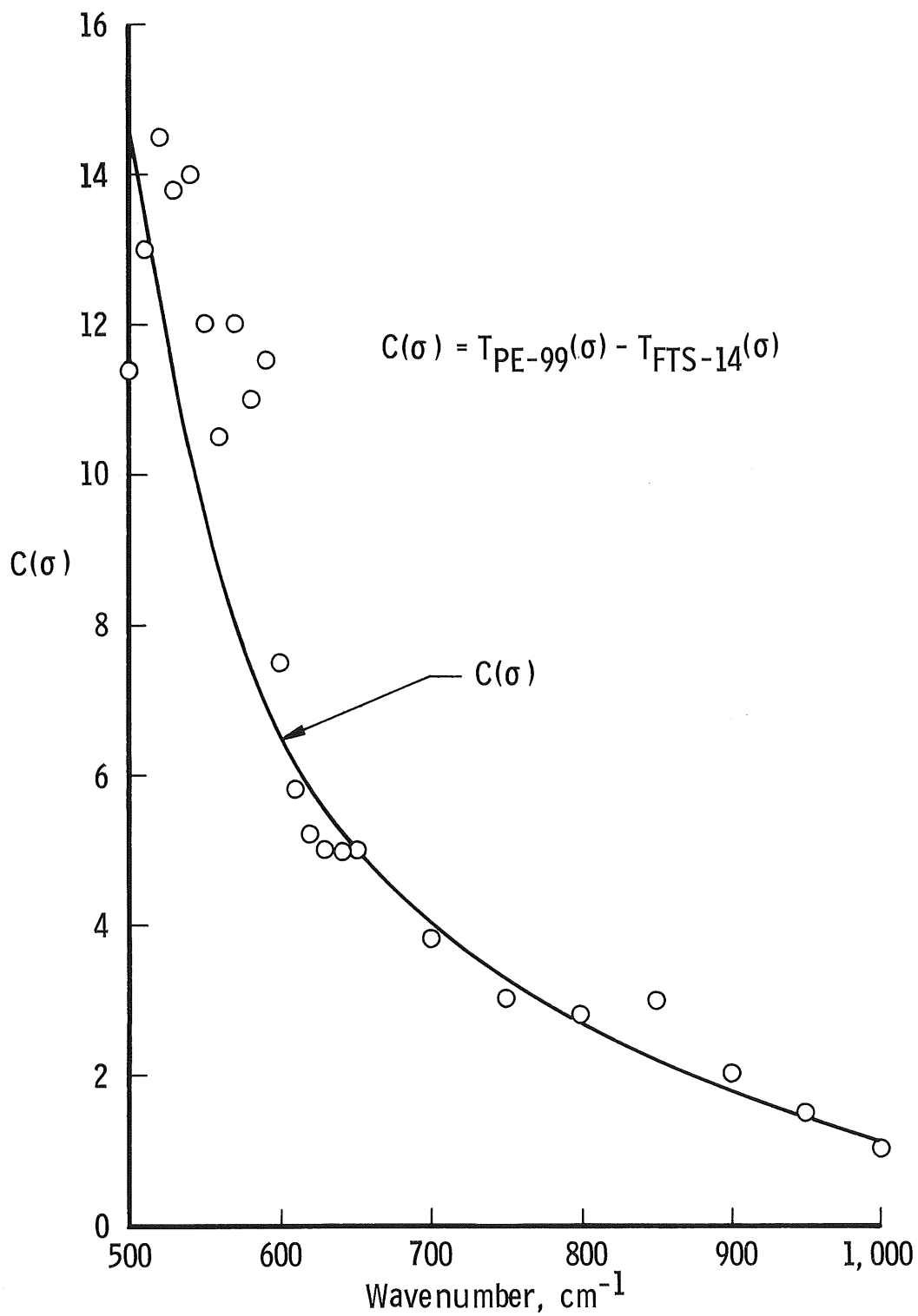


Figure 20. Correction percentage ( $C(\sigma)$ ) for FTS-14 80°K germanium transmission data attributable to emission problem.

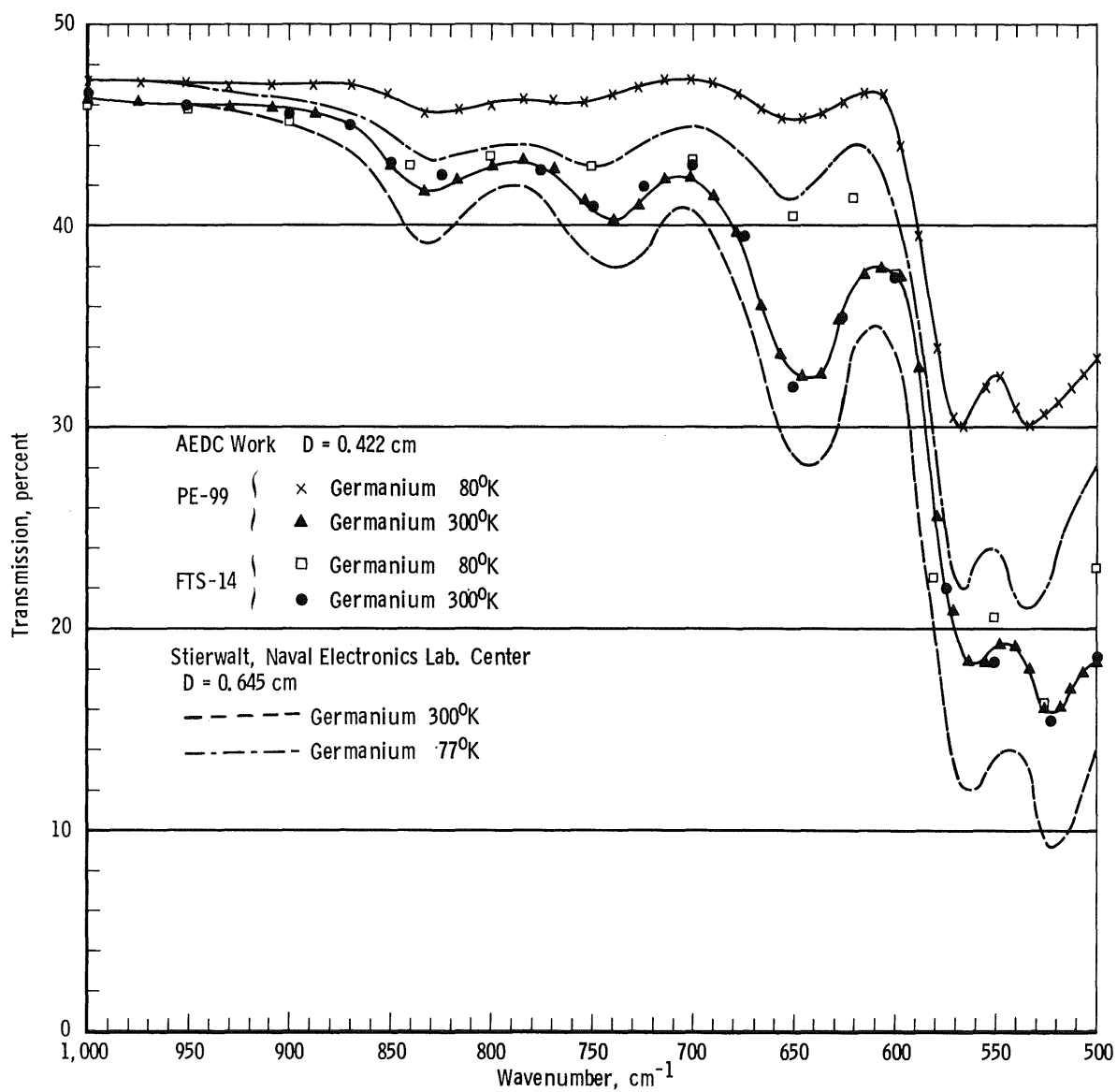


Figure 21. Summary of transmission data for  $300^\circ\text{K}$  and  $80^\circ\text{K}$  germanium windows.



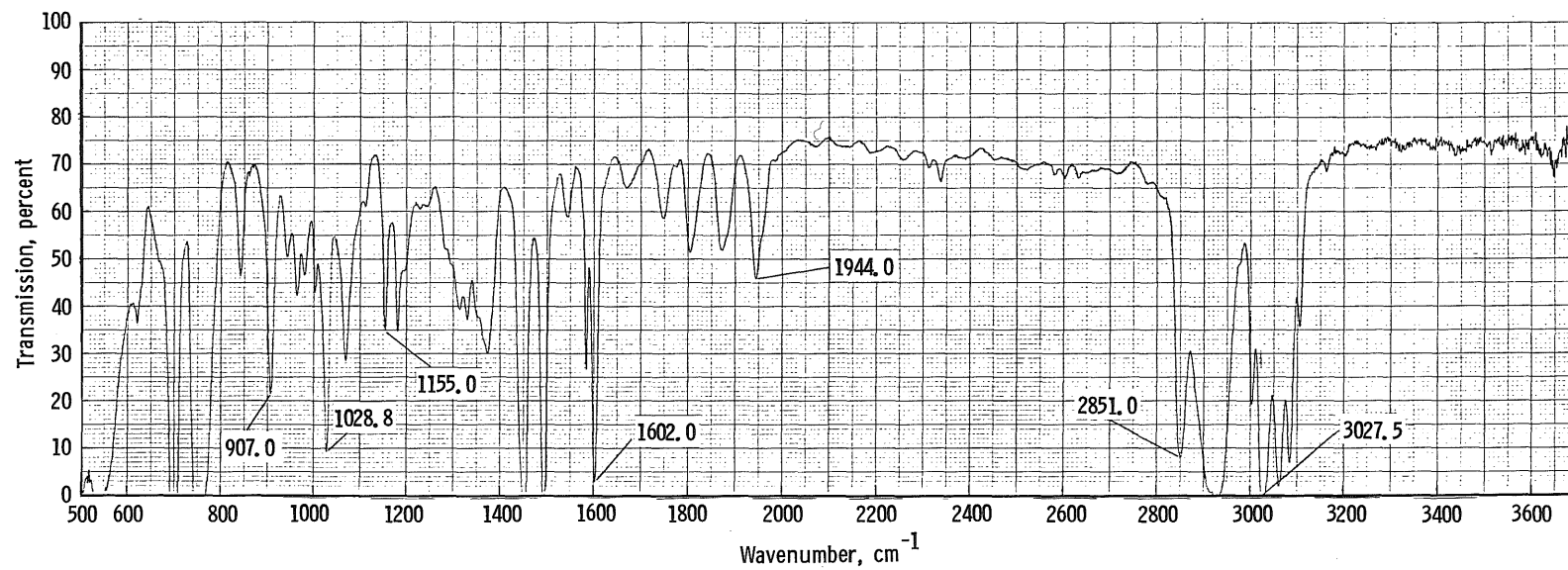


Figure 22. Transmission of 300°K polystyrene sandwiched between two 4-mm-thick NaCl windows.

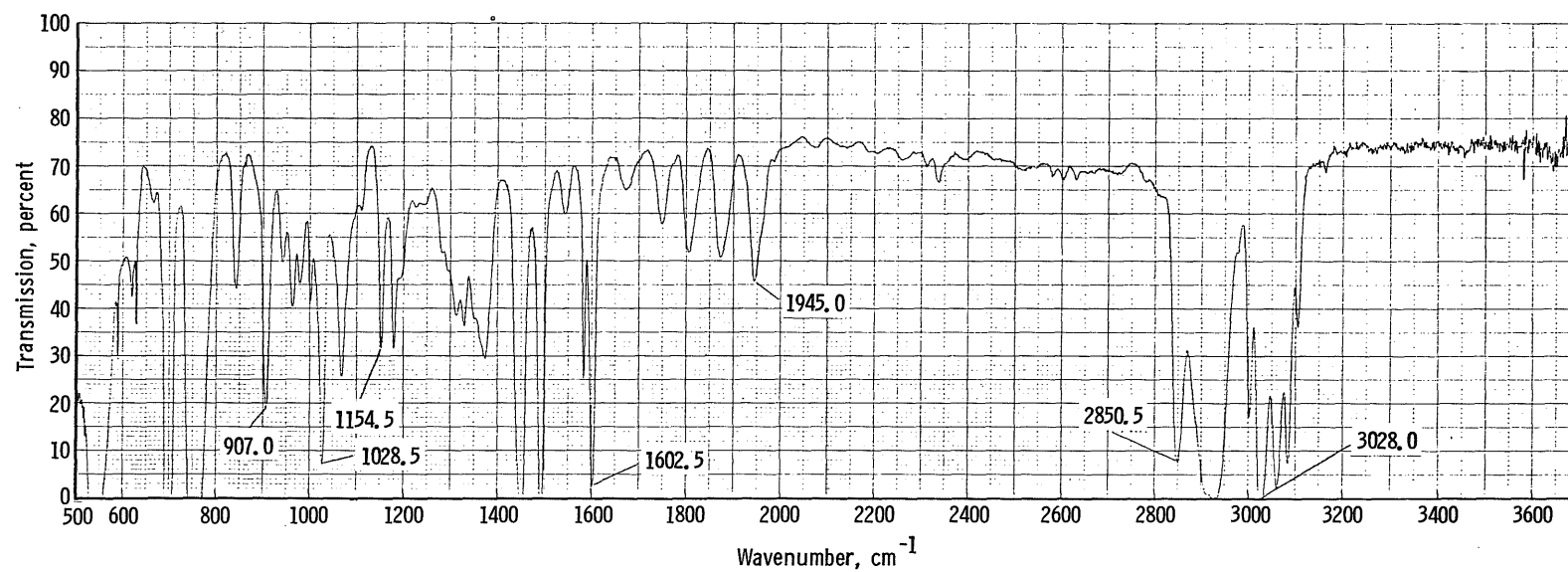
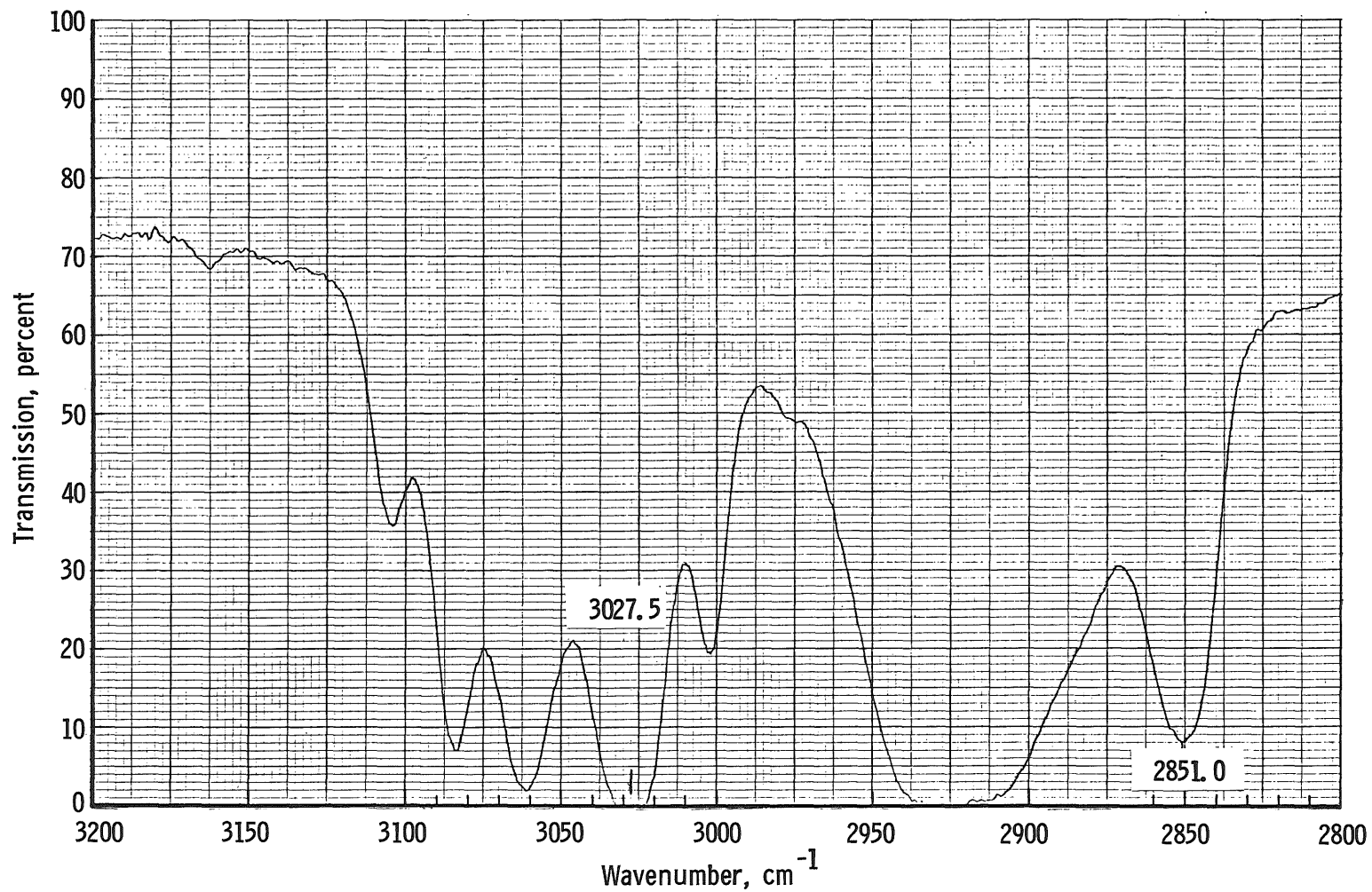
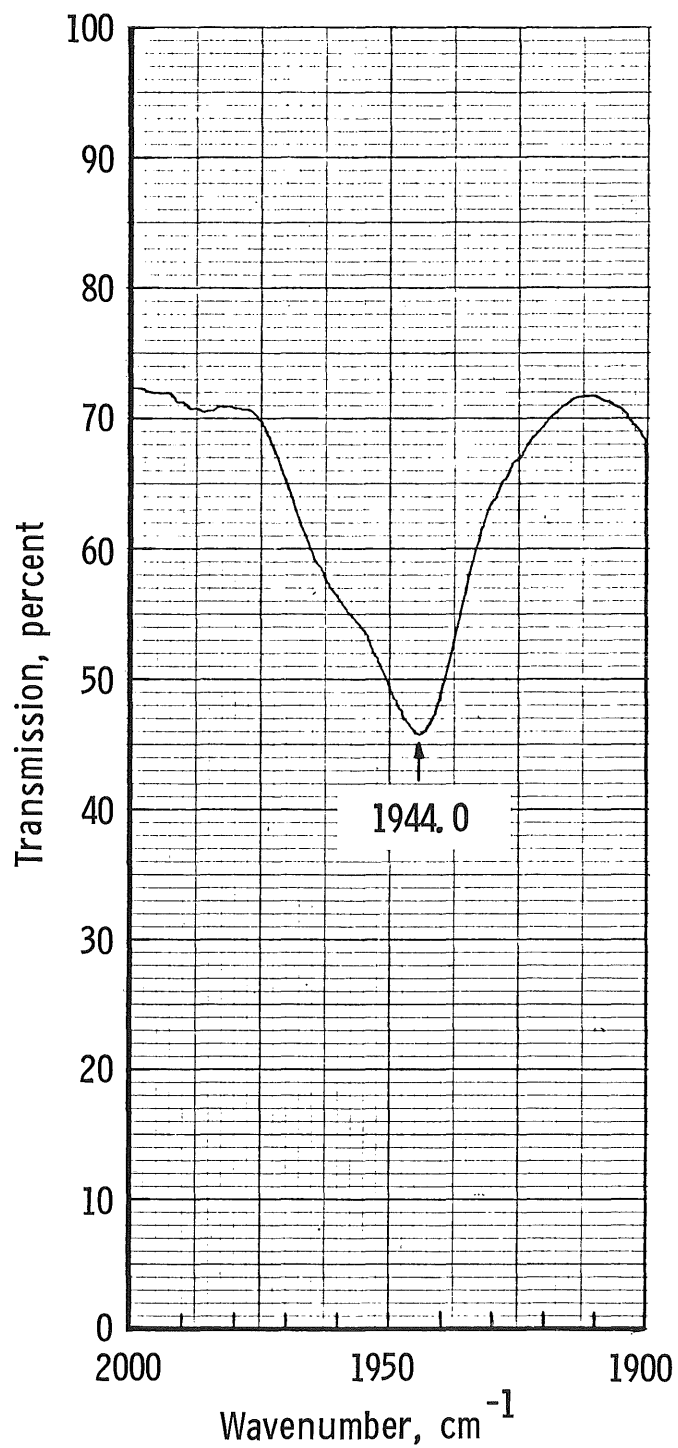


Figure 23. Transmission of 20°K polystyrene.

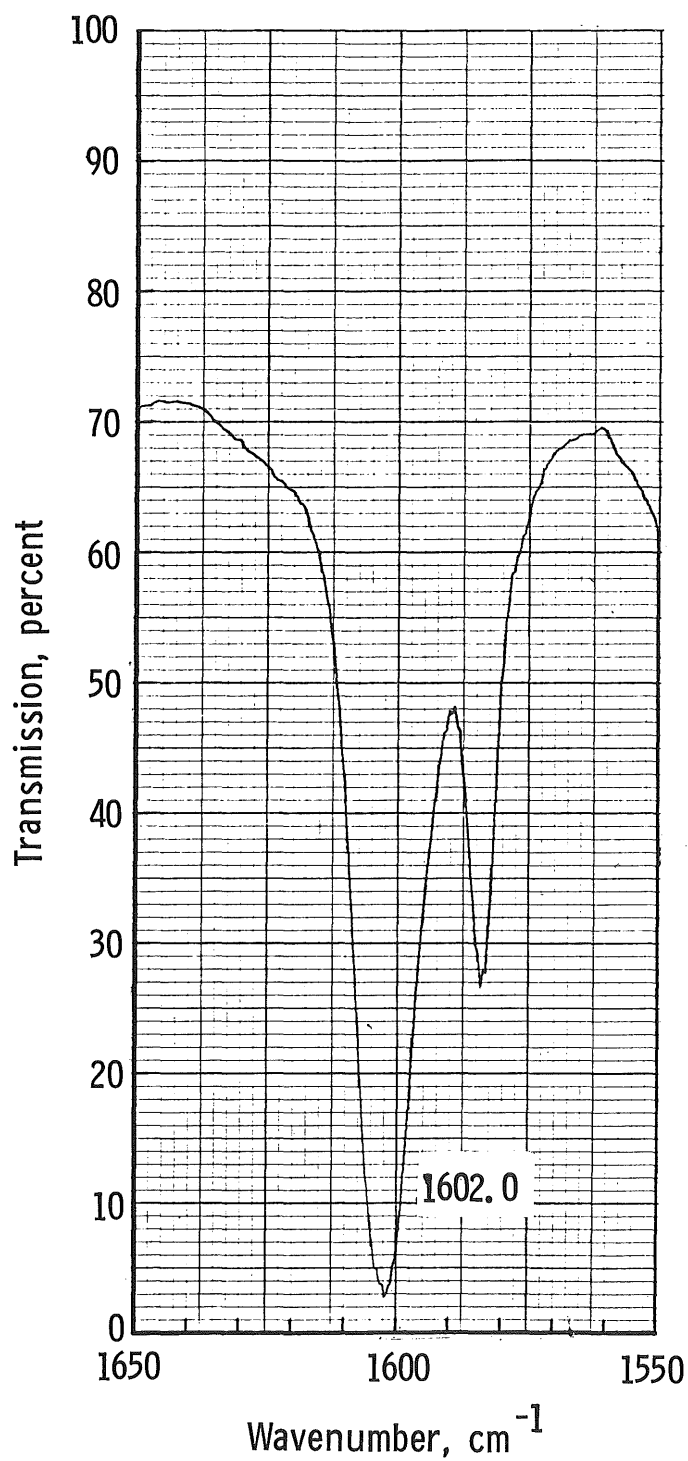


a. 2,800 to 3,200  $\text{cm}^{-1}$  region

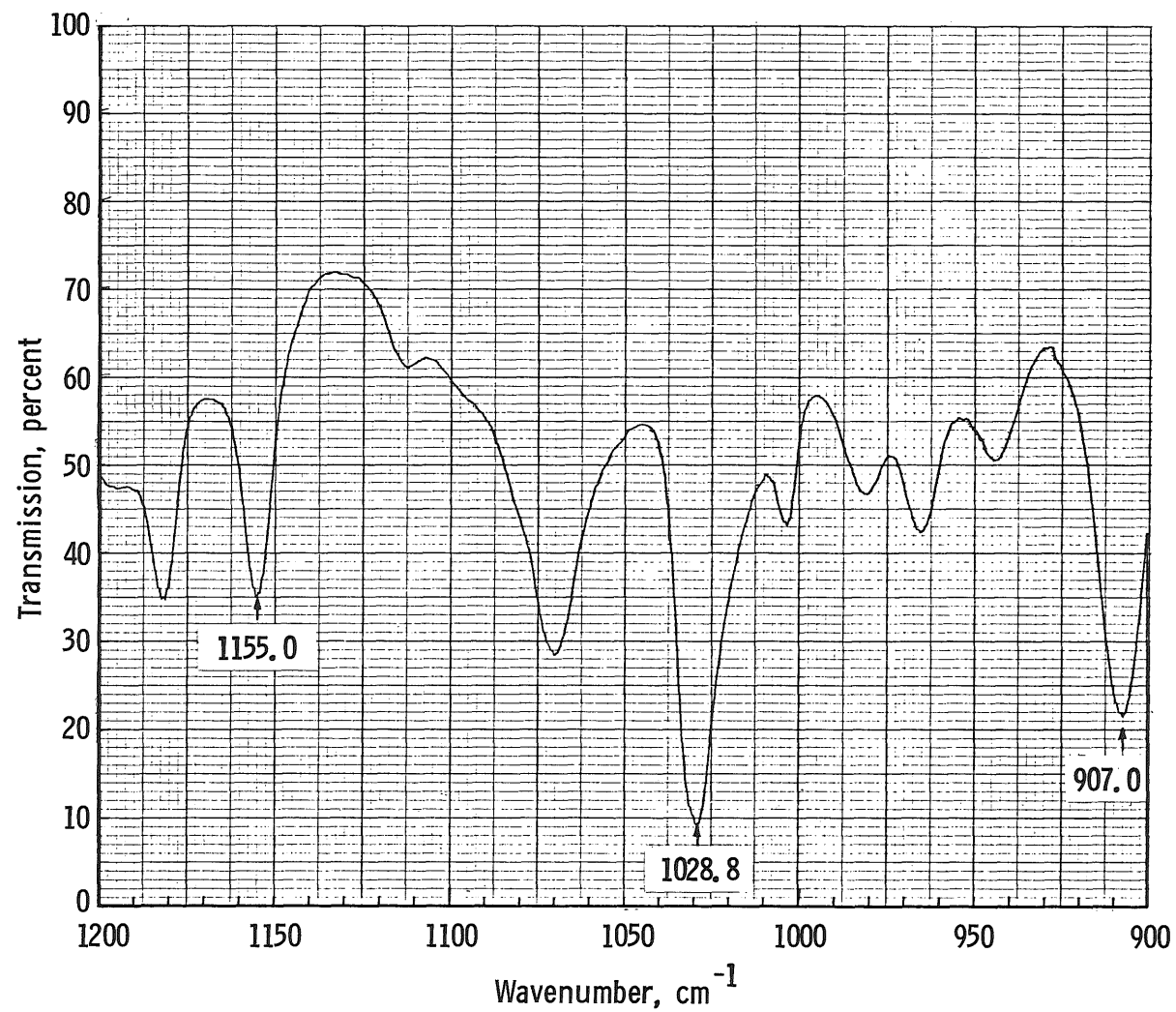
Figure 24. 25- $\text{cm}^{-1}$ /in. plots of 300°K polystyrene.



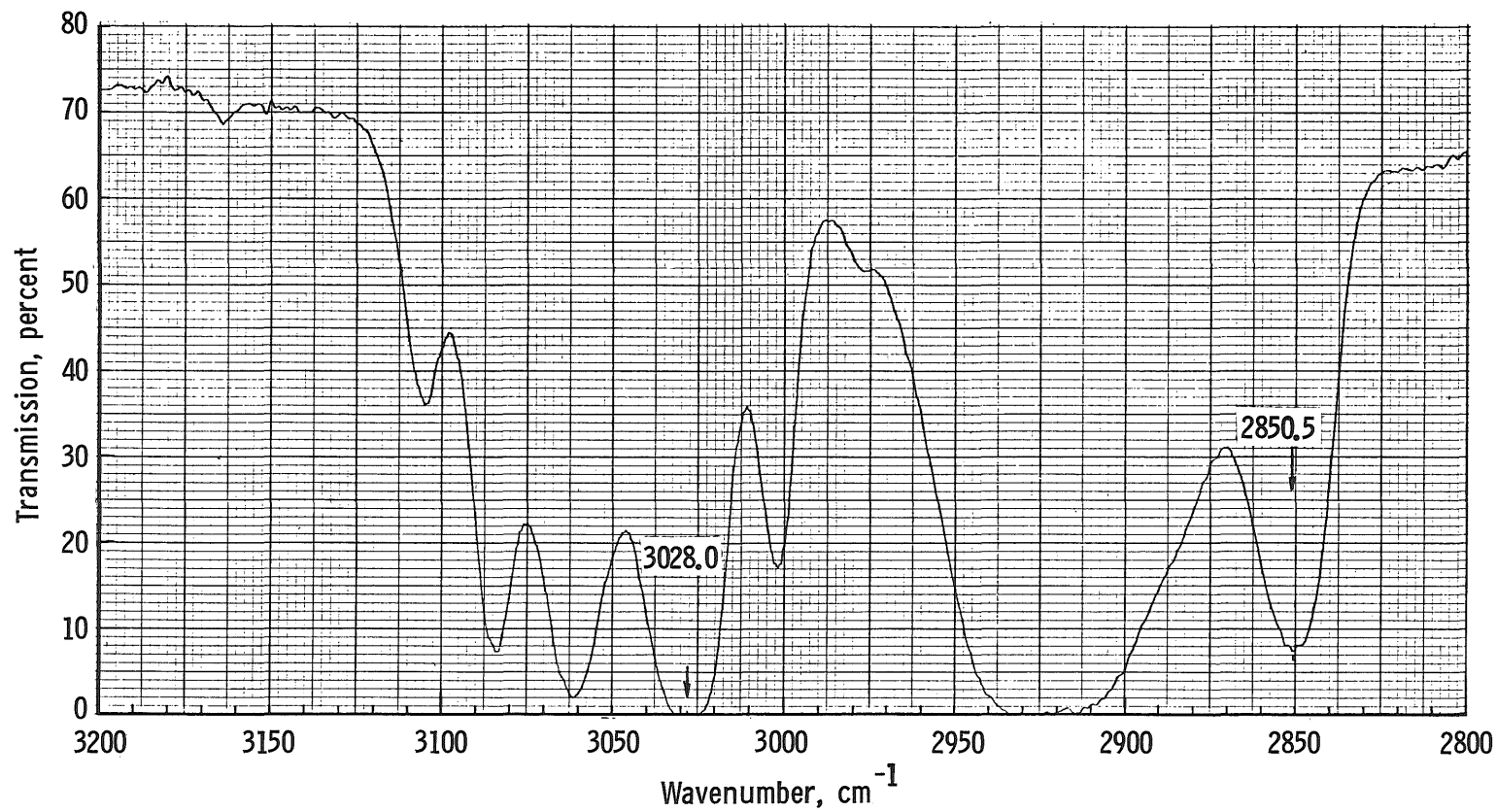
b. 1,900 to 2,000  $\text{cm}^{-1}$  region  
Figure 24. Continued.



c. 1,550 to 1,650 cm<sup>-1</sup> region  
Figure 24. Continued.

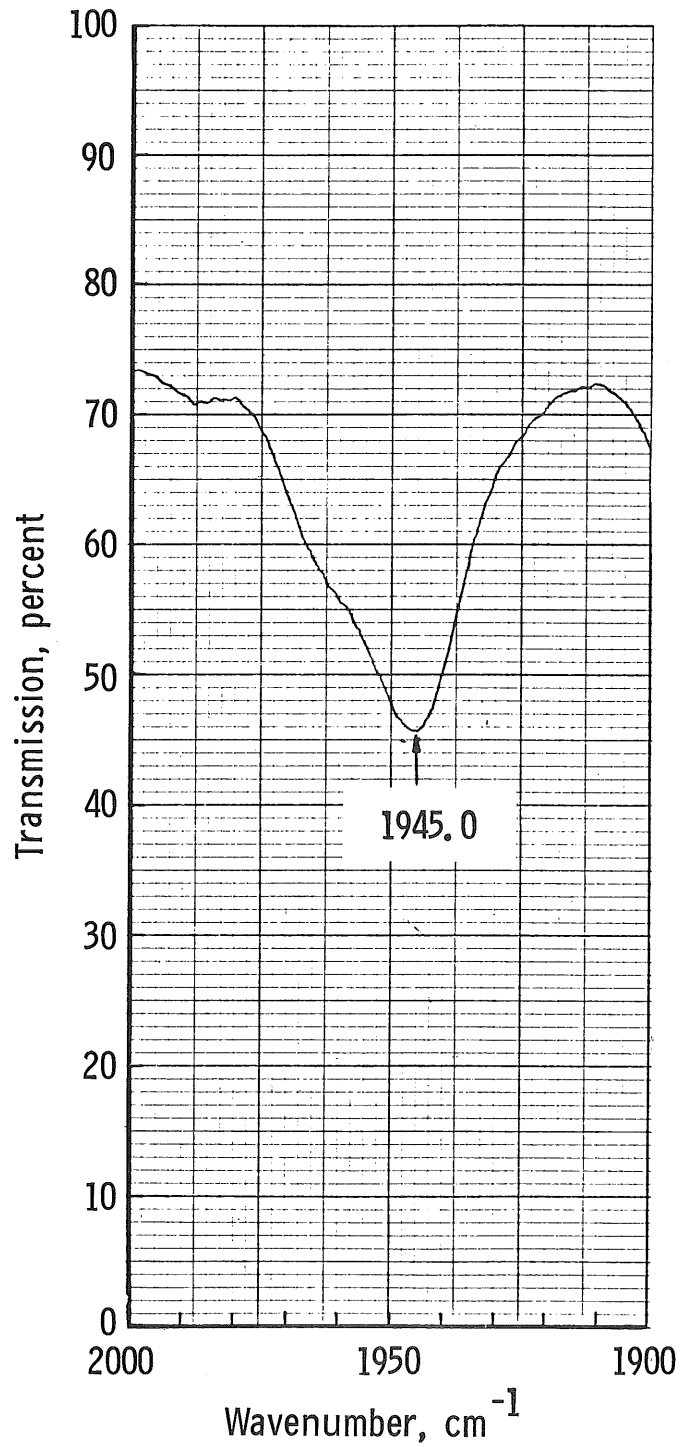


d. 900 to 1,200 cm<sup>-1</sup> region  
Figure 24. Concluded.



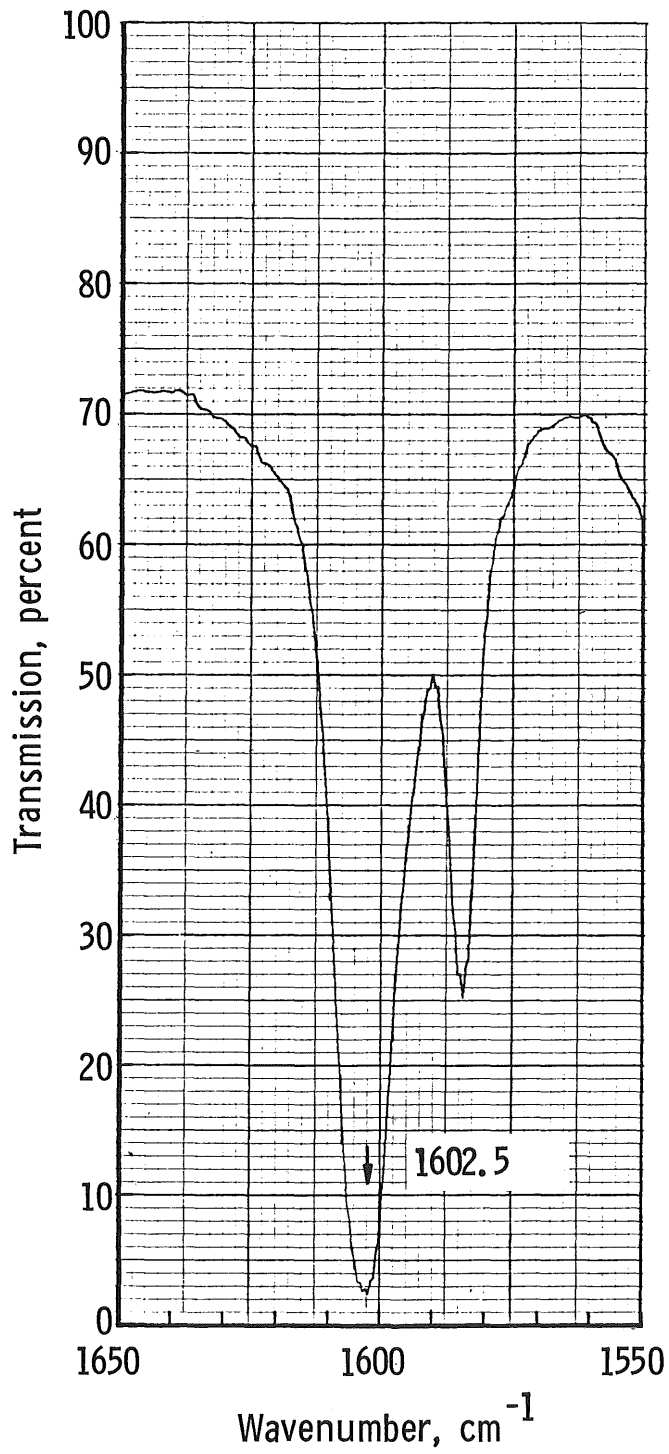
a. 2,800 to 3,200  $\text{cm}^{-1}$  region

Figure 25. 25- $\text{cm}^{-1}$ /in. plots of 20° K polystyrene.

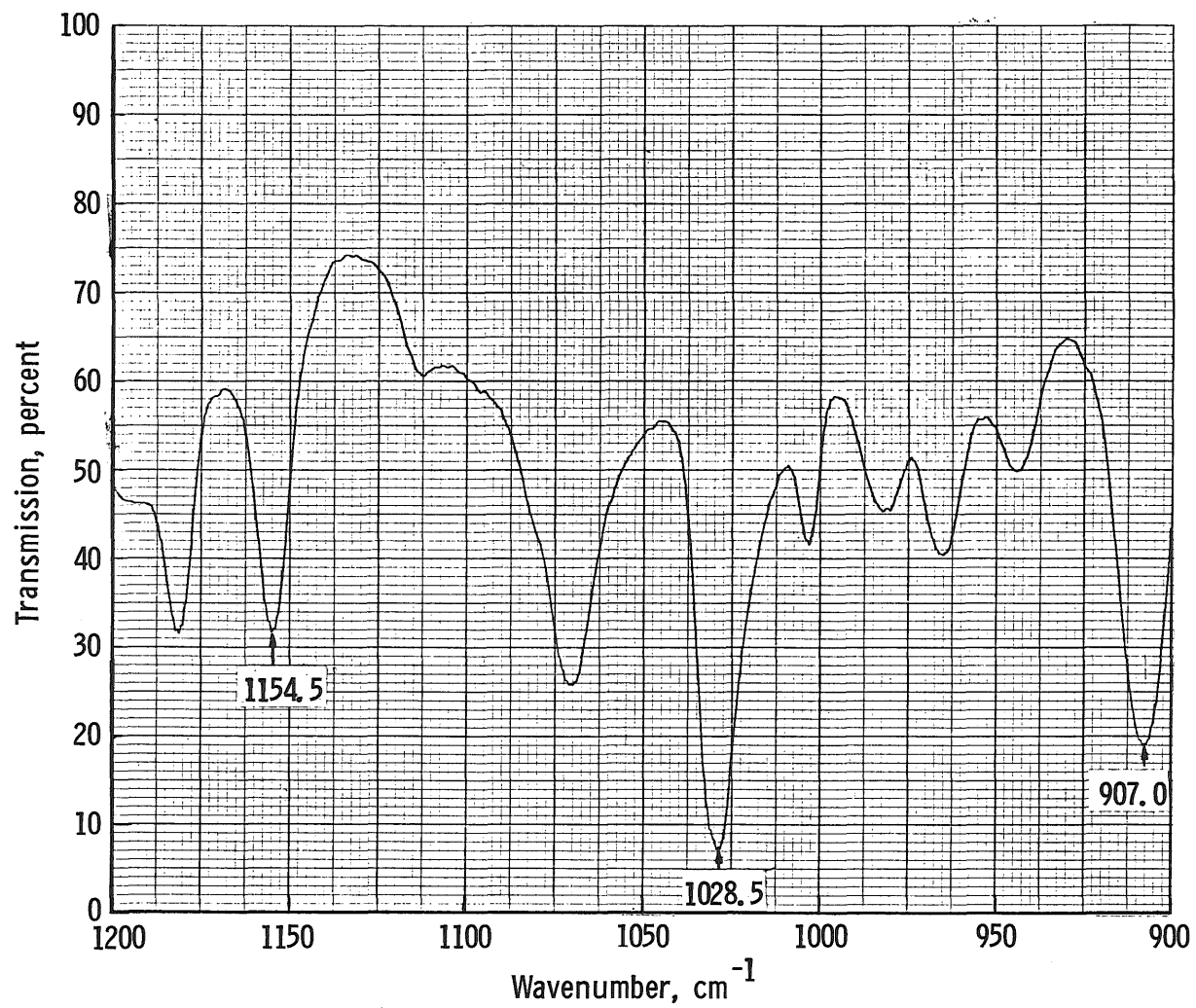


b. 1,900 to 2,000  $\text{cm}^{-1}$  region  
Figure 25. Continued.





c. 1,550 to 1,650 cm<sup>-1</sup> region  
Figure 25. Continued.



d. 900 to 1,200 cm<sup>-1</sup> region  
Figure 25. Concluded.

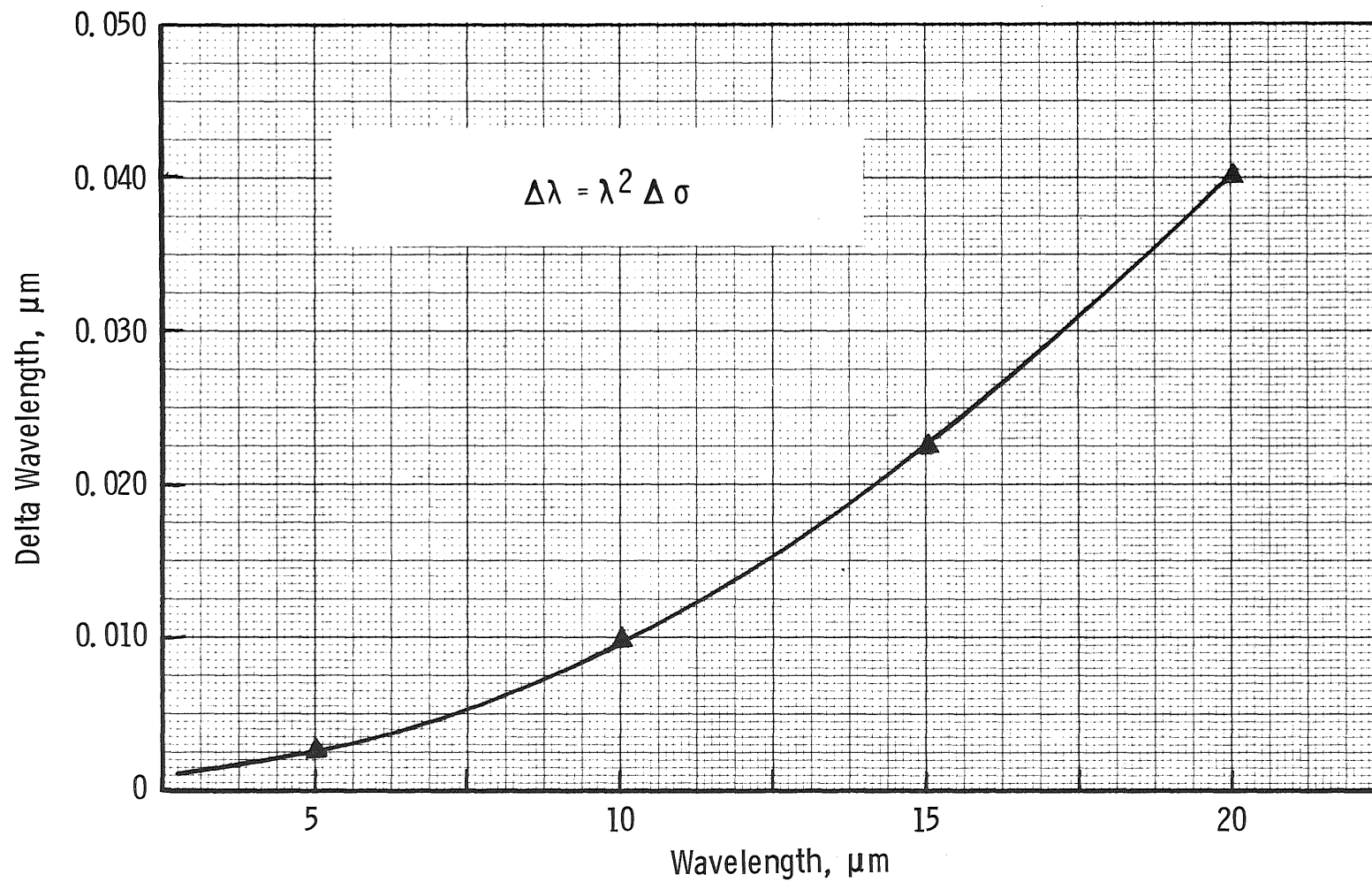


Figure 26. Conversion plot for a  $1\text{-cm}^{-1}$  increment in wavenumber to the corresponding increment in wavelength.

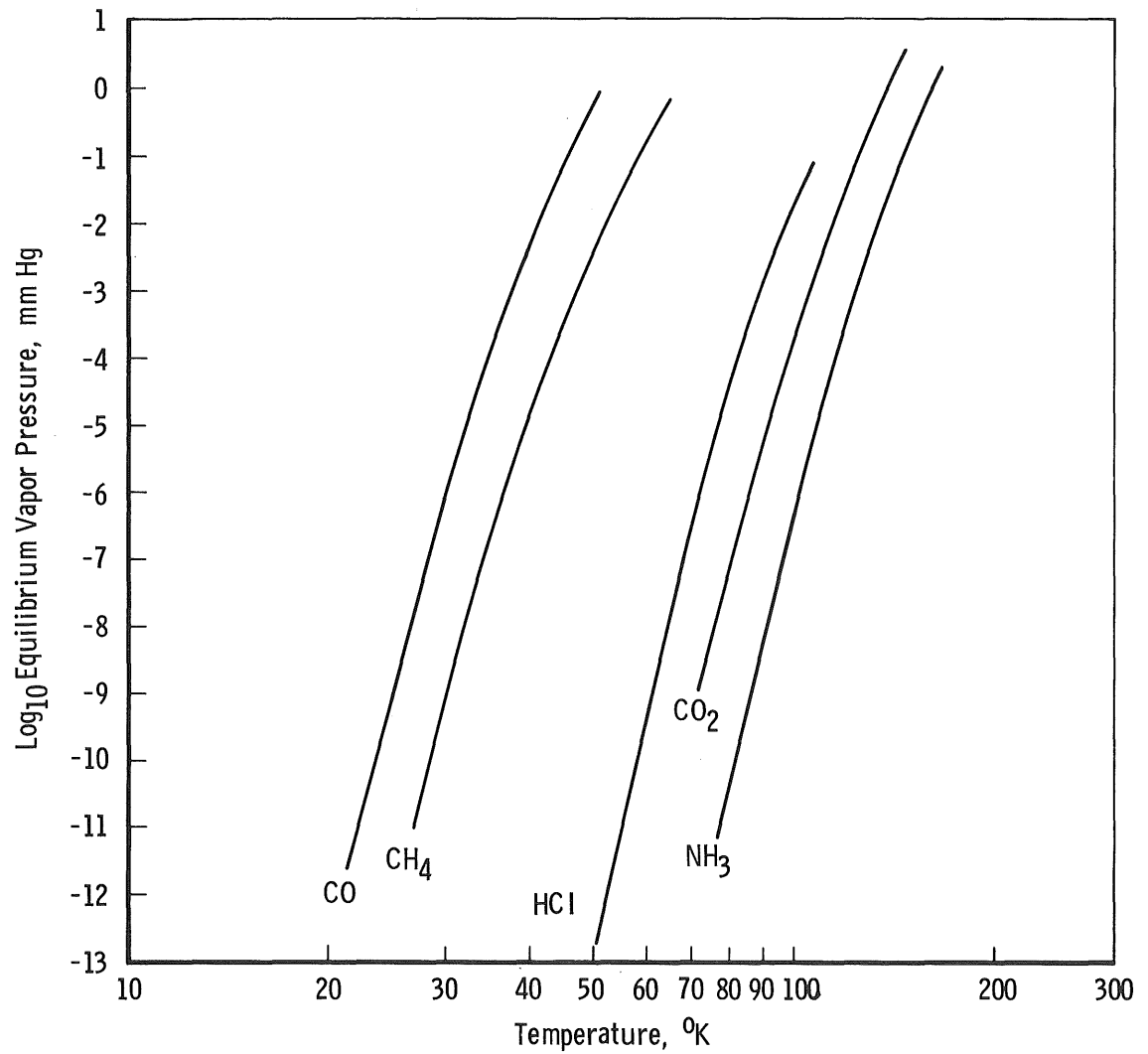
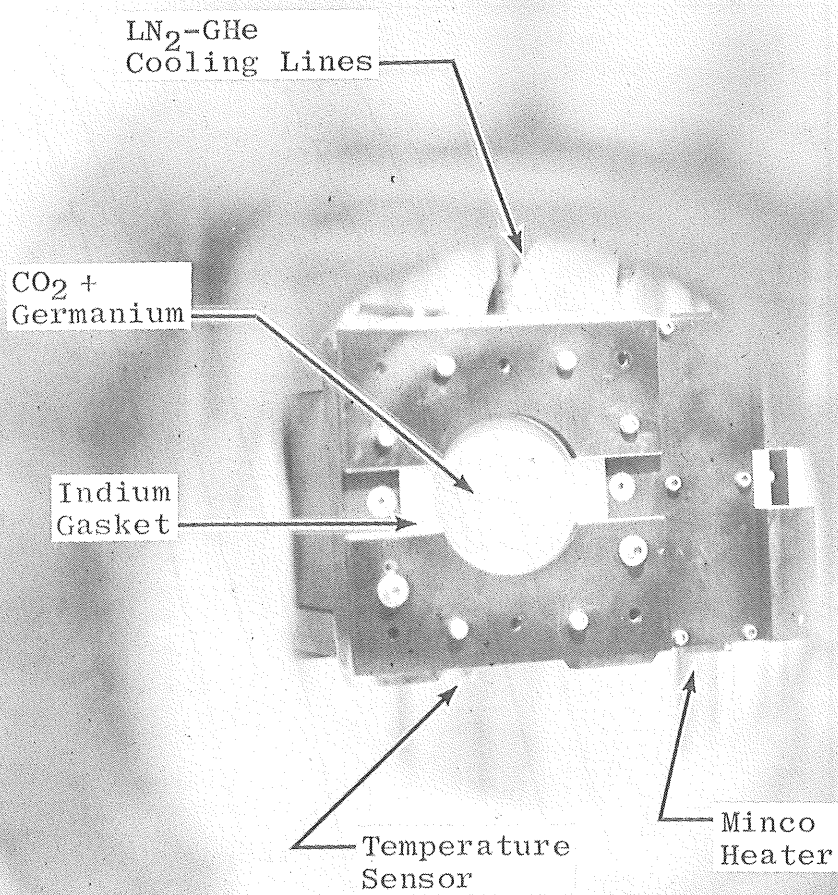
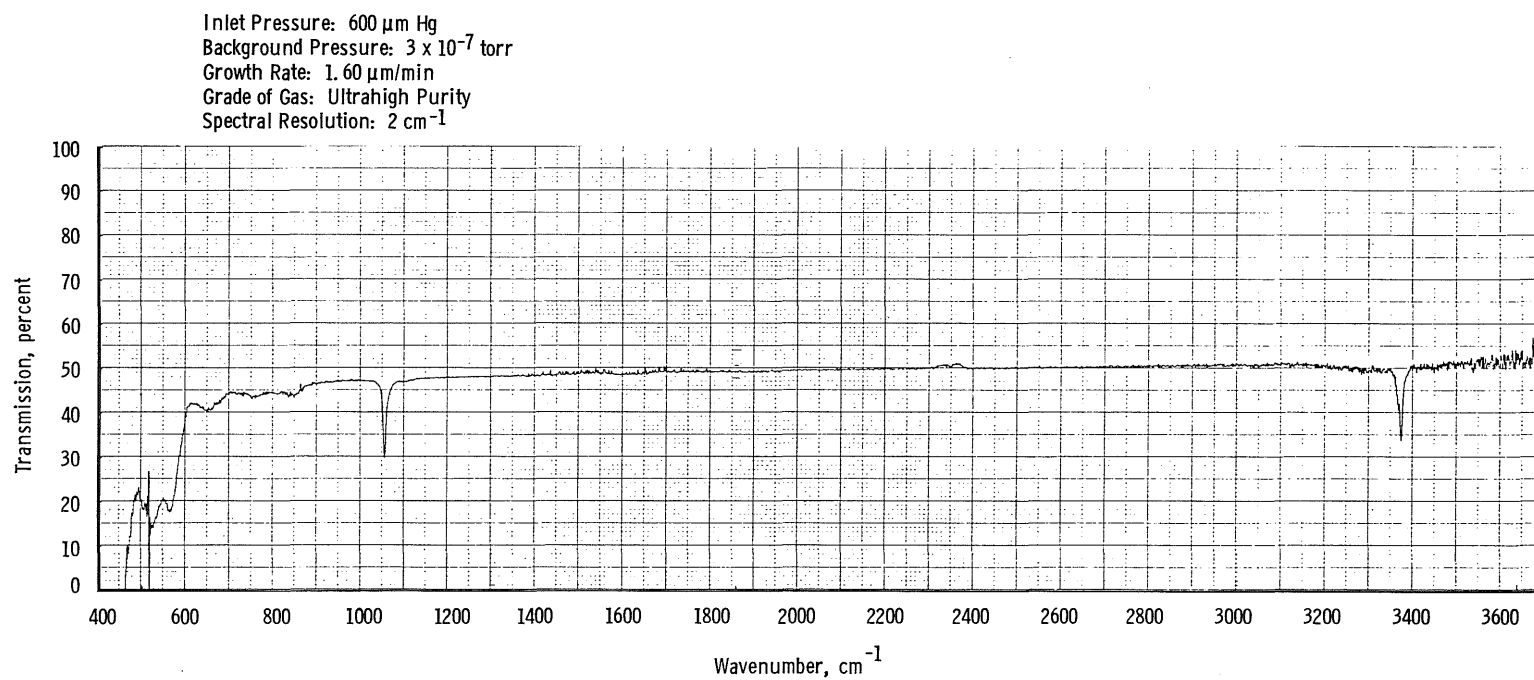


Figure 27. Equilibrium vapor pressure as a function of temperature for gases investigated in this study.



A E D C  
2577-75

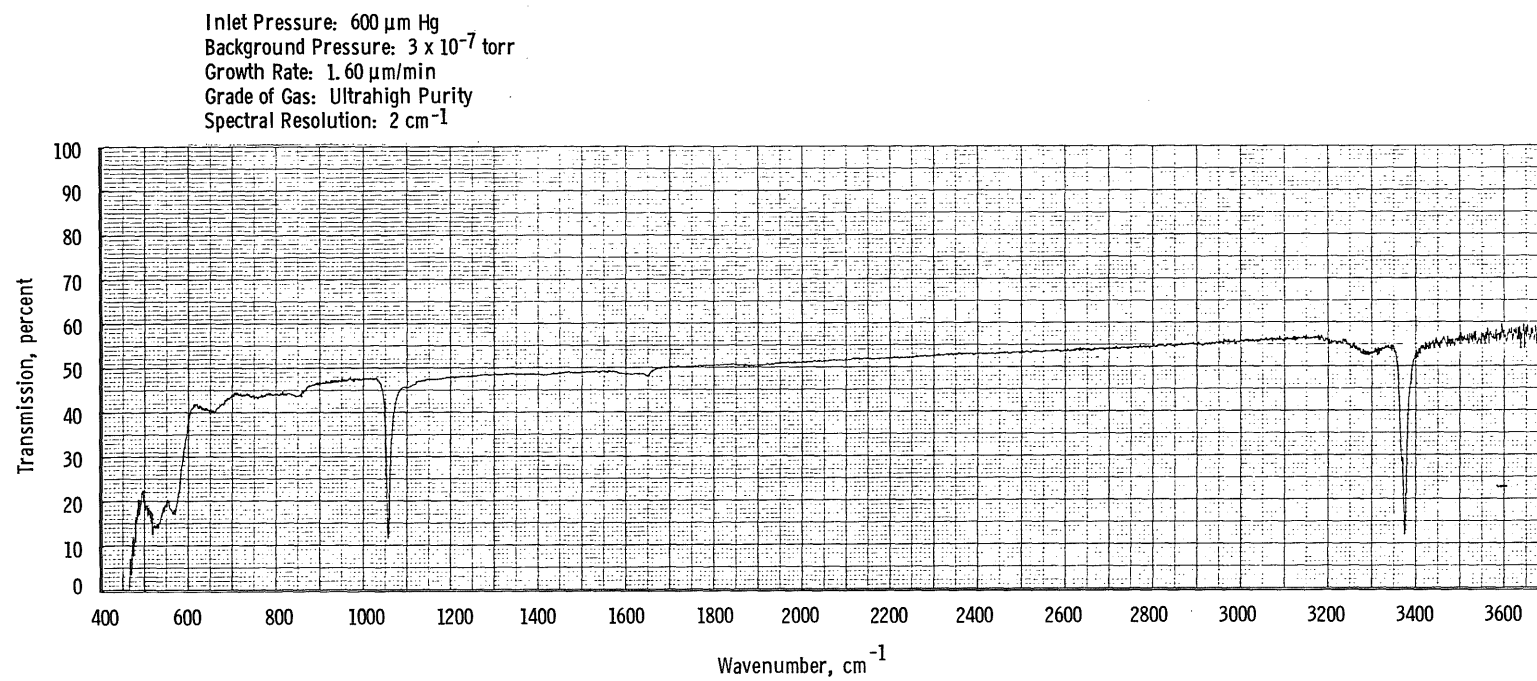
Figure 28. Photograph of 5.0- $\mu$ m-thick CO<sub>2</sub> deposit on an 80°K germanium window.



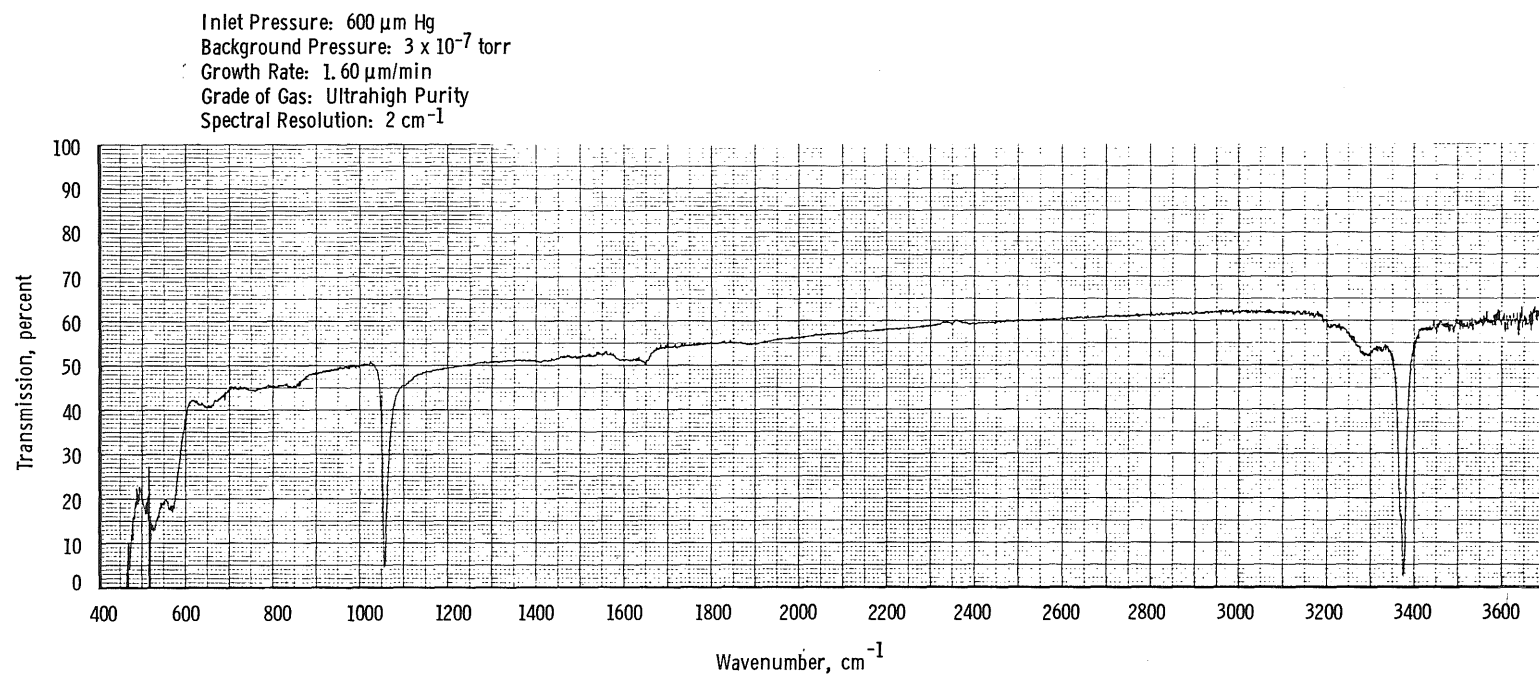
a. 0.111- $\mu\text{m}$ -thick deposit

Figure 29. Transmission of 80° K germanium window with various  $\text{NH}_3$  deposit thicknesses.

88

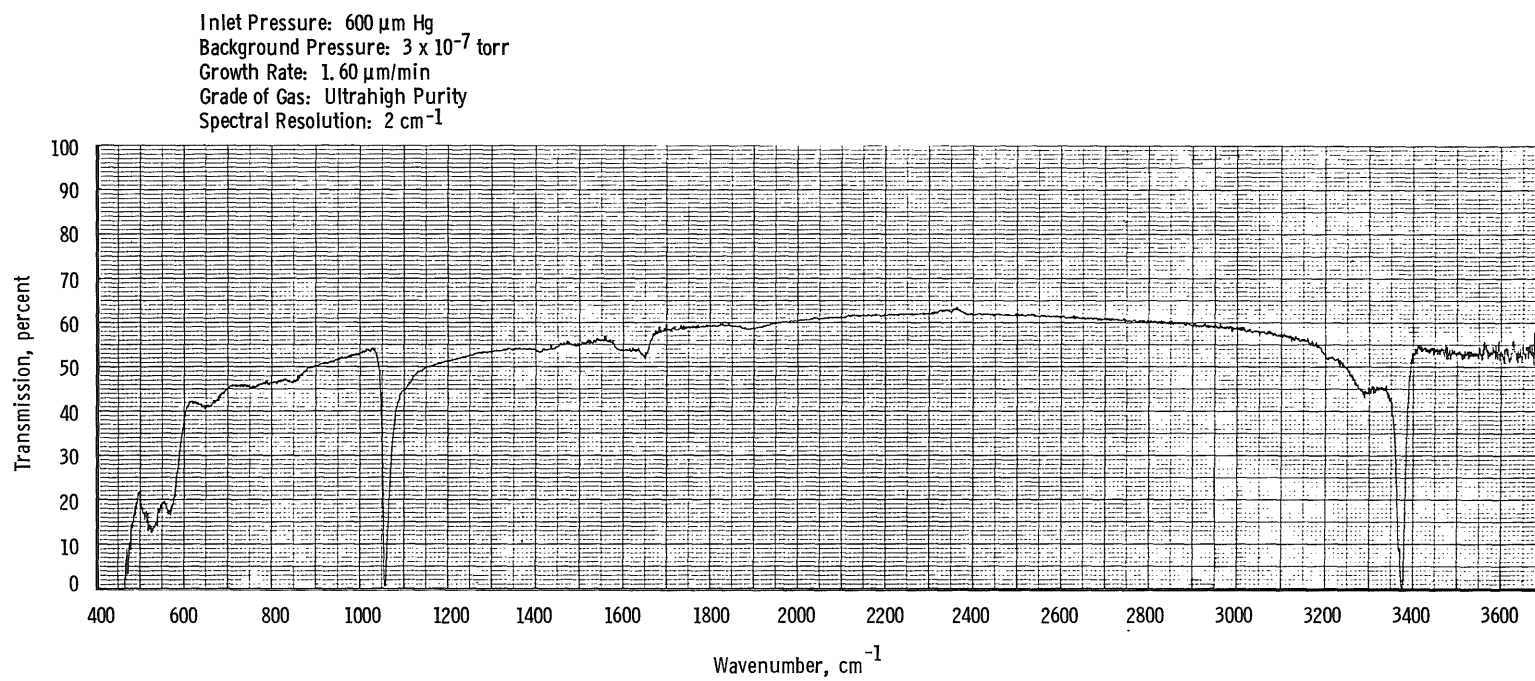


b. 0.334- $\mu\text{m}$ -thick deposit  
Figure 29. Continued.

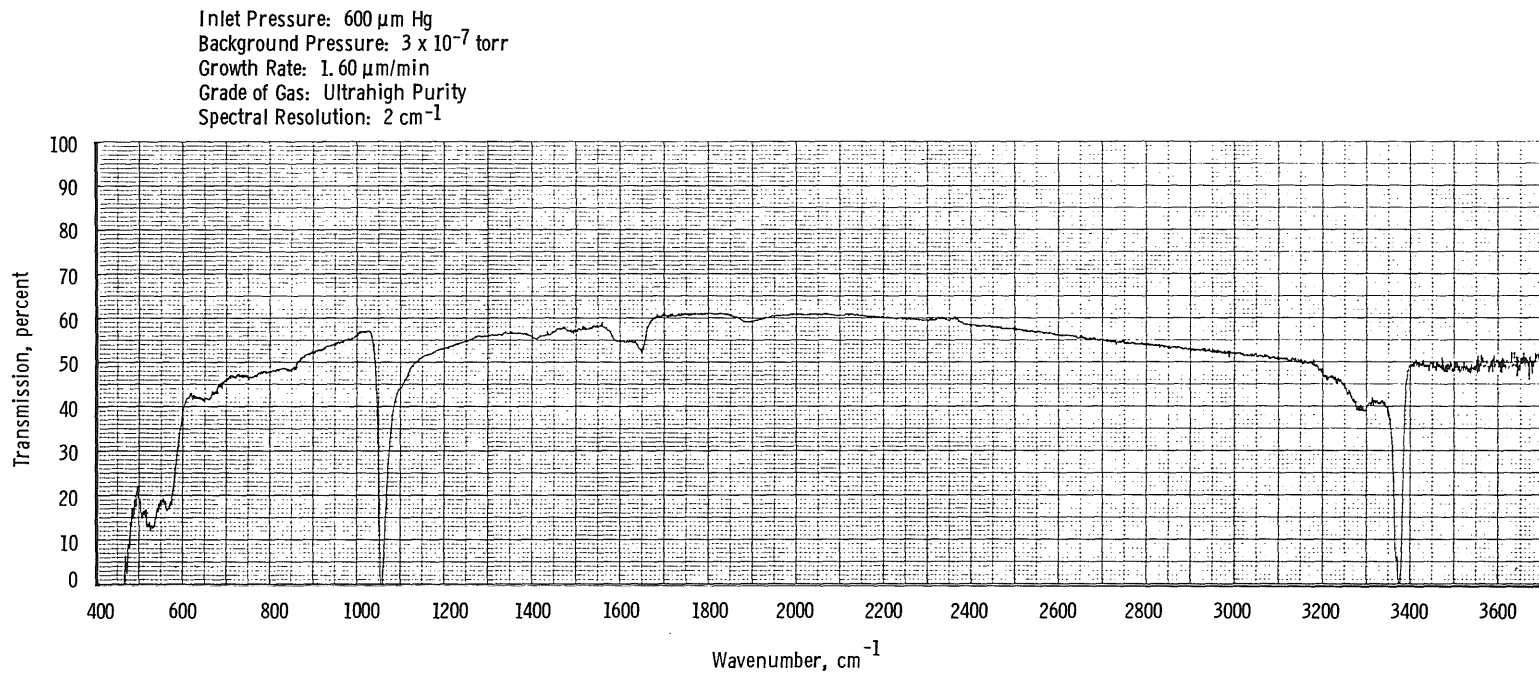


c. 0.557- $\mu\text{m}$ -thick deposit  
Figure 29. Continued.

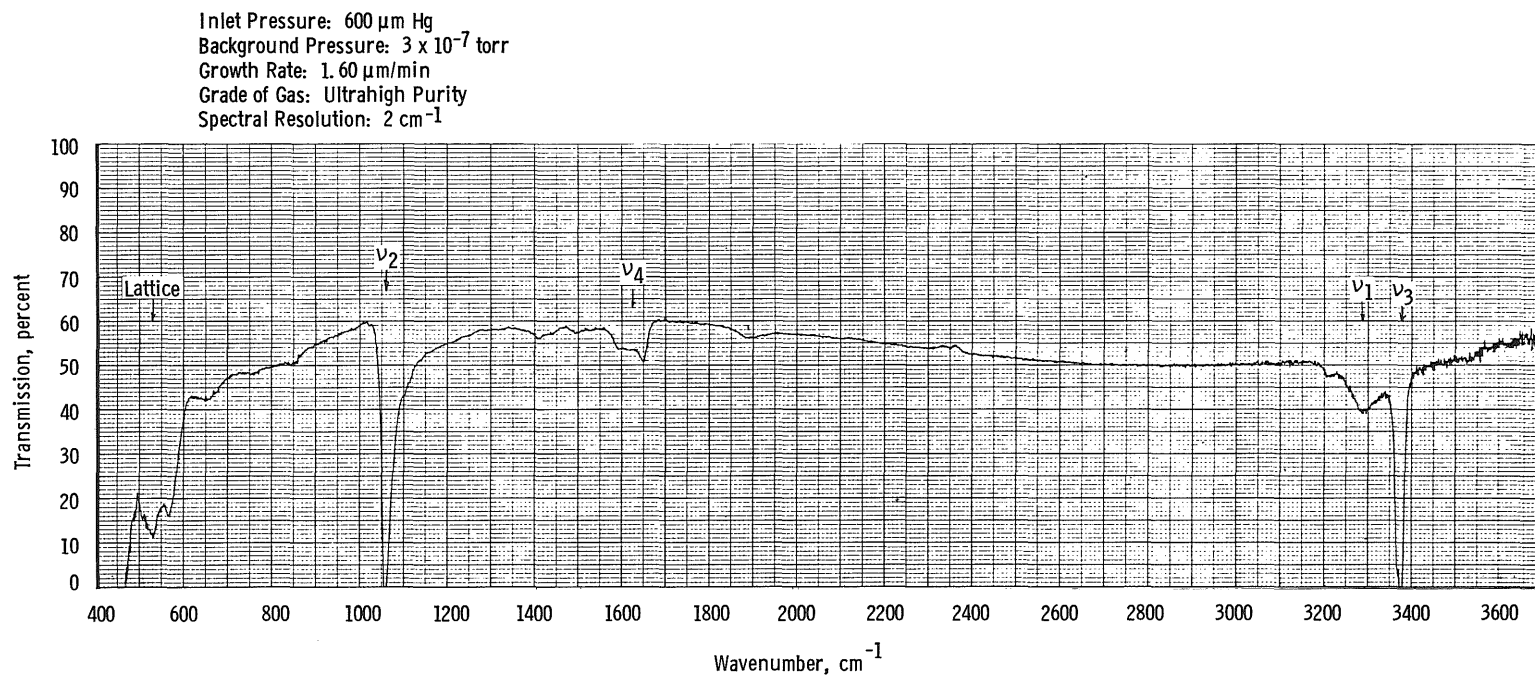




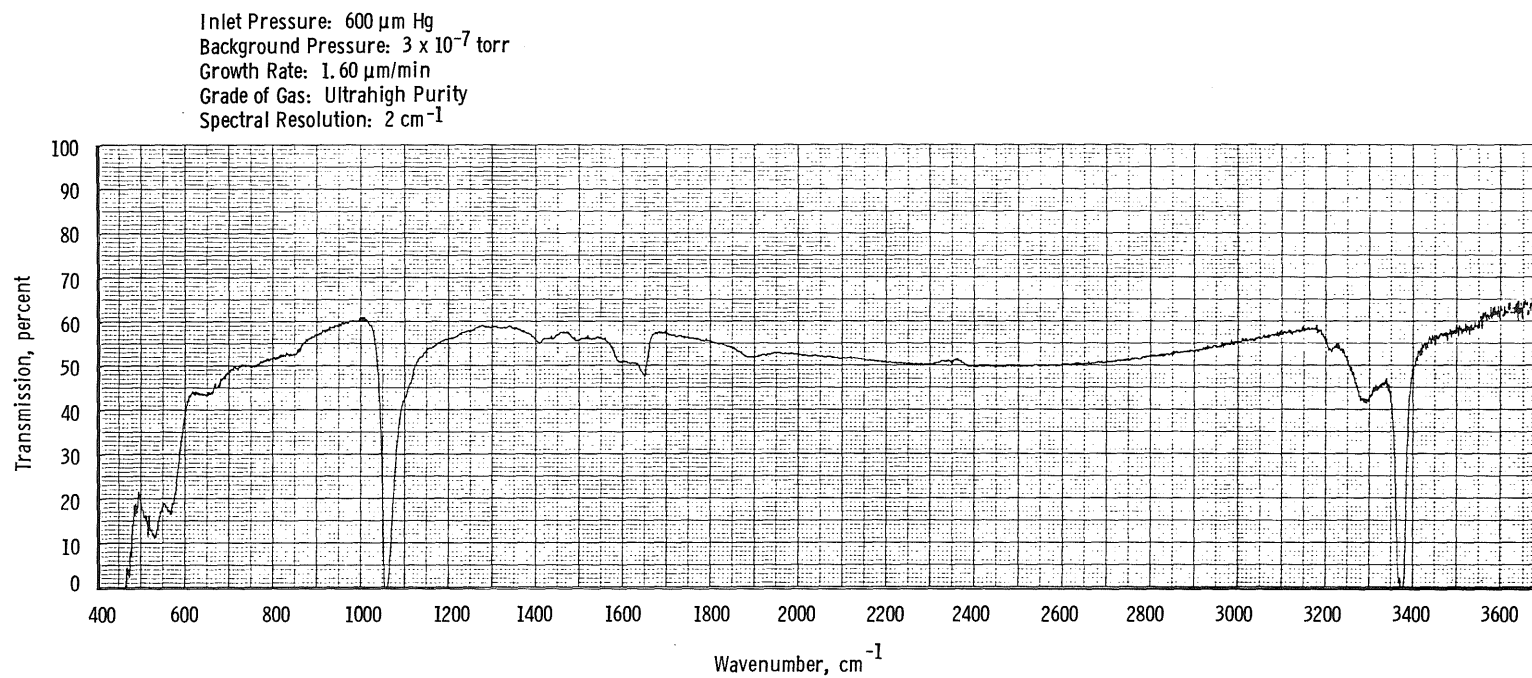
d. 0.780- $\mu\text{m}$ -thick deposit  
Figure 29. Continued.



e. 1.003- $\mu\text{m}$ -thick deposit  
Figure 29. Continued.

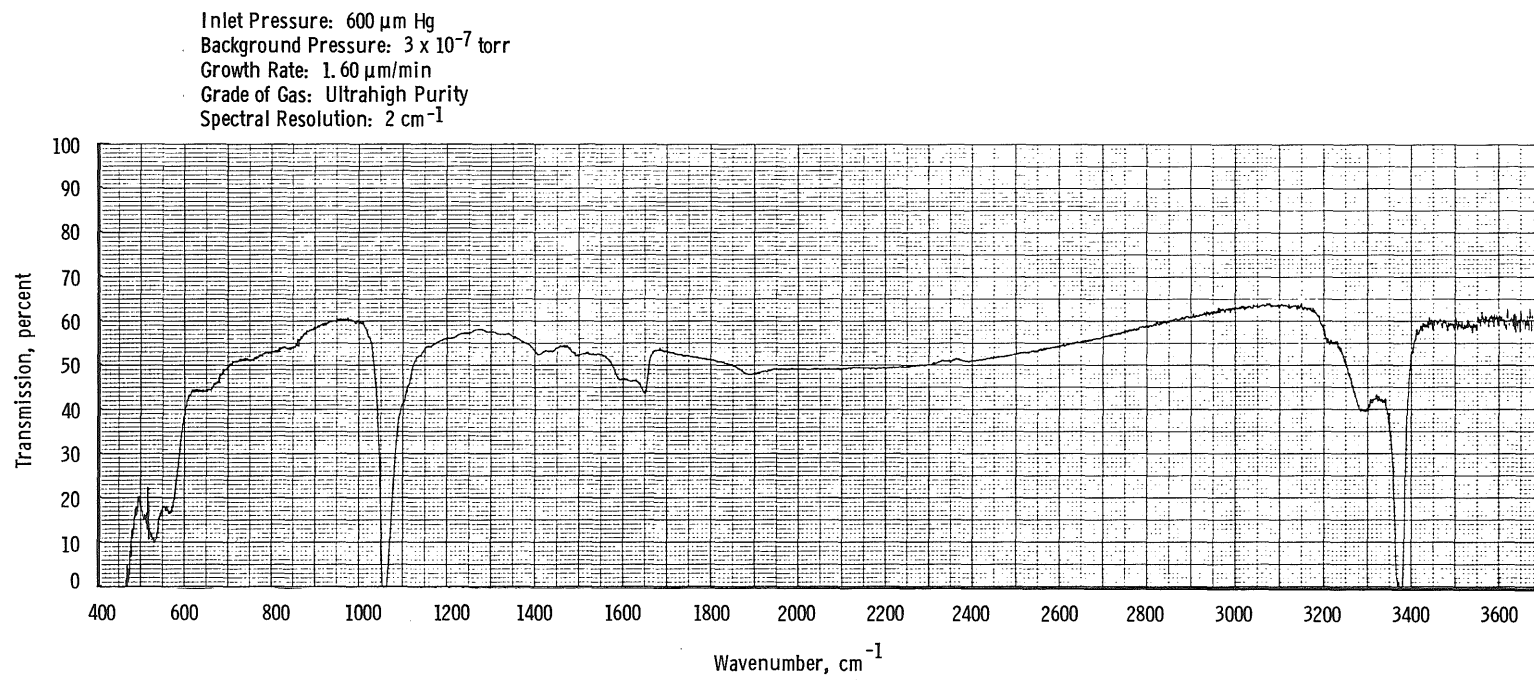


f. 1.225- $\mu\text{m}$ -thick deposit  
Figure 29. Continued.

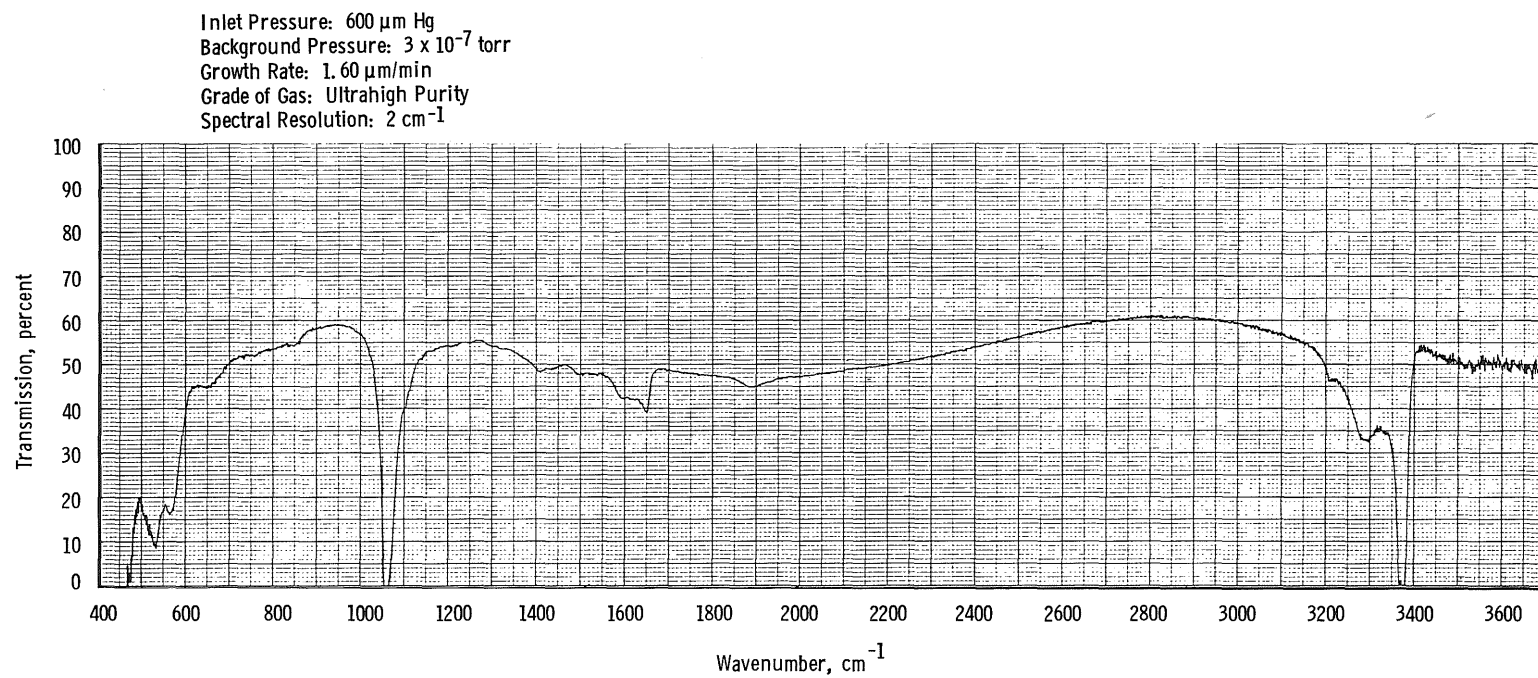


g. 1.449- $\mu\text{m}$ -thick deposit  
Figure 29. Continued.

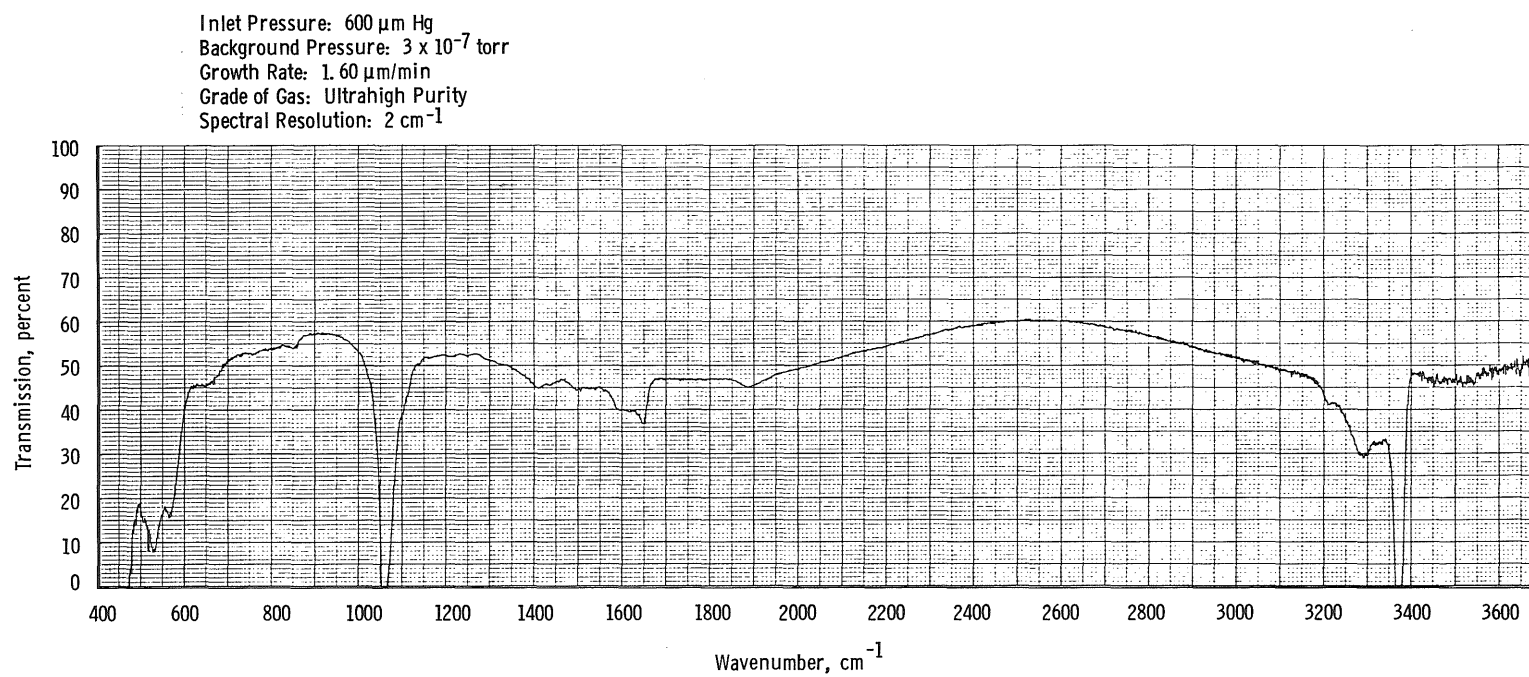
94



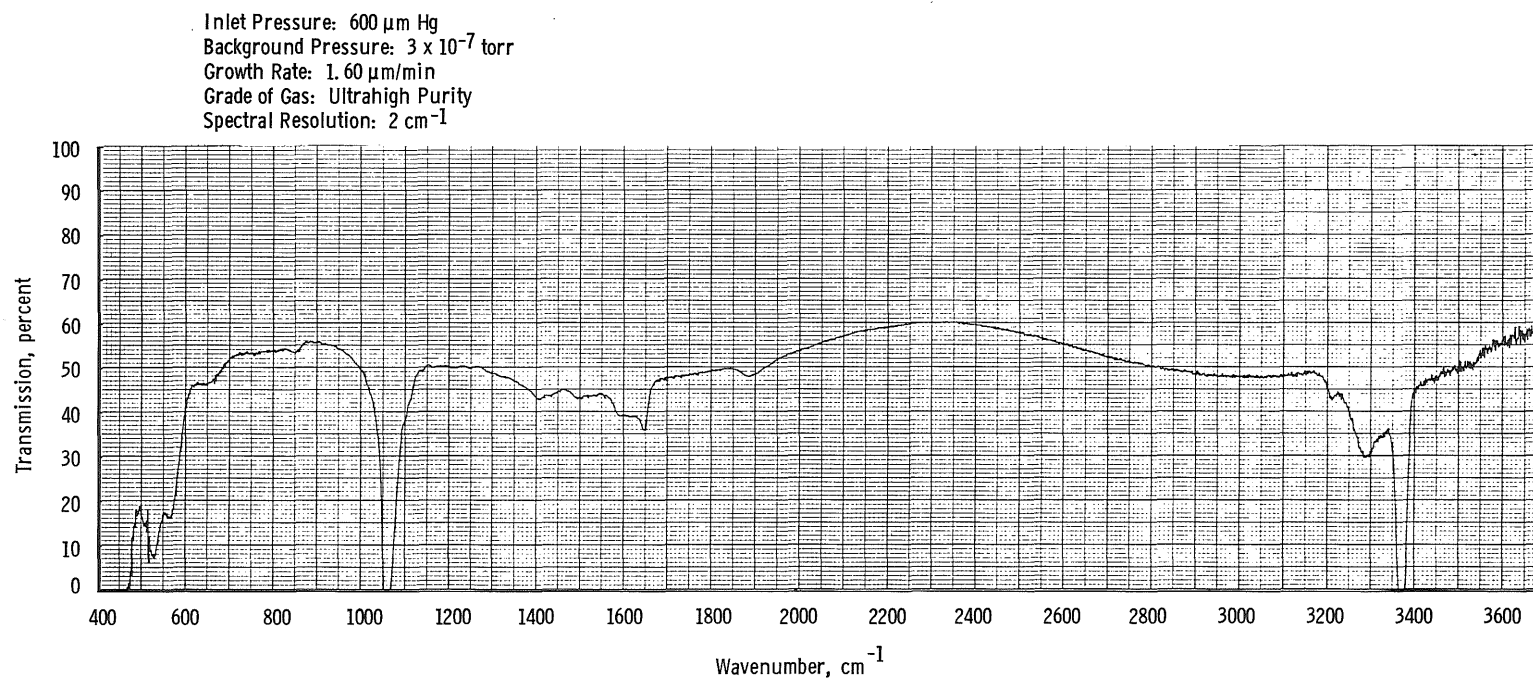
h. 1.671- $\mu\text{m}$ -thick deposit  
Figure 29. Continued.



i. 1.894- $\mu\text{m}$ -thick deposit  
Figure 29. Continued.

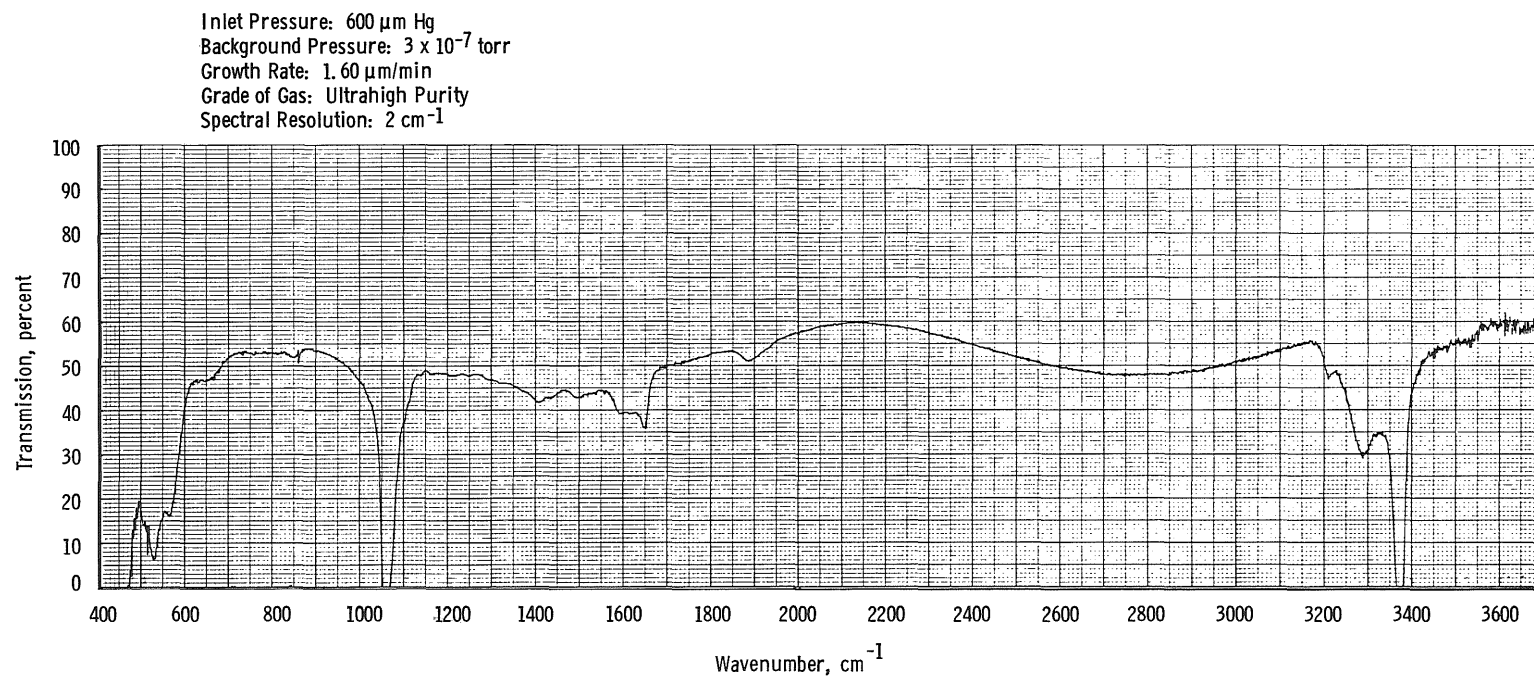


j. 2.117- $\mu\text{m}$ -thick deposit  
Figure 29. Continued.

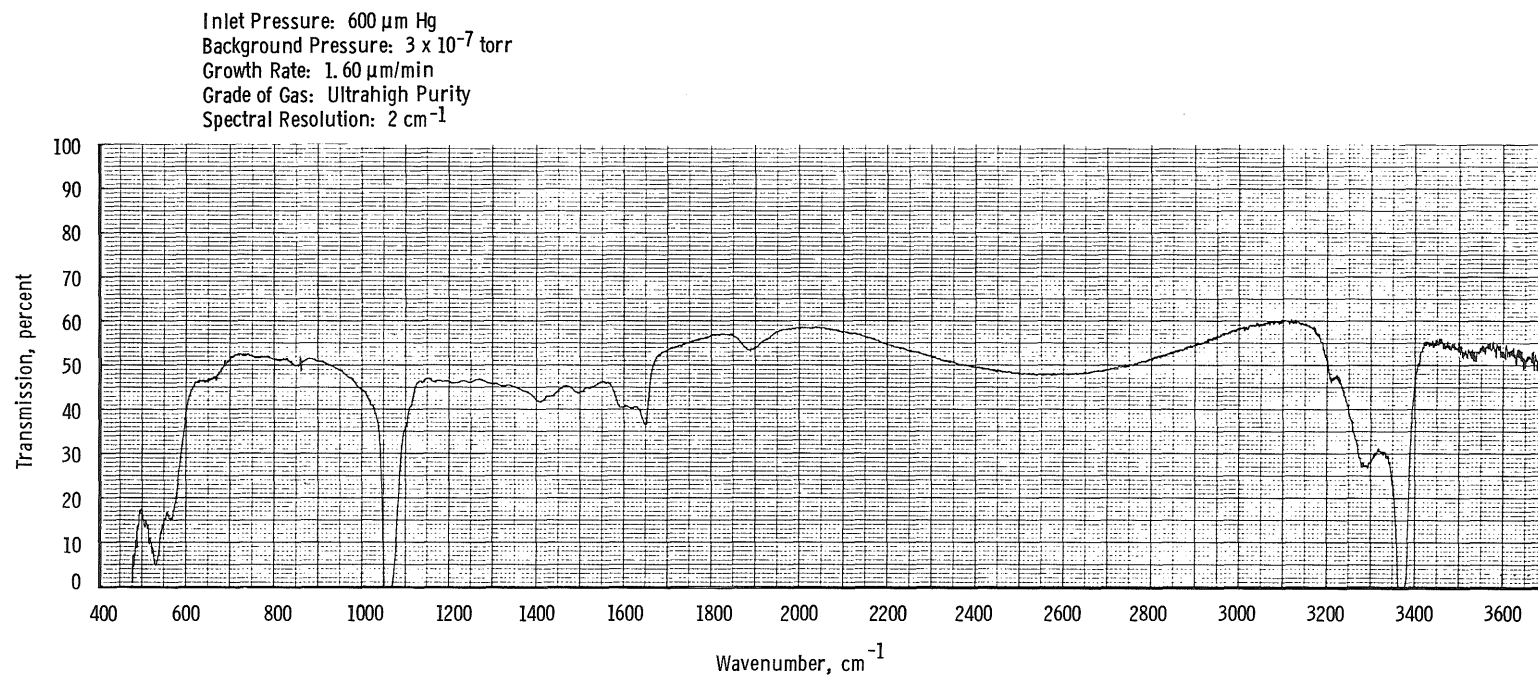


k. 2.340- $\mu\text{m}$ -thick deposit  
Figure 29. Continued.





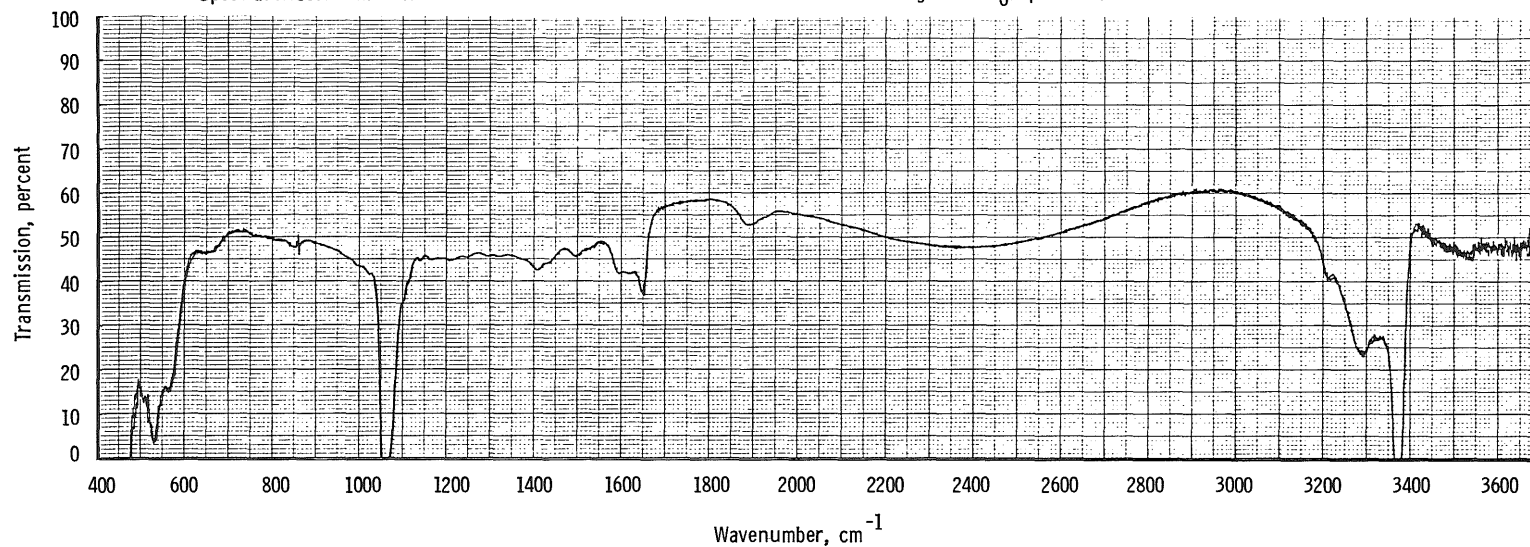
I. 2.562- $\mu\text{m}$ -thick deposit  
Figure 29. Continued.



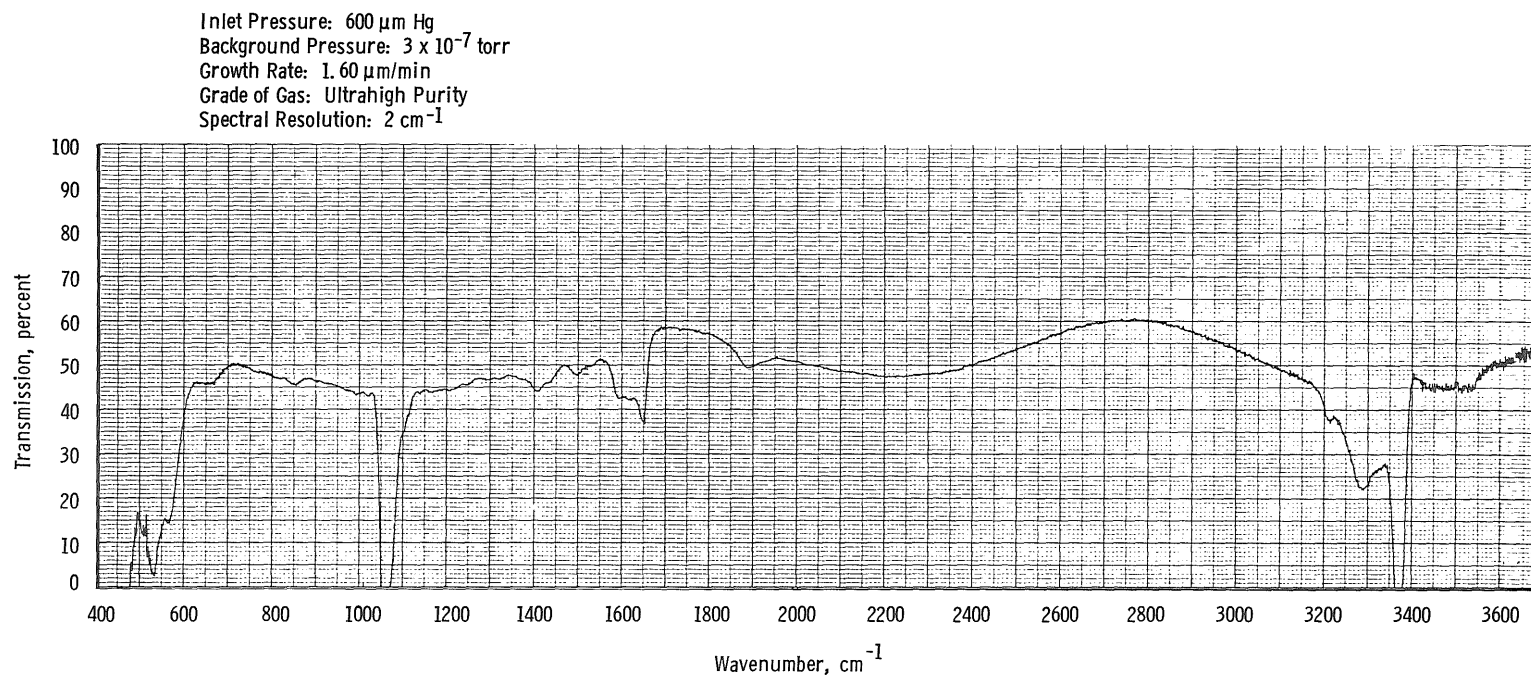
m. 2.785- $\mu\text{m}$ -thick deposit  
Figure 29. Continued.

Inlet Pressure: 600  $\mu\text{m Hg}$   
 Background Pressure:  $3 \times 10^{-7}$  torr  
 Growth Rate: 1.60  $\mu\text{m/min}$   
 Grade of Gas: Ultrahigh Purity  
 Spectral Resolution: 2  $\text{cm}^{-1}$

NOTES: The two traces are from separate background spectra, one taken earlier before deposition began and then one taken when  $\text{NH}_3$  was 3  $\mu\text{m}$  thick. The excellent reproducibility implies no drift in infrared light source and other parameters that dictate the background ( $I_0$ ) spectrum.

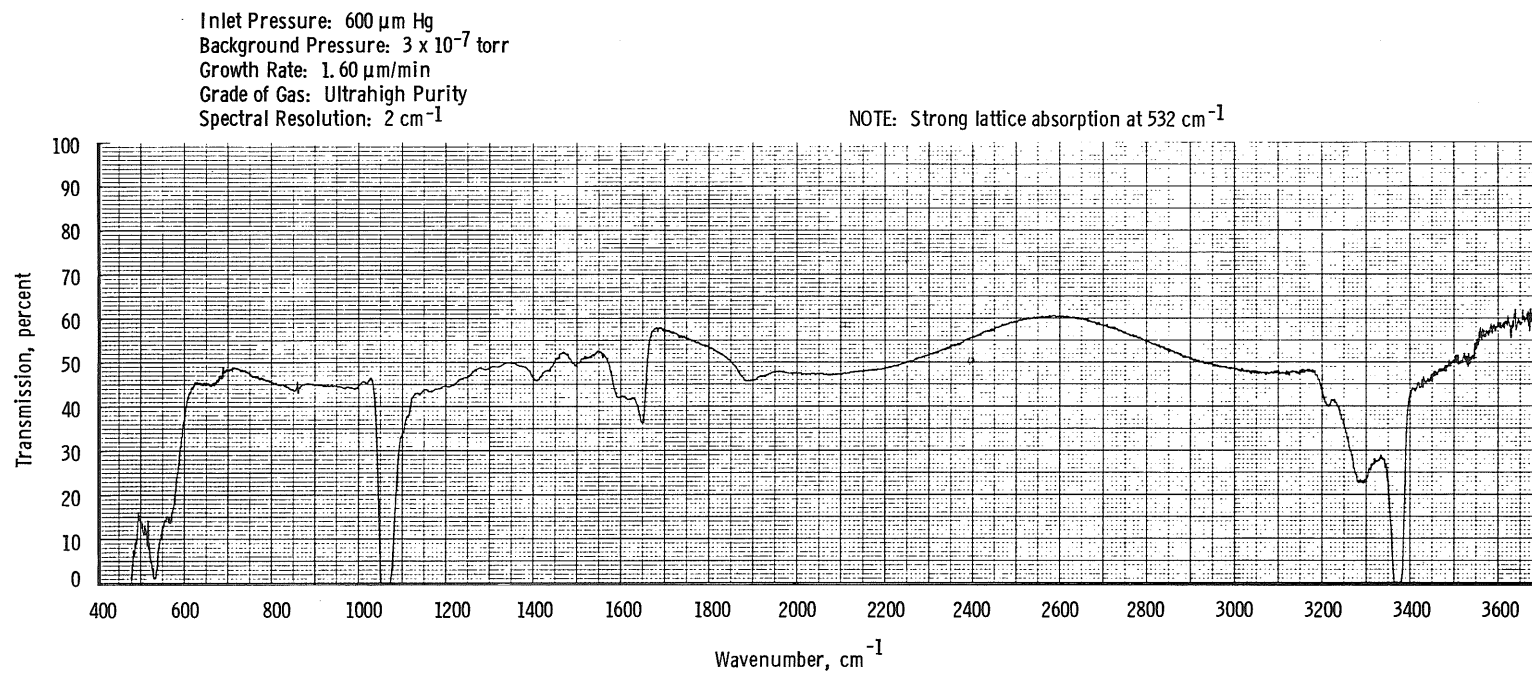


n. 3.010- $\mu\text{m}$ -thick deposit  
 Figure 29. Continued.

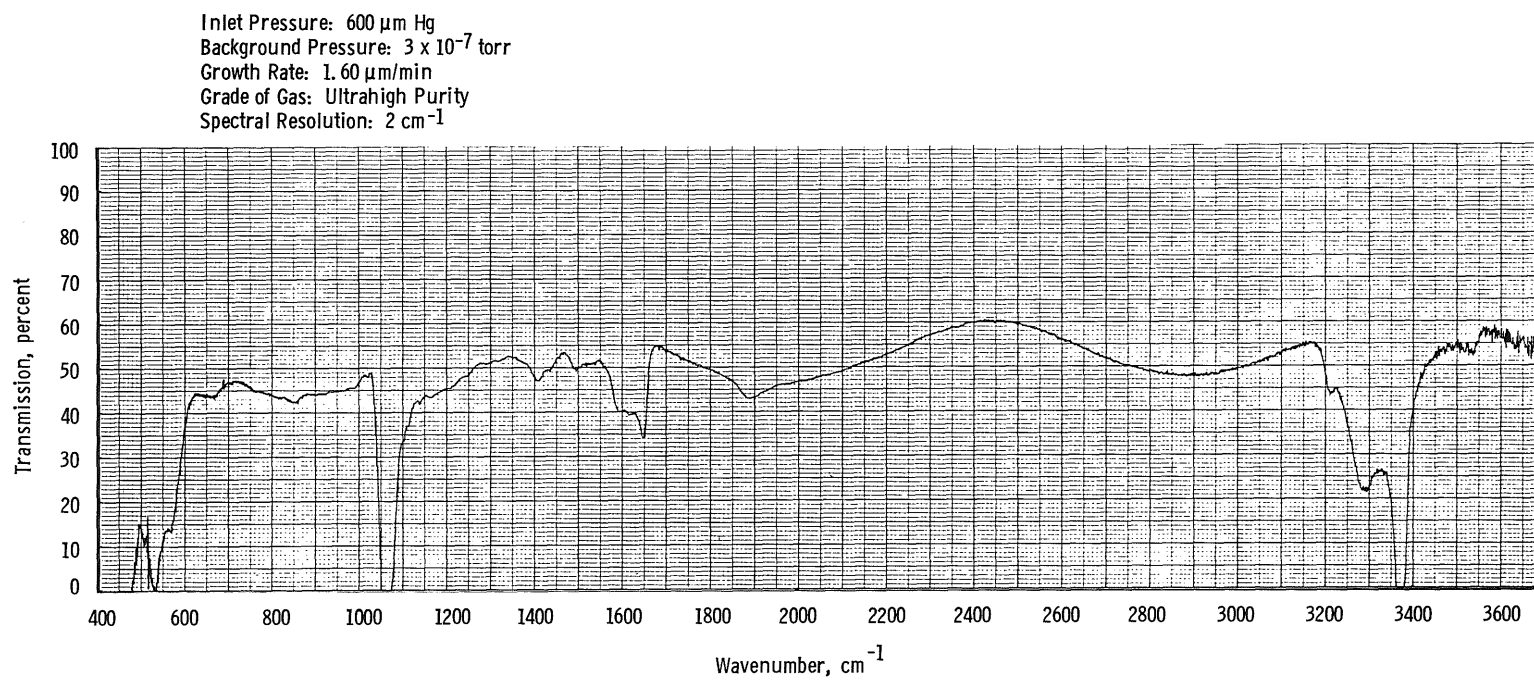


o. 3.231- $\mu\text{m}$ -thick deposit  
Figure 29. Continued.

102

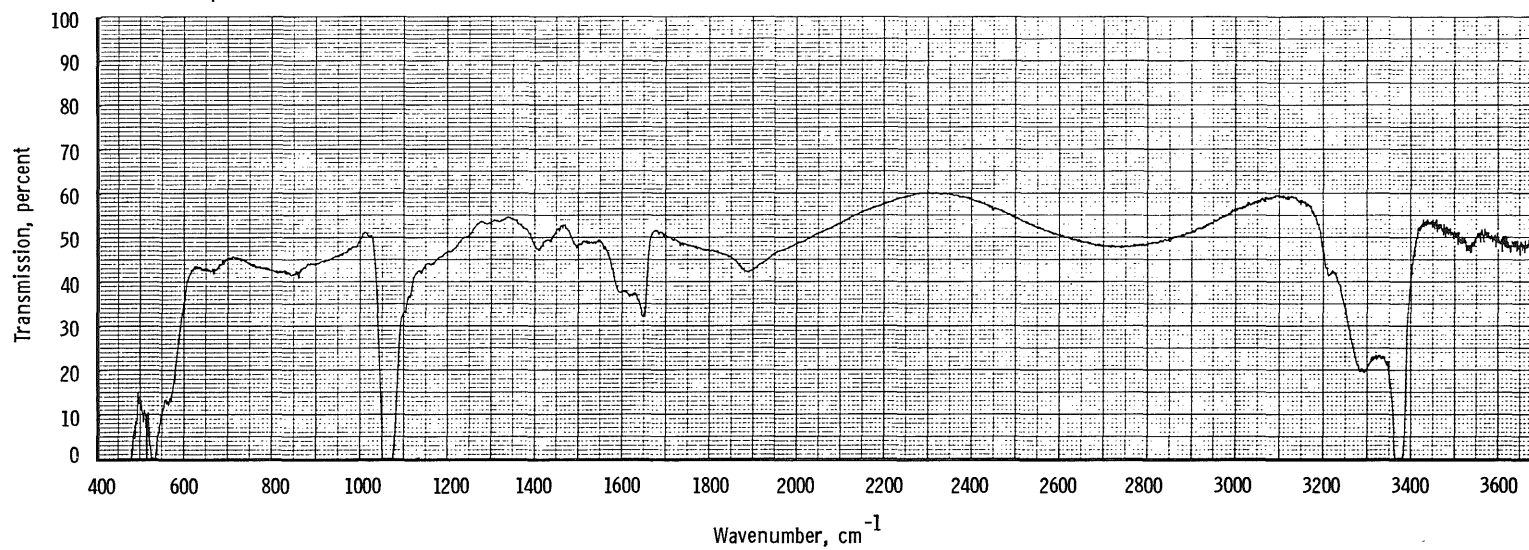


p. 3.454- $\mu\text{m}$ -thick deposit  
Figure 29. Continued.

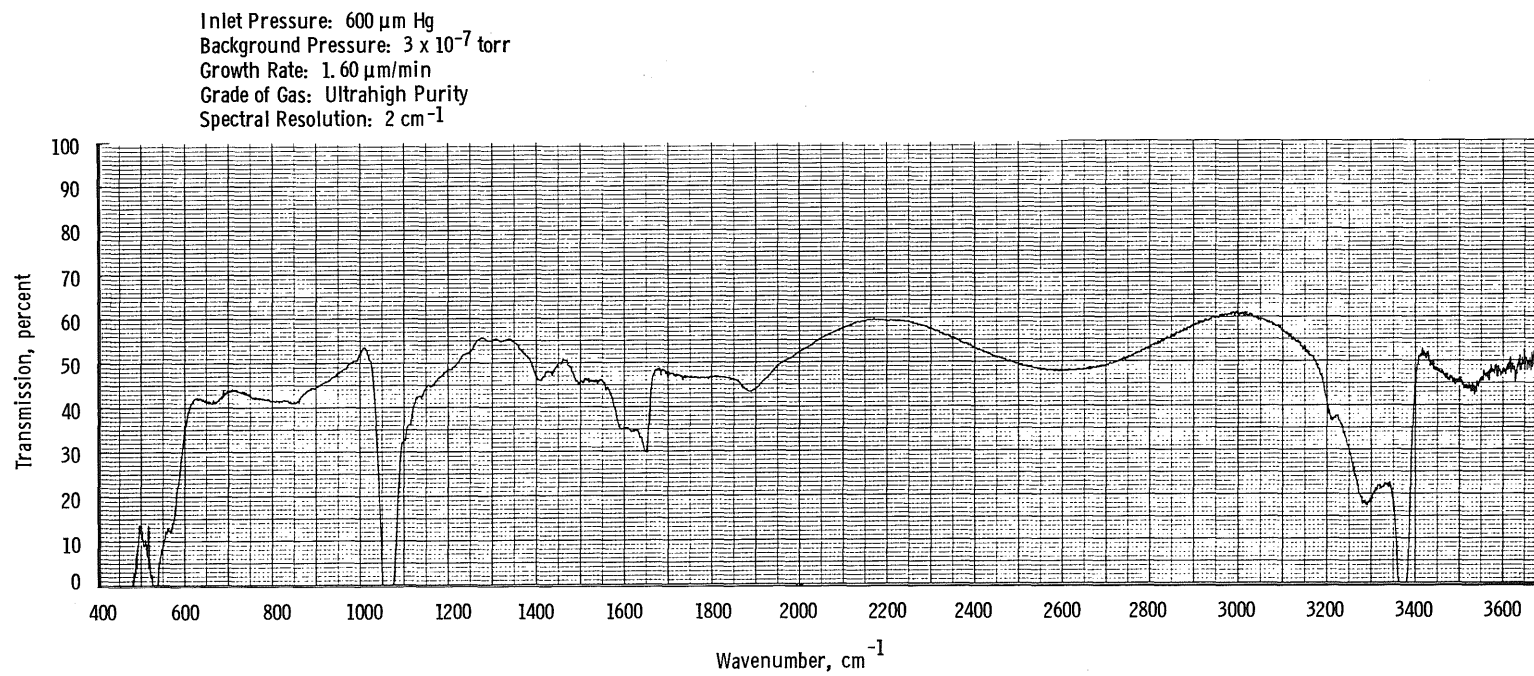


q. 3.676- $\mu\text{m}$ -thick deposit  
Figure 29. Continued.

Inlet Pressure: 600  $\mu\text{m Hg}$   
Background Pressure:  $3 \times 10^{-7}$  torr  
Growth Rate: 1.60  $\mu\text{m/min}$   
Grade of Gas: Ultrahigh Purity  
Spectral Resolution: 2  $\text{cm}^{-1}$



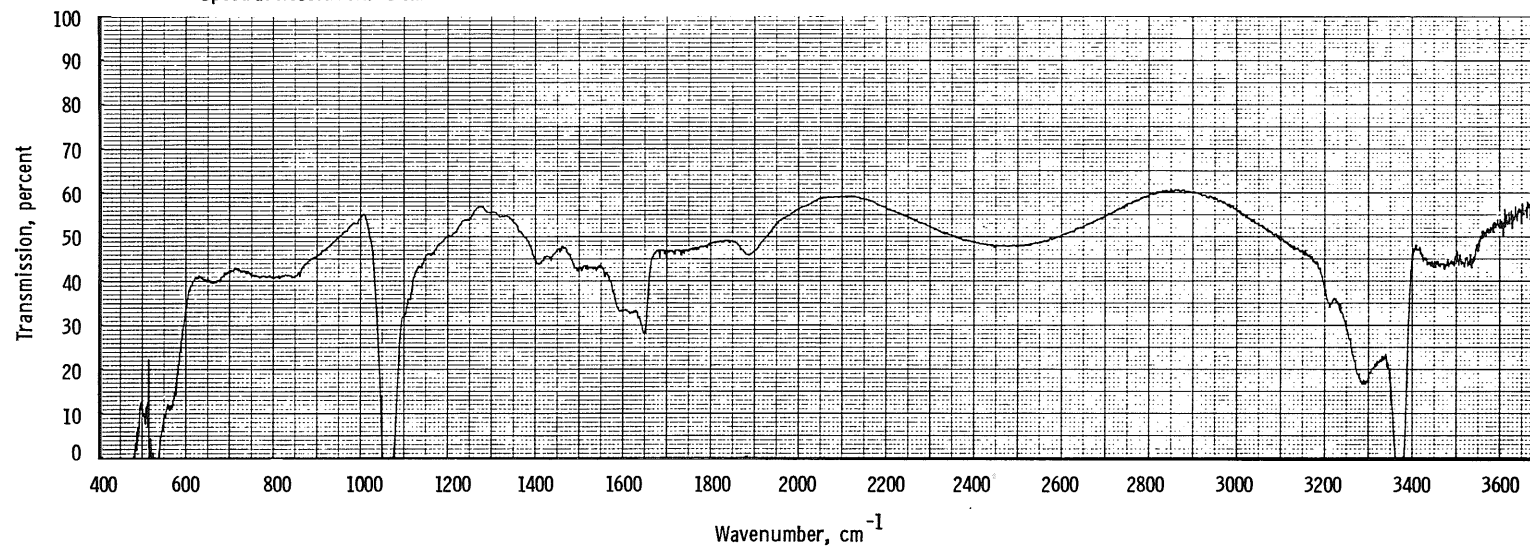
r. 3.990- $\mu\text{m}$ -thick deposit  
Figure 29. Continued.



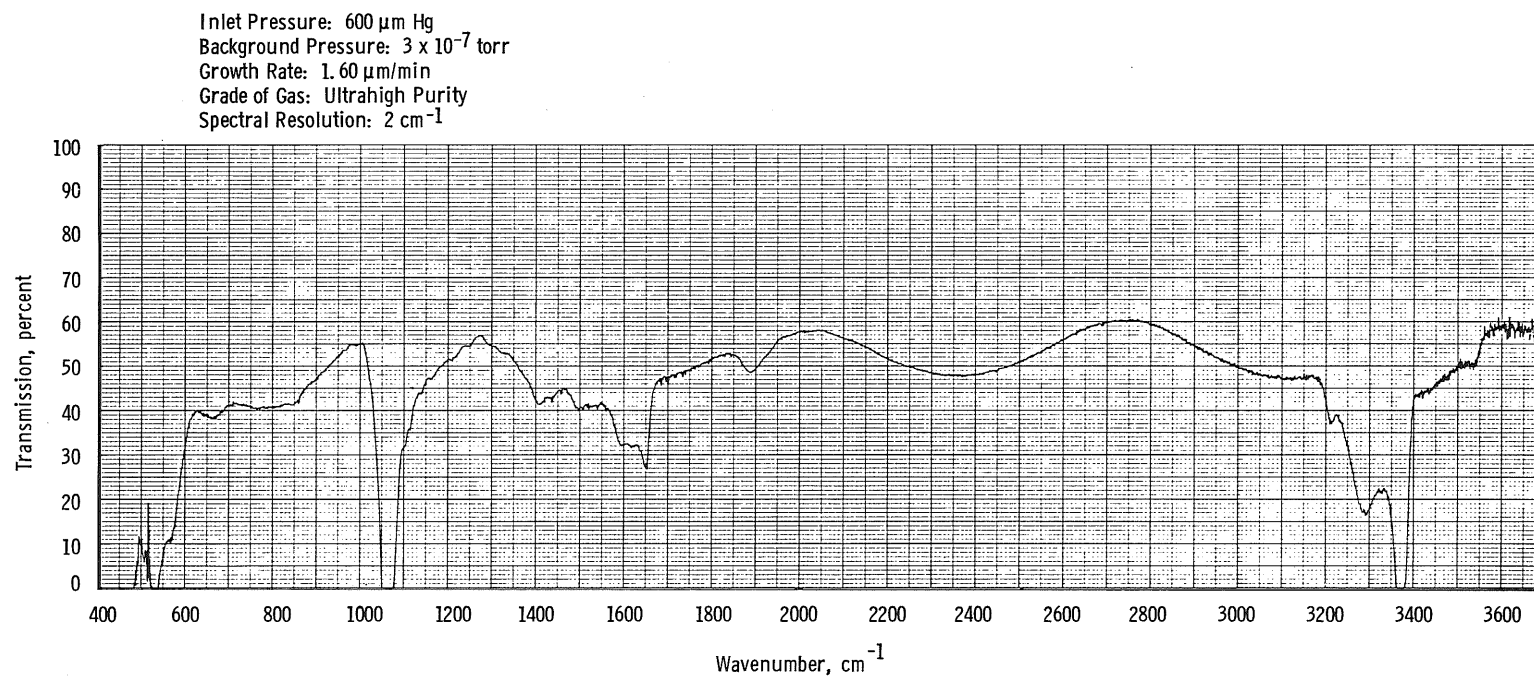
s. 4.120- $\mu\text{m}$ -thick deposit  
Figure 29. Continued.



Inlet Pressure: 600  $\mu\text{m Hg}$   
Background Pressure:  $3 \times 10^{-7}$  torr  
Growth Rate: 1.60  $\mu\text{m/min}$   
Grade of Gas: Ultrahigh Purity  
Spectral Resolution: 2  $\text{cm}^{-1}$

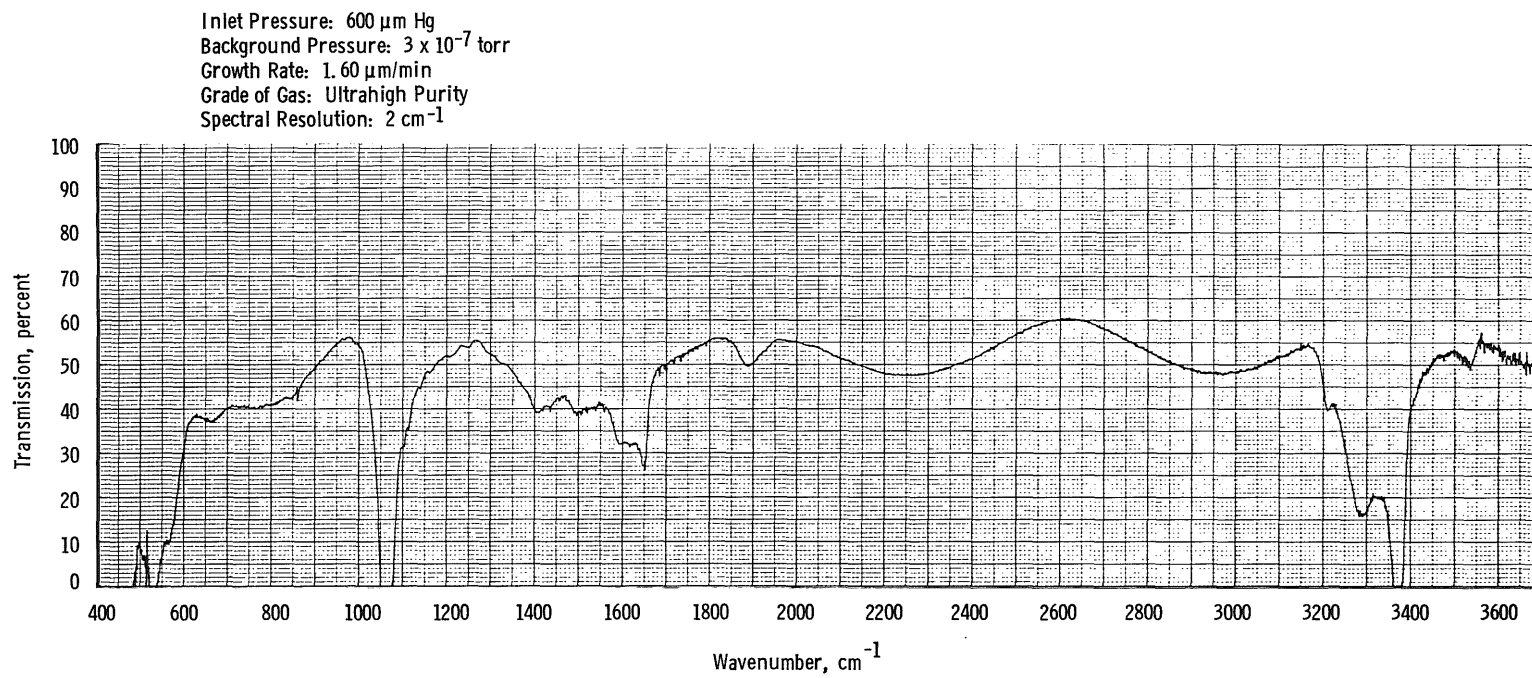


t. 4.340- $\mu\text{m}$ -thick deposit  
Figure 29. Continued.

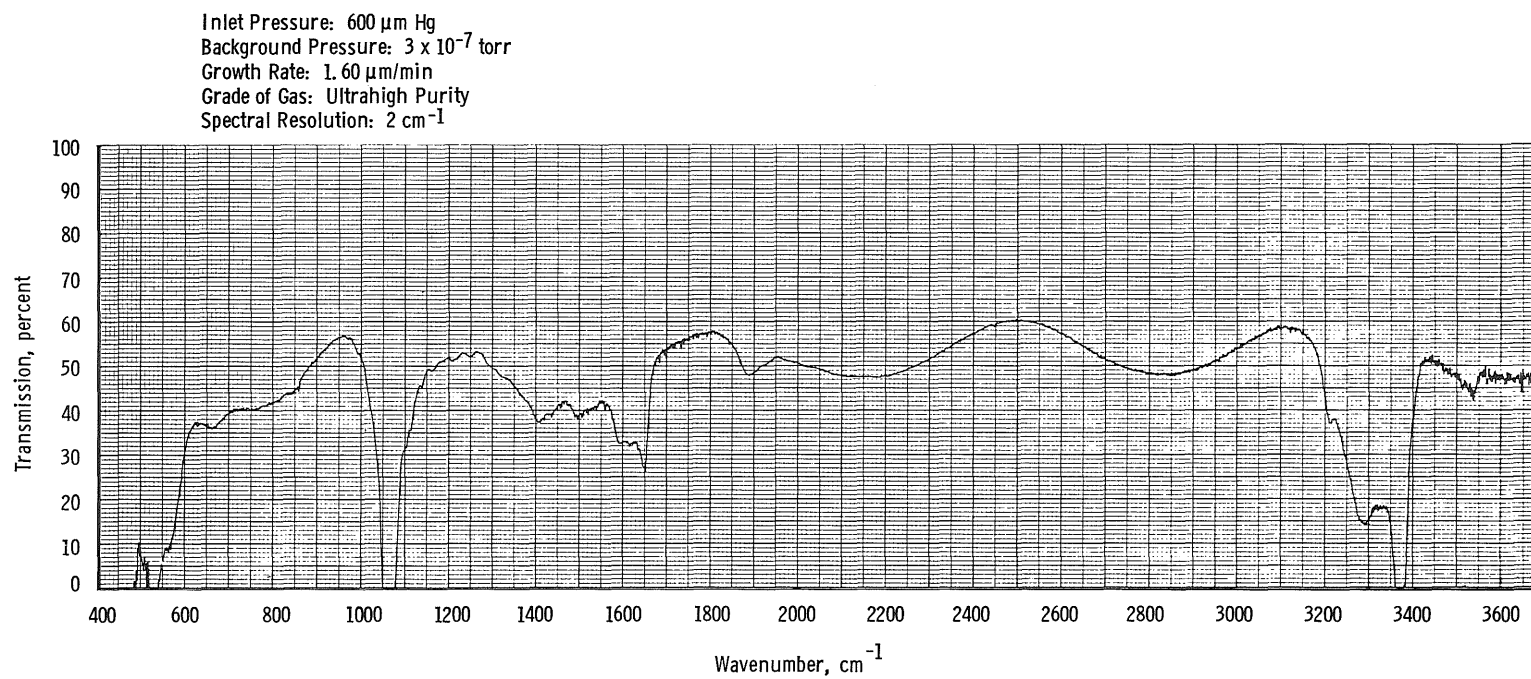


u. 4.570- $\mu\text{m}$ -thick deposit  
Figure 29. Continued.

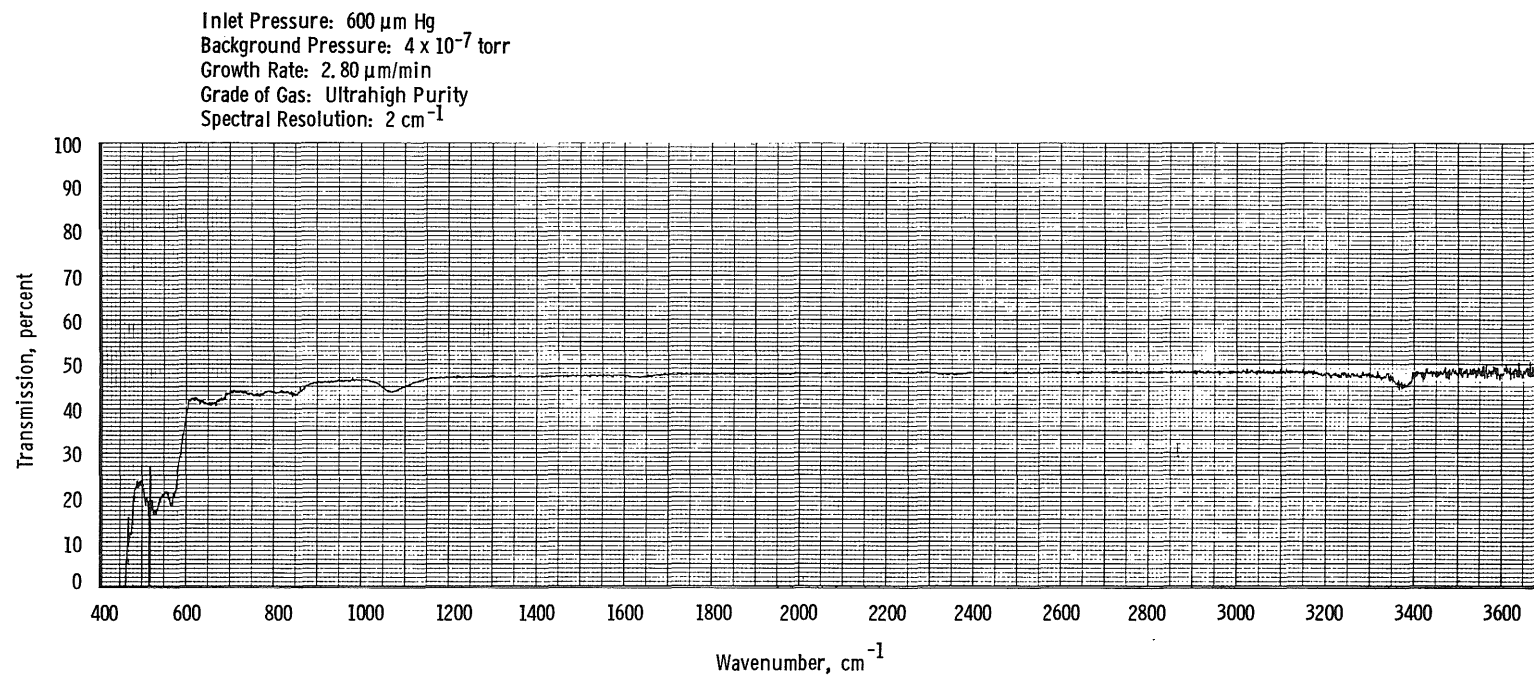
801



v. 4.790- $\mu\text{m}$ -thick deposit  
Figure 29. Continued.

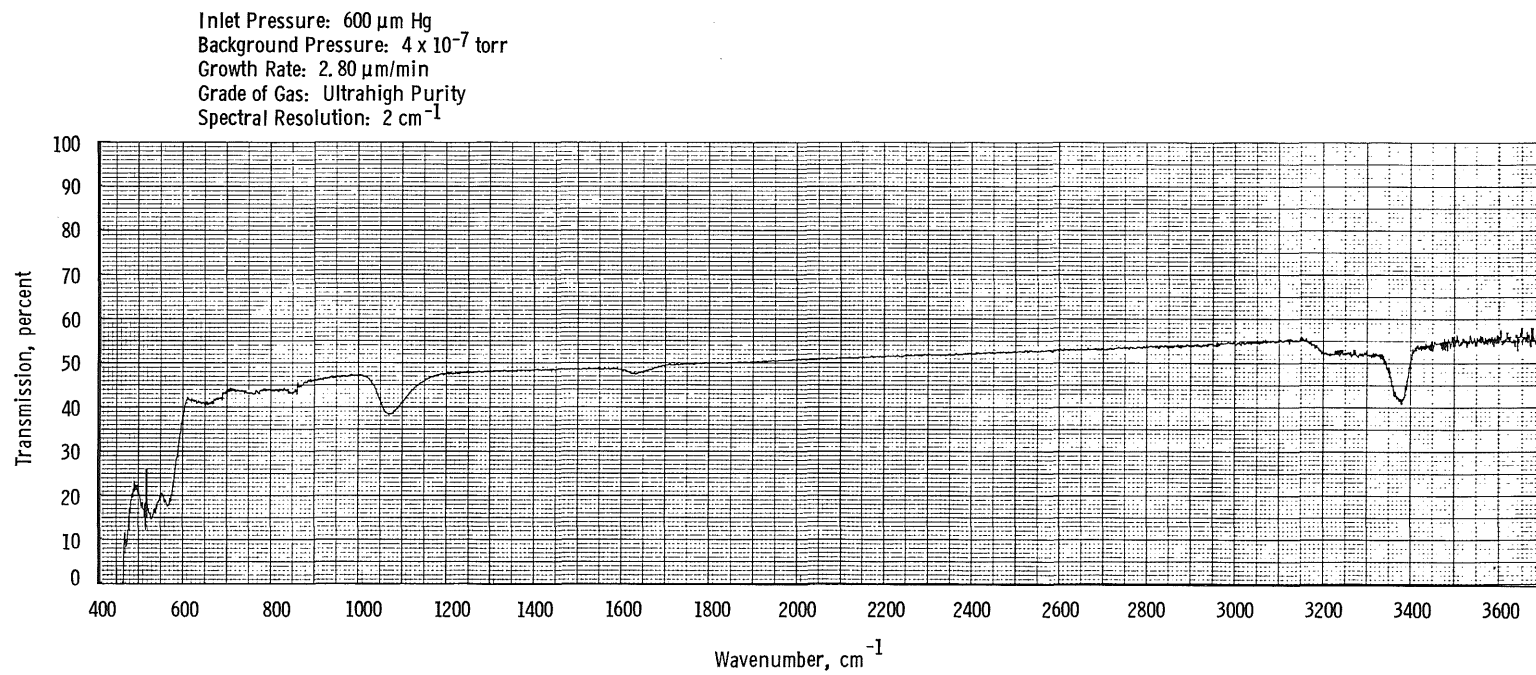


w. 5.010- $\mu\text{m}$ -thick deposit  
Figure 29. Concluded.



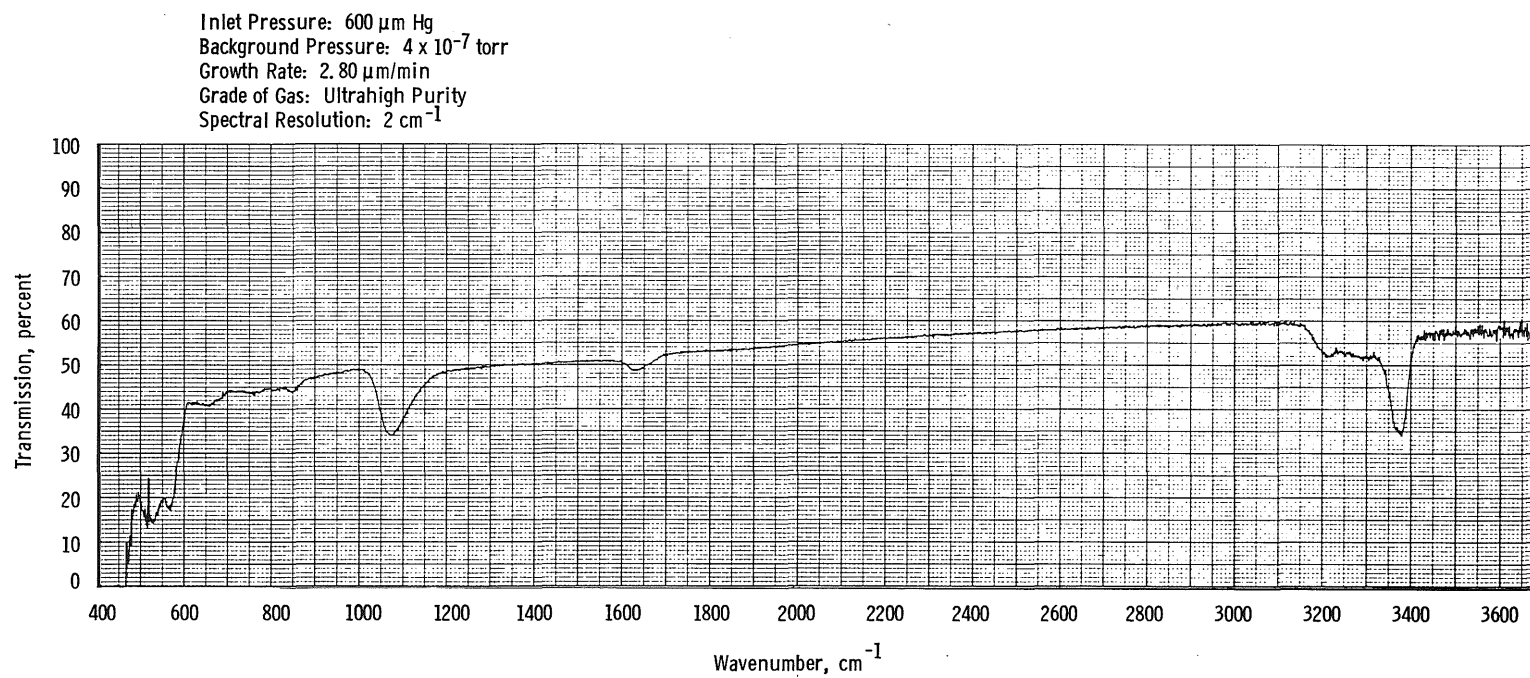
a. 0.111- $\mu\text{m}$ -thick deposit

Figure 30. Transmission of 20°K germanium window with various  $\text{NH}_3$  deposit thicknesses.

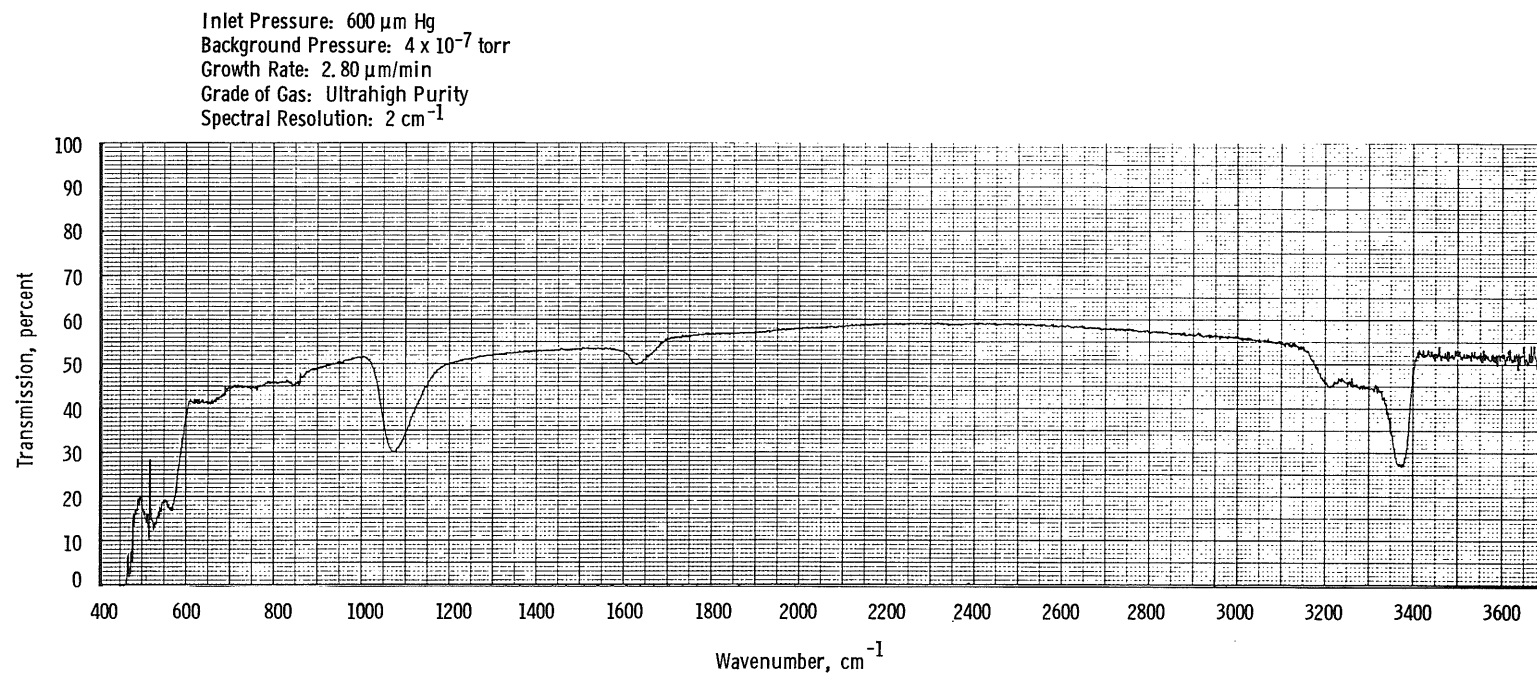


b. 0.334- $\mu\text{m}$ -thick deposit  
Figure 30. Continued.

112



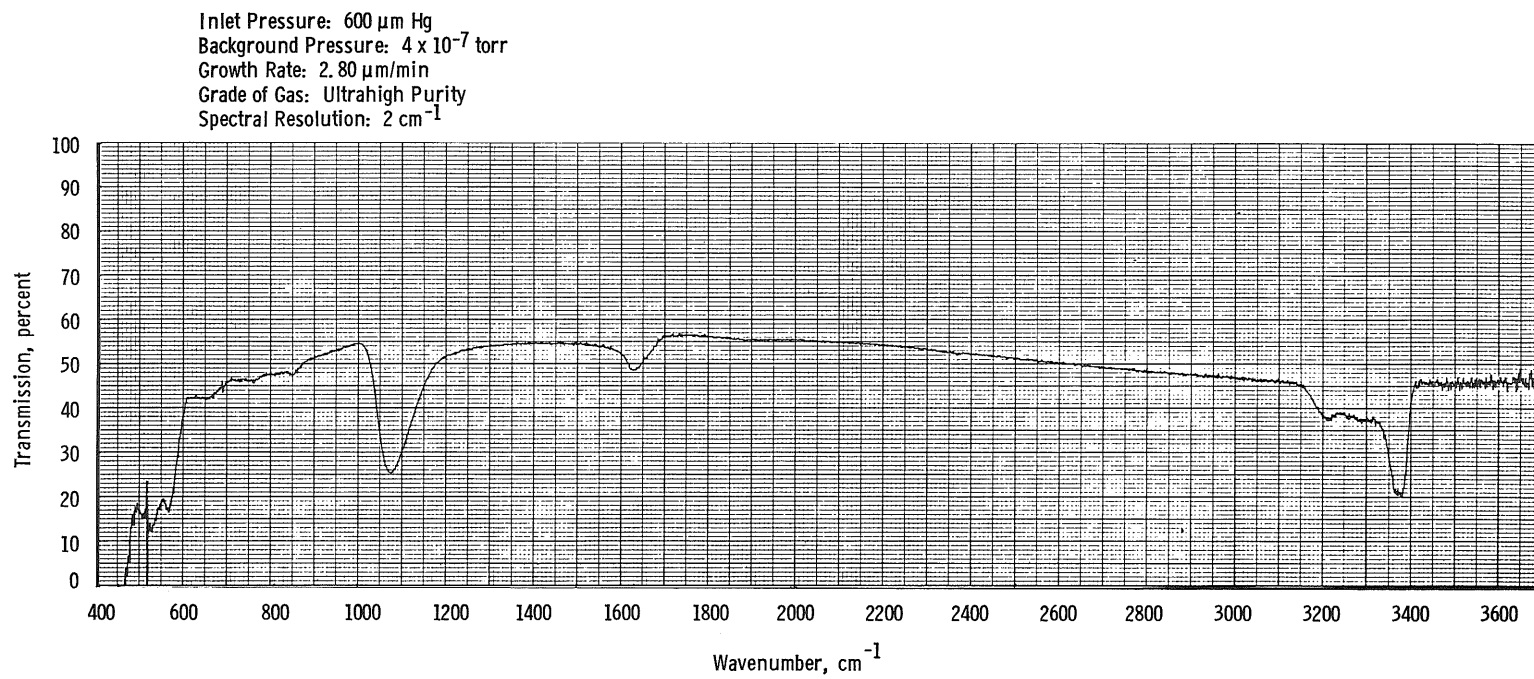
c. 0.557- $\mu\text{m}$ -thick deposit  
Figure 30. Continued.



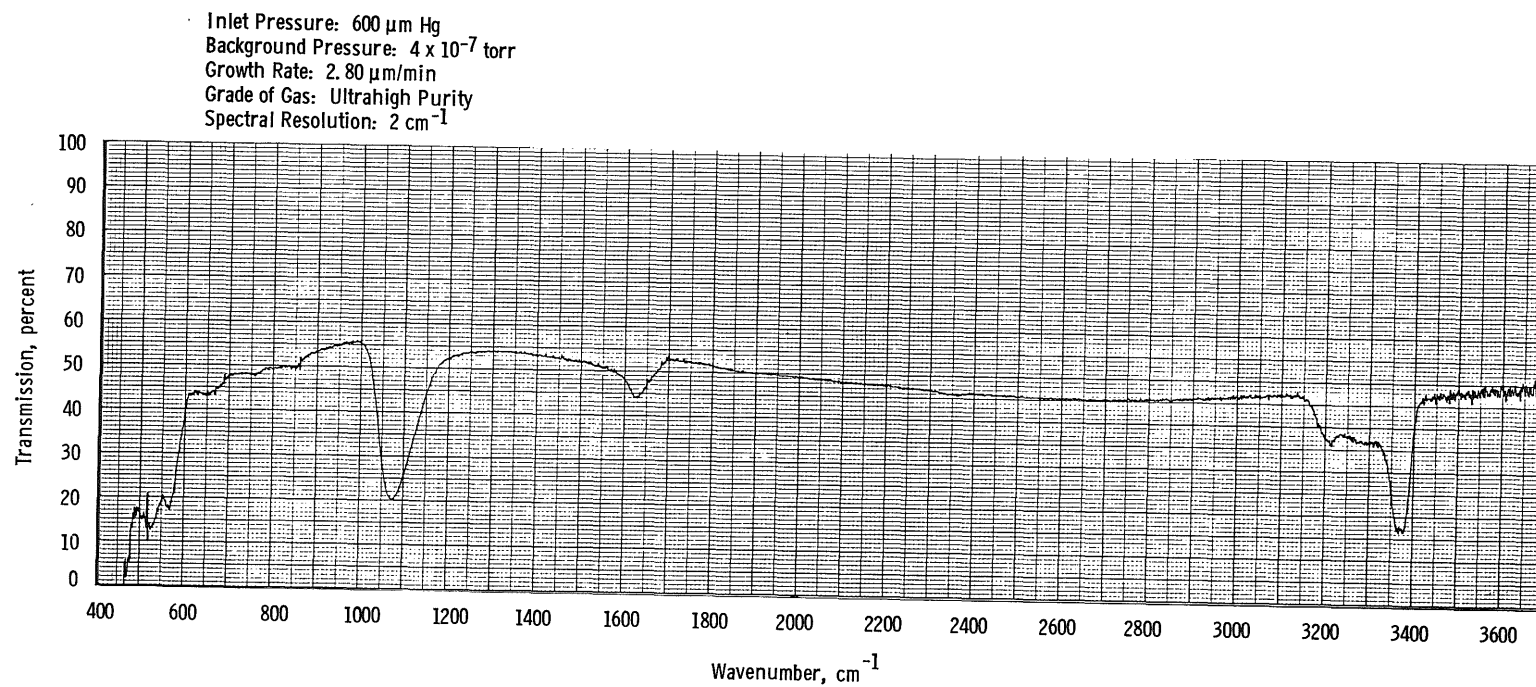
d. 0.780- $\mu\text{m}$ -thick deposit  
Figure 30. Continued.



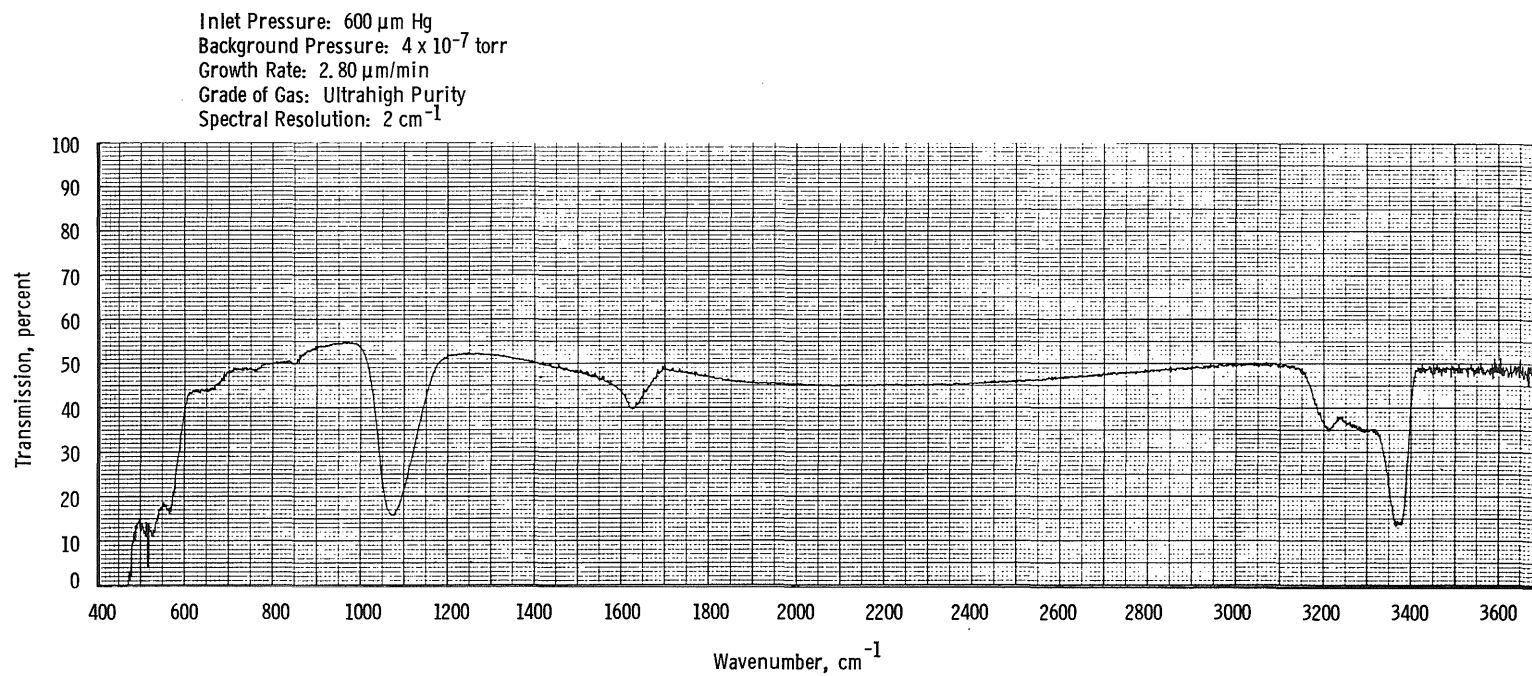
114



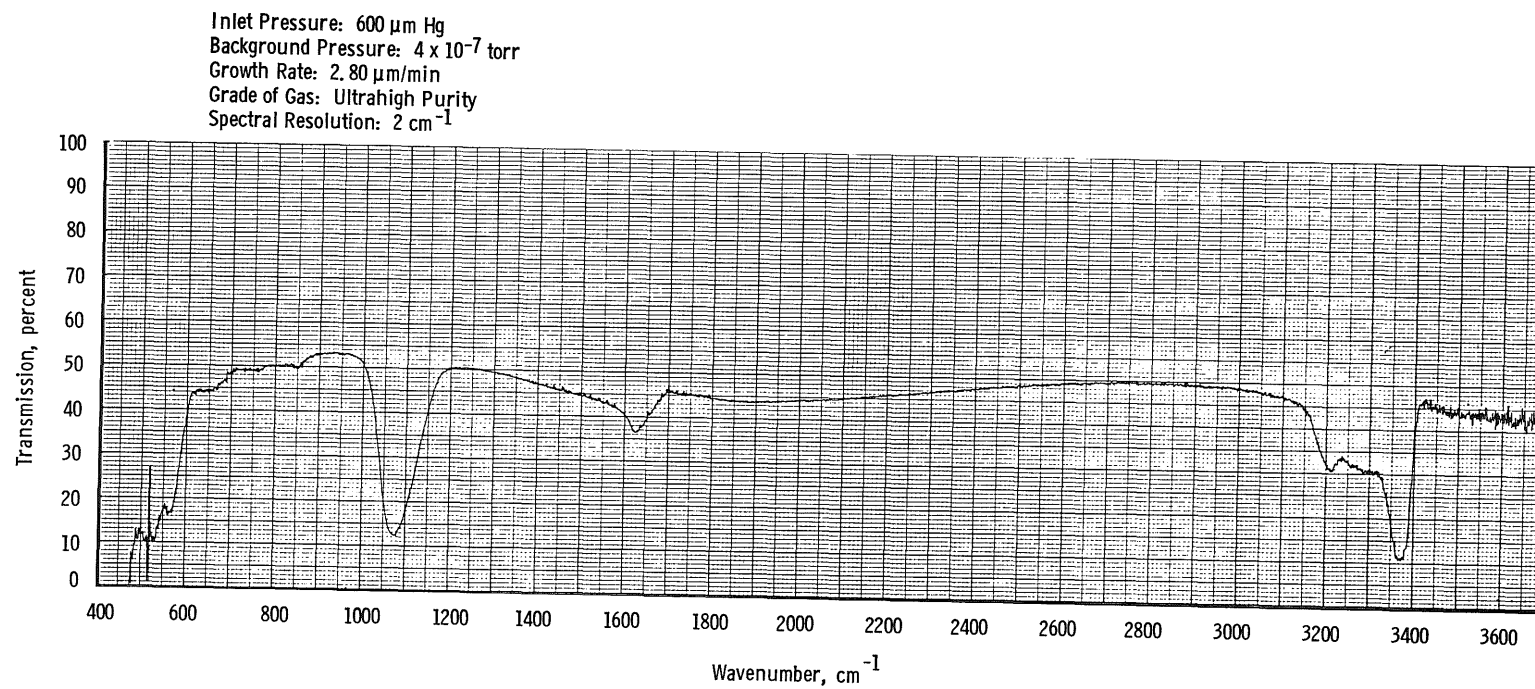
e. 1.003- $\mu\text{m}$ -thick deposit  
Figure 30. Continued.



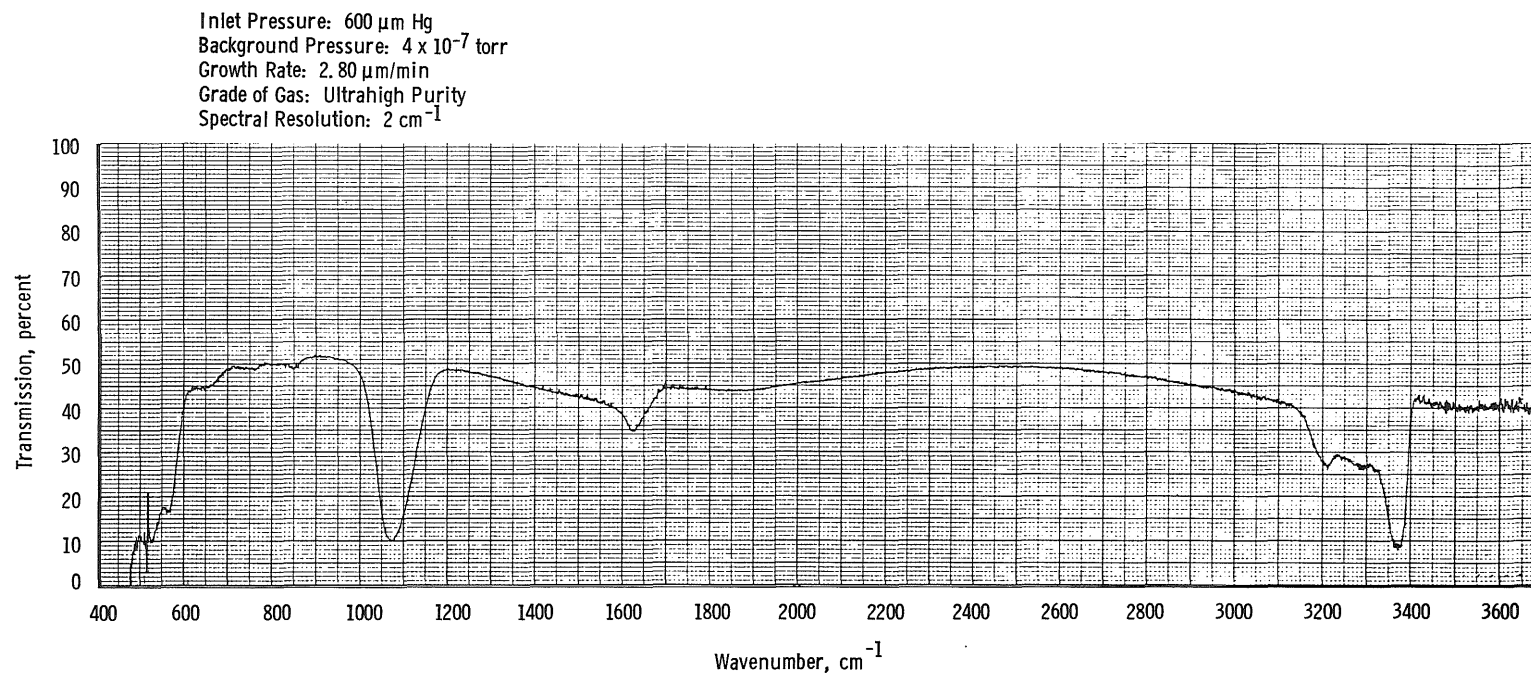
f. 1.225- $\mu\text{m}$ -thick deposit  
Figure 30. Continued.



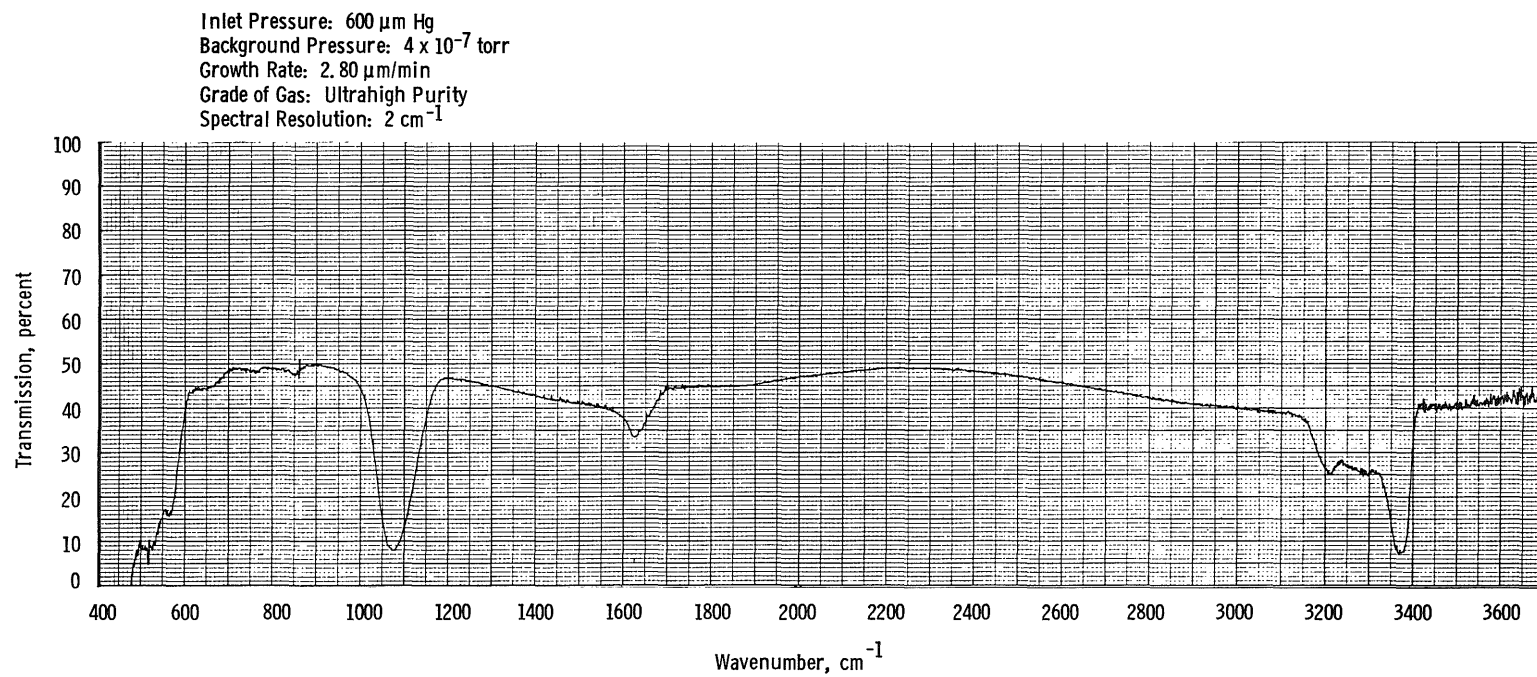
g. 1.448- $\mu\text{m}$ -thick deposit  
Figure 30. Continued.



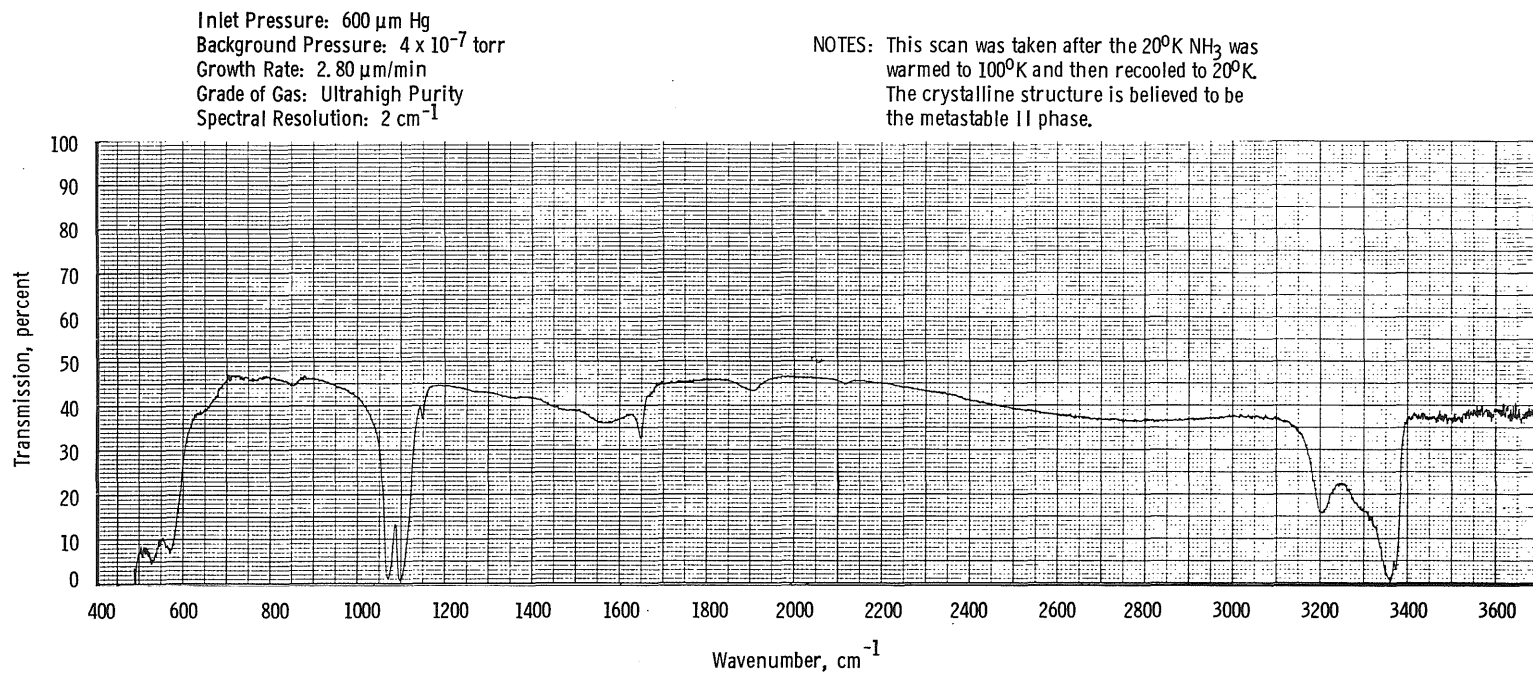
h. 1.671- $\mu\text{m}$ -thick deposit  
Figure 30. Continued.



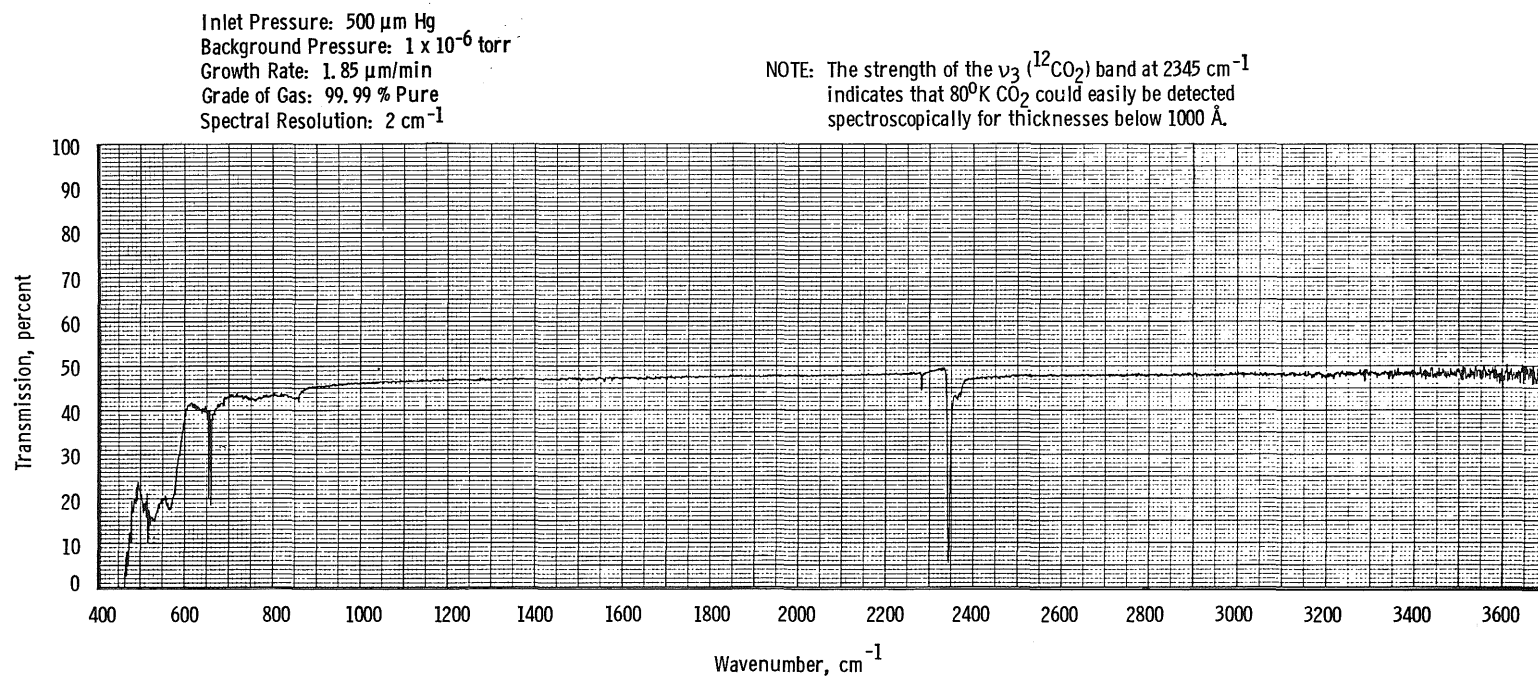
i. 1.894- $\mu\text{m}$ -thick deposit  
Figure 30. Continued.



j. 2.117- $\mu\text{m}$ -thick deposit  
Figure 30. Continued.



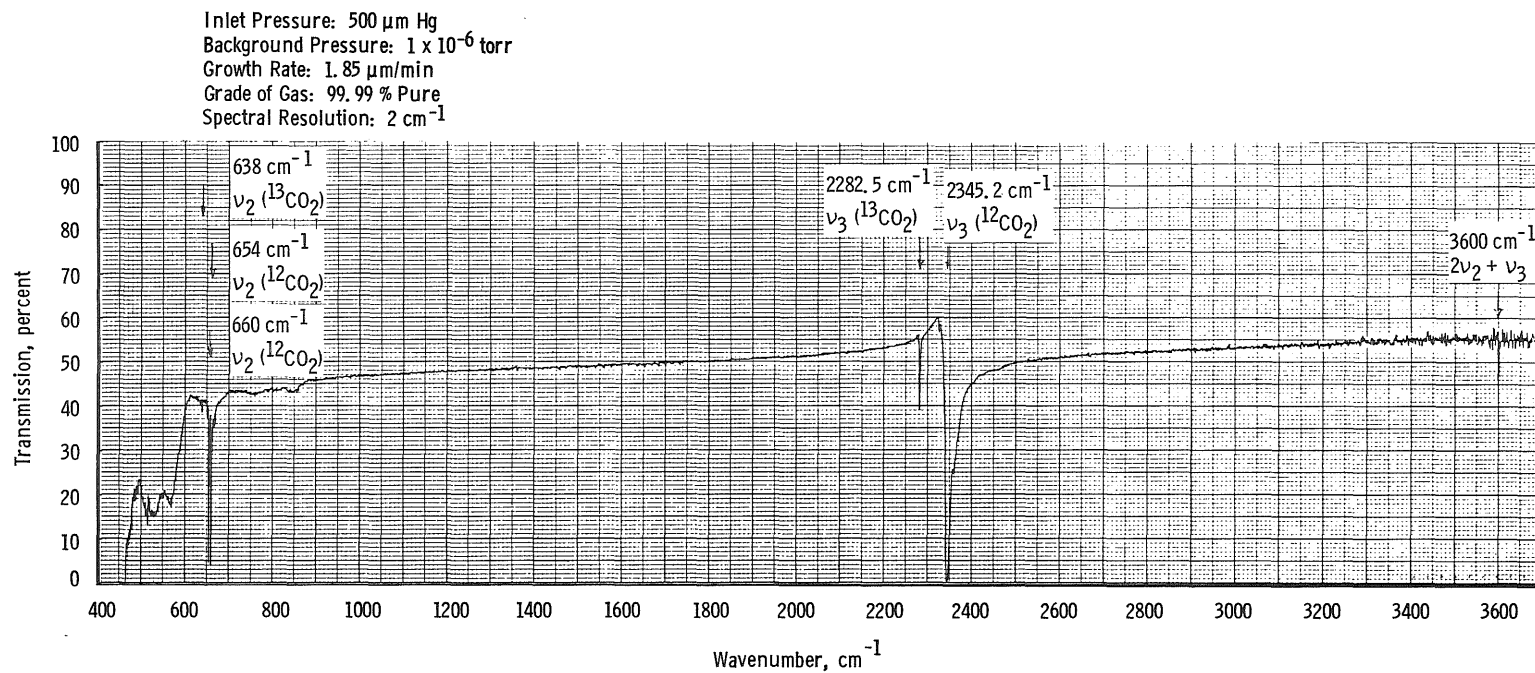
k. 1.80-2.10- $\mu\text{m}$ -thick deposit  
Figure 30. Concluded.



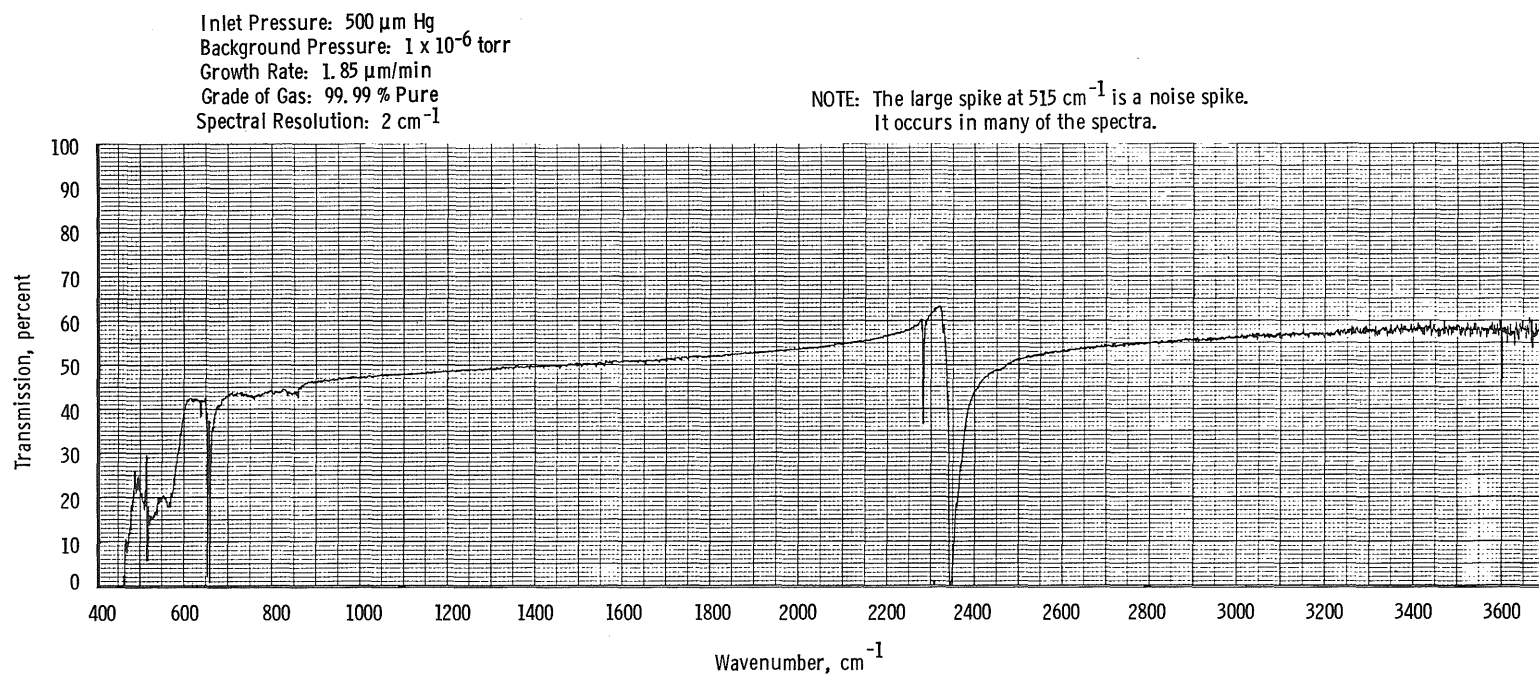
a. 0.111- $\mu\text{m}$ -thick deposit

Figure 31. Transmission of  $80^\circ\text{K}$  germanium window with various  $\text{CO}_2$  deposit thicknesses.

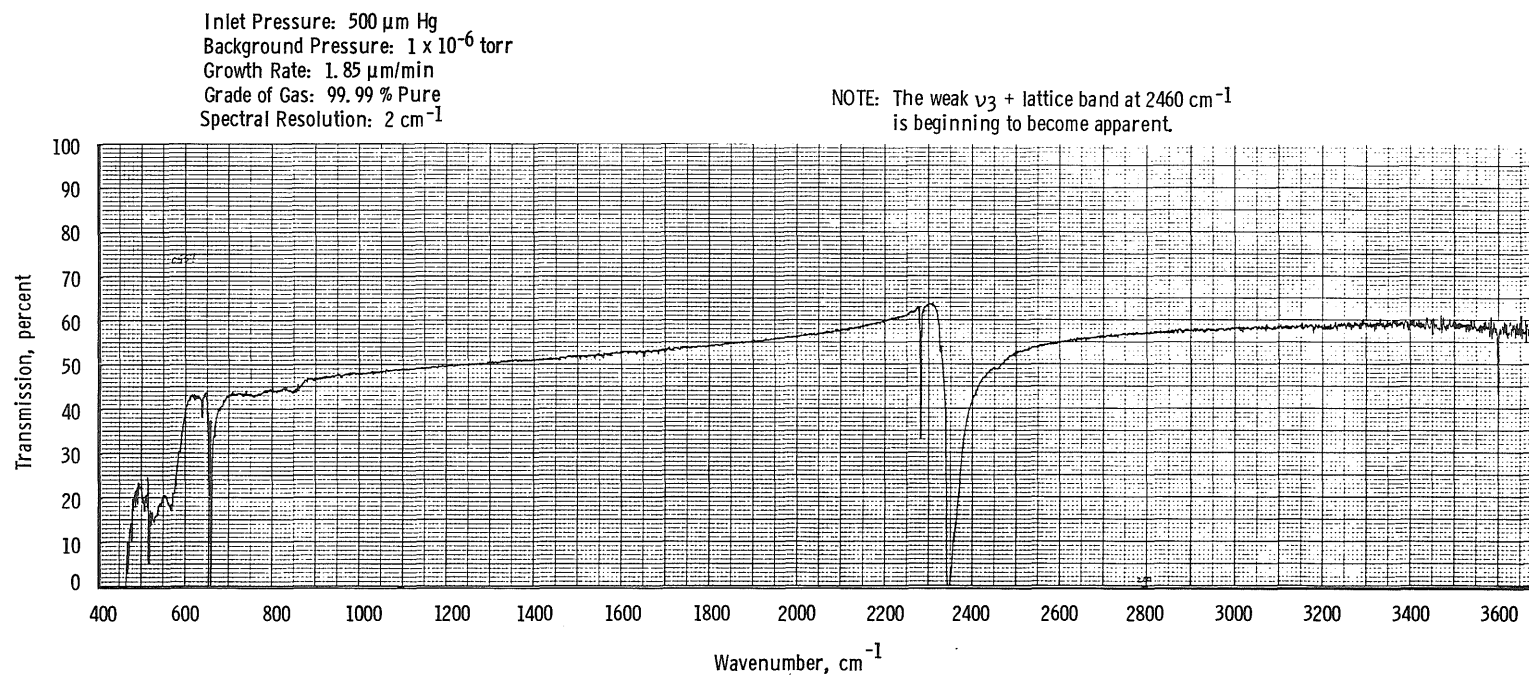




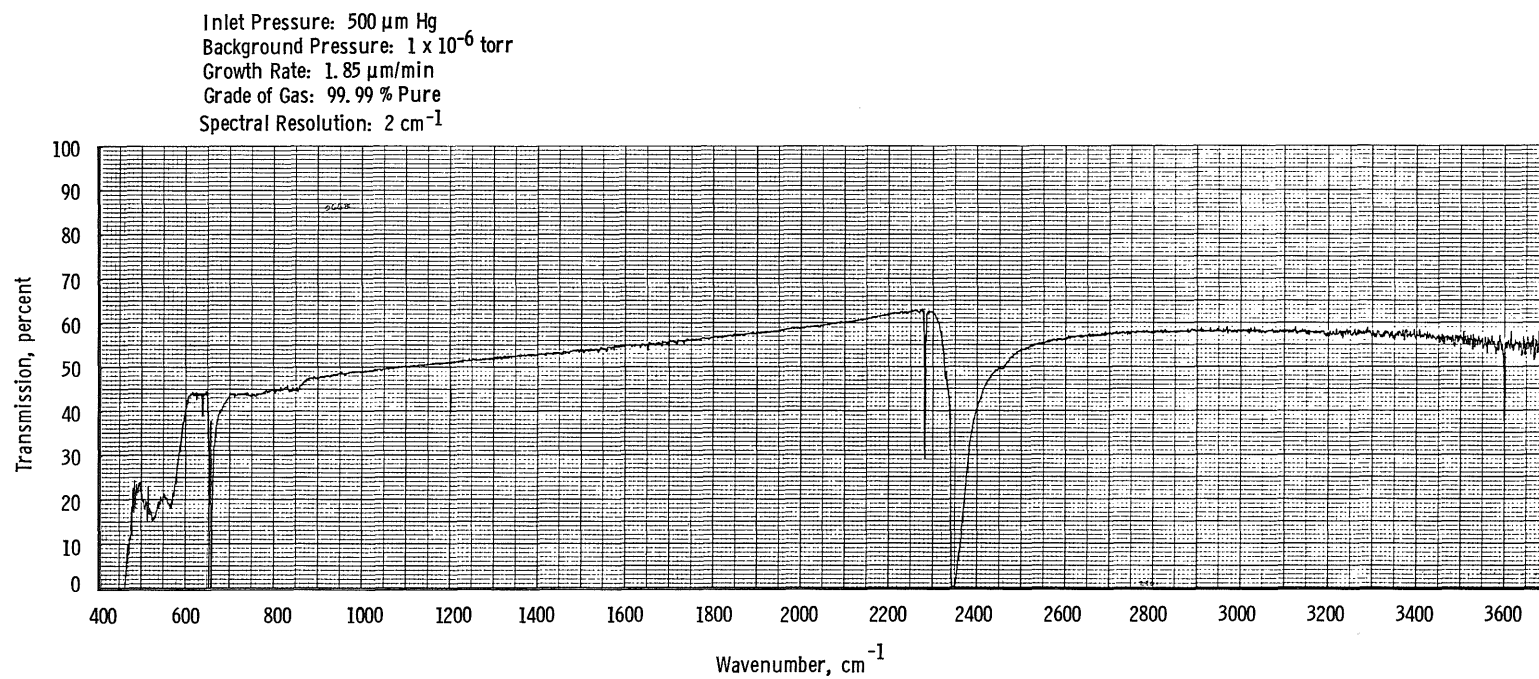
b. 0.334- $\mu\text{m}$ -thick deposit  
 Figure 31. Continued.



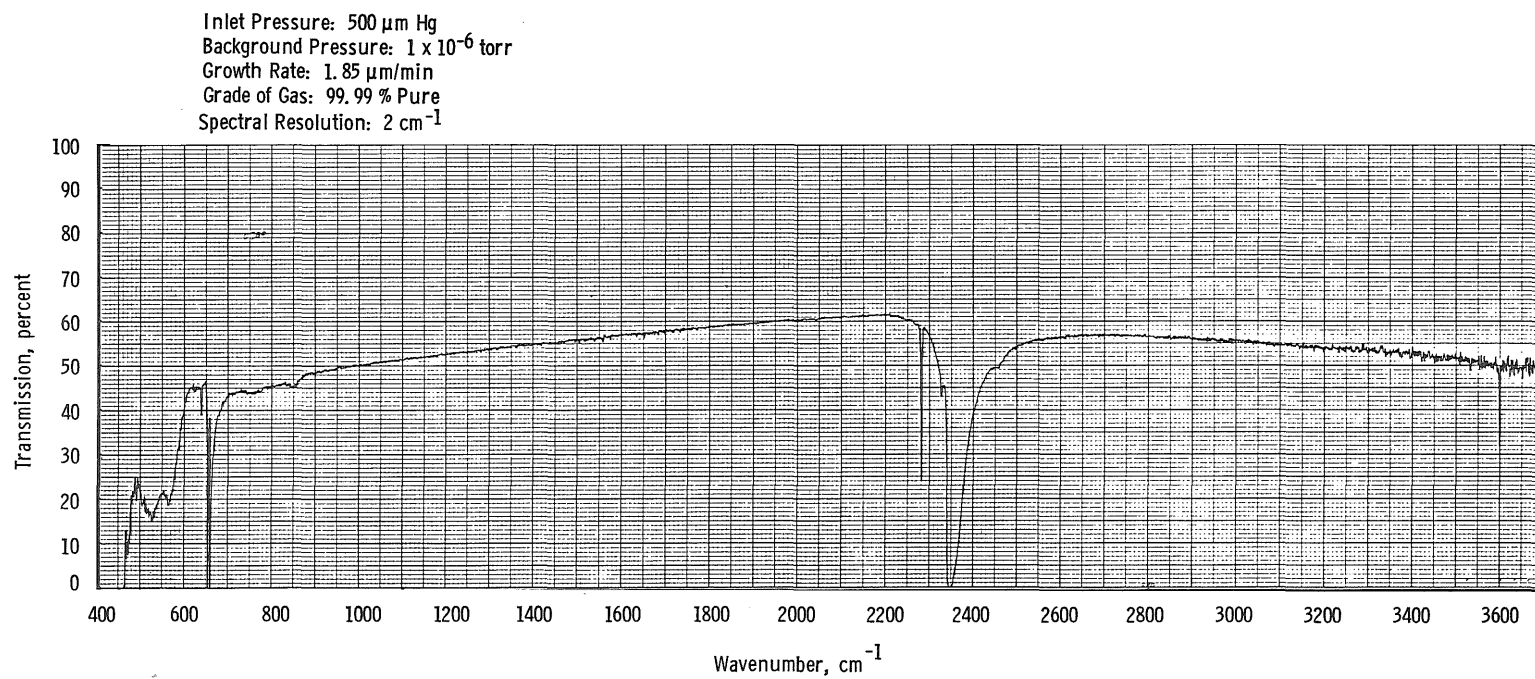
c. 0.446- $\mu\text{m}$ -thick deposit  
Figure 31. Continued.



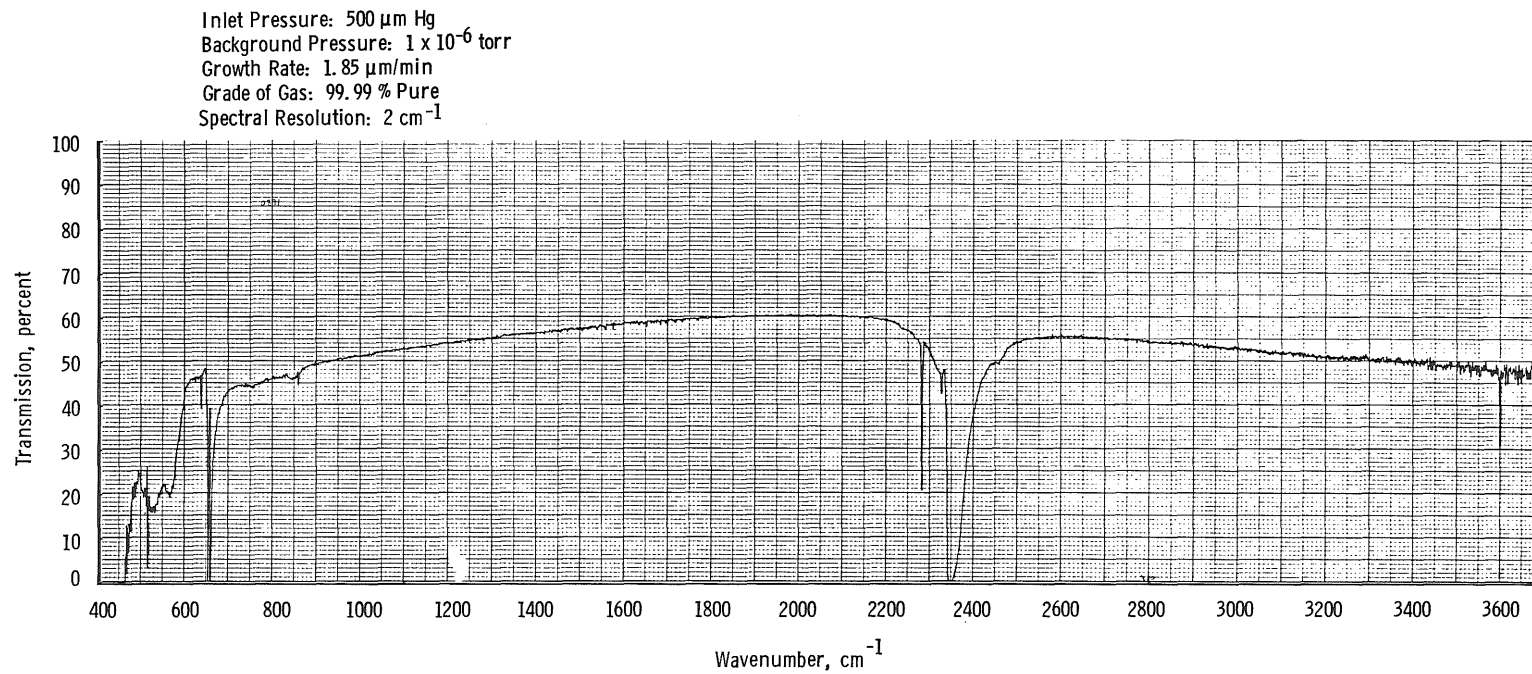
d. 0.557- $\mu\text{m}$ -thick deposit  
Figure 31. Continued.



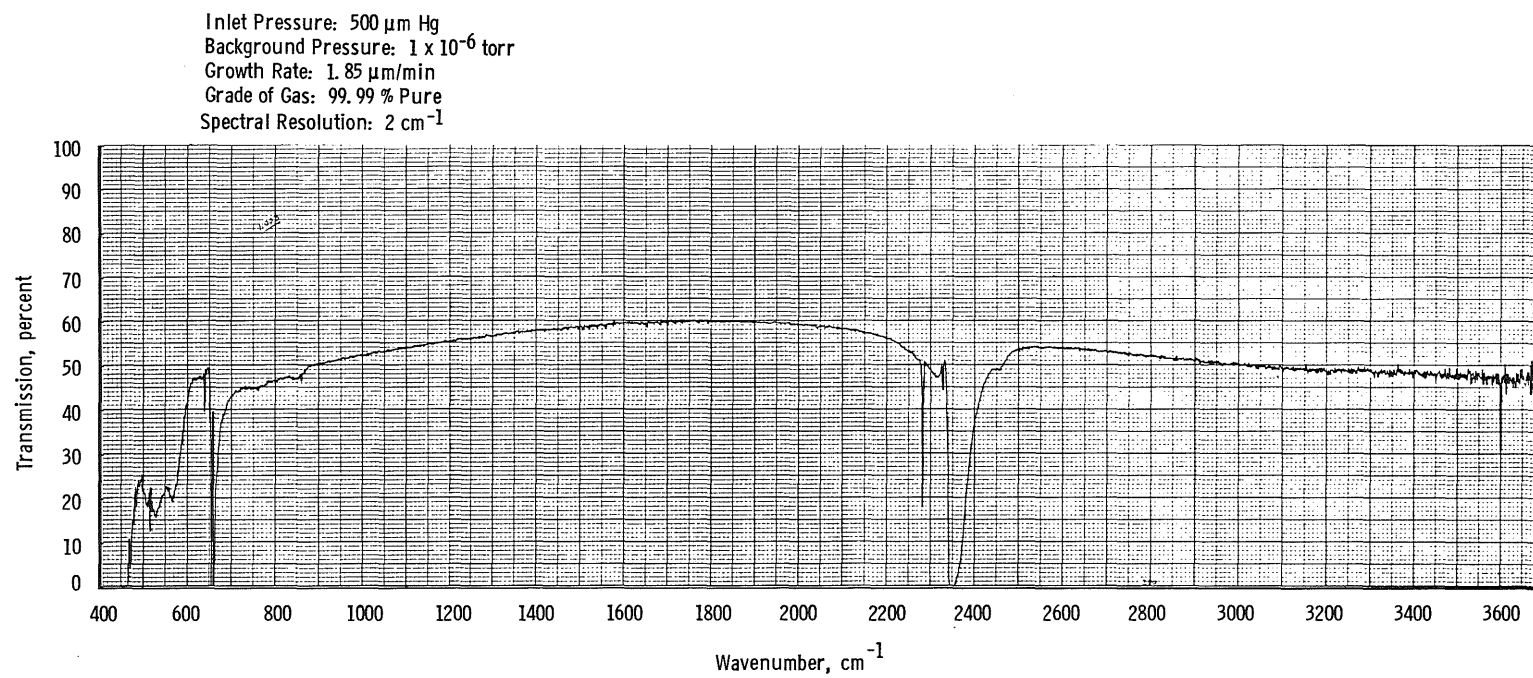
e. 0.668- $\mu\text{m}$ -thick deposit  
Figure 31. Continued.



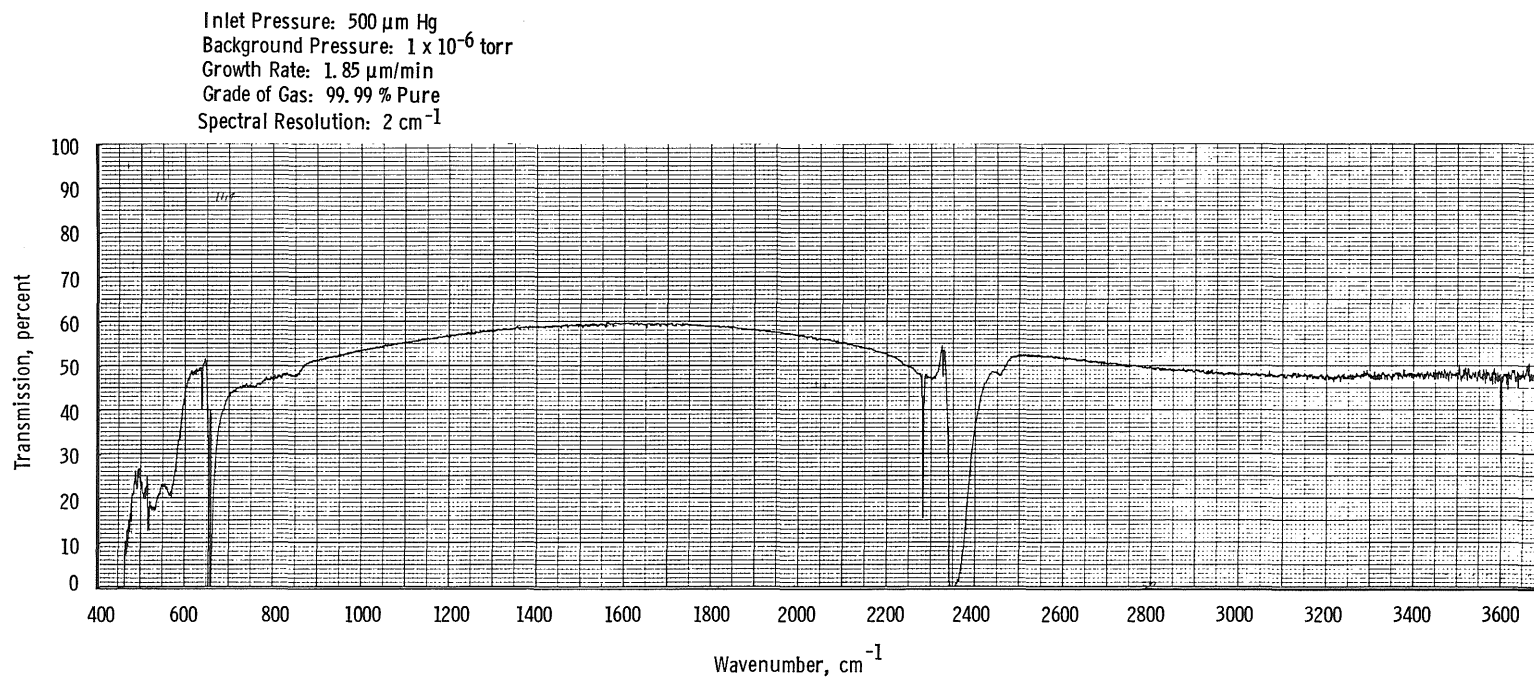
f. 0.780- $\mu\text{m}$ -thick deposit  
Figure 31. Continued.



g. 0.891- $\mu\text{m}$ -thick deposit  
Figure 31. Continued.



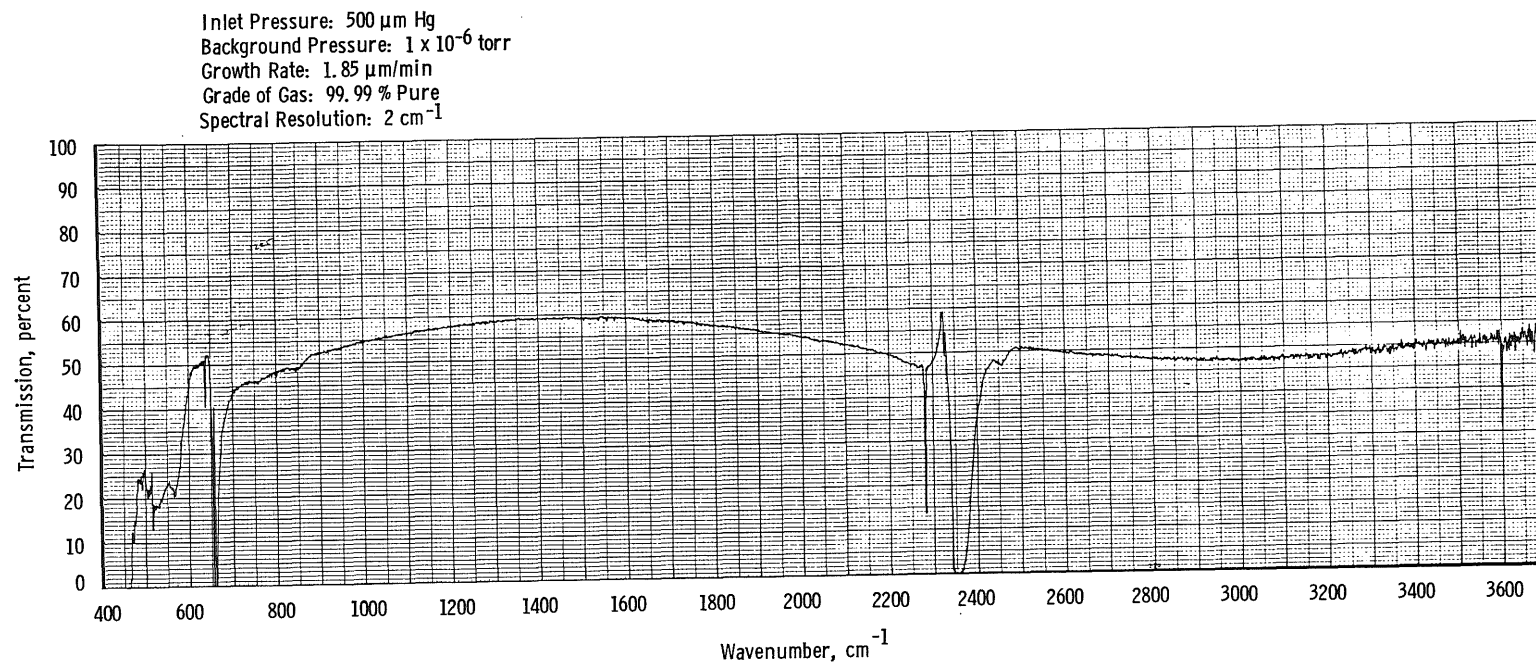
h. 1.003- $\mu\text{m}$ -thick deposit  
Figure 31. Continued.



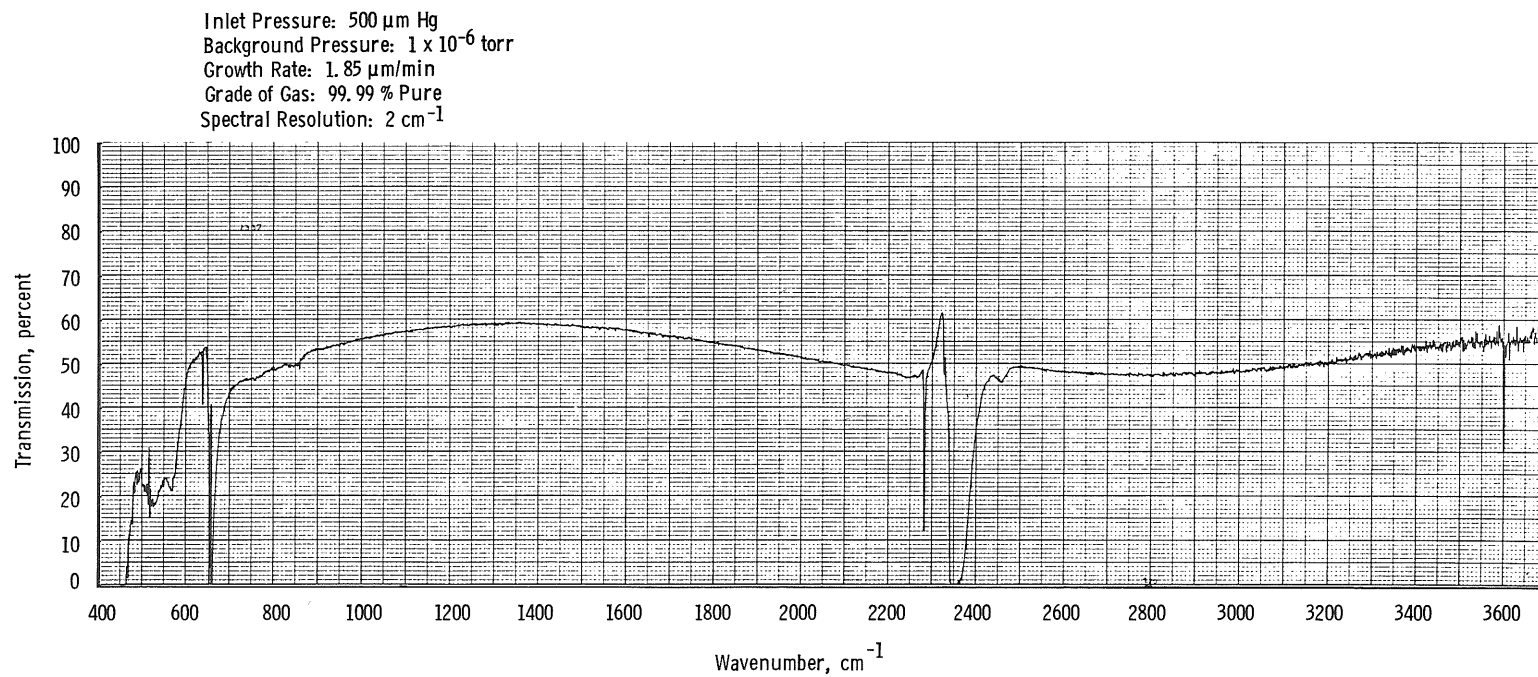
i. 1.114- $\mu\text{m}$ -thick deposit  
Figure 31. Continued.



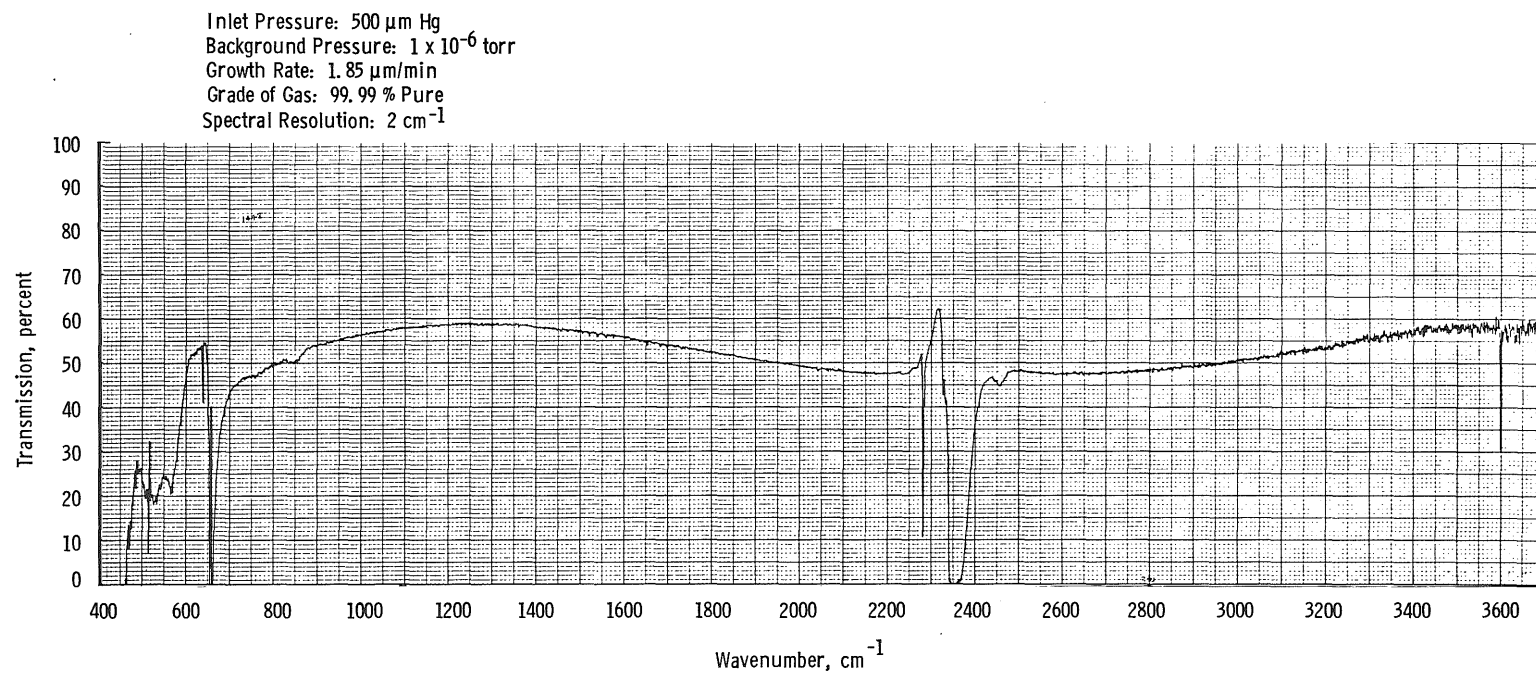
130



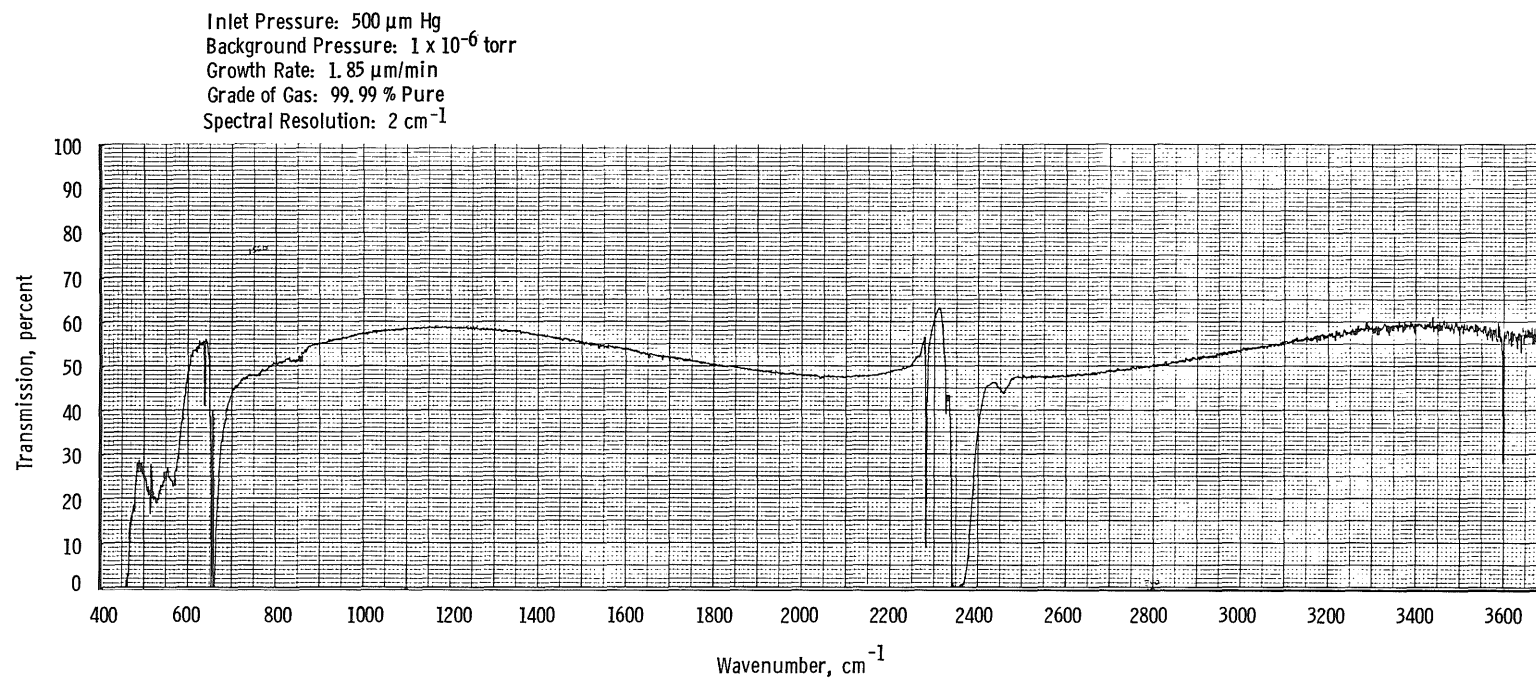
j. 1.225- $\mu\text{m}$ -thick deposit  
Figure 31. Continued.



k. 1.337- $\mu\text{m}$ -thick deposit  
Figure 31. Continued.

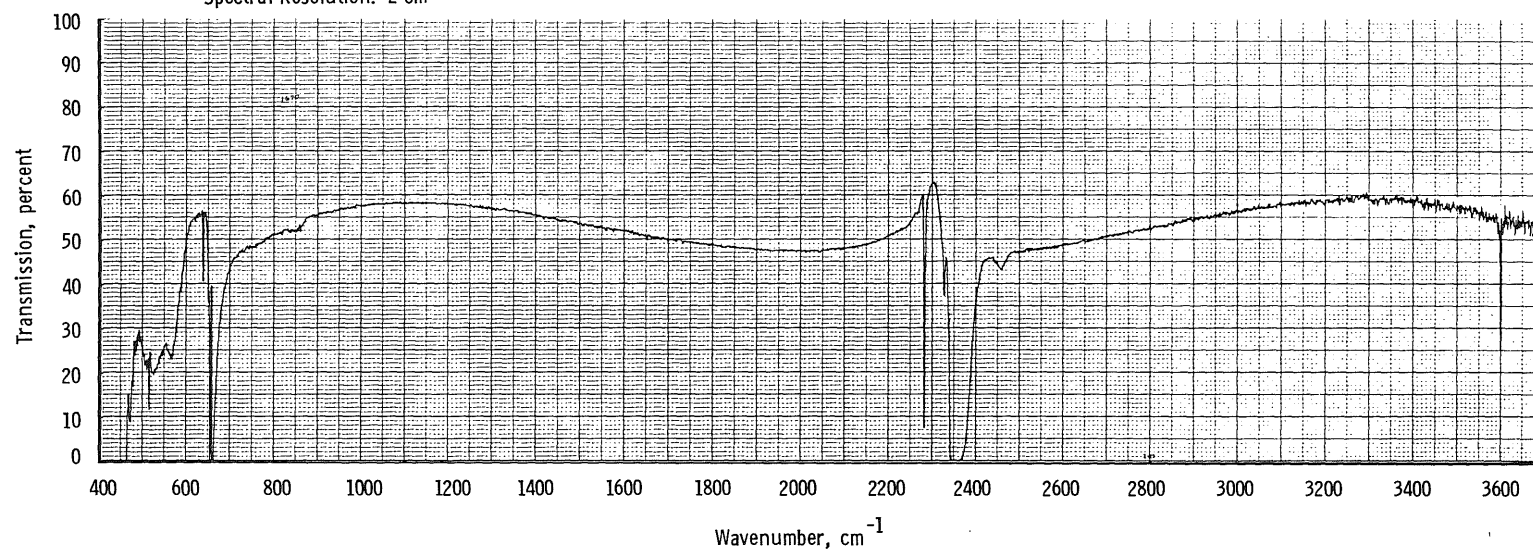


I. 1.448- $\mu\text{m}$ -thick deposit  
Figure 31. Continued.

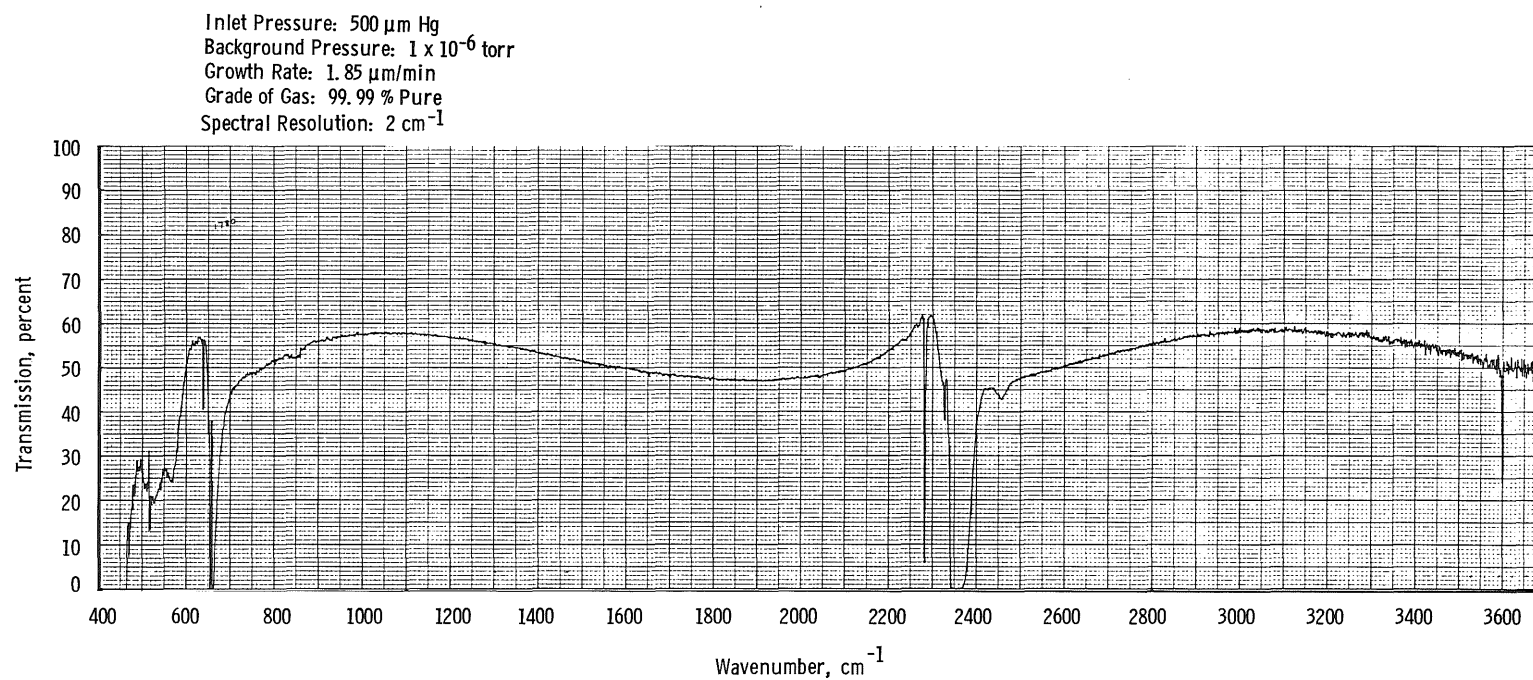


m. 1.560- $\mu\text{m}$ -thick deposit  
Figure 31. Continued.

Inlet Pressure: 500  $\mu\text{m Hg}$   
Background Pressure:  $1 \times 10^{-6}$  torr  
Growth Rate: 1.85  $\mu\text{m/min}$   
Grade of Gas: 99.99 % Pure  
Spectral Resolution: 2  $\text{cm}^{-1}$

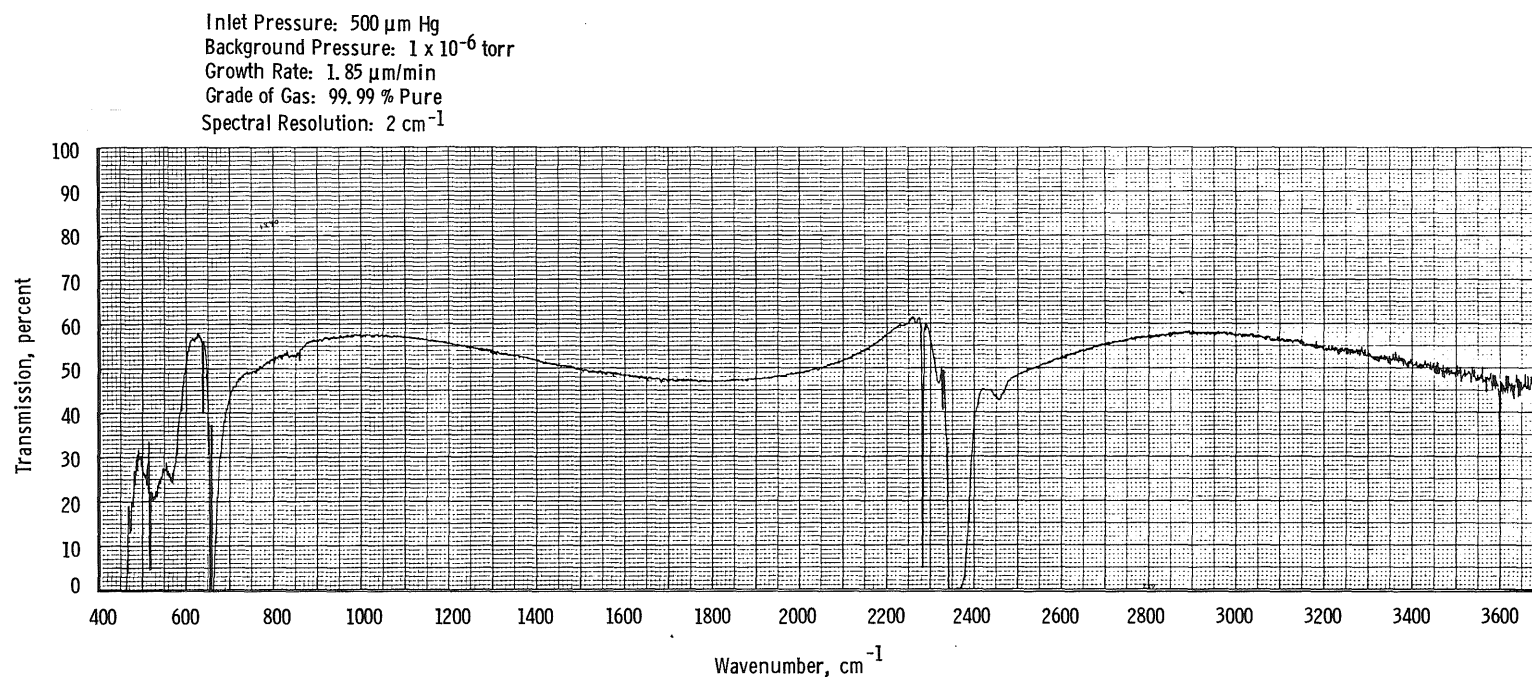


n. 1.670- $\mu\text{m}$ -thick deposit  
Figure 31. Continued.

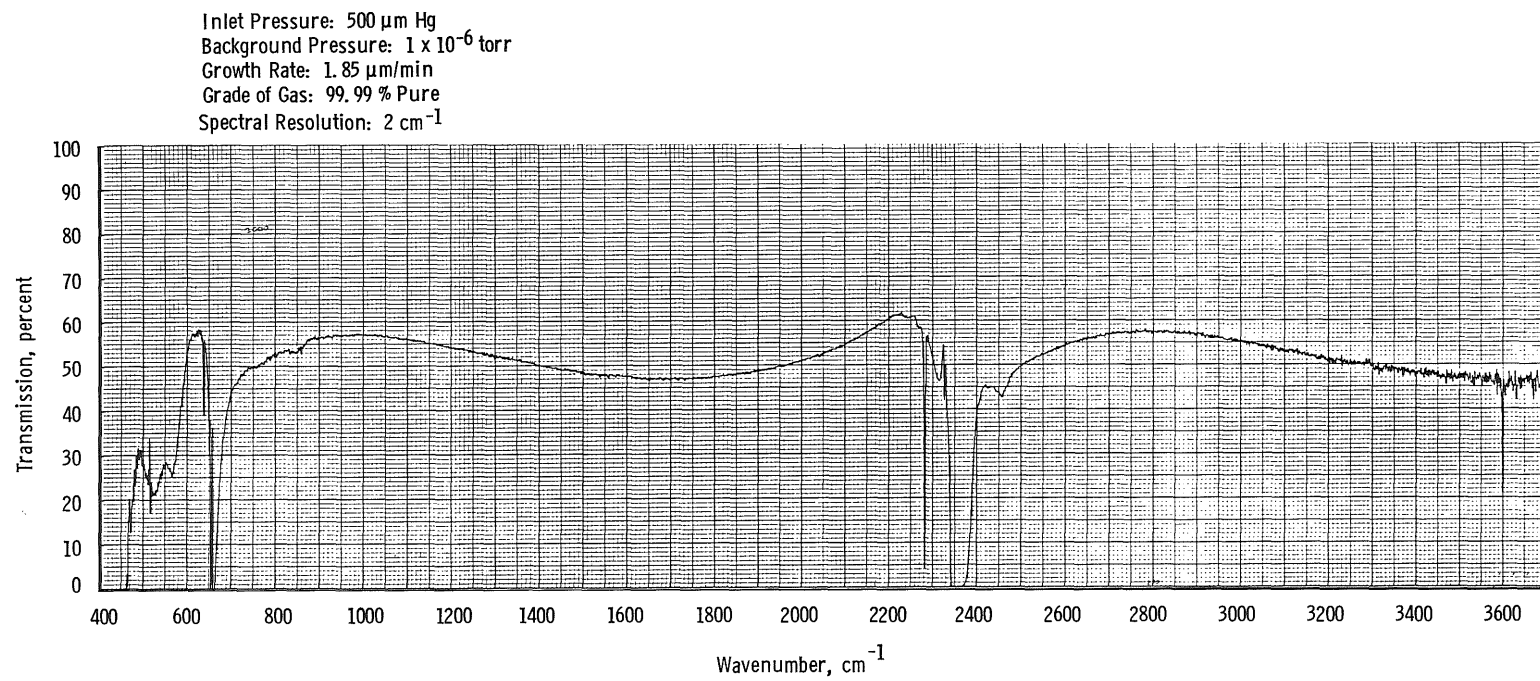


o. 1.780- $\mu\text{m}$ -thick deposit  
Figure 31. Continued.

136

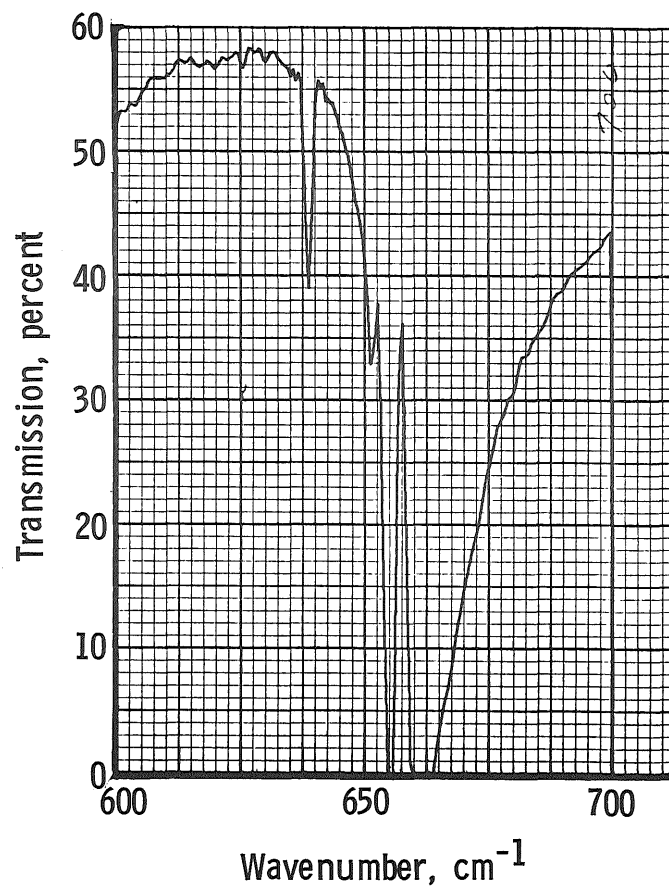


p. 1.890- $\mu\text{m}$ -thick deposit  
Figure 31. Continued.



q. 2.000- $\mu\text{m}$ -thick deposit  
Figure 31. Concluded.



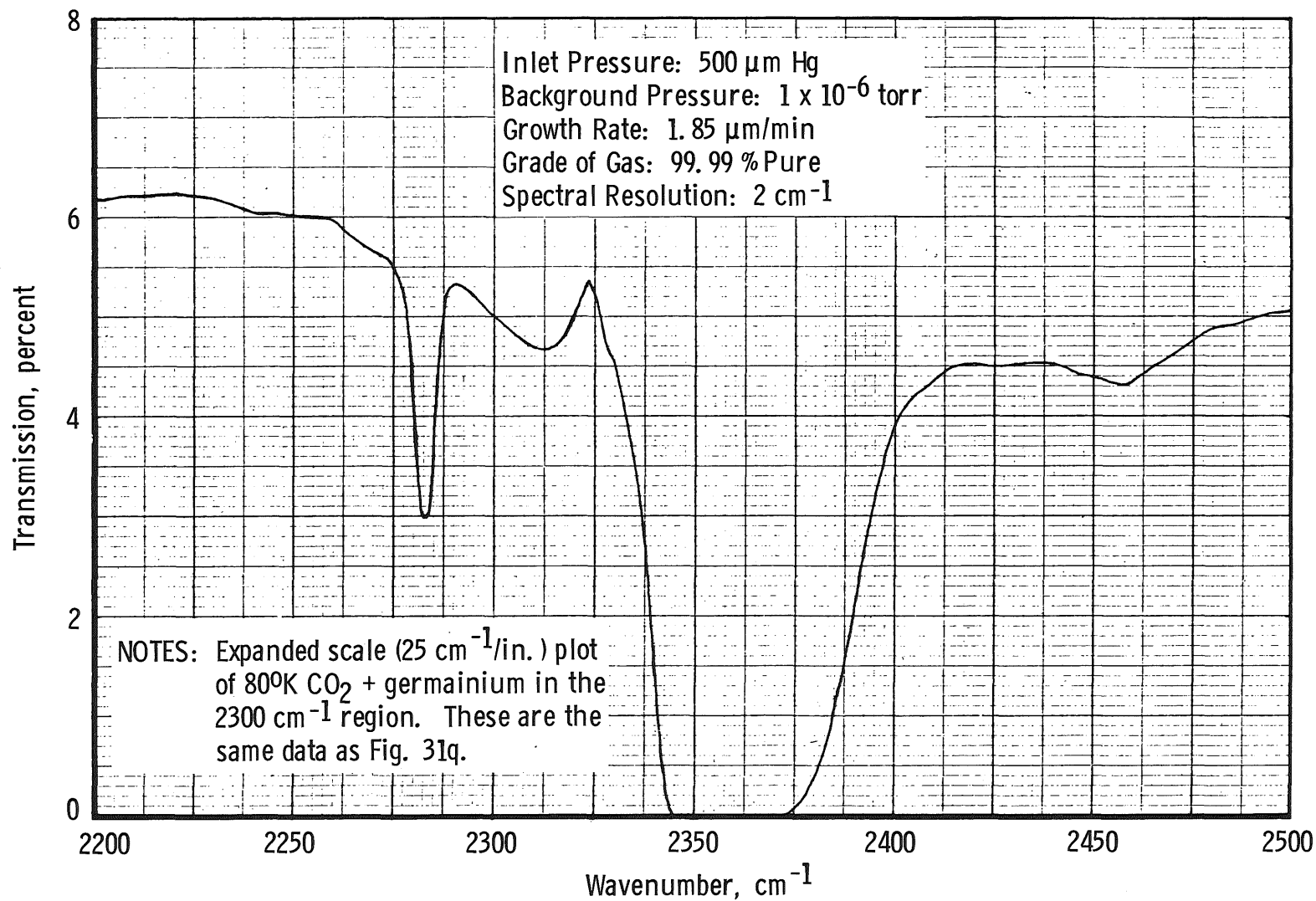


Inlet Pressure: 500  $\mu\text{m Hg}$   
 Background Pressure:  $1 \times 10^{-6}$  torr  
 Growth Rate: 1.85  $\mu\text{m/min}$   
 Grade of Gas: 99.99 % Pure  
 Spectral Resolution: 2  $\text{cm}^{-1}$

NOTES: Expanded scale (25  $\text{cm}^{-1}/\text{in.}$ ) plot of 80°K  $\text{CO}_2$  + germanium in the 650  $\text{cm}^{-1}$  region. These are the same data as Fig. 31q.

a. 650- $\text{cm}^{-1}$  region

Figure 32. Transmission of 80°K germanium window with a 2.000- $\mu\text{m}$ -thick  $\text{CO}_2$  deposit, expanded abscissa scale.



b.  $2,300\text{-cm}^{-1}$  region  
Figure 32. Concluded.

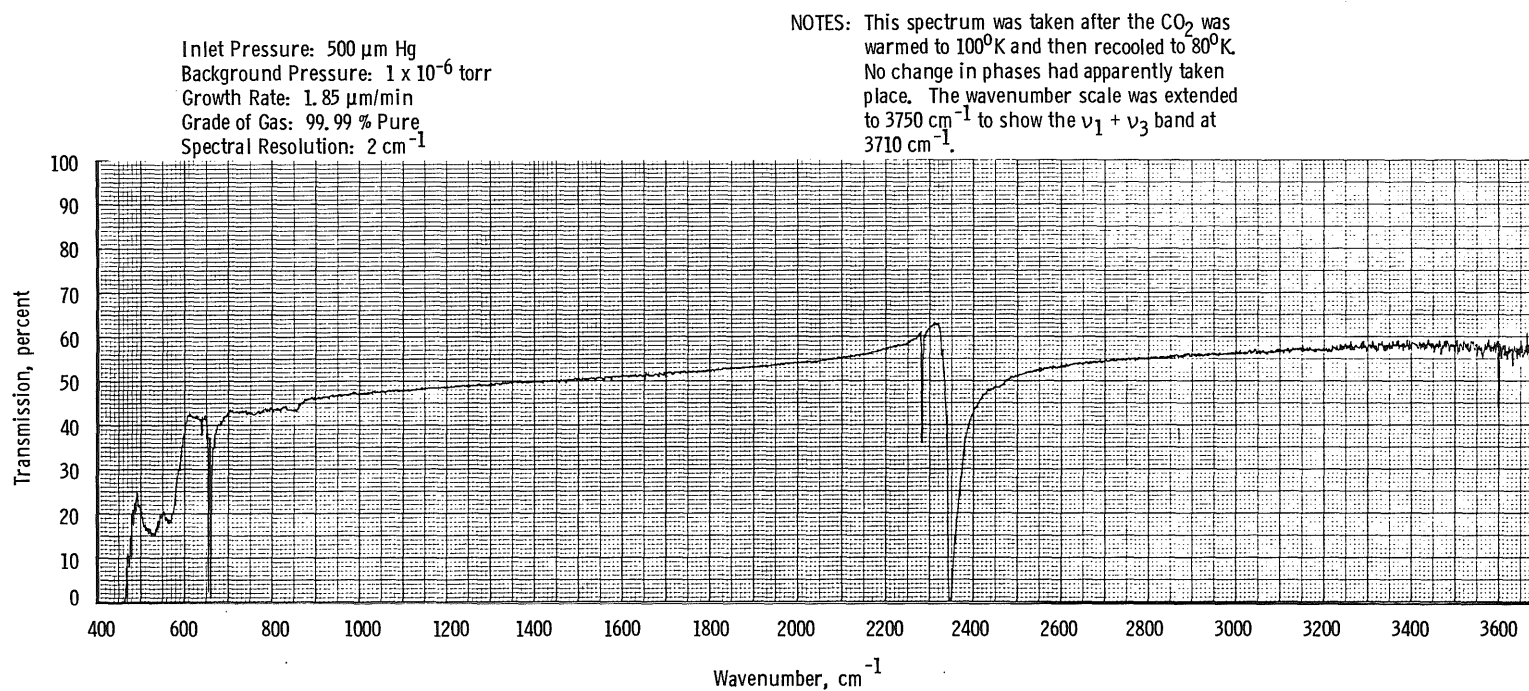
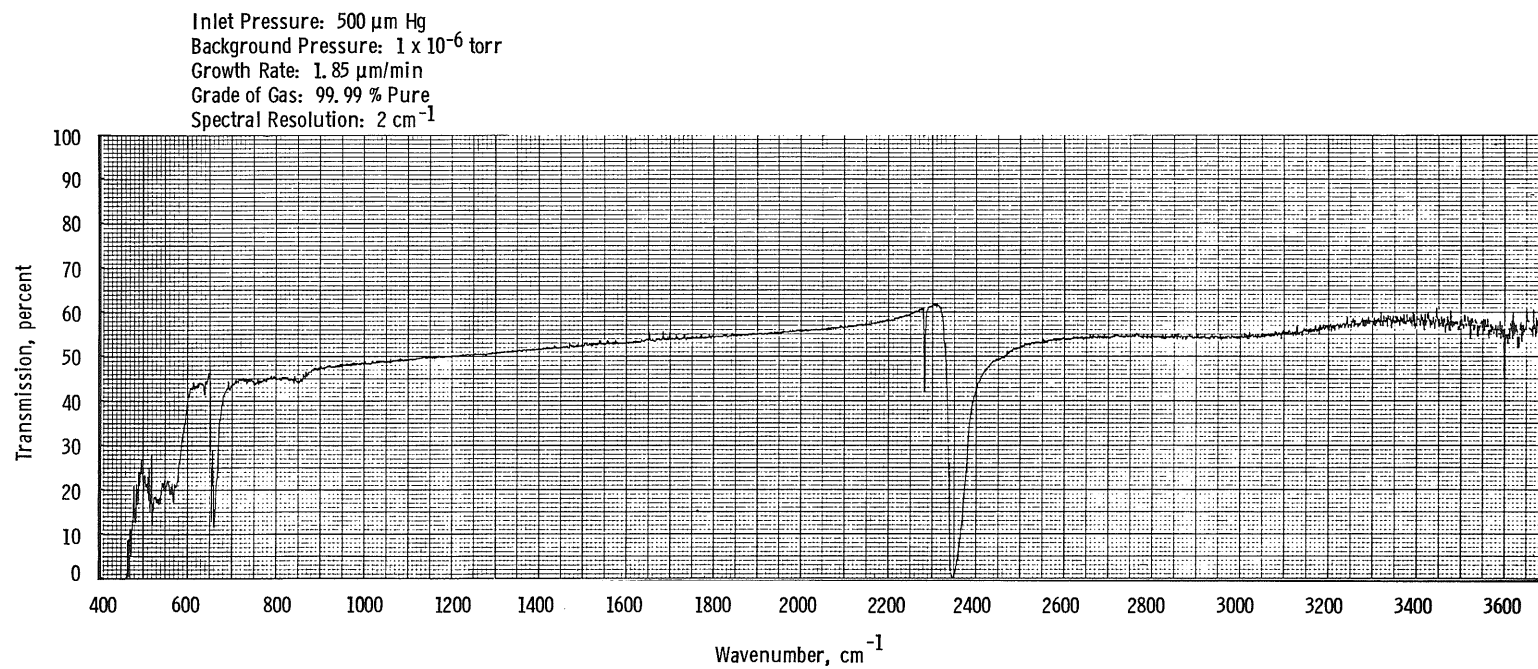
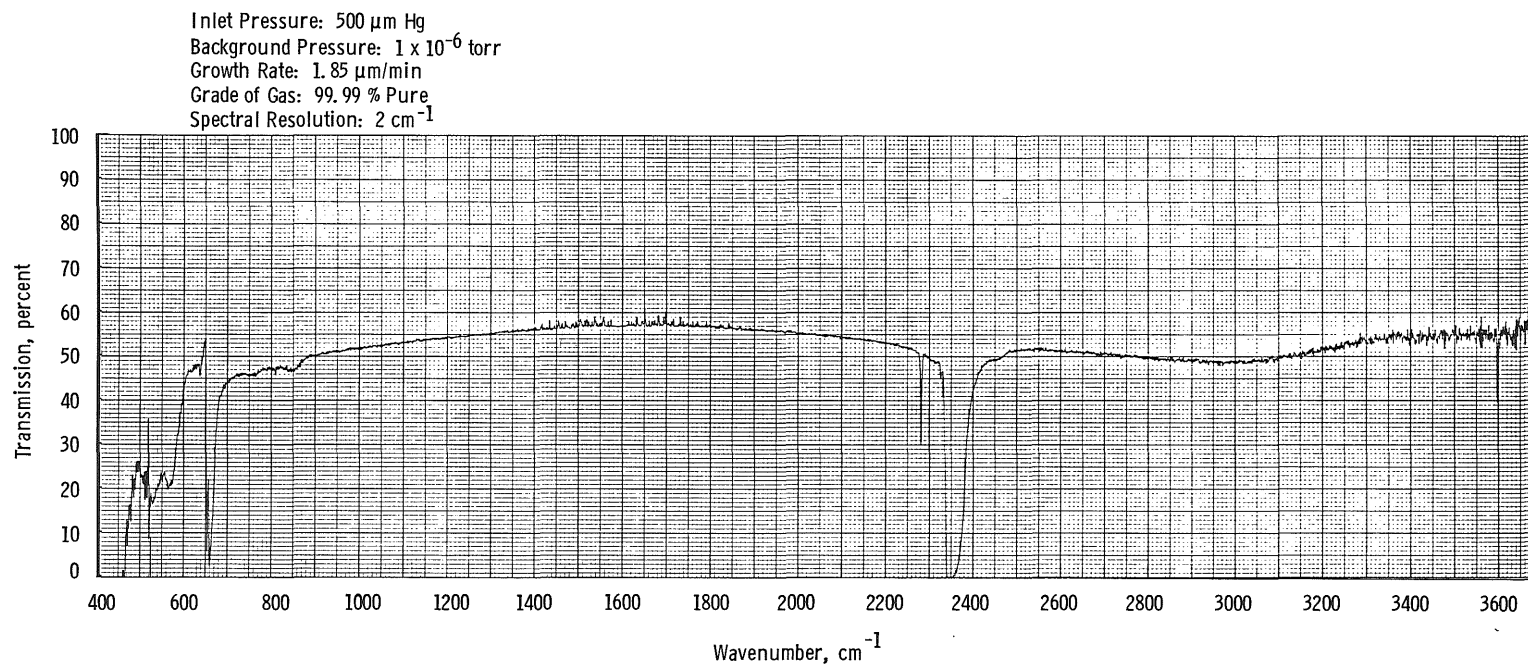


Figure 33. Transmission of germanium window with a 2.000- $\mu\text{m}$ -thick  $\text{CO}_2$  deposit after warming to  $100^\circ\text{K}$  and cooling back down to  $80^\circ\text{K}$ .

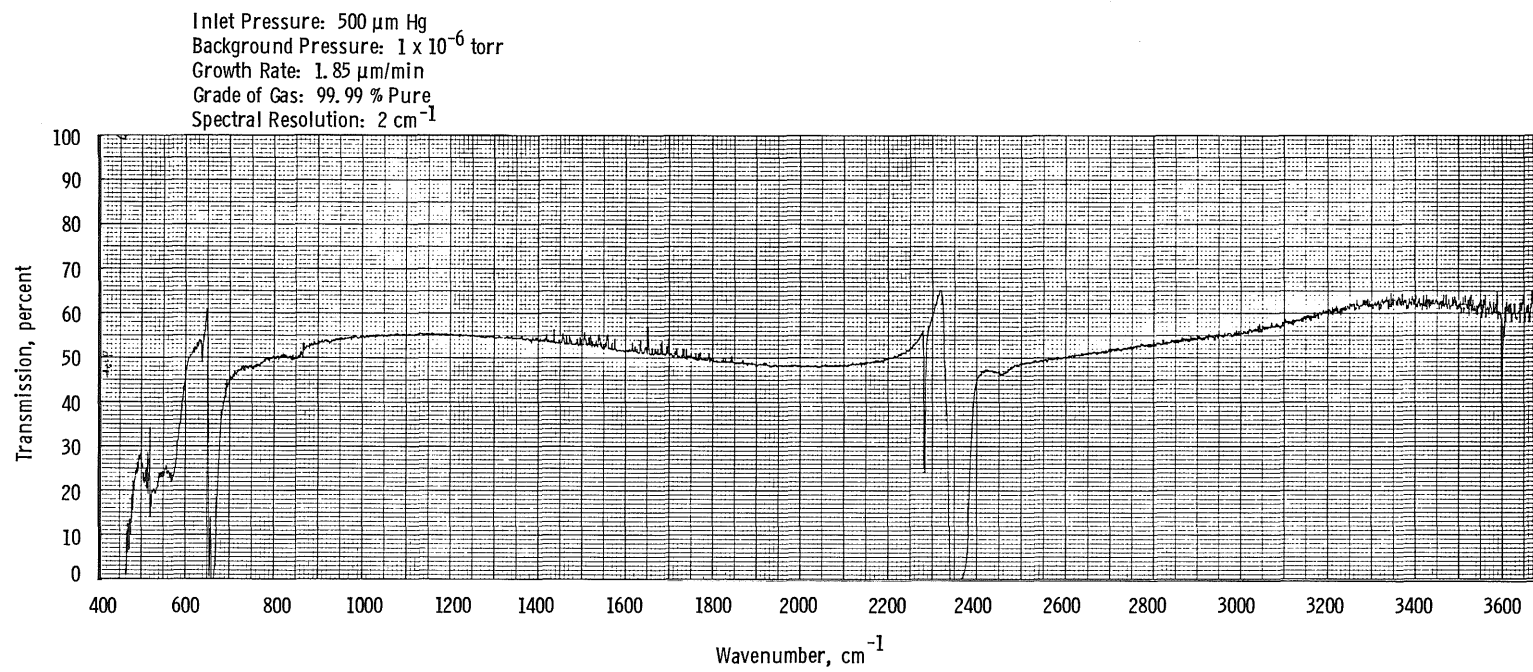


a. 0.668- $\mu\text{m}$ -thick deposit

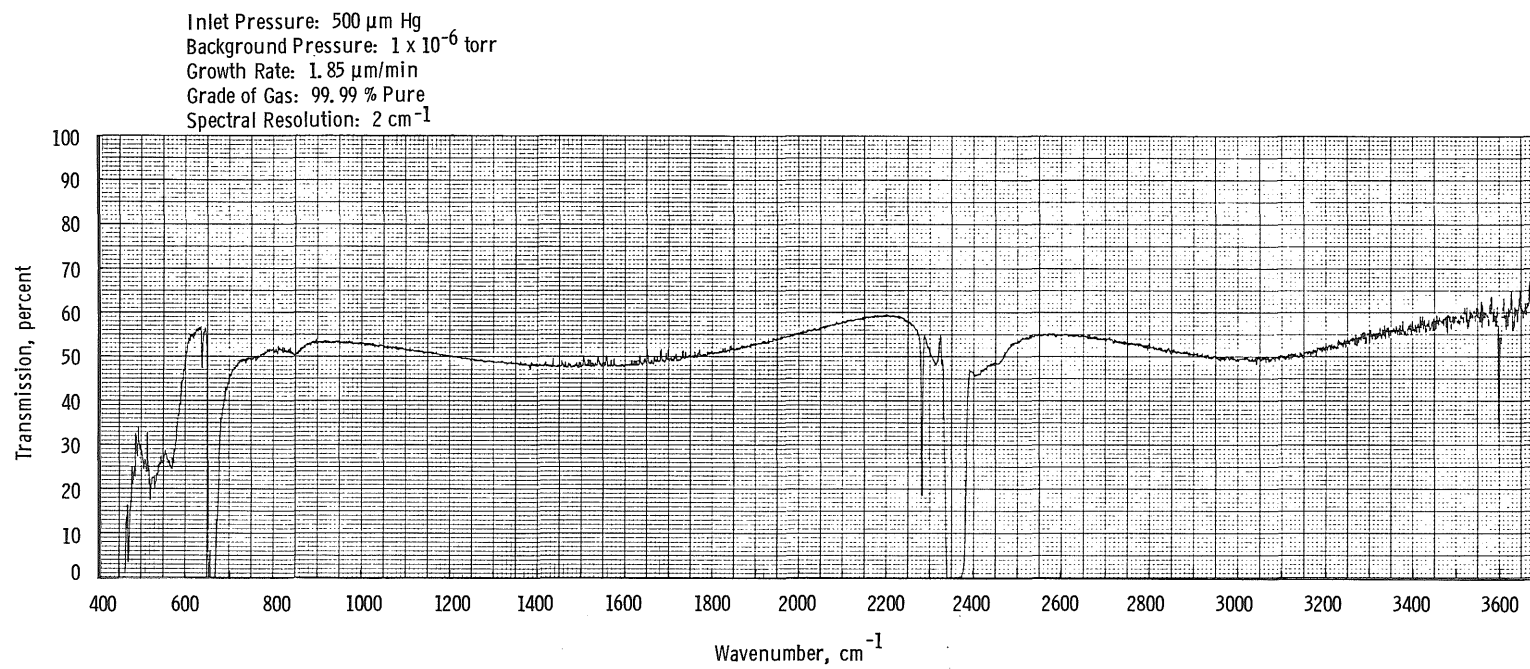
Figure 34. Transmission of 20° K germanium window with various  $\text{CO}_2$  deposit thicknesses.



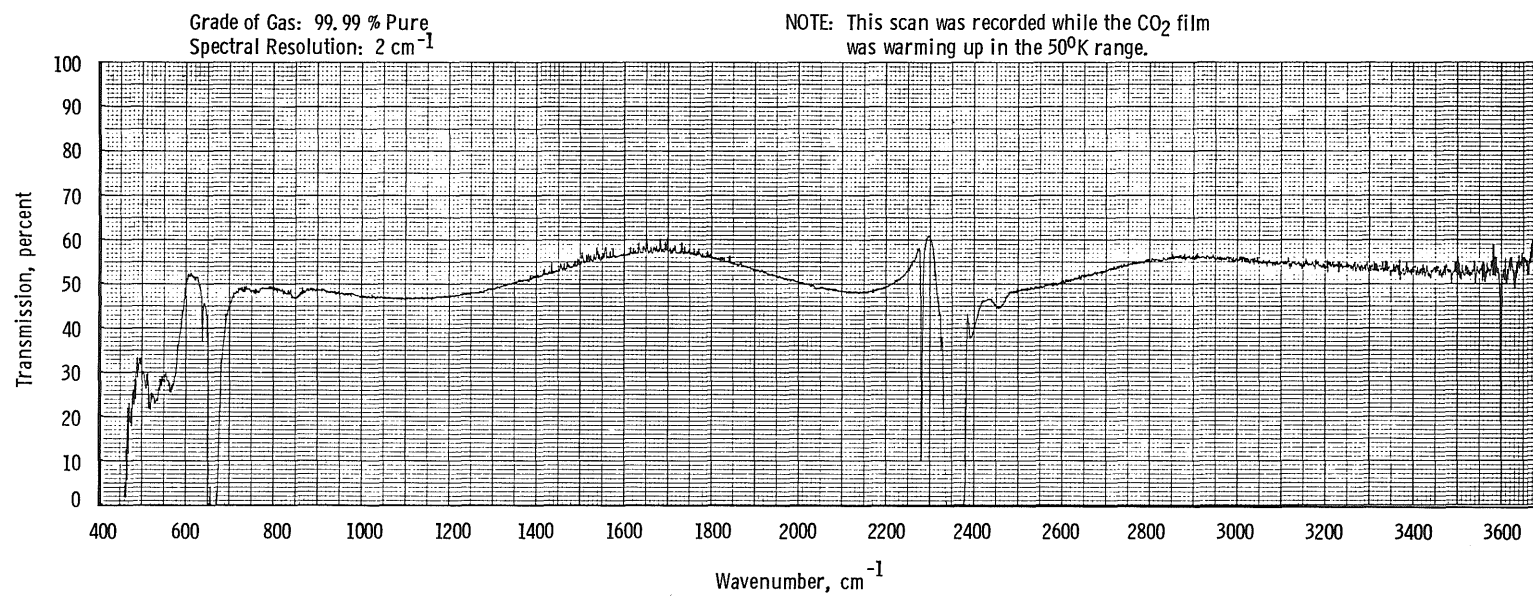
b. 1.114- $\mu\text{m}$ -thick deposit  
Figure 34. Continued.



c. 1.890- $\mu\text{m}$ -thick deposit  
Figure 34. Continued.



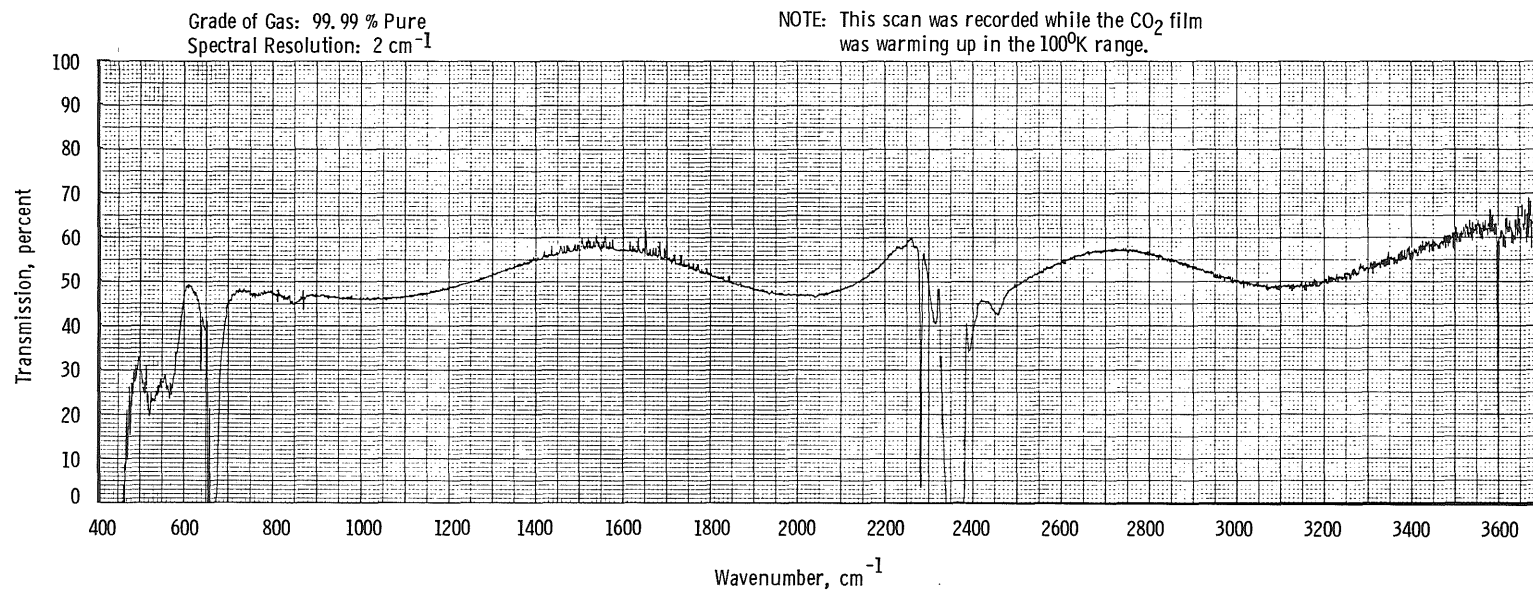
d. 2.560- $\mu\text{m}$ -thick deposit  
Figure 34. Concluded.



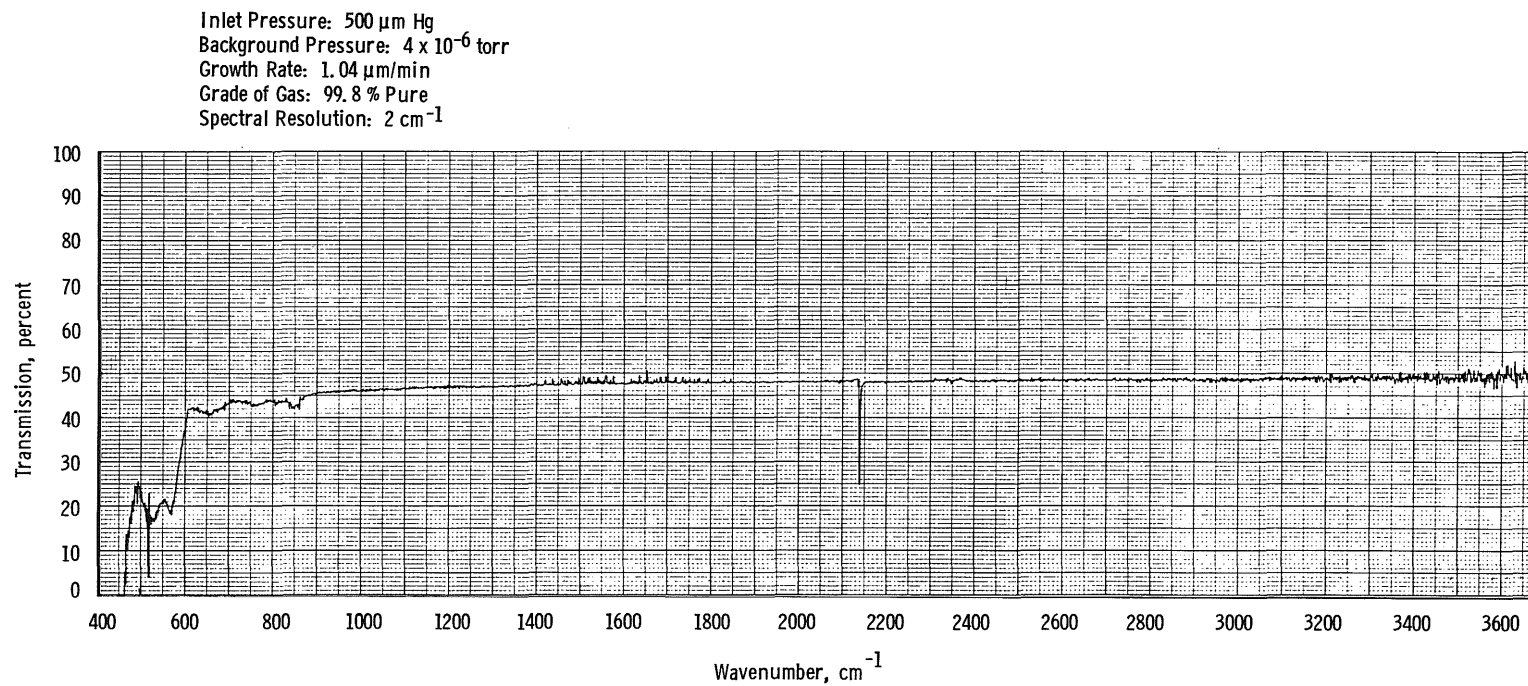
a. From  $20^\circ\text{K}$  to  $50^\circ\text{K}$

Figure 35. Transmission of germanium window with a  $\text{CO}_2$  deposit after warming.



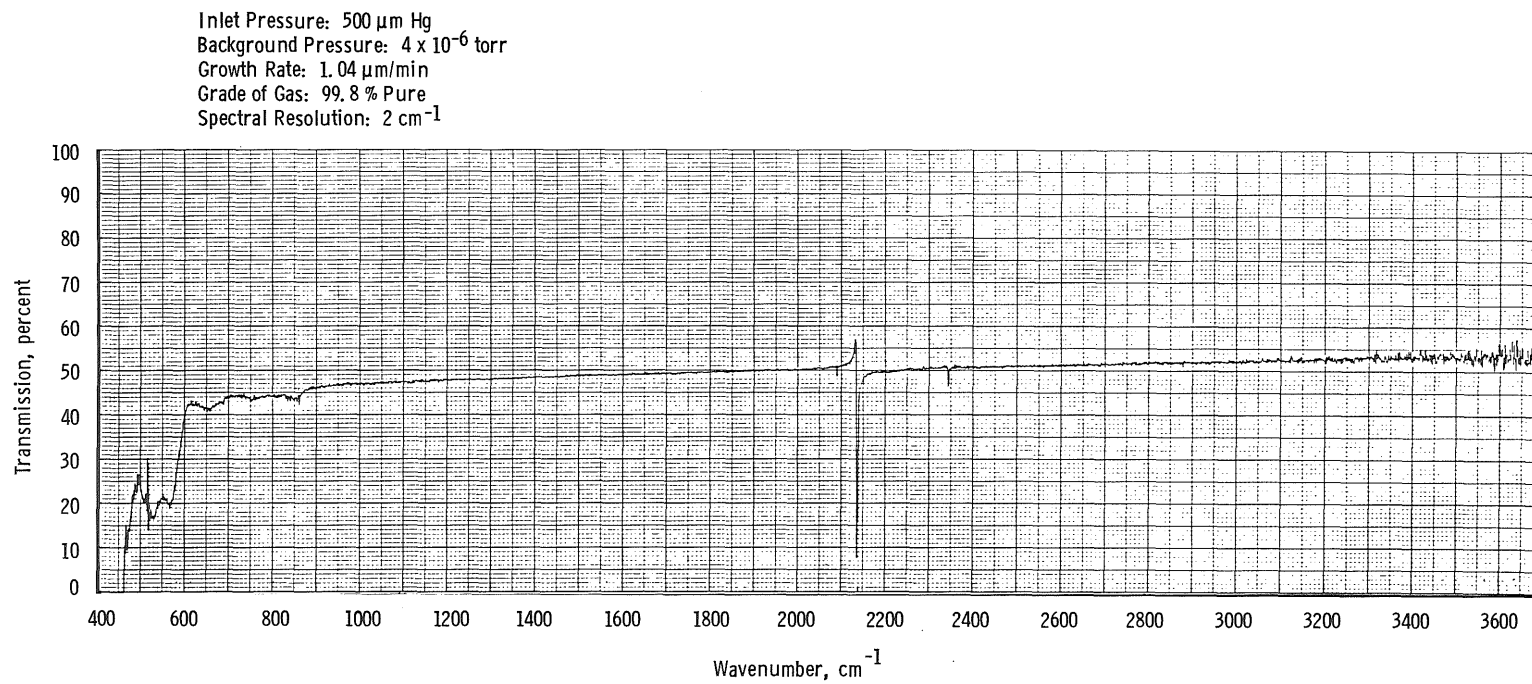


b. From  $20^\circ\text{K}$  to  $100^\circ\text{K}$   
Figure 35. Concluded.

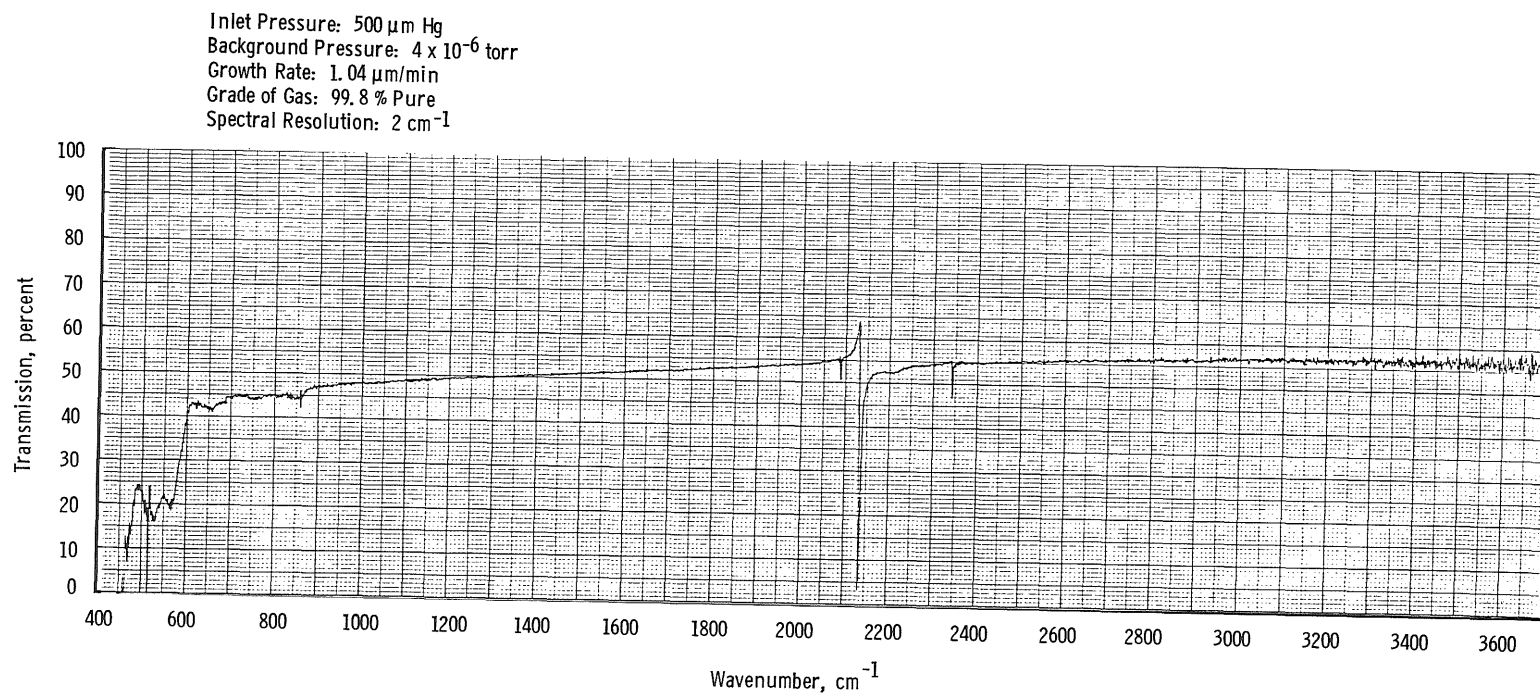


a. 0.130- $\mu\text{m}$ -thick deposit

Figure 36. Transmission of 20°K germanium window with various CO deposit thicknesses.

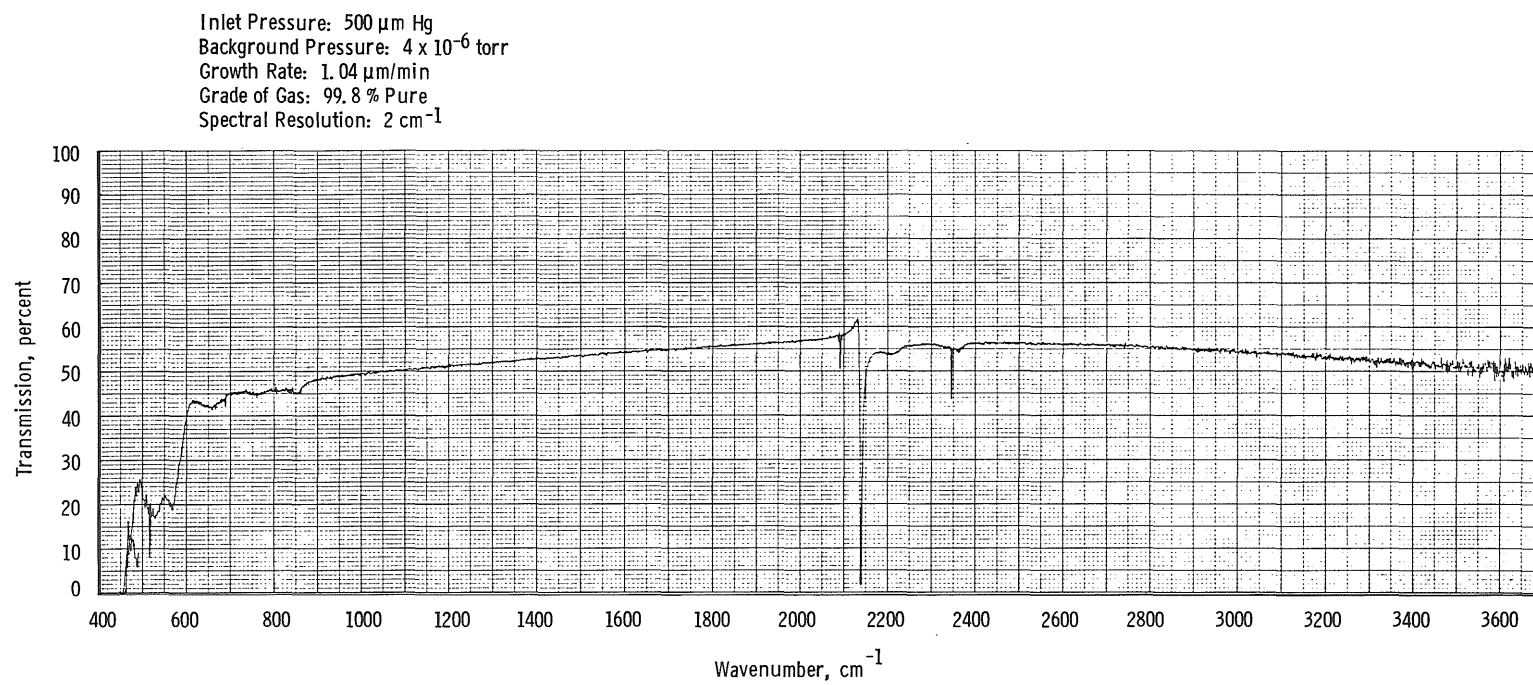


b. 0.390- $\mu\text{m}$ -thick deposit  
Figure 36. Continued.

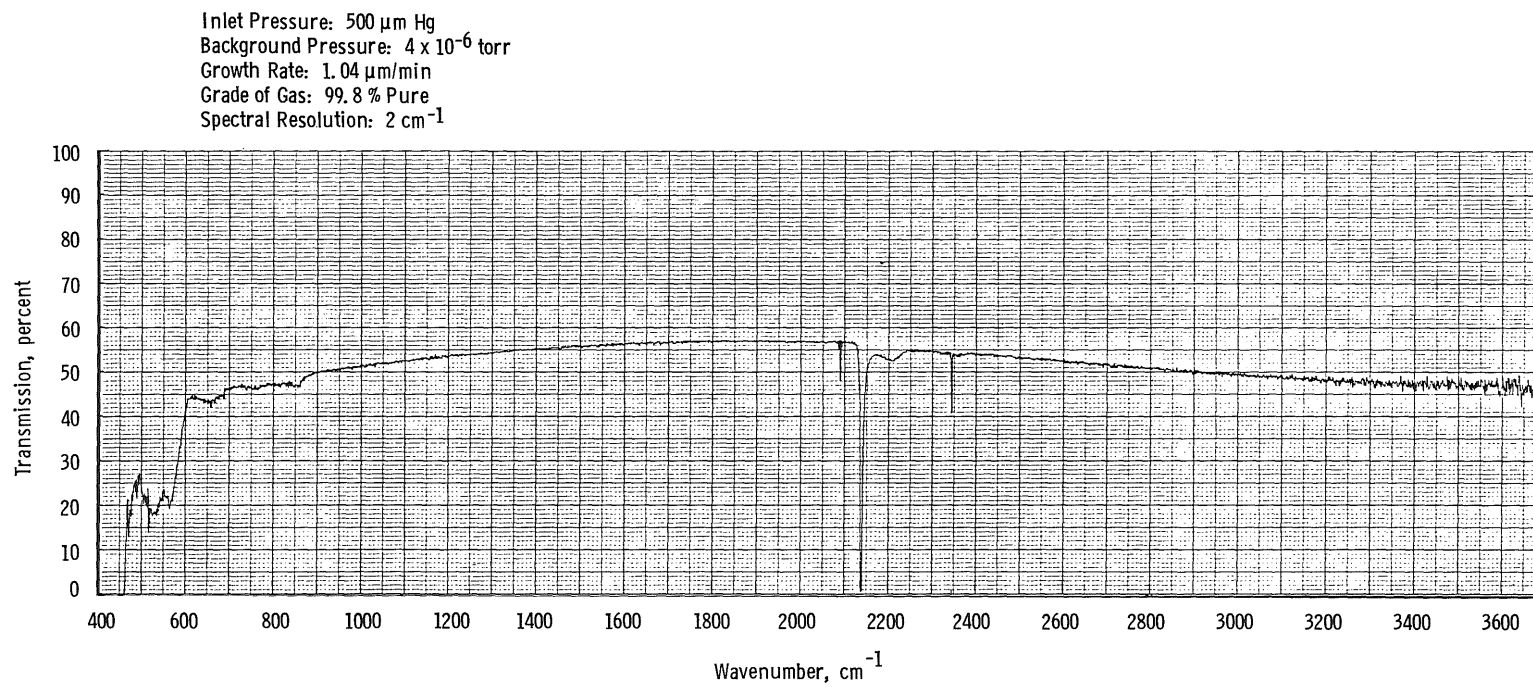


c. 0.648- $\mu\text{m}$ -thick deposit  
Figure 36. Continued.

150

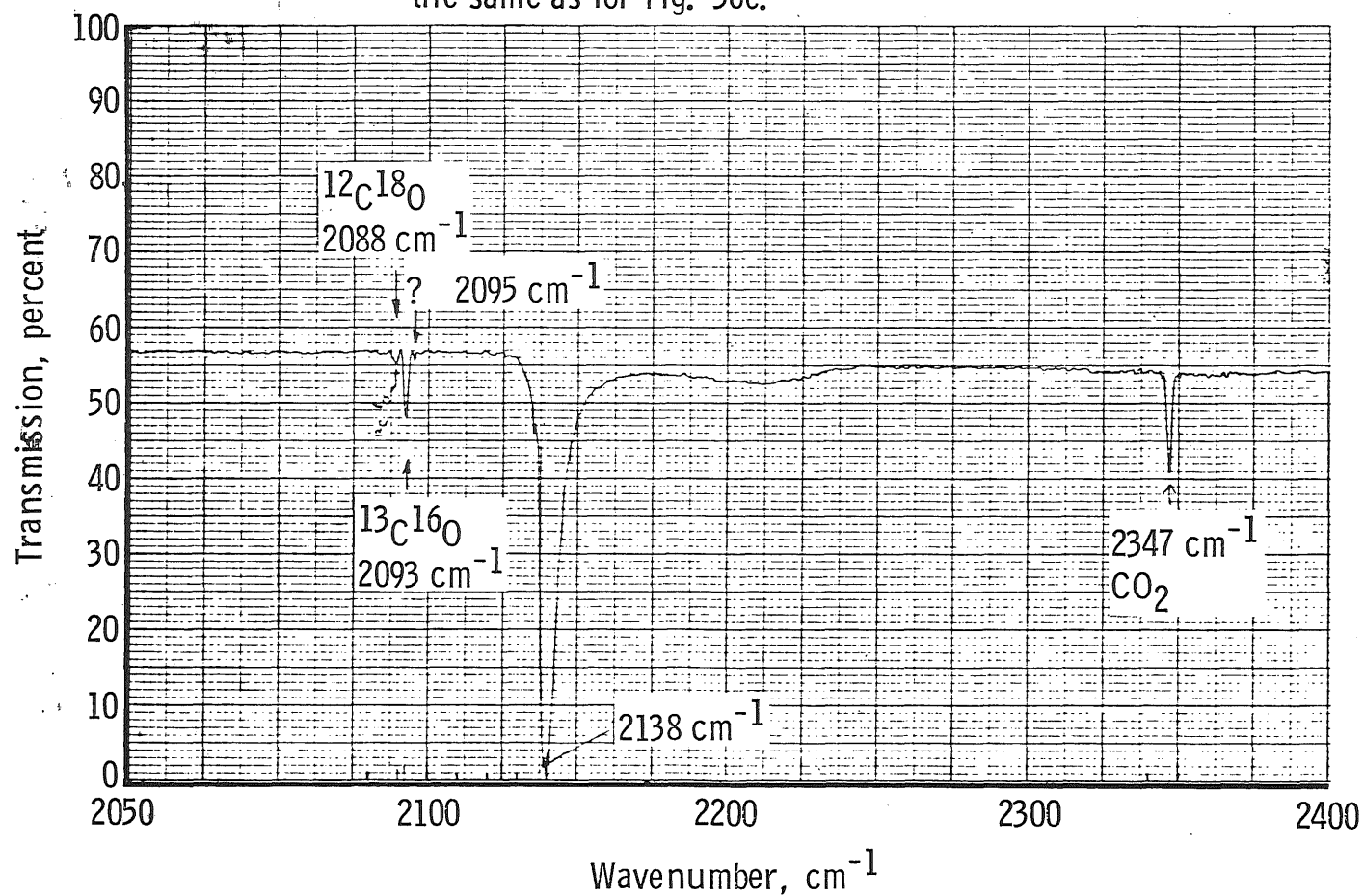


d. 0.908- $\mu\text{m}$ -thick deposit  
Figure 36. Continued.



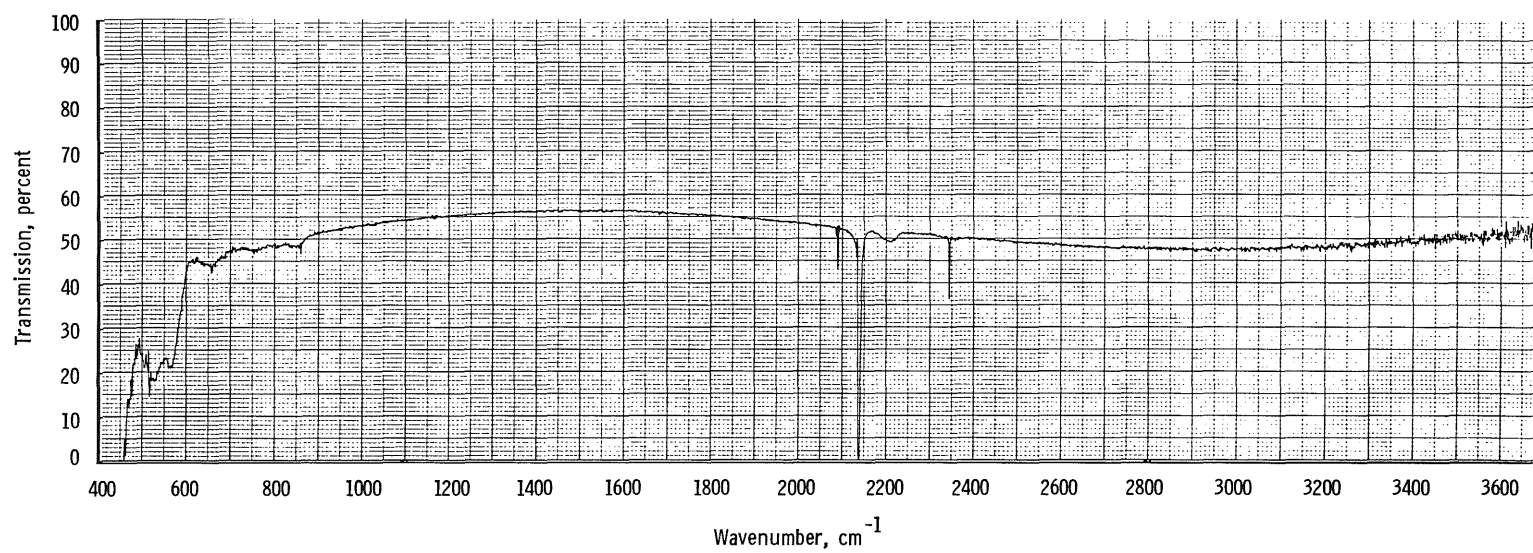
e. 1.167- $\mu\text{m}$ -thick deposit  
Figure 36. Concluded.

NOTES: The wavenumber scale was expanded to  $25 \text{ cm}^{-1}/\text{in.}$  for the  $2200 \text{ cm}^{-1}$  region; thickness of solid CO was the same as for Fig. 36e.



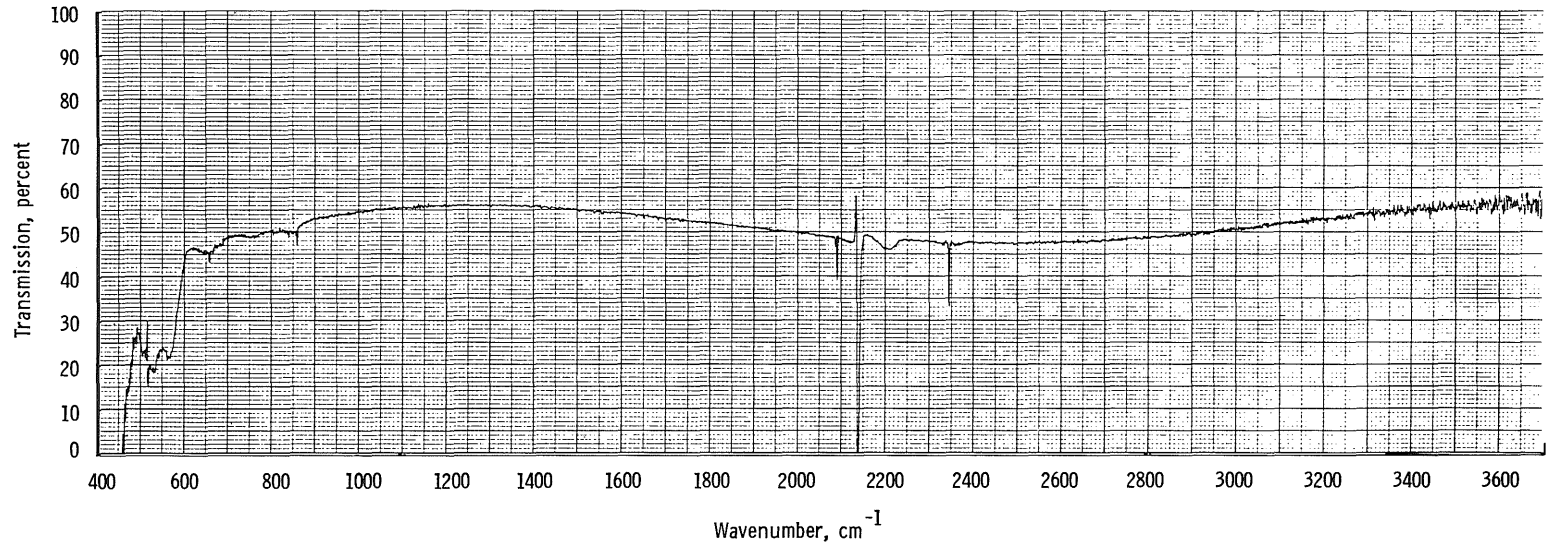
a.  $1.167\text{-}\mu\text{m}$ -thick deposit (expanded abscissa scale in  $2,200\text{-cm}^{-1}$  region)

Figure 37. Transmission of  $20^\circ\text{K}$  germanium window with various CO deposit thicknesses.

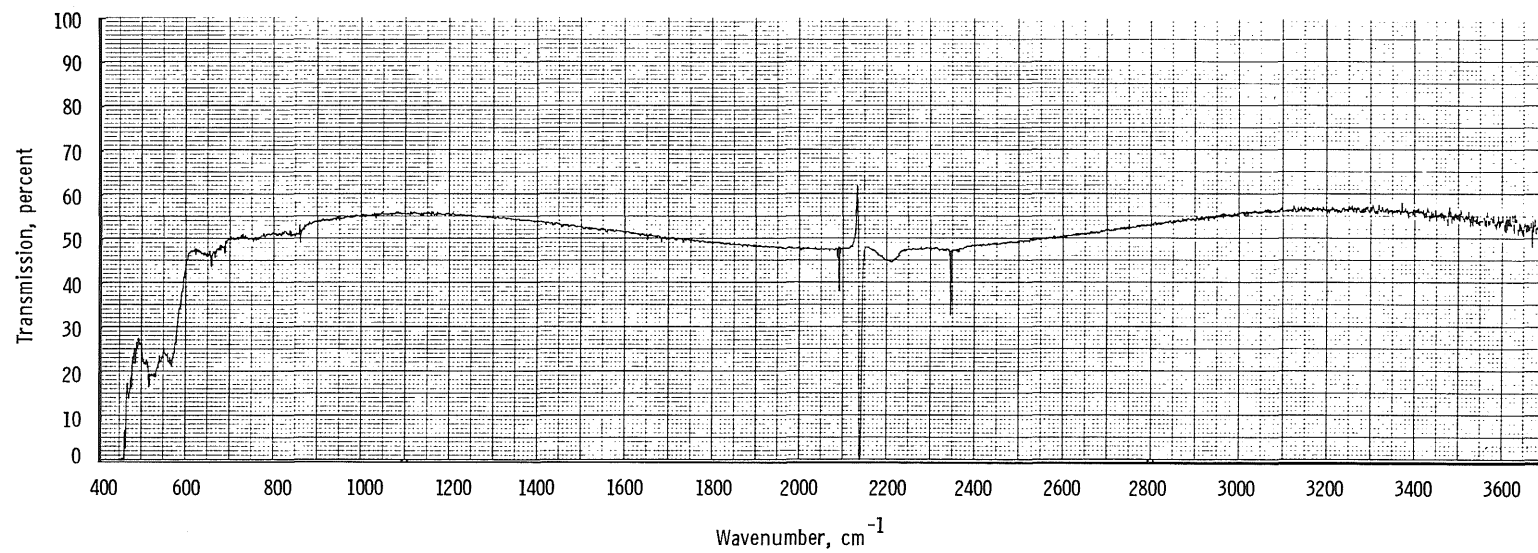


b. 1.426- $\mu\text{m}$ -thick deposit  
Figure 37. Continued.



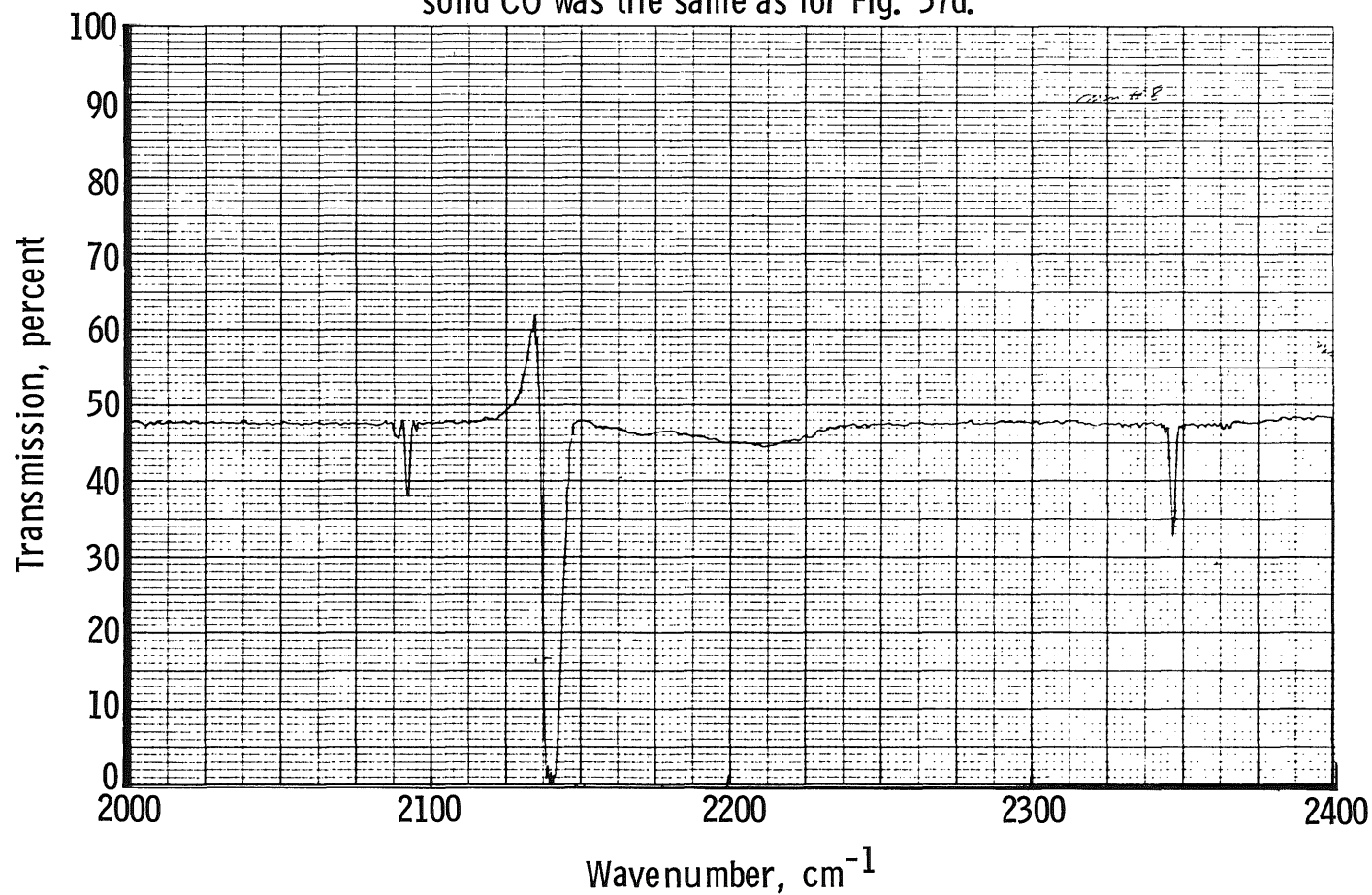


c. 1.686- $\mu$ m-thick deposit  
Figure 37. Continued.



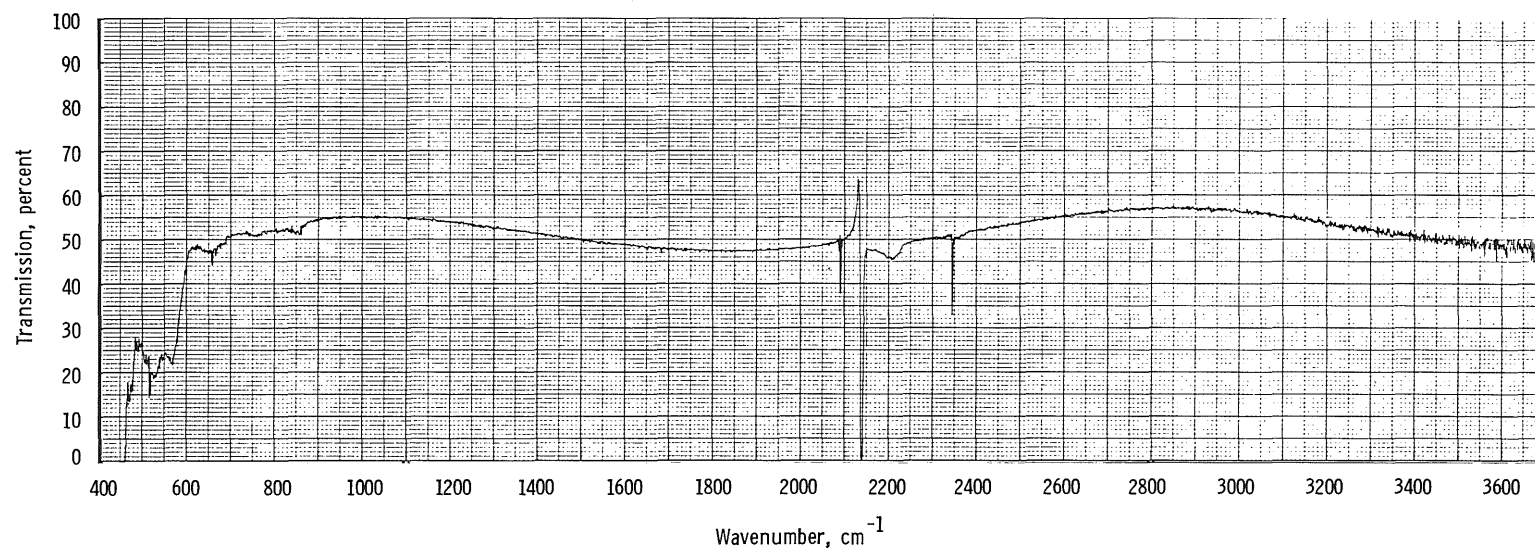
d. 1.945- $\mu$ m-thick deposit  
Figure 37. Continued.

NOTES: The wavenumber scale was expanded to  $25 \text{ cm}^{-1}/\text{in.}$  for the  $2200 \text{ cm}^{-1}$  region. The thickness of the solid CO was the same as for Fig. 37d.



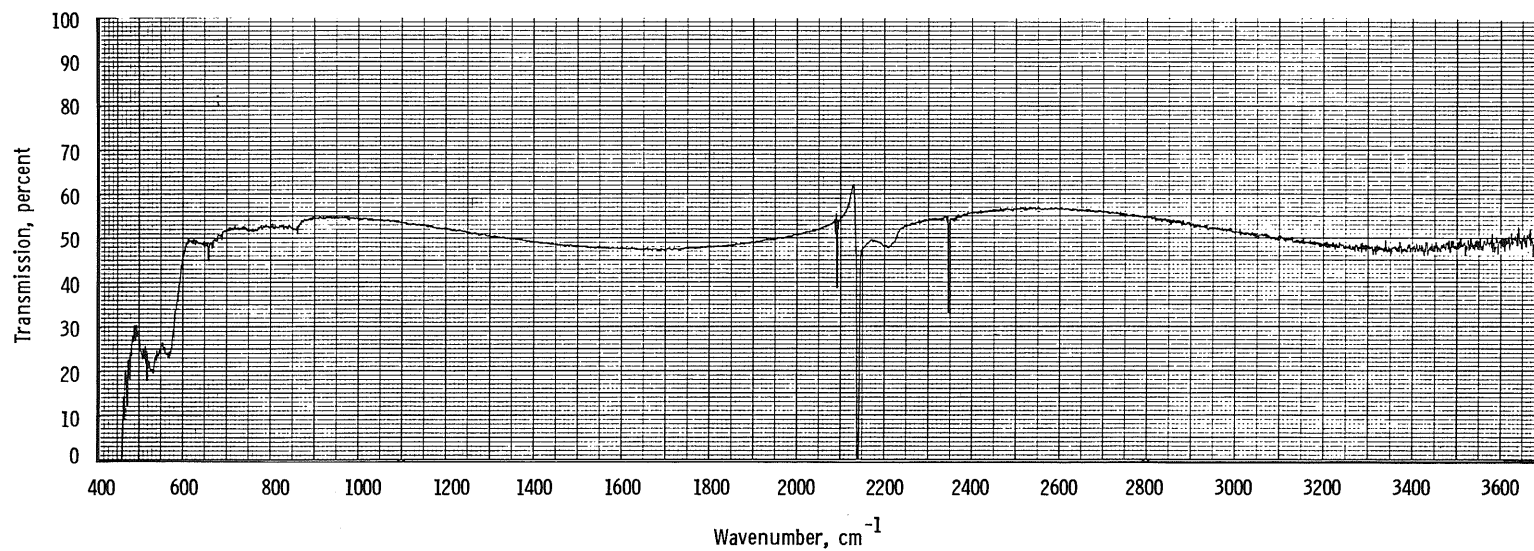
e.  $1.945\text{-}\mu\text{m}$ -thick deposit (expanded abscissa scale in  $2,200\text{-cm}^{-1}$  region)

Figure 37. Continued.

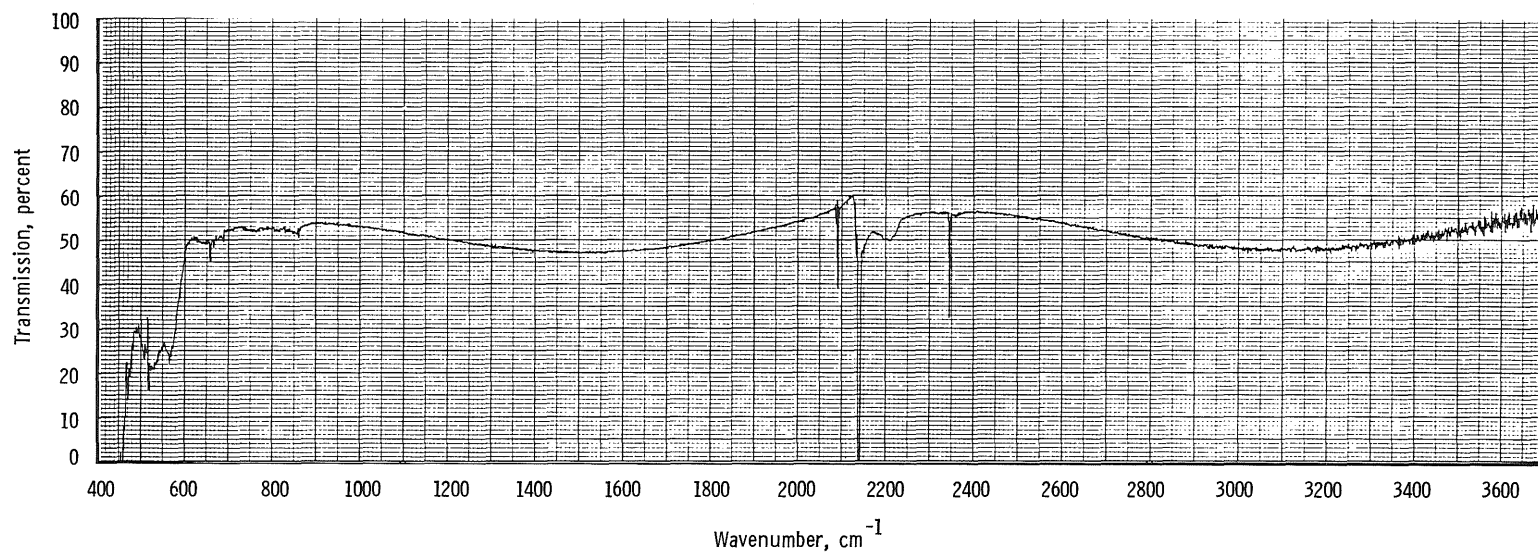


f. 2.204- $\mu\text{m}$ -thick deposit  
Figure 37. Continued.

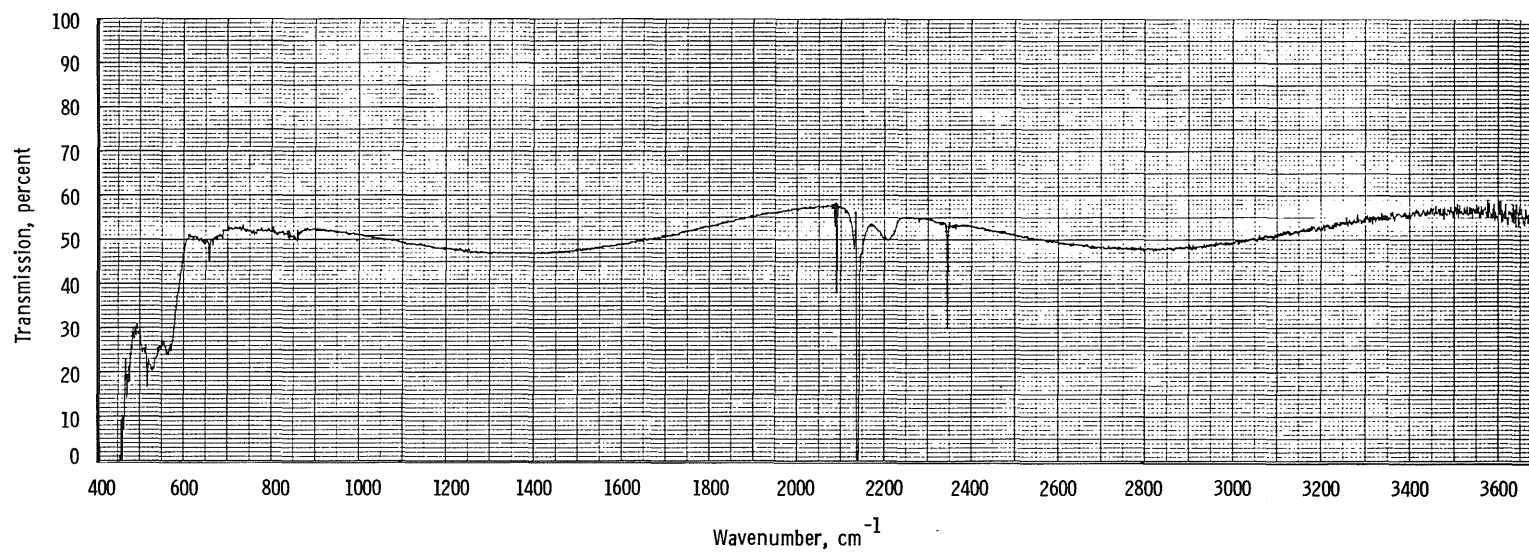
158



g. 2.464- $\mu\text{m}$ -thick deposit  
Figure 37. Continued.

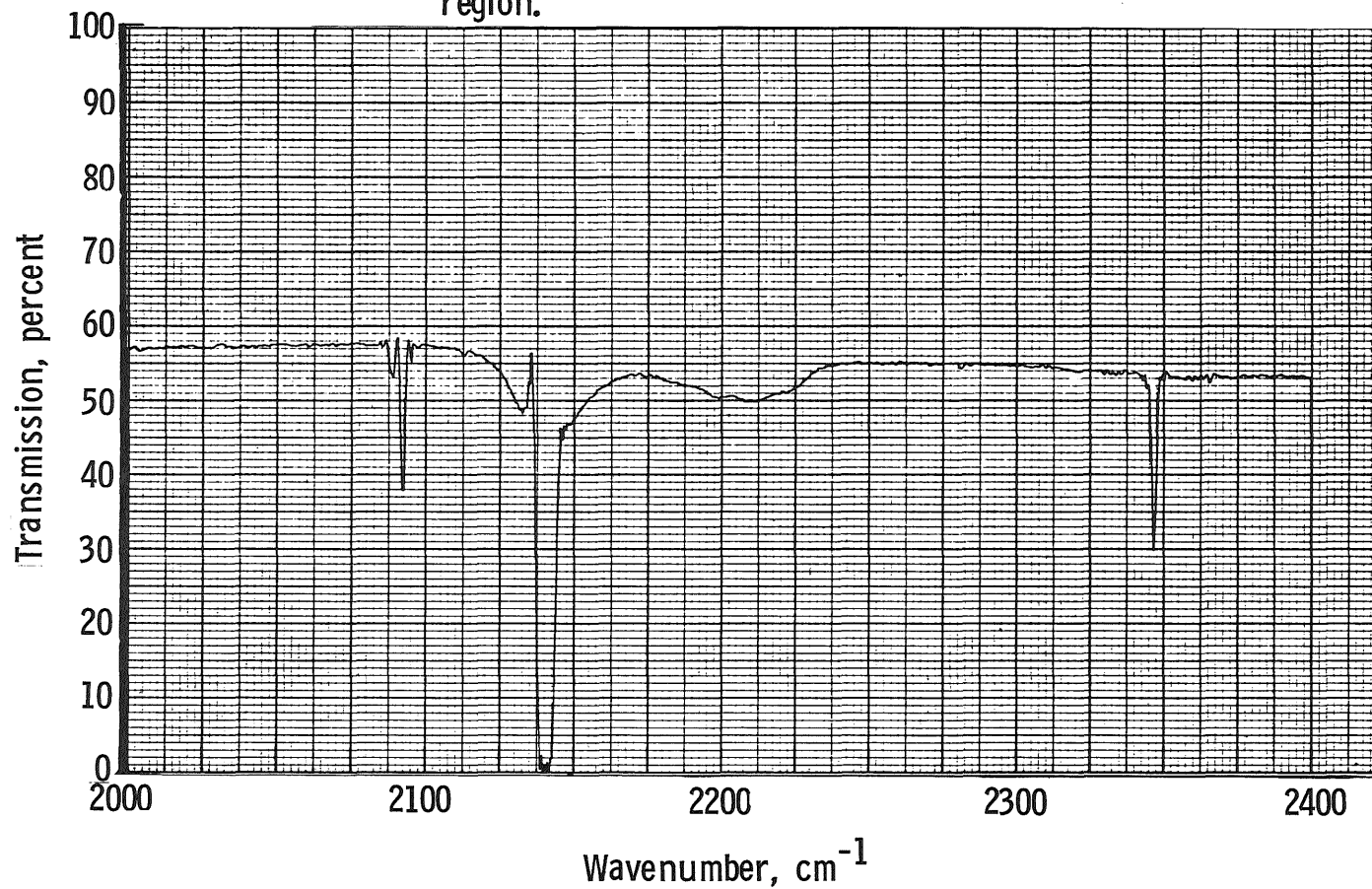


**h. 2.723- $\mu\text{m}$ -thick deposit**  
**Figure 37. Continued.**



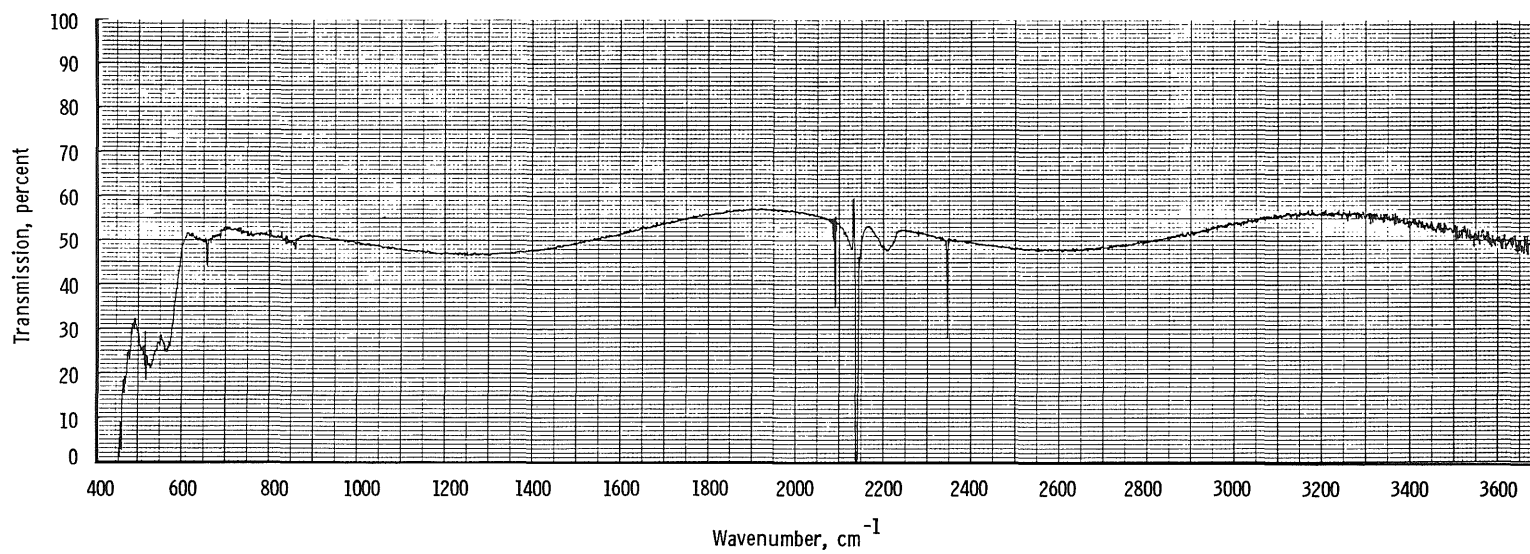
i. 2.982- $\mu\text{m}$ -thick deposit  
Figure 37. Continued.

NOTES: The wavenumber scale was expanded to 25  $\text{cm}^{-1}/\text{in.}$   
in order to show detailed structure in the 2200  $\text{cm}^{-1}$   
region.

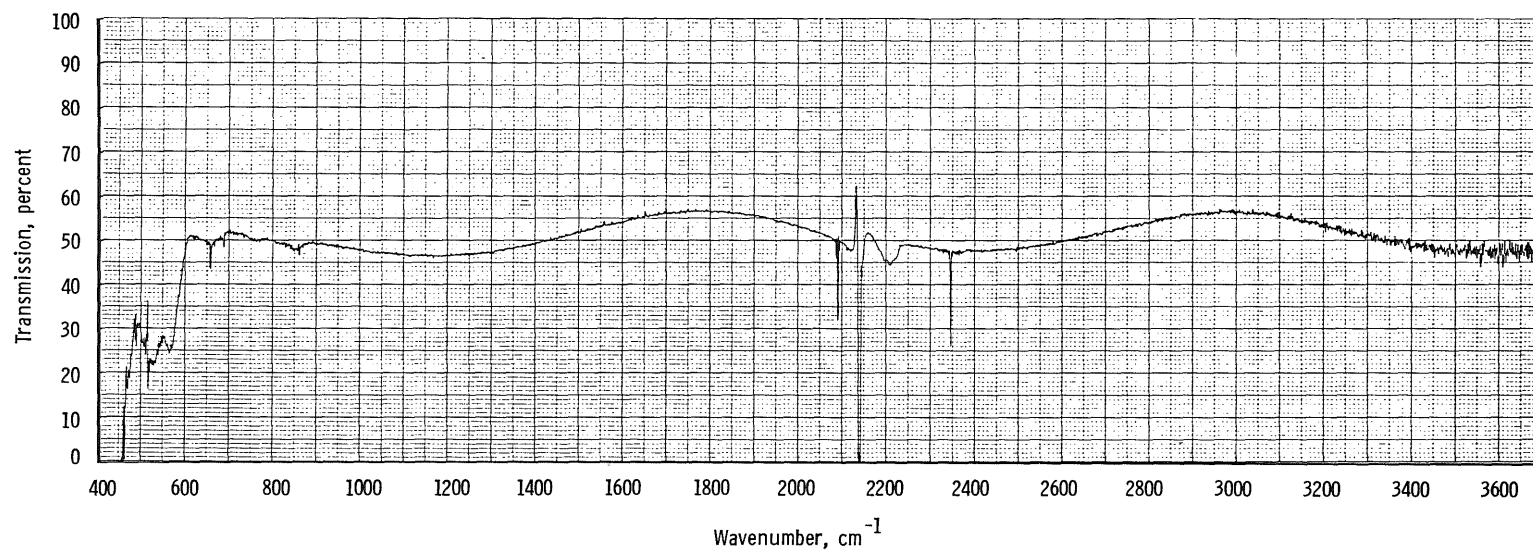


j. 2.982- $\mu\text{m}$ -thick deposit (expanded abscissa scale in 2,200- $\text{cm}^{-1}$  region)  
Figure 37. Continued.

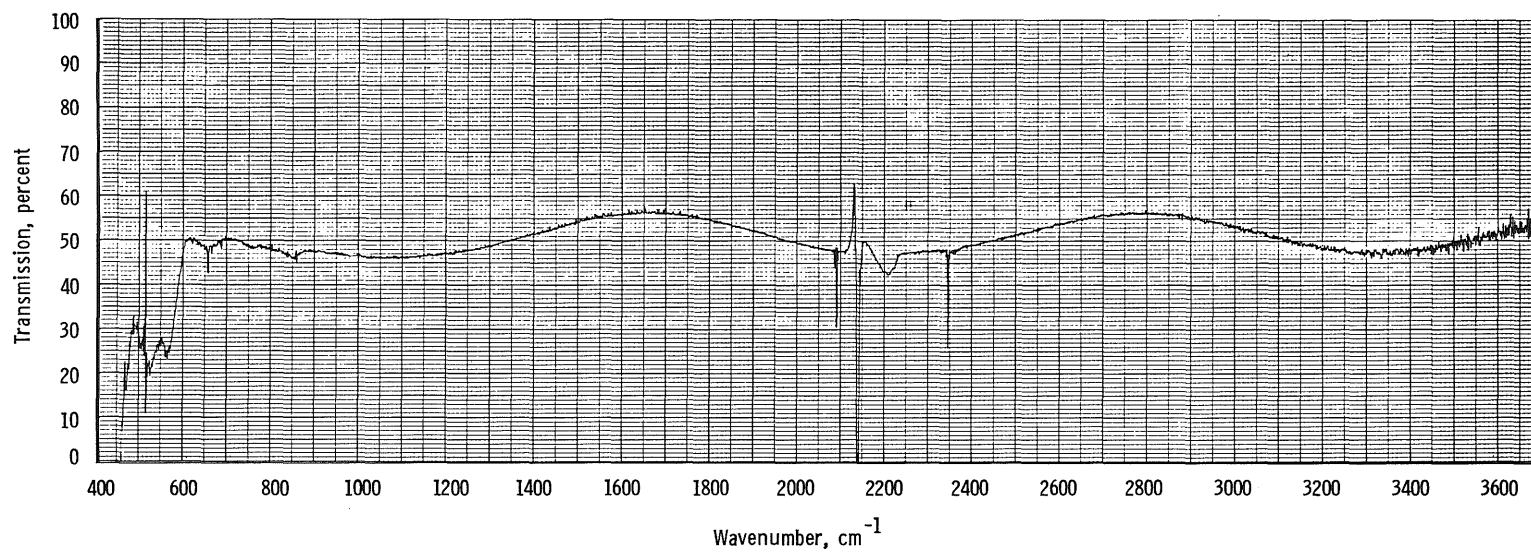




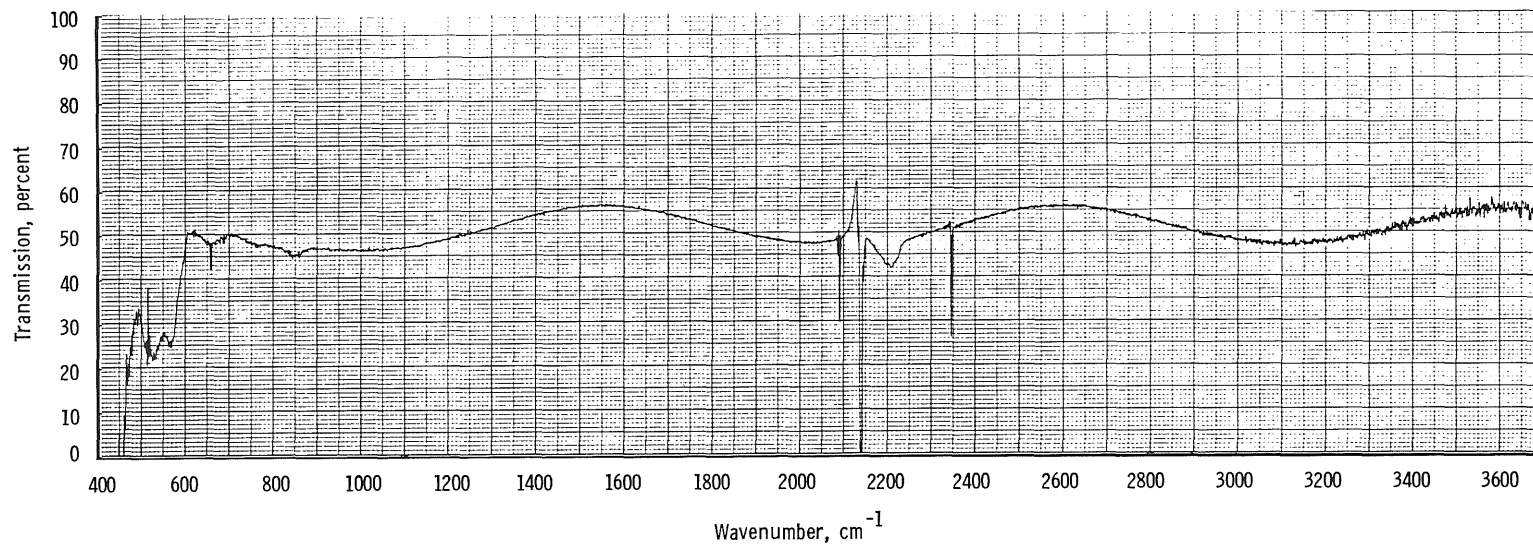
k. 3.242- $\mu\text{m}$ -thick deposit  
Figure 37. Continued.



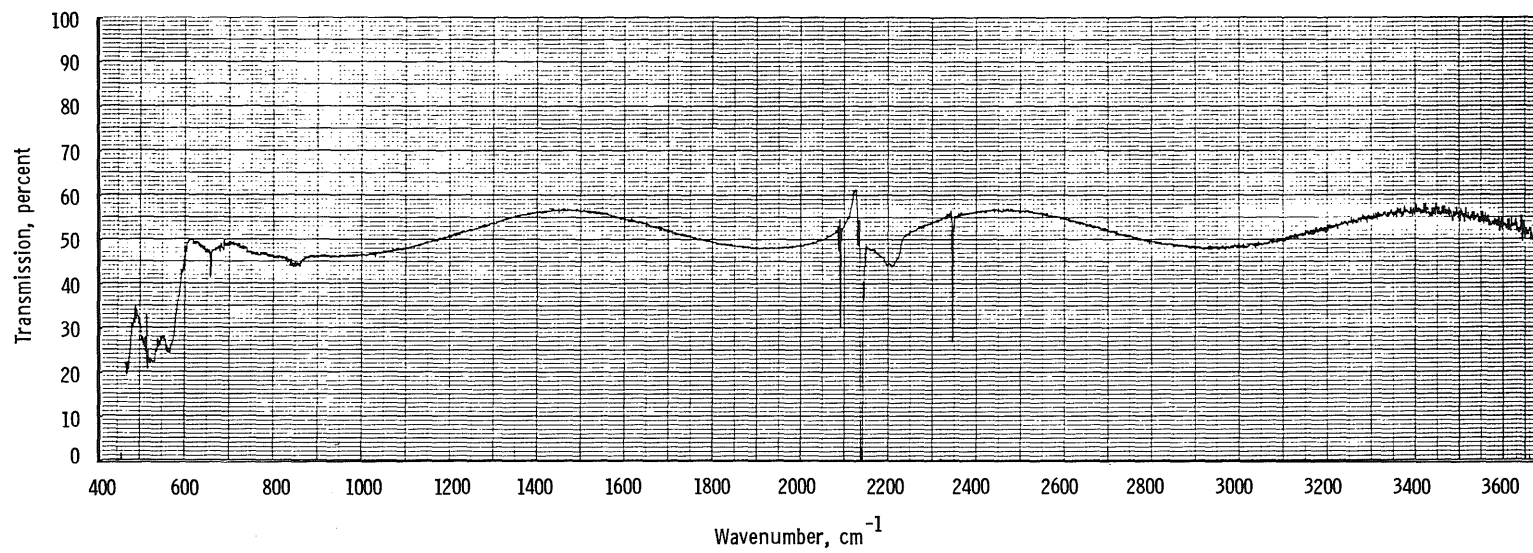
I. 3.501- $\mu$ m-thick deposit  
Figure 37. Continued.



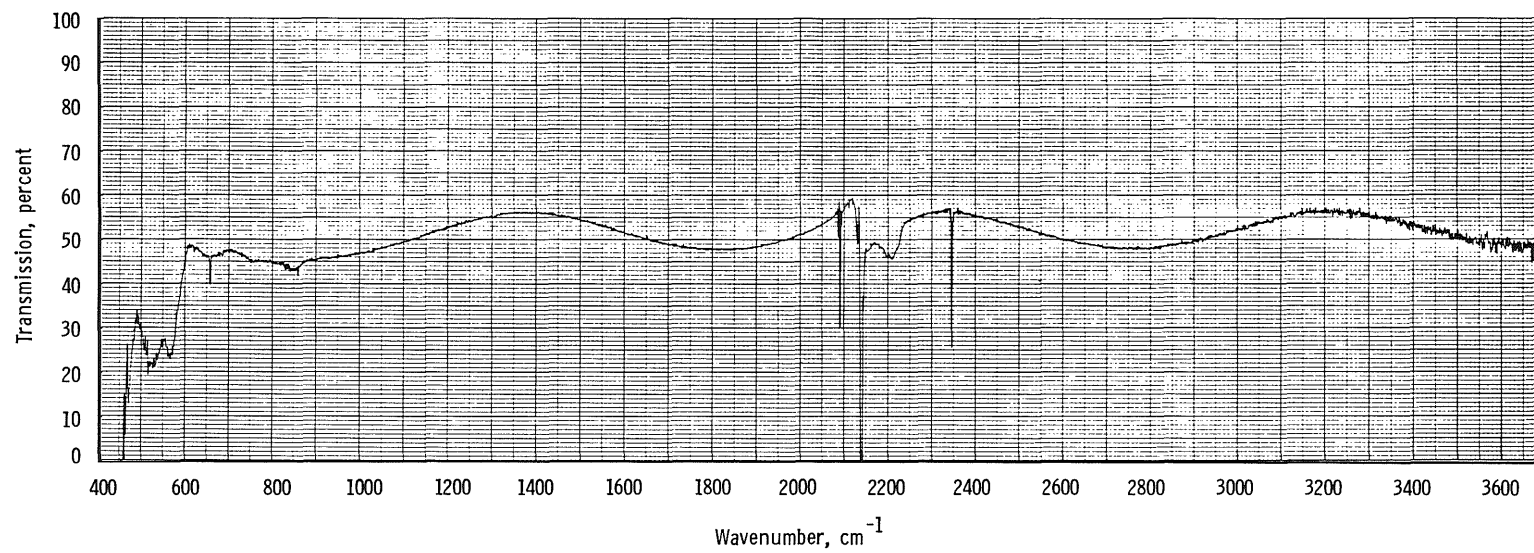
m. 3.760- $\mu\text{m}$ -thick deposit  
Figure 37. Continued.



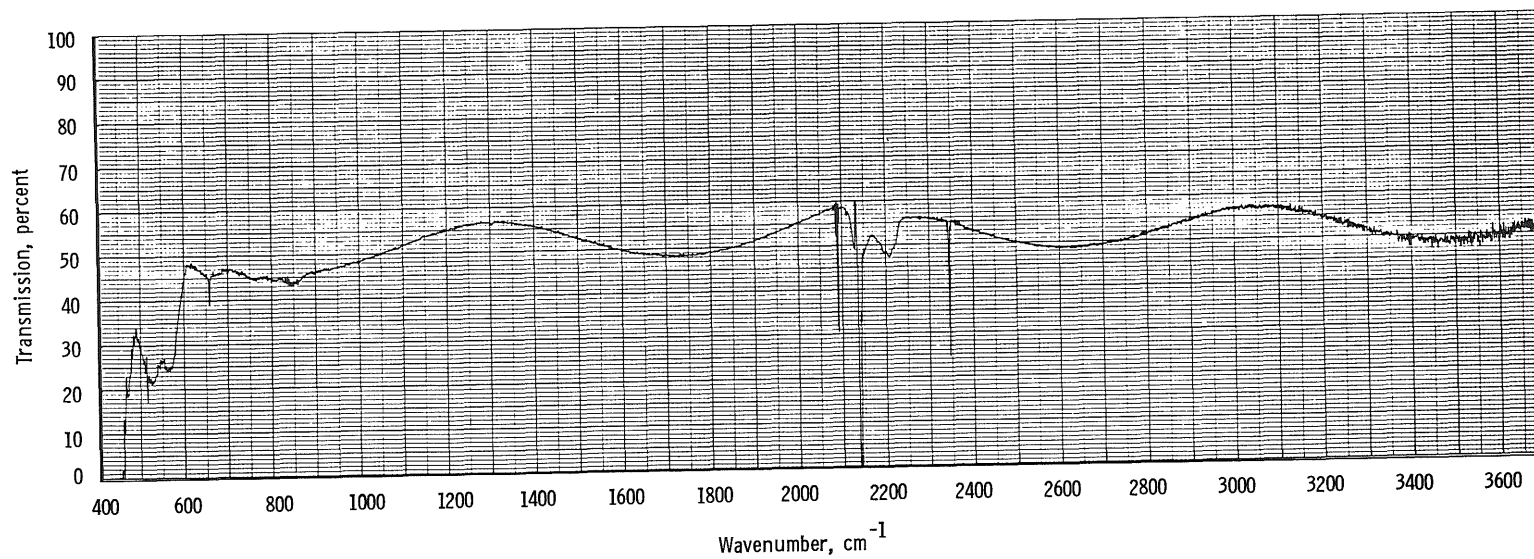
n. 4.020- $\mu$ m-thick deposit  
Figure 37. Continued.



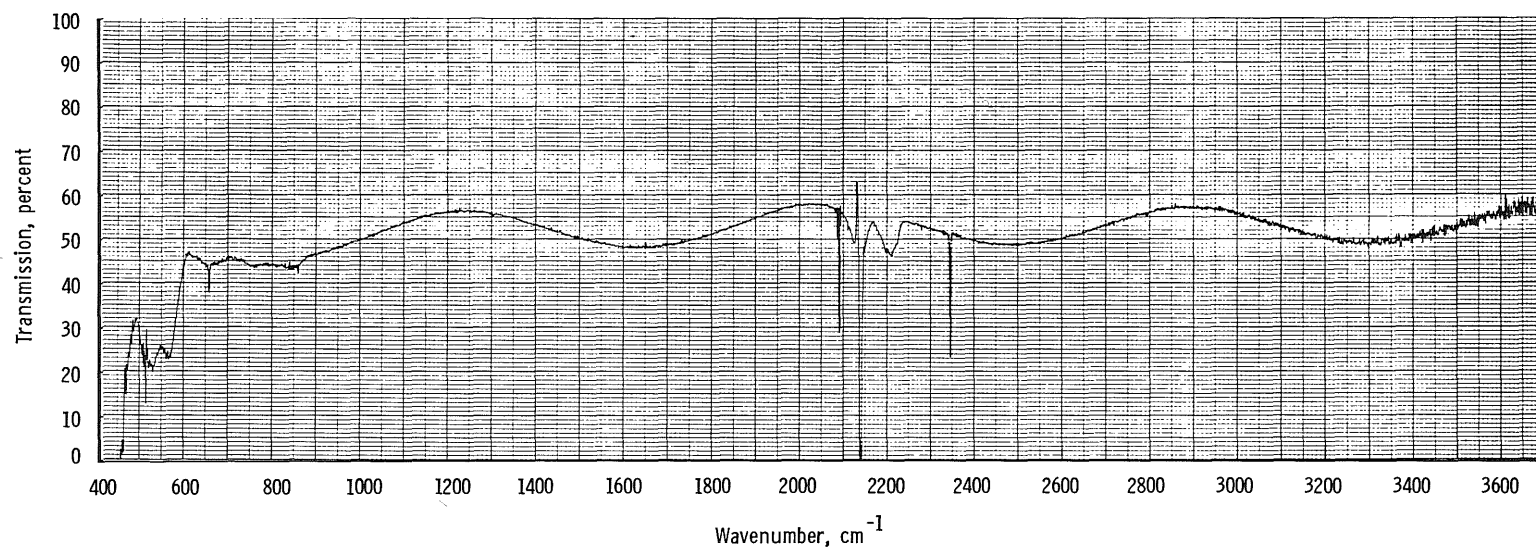
o. 4.280- $\mu\text{m}$ -thick deposit  
Figure 37. Continued.



p. 4.538- $\mu\text{m}$ -thick deposit  
Figure 37. Continued.

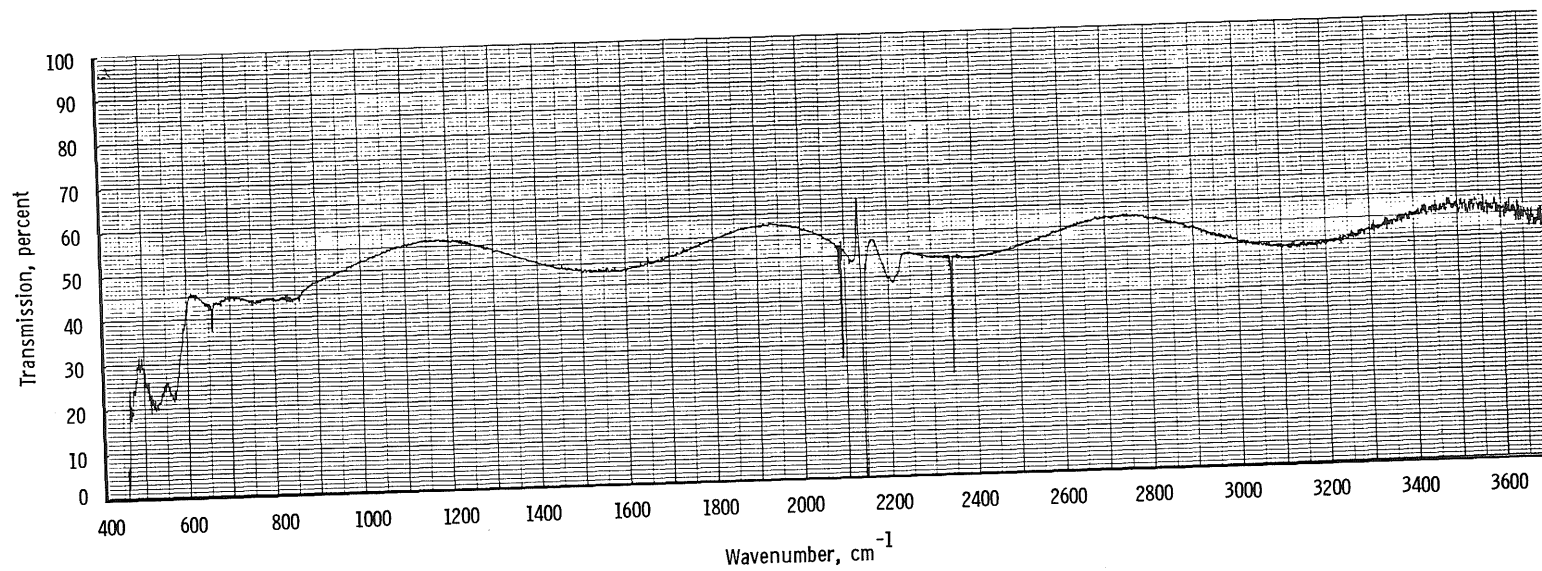


q. 4.798- $\mu\text{m}$ -thick deposit  
Figure 37. Continued.

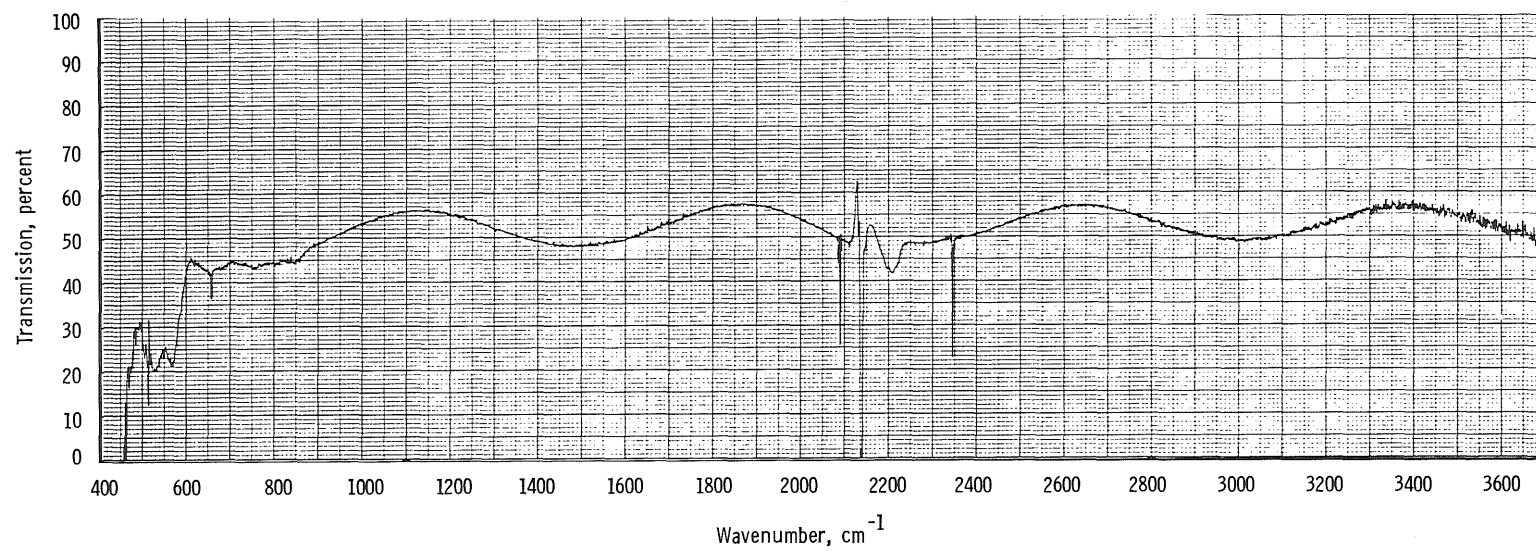


r. 5.057- $\mu\text{m}$ -thick deposit  
Figure 37. Continued.

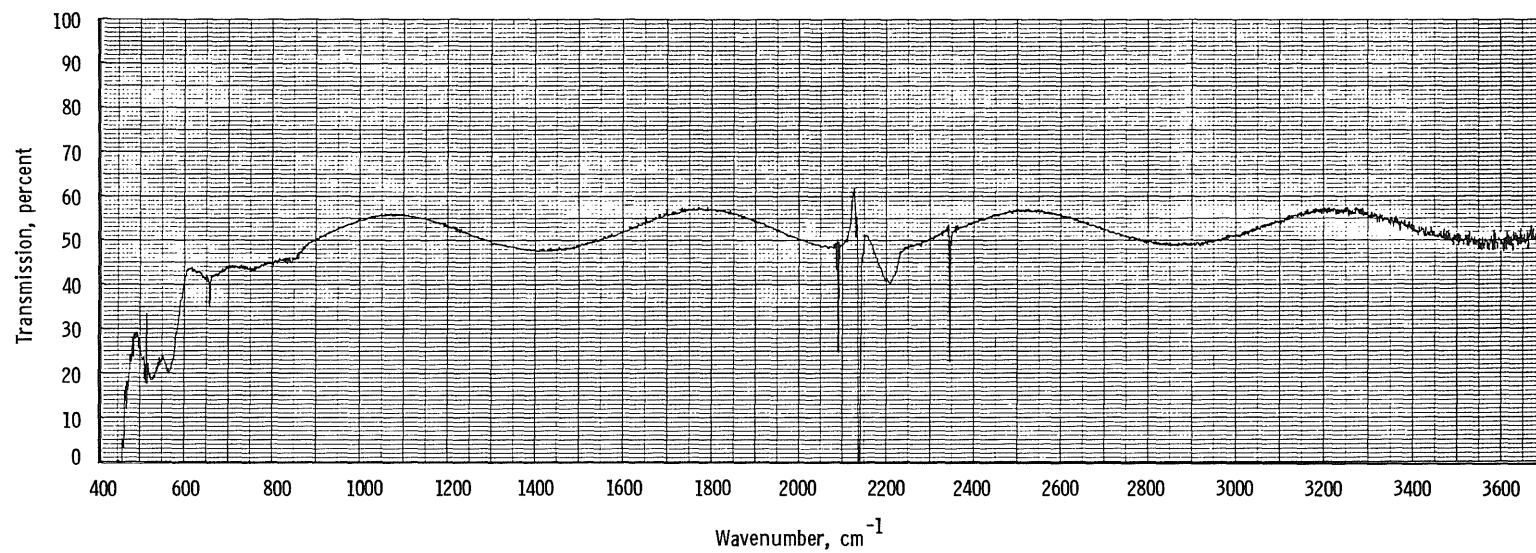




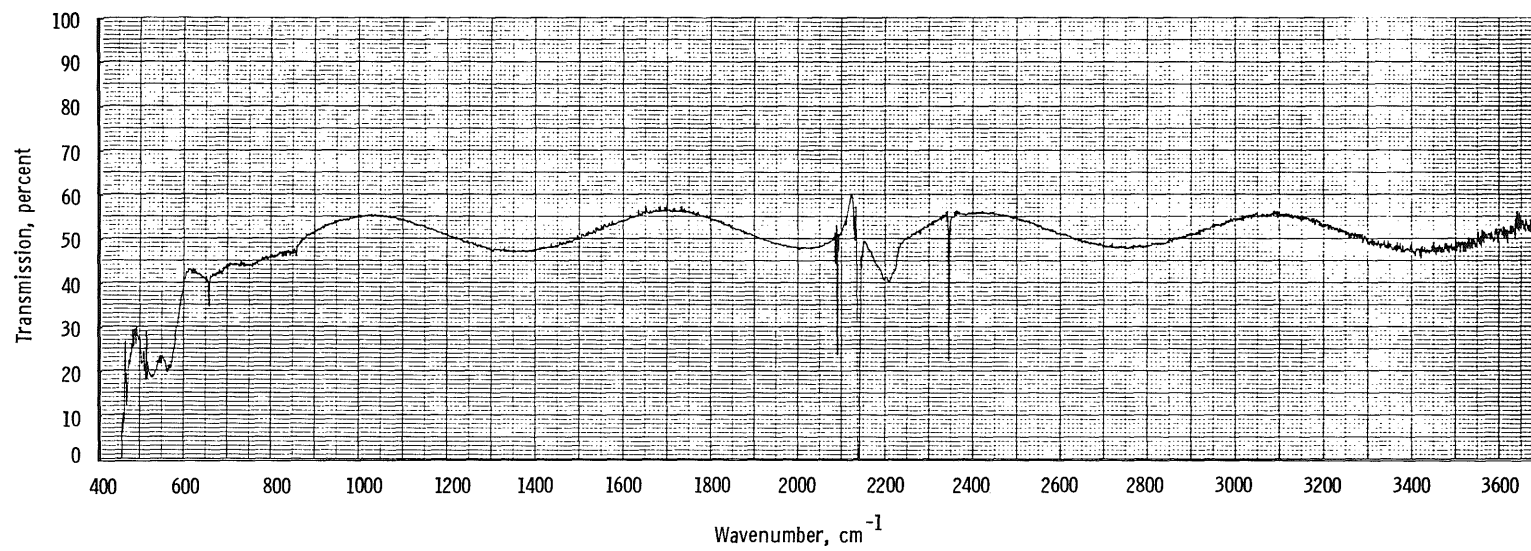
s. 5.316- $\mu\text{m}$ -thick deposit  
Figure 37. Continued.



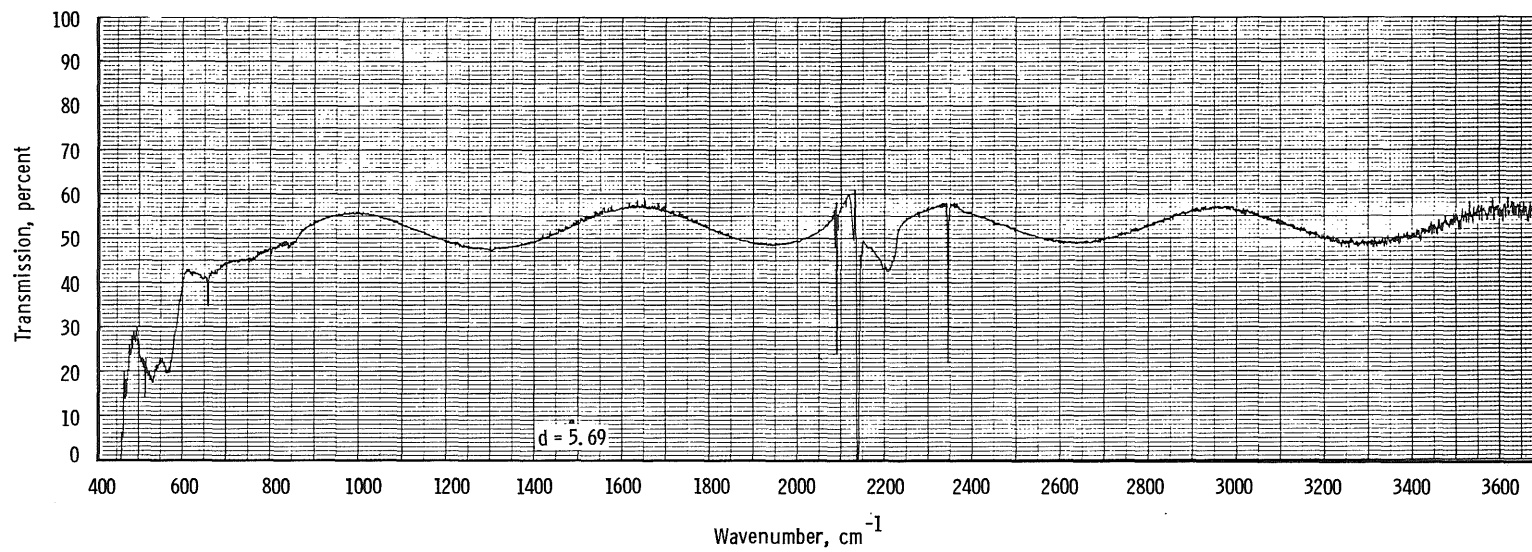
t. 5.576- $\mu\text{m}$ -thick deposit  
Figure 37. Continued.



u. 5.835- $\mu\text{m}$ -thick deposit  
Figure 37. Continued.



v. 6.095- $\mu\text{m}$ -thick deposit  
Figure 37. Continued.



w. 6.354- $\mu\text{m}$ -thick deposit  
Figure 37. Concluded.

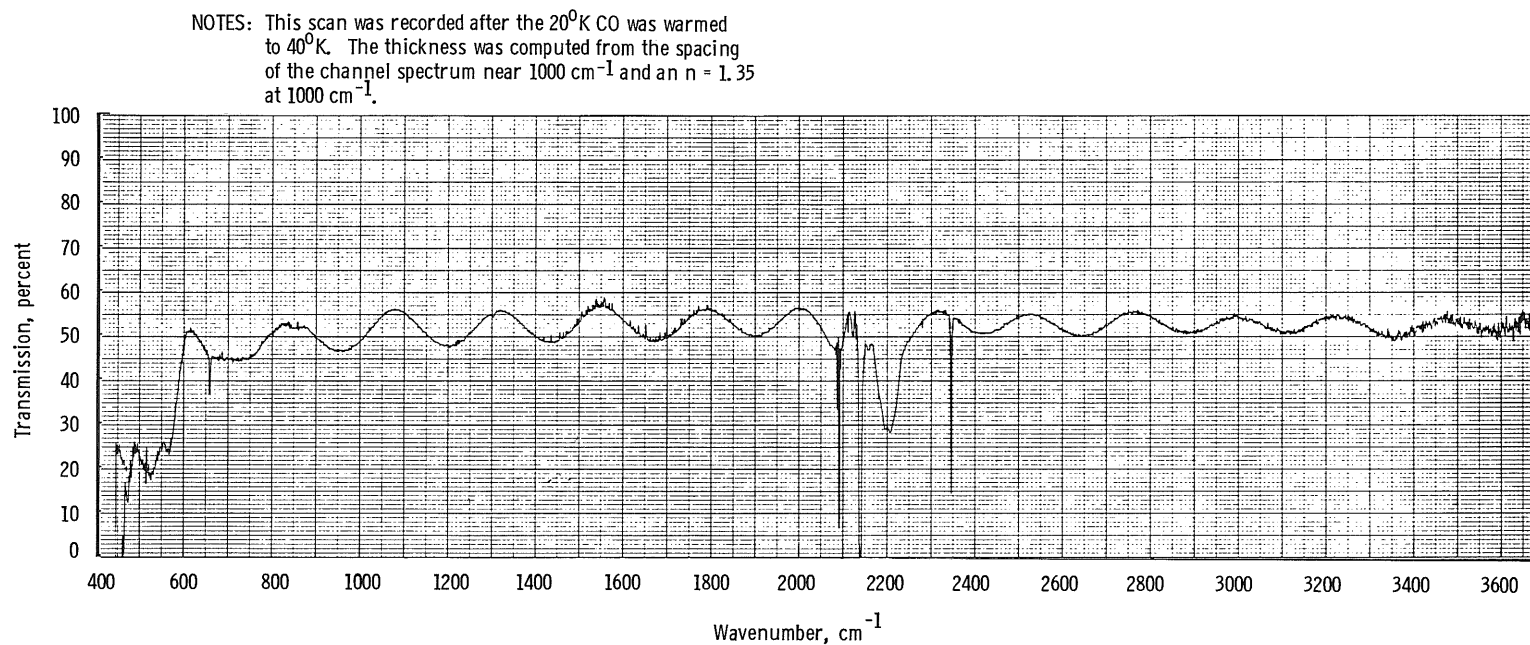
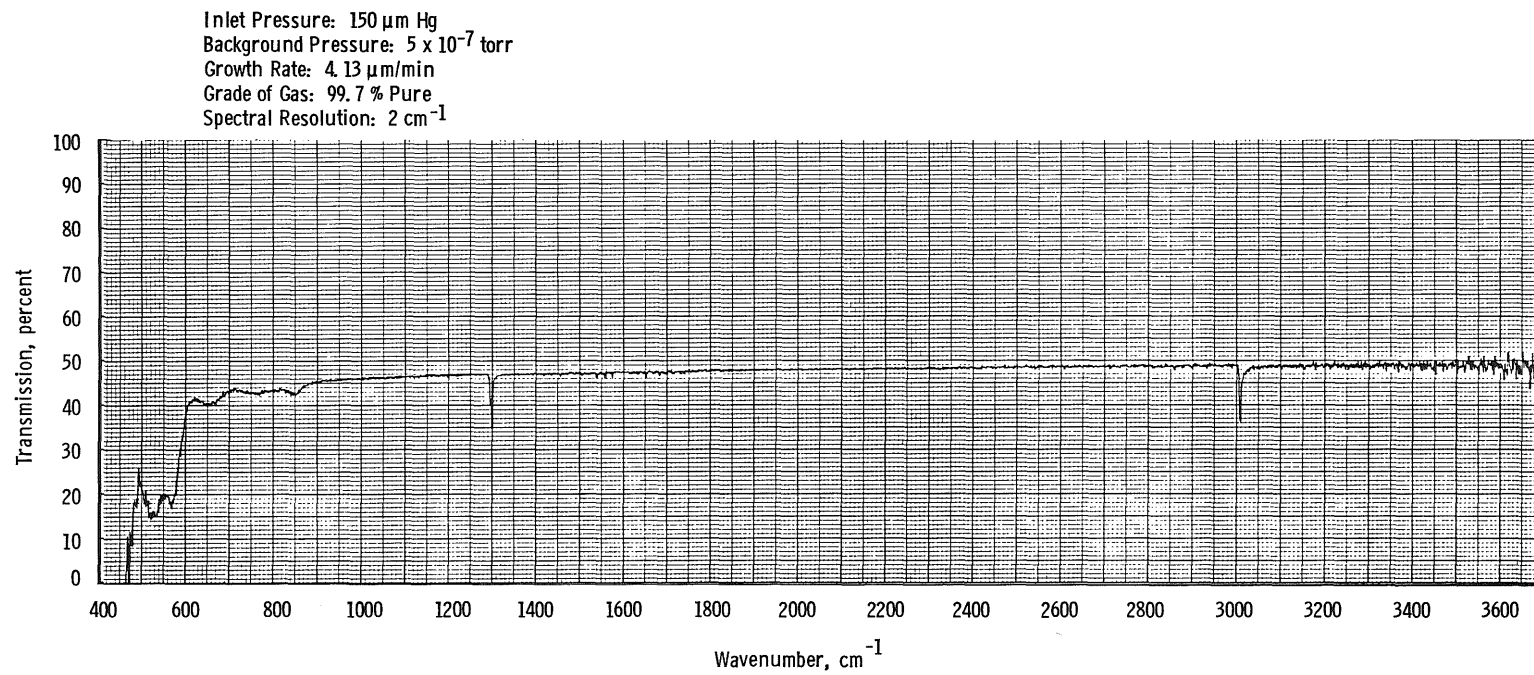
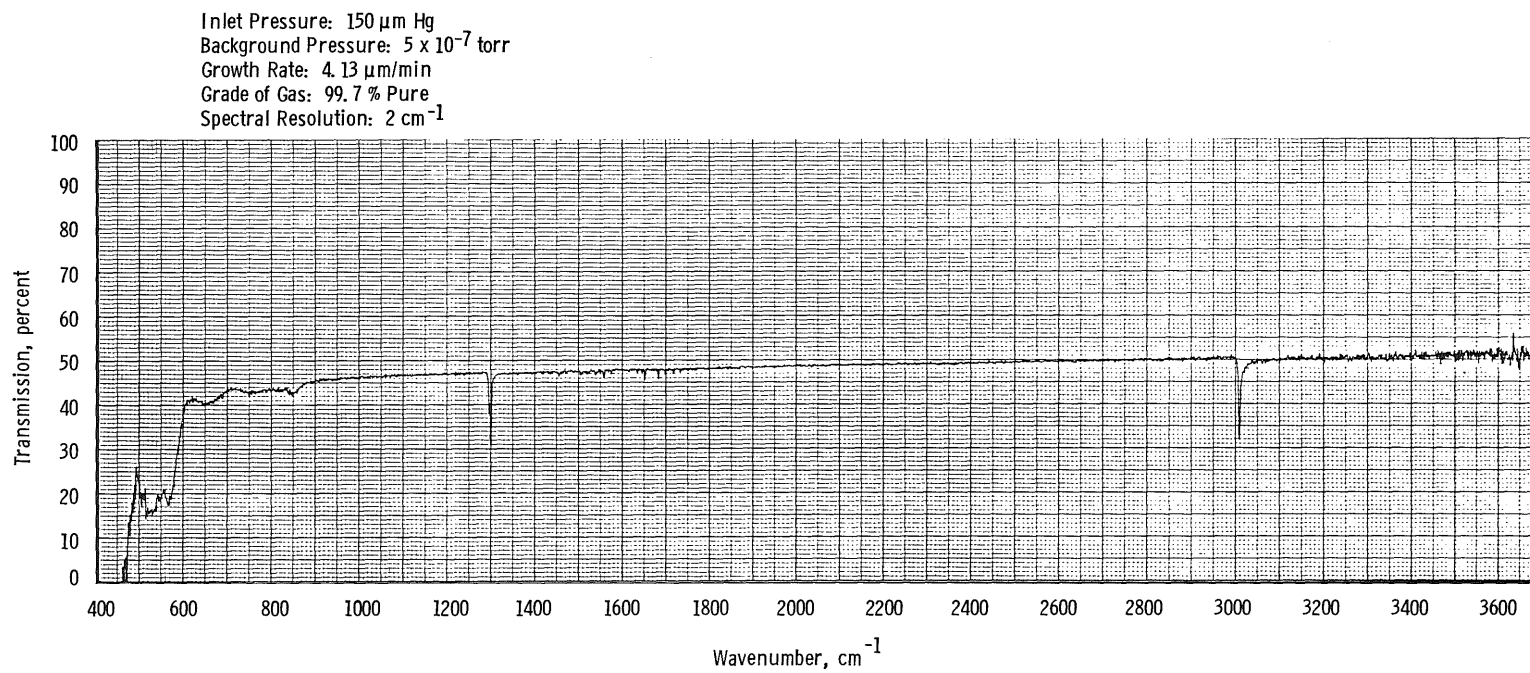


Figure 38. Transmission of germanium window with a  $15\text{-}\mu\text{m}$ -thick CO deposit after warming from  $20^{\circ}\text{K}$  to  $40^{\circ}\text{K}$ .



a. 0.114- $\mu\text{m}$ -thick deposit

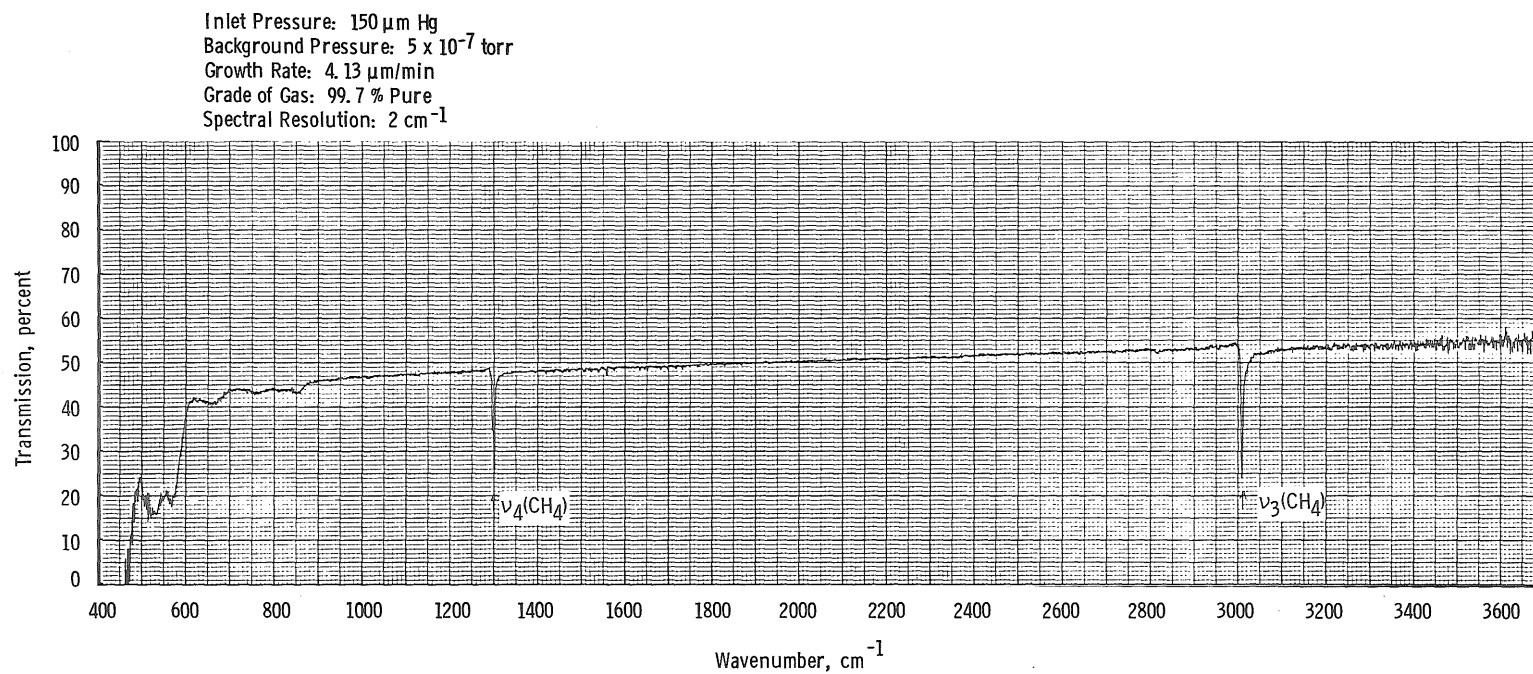
Figure 39. Transmission of 20°K germanium window with various  $\text{CH}_4$  deposit thicknesses.



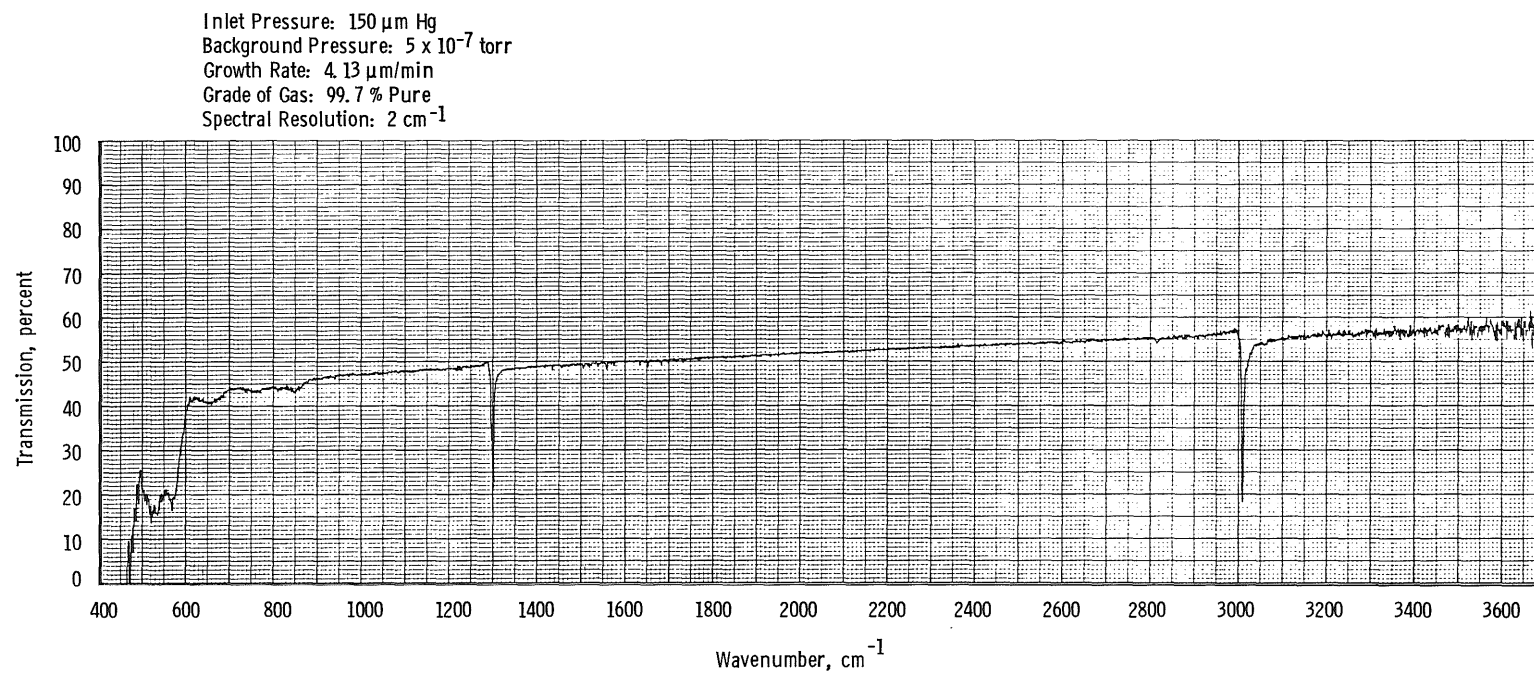
b. 0.229- $\mu\text{m}$ -thick deposit  
Figure 39. Continued.



178

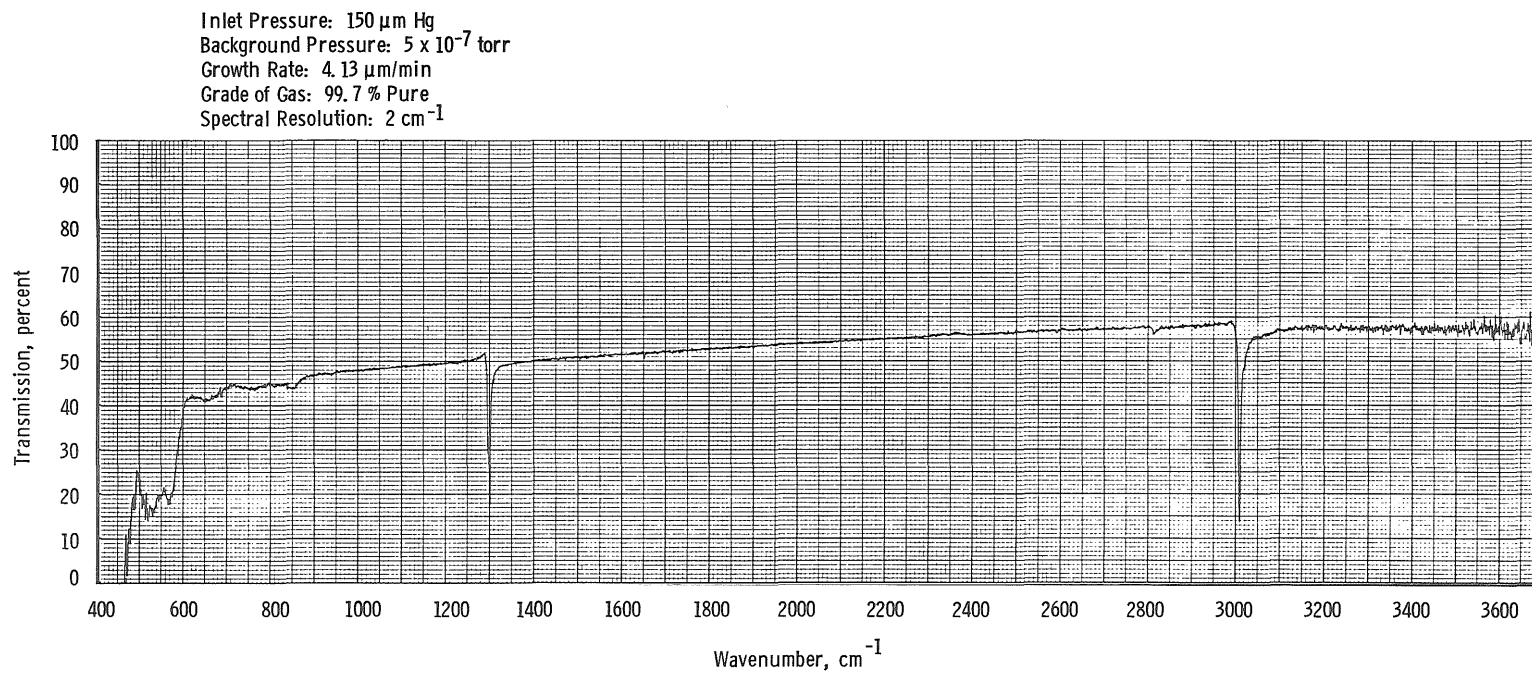


c. 0.344- $\mu\text{m}$ -thick deposit  
Figure 39. Continued.

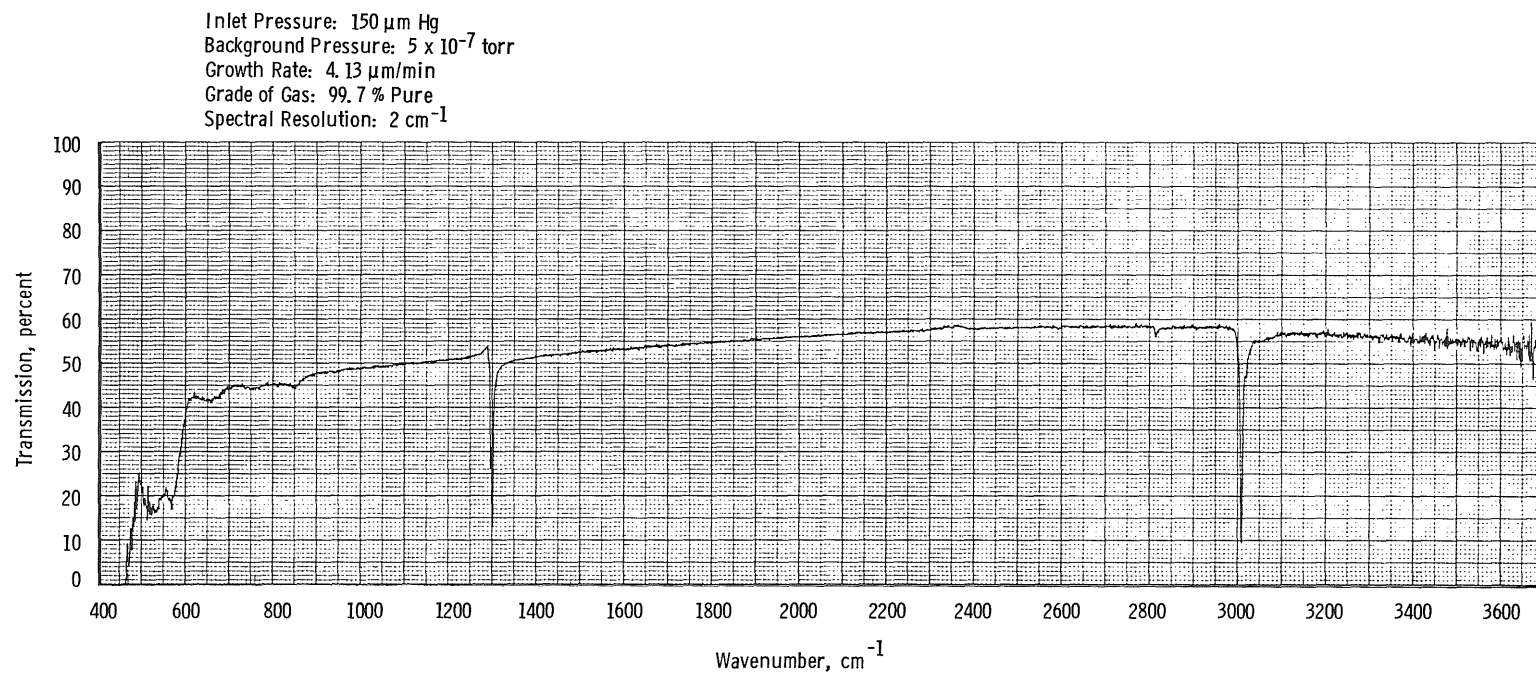


d. 0.458- $\mu\text{m}$ -thick deposit  
Figure 39. Continued.

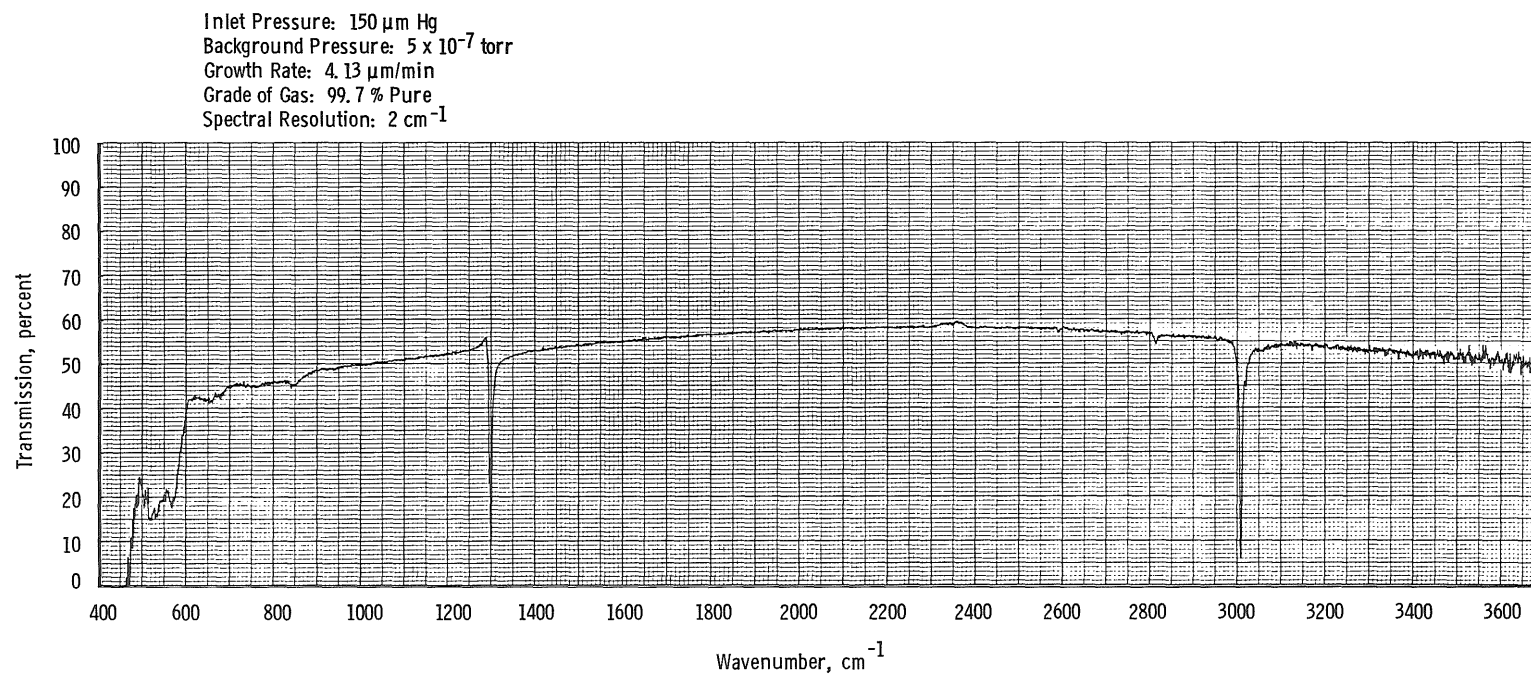
180



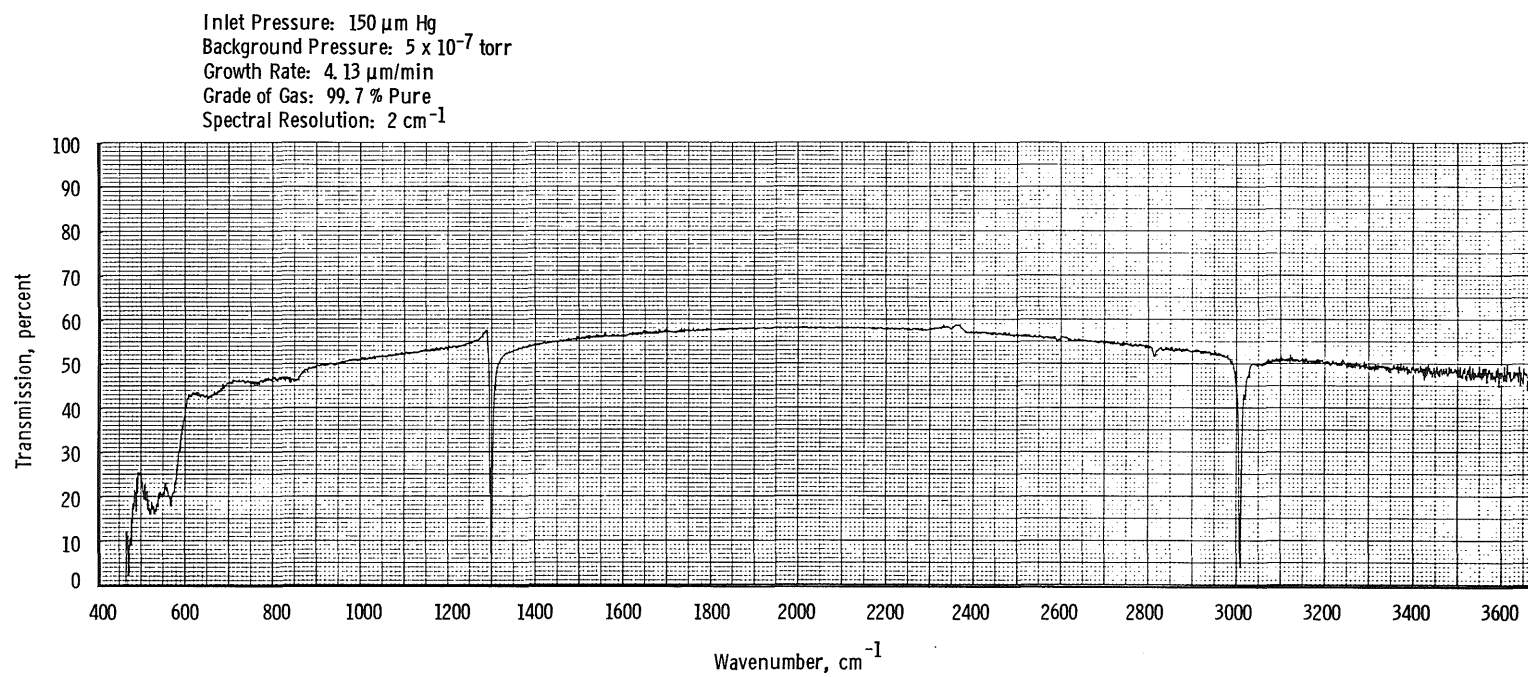
e. 0.573- $\mu\text{m}$ -thick deposit  
Figure 39. Continued.



f. 0.688- $\mu\text{m}$ -thick deposit  
Figure 39. Continued.

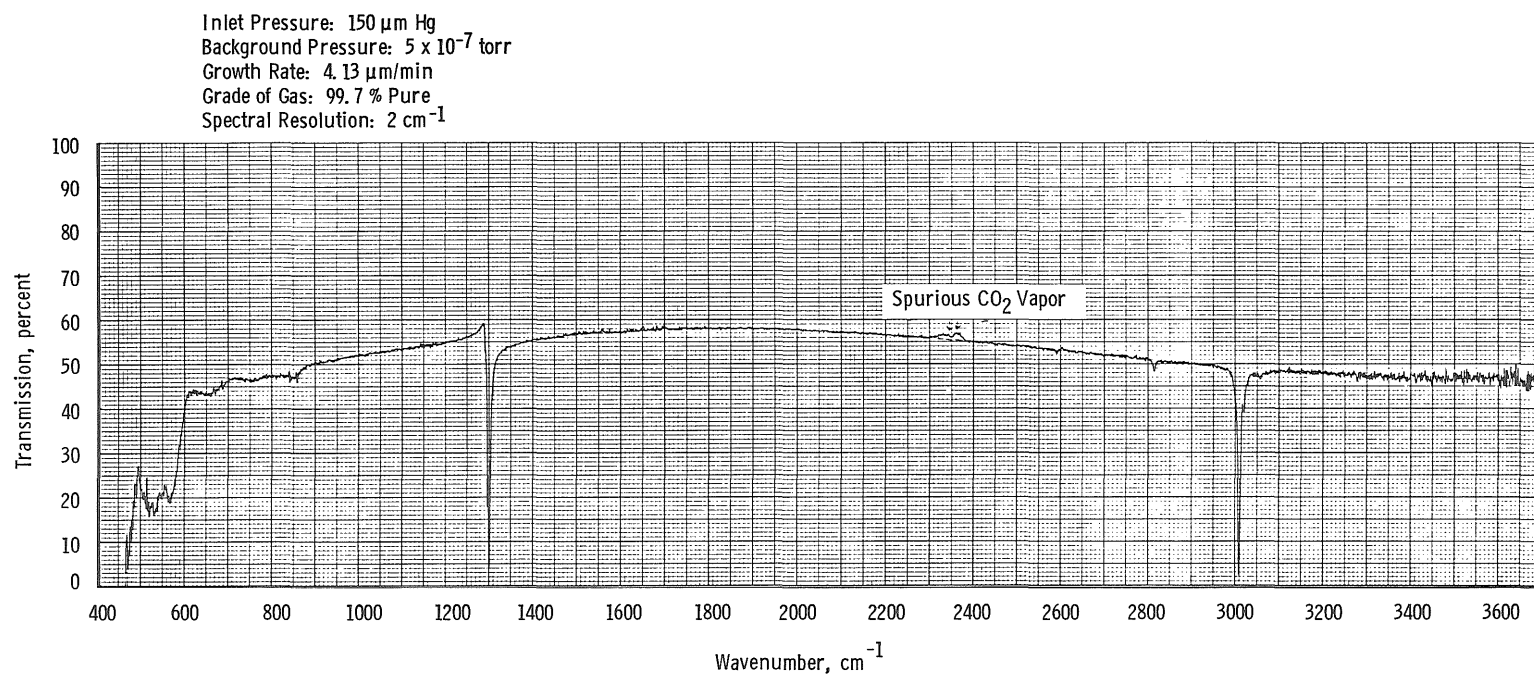


**g. 0.802- $\mu\text{m}$ -thick deposit**  
**Figure 39. Continued.**

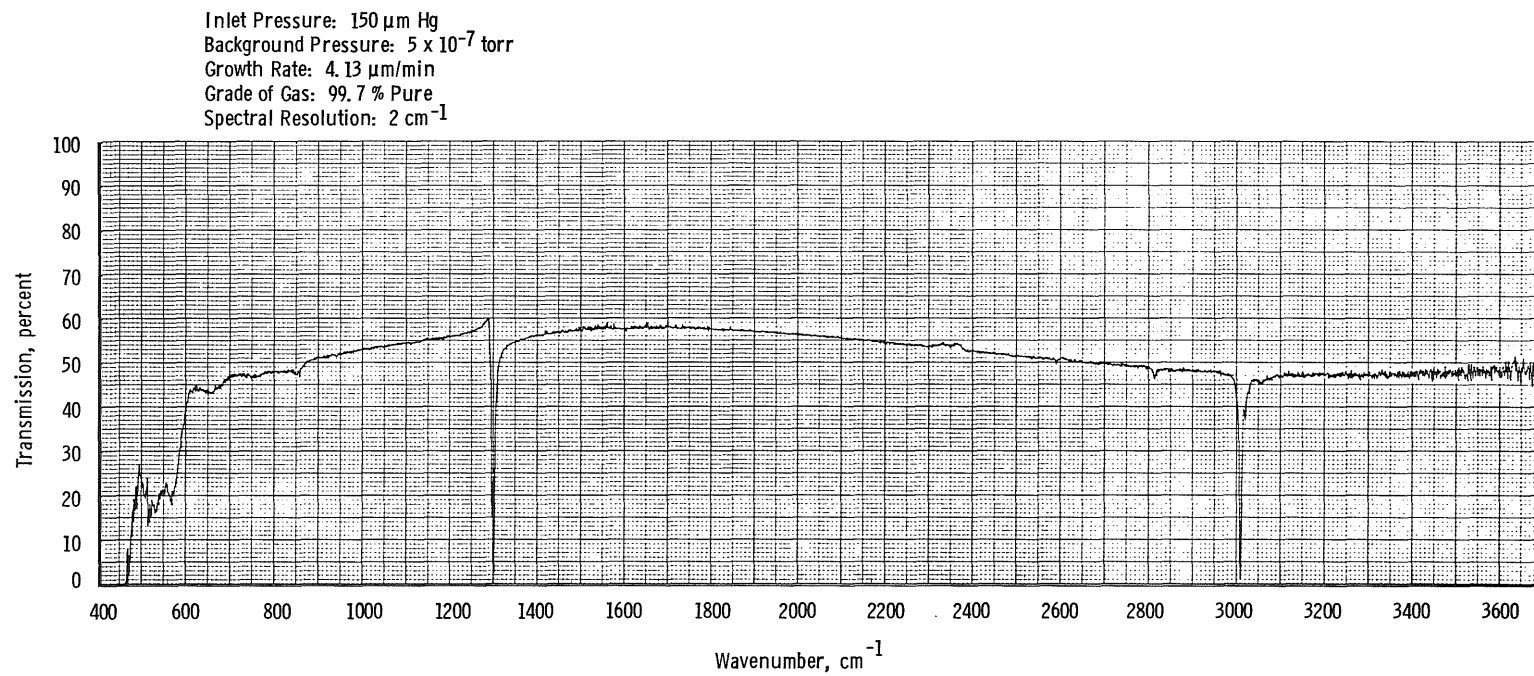


**h. 0.917- $\mu\text{m}$ -thick deposit**  
**Figure 39. Continued.**

184



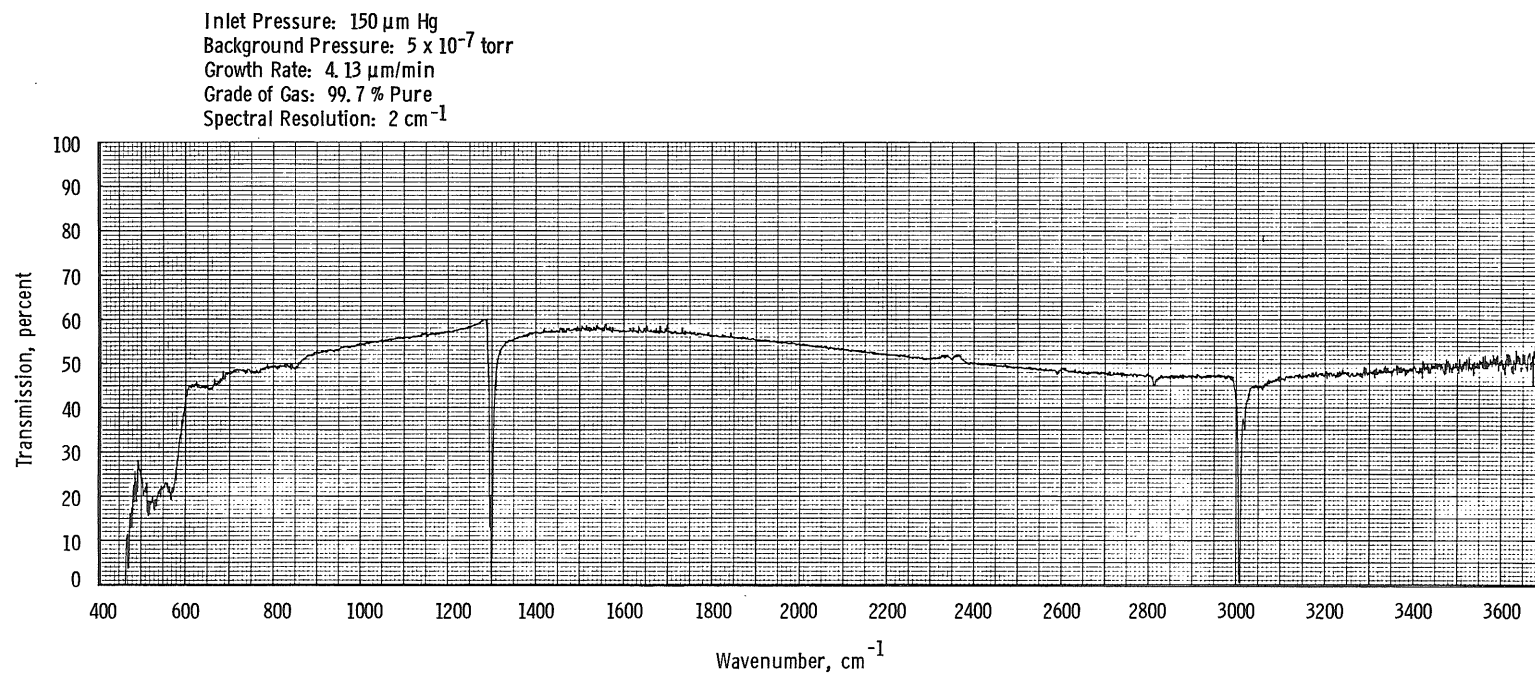
i. 1.030- $\mu\text{m}$ -thick deposit  
Figure 39. Continued.



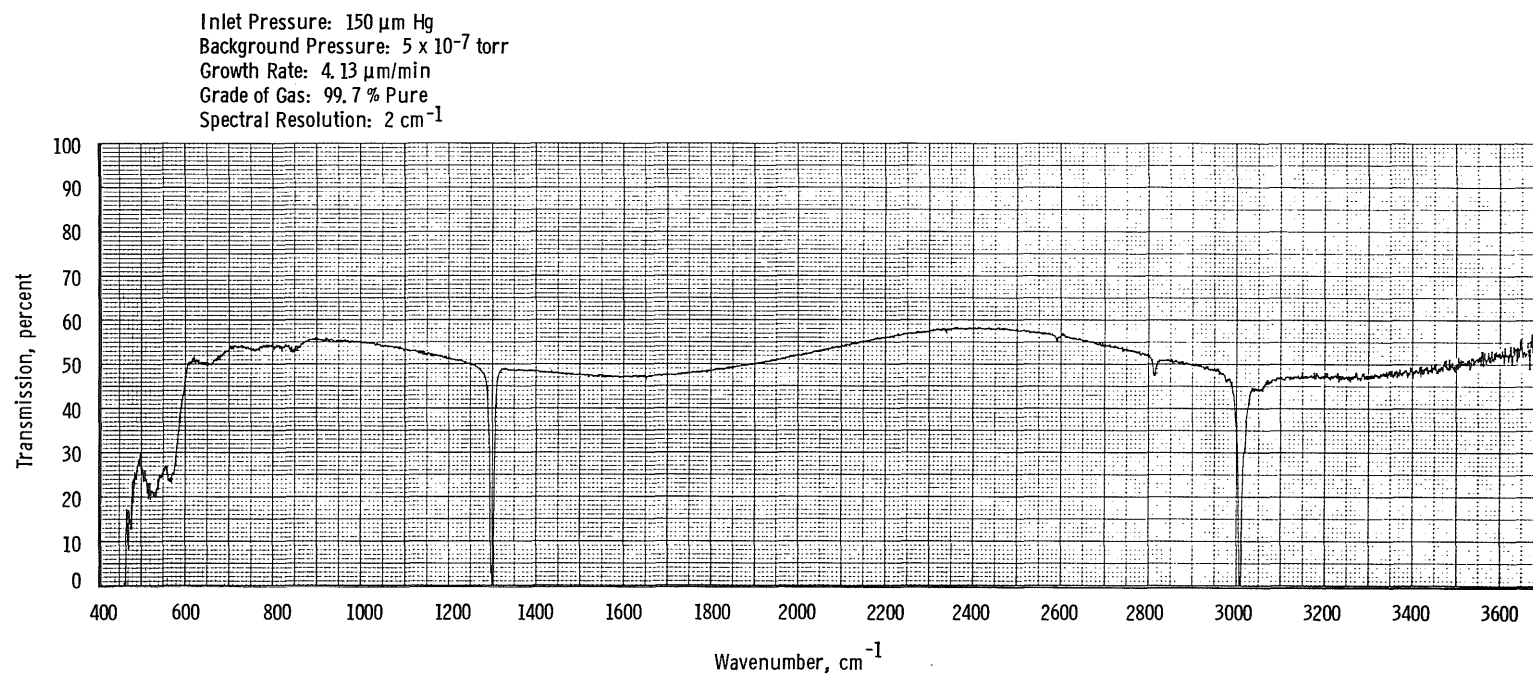
j. 1.150- $\mu\text{m}$ -thick deposit  
Figure 39. Continued.



186

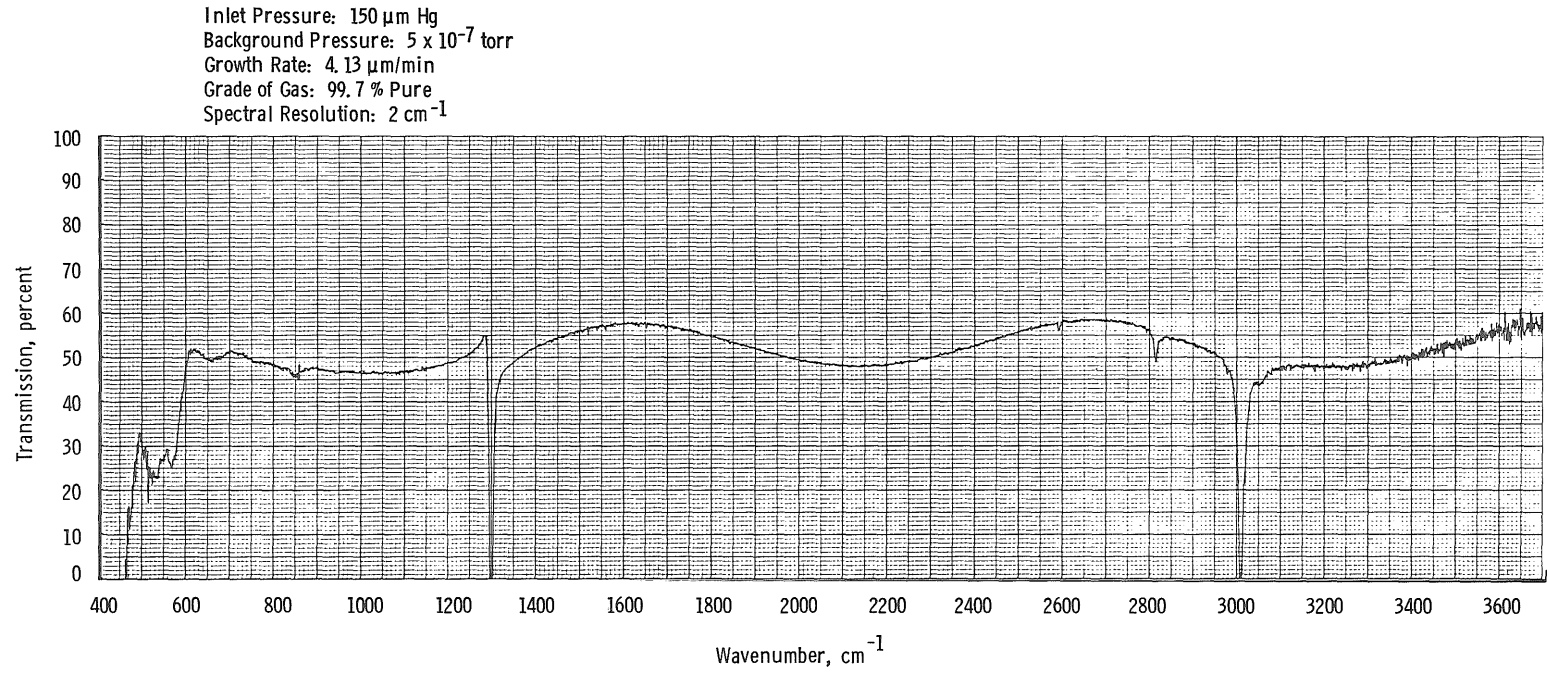


k. 1.260- $\mu\text{m}$ -thick deposit  
Figure 39. Continued.

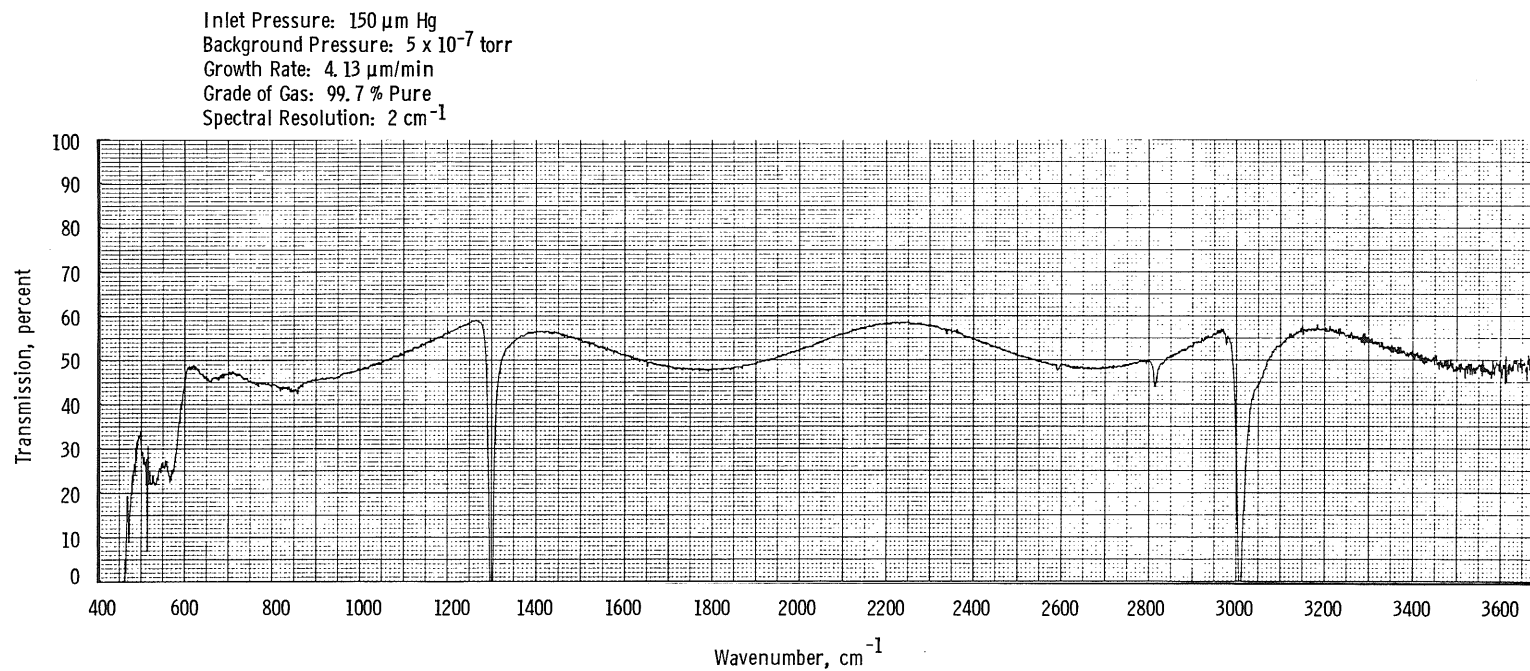


I. 2.290- $\mu\text{m}$ -thick deposit  
Figure 39. Continued.

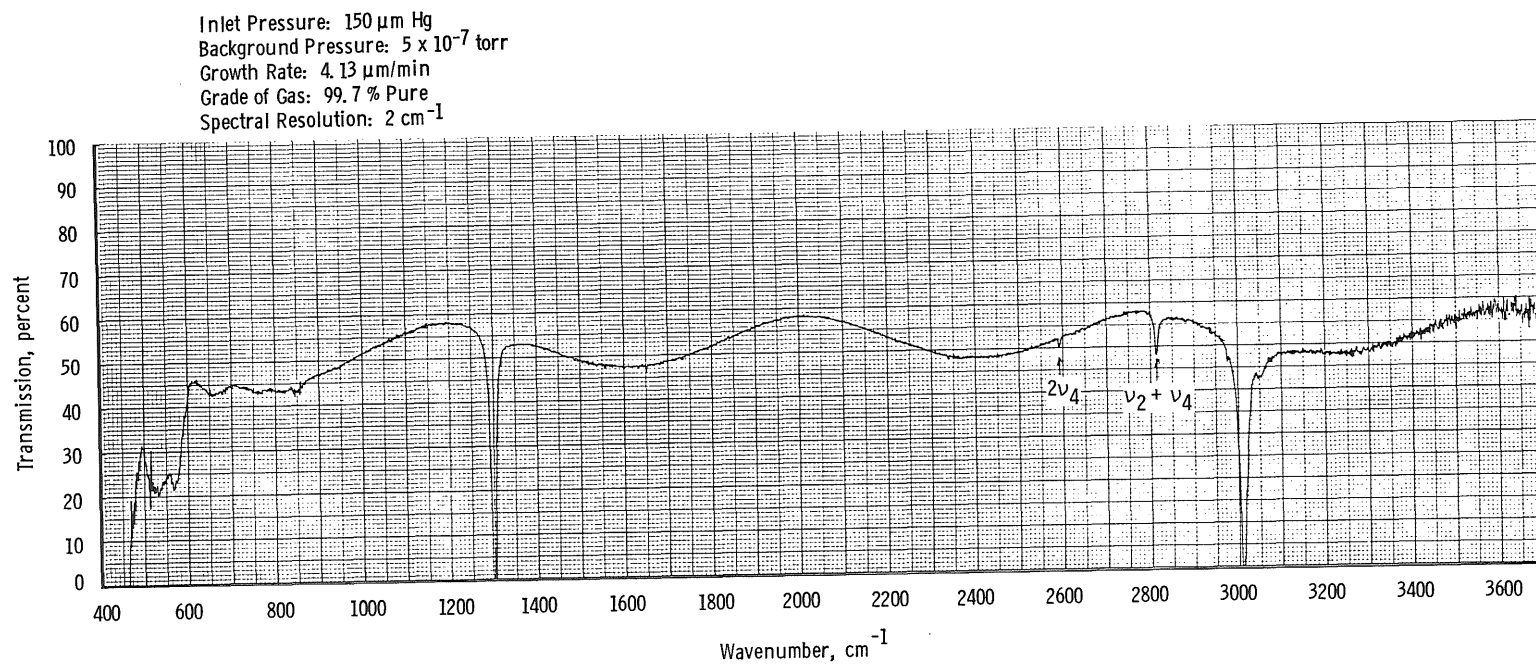
188



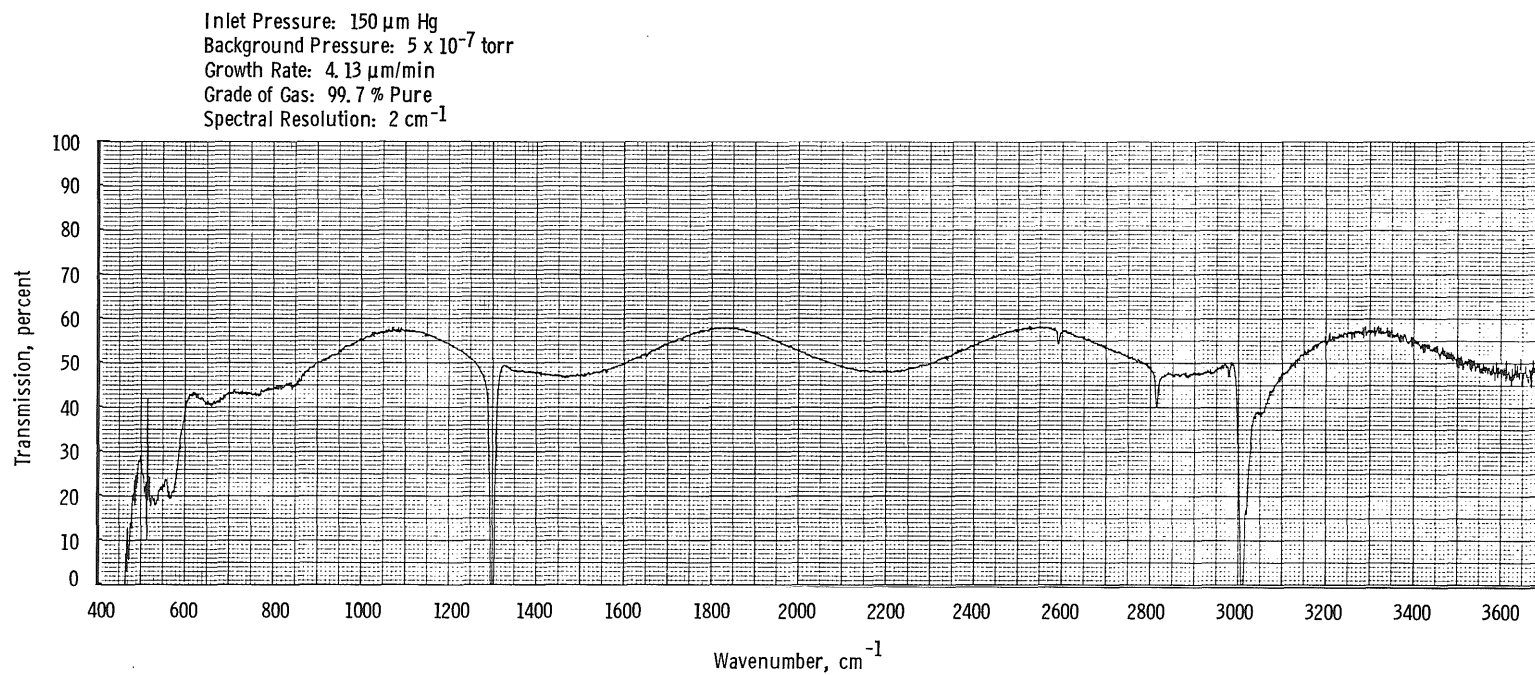
m. 3.44- $\mu\text{m}$ -thick deposit  
Figure 39. Continued.



n. 4.127- $\mu\text{m}$ -thick deposit  
Figure 39. Continued.

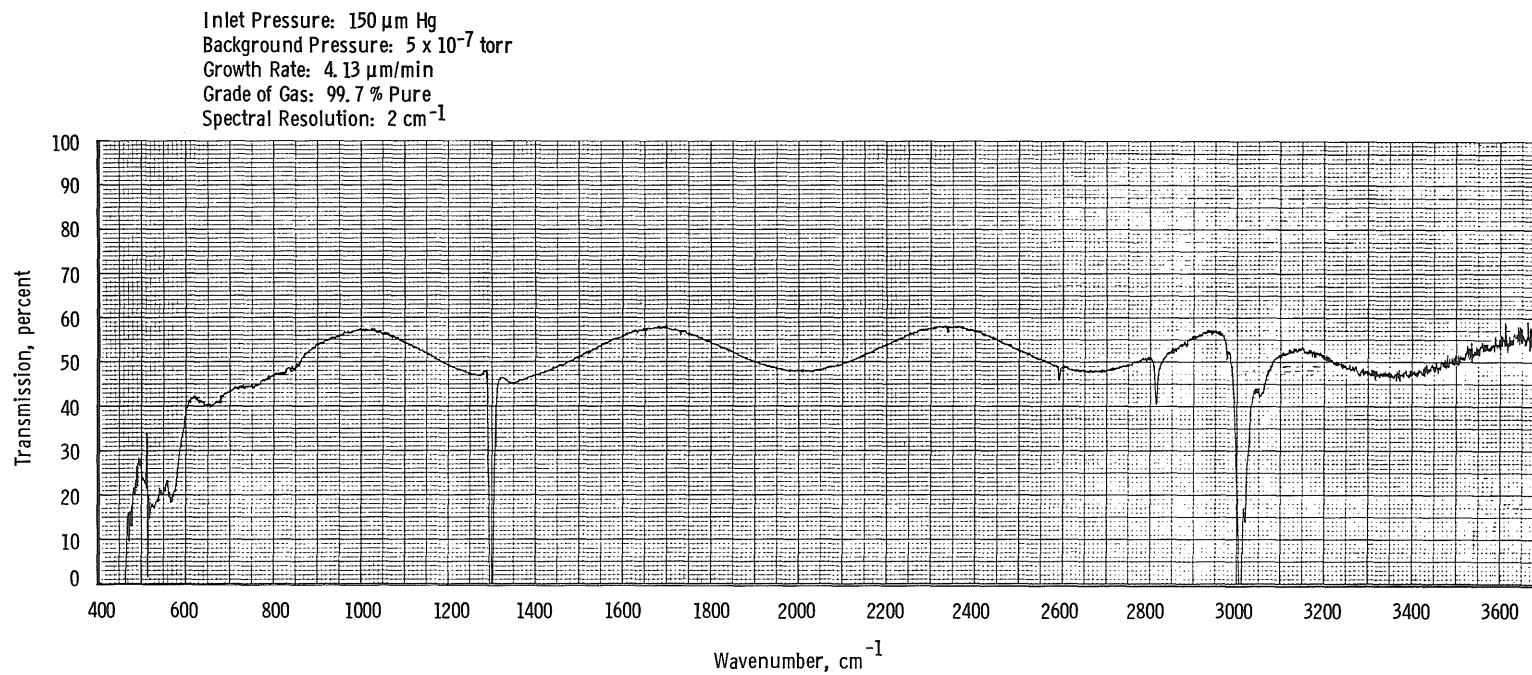


o. 4.580- $\mu\text{m}$ -thick deposit  
Figure 39. Continued.

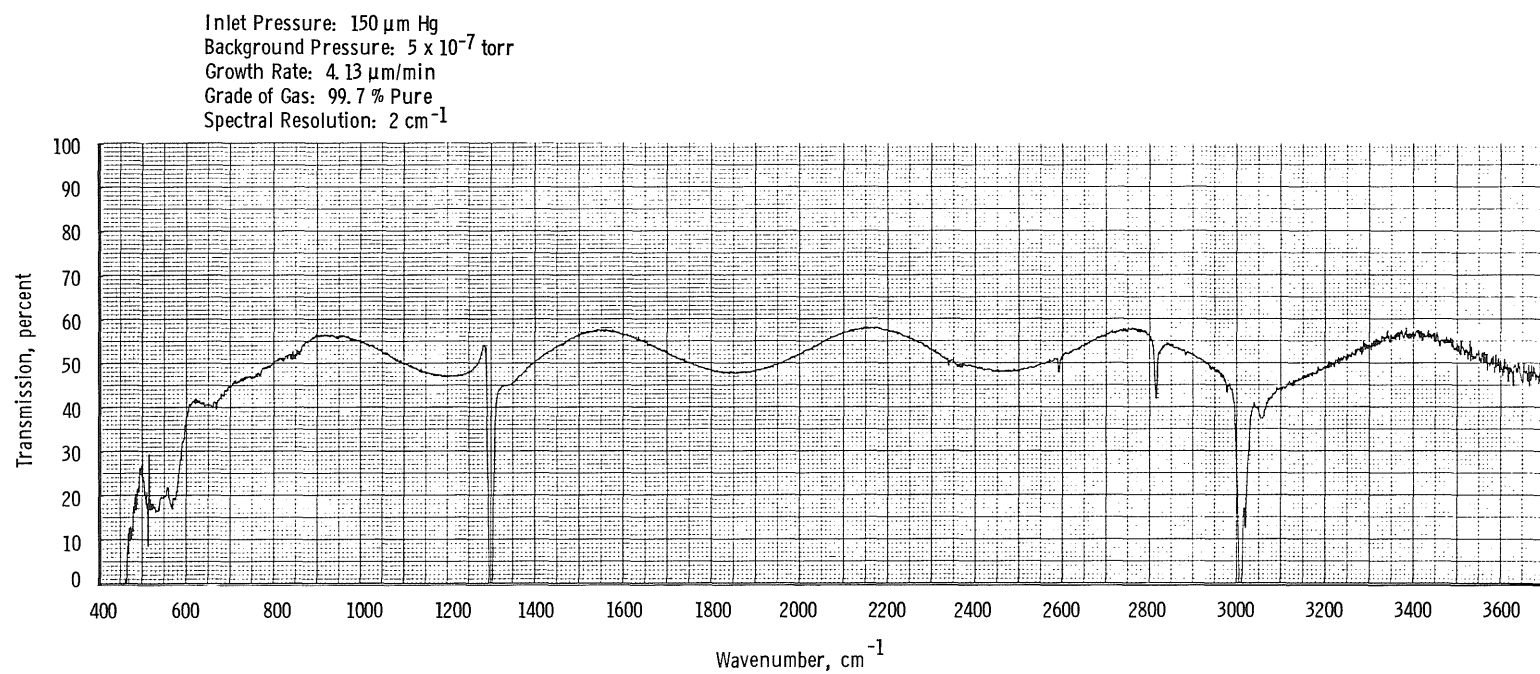


p. 5.040- $\mu\text{m}$ -thick deposit  
Figure 39. Continued.

192



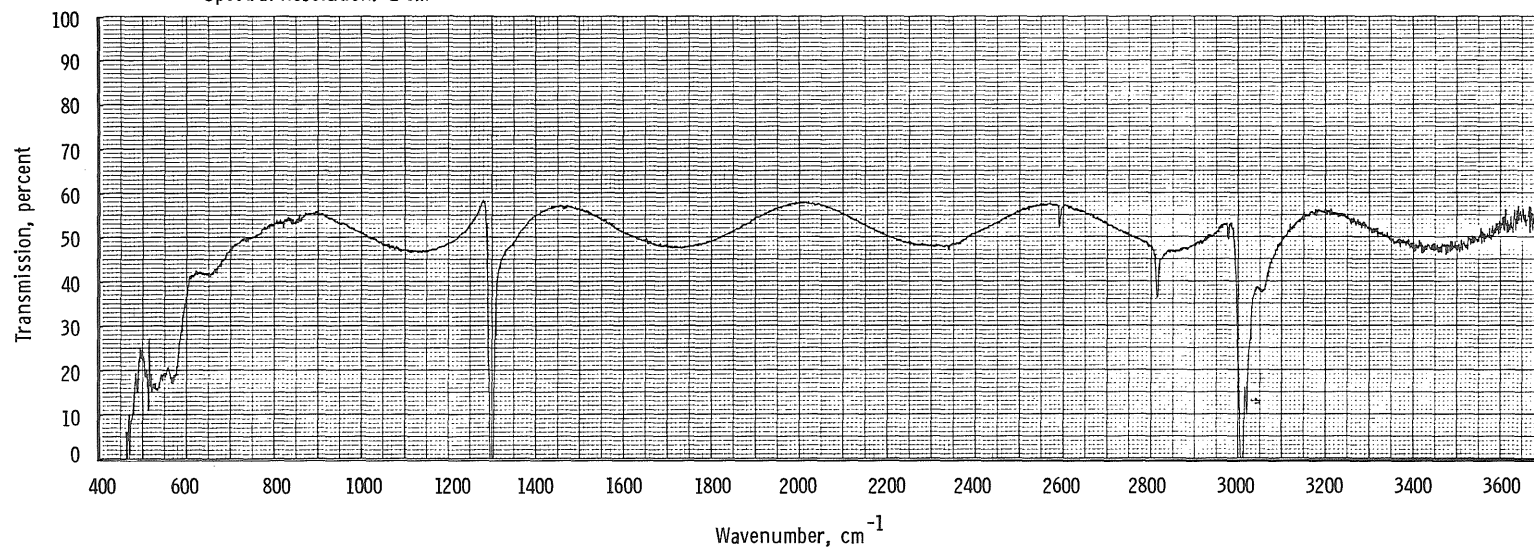
q. 5.500- $\mu\text{m}$ -thick deposit  
Figure 39. Continued.



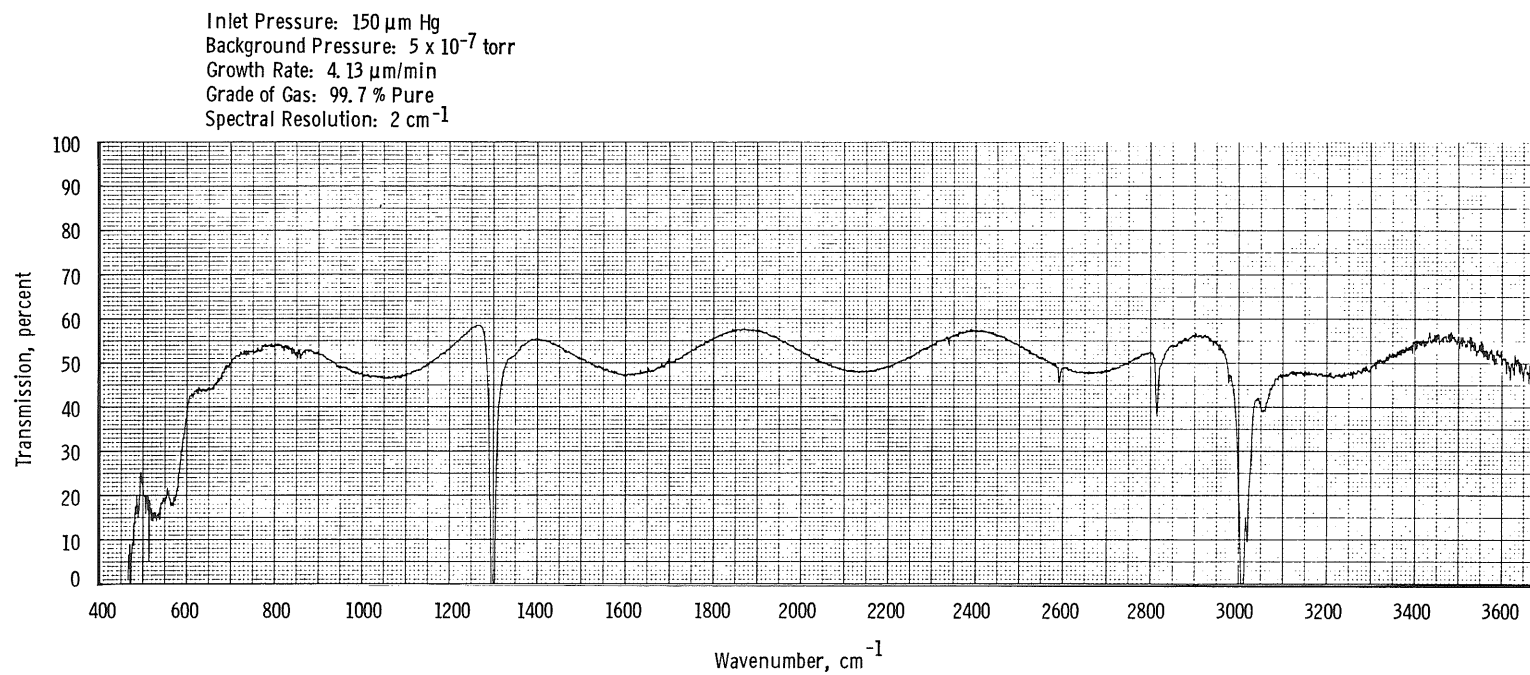
r. 5.960- $\mu\text{m}$ -thick deposit  
Figure 39. Continued.



Inlet Pressure: 150  $\mu\text{m Hg}$   
Background Pressure:  $5 \times 10^{-7}$  torr  
Growth Rate: 4.13  $\mu\text{m/min}$   
Grade of Gas: 99.7 % Pure  
Spectral Resolution: 2  $\text{cm}^{-1}$

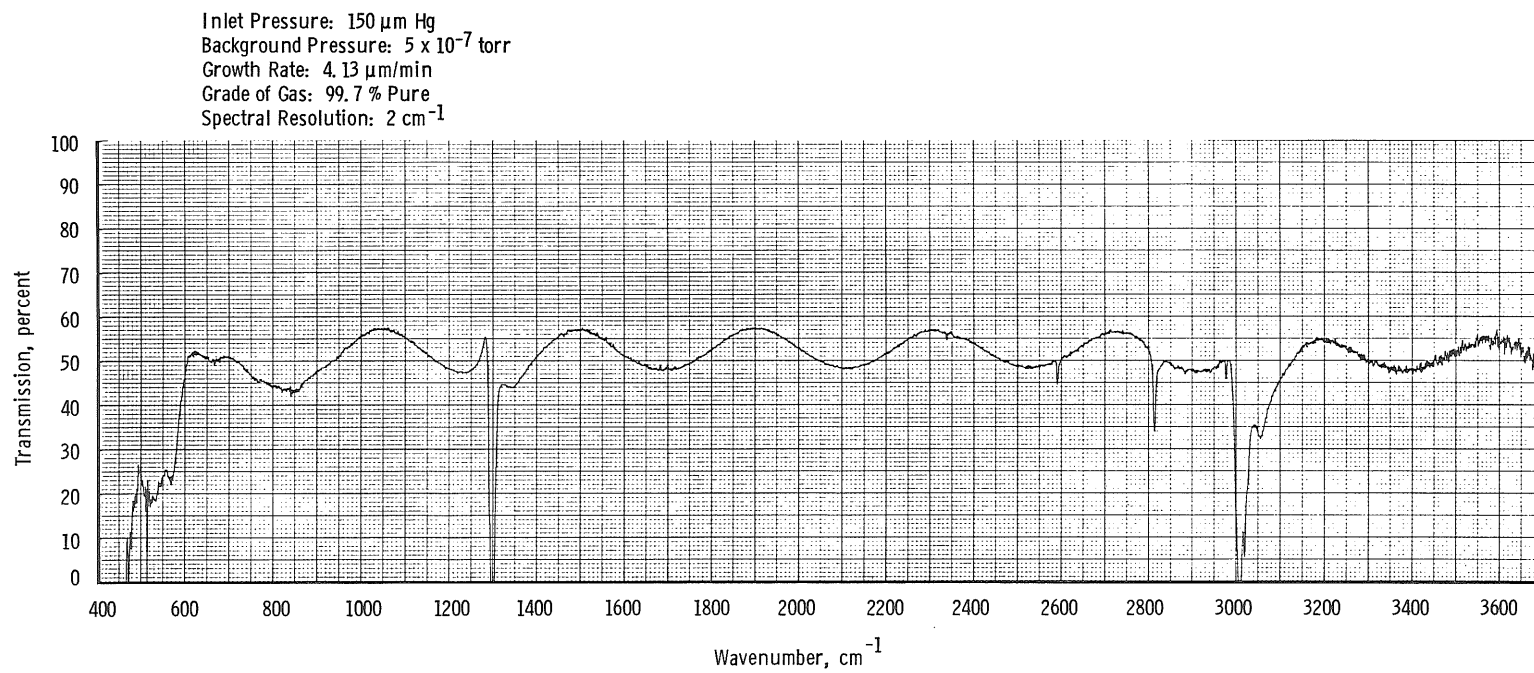


s. 6.420- $\mu\text{m}$ -thick deposit  
Figure 39. Continued.

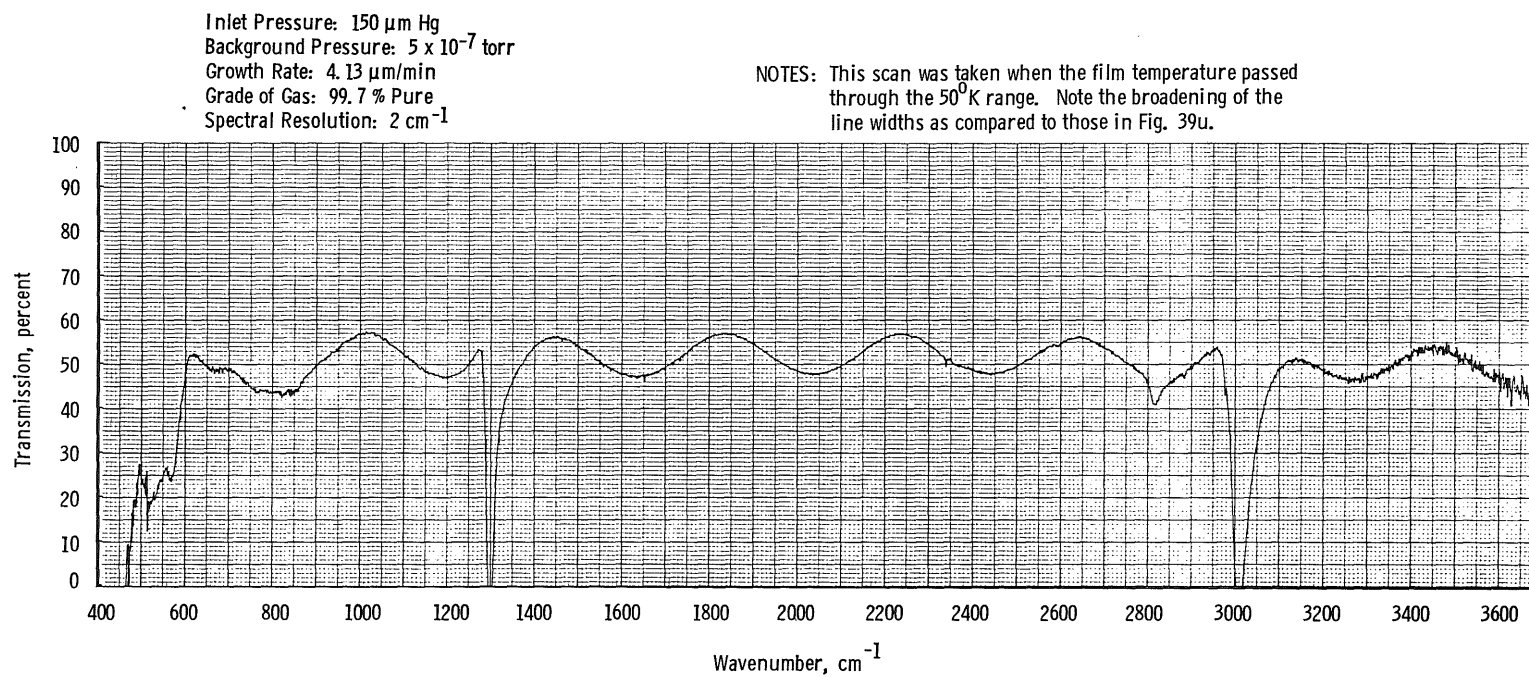


t. 6.880- $\mu\text{m}$ -thick deposit  
Figure 39. Continued.

196



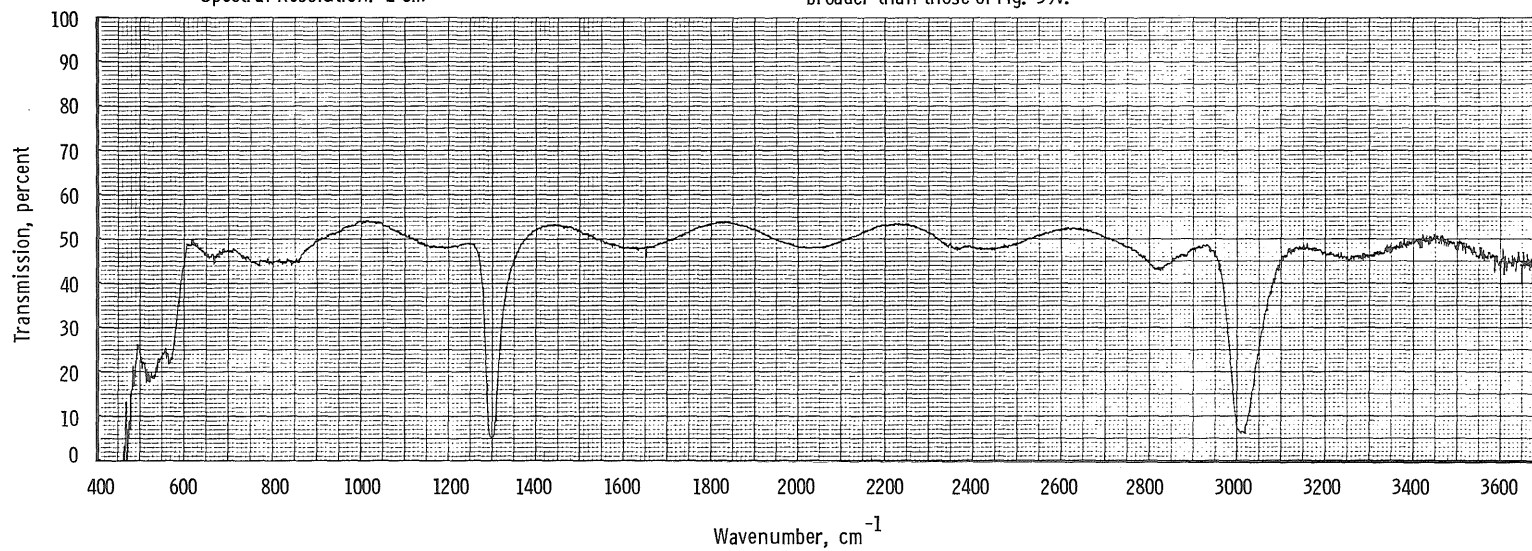
u. 8.710- $\mu\text{m}$ -thick deposit  
Figure 39. Continued.



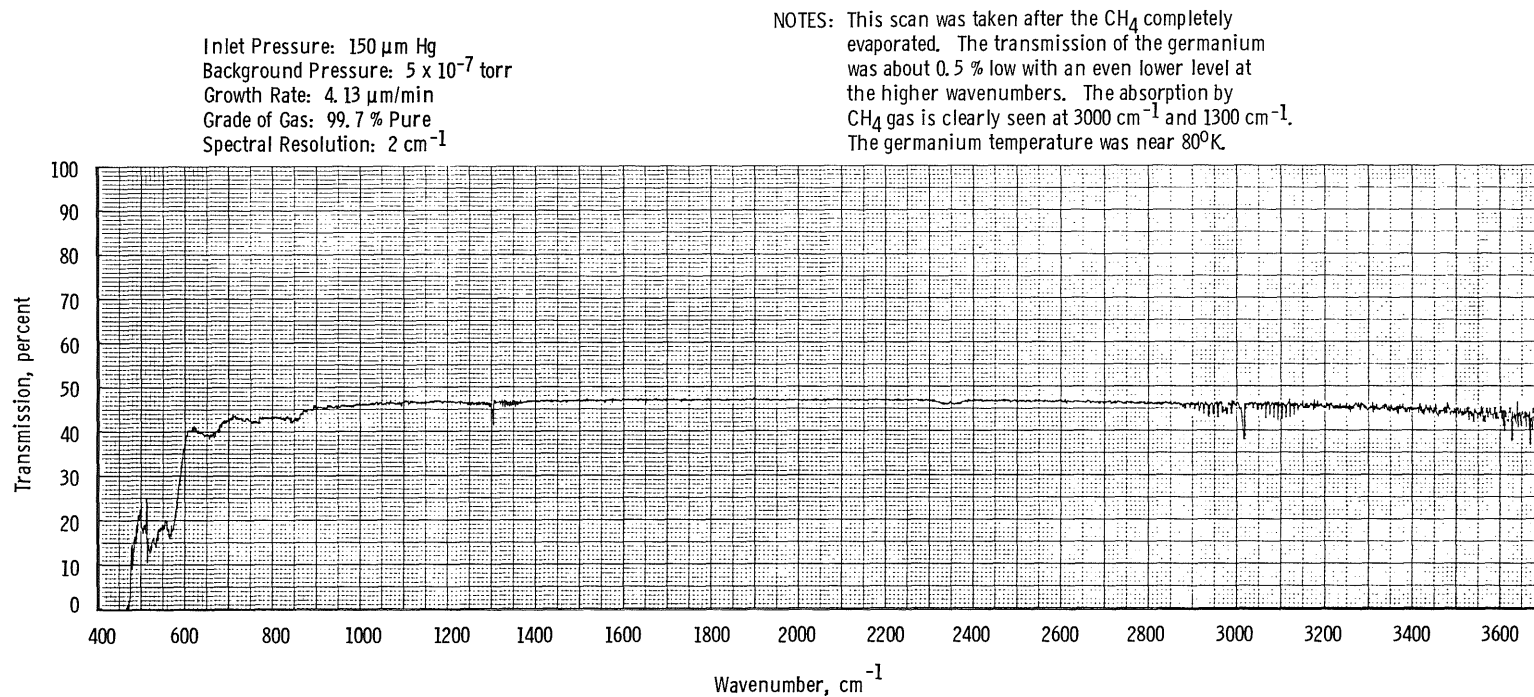
v. After warming from 20°K to 50°K  
Figure 39. Continued.

Inlet Pressure: 150  $\mu$ m Hg  
Background Pressure:  $5 \times 10^{-7}$  torr  
Growth Rate: 4.13  $\mu$ m/min  
Grade of Gas: 99.7 % Pure  
Spectral Resolution: 2  $\text{cm}^{-1}$

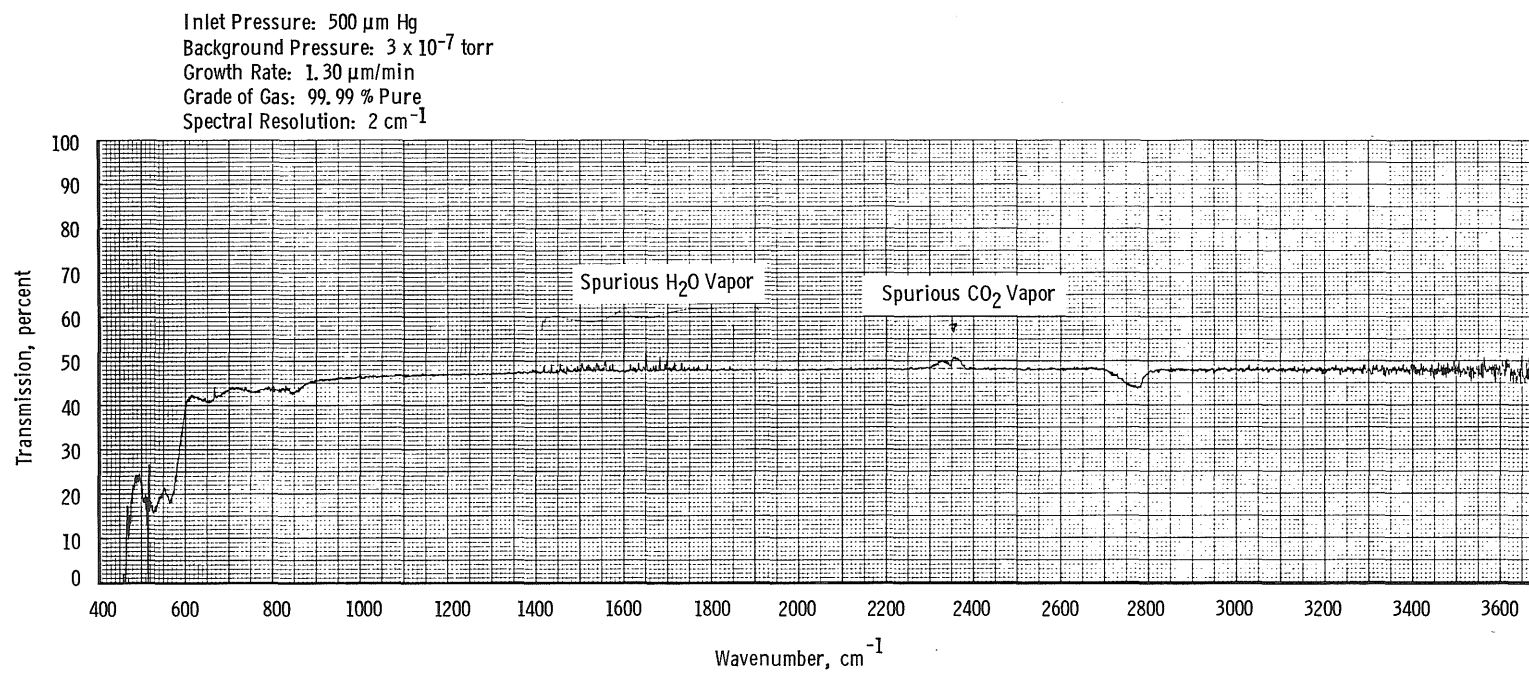
NOTES: This scan was taken just before the  $\text{CH}_4$  completely evaporated. In visible light the film appeared very polycrystalline, indicating that a phase transition had taken place. The bands have become even broader than those of Fig. 39v.



w. Just before  $\text{CH}_4$  evaporated  
Figure 39. Continued.

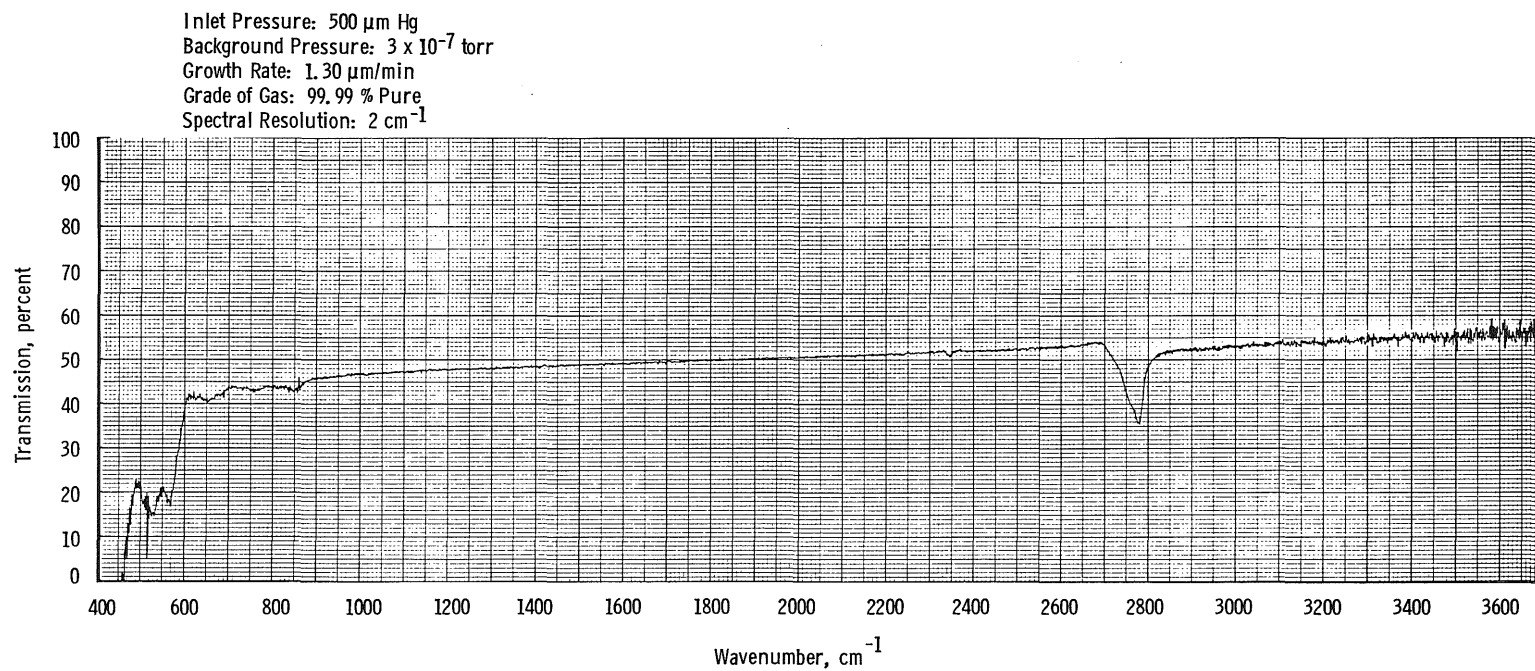


x. After  $\text{CH}_4$  deposit had completely evaporated  
Figure 39. Concluded.



a. First interference minimum

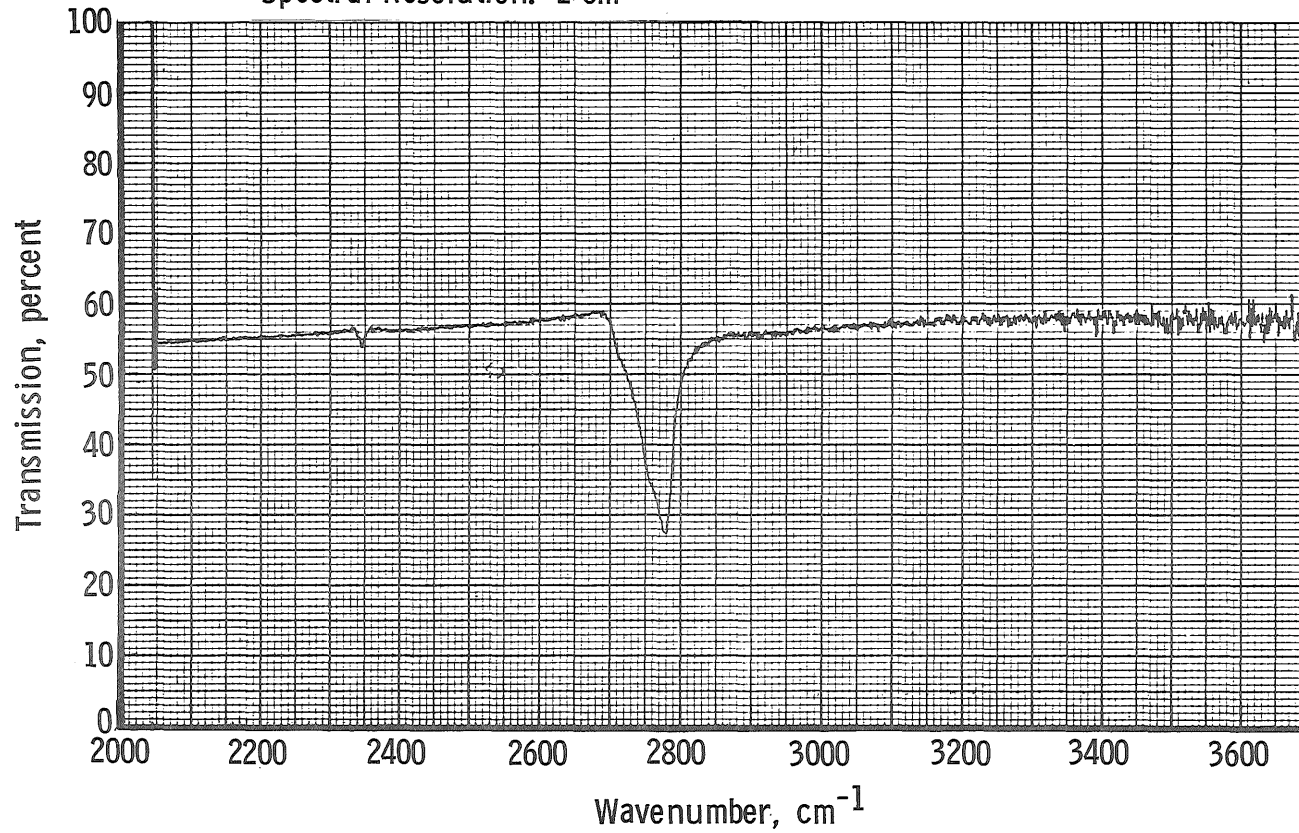
Figure 40. Transmission of 20°K germanium window with an HC1 deposit (see Table 5).



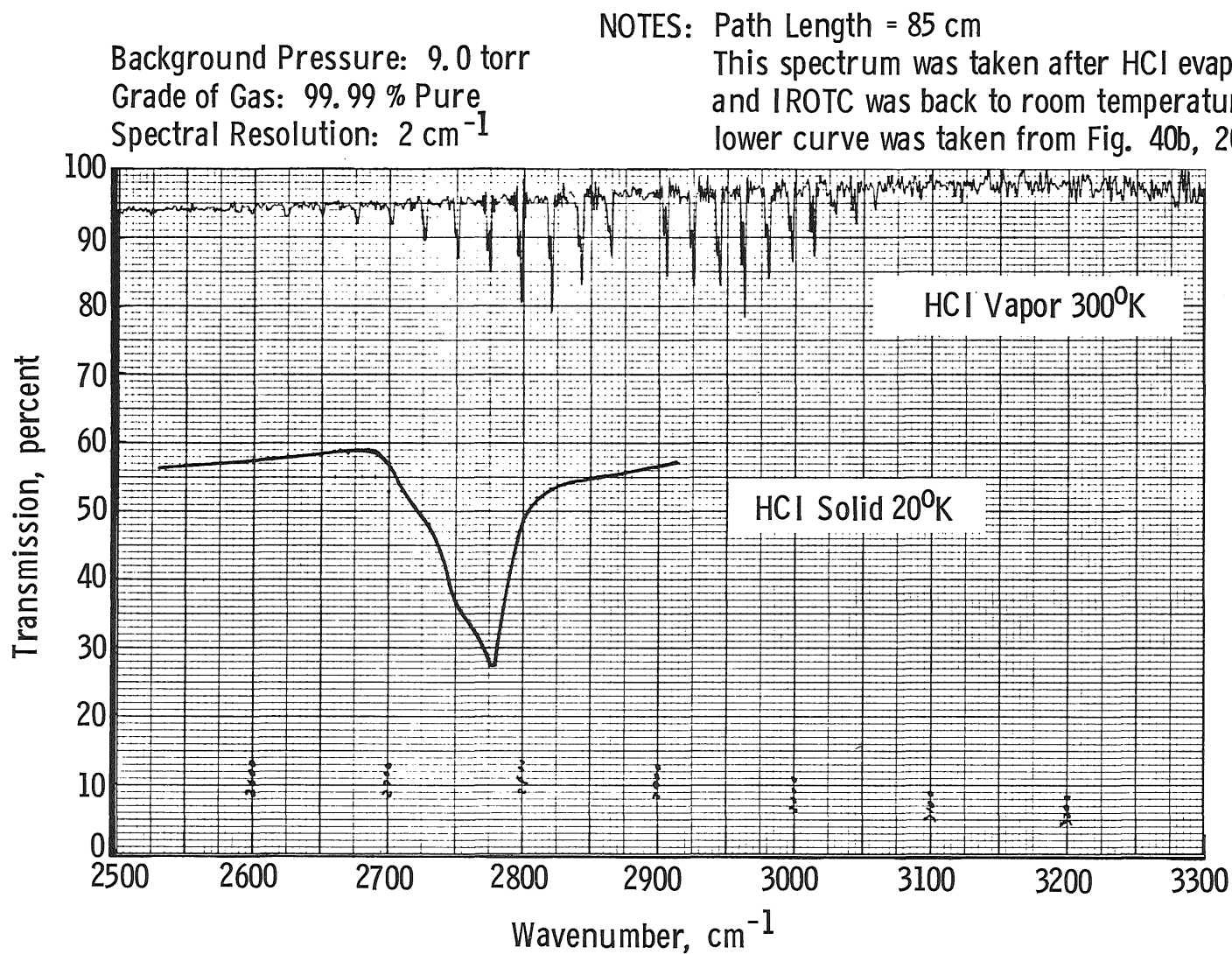
b. Second interference minimum  
Figure 40. Continued.

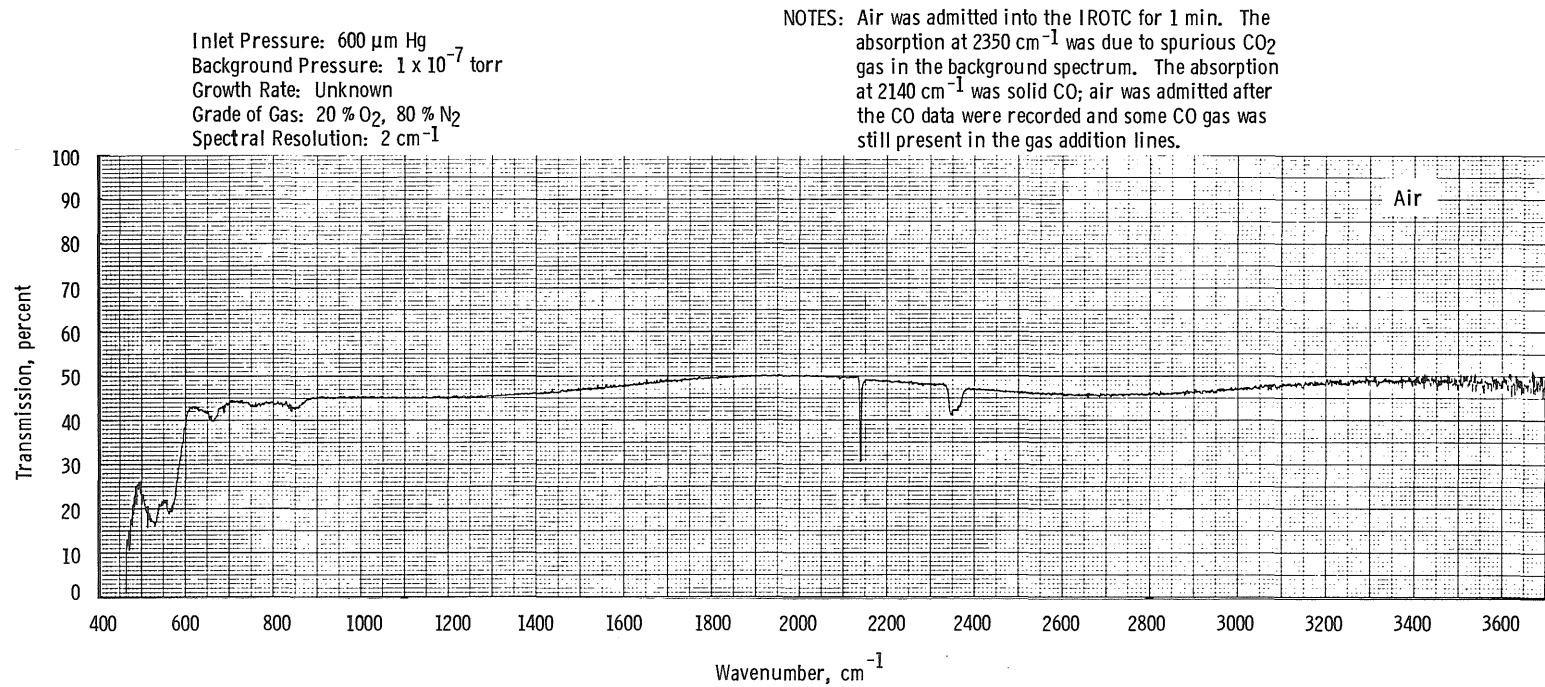


Inlet Pressure: 500  $\mu\text{m Hg}$   
 Background Pressure:  $3 \times 10^{-7}$  torr  
 Growth Rate: 1.30  $\mu\text{m/min}$   
 Grade of Gas: 99.99 % Pure  
 Spectral Resolution: 2  $\text{cm}^{-1}$



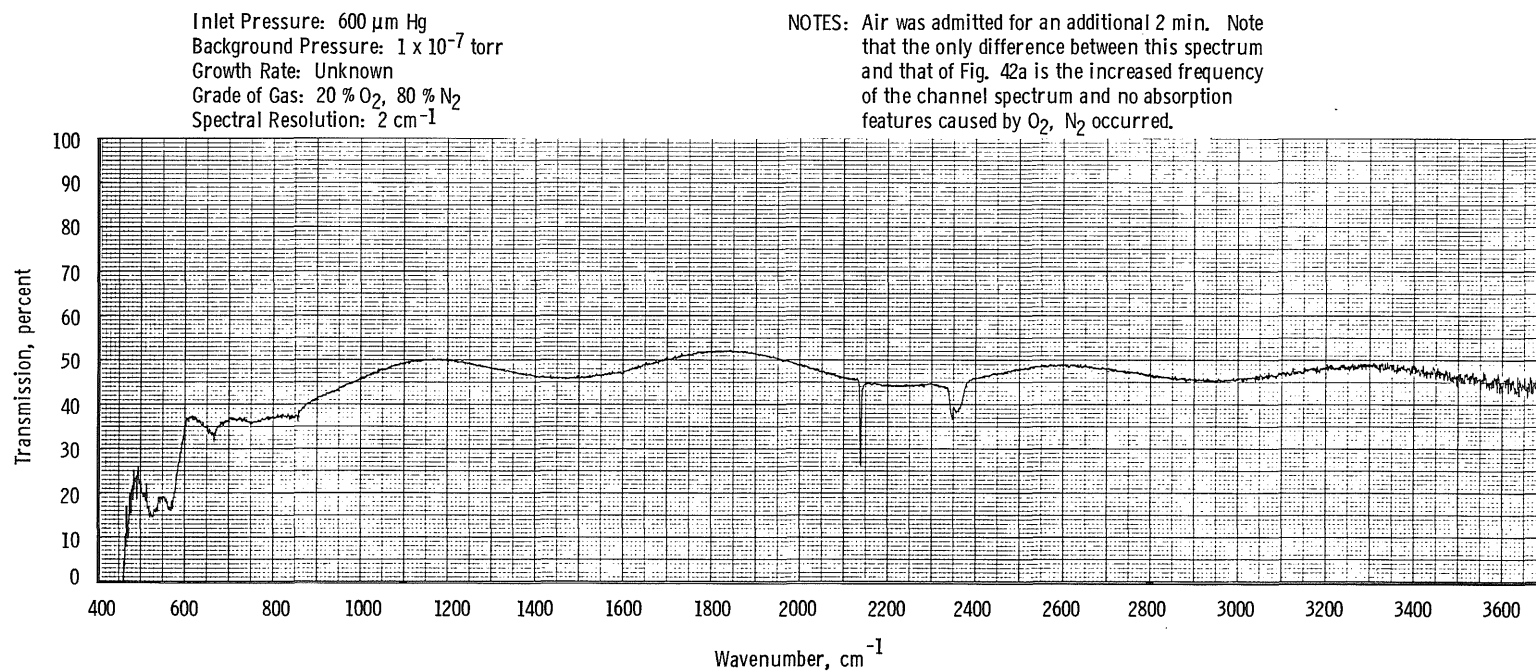
c. Third interference minimum  
 Figure 40. Concluded.

Figure 41. Transmission of  $300^{\circ}\text{K}$  HCl, 95-cm path length.



a. 1-min deposition time

Figure 42. Transmission of 20°K germanium window with an air cryodeposit.



**b. 3-min deposition time**  
**Figure 42. Concluded.**

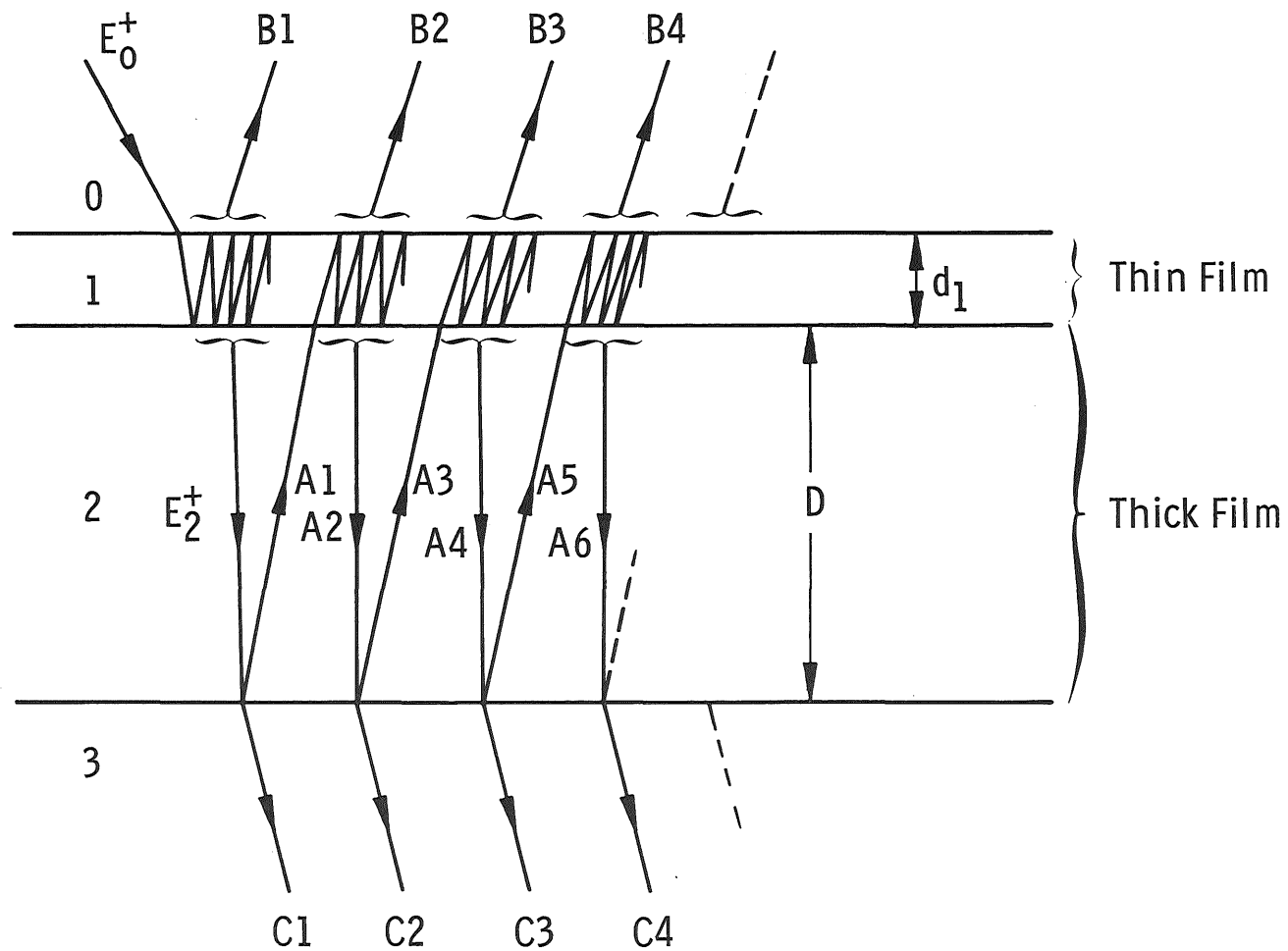
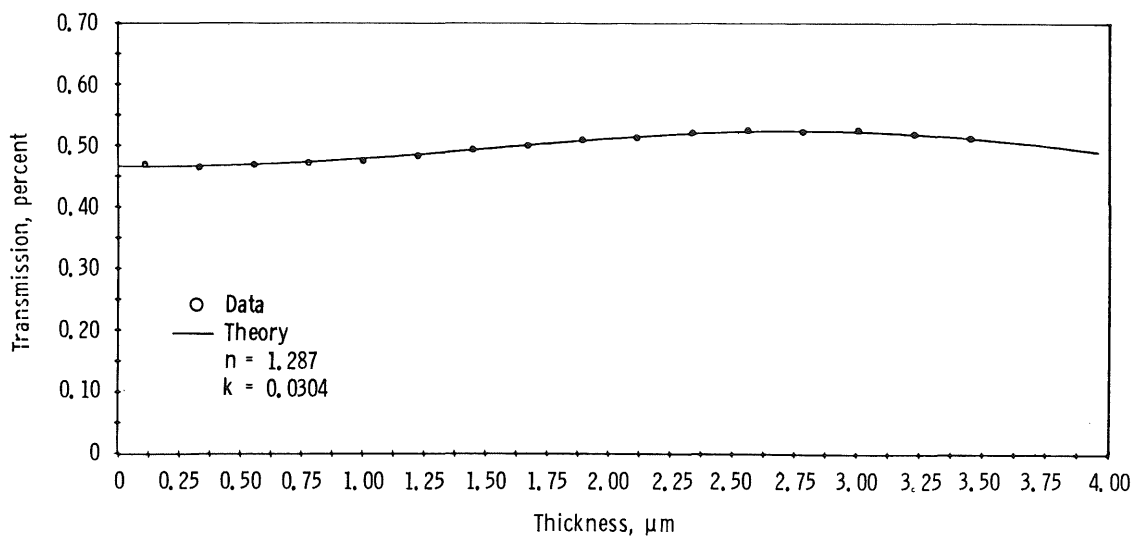
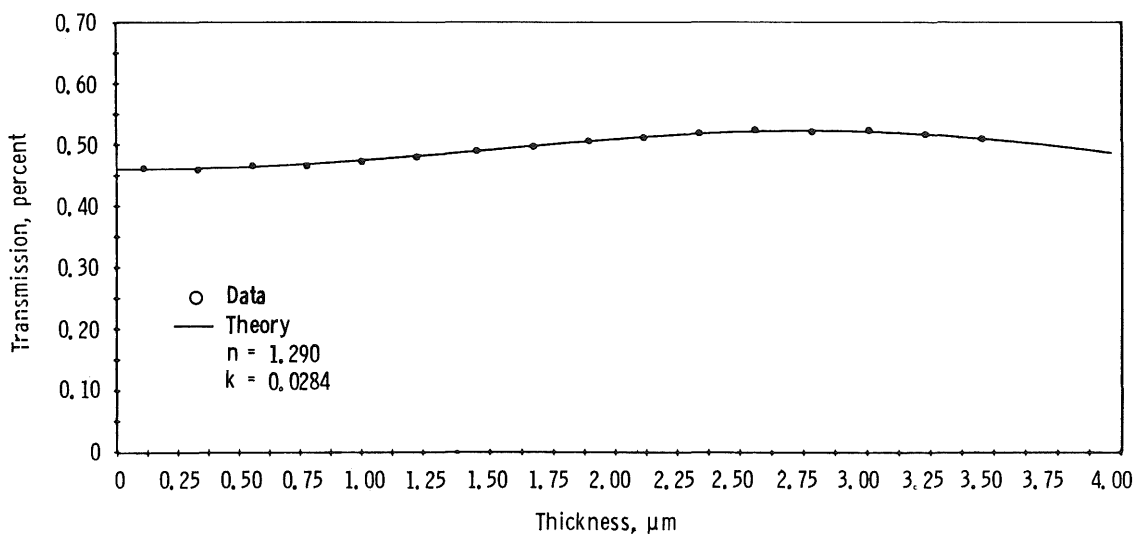


Figure 43. Geometry depicting analytical model for a thin film formed upon a thick film.

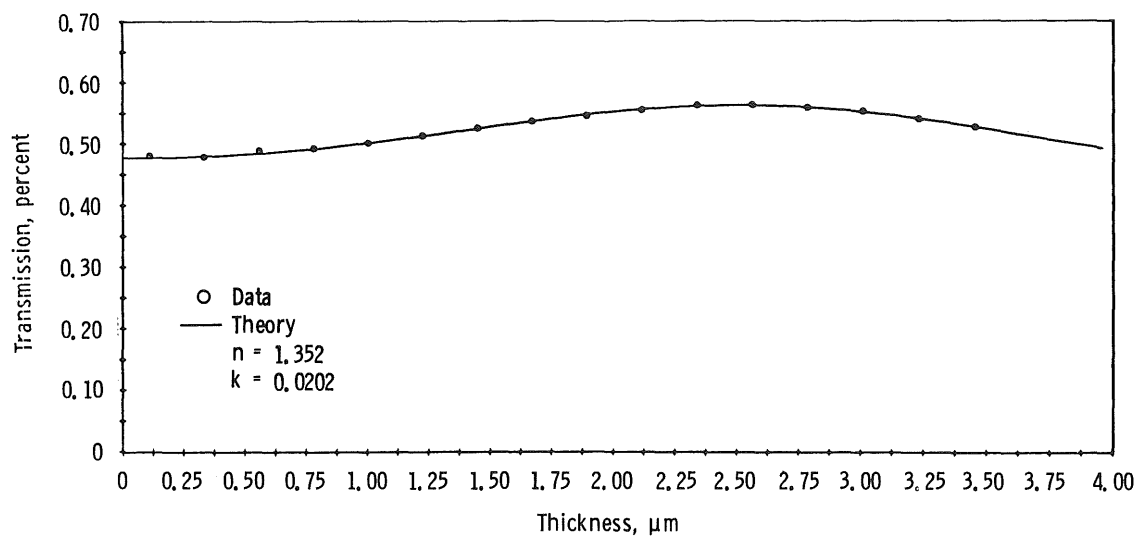


a.  $\lambda = 15.873 \mu\text{m}$

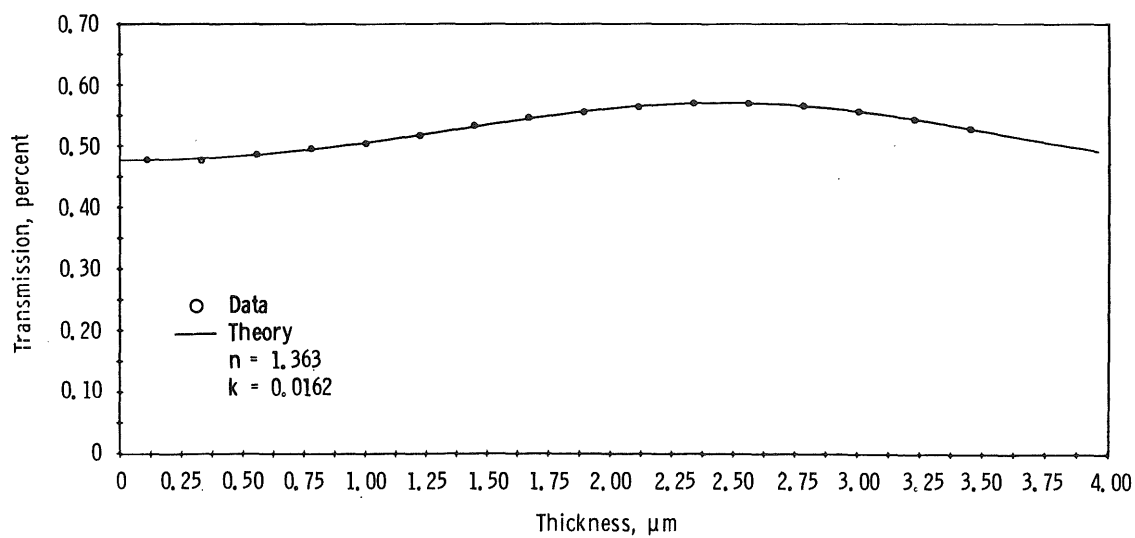


b.  $\lambda = 15.625 \mu\text{m}$

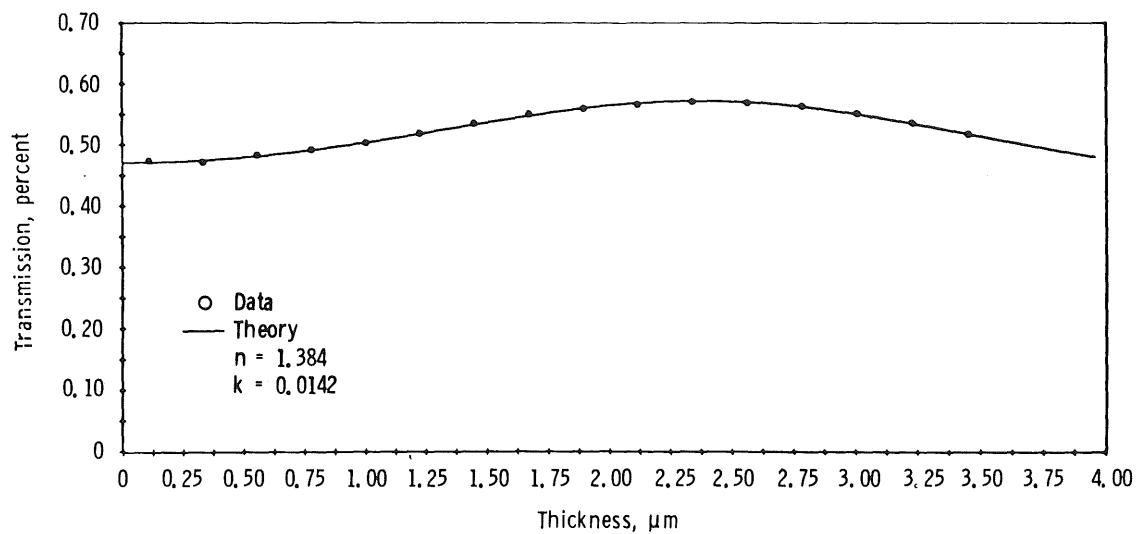
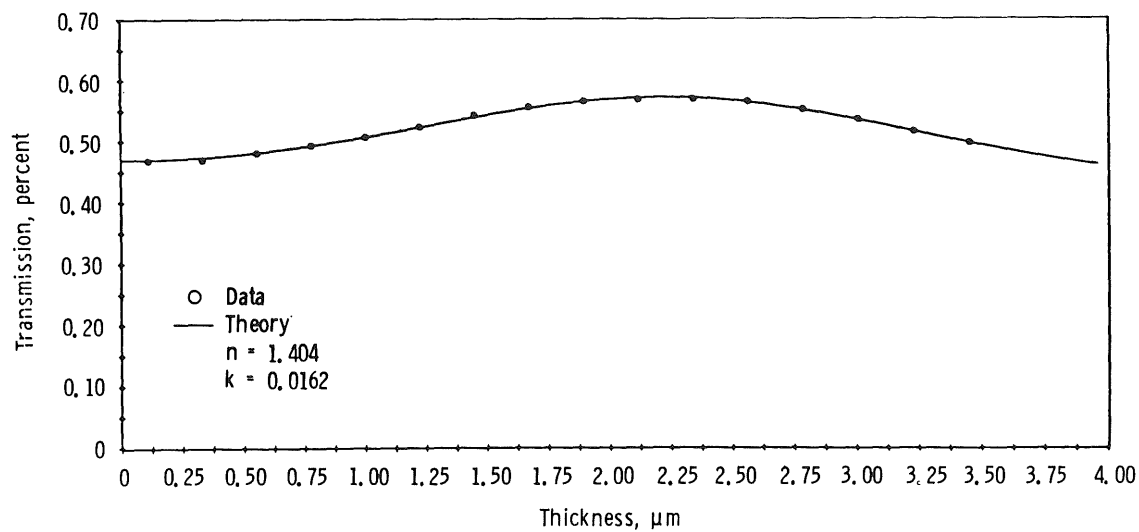
Figure 44. Comparison of theory and transmission data for  $\text{NH}_3$  deposits on  $80^\circ\text{K}$  germanium.



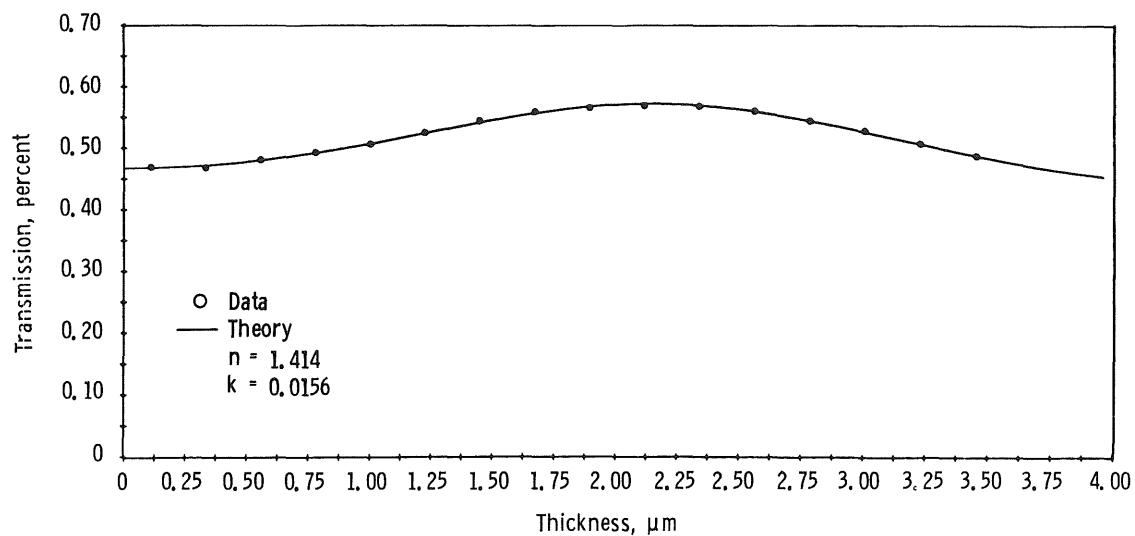
c.  $\lambda = 14.286 \mu\text{m}$



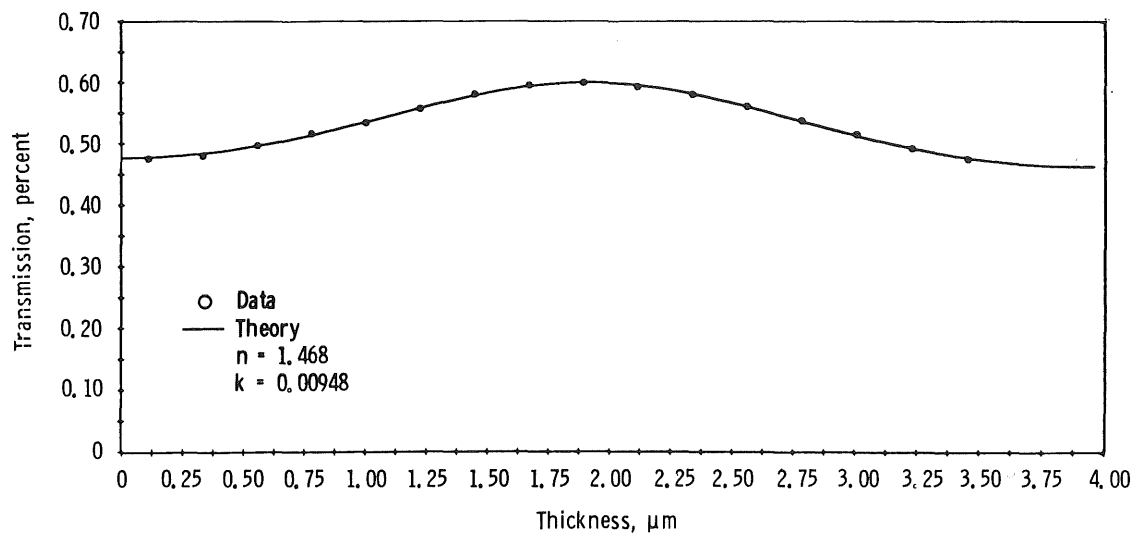
d.  $\lambda = 13.889 \mu\text{m}$   
Figure 44. Continued.

e.  $\lambda = 13.514 \mu\text{m}$ f.  $\lambda = 12.821 \mu\text{m}$   
Figure 44. Continued.

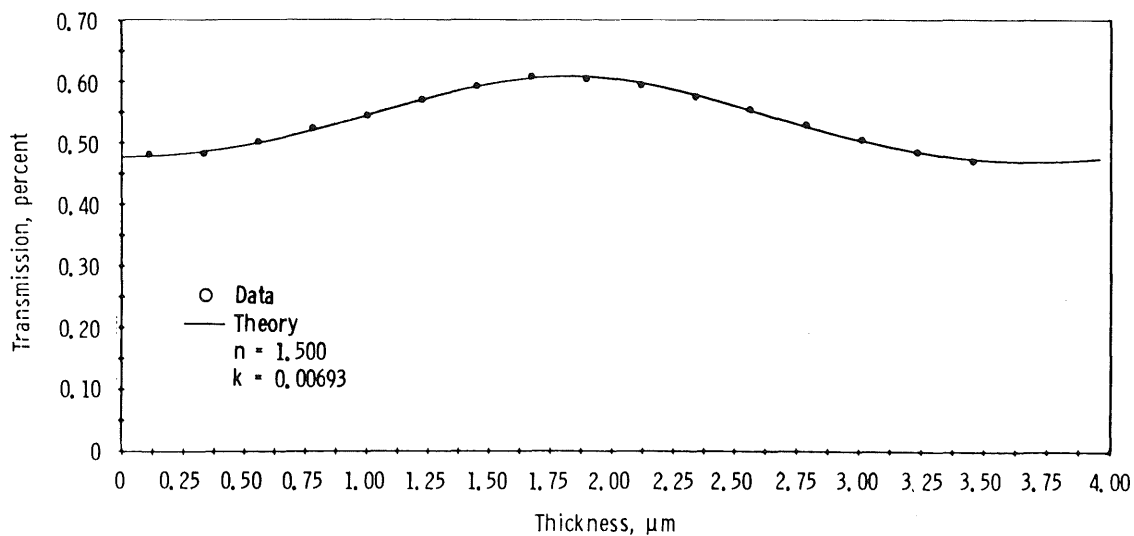




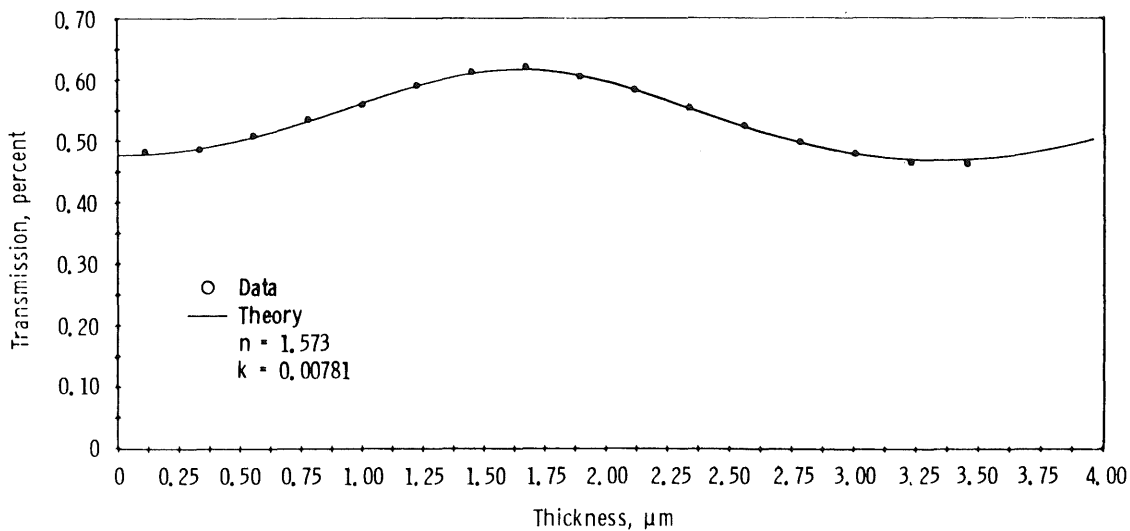
g.  $\lambda = 12.500 \mu\text{m}$



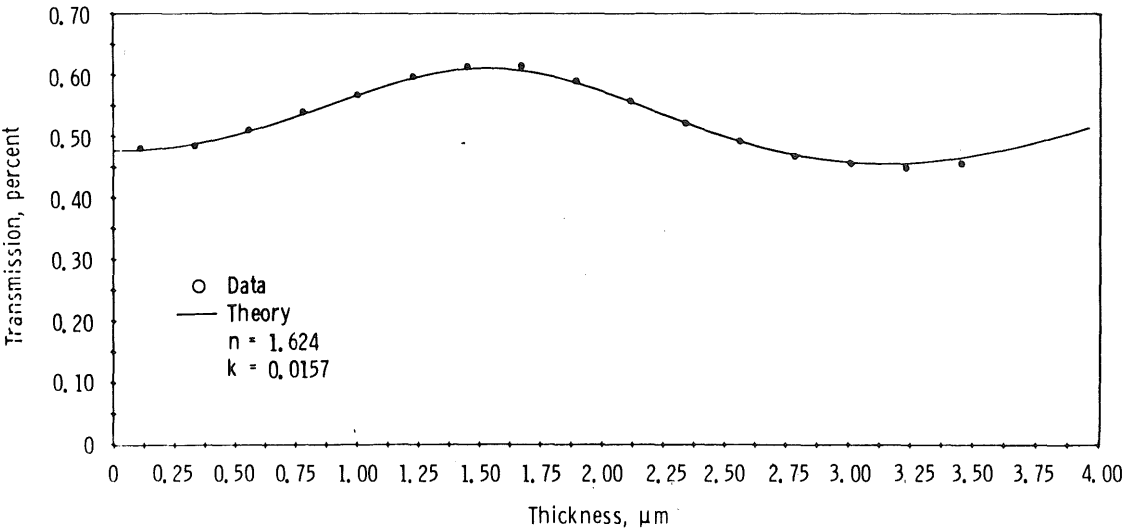
h.  $\lambda = 11.364 \mu\text{m}$   
Figure 44. Continued.



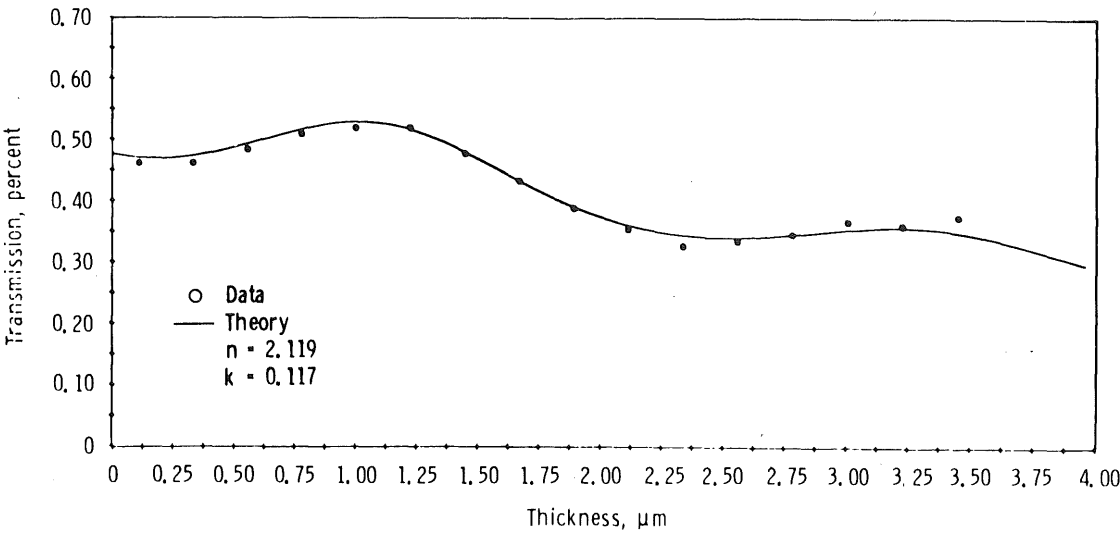
i.  $\lambda = 10.989 \mu\text{m}$



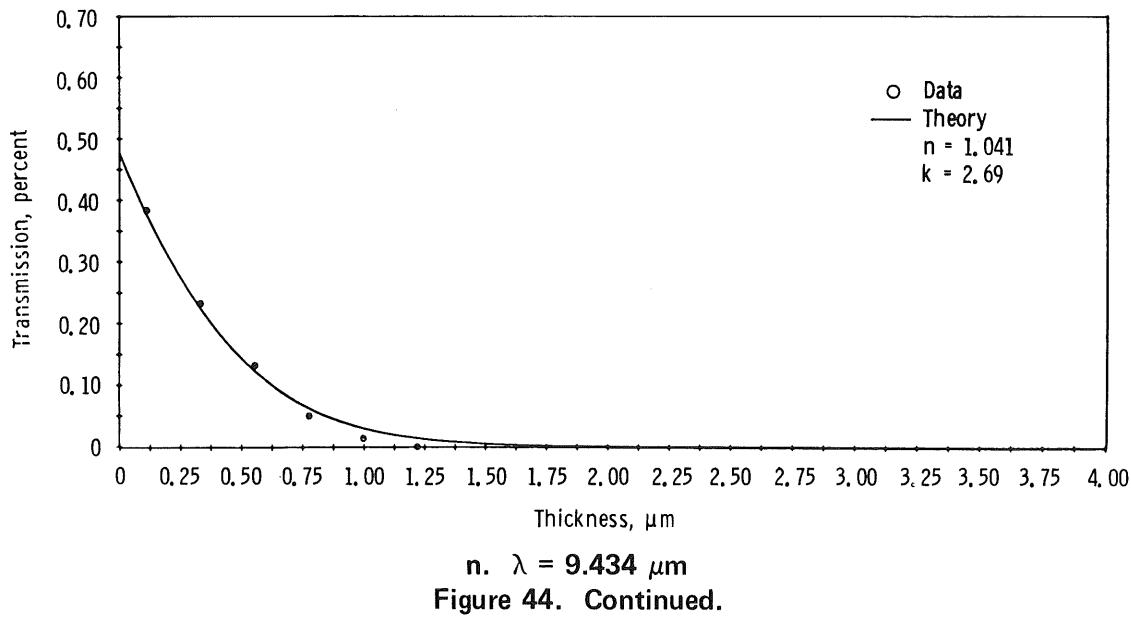
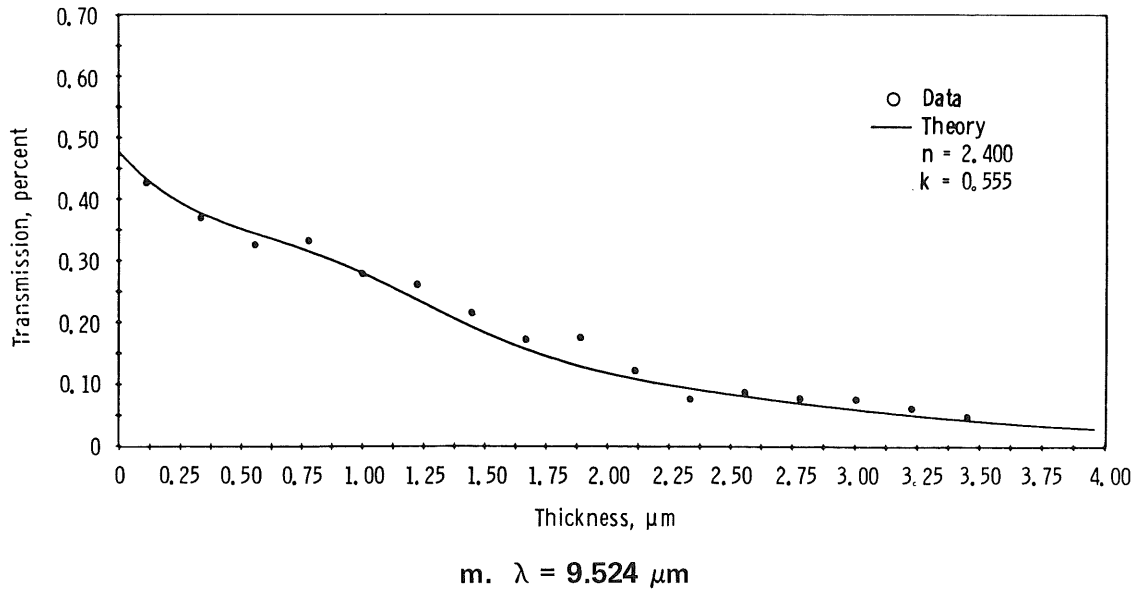
j.  $\lambda = 10.417 \mu\text{m}$   
Figure 44. Continued.

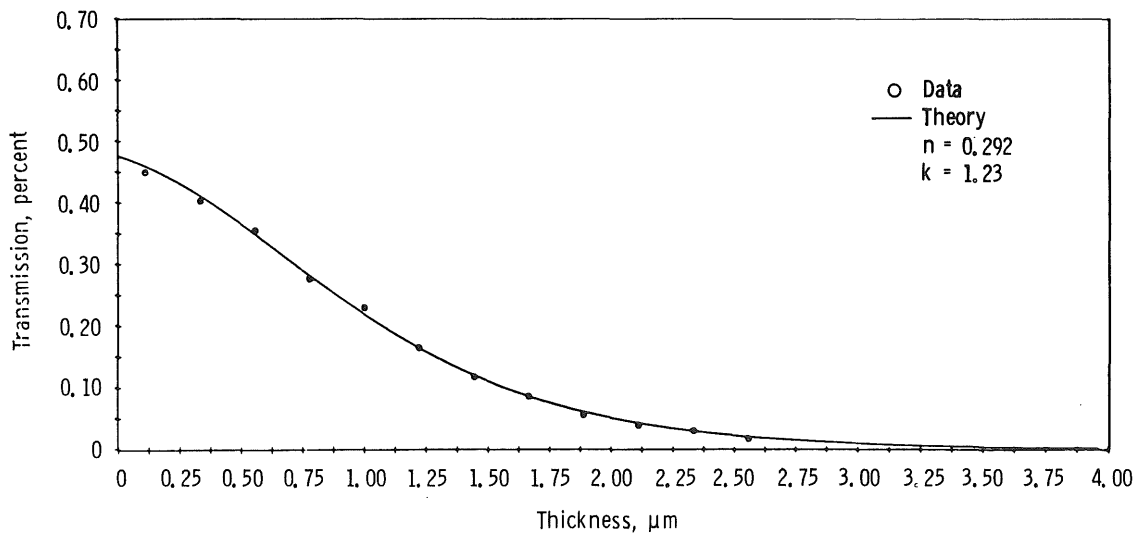


k.  $\lambda = 10.101 \mu\text{m}$

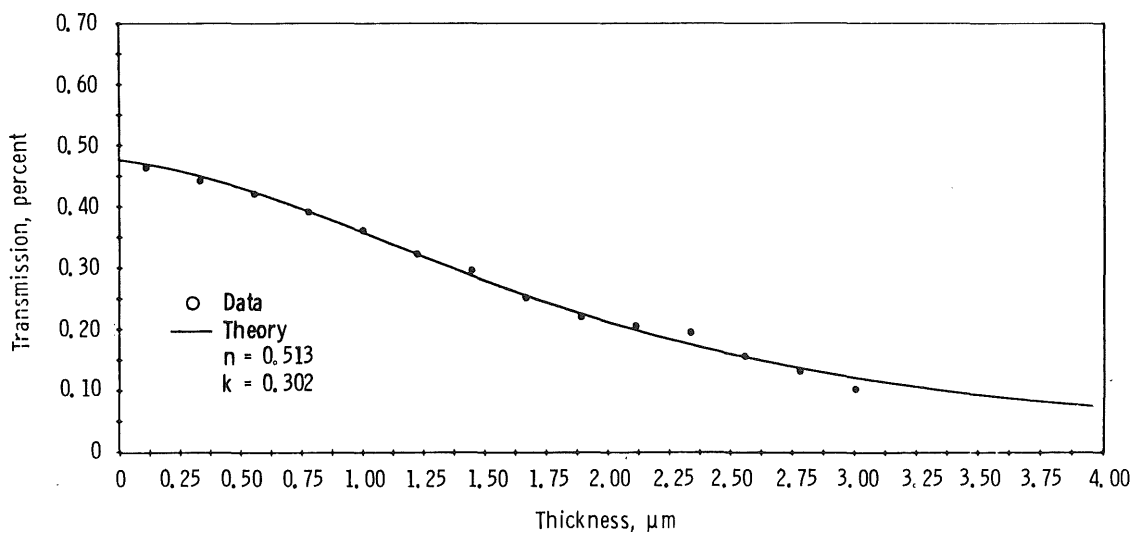


l.  $\lambda = 9.615 \mu\text{m}$   
Figure 44. Continued.

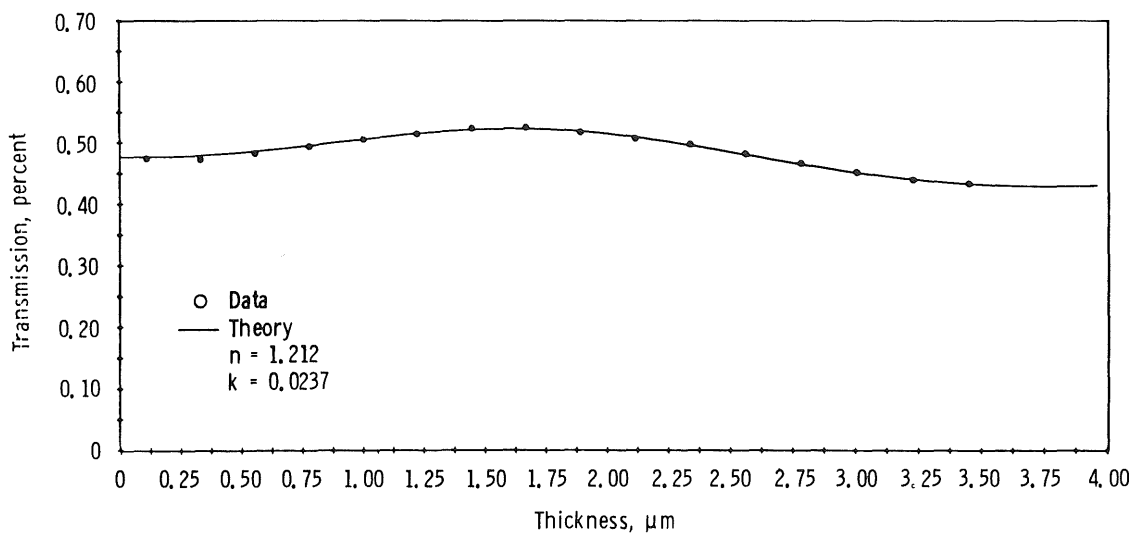




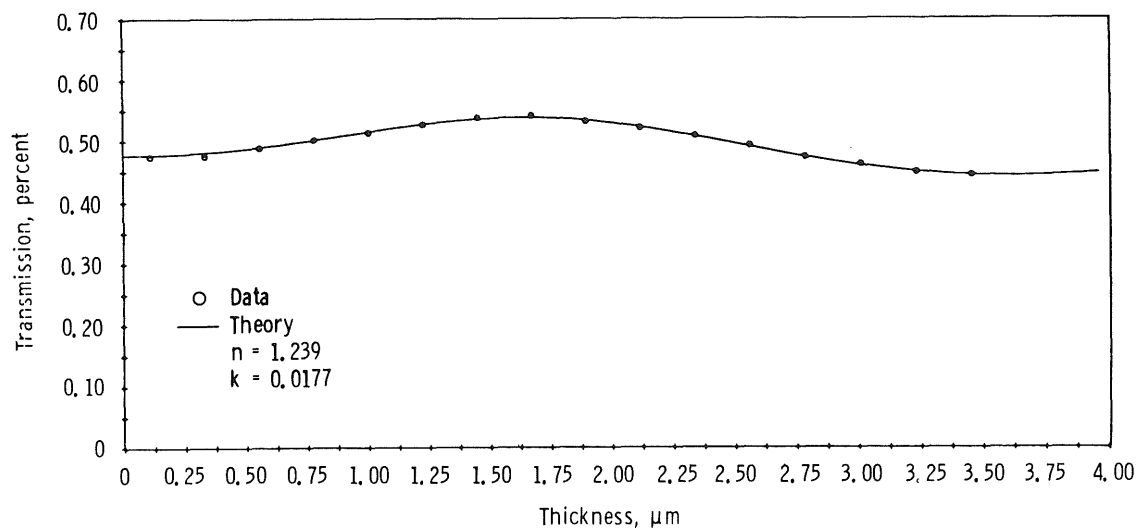
o.  $\lambda = 9.346 \mu\text{m}$



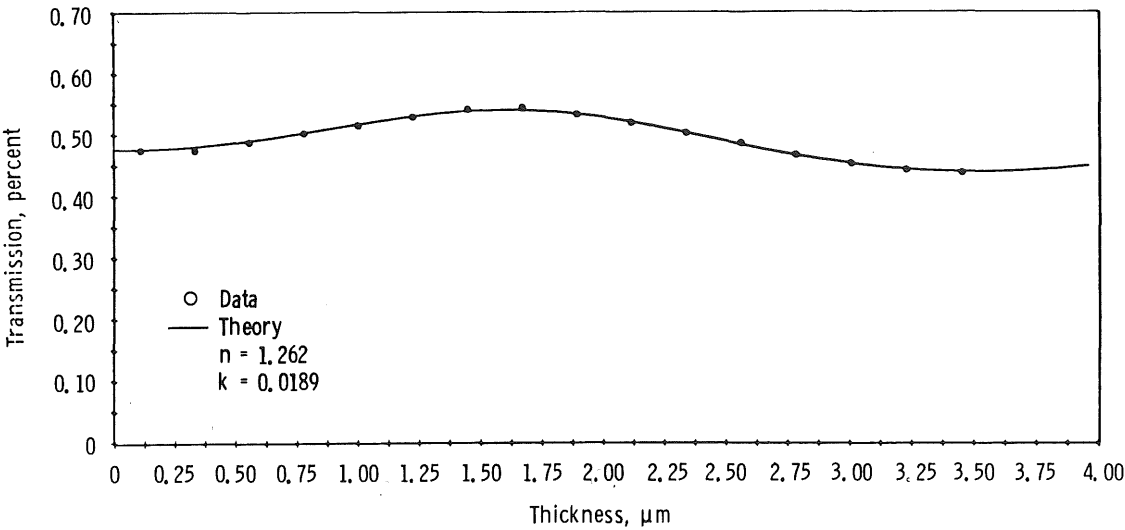
p.  $\lambda = 9.259 \mu\text{m}$   
Figure 44. Continued.



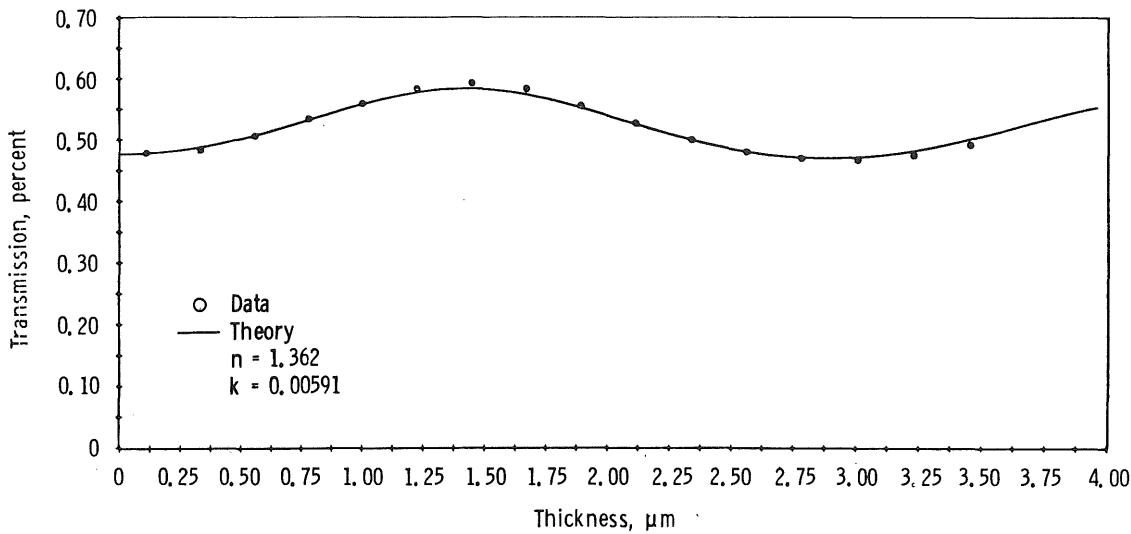
q.  $\lambda = 8.772 \mu\text{m}$



r.  $\lambda = 8.696 \mu\text{m}$   
Figure 44. Continued.

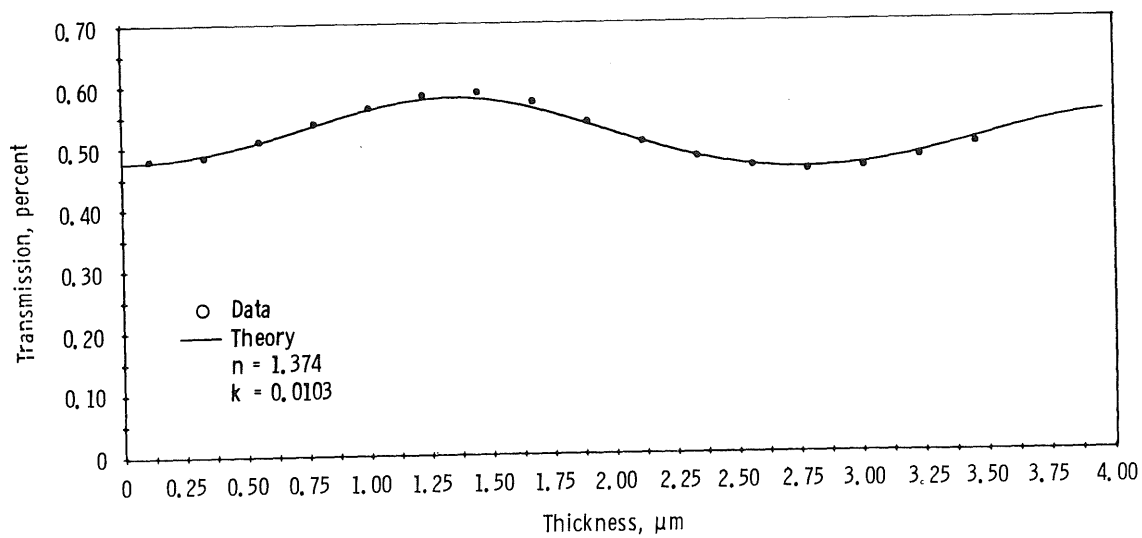


s.  $\lambda = 8.621 \mu\text{m}$

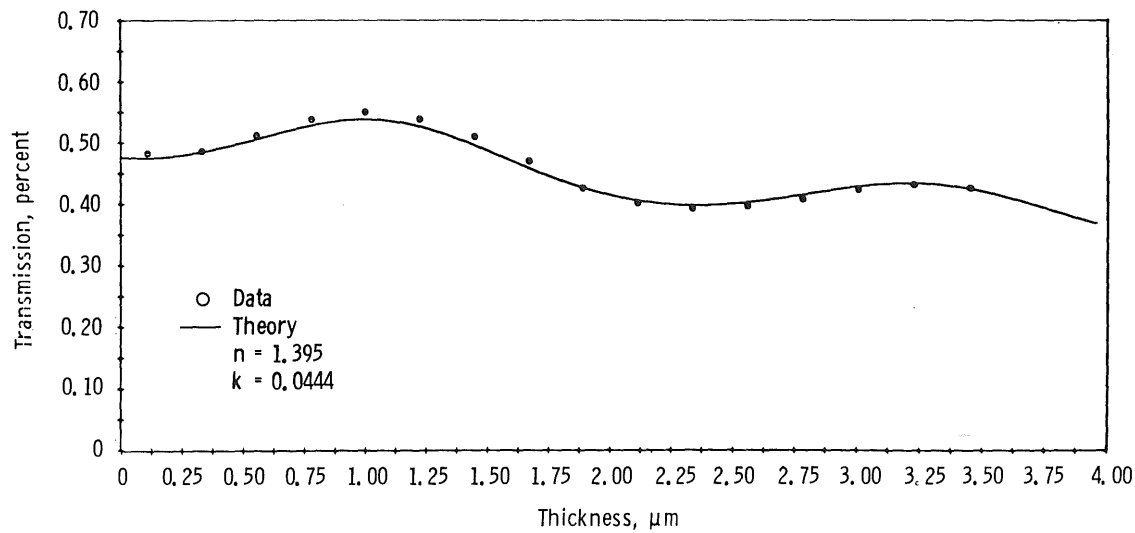


t.  $\lambda = 7.812 \mu\text{m}$

Figure 44. Continued.



u.  $\lambda = 7.519 \mu\text{m}$



v.  $\lambda = 6.250 \mu\text{m}$

Figure 44. Continued.



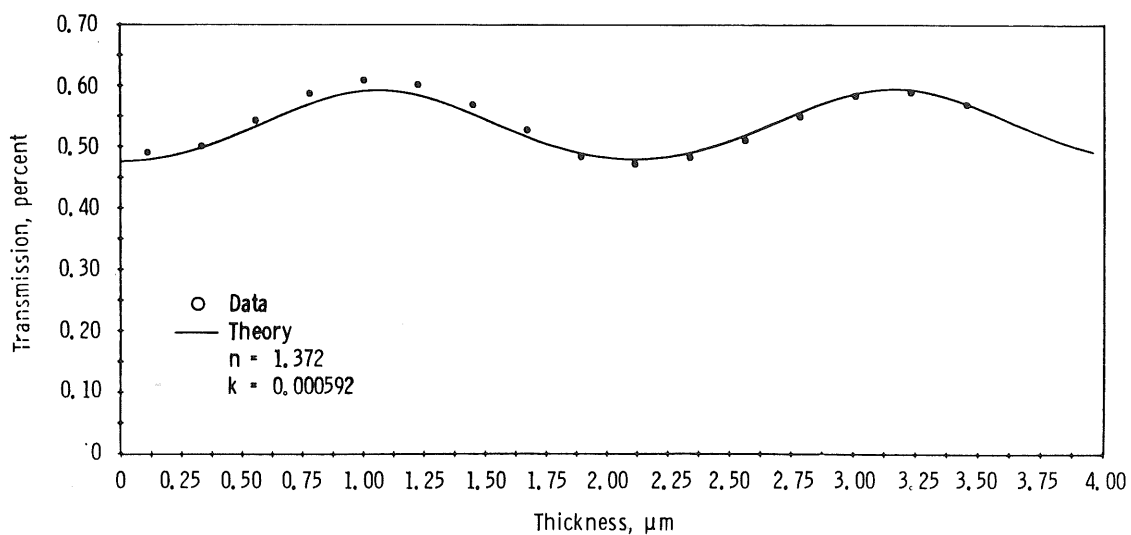
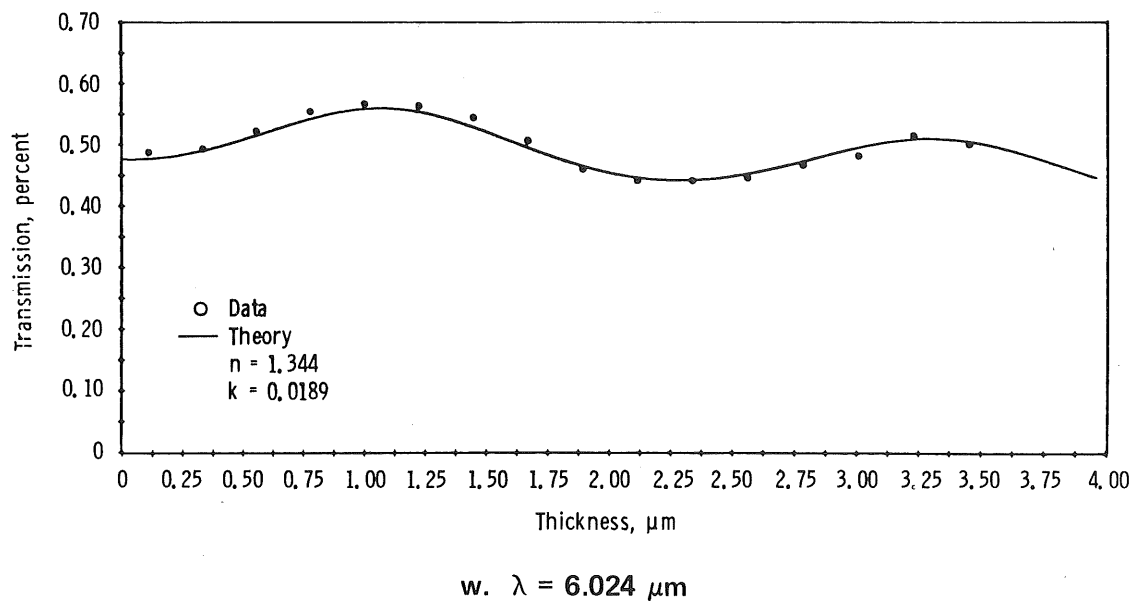
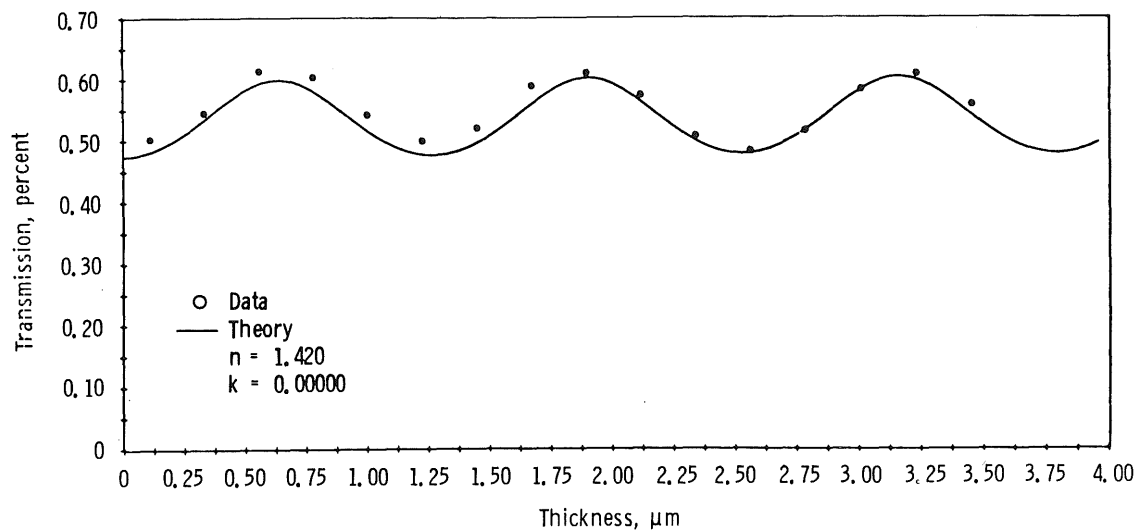
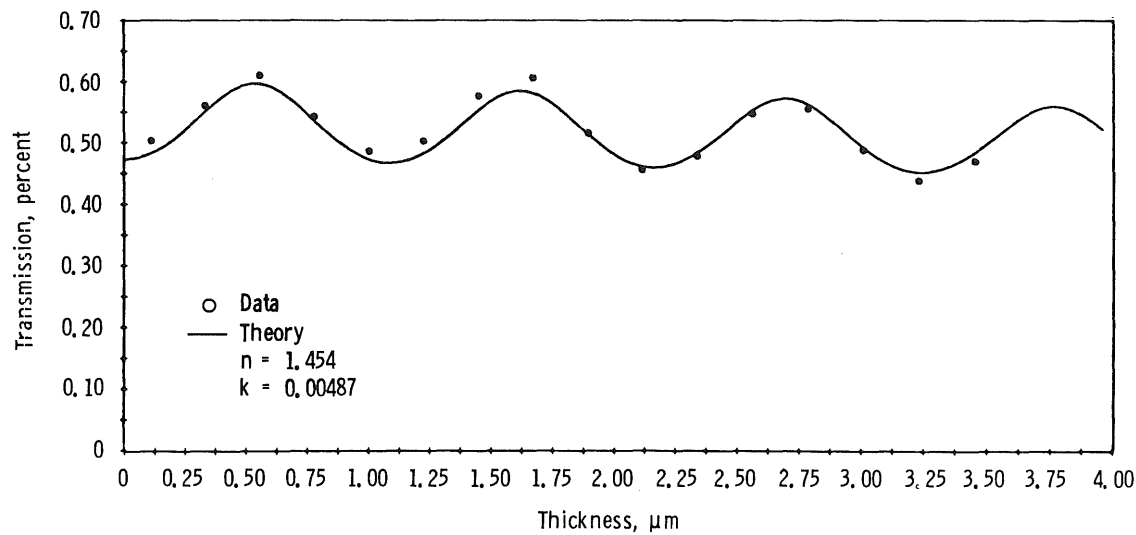


Figure 44. Continued.

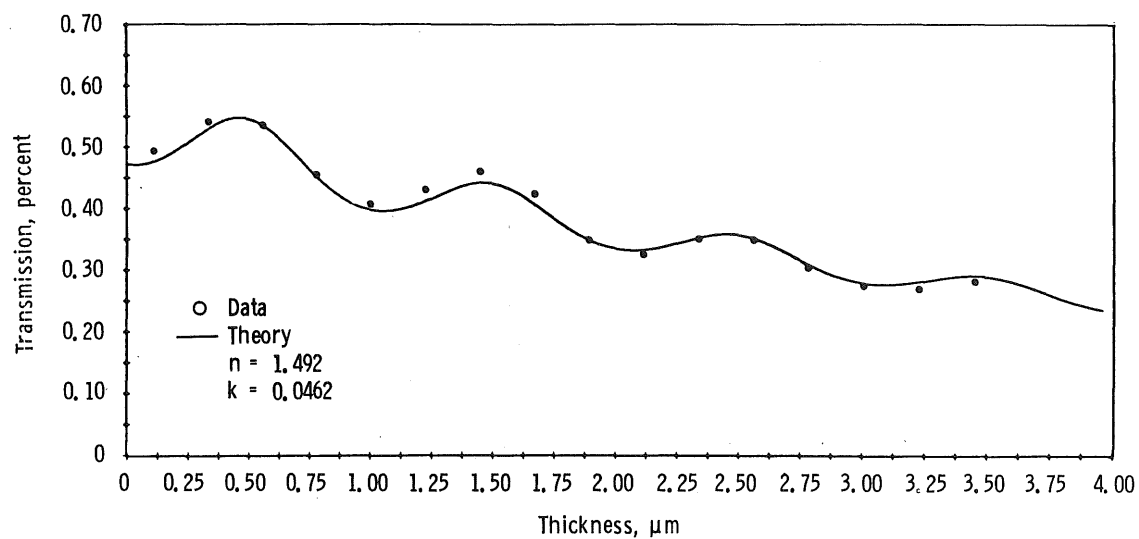


y.  $\lambda = 3.584 \mu\text{m}$

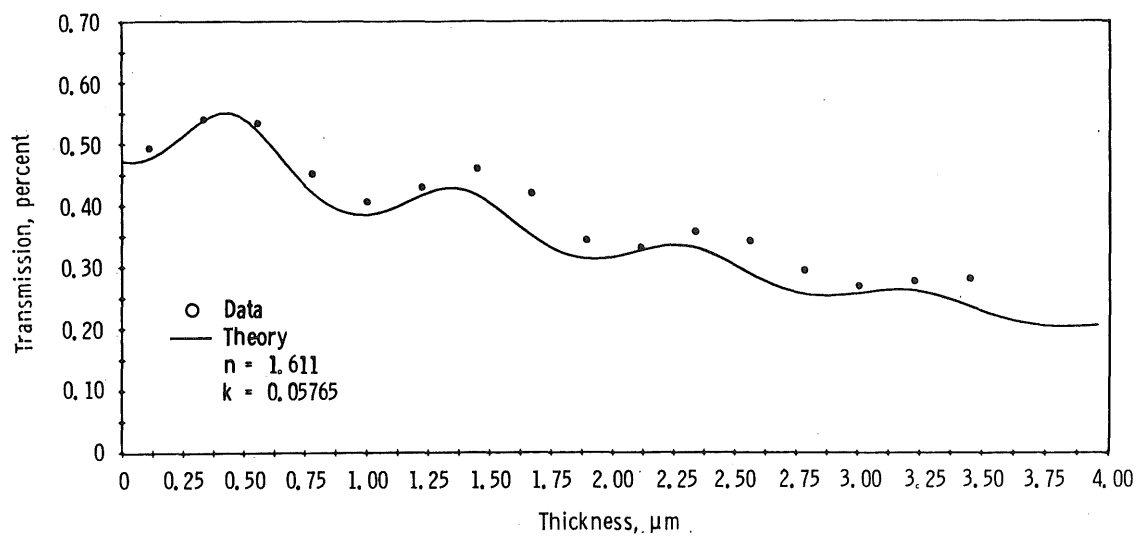


z.  $\lambda = 3.584 \mu\text{m}$

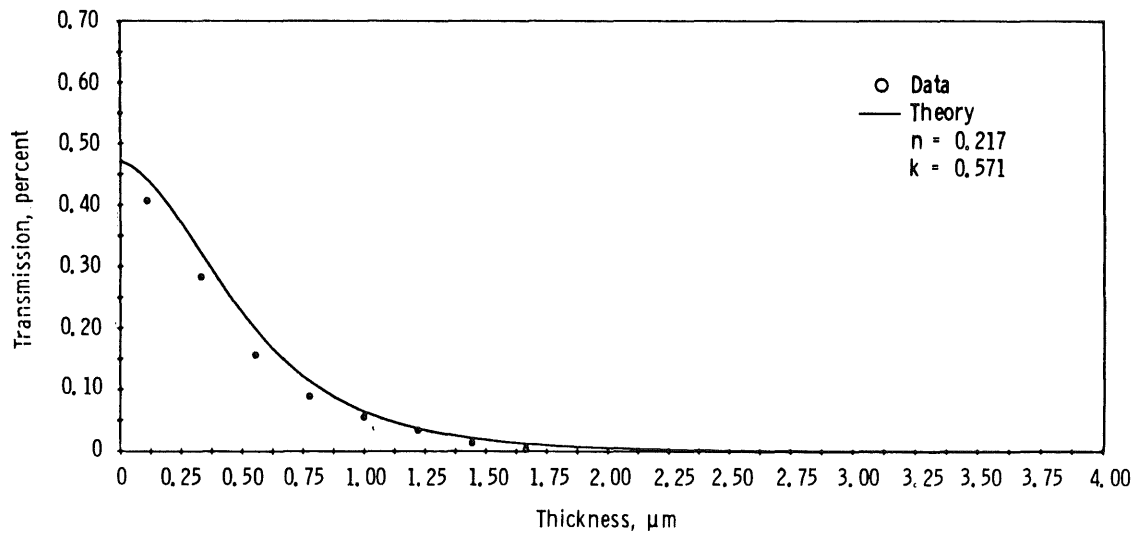
Figure 44. Continued.



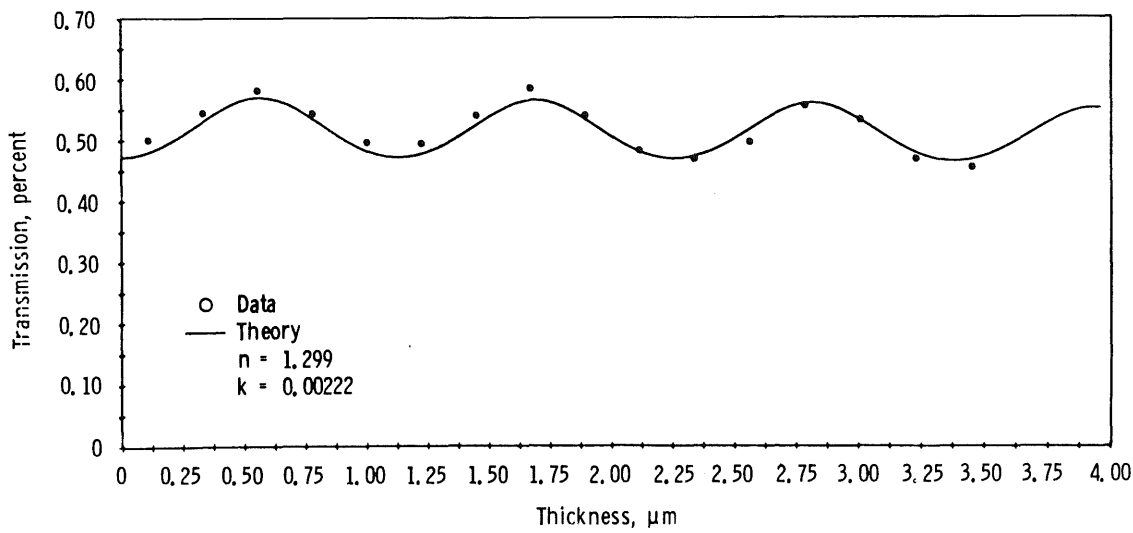
aa.  $\lambda = 3.003 \mu\text{m}$



bb.  $\lambda = 2.994 \mu\text{m}$   
Figure 44. Continued.

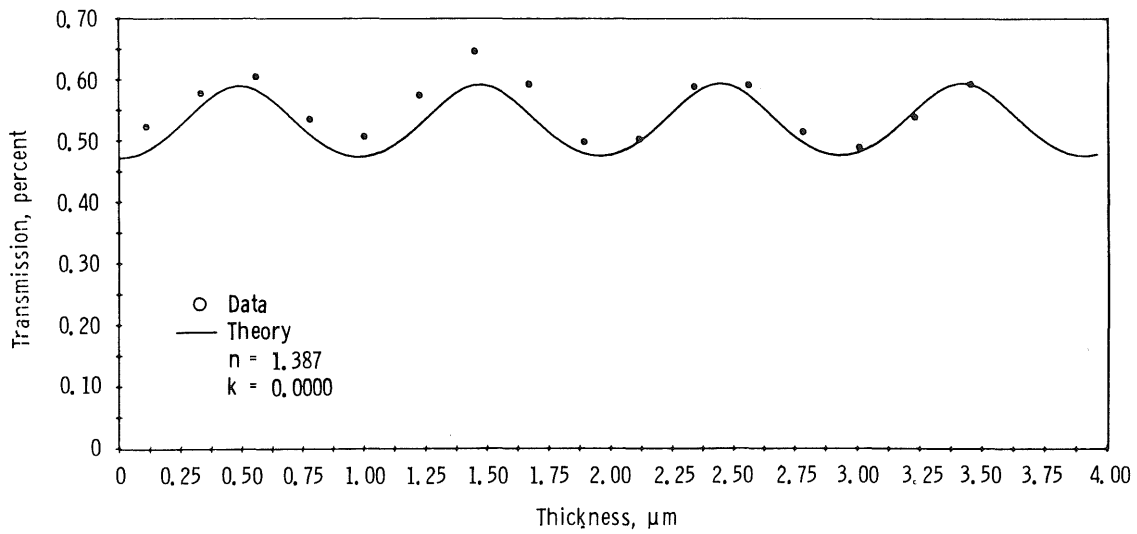


cc.  $\lambda = 2.967 \mu\text{m}$

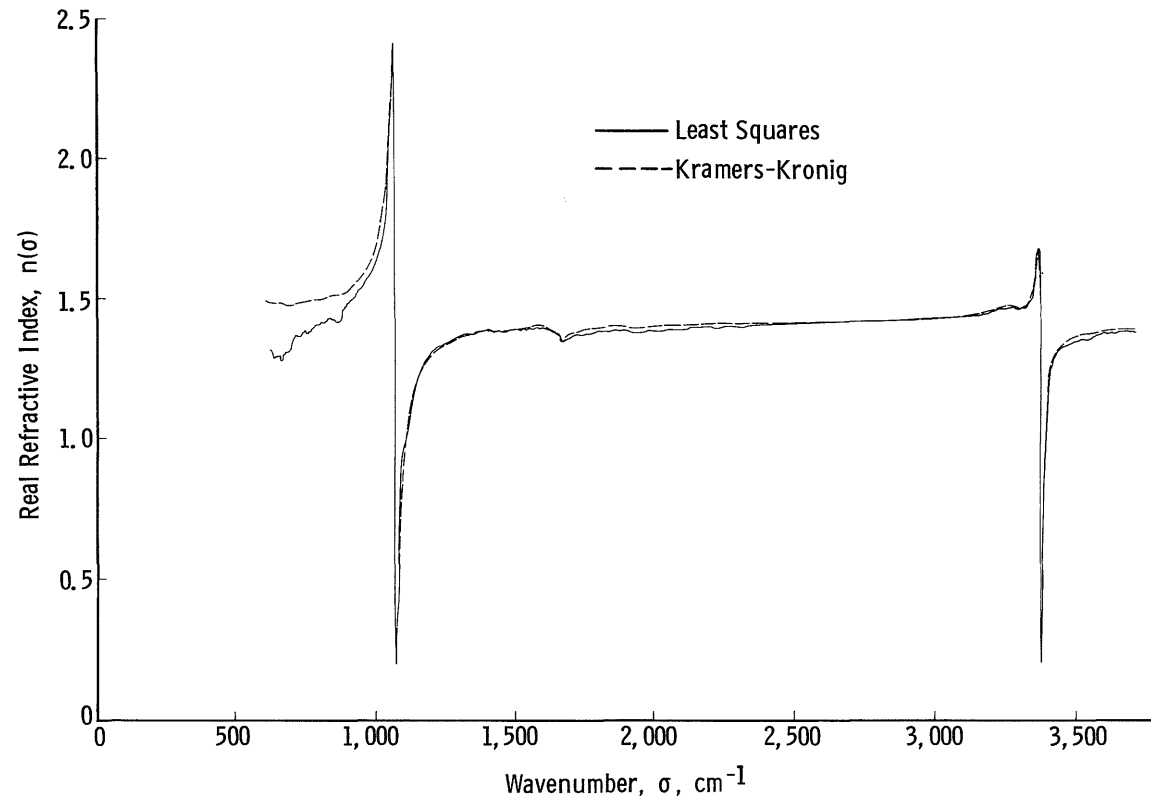


dd.  $\lambda = 2.924 \mu\text{m}$

Figure 44. Continued.

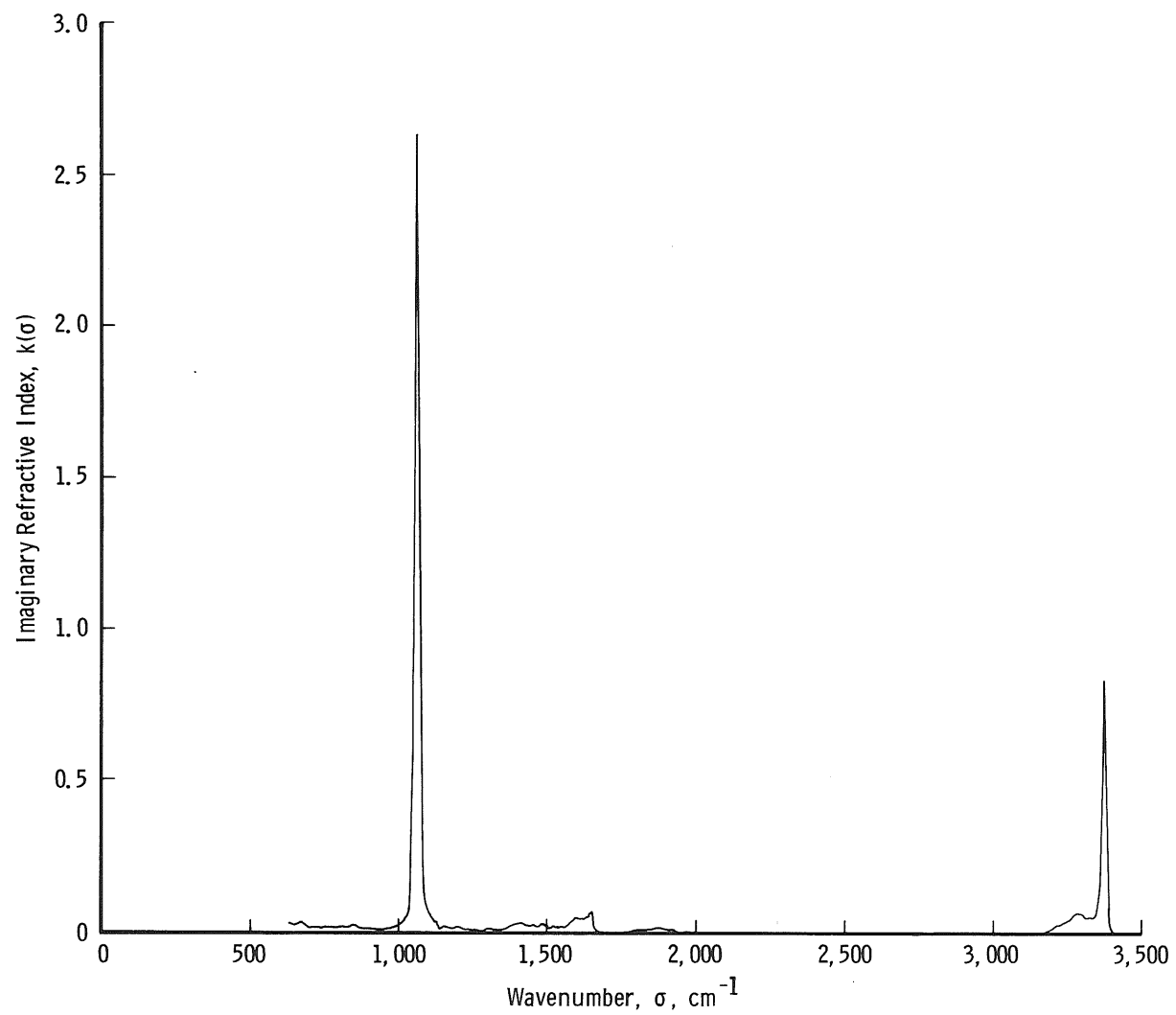


ee.  $\lambda = 2.710 \mu\text{m}$   
Figure 44. Concluded.

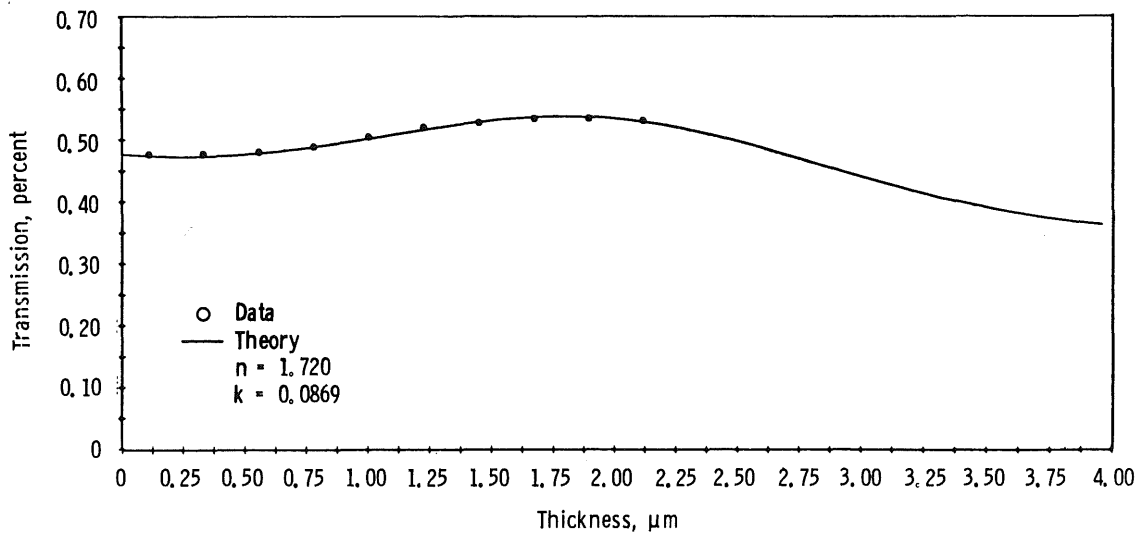


a. Real component

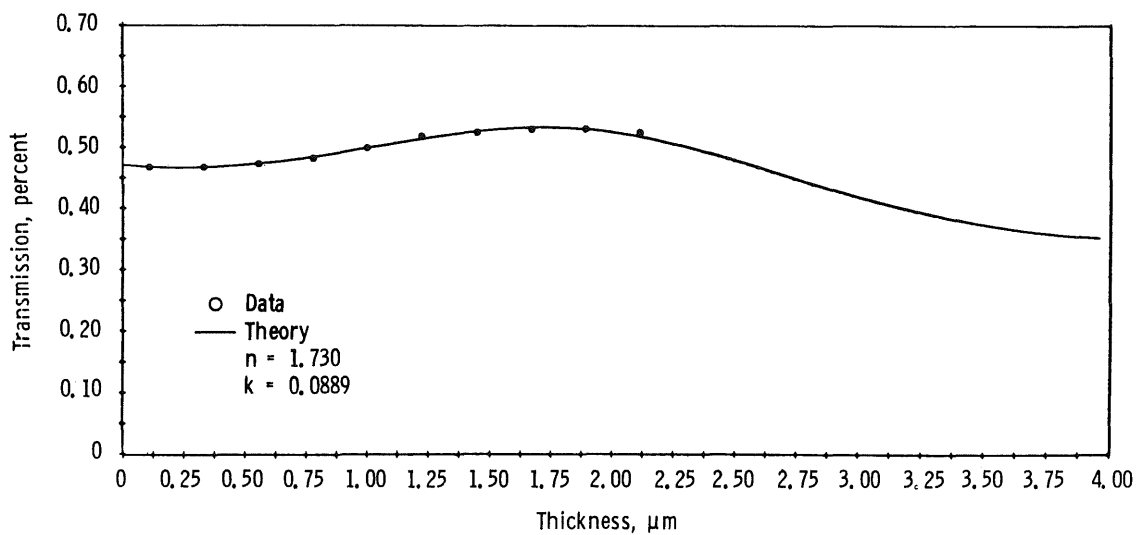
Figure 45. Complex refractive index for  $\text{NH}_3$  on  $80^\circ\text{K}$ .



b. Imaginary component  
Figure 45. Concluded.



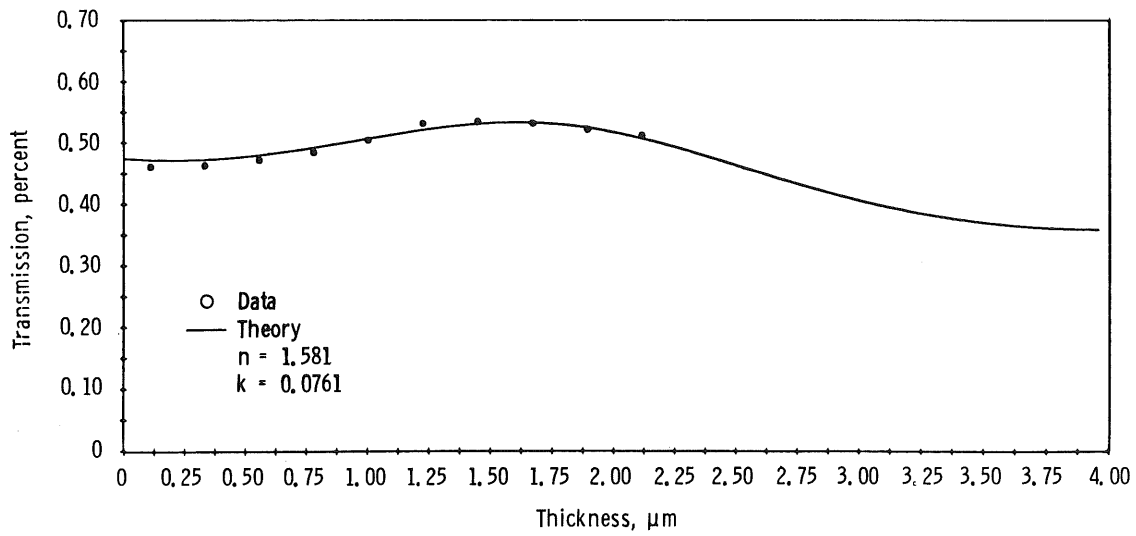
a.  $\lambda = 14.085 \mu\text{m}$



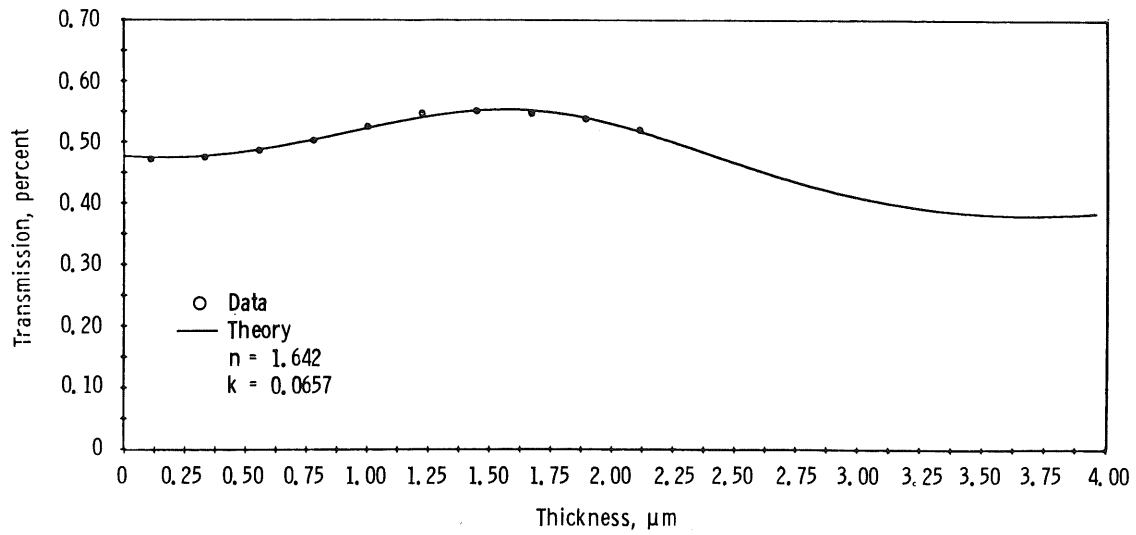
b.  $\lambda = 13.514 \mu\text{m}$

**Figure 46. Comparison of theory and transmission data for  $\text{NH}_3$  on  $20^\circ\text{K}$  germanium.**

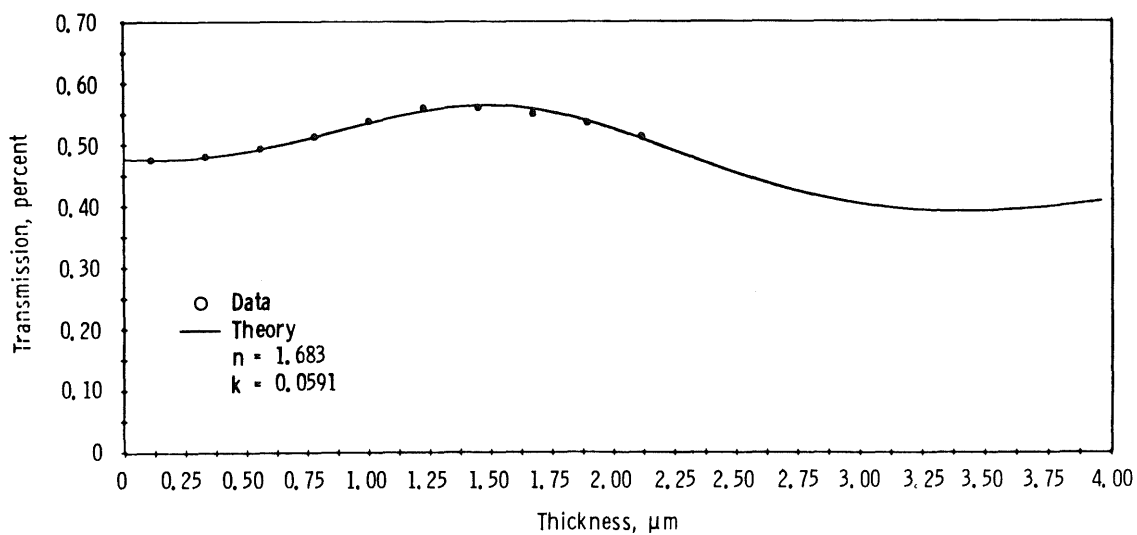




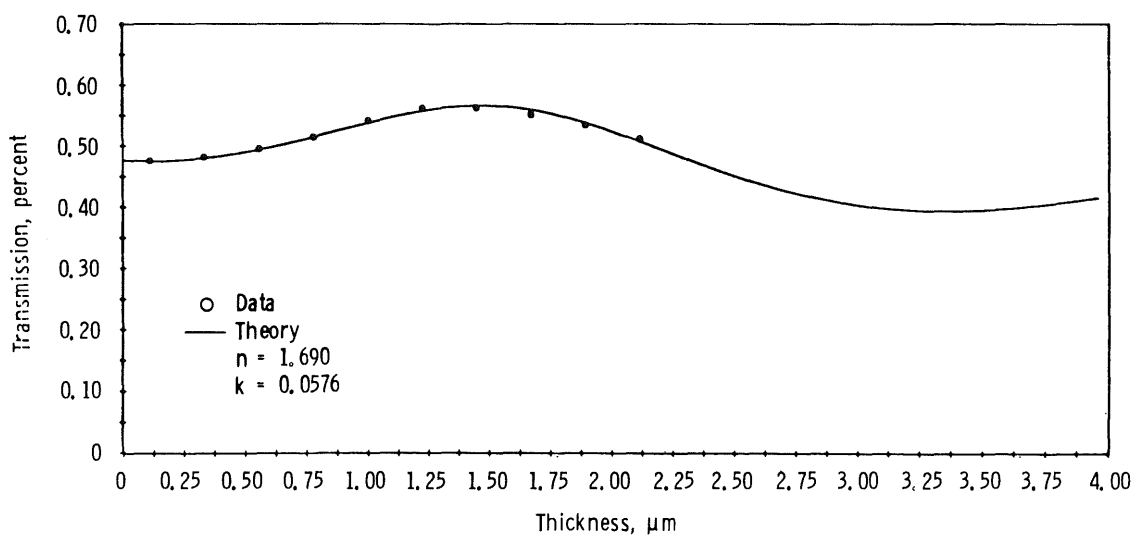
c.  $\lambda = 11.628 \mu\text{m}$



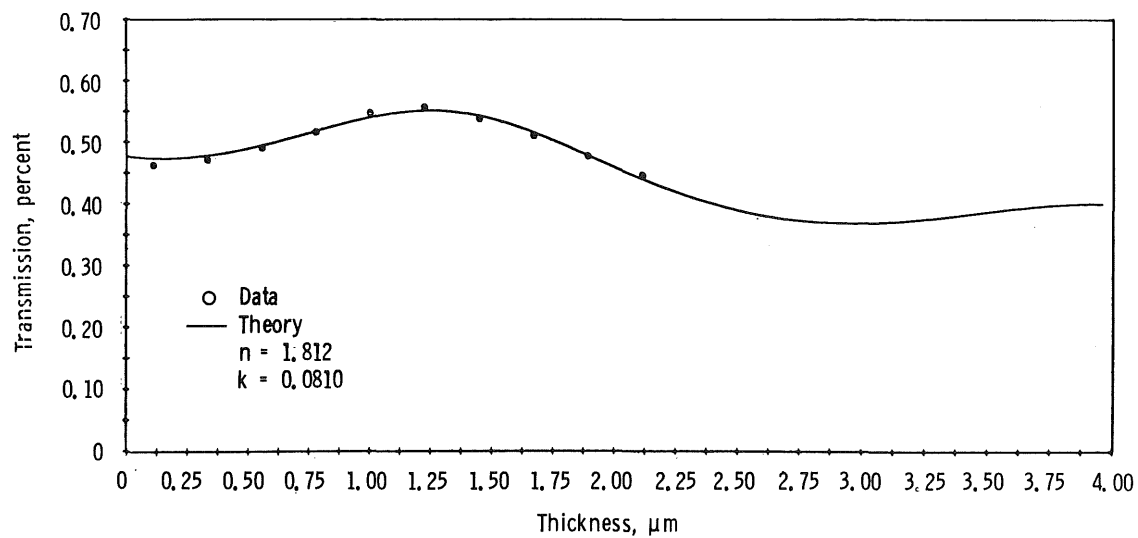
d.  $\lambda = 11.364 \mu\text{m}$   
Figure 46. Continued.



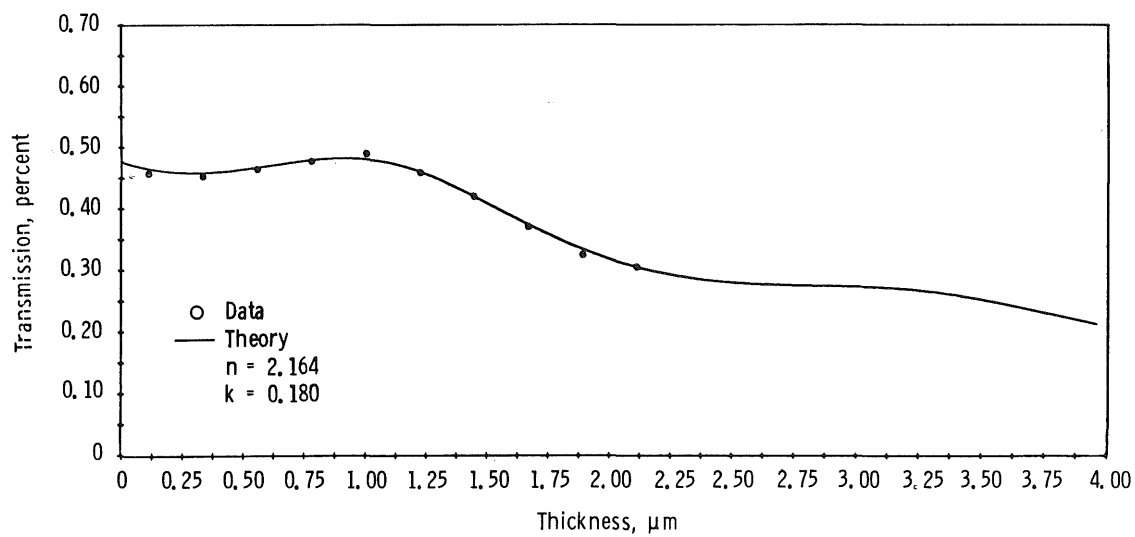
e.  $\lambda = 10.870 \mu\text{m}$



f.  $\lambda = 10.753 \mu\text{m}$   
Figure 46. Continued.



g.  $\lambda = 10.000 \mu\text{m}$



h.  $\lambda = 9.709 \mu\text{m}$   
Figure 46. Continued.

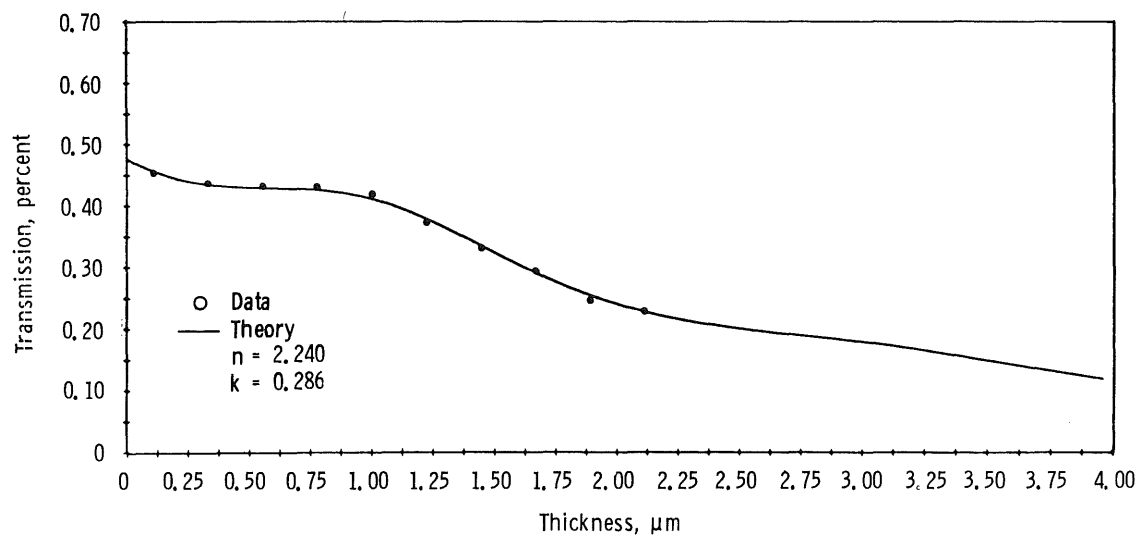
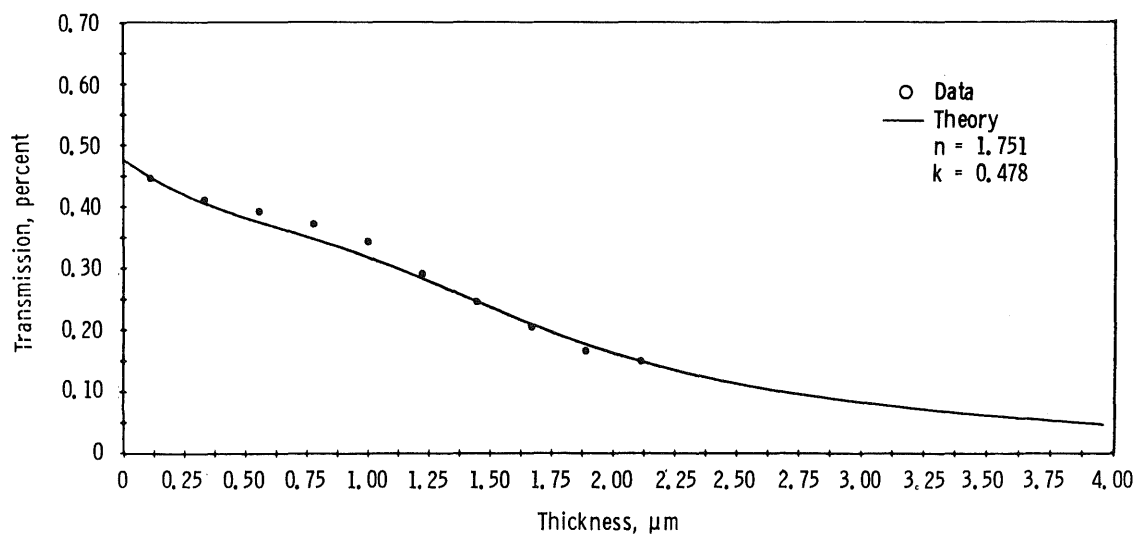
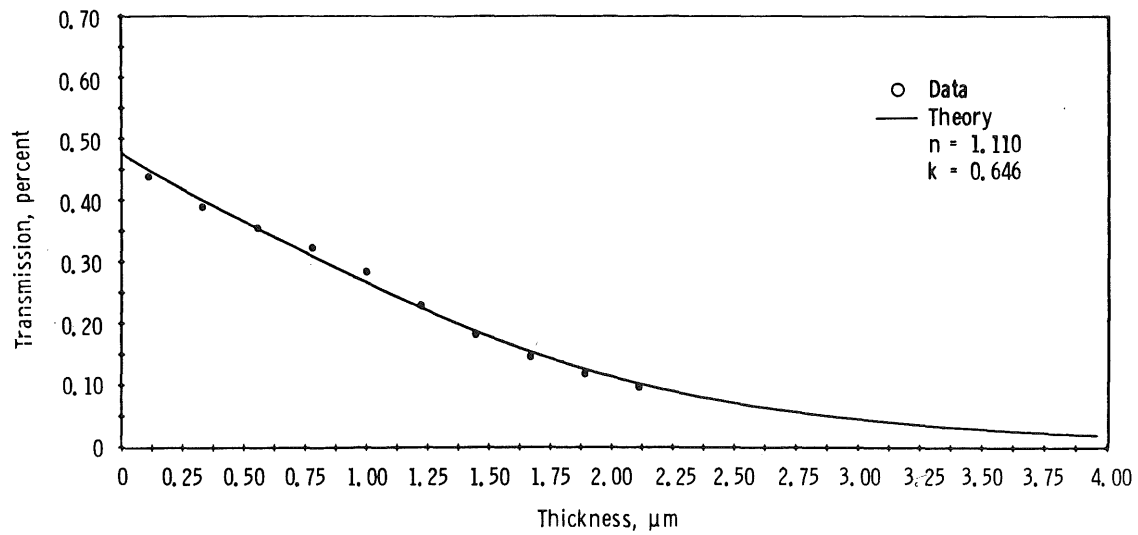
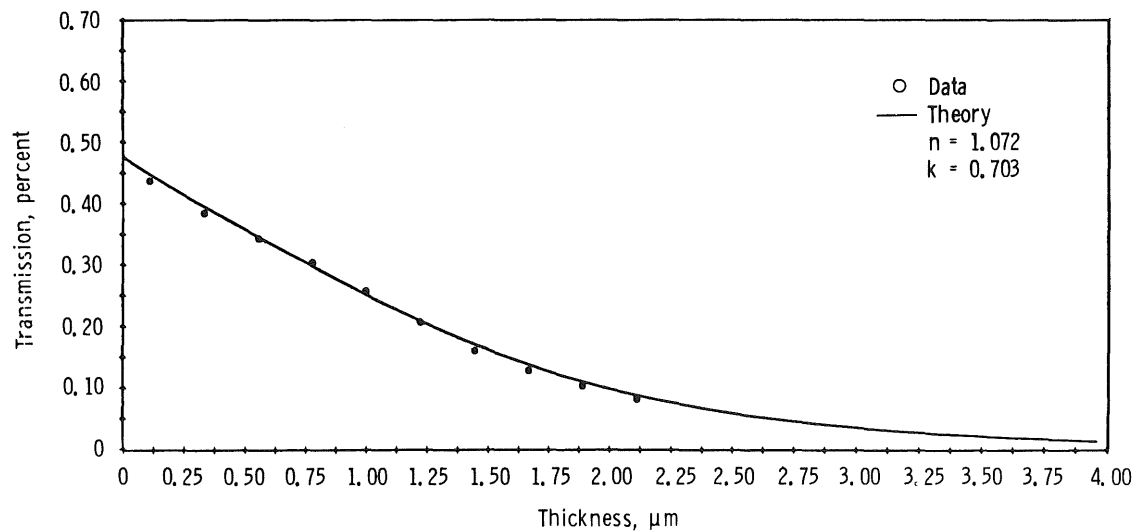
i.  $\lambda = 9.615 \mu\text{m}$ j.  $\lambda = 9.524 \mu\text{m}$ 

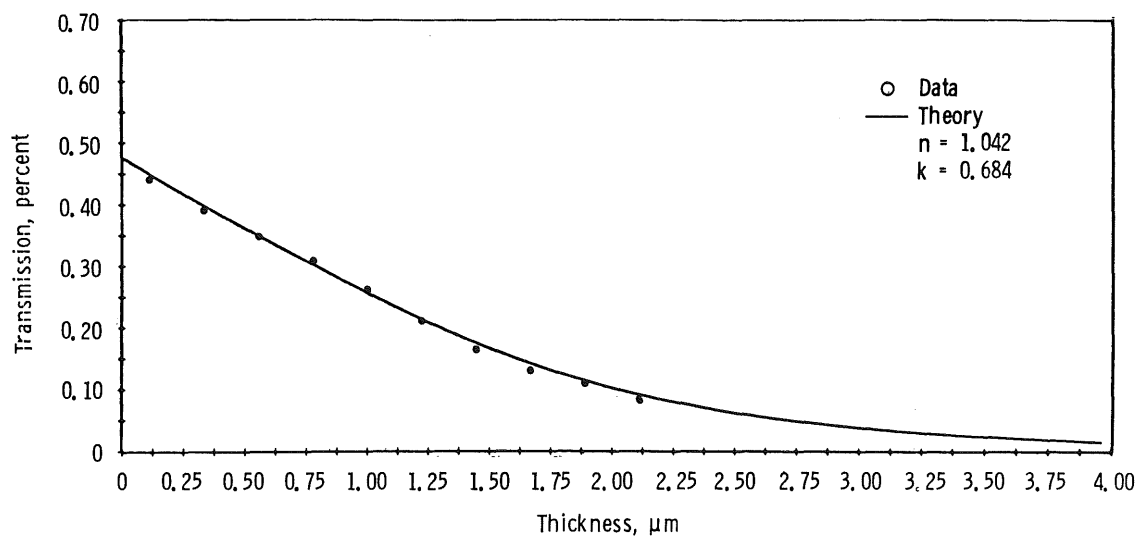
Figure 46. Continued.



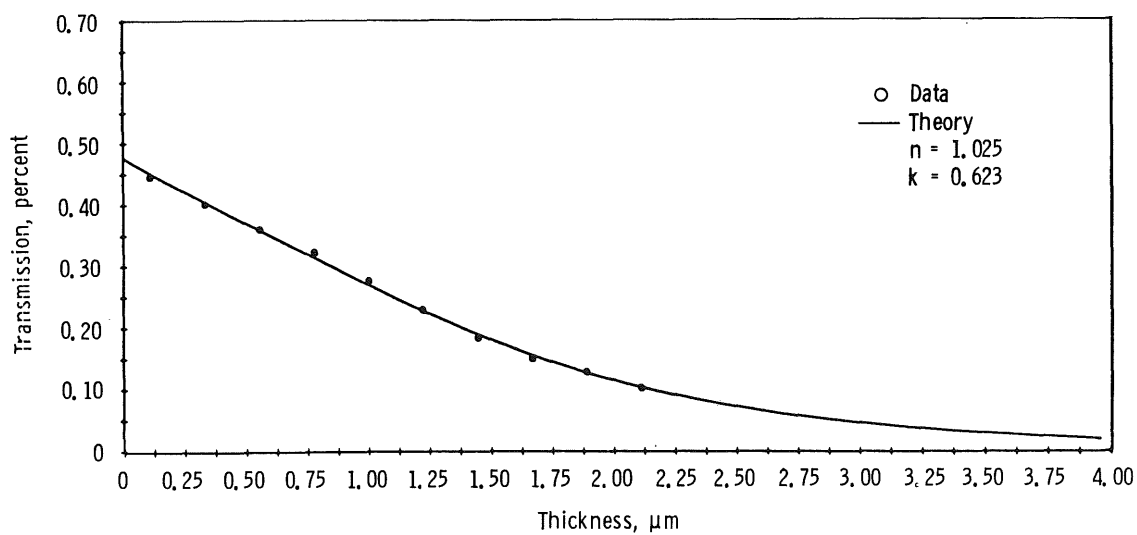
k.  $\lambda = 9.434 \mu\text{m}$



l.  $\lambda = 9.346 \mu\text{m}$   
Figure 46. Continued.

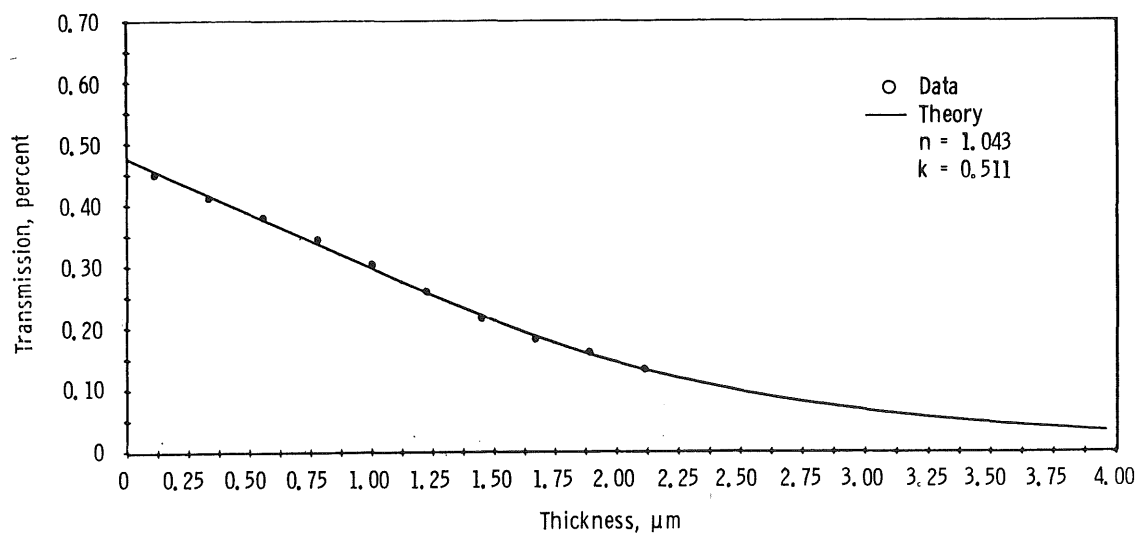


m.  $\lambda = 9.259 \mu\text{m}$

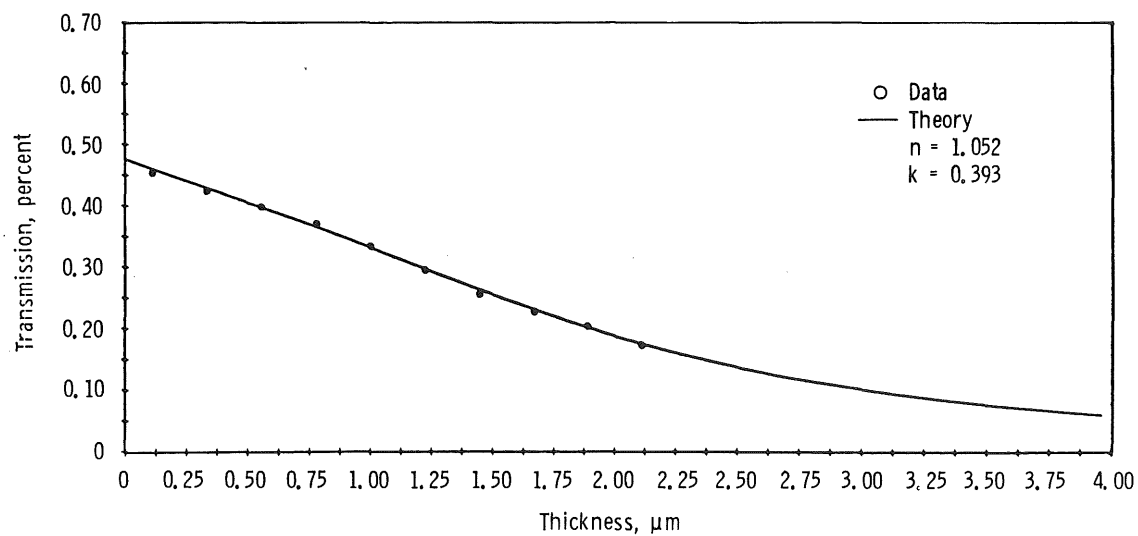


n.  $\lambda = 9.174 \mu\text{m}$

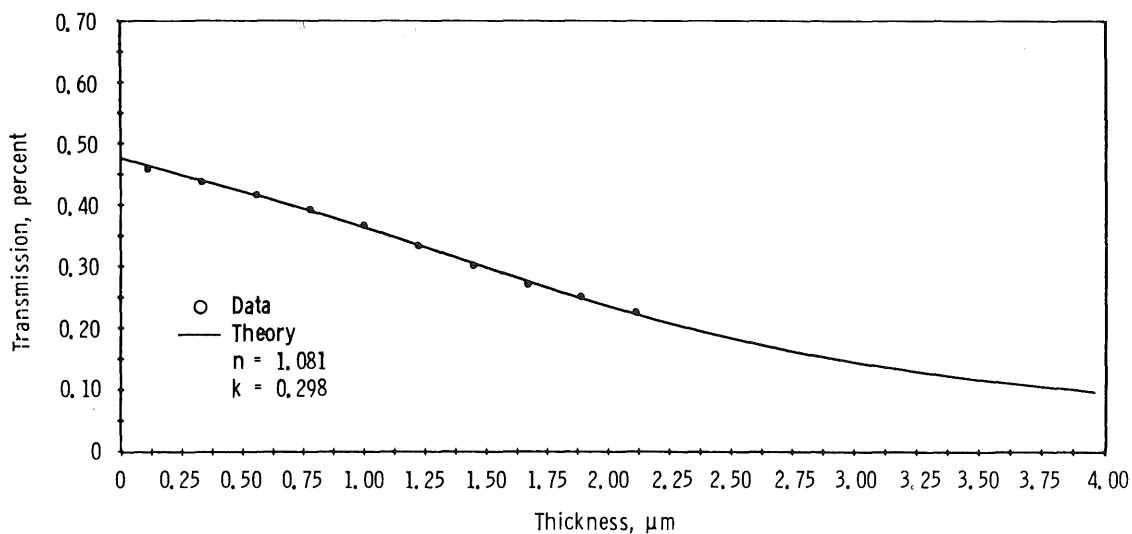
Figure 46. Continued.



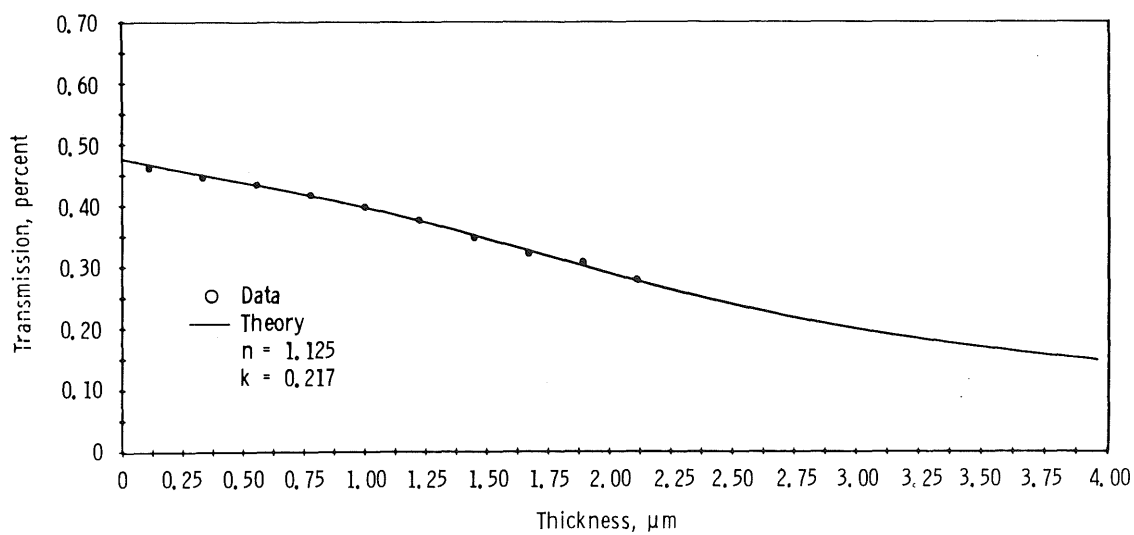
o.  $\lambda = 9.091 \mu\text{m}$



p.  $\lambda = 9.009 \mu\text{m}$   
Figure 46. Continued.



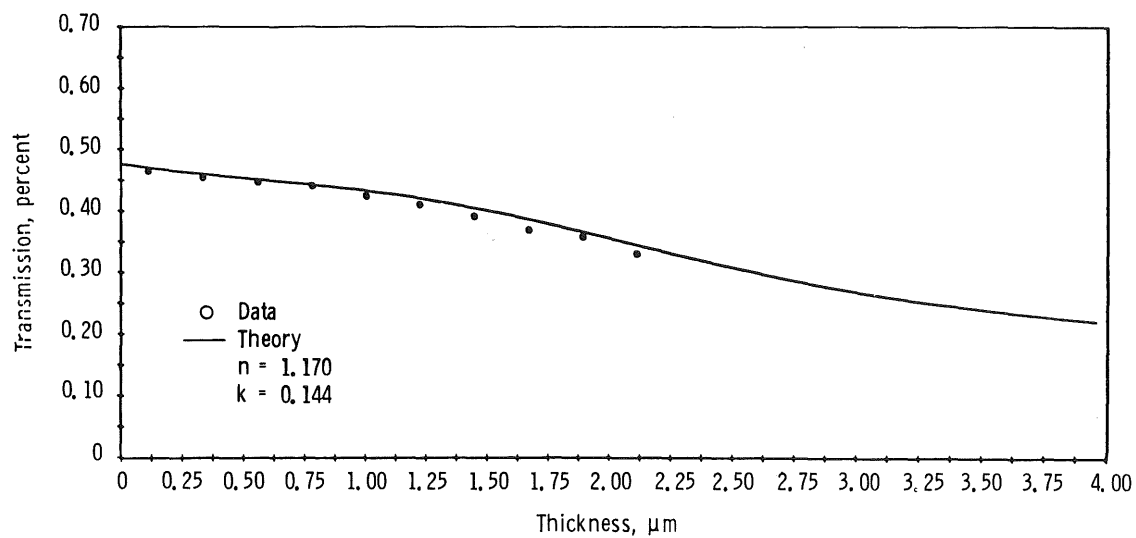
q.  $\lambda = 8.929 \mu\text{m}$



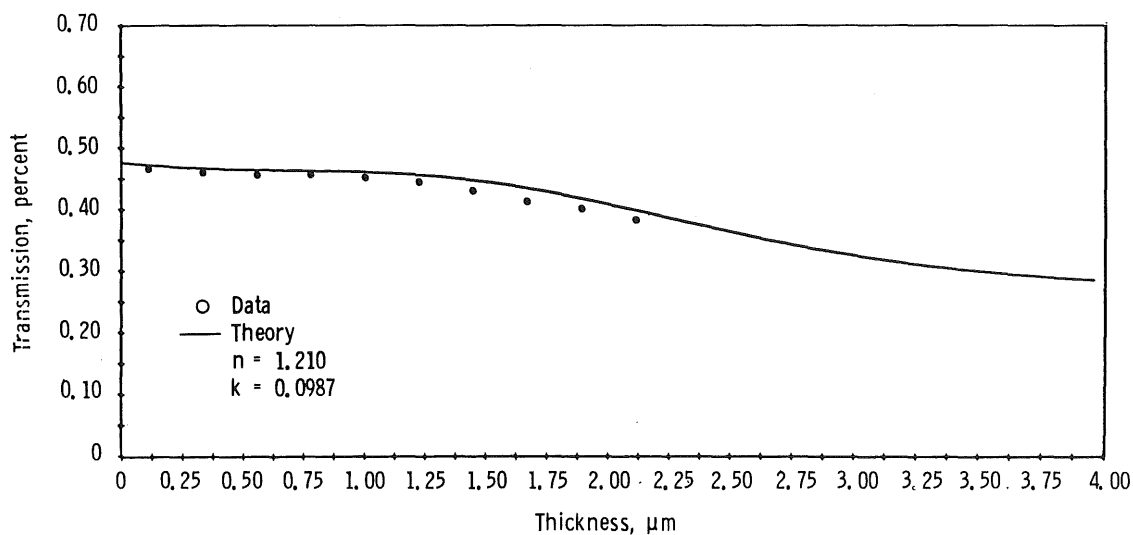
r.  $\lambda = 8.850 \mu\text{m}$

Figure 46. Continued.



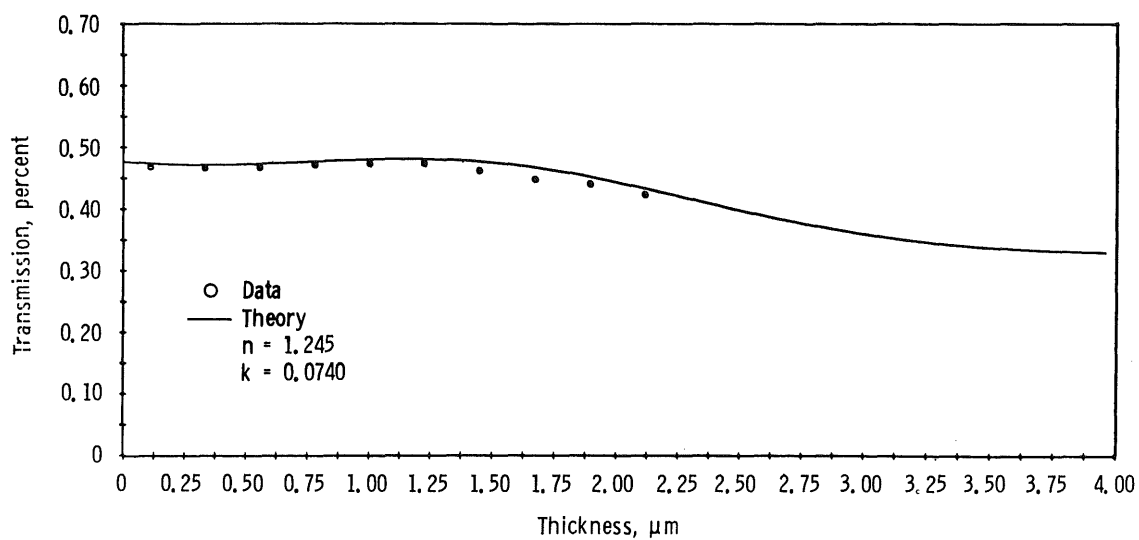


s.  $\lambda = 8.772 \mu\text{m}$

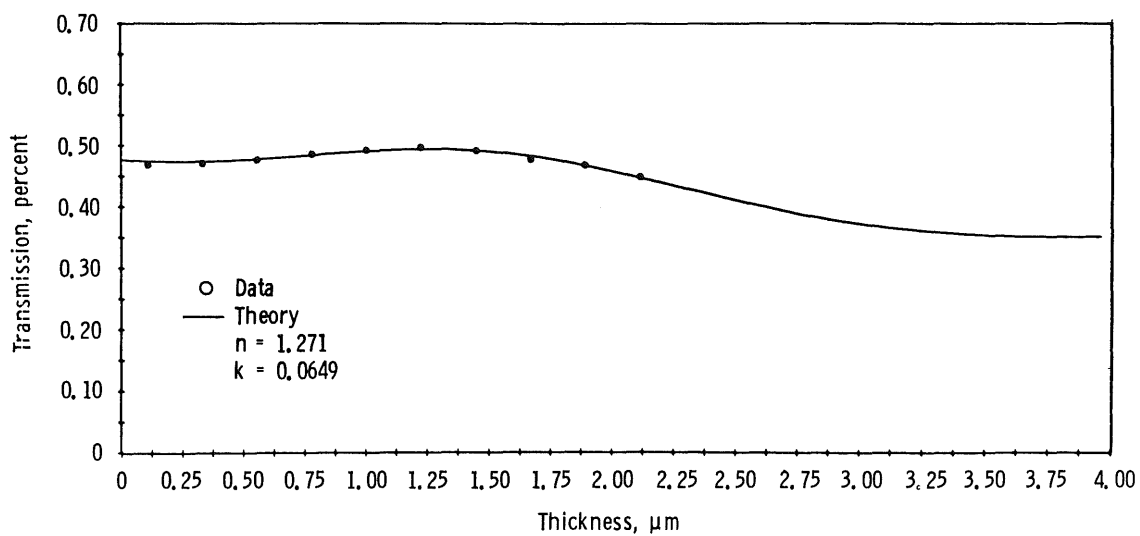


t.  $\lambda = 8.696 \mu\text{m}$

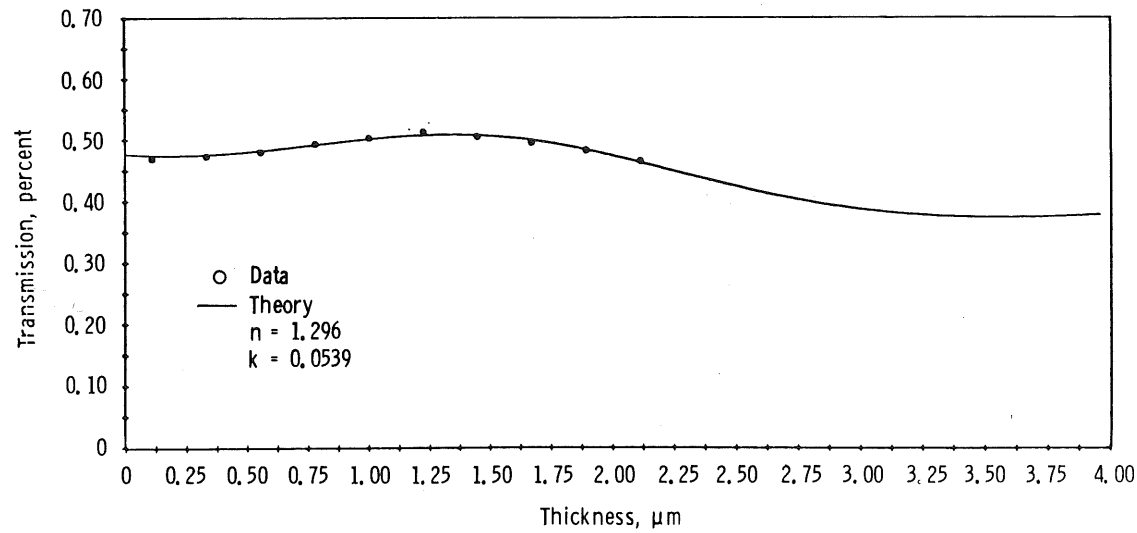
Figure 46. Continued.



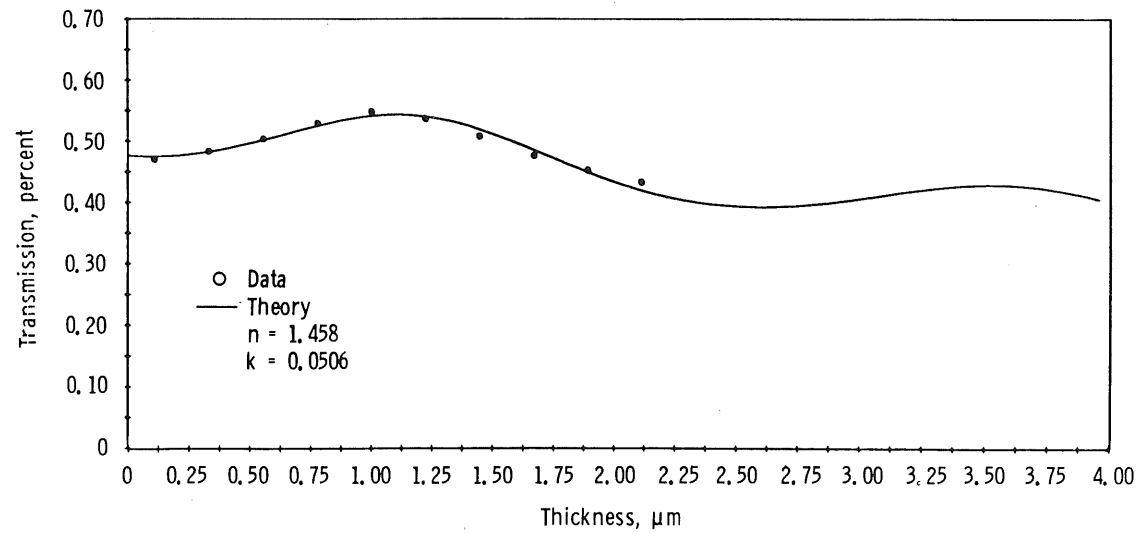
u.  $\lambda = 8.621 \mu\text{m}$



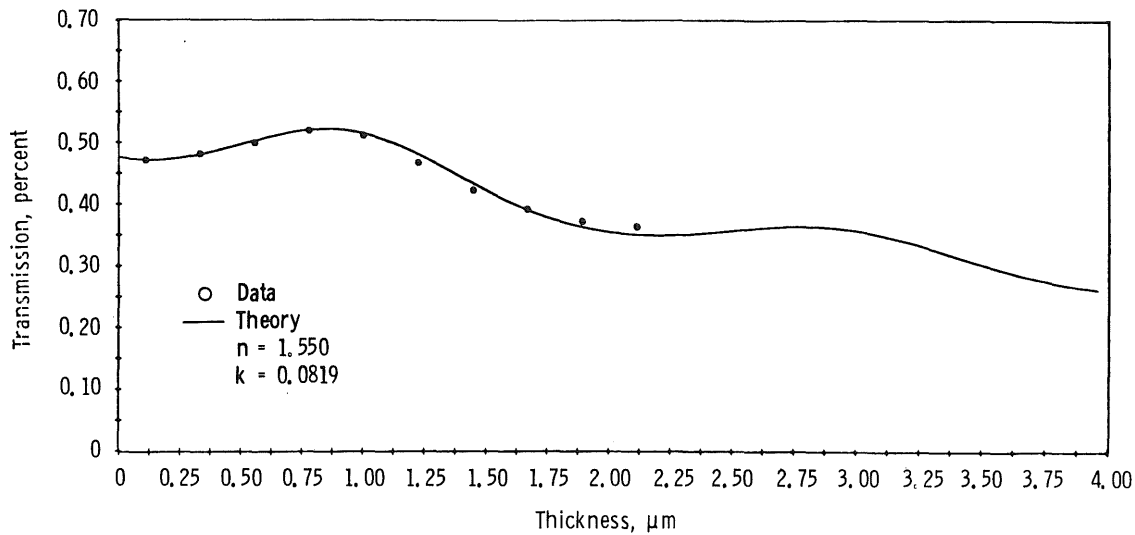
v.  $\lambda = 8.547 \mu\text{m}$   
Figure 46. Continued.



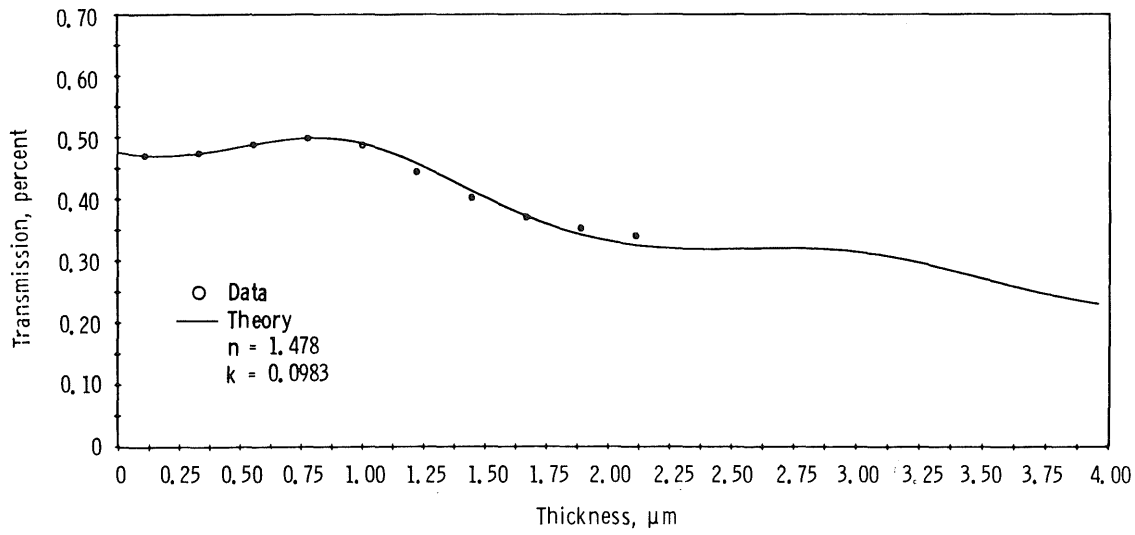
w.  $\lambda = 8.475 \mu\text{m}$



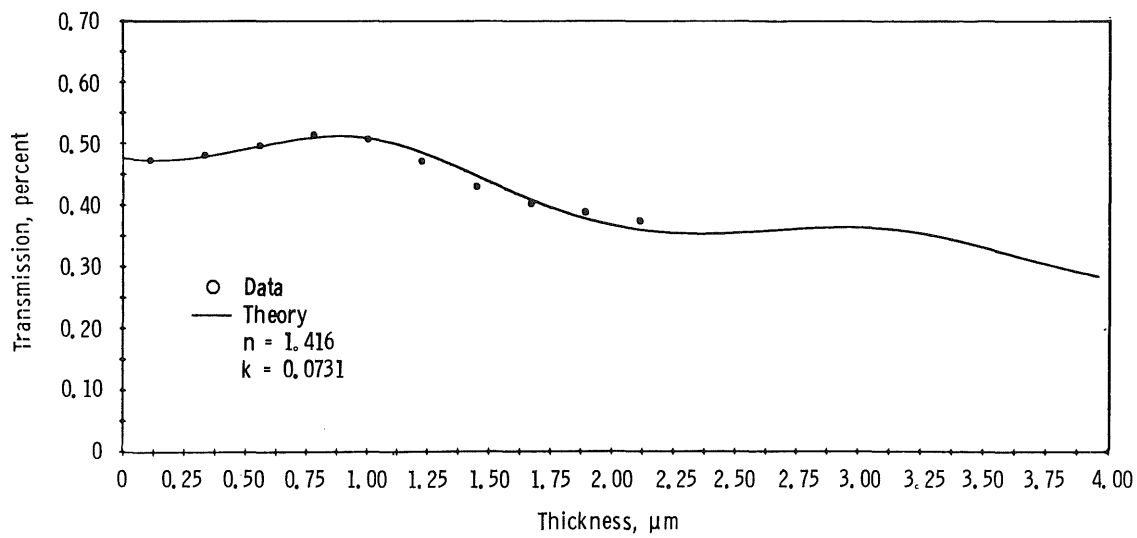
x.  $\lambda = 7.194 \mu\text{m}$   
Figure 46. Continued.



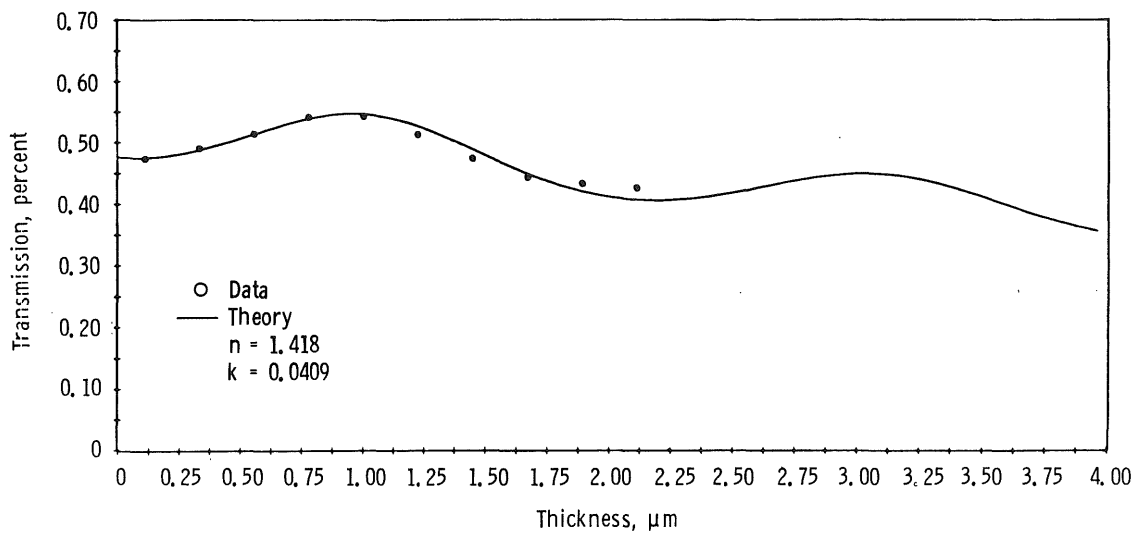
y.  $\lambda = 6.211 \mu\text{m}$



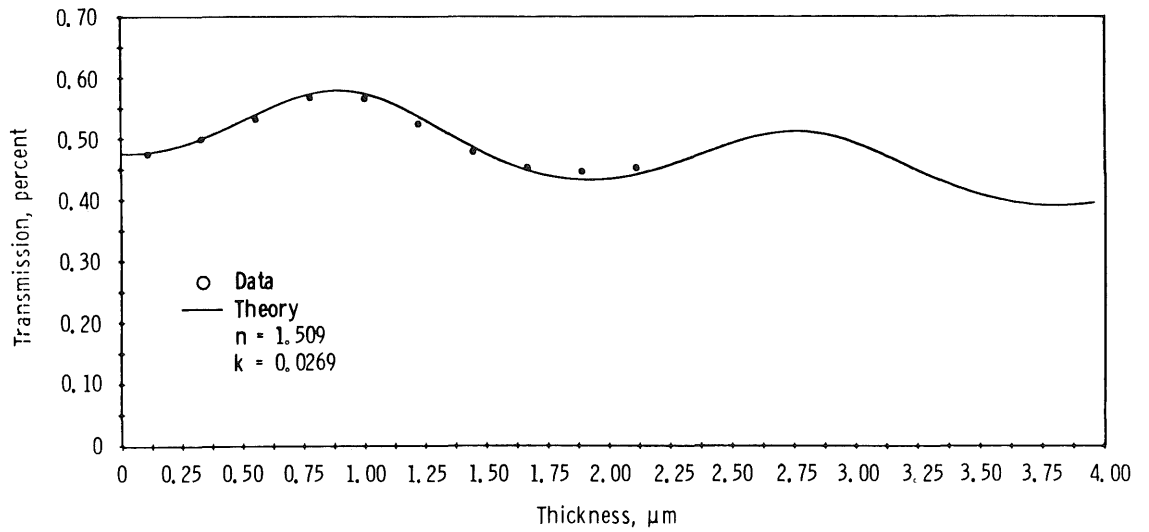
z.  $\lambda = 6.135 \mu\text{m}$   
Figure 46. Continued.



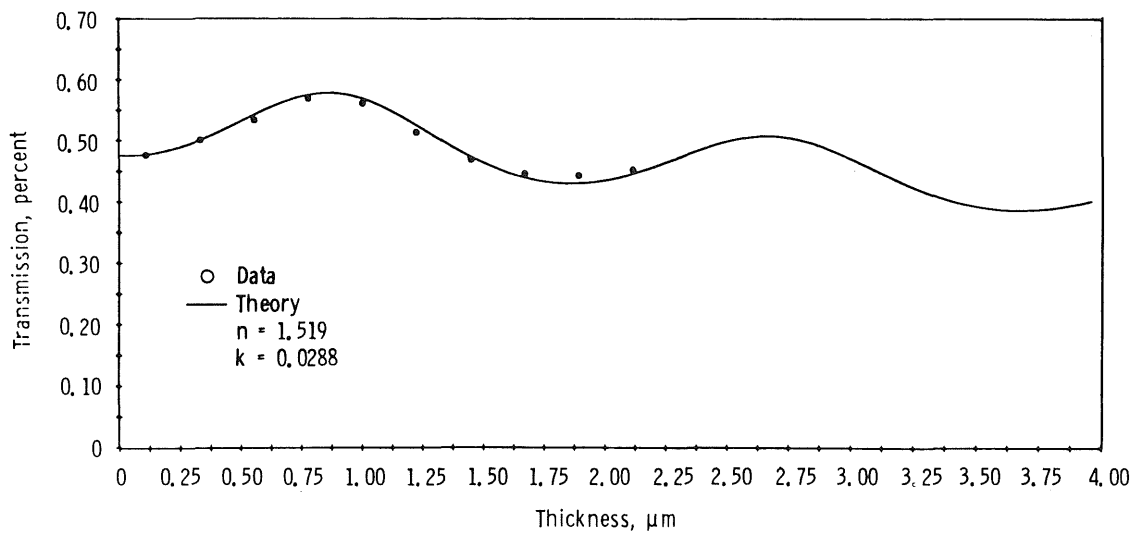
aa.  $\lambda = 6.061 \mu\text{m}$



bb.  $\lambda = 5.952 \mu\text{m}$   
Figure 46. Continued.

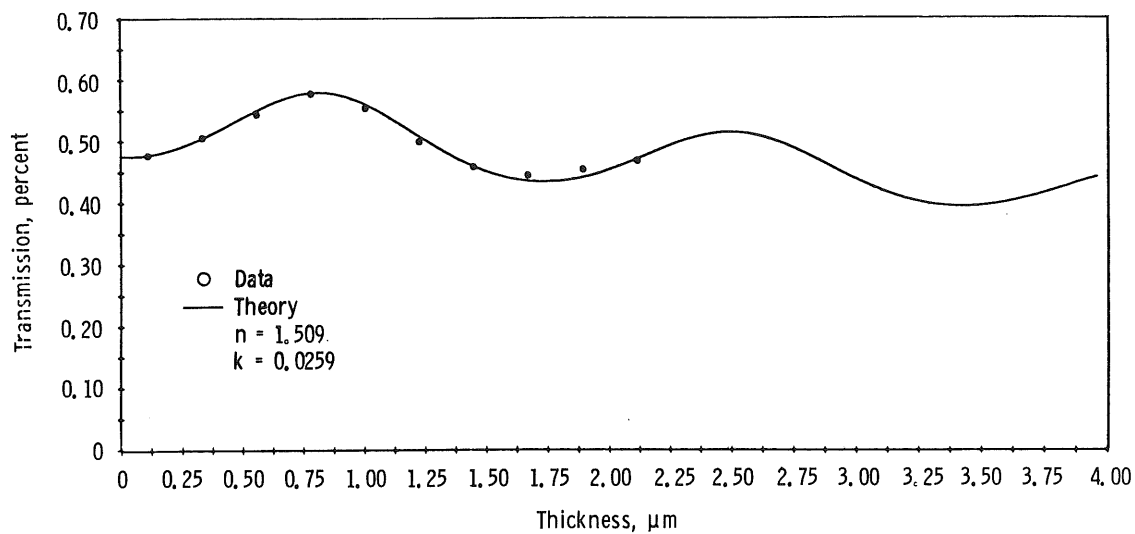


cc.  $\lambda = 5.650 \mu\text{m}$

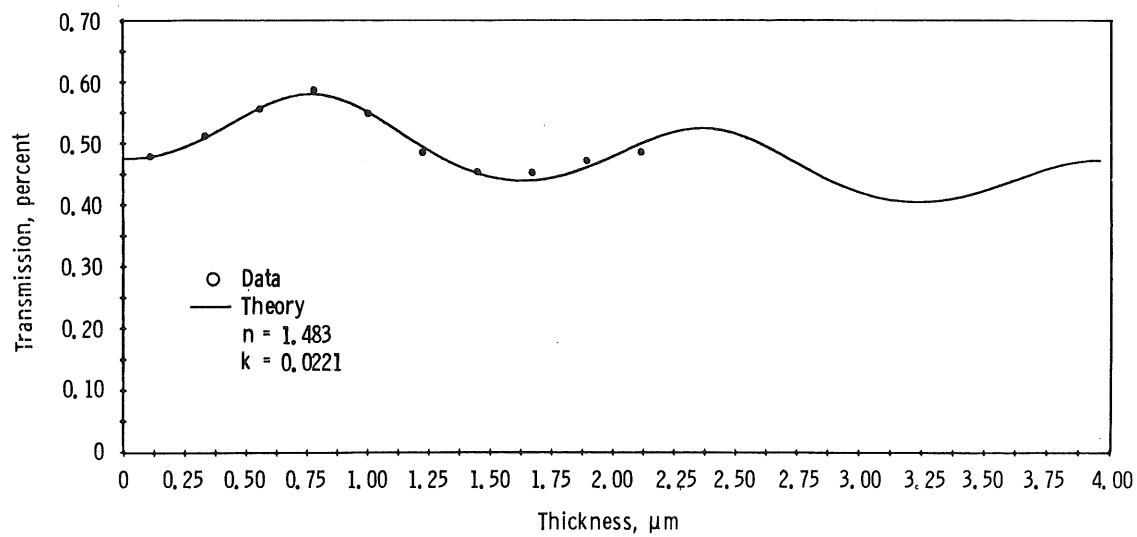


dd.  $\lambda = 5.494 \mu\text{m}$

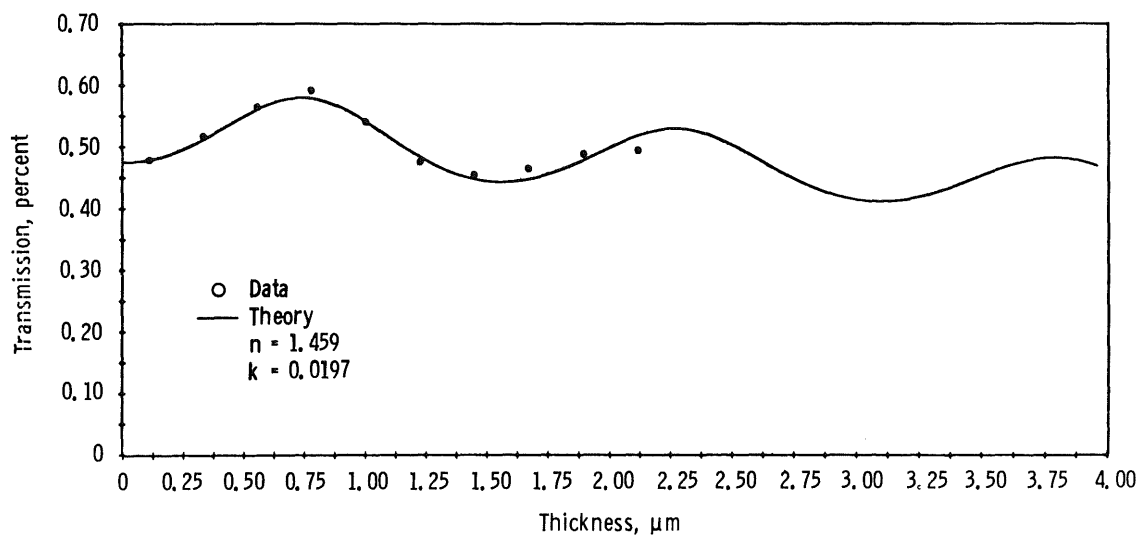
Figure 46. Continued.



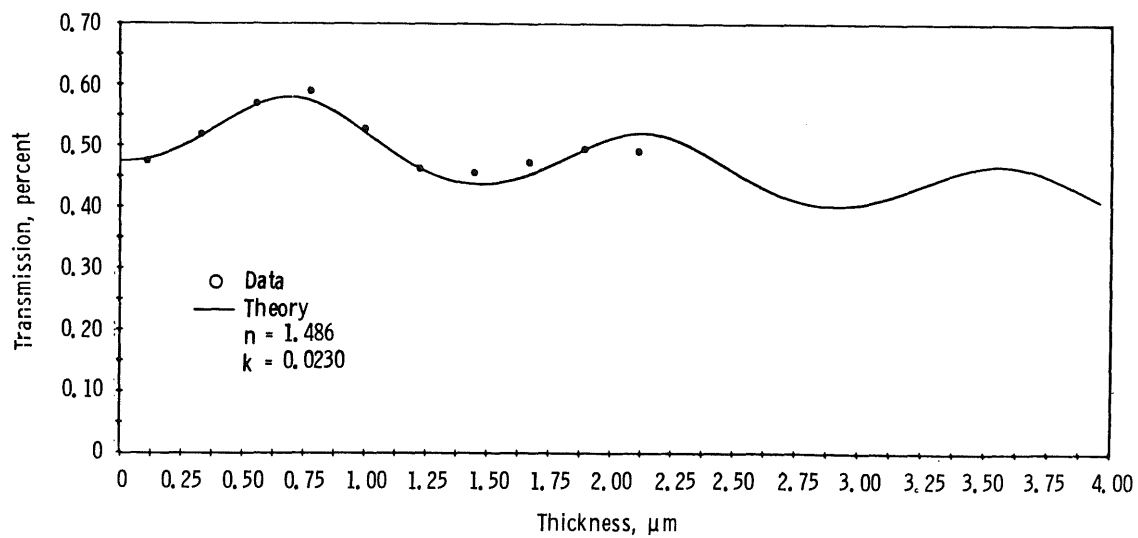
ee.  $\lambda = 5.102 \mu\text{m}$



ff.  $\lambda = 4.739 \mu\text{m}$   
Figure 46. Continued.

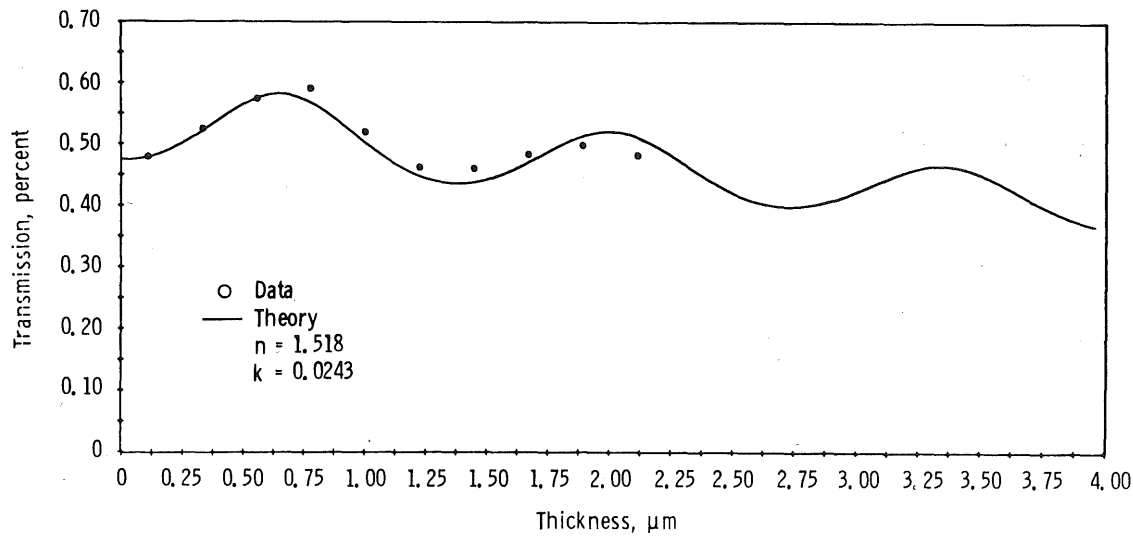


gg.  $\lambda = 4.464 \mu\text{m}$

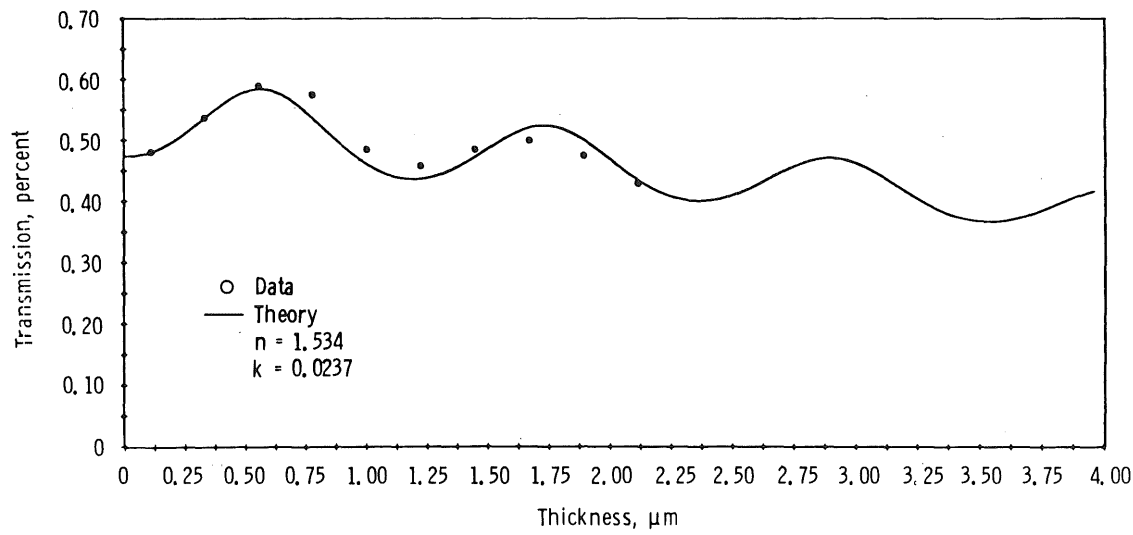


hh.  $\lambda = 4.273 \mu\text{m}$   
Figure 46. Continued.

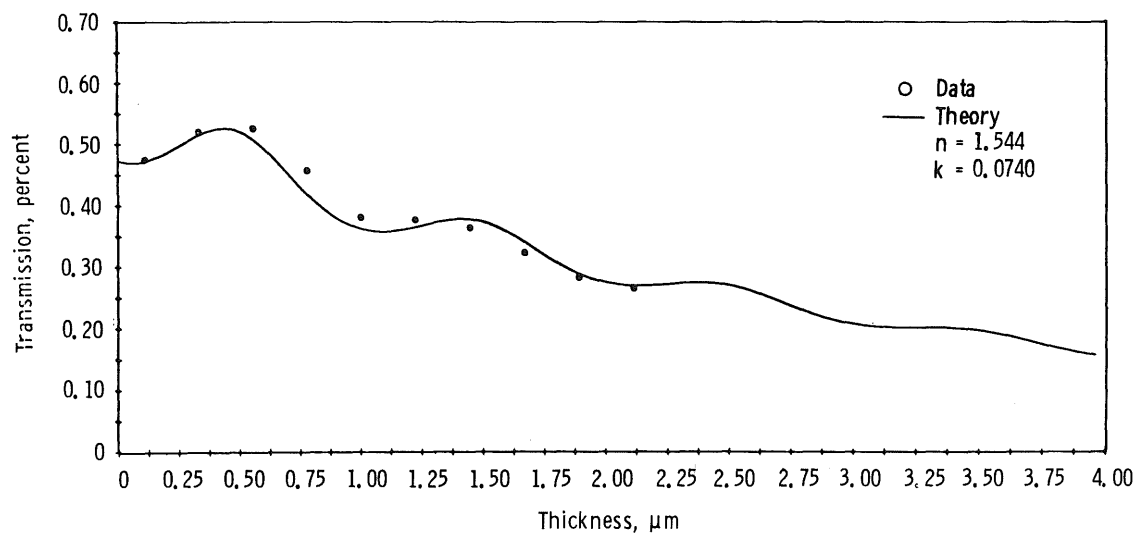




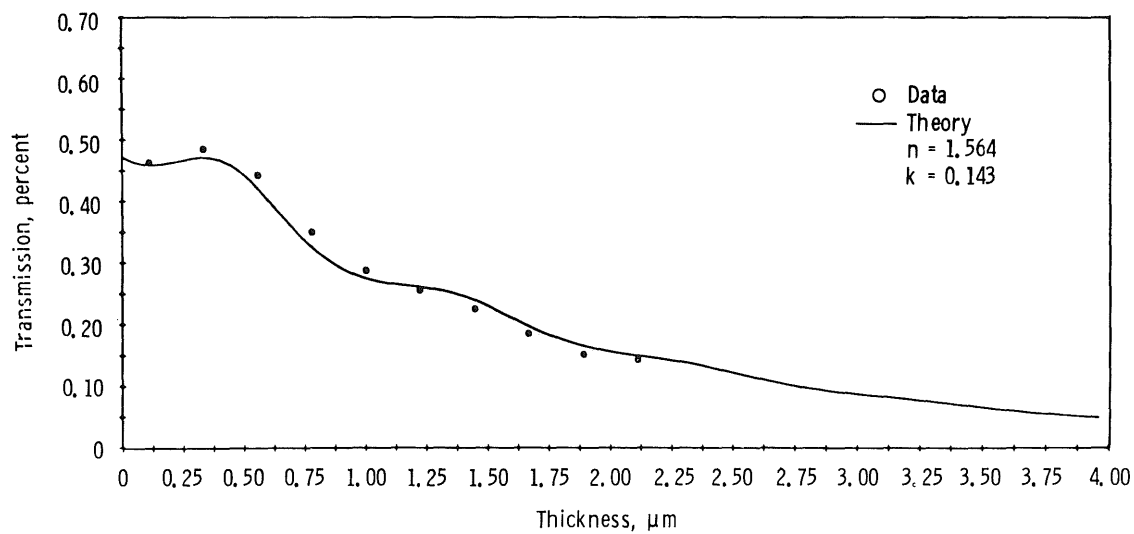
ii.  $\lambda = 4.098 \mu\text{m}$



jj.  $\lambda = 3.584 \mu\text{m}$   
Figure 46. Continued.

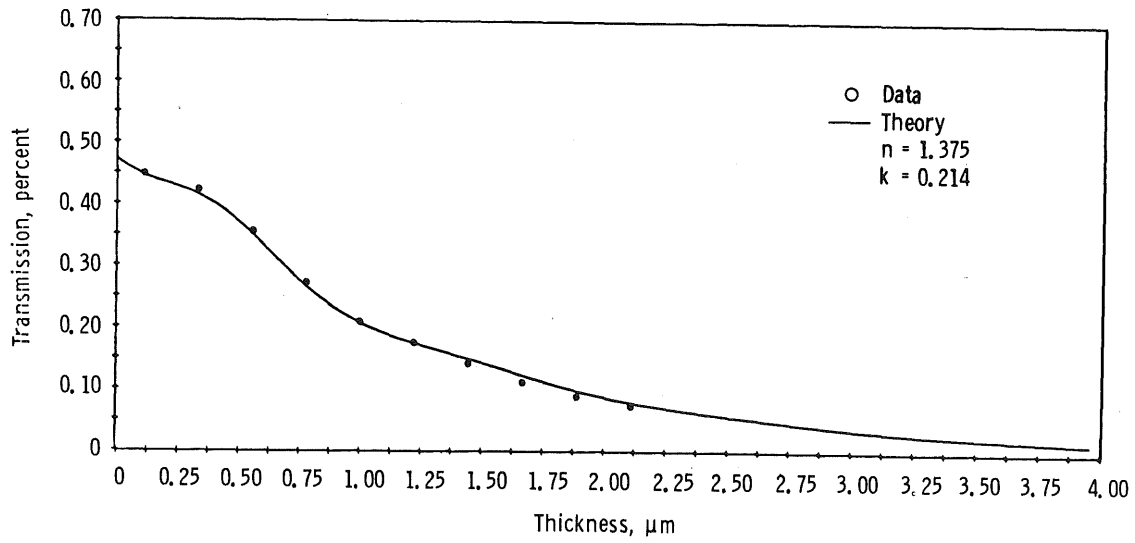


kk.  $\lambda = 3.106 \mu\text{m}$

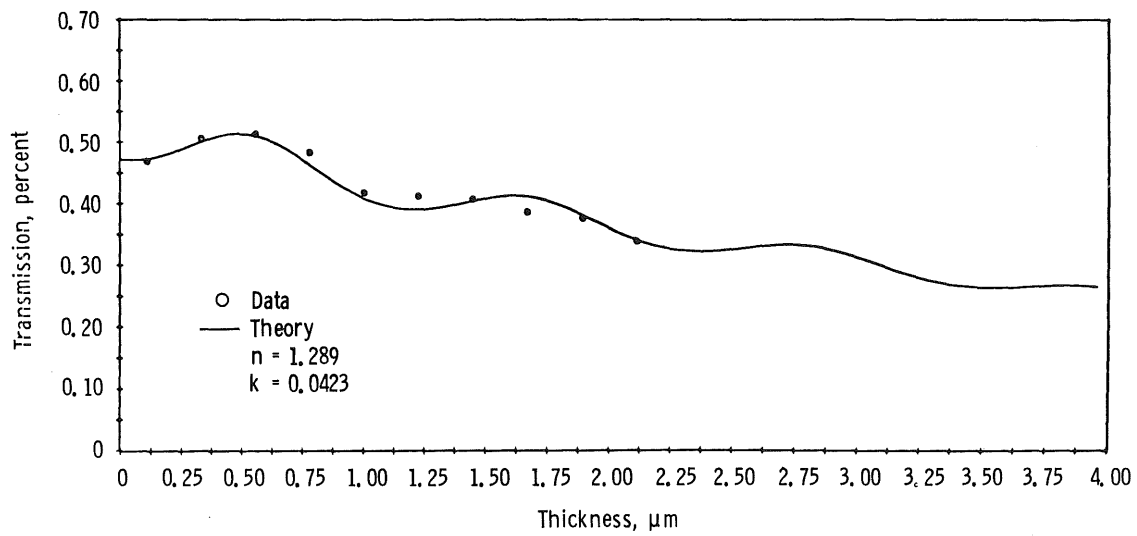


II.  $\lambda = 2.985 \mu\text{m}$

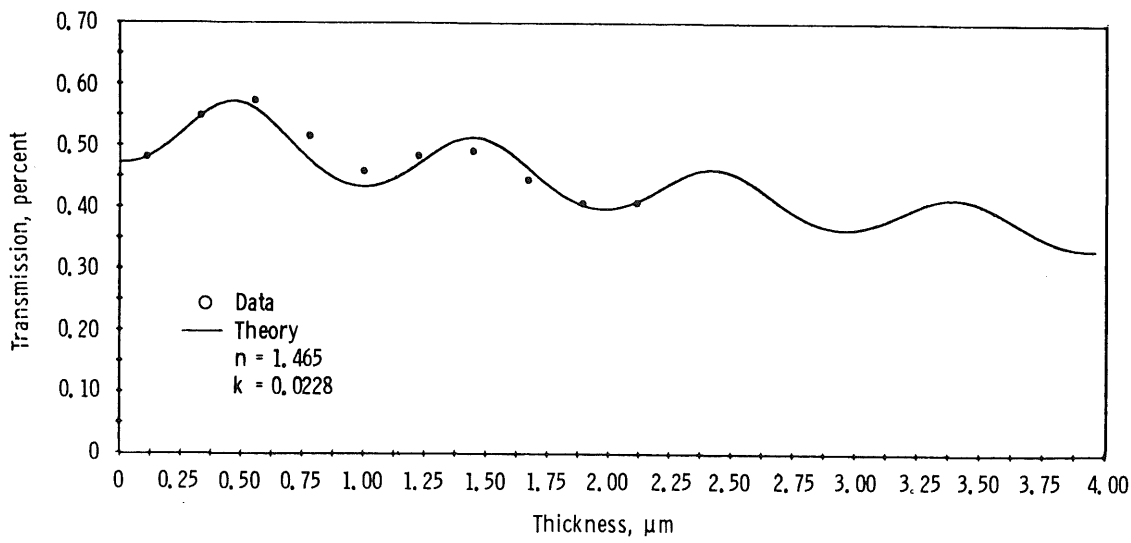
Figure 46. Continued.



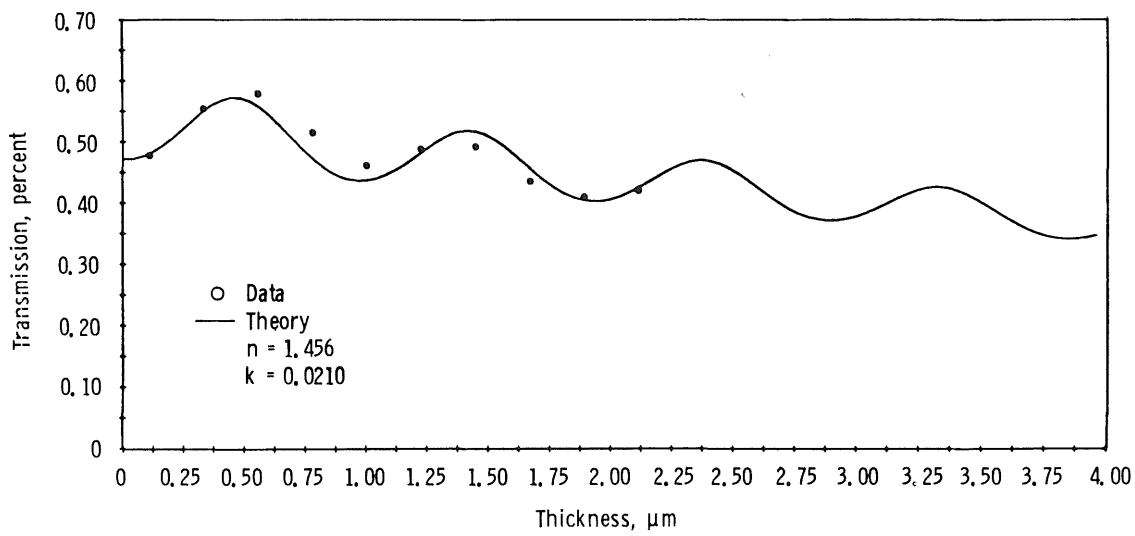
mm.  $\lambda = 2.967 \mu\text{m}$



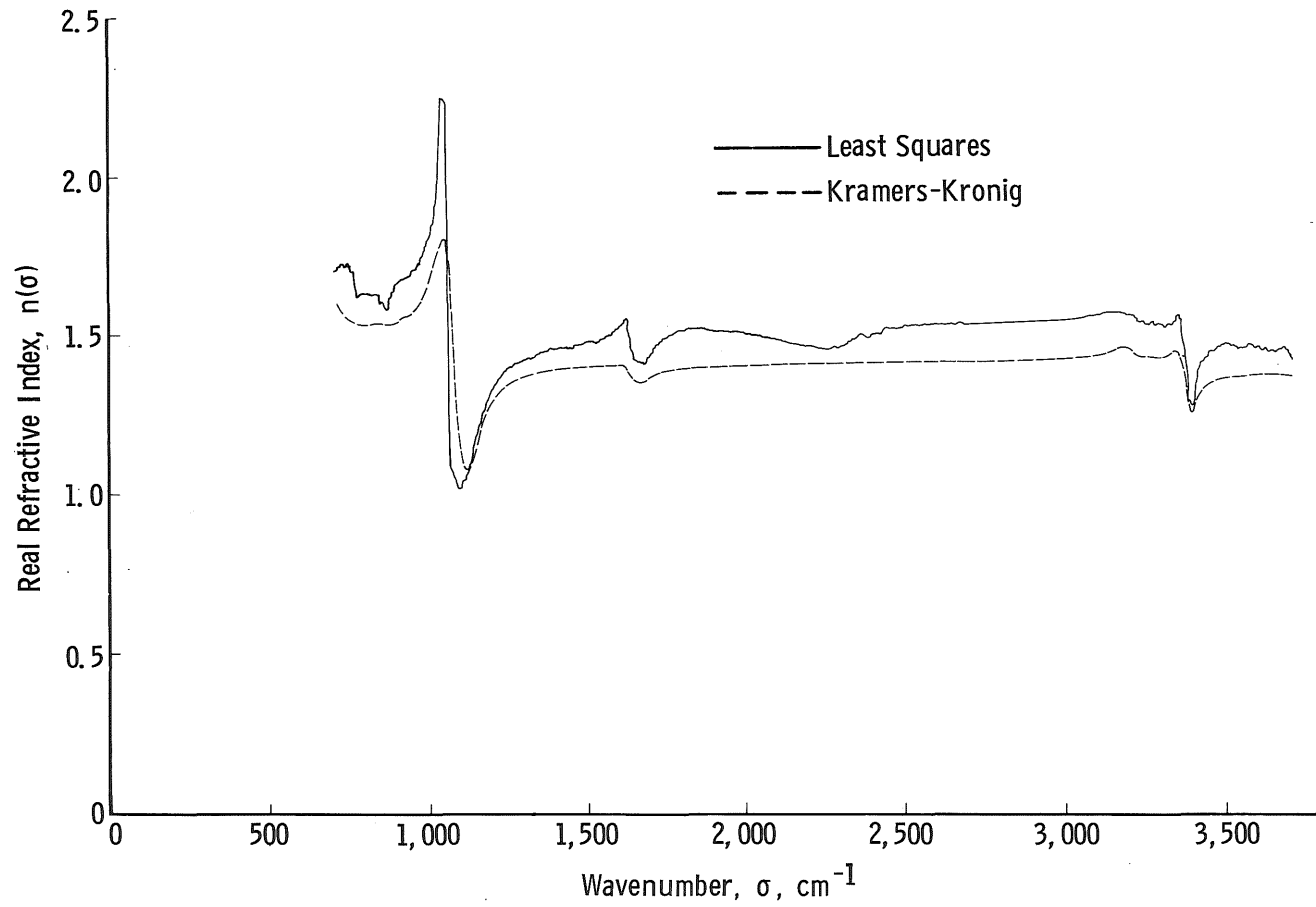
nn.  $\lambda = 2.941 \mu\text{m}$   
Figure 46. Continued.



oo.  $\lambda = 2.865 \mu\text{m}$

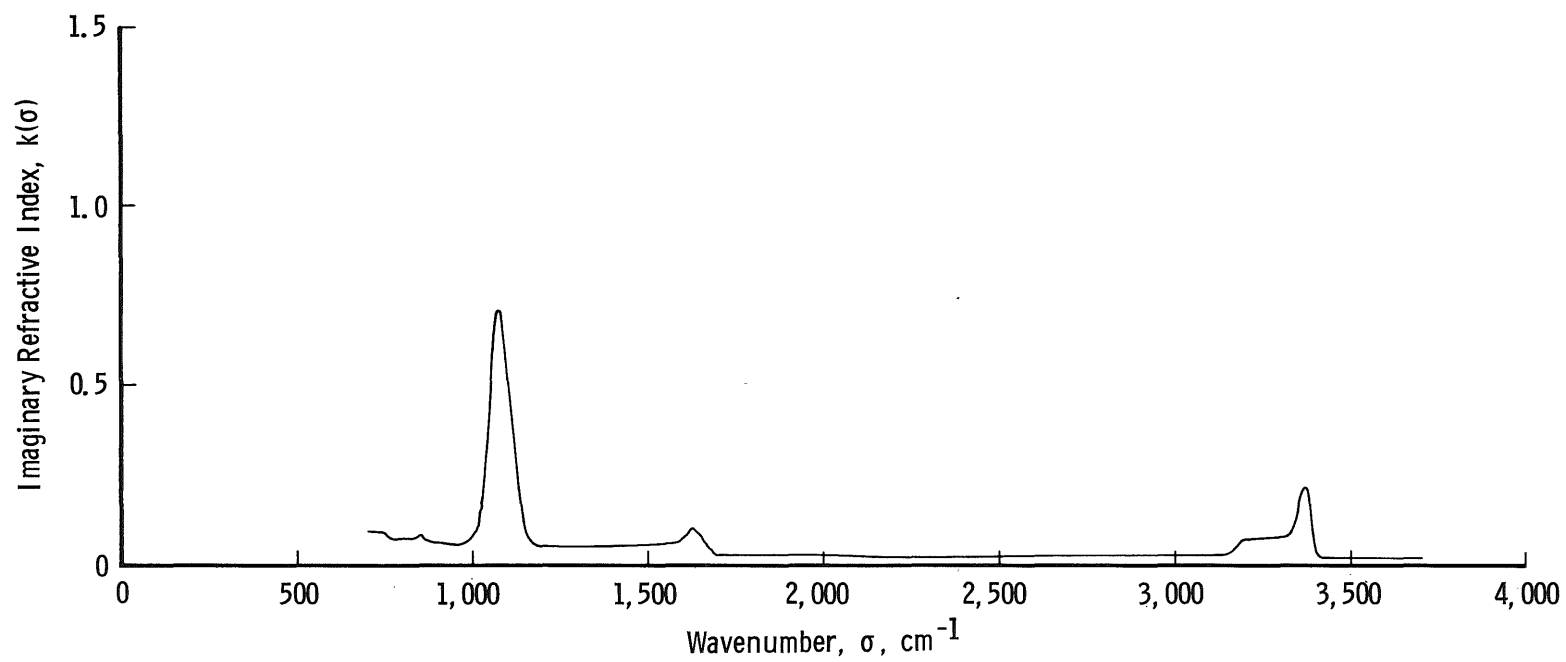


pp.  $\lambda = 2.786 \mu\text{m}$   
Figure 46. Concluded.



a. Real component

Figure 47. Complex refractive index for  $\text{NH}_3$  on  $20^\circ\text{K}$  germanium.



b. Imaginary component  
Figure 47. Concluded.

Table 1. Growth Conditions for Solid Gases Studied

Solid Gas	Substrate Temperature, °K	Refractive Index at He-Ne .6328 $\mu$ m	Linear Growth Rate, $\mu$ m/min	Inlet Pressure (MKS Baratron), $\mu$ m Hg	IROT Background Pressure during Deposition, torr	Equilibrium Vapor Pressure, torr, at Substrate Temperature	Grade of Gas Employed
NH <sub>3</sub> (This Study)	80	1.42 $\pm$ .02	1.60	600	3 x 10 <sup>-7</sup>	6 x 10 <sup>-11</sup>	Ultrahigh Pure 99.999%
NH <sub>3</sub> (This Study)	20	1.42 $\pm$ .02	2.80	600	4 x 10 <sup>-7</sup>	<10 <sup>-13</sup>	Ultrahigh Pure 99.999%
NH <sub>3</sub> (Ref. 2)	30-60	1.38 $\pm$ .05					
CO <sub>2</sub> (This Study)	80	1.42 $\pm$ .02	1.85	500	1 x 10 <sup>-6</sup>	.8 x 10 <sup>-8</sup>	Coleman Grade 99.999%
CO <sub>2</sub> (This Study)	20	1.42 $\pm$ .02	1.85	500	1 x 10 <sup>-6</sup>	<10 <sup>-13</sup>	Coleman Grade 99.999%
CO <sub>2</sub> (Ref. 2)	24 and 77	1.34 $\pm$ .06					
CO <sub>2</sub> (Ref. 8)	82	1.42 $\pm$ .01	1.3				High Purity 99.98%
CO <sub>2</sub> (Viehman, NASA)	77	1.41					
CO	20	1.22 $\pm$ .02	1.04	500	4 x 10 <sup>-6</sup>	5 x 10 <sup>-13</sup>	Ultrahigh Pure 99.8%
CH <sub>4</sub>	20	1.38 $\pm$ .02	4.13	150	5 x 10 <sup>-7</sup>	<10 <sup>-13</sup>	Instrument Grade 99.7%
HCL	20		1.30	500	3 x 10 <sup>-7</sup>	<10 <sup>-13</sup>	Electronic Grade 99.99%
H <sub>2</sub> O (This Study)	77	1.26 $\pm$ .01					
H <sub>2</sub> O (Ref. 2)	24 and 80	1.32 $\pm$ .05					
H <sub>2</sub> O (Ref. 8)	82	1.26 $\pm$ .01	1.8				
H <sub>2</sub> O (Viehman, NASA)	77	1.268					

Table 2. Transmission of Germanium as a Function of Temperature

$\sigma$ , $\text{cm}^{-1}$	$\lambda$ , $\mu\text{m}$	Temperature, $^{\circ}\text{K}$		
		300	200	80
		T, %		
6451.6	1.55	0.0	0.00	3.00
6250.0	1.60	0.0	0.00	16.00
6060.1	1.65	0.0	2.00	36.00
5882.3	1.70	0.0	12.00	44.40
5714.3	1.75	0.0	24.00	45.30
5555.5	1.80	4.0	34.00	46.0
5405.4	1.85	14.0	40.00	46.2
5263.2	1.90	24.0	44.00	46.5
5128.2	1.95	34.0	45.00	46.8
5000.0	2.00	43.0	45.20	47.0
4444.4	2.25	45.8	46.50	47.5
4000.0	2.50	46.5	47.10	47.8
3636.4	2.75	46.8	47.30	48.0
3333.3	3.00	47.0	47.40	48.0
3076.9	3.25	47.0	47.50	48.0
2857.1	3.50	47.0	47.50	48.0
2666.6	3.75	47.0	47.50	48.0
2500.0	4.00	47.0	47.50	48.0
2222.2	4.50	47.0	47.50	48.0
2000.0	5.00	47.0	47.50	48.0
1818.2	5.50	47.0	47.50	48.0
1666.6	6.00	47.0	47.50	48.0
1538.5	6.50	47.0	47.50	48.0
1428.5	7.00	46.9	47.50	48.0
1333.3	7.50	46.7	47.40	48.0
1250.0	8.00	46.5	47.30	47.8
1176.5	8.50	46.5	47.10	47.7
1111.1	9.00	46.4	47.00	47.5
1052.6	9.50	46.4	47.00	47.3
1000.0	10.00	46.3	46.90	47.2
975.4	10.25	46.2	46.80	47.2
952.4	10.50	46.1	46.80	47.1
930.0	10.75	46.0	46.70	47.0
909.0	11.00	45.9	46.70	47.0
888.8	11.25	45.6	46.60	47.0

$\sigma$ , $\text{cm}^{-1}$	$\lambda$ , $\mu\text{m}$	Temperature, $^{\circ}\text{K}$		
		300	200	80
		T, %		
869.5	11.50	45.1	46.00	47.0
851	11.75	43.0	45.00	46.5
833	12.00	41.7	45.00	45.7
816.3	12.25	42.2	45.40	45.8
800	12.50	43.0	45.9	46.0
784.3	12.75	43.2	46.0	46.3
769.2	13.00	42.8	45.90	46.3
754.7	13.25	41.2	45.70	46.2
740.7	13.50	40.2	45.90	46.5
727	13.75	41.0	46.40	46.9
714	14.00	42.3	46.50	47.3
701	14.25	42.3	46.50	47.3
689.6	14.50	41.5	47.0	47.1
678	14.75	39.6	46.5	46.5
666.6	15.00	36.2	44.7	45.8
655.7	15.25	33.6	42.5	45.4
645	15.50	32.5	41.6	45.4
635	15.75	32.6	41.8	45.6
625	16.00	35.4	42.4	46.1
615.4	16.25	37.7	42.5	46.6
606	16.50	38.0	42.0	46.4
597.0	16.75	37.5	40.4	44.0
588	17.00	33.0	36.4	39.5
579.7	17.25	25.5	31.0	34.0
571.4	17.50	20.8	25.5	30.5
563.4	17.75	18.4	23.0	30.0
555.5	18.00	18.5	24.0	32.0
548.0	18.25	19.2	25.0	32.5
540.5	18.50	19.1	24.2	31.0
533.3	18.75	18.0	22.8	30.0
526.3	19.00	16.0	21.0	30.5
519.5	19.25	16.0	20.0	31.2
512.8	19.50	17.0	20.4	32.0
506.3	19.75	17.8	21.7	32.6
500.0	20.00	18.3	23.2	33.4



**Table 3. Transmission Measurements of 80°K Germanium Using PE-99  
and Correction Factor C for FTS-14**

$\sigma, \text{ cm}^{-1}$	$\alpha_g, \text{ cm}^{-1}$	$k_g \times 10^4$	T, %	C, %
1000	0.00	0.00	47.2	1.00
990	↓	↓	47.2	1.18
980			47.2	1.21
970			47.1	1.30
960			47.1	1.38
950			47.1	1.41
940			47.1	1.50
930			47.0	1.58
920			47.0	1.62
910			47.0	1.70
900			47.0	1.80
890			47.0	1.85
880			47.0	1.90
870			47.0	2.00
860	0.010	↓	46.8	2.10
850	0.025		46.5	2.20
840	0.040		46.0	2.30
830	0.051		45.7	2.40
820	0.051		45.7	2.50
810	0.050		45.8	2.60
800	0.040		46.0	2.70
790	0.030		46.2	2.80
780	0.030		46.2	2.90
770	0.035		46.1	3.10
760	0.040		46.0	3.15
750	0.030		46.2	3.30

Table 3. Concluded

$\sigma$ , $\text{cm}^{-1}$	$\alpha_g$ , $\text{cm}^{-1}$	$k_g \times 10^{-4}$	T, %	C, %
740	0.025	↓	46.5	3.41
730	0.010		46.8	3.57
720	0.000		47.1	3.70
710	0.000		47.0	3.90
700	0.000		47.0	4.02
690	0.0000	0.0000	47.1	4.15
680	0.0015	0.0017	46.7	4.30
670	0.0400	0.0475	46.0	4.50
660	0.0650	0.0784	45.4	4.70
650	0.0770	0.0943	45.1	4.95
640	0.0650	0.0808	45.5	5.20
630	0.0400	0.0505	46.0	5.45
620	0.0250	0.0321	46.4	5.70
610	0.0250	0.0326	46.5	6.05
600	0.090	0.1194	44.8	6.45
590	0.285	0.3844	40.4	6.90
580	0.620	0.8506	34.2	7.40
570	0.870	1.2150	30.2	8.00
560	0.820	1.1650	31.0	8.70
550	0.710	1.0273	32.7	9.40
540	0.820	1.2084	30.9	10.20
530	0.870	1.3063	30.2	11.20
520	0.800	1.2243	31.2	12.10
510	0.730	1.1391	32.3	13.30
500	0.660	1.0504	33.4	14.50

Table 4. Summary of Band Center Frequencies for 300°K and 20°K Polystyrene

Beckman Wavelength Calibrator Card. 300°K IUPAC 1961	3027.9 cm <sup>-1</sup> 3.303 μm	2851.5 cm <sup>-1</sup> 3.507 μm	1944.5 cm <sup>-1</sup> 5.143 μm	1601.8 cm <sup>-1</sup> 6.243 μm	1154.6 cm <sup>-1</sup> 8.661 μm	1028.3 cm <sup>-1</sup> 9.725 μm	906.9 cm <sup>-1</sup> 11.027 μm
Plyer et al. Ref. 14 300°K	3027.9 cm <sup>-1</sup> 3.303 μm	2851.5 cm <sup>-1</sup> 3.507 μm	1946.3 cm <sup>-1</sup> 5.138 μm	1603.1 cm <sup>-1</sup> 6.238 μm	1154.5 cm <sup>-1</sup> 8.662 μm	1028.4 cm <sup>-1</sup> 9.724 μm	906.8 cm <sup>-1</sup> 11.027 μm
This Work 300°K	3027.5 cm <sup>-1</sup> 3.303 μm	2851.0 cm <sup>-1</sup> 3.507	1944.0 cm <sup>-1</sup> 5.144 μm	1602.0 cm <sup>-1</sup> 6.242 μm	1155.0 cm <sup>-1</sup> 8.658 μm	1028.8 cm <sup>-1</sup> 9.720 μm	907.0 cm <sup>-1</sup> 11.025 μm
This Work 20°K	3028.0 cm <sup>-1</sup> 3.303 μm	2850.5 cm <sup>-1</sup> 3.508	1945.0 cm <sup>-1</sup> 5.141 μm	1602.5 cm <sup>-1</sup> 6.240 μm	1154.5 8.662 μm	1028.5 cm <sup>-1</sup> 9.723 μm	907.0 cm <sup>-1</sup> 11.025 μm

Table 5. Summary of Film Thicknesses, Gas Specie, and Substrate Temperature for Plots Given in Figs. 29 through 42

80°K NH <sub>3</sub>		20°K NH <sub>3</sub>		80°K CO <sub>2</sub>		20°K CO <sub>2</sub>		20°K CO		20°K CH <sub>4</sub>		20°K HCL		20°K Air	
Figure Number	Thickness, $\mu\text{m}$	Figure Number	Thickness, $\mu\text{m}$	Figure Number	Thickness, $\mu\text{m}$	Figure Number	Thickness, $\mu\text{m}$	Figure Number	Thickness, $\mu\text{m}$	Figure Number	Thickness, $\mu\text{m}$	Figure Number	Thickness, $\mu\text{m}$	Figure Number	Thickness, $\mu\text{m}$
29a	0.111 Min, 0	30a	0.111 Min, 0	31a	0.111 Min, 0	34a	0.668 Max, 3	36a	0.130 Min, 0	39a	0.114 Min, 0	40a	Min, 1	42a	Unknown
29b	0.334 Min, 1	30b	0.334 Min, 1	31b	0.334 Min, 1	34b	1.114 Max, 5	36b	0.390 Min, 1	39b	0.229 Max, 1	40b	Min, 2	42b	Unknown
29c	0.557 Min, 2	30c	0.557 Min, 2	31c	0.446 Max, 2	34c	1.890 Min, 8	36c	0.648 Min, 2	39c	0.344 Min, 1	40c	Min, 3		
29d	0.780 Min, 3	30d	0.780 Min, 3	31d	0.557 Min, 2	34d	2.560 Min, 11	36d	0.908 Min, 3	39d	0.458 Max, 2	41	Gas		
29e	1.003 Min, 4	30e	1.003 Min, 4	31e	0.668 Max, 3	35a	Unknown	36e	1.167 Min, 4	39e	0.573 Min, 2				
29f	1.225 Min, 5	30f	1.225 Min, 5	31f	0.780 Min, 3	35b	Unknown	37a	1.167 Min, 4	39f	0.688 Max, 3				
29g	1.448 Min, 6	30g	1.448 Min, 6	31g	0.891 Max, 4			37b	1.426 Min, 5	39g	0.802 Min, 3				
29h	1.671 Min, 7	30h	1.671 Min, 7	31h	1.003 Min, 4			37c	1.686 Min, 6	39h	0.917 Max, 4				
29i	1.894 Min, 8	30i	1.894 Min, 8	31i	1.114 Max, 5			37d	1.945 Min, 7	39i	1.030 Min, 4				
29j	2.117 Min, 9	30j	2.117 Min, 9	31j	1.225 Min, 5			37e	1.945 Min, 7	39j	1.150 Max, 5				
29k	2.340 Min, 10	30k	1.80-2.10	31k	1.337 Max, 6			37f	2.204 Min, 8	39k	1.260 Min, 5				
29l	2.562 Min, 11			31l	1.448 Min, 6			37g	2.464 Min, 9	39l	2.29 Max, 10				
29m	2.785 Min, 12			31m	1.560 Max, 7			37h	2.723 Min, 10	39m	3.44 Max, 15				
29n	3.010 Min, 13			31n	1.670 Min, 7			37i	2.982 Min, 11	39n	4.127 Max, 18				
29o	3.231 Min, 14			31o	1.780 Max, 8			37j	2.982 Min, 11	39o	4.580 Max, 20				
29p	3.454 Min, 15			31p	1.890 Min, 8			37k	3.242 Min, 12	39p	5.040 Max, 22				

Table 5. Concluded

80°K NH <sub>3</sub>		20°K NH <sub>3</sub>		80°K CO <sub>2</sub>		20°K CO <sub>2</sub>		20°K CO		20°K CH <sub>4</sub>		20°K HCL		20°K Air	
Figure Number	Thickness, $\mu\text{m}$	Figure Number	Thickness, $\mu\text{m}$	Figure Number	Thickness, $\mu\text{m}$	Figure Number	Thickness, $\mu\text{m}$	Figure Number	Thickness, $\mu\text{m}$	Figure Number	Thickness, $\mu\text{m}$	Figure Number	Thickness, $\mu\text{m}$	Figure Number	Thickness, $\mu\text{m}$
29q	3.676 Min, 16			31q	2.000 Max, 9			37l	3.501 Min, 13	39q	5.500 Max, 24				
29r	3.990 Min, 17			32a	2.000 Max, 9			37m	3.760 Min, 14	39r	5.960 Max, 26				
29s	4.120 Min, 18			32b	2.000 Max, 9			37n	4.020 Min, 15	39s	6.420 Max, 28				
29t	4.340 Min, 19			33	0.500 Max, 9			37o	4.280 Min, 16	39t	6.880 Max, 30				
29u	4.570 Min, 20							37p	4.538 Min, 17	39u	8.710 Max, 38				
29v	4.790 Min, 21							37q	4.798 Min, 18	39v	Unknown				
29w	5.010 Min, 22							37r	5.057 Min, 19	39w	Unknown				
								37s	5.316 Min, 20	39x	Unknown				
								37t	5.576 Min, 21						
								37u	5.835 Min, 22						
								37v	6.095 Min, 23						
								37w	6.354 Min, 24						
								38	15.00						

Table 6. Molecular Band of 20°K and 80°K Solid NH<sub>3</sub>

Band	Metastable I	Amorphous (20°K)	Metastable II (Warmed to 100°K)
Lattice	530 cm <sup>-1</sup>		530 cm <sup>-1</sup>
$\nu_2$	1,060 cm <sup>-1</sup>	1,075 cm <sup>-1</sup>	1,100 cm <sup>-1</sup>
$\nu_4$	1,625 cm <sup>-1</sup>	1,625 cm <sup>-1</sup>	1,575 cm <sup>-1</sup>
$\nu_1$	3,290 cm <sup>-1</sup>	3,210 cm <sup>-1</sup>	3,205 cm <sup>-1</sup>
$\nu_3$	3,375 cm <sup>-1</sup>	3,375 cm <sup>-1</sup>	3,360 cm <sup>-1</sup>

Table 7. Complex Refractive Index ( $\bar{n} = n - ik$ )  
for  $\text{NH}_3$  on  $80^\circ\text{K}$  Germanium

$\sigma, \text{ cm}^{-1}$	$n(\sigma)$	$k(\sigma)$	$\lambda, \mu$
630	1.287	$3.04 \times 10^{-2}$	15.875
640	1.290	2.84	15.625
650	1.277	2.70	15.385
660	1.283	2.96	15.152
670	1.307	3.37	14.925
680	1.308	2.88	14.706
690	1.328	2.37	14.493
700	1.352	2.02	14.286
710	1.368	1.73	14.085
720	1.363	1.62	13.889
730	1.379	1.62	13.699
740	1.384	1.42	13.514
750	1.375	1.48	13.333
760	1.383	1.56	13.158
770	1.395	1.56	12.987
780	1.404	1.62	12.821
790	1.407	1.66	12.658
800	1.414	1.56	12.500
810	1.412	1.39	12.346
820	1.428	1.30	12.195
830	1.428	1.23	12.048
840	1.421	1.69	11.905
850	1.413	2.11	11.765
860	1.414	1.85	11.628
870	1.448	1.33	11.494
880	1.468	$9.48 \times 10^{-3}$	11.364
890	1.479	7.82	11.236
900	1.494	7.60	11.111

Table 7. Continued

$\sigma$ , $\text{cm}^{-1}$	$n(\sigma)$	$k(\sigma)$	$\lambda$ , $\mu$
910	1.500	$6.93 \times 10^{-3}$	10.989
920	1.511	6.75	10.870
930	1.531	6.08	10.753
940	1.537	6.32	10.638
950	1.556	6.75	10.526
960	1.573	7.81	10.417
970	1.584	9.86	10.309
980	1.602	$1.18 \times 10^{-2}$	10.204
990	1.624	1.57	10.101
1000	1.650	2.60	10.000
1010	1.699	2.85	9.901
1020	1.776	4.16	9.804
1030	1.899	5.48	9.709
1040	2.119	11.7	9.615
1050	2.400	55.5	9.524
1060	1.041	269.0	9.434
1070	0.292	123.0	9.346
1080	0.513	30.2	9.259
1090	0.947	11.8	9.174
1100	1.001	7.21	9.091
1110	1.048	4.88	9.009
1120	1.120	3.34	8.729
1130	1.175	2.31	8.850
1140	1.212	2.37	8.772
1150	1.239	1.77	8.696
1160	1.262	1.89	8.621
1170	1.280	1.80	8.547
1180	1.294	1.62	8.475
1190	1.307	1.52	8.403
1200	1.318	1.44	8.333



Table 7. Continued

$\sigma, \text{ cm}^{-1}$	$n(\sigma)$	$k(\sigma)$	$\lambda, \mu$
1210	1.323	$1.48 \times 10^{-2}$	8.264
1220	1.330	1.33	8.197
1230	1.335	1.01	8.130
1240	1.341	$9.75 \times 10^{-3}$	8.065
1250	1.345	9.86	8.000
1260	1.349	6.75	7.937
1270	1.355	5.20	7.874
1280	1.362	5.91	7.812
1290	1.365	8.65	7.752
1300	1.366	8.88	7.692
1310	1.369	8.88	7.634
1320	1.372	$1.04 \times 10^{-2}$	7.576
1330	1.374	1.03	7.519
1340	1.378	$9.86 \times 10^{-3}$	7.463
1350	1.382	$1.22 \times 10^{-2}$	7.407
1360	1.382	1.39	7.353
1370	1.385	1.67	7.299
1380	1.389	1.90	7.246
1390	1.389	2.22	7.194
1400	1.392	2.85	7.143
1410	1.379	2.96	7.092
1420	1.383	2.60	7.042
1430	1.385	2.44	6.993
1440	1.378	2.22	6.944
1450	1.378	1.78	6.897
1460	1.385	1.48	6.849
1470	1.387	1.48	6.803
1480	1.388	1.78	6.757
1490	1.389	2.22	6.711
1500	1.390	2.28	6.667
1510	1.388	2.03	6.623

Table 7. Continued

$\sigma$ , $\text{cm}^{-1}$	$n(\sigma)$	$k(\sigma)$	$\lambda$ , $\mu$
1520	1.392	$1.95 \times 10^{-2}$	6.579
1530	1.387	1.89	6.536
1540	1.393	1.78	6.494
1550	1.393	1.67	6.452
1560	1.394	1.85	6.410
1570	1.398	2.22	6.369
1580	1.395	3.25	6.329
1590	1.399	4.44	6.289
1600	1.395	4.44	6.250
1610	1.390	4.45	6.211
1620	1.387	4.49	6.173
1630	1.384	4.44	6.135
1640	1.375	5.07	6.098
1650	1.375	6.08	6.061
1660	1.344	1.89	6.024
1670	1.353	$3.43 \times 10^{-3}$	5.988
1680	1.356	$5.96 \times 10^{-4}$	5.952
1690	1.363	1.00	5.917
1700	1.368	1.72	5.882
1710	1.368	2.35	5.848
1720	1.370	3.02	5.814
1730	1.372	5.92	5.780
1740	1.376	7.04	5.747
1750	1.374	5.60	5.714
1760	1.376	6.15	5.682
1770	1.377	8.34	5.650
1780	1.378	9.74	5.618
1790	1.380	8.90	5.587
1800	1.381	7.18	5.556
1810	1.382	$1.14 \times 10^{-3}$	5.525

Table 7. Continued

$\sigma$ , $\text{cm}^{-1}$	$n(\sigma)$	$k(\sigma)$	$\lambda$ , $\mu$
1820	1.385	$1.56 \times 10^{-3}$	5.495
1830	1.385	2.00	5.464
1840	1.387	2.70	5.435
1850	1.389	3.79	5.405
1860	1.389	5.77	5.376
1870	1.389	9.13	5.348
1880	1.388	$1.18 \times 10^{-2}$	5.319
1890	1.385	1.22	5.291
1900	1.383	1.11	5.263
1910	1.382	$9.23 \times 10^{-3}$	5.236
1920	1.383	7.60	5.208
1930	1.381	6.08	5.181
1940	1.383	4.27	5.155
1950	1.383	$2.85 \times 10^{-3}$	5.128
1960	1.384	2.14	5.102
1970	1.387	1.67	5.076
1980	1.388	1.37	5.051
1990	1.388	1.04	5.025
2000	1.387	$6.93 \times 10^{-4}$	5.000
2010	1.389	4.72	4.975
2020	1.388	3.19	4.950
2030	1.388	1.01	4.926
2040	1.391	$<1.0 \times 10^{-6}$	4.902
2050	1.391		4.878
2060	1.392		4.854
2070	1.393		4.831
2080	1.394		4.808
2090	1.395		4.785
2100	1.394		4.762

Table 7. Continued

$\sigma$ , $\text{cm}^{-1}$	$n(\sigma)$	$k(\sigma)$	$\lambda$ , $\mu$
2110	1.395	$< 1.0 \times 10^{-6}$ ↓	4.739
2120	1.397		4.717
2130	1.398		4.695
2140	1.397		4.673
2150	1.397		4.651
2160	1.397		4.630
2170	1.397		4.608
2180	1.397		4.587
2190	1.398		4.566
2200	1.398		4.545
2210	1.399		4.525
2220	1.399		4.505
2230	1.339		4.484
2240	1.399		4.464
2250	1.400		4.444
2260	1.400		4.425
2270	1.400		4.405
2280	1.401		4.386
2290	1.402		4.367
2300	1.401		4.348
2310	1.403		4.329
2320	1.403	$1.0 \times 10^{-6}$ ↓	4.310
2330	1.404		4.292
2340	1.405		4.274
2350	1.405		4.255
2360	1.404		4.237
2370	1.404		4.219
2380	1.404		4.202
2390	1.404		4.184
2400	1.405		4.167

Table 7. Continued

$\sigma$ , $\text{cm}^{-1}$	$n(\sigma)$	$k(\sigma)$	$\lambda$ , $\mu$
2410	1.406	1.0 x 10 <sup>-6</sup> ↓	4.149
2420	1.408		4.132
2430	1.408		4.115
2440	1.408		4.098
2450	1.409		4.082
2460	1.410		4.065
2470	1.410		4.049
2480	1.411		4.032
2490	1.412		4.016
2500	1.413		4.000
2510	1.414		3.984
2520	1.415		3.968
2530	1.415		8.953
2540	1.415		3.937
2550	1.415		3.922
2560	1.416		3.906
2570	1.415		3.891
2580	1.417		3.876
2590	1.417		3.861
2600	1.417		3.846
2610	1.417		3.831
2620	1.419		3.817
2630	1.419		3.802
2640	1.419		3.788
2650	1.418		3.774
2660	1.417		3.759
2670	1.418		3.745
2680	1.418		3.731
2690	1.416		3.717
2700	1.417		3.704

Table 7. Continued

$\sigma$ , $\text{cm}^{-1}$	$n(\sigma)$	$k(\sigma)$	$\lambda$ , $\mu$
2710	1.417	1.0 x 10 <sup>-6</sup> ↓	3.690
2720	1.418		3.676
2730	1.419		3.663
2740	1.418		3.650
2750	1.419		3.636
2760	1.419		3.623
2770	1.419		3.610
2780	1.420		3.597
2790	1.420		3.584
2800	1.421		3.571
2810	1.421		3.559
2820	1.422		3.546
2830	1.422		3.534
2840	1.422		3.521
2850	1.422		3.509
2860	1.423		3.497
2870	1.423		3.484
2880	1.424		3.472
2890	1.424		3.460
2900	1.425		3.448
2910	1.425		3.436
2920	1.425		3.425
2930	1.427		3.413
2940	1.427		3.401
2950	1.429		3.390
2960	1.429		3.378
2970	1.430		3.367
2980	1.430		3.356
2990	1.430		3.344
3000	1.432		3.333
3010	1.434		3.322

Table 7. Continued

$\sigma$ , $\text{cm}^{-1}$	$n(\sigma)$	$k(\sigma)$	$\lambda$ , $\mu$
3020	1.435	$1.0 \times 10^{-6}$	3.311
3030	1.435	↓	3.300
3040	1.435		3.289
3050	1.435		3.279
3060	1.438		3.268
3070	1.438		3.257
3080	1.439		3.247
3090	1.440		3.236
3100	1.439		3.226
3110	1.441		3.215
3120	1.443		3.205
3130	1.443		3.195
3140	1.443		3.185
3150	1.445	$1.77 \times 10^{-5}$	3.175
3160	1.446		3.165
3170	1.447	6.25 ↓	3.155
3180	1.453	$2.34 \times 10^{-3}$	3.145
3190	1.454	4.87 ↓	3.135
3200	1.458	$1.08 \times 10^{-2}$	3.125
3210	1.459	1.69	3.115
3220	1.457	1.58	3.106
3230	1.463	1.68	3.096
3240	1.470	2.16	3.086
3250	1.468	2.78	3.076
3260	1.463	3.60	3.067
3270	1.476	4.62	3.058
3280	1.475	5.61	3.049
3290	1.467	5.77	3.040
3300	1.465	5.55	3.030
3310	1.472	4.88 ↓	3.021

Figure 7. Continued.

$\sigma$ , $\text{cm}^{-1}$	$n(\sigma)$	$k(\sigma)$	$\lambda$ , $\mu$
3320	1.472	$4.62 \times 10^{-2}$	3.012
3330	1.492	4.62	3.003
3340	1.504	4.62	2.994
3350	1.611	5.76	2.985
3360	1.679	15.8	2.976
3370	0.981	57.1	2.967
3380	0.217	57.1	2.959
3390	1.103	3.23	2.950
3400	1.229	$7.78 \times 10^{-3}$	2.941
3410	1.275	3.70	2.933
3420	1.299	2.22	2.924
3430	1.316	1.90	2.915
3440	1.328	2.02	2.907
3450	1.335	2.14	2.899
3460	1.341	1.71	2.890
3470	1.344	1.95	2.882
3480	1.348	2.22	2.874
3490	1.351	1.85	2.865
3500	1.354	1.67	2.857
3510	1.359	2.34	2.849
3520	1.360	2.37	2.841
3530	1.357	2.37	2.833
3540	1.356	2.02	2.872
3550	1.362	$<10^{-6}$	2.817
3560	1.373		2.809
3570	1.374		2.801
3580	1.380		2.793
3590	1.381		2.786
3600	1.385		2.778



Table 7. Concluded


$\sigma, \text{ cm}^{-1}$	$n(\sigma)$	$k(\sigma)$	$\lambda, \mu$
3610	1.381	$<10^{-6}$ 	2.770
3620	1.384		2.762
3630	1.383		2.755
3640	1.388		2.747
3650	1.389		2.740
3660	1.390		2.732
3670	1.391		2.725
3680	1.390		2.717
3690	1.388		2.710
3700	1.387		2.703

Table 8. Complex Refractive Index ( $\bar{n} = n - ik$ )  
for  $\text{NH}_3$  on 20°K Germanium

$\sigma, \text{ cm}^{-1}$	$n(\sigma)$	$k(\sigma)$	$\lambda, \mu\text{m}$
700	1.634	$8.44 \times 10^{-2}$	14.286
710	1.651	8.05	14.085
720	1.614	7.95	13.889
730	1.601	8.11	13.699
740	1.589	8.14	13.513
750	1.566	8.20	13.333
760	1.536	8.15	13.158
770	1.548	7.81	12.987
780	1.562	7.49	12.821
790	1.556	7.33	12.658
800	1.552	7.45	12.500
810	1.549	7.46	12.346
820	1.539	7.30	12.195
830	1.542	7.45	12.048
840	1.515	7.51	11.905
850	1.507	7.85	11.765
860	1.519	7.06	11.628
870	1.568	6.47	11.494
880	1.591	6.04	11.364
890	1.609	5.81	11.236
900	1.612	5.62	11.111
910	1.623	5.56	10.989
920	1.629	5.49	10.870
930	1.636	5.36	10.753
940	1.648	5.33	10.638
950	1.653	5.38	10.526
960	1.671	5.32	10.417
970	1.688	5.41	10.309
980	1.707	5.57	10.204
990	1.739	5.79	10.101
1000	1.751	7.62	10.000
1010	1.808	8.98	9.901

Table 8. Continued

$\sigma$ , $\text{cm}^{-1}$	$n(\sigma)$	$k(\sigma)$	$\lambda$ , $\mu\text{m}$
1020	1.922	11.9 x $10^{-2}$	9.804
1030	2.104	17.7	9.709
1040	2.239	27.5	9.615
1050	2.378	40.7	9.524
1060	2.309	54.3	9.434
1070	1.190	67.8	9.346
1080	1.023	67.3	9.259
1090	1.012	59.5	9.174
1100	1.039	48.5	9.091
1110	1.122	38.2	9.009
1120	1.076	28.3	8.729
1130	1.099	20.4	8.850
1140	1.126	14.5	8.772
1150	1.154	10.2	8.696
1160	1.186	7.28	8.621
1170	1.246	5.89	8.547
1180	1.271	4.85	8.475
1190	1.296	4.51	8.403
1200	1.318	4.42	8.333
1210	1.329	4.37	8.264
1220	1.340	4.35	8.197
1230	1.351	4.27	8.130
1240	1.360	4.23	8.065
1250	1.367	4.25	8.000
1260	1.373	4.24	7.937
1270	1.381	4.21	7.874
1280	1.389	4.26	7.812
1290	1.393	4.24	7.752
1300	1.397	4.24	7.692
1310	1.401	4.27	7.634
1320	1.401	4.28	7.576
1330	1.407	4.30	7.519

Table 8. Continued

$\sigma$ , $\text{cm}^{-1}$	$n(\sigma)$	$k(\sigma)$	$\lambda$ , $\mu$
1340	1.410	$4.35 \times 10^{-2}$	7.463
1350	1.415	4.42	7.407
1360	1.418	4.43	7.353
1370	1.421	4.44	7.299
1380	1.424	4.52	7.246
1390	1.425	4.55	7.194
1400	1.427	4.57	7.143
1410	1.431	4.61	7.092
1420	1.432	4.64	7.042
1430	1.433	4.70	6.993
1440	1.433	4.76	6.944
1450	1.438	4.79	6.897
1460	1.441	4.77	6.849
1470	1.442	4.83	6.803
1480	1.445	4.88	6.757
1490	1.447	4.91	6.711
1500	1.451	4.92	6.667
1510	1.452	4.94	6.523
1520	1.449	4.96	6.579
1530	1.457	5.10	6.536
1540	1.456	5.11	6.494
1550	1.462	5.32	6.452
1560	1.468	5.44	6.410
1570	1.471	5.60	6.369
1580	1.482	5.87	6.329
1590	1.490	6.21	6.289
1600	1.492	6.73	6.250
1610	1.516	7.76	6.211
1620	1.487	9.32	6.173
1630	1.447	9.29	6.135
1640	1.412	8.26	6.098
1650	1.393	6.83	6.061

Table 8. Continued

$\sigma$ , $\text{cm}^{-1}$	$n(\sigma)$	$k(\sigma)$	$\lambda$ , $\mu$
1660	1.394	$5.75 \times 10^{-2}$	6.024
1670	1.379	4.62	5.988
1680	1.395	3.72	5.952
1690	1.410	2.91	5.917
1700	1.419	2.45	5.882
1710	1.435	2.49	5.848
1720	1.443	2.50	5.814
1730	1.452	2.51	5.780
1740	1.451	2.44	5.747
1750	1.457	1.43	5.714
1760	1.462	2.46	5.682
1770	1.465	2.46	5.650
1780	1.469	2.52	5.618
1790	1.467	2.51	5.587
1800	1.471	2.56	5.556
1810	1.474	2.62	5.525
1820	1.472	2.63	5.495
1830	1.471	2.66	5.464
1840	1.474	2.69	5.435
1850	1.473	2.71	5.405
1860	1.474	2.72	5.376
1870	1.471	2.72	5.348
1880	1.468	2.71	5.319
1890	1.467	2.69	5.291
1900	1.463	2.62	5.263
1910	1.465	2.60	5.236
1920	1.463	2.56	5.208
1930	1.461	2.51	5.181
1940	1.462	2.46	5.155
1950	1.458	2.40	5.128
1960	1.459	2.36	5.102
1970	1.458	2.33	5.076
1980	1.456	2.28	5.051

Table 8. Continued

$\sigma$ , $\text{cm}^{-1}$	$n(\sigma)$	$k(\sigma)$	$\lambda$ , $\mu$
1990	1.453	$2.23 \times 10^{-2}$	5.025
2000	1.452	2.18	5.000
2010	1.453	2.18	4.975
2020	1.450	2.19	4.950
2030	1.148	2.16	4.926
2040	1.448	2.15	4.902
2050	1.447	2.14	4.878
2060	1.444	2.10	4.854
2070	1.441	2.06	4.831
2080	1.439	2.06	4.808
2090	1.439	2.04	4.785
2100	1.436	2.01	4.762
2110	1.435	1.99	4.739
2120	1.435	1.95	4.717
2130	1.430	1.91	4.695
2140	1.426	1.88	4.673
2150	1.427	1.89	4.651
2160	1.424	1.85	4.630
2170	1.424	1.85	4.608
2180	1.422	1.81	4.587
2190	1.422	1.79	4.566
2200	1.420	1.78	4.545
2210	1.418	1.78	4.525
2220	1.417	1.79	4.505
2230	1.415	1.77	4.484
2240	1.417	1.81	4.464
2250	1.415	1.79	4.444
2260	1.415	1.81	4.425
2270	1.418	1.82	4.405
2280	1.419	1.84	4.386
2290	1.421	1.86	4.367
2300	1.424	1.90	4.348
2310	1.428	1.93	4.329

Table 8. Continued

$\sigma$ , $\text{cm}^{-1}$	$n(\sigma)$	$k(\sigma)$	$\lambda$ , $\mu$
2320	1.438	$2.01 \times 10^{-2}$	4.310
2330	1.443		4.292
2340	1.444		4.275
2350	1.450		4.255
2360	1.456		4.237
2370	1.453		4.219
2380	1.452		4.202
2390	1.455		4.184
2400	1.458		4.167
2410	1.459		4.149
2420	1.464		4.132
2430	1.467		4.115
2440	1.473		4.098
2450	1.471		4.082
2460	1.475		4.065
2470	1.475		4.049
2480	1.477		4.032
2490	1.477		4.016
2500	1.481		4.000
2510	1.480		3.984
2520	1.482		3.968
2530	1.483		3.953
2540	1.481		3.937
2550	1.482		3.922
2560	1.485		3.906
2570	1.484		3.891
2580	1.485		3.876
2590	1.486		3.861
2600	1.486		3.846
2610	1.487		3.831
2620	1.486		3.817
2630	1.485		3.802
2640	1.486		3.788

Table 8. Continued

$\sigma$ , $\text{cm}^{-1}$	$n(\sigma)$	$k(\sigma)$	$\lambda$ , $\mu$
2650	1.487	$2.26 \times 10^{-2}$	3.774
2660	1.486	2.23	3.759
2670	1.486	2.21	3.745
2680	1.489	2.22	3.731
2690	1.487	2.22	3.717
2700	1.487	2.22	3.704
2710	1.487	2.22	3.690
2720	1.488	2.19	3.676
2730	1.487	2.18	3.663
2740	1.488	2.19	3.650
2750	1.488	2.20	3.636
2760	1.489	2.20	3.623
2770	1.486	2.22	3.610
2780	1.486	2.22	3.597
2790	1.487	2.18	3.584
2800	1.487	2.20	3.571
2810	1.488	2.18	3.559
2820	1.487	2.17	3.546
2830	1.491	2.17	3.534
2840	1.490	2.17	3.521
2850	1.491	2.19	3.509
2860	1.491	2.19	3.497
2870	1.492	2.18	3.484
2880	1.492	2.19	3.472
2890	1.493	2.19	3.460
2900	1.494	2.19	3.448
2910	1.495	2.14	3.436
2920	1.493	2.20	3.425



Table 8. Continued

$\sigma$ , $\text{cm}^{-1}$	$n(\sigma)$	$k(\sigma)$	$\lambda$ , $\mu$
2930	1.494	$2.15 \times 10^{-2}$	3.413
2940	1.495	2.14	3.401
2950	1.495	2.13	3.390
2960	1.498	2.13	3.378
2970	1.498	2.13	3.367
2980	1.499	2.13	3.356
2990	1.498	2.12	3.344
3000	1.501	2.15	3.333
3010	1.503	2.18	3.322
3020	1.503	2.19	3.311
3030	1.503	2.19	3.300
3040	1.504	2.21	3.289
3050	1.503	2.24	3.279
3060	1.505	2.25	3.268
3070	1.508	2.24	3.257
3080	1.508	2.26	3.247
3090	1.512	2.29	3.236
3100	1.511	2.32	3.226
3110	1.512	2.34	3.215
3120	1.513	2.41	3.205
3130	1.511	2.45	3.195
3140	1.512	2.59	3.185
3150	1.519	2.82	3.175
3160	1.519	3.17	3.165
3170	1.528	4.11	3.155
3180	1.524	5.19	3.145
3190	1.522	6.15	3.135
3200	1.516	6.93	3.125
3210	1.510	7.45	3.115
3220	1.494	6.97	3.106
3230	1.490	6.40	3.096

Table 8. Continued

$\sigma$ , $\text{cm}^{-1}$	$n(\sigma)$	$k(\sigma)$	$\lambda$ , $\mu$
3240	1.496	$6.35 \times 10^{-2}$	3.086
3250	1.485	6.62	3.076
3260	1.488	6.78	3.067
3270	1.493	6.97	3.058
3280	1.488	7.13	3.049
3290	1.487	7.28	3.040
3300	1.485	7.23	3.030
3310	1.483	7.22	3.021
3320	1.486	7.32	3.012
3330	1.491	8.11	3.003
3340	1.503	10.0	2.994
3350	1.522	3.7	2.985
3360	1.477	8.6	2.976
3370	1.439	0.6	2.967
3380	1.322	20.1	2.959
3390	1.260	12.0	2.950
3400	1.266	3.96	2.941
3410	1.351	2.06	2.933
3420	1.374	1.94	2.924
3430	1.381	1.95	2.915
3440	1.391	1.94	2.907
3450	1.405	2.02	2.899
3460	1.403	1.99	2.890
3470	1.412	2.09	2.882
3480	1.416	2.09	2.874
3490	1.416	2.07	2.865
3500	1.424	2.06	2.857
3510	1.415	2.12	2.849
3520	1.414	2.01	2.841
3530	1.405	2.06	2.833
3540	1.410	2.03	2.825

Table 8. Concluded

$\sigma, \text{ cm}^{-1}$	$n(\sigma)$	$k(\sigma)$	$\lambda, \mu$
3550	1.410	$1.98 \times 10^{-2}$	2.817
3560	1.411	1.95	2.809
3570	1.419	2.05	2.801
3580	1.418	1.98	2.793
3590	1.408	1.94	2.786
3600	1.414	1.86	2.778
3610	1.402	1.88	2.770
3620	1.408	1.92	2.762
3630	1.400	1.89	2.755
3640	1.400	1.84	2.747
3650	1.390	1.76	2.740
3660	1.406	1.98	2.732
3670	1.407	1.87	2.725
3680	1.417	1.96	2.717
3690	1.398	1.88	2.710
3700	1.379	1.94	2.703

## APPENDIX A

### $\Delta n_g / \Delta t$ OF GERMANIUM AT 10.6 $\mu\text{m}$

This appendix describes the results of measurements of the change in real refractive index of germanium with temperature. As noted in Section 4.1, the transmission of germanium in the 2- to 10- $\mu\text{m}$  wavelength range increases approximately one percent upon cooling to 80°K. This small transmission change is actually within the error bars of the measurements reported and therefore cannot be employed to deduce quantitative values of  $\Delta n_g / \Delta t$  where  $n_g \equiv$  real refractive index of germanium, and  $t \equiv$  absolute temperature. The method described in Ref. A-1 has therefore been adapted to the IROTC and  $\Delta n_g / \Delta t$  measurements conducted. The effort spent in this area was of a demonstrative nature and intended to exemplify the flexibility of the IROTC in the research of transmission at cryogenic temperatures.

The optical system employed is centered about a CO<sub>2</sub> laser that provides IR radiation at 10.6  $\mu\text{m}$  of sufficient coherent length so that the  $D = 0.422\text{-cm}$ -thick germanium window actually acts as a "thin film," i. e., interference between multiple internal reflections is readily observed. The expression for transmission through a thin film thus applies:

$$T = 4n_g^2 / \left[ 4n_g^2 + (n_g^2 - 1)^2 \sin^2 \left( \frac{2\pi n_g D}{\lambda} \right) \right] \quad (\text{A-1})$$

The maxima in transmission occur when  $m\lambda = 2n_g D$ , where  $m$  is an integer. As the germanium window is cooled the thickness decreases, the value of  $n_g$  changes, and the order of interference changes; hence,

$$\frac{\partial}{\partial t} (m\lambda) = \frac{\partial}{\partial t} (2n_g D) \quad (\text{A-2})$$

where  $t$  is absolute temperature, or

$$\frac{\partial m}{\partial t} \lambda + \frac{m \partial \lambda}{\partial t} = 2n_g \Big|_{t_0} \frac{\partial D}{\partial t} + \frac{2 \partial n_g}{\partial t} D \Big|_{t_0} \quad (\text{A-3})$$

where  $t_0$  is the base temperature before cooling starts. Approximating the partial derivatives with incremental changes, and noting that  $\frac{\partial \lambda}{\partial t} = 0$ , gives

$$\frac{\Delta m}{\Delta t} \lambda = 2n_g \Big|_{t_0} \frac{\Delta D}{\Delta t} + \frac{2 \Delta n_g}{\Delta t} D \Big|_{t_0} \quad (\text{A-4})$$

but by definition  $\frac{1}{D} \left| \frac{\Delta D}{\Delta t} \right|_{t_0} = \gamma \Big|_{t_0}$ , is the thermal expansion coefficient of the germanium. Solving for  $\Delta n_g / \Delta t$  and substituting for  $\gamma$  yields

$$\frac{\Delta n_g}{\Delta t} = \frac{\lambda}{2D} \Big|_{t_0} \frac{1}{\Delta t / \Delta m} - \gamma^n_g \Big|_{t_0} \quad (\text{A-5})$$

All of the terms on the right-hand side of Eq. (A-5) are known. The value of  $\Delta t / \Delta m$  was obtained with the system shown in Fig. A-1. The CO<sub>2</sub> laser was chopped, directed through the germanium window, and entered a small 0.5-in. -diam (13-mm) gold-coated integrating sphere after passing out of the IROTC. A Reeder® thermocouple IR detector located in an aperture in the integrating sphere was used to monitor the transmitted CO<sub>2</sub> beam intensity. With the germanium window precooled to 80°K the LN<sub>2</sub> flow was shut off and a warming rate of 0.66°K/min occurred. As the window warmed, the transmission oscillated as shown in Fig. A-2. The absolute values are not consistent with Eq. (A-5), and this is believed to be due to poor interference of multiple reflections attributable to the divergence of the CO<sub>2</sub> laser beam and irregularities in the germanium window. However, the important parameter is the change in temperature of the window for a  $\Delta m = 1$ . The value of  $\Delta m / \Delta t$  ranged from 1.0/5.32 °K<sup>-1</sup> for the 80 to 100°K range to 1.0/3.00 °K<sup>-1</sup> for the 273 to 300°K range. The values of  $\gamma$  were extracted from Ref. A-2, NBS Monogram 29, and are shown plotted in Fig. A-3. The value of  $n_g$  on the right-hand side of Eq. (A-5) was taken to be constant, 4.01. The results for  $\Delta n_g / \Delta t$  found from Eq. (A-5) are shown in Fig. A-4. To the knowledge of the authors no such measurement of  $\Delta n_g / \Delta t$  at low temperatures has been carried out and therefore no comparison is possible. The errors in  $\Delta n_g / \Delta t$  are results of errors in temperature measurement, possible errors in  $\gamma$ , and errors in selecting the maximum transmission; however, the combined total error is believed to be  $\pm 5$  percent.

## REFERENCES

- A-1. Skolnik, L. H. and Clark, O. M. "Temperature Change of the Refractive Index of CVD ZnSe at 10.6  $\mu\text{m}$ ." Applied Optics, Vol. 13, No. 9, September 1974, pp. 1999-2001.
- A-2. Corrucini, R. J. and Gniewek, J. J. "Thermal Expansion of Technical Solids at Low Temperatures: A Computation from the Literature." NBS Monograph 29, Government Printing Office, Washington, D. C., 1961, p. 4.

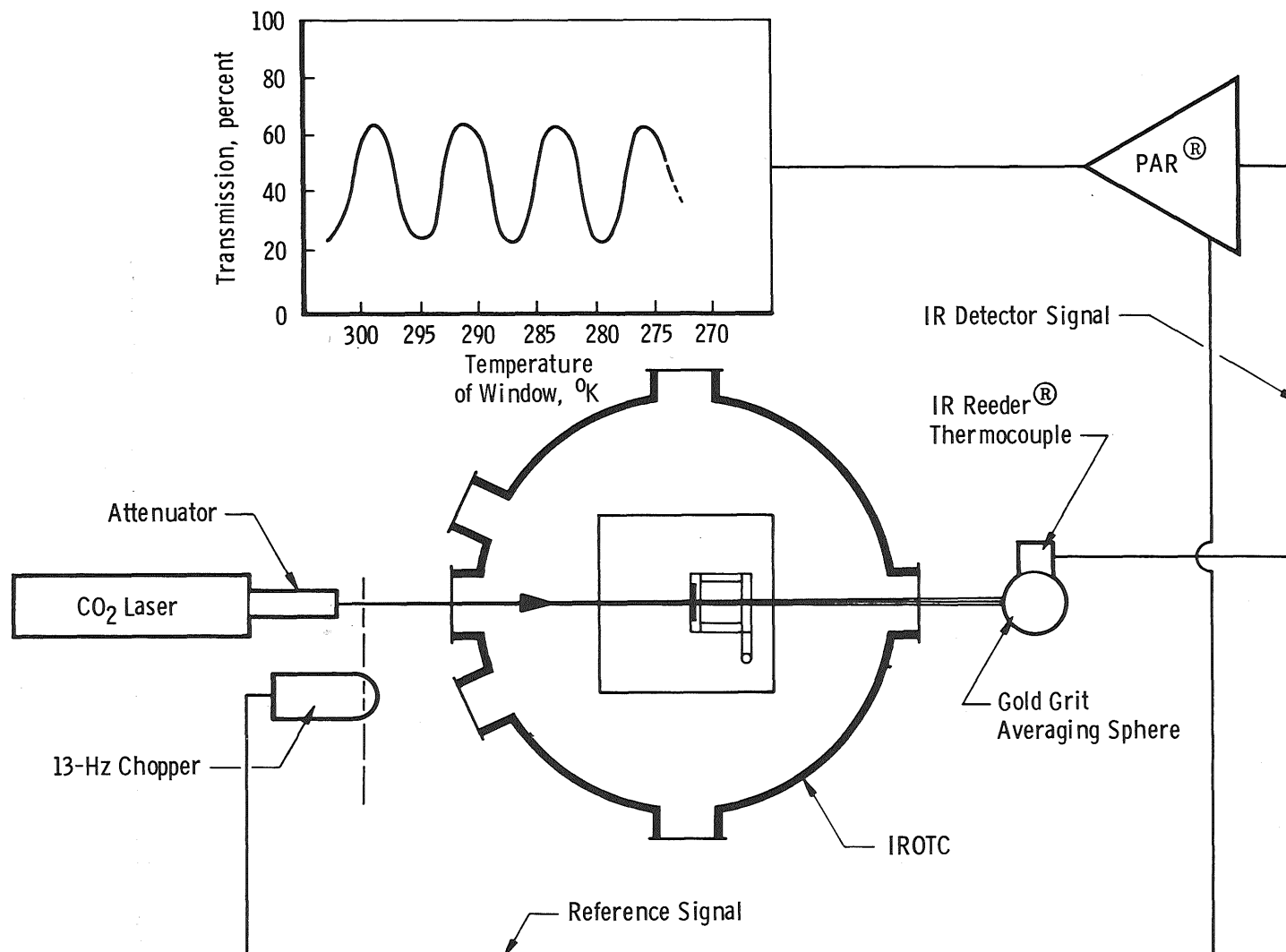


Figure A-1. Experimental setup for measuring  $\Delta n_g / \Delta t$ .

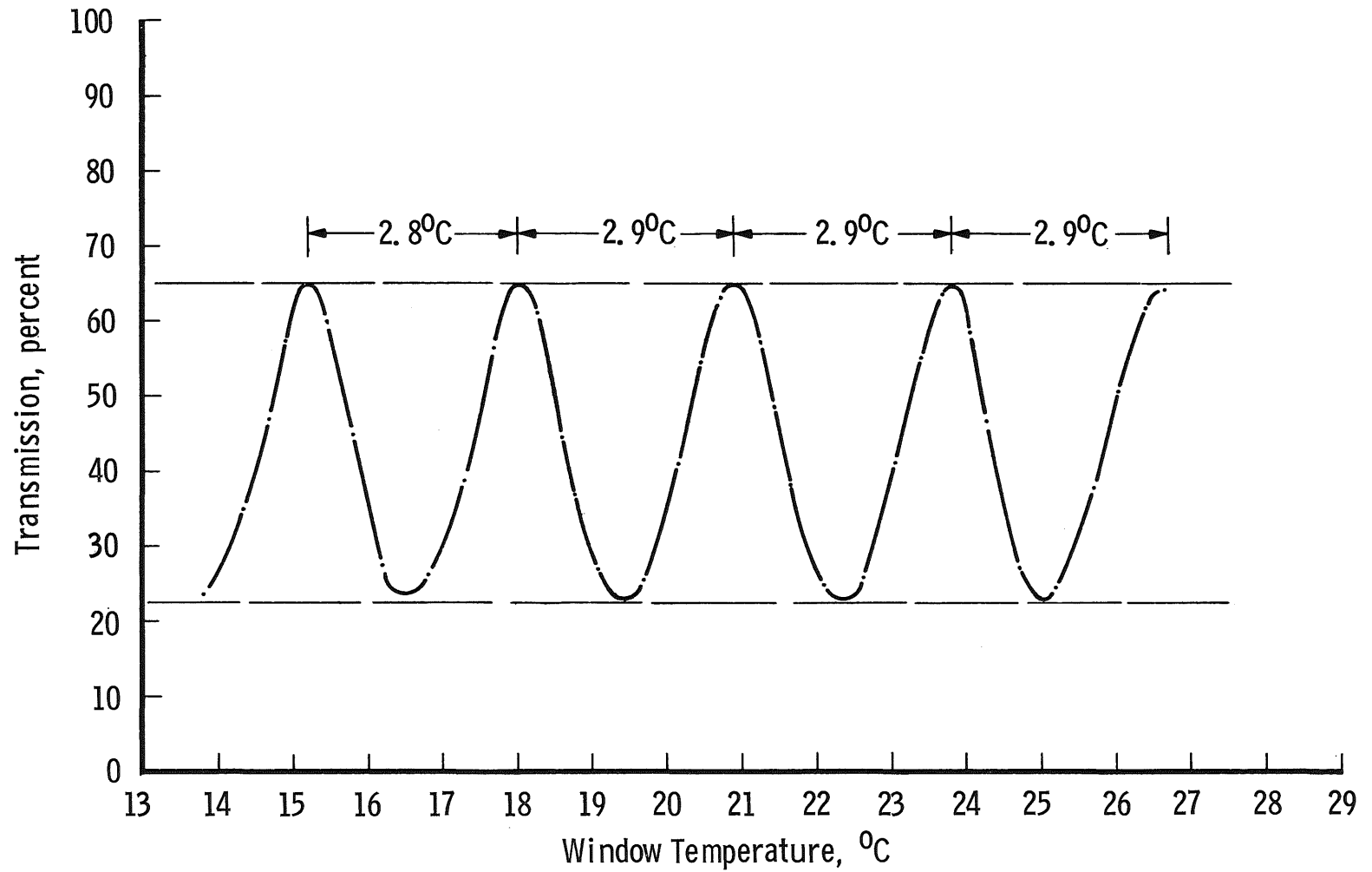


Figure A-2. Transmission of germanium versus temperature for CO<sub>2</sub> laser,  $\lambda = 10.28 \mu\text{m}$ .

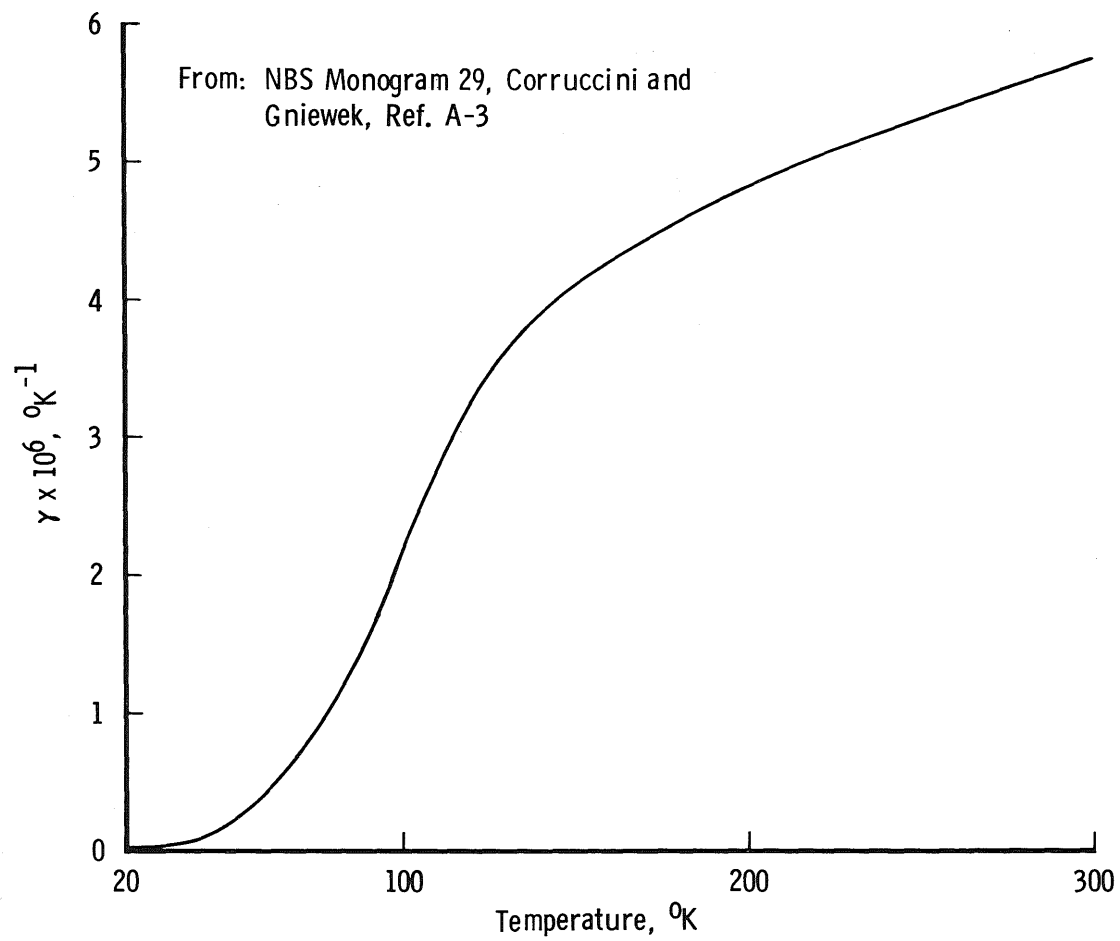


Figure A-3. Expansion coefficient of germanium  $\gamma = \frac{10^6}{D_{273}} \frac{dD}{dt}, ^\circ\text{K}^{-1}$ .



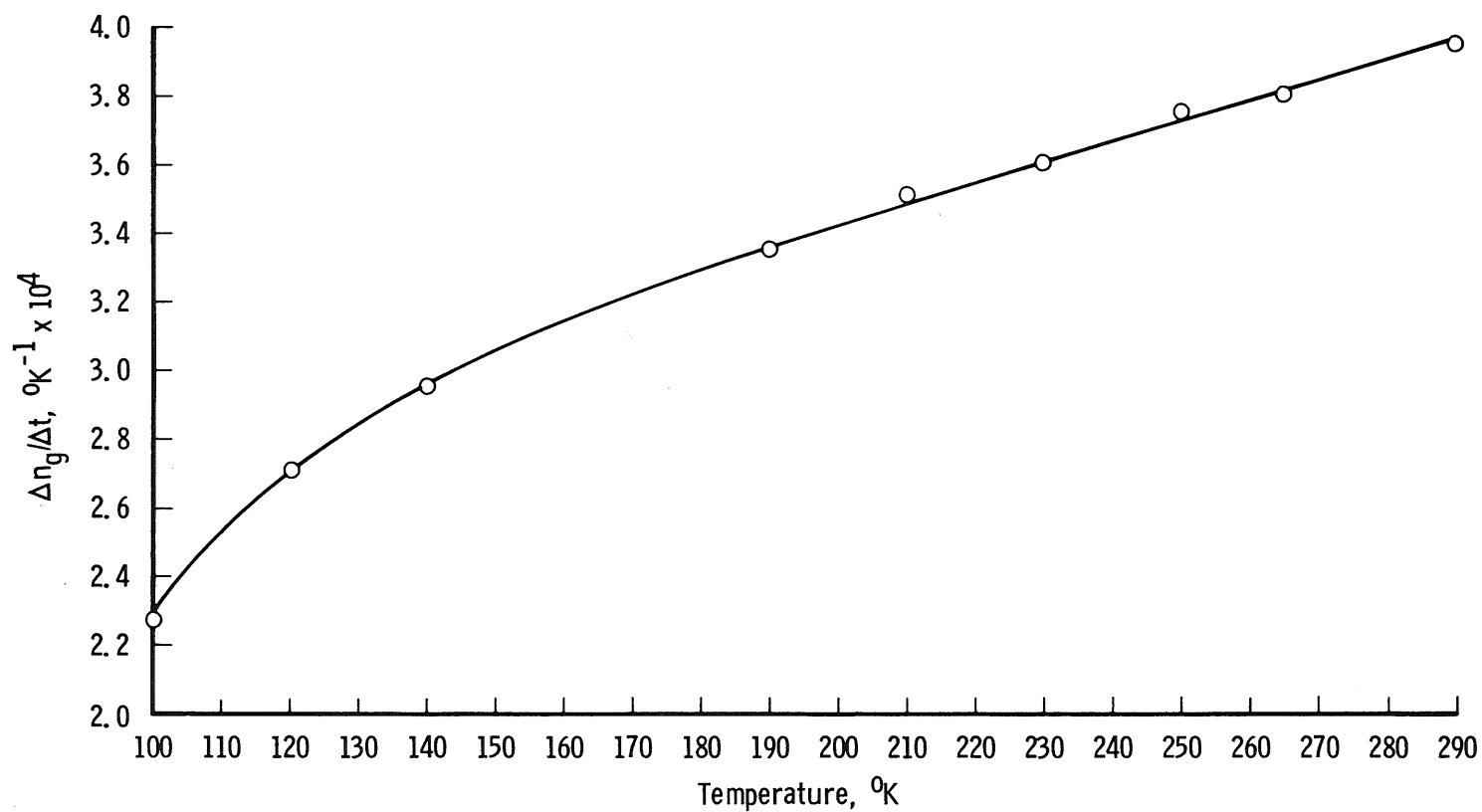


Figure A-4.  $\Delta n_g / \Delta t$  for germanium at 10.6  $\mu\text{m}$  as a function of temperature.

## APPENDIX B

### REFLECTANCE OF 77°K NH<sub>3</sub> FROSTS BETWEEN 0.5 AND 3.0 $\mu$ m

The spectral hemispherical-directional reflectance of thick 77°K NH<sub>3</sub> frosts is presented for near normal incidence. The reflectance measurements were obtained in an 8-in. IR integrating sphere, the details of which are given in Refs. B-1 and B-2. The spectral range is from 0.5 to 3.0  $\mu$ m for measurements reported here, with a spectral resolution of between 0.03 and 0.10  $\mu$ m as fixed by energy limitations and the CaF<sub>2</sub> prism of the Perkin-Elmer Model 98 spectrometer. The reflectance of the NH<sub>3</sub> frosts is presented to complement the 2.7- to 20- $\mu$ m transmission data discussed in the main body of the report. The results show the absorption bands that can only be detected if thick specimens are employed and reflectance is observed. To the authors' knowledge, the only other NH<sub>3</sub> frost data are those of Pilcher, et al., Ref. B-3, which are relevant to the interpretation of the albedo of Saturn's Rings. The spectra presented here are in good agreement with the above work; however, the texture of the frost could not be varied as was done with the tests discussed in Ref. B-3. Therefore, the dependence of absorption bandwidth on texture could not be confirmed.

The reflectance for two thicknesses, 100 and 500  $\mu$ m, of 77°K NH<sub>3</sub> frosts is shown in Figs. B-1 and B-2. The band at 3.0  $\mu$ m is by far the strongest. Other bands at 2.30, 2.04, 1.66, 1.54, 1.24, and 1.04  $\mu$ m are evident and are in line with the results of Ref. B-3. It is believed that the frosts are cubic polycrystalline frosts since spectra taken after warming them to temperatures near 150°K and recooling to 77°K showed no change in band shape or wavelength location.

Error in absolute reflectance is estimated to be  $\pm 3$  percent, as indicated by reflectance measurements of the bare stainless steel substrate (of known reflectance). The errors in thickness, shown in the figures, are probably up to 20 percent.

## REFERENCES

- B-1. Wood, B. E., Smith, A. M., Roux, J. A., and Seiber, B. A.  
"Spectral Absolute Reflectance of CO<sub>2</sub> Frosts from 0.5 to  
12.0  $\mu$ ." AIAA Journal, 9, July 1971, pp. 1338-1344.

- B-2. Wood, B. E., Smith, A. M., Roux, J. A. and Seiber, B. A.  
 "Spectral Infrared Reflectance of  $\text{H}_2\text{O}$  Condensed on  $\text{LN}_2$ -Cooled Surfaces in Vacuum." AIAA Journal, 9, September 1971, pp. 1836-1842.
- B-3. Pilcher, C. B., Chapman, C. R., Lebofsky, L. A., and Kieffer, H. H. "Saturn's Rings: Identification of Water Frost." Science, 167, March 1970, pp. 1372-1373.

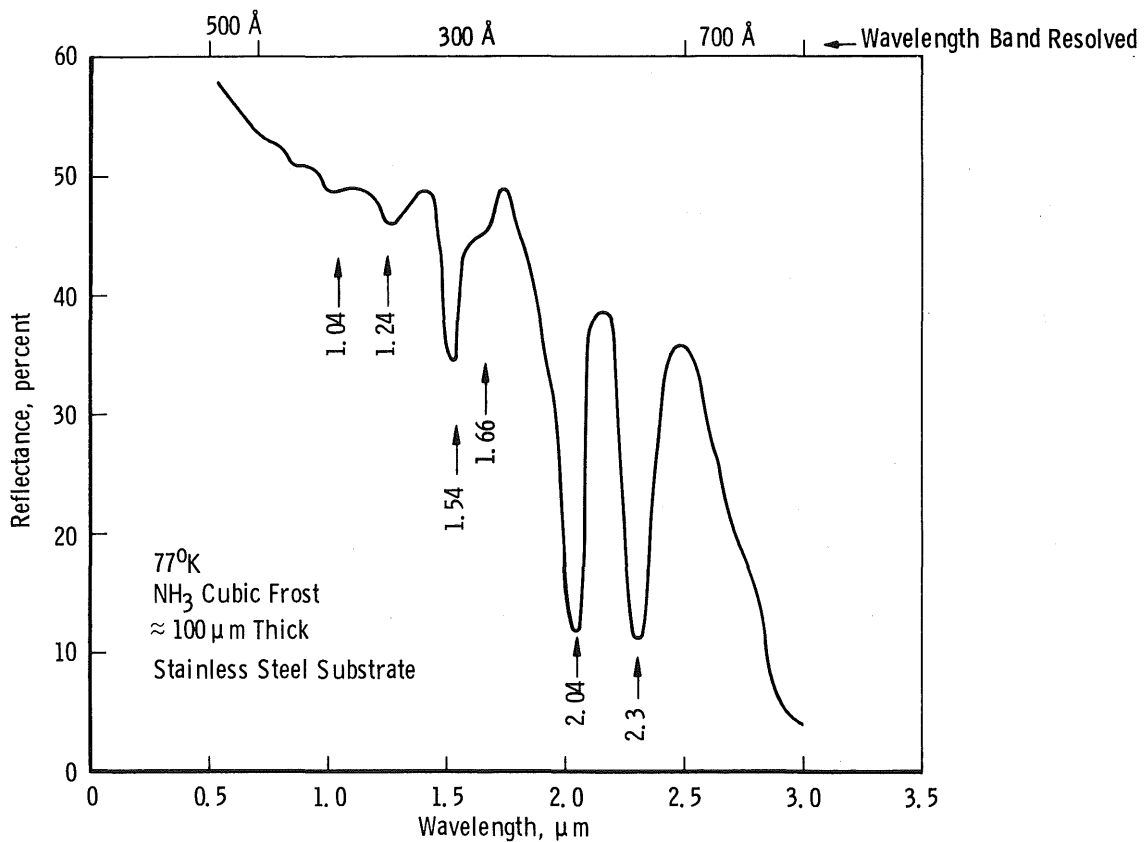


Figure B-1. Reflectance of 100- $\mu\text{m}$ -thick  $\text{NH}_3$  frost at 77°K.

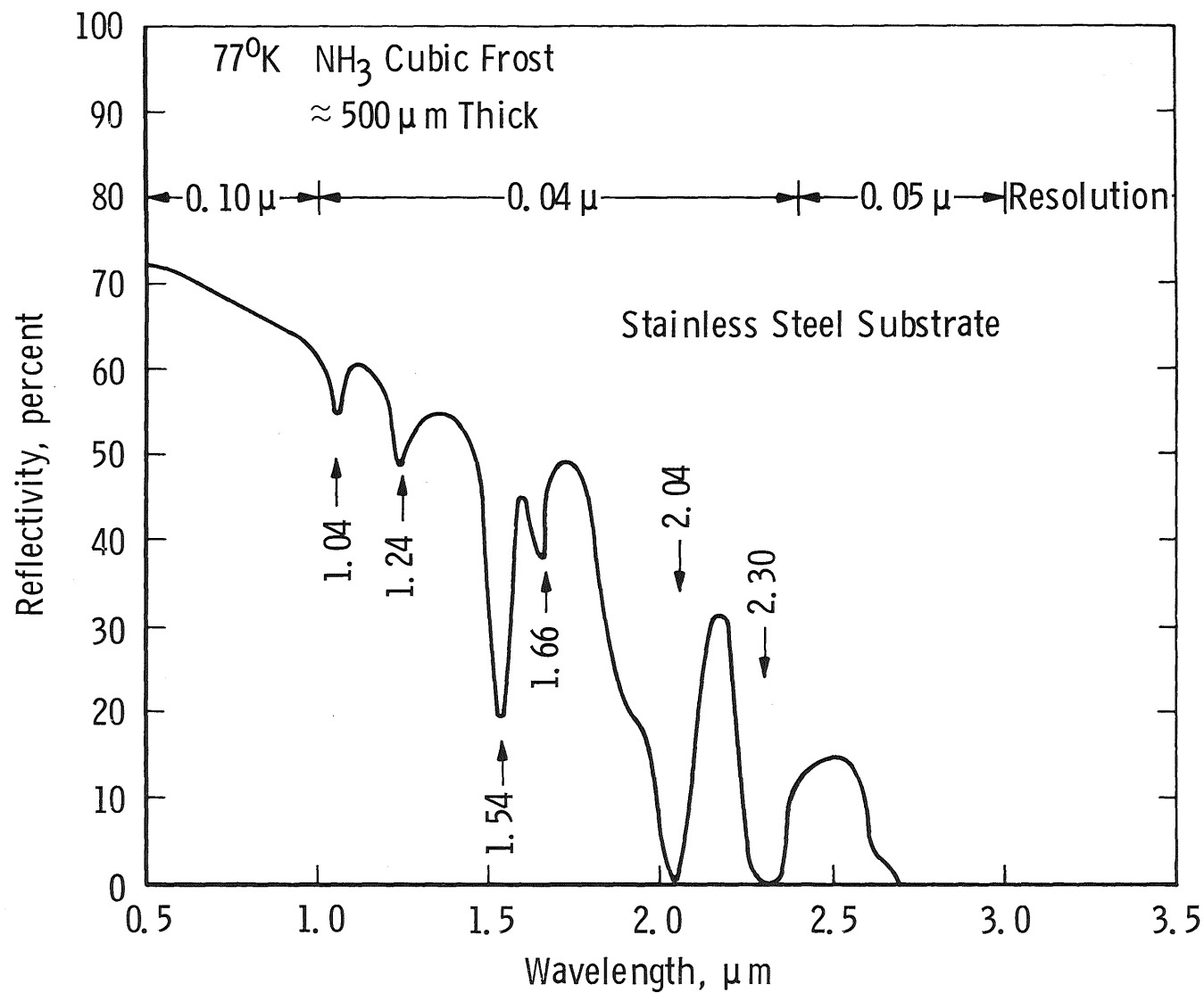


Figure B-2. Reflectance of 500-μm-thick NH<sub>3</sub> frost at 77°K.

## APPENDIX C NOTES ON NONCUBIC NH<sub>3</sub>

by

F. A. Mauer, L. H. Bolz, H. S. Peiser, and H. F. McMurdie  
National Bureau of Standards  
Washington, D. C. 20234

All X-ray specimens were prepared using NH<sub>3</sub> from a commercial source. The analysis supplied by the manufacturer indicated that the gas was at least 99.9 percent pure. Further purification by vacuum distillation and by melting in contact with freshly cut sodium to remove any traces of water did not alter the type of X-ray patterns obtained. Further confirmation of the purity of the sample is the fact that on warming to approximately 140°K the sample always transformed to the well-known cubic phase of NH<sub>3</sub>. There was no evidence that any impurity was released as a gas or remained as a solid residue.

Low temperature X-ray powder patterns were recorded with the diffractometer cryostat. Specimens were prepared by freezing ammonia gas on a gold-plated copper surface cooled by LN<sub>2</sub> (77°K) or LHe (4.3°K). In a typical experiment, a layer approximately 0.4 mm thick was deposited in 60 minutes. In other cases, the thickness varied from approximately 0.01 to 0.5 mm and the rate of deposition from 0.0006 to 0.03 mm per minute.

A combined list of the X-ray powder diffraction peaks obtained in three selected experiments is given in Table C-1 for convenience in comparing the patterns and in determining the regions in which small peaks might be obscured by peaks of the cubic phase or the gold substrate, which are present in all the patterns. The two-theta scale of the individual patterns has been corrected by using the cubic phase as an internal standard. There are at least 27 peaks that cannot be attributed to the cubic phase. In 15 to 20 separate experiments, these same peaks have been found to occur, but with widely different relative intensities. It is possible to recognize two extreme types of patterns in each of which some of the principal peaks that characterize the other are weak or missing altogether. The patterns from which the data in Table C-1 were obtained were chosen to represent these two types. The question of whether these represent two noncubic phases or a single phase growing with two different preferential orientations has to be considered. The noncubic phase (or phases) predominated in samples deposited at 77°K from the gas, but single-phase patterns have not been prepared and the powder patterns have not been indexed.

Samples deposited at 4.2°K were amorphous, but crystallized when warmed above about 40°K, giving a mixture of phases. All samples transformed to the cubic phase about 140°K. No phase change in either cubic or noncubic ammonia was achieved by cooling. It seems safe to assume that the solid prepared by freezing liquid  $\text{NH}_3$  at the melting point remains cubic at all lower temperatures.

When specimens deposited at 77°K are permitted to warm up, those that give predominantly type I patterns on the one hand, or type II patterns on the other, both transform to cubic  $\text{NH}_3$ , but the temperature range seems to be different. Specimens giving a type II pattern always transform at a lower temperature. This was at first taken as an indication that two different noncubic phases were involved. However, when specimens that give the strongest lines of both patterns are warmed, the type II lines disappear only four or five minutes before the type I lines, while the substrate temperature rises through the range 125 to 140°K. The temperature range of 15°K is not unlike that of 185 to 195°K observed for melting in equilibrium with the vapor at the triple point which should occur at 195.4°K. The wide temperature range is believed to result from the rapid warmup and the low conductivity of the loosely compacted specimen. The fact that some lines in the X-ray pattern disappear before others of similar intensity is believed to be related to the morphology of the crystallites. The thicker deposits looked much like frost on a window pane, with dendrites growing out from the surface. Some contained crystallites that were visible to the naked eye. The dendrites are preferentially oriented and, it is believed, give rise to the type I pattern. Branching of the dendrites may result in a second type of preferential orientation giving patterns of type II. The heat path from the branches to the substrate is long, so the branches warm ahead of the main stems of the dendrites. The peaks they contribute to the X-ray patterns disappear first. This hypothesis is supported by the fact that X-ray patterns made by tracing a portion of the pattern repeatedly during deposition show that the strongest peaks of the type I pattern are always seen at first, even while depositing specimens that eventually give a type II pattern.

The conditions of preparation and their control to get either type of noncubic pattern at will have not been defined. Early results suggested that low deposition rates produced specimens that gave type II patterns. The slowest deposit made was by distillation from solid  $\text{NH}_3$  in a side tube cooled by solid  $\text{CO}_2$ . A layer 0.5 mm thick was deposited in 13.5 hours. The pattern from this specimen was of type II.

Table C-1. X-Ray Diffraction Peaks

No.	$2\theta$	Gold Substrate		Cubic $\text{NH}_3$		Noncubic Type I		Noncubic Type II	
		hk $\ell$	I	hk $\ell$	I	d	I	d	I
1.	22.85					3.892	5		
2.	24.45					3.640	12		
3.	24.77			110	27				
4.	25.63							3.137 $\beta$	1
5.	26.09					3.416	19		
6.	26.19							3.402	2
7.	27.64					3.227	17	3.227	3
8.	28.44							3.138	100
9.	29.14							3.064	50
10.	29.62					3.061	100		
11.	30.45			111	100				
12.	31.41					2.845	24		
13.	31.45							2.845	2
14.	33.23					2.696	5		
15.	34.72							2.584	4
16.	34.55	111 $\beta$	1						
17.	35.31			220	20				
18.	38.29	111	100						
19.	39.39					2.288	5		
20.	39.64			210	7				
21.	40.01								
22.	40.87					2.208	19		
23.	43.61			211					

### Table C-1. Concluded

No.	2 $\theta$	Gold Substrate		Cubic NH <sub>3</sub>		Noncubic Type I		Noncubic Type II	
	CuK $\alpha$	hkl	I	hkl	I	d	I	d	I
24.	44.50	200	52						
25.	46.18							1.966	<1
26.	47.55					1.912	5		
27.	47.68							1.907	<1
28.	50.79			220	7				
29.	53.60							1.710	2
30.	53.68					1.707	10		
31.	54.12			221/300					
32.	54.56							1.682	<1
33.	57.30			310					
34.	60.38			311	14				
35.	61.13							1.516	3
36.	62.41							1.488	<1
37.	64.76	220	32						
38.	69.13			321	5				
39.	74.37							1.276	<1
40.	74.43			400		1.275	5		
41.	77.79	311	36						
42.	81.97	222	12						
43.	90.20							1.088	<1
44.	94.75							1.048	<1
45.	96.5~							1.033	1
46.	98.45	400	6						